OCTOBER 2020

AJNR

VOLUME 41 • PP 1759–1962

AJNR

AMERICAN JOURNAL OF NEURORADIOLOGY

OCTOBER 2020
VOLUME 41
NUMBER 10
WWW.AJNR.ORG

THE JOURNAL OF DIAGNOSTIC AND INTERVENTIONAL NEURORADIOLOGY

Mechanical thrombectomy during the COVID-19 pandemic
Tentorial venous anatomy
Colloid cyst correlation with histology and ventricular obstruction
Transcranial MR imaging-guided focused ultrasound

Official Journal ASNR • ASFNR • ASHNR • ASPNR • ASSR

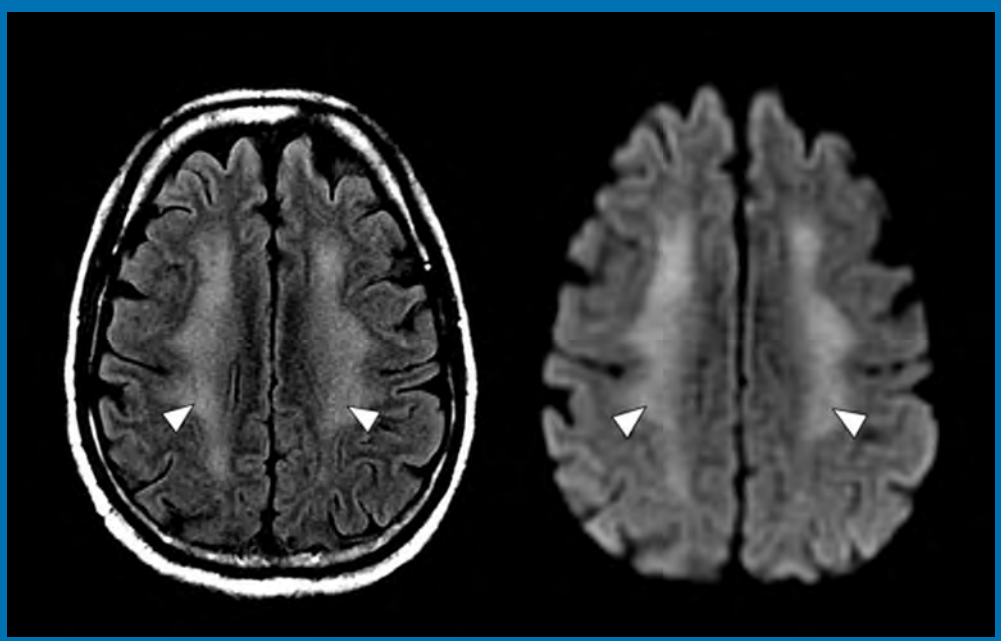

The New Standard of **Ease and Simplicity** in Flow Diversion Treatment.

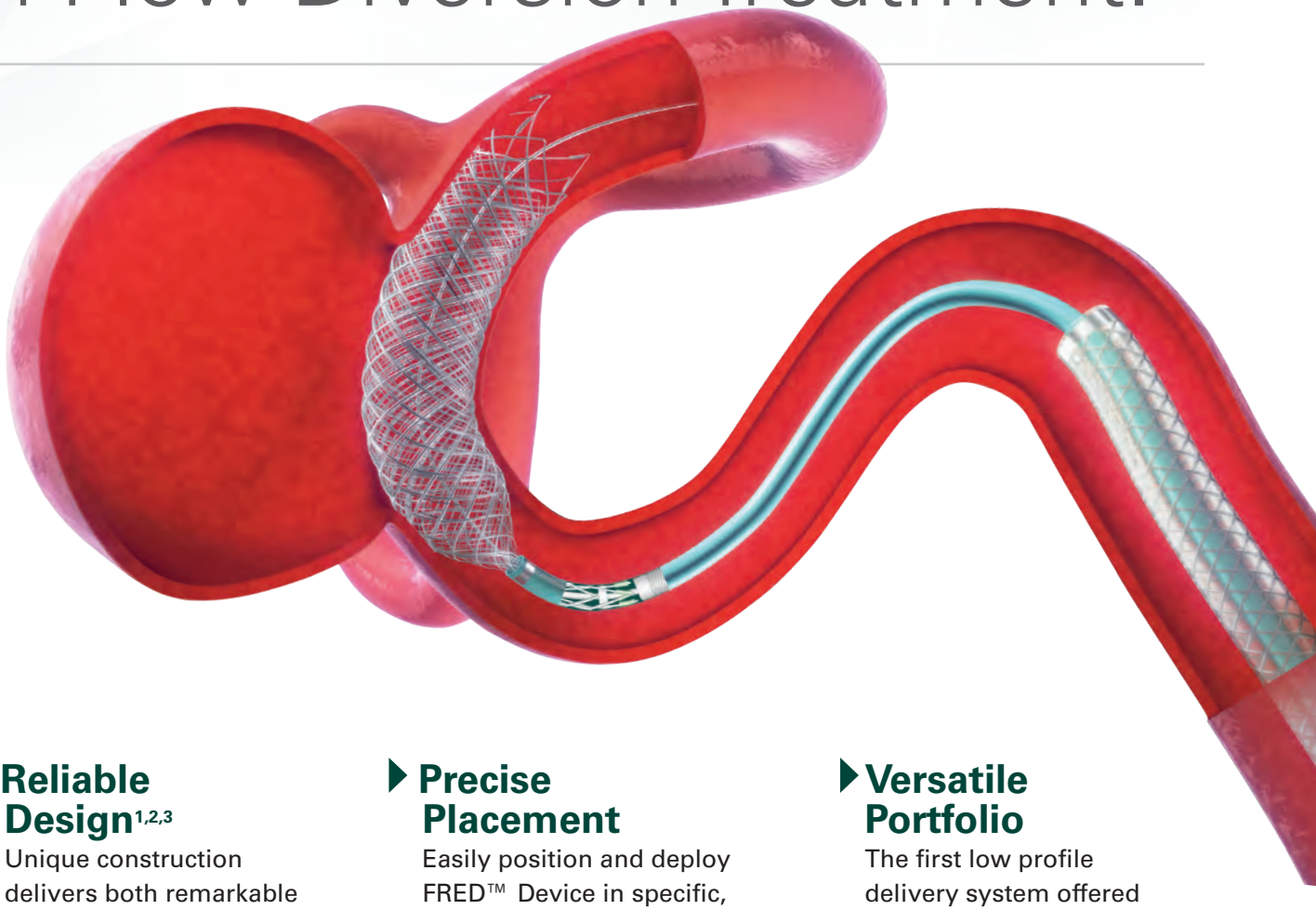

Reliable Design[1,2,3]

Unique construction delivers both remarkable ease of use and excellent flow diversion[1,2,3]

Precise Placement

Easily position and deploy FRED™ Device in specific, targeted locations[4,5,6]

Versatile Portfolio

The first low profile delivery system offered in combination with large diameter and long length options

References:
1. TR11-211 2. TR13-171 3. TR15-055 4. TR13-192 5. TR15-072 6. TR19-145

The Flow Re-Direction Endoluminal Device (FRED™) System is indicated for use in the internal carotid artery from the petrous segment to the terminus for the endovascular treatment of adult patients (22 years of age or older) with wide-necked (neck width ≥ 4 mm or dome-to-neck ratio < 2) saccular or fusiform intracranial aneurysms arising from a parent vessel with a diameter ≥ 2.0 mm and ≤ 5.0 mm.

Use of the FRED™ System is contraindicated under these circumstances: Patients in whom anticoagulant, anti-platelet therapy, or thrombolytic drugs are contraindicated. Patients with known hypersensitivity to metal such as nickel-titanium and metal jewelry. Patients with anatomy that does not permit passage or deployment of the FRED™ System. Patients with an active bacterial infection. Patients with a pre-existing stent in place at the target aneurysm. Patients in whom the parent vessel size does not fall within the indicated range. Patients who have not received dual anti-platelet agents prior to the procedure. For complete indications, contraindications, potential complications, warnings, precautions, and instructions, see instructions for use (IFU provided in the device).

RX Only: Federal (United States) law restricts this device to sale by or on the order of a physician.

MICROVENTION™ and FRED™ are registered trademarks of MicroVention, Inc. in the United States and other jurisdictions. © 2020 MicroVention, Inc. 04/2020.

DOTAREM®
(gadoterate meglumine) Injection

REAL-WORLD TESTED.
REAL-WORLD PROVEN.

The Dotarem® safety profile has been tested and proven in both studies and 30 years of global clinical use.*

0.007% **Spontaneously Reported Worldwide Adverse Events. (>50 million doses)[3-10]**

Dotarem remains an industry standard for contrast imaging with a low incidence of immediate adverse events for patients of all ages.[2-10]

1 Dotarem®
The first and only macrocyclic and ionic GBCA molecule.[1]

A low incidence of adverse events can help your patient focus on what matters most in their life.

Guerbet | COMMITTED

For more information on Dotarem, please see Full Prescribing Information including Boxed Warning and Medication Guide

IMPORTANT SAFETY INFORMATION[1]

WARNING: NEPHROGENIC SYSTEMIC FIBROSIS (NSF)

Gadolinium-based contrast agents (GBCAs) increase the risk for NSF among patients with impaired elimination of the drugs. Avoid use of GBCAs in these patients unless the diagnostic information is essential and not available with non-contrasted MRI or other modalities. NSF may result in fatal or debilitating fibrosis affecting the skin, muscle and internal organs.

- The risk for NSF appears highest among patients with:
  - Chronic, severe kidney disease (GFR < 30 mL/min/1.73m2), or
  - Acute kidney injury.
- Screen patients for acute kidney injury and other conditions that may reduce renal function. For patients at risk for chronically reduced renal function (e.g. age > 60 years, hypertension, diabetes), estimate the glomerular filtration rate (GFR) through laboratory testing.
- For patients at highest risk for NSF, do not exceed the recommended DOTAREM dose and allow a sufficient period of time for elimination of the drug from the body prior to any re-administration.

GUERBET CELEBRATING 30 YEARS* DOTAREM® (gadoterate meglumine) Injection TOGETHER WE BUILD THE FUTURE

Indications and Usage

DOTAREM® (gadoterate meglumine) injection is a prescription gadolinium-based contrast agent indicated for intravenous use with magnetic resonance imaging (MRI) in brain (intracranial), spine and associated tissues in adult and pediatric patients (including term neonates) to detect and visualize areas with disruption of the blood brain barrier (BBB) and/or abnormal vascularity.

Contraindications

History of clinically important hypersensitivity reactions to DOTAREM.

Warnings and Precautions

- Hypersensitivity Reactions: Anaphylactic and anaphylactoid reactions have been reported with DOTAREM, involving cardiovascular, respiratory, and/or cutaneous manifestations. Some patients experienced circulatory collapse and died. In most cases, initial symptoms occurred within minutes of DOTAREM administration and resolved with prompt emergency treatment.
- Before DOTAREM administration, assess all patients for any history of a reaction to contrast media, bronchial asthma and/or allergic disorders. These patients may have an increased risk for a hypersensitivity reaction to DOTAREM.
- Administer DOTAREM only in situations where trained personnel and therapies are promptly available for the treatment of hypersensitivity reactions, including personnel trained in resuscitation.
- Gadolinium Retention: Gadolinium is retained for months or years in several organs. The highest concentrations have been identified in the bone, followed by brain, skin, kidney, liver and spleen. The duration of retention also varies by tissue, and is longest in bone. Linear GBCAs cause more retention than macrocyclic GBCAs.
- Consequences of gadolinium retention in the brain have not been established. Adverse events involving multiple organ systems have been reported in patients with normal renal function without an established causal link to gadolinium retention.
- Acute Kidney Injury: In patients with chronically reduced renal function, acute kidney injury requiring dialysis has occurred with the use of GBCAs. The risk of acute kidney injury may increase with increasing dose of the contrast agent; administer the lowest dose necessary for adequate imaging.
- Extravasation and Injection Site Reactions: Ensure catheter and venous patency before the injection of DOTAREM. Extravasation into tissues during DOTAREM administration may result in tissue irritation.

Adverse Reactions

- The most common adverse reactions associated with DOTAREM in clinical trials were nausea, headache, injection site pain, injection site coldness and rash.
- Serious adverse reactions in the Postmarketing experience have been reported with DOTAREM. These serious adverse reactions include but are not limited to: arrhythmia, cardiac arrest, respiratory arrest, pharyngeal edema, laryngospasm, bronchospasm, coma and convulsion.

Use in Specific Populations

- **Pregnancy:** GBCAs cross the human placenta and result in fetal exposure and gadolinium retention. Use only if imaging is essential during pregnancy and cannot be delayed.
- **Lactation:** There are no data on the presence of gadoterate in human milk, the effects on the breastfed infant, or the effects on milk production. However, published lactation data on other GBCAs indicate that 0.01 to 0.04% of the maternal gadolinium dose is present in breast milk.
- **Pediatric Use:** The safety and efficacy of DOTAREM at a single dose of 0.1 mmol/kg has been established in pediatric patients from birth (term neonates ≥ 37 weeks gestational age) to 17 years of age based on clinical data. The safety of DOTAREM has not been established in preterm neonates. No cases of NSF associated with DOTAREM or any other GBCA have been identified in pediatric patients age 6 years and younger.

You are encouraged to report negative side effects of prescription drugs to the FDA. Visit www.fda.gov/medwatch or call 1-800-FDA-1088.
Please see the full Prescribing Information, including the patient Medication Guide, for additional important safety information.
*Dotarem was launched globally in 1989 and approved by the FDA for use in the US in 2013.

References:

1. Dotarem [package insert]. Princeton, NJ: Guerbet LLC; July 2019. **2.** Internal data as of May 2019. **3.** de Kerviler E et al. Adverse reactions to gadoterate meglumine: review of over 25 years of clinical use and more than 50 million doses. Invest Radiol. 2016 Sep;51(9):544-51. **4.** Briand et al. Efficacy and safety of the macrocyclic complex Gd-DOTA in Children: Results of a Multi-Centre Study. Proceedings of the 29th Congress ofthe European Society of Pediatric Radiology. 1992; 128 **5.** Briand Y. Daily Paediatric Use of MRI Contrast Agents: Results of a Multi-Centre Survey. Proceedings of the 29th Congress of the European Society of Pediatric Radiology. 1992. **6.** Ishiguchi T & Takahashi S. Safety of gadoterate meglumine (Gd-DOTA) as a contrast agent for magnetic resonance imaging: results of a post-marketing surveillance study in Japan. Drugs R D. 2010;10(3):133-45. **7.** Emond S & Brunelle F. Gd-DOTA administration at MRI in children younger than 18 months of age: immediate adverse reactions. Pediatr Radiol. 2011 Nov;41(11):1401-6. **8.** Maurer M et al. Tolerability and diagnostic value of gadoteric acid in the general population and in patients with risk factors: results in more than 84,000 patients. Eur J Radiol. 2012 May;81(5):885-90. **9.** Soyer et al. Observational Study on the Safety Pro le of Gadoterate Megluminein 35,499 Patients: The SECURE Study. J. Magn. Reson. Imag. 2017; 45, 988-997 **10.** Radbruch A et al. Gadolinium retention in the dentate nucleus and globus pallidus is dependent on the class of contrast agent. Radiology. 2015 Jun;275(3):783-97.

GU09191202

stryker

We make the solutions.

You make the difference.

Looking for customizable fracture care? Stryker puts the possibilities in your hands.

strykerIVS.com/VCF

Stryker or its affiliated entities own, use, or have applied for the following trademarks or service marks: AVAflex, iVAS, SpineJack and Stryker. All other trademarks are trademarks of their respective owners or holders.

The absence of a product, feature, or service name, or logo from this list does not constitute a waiver of Stryker's trademark or other intellectual property rights concerning that name or logo.

V0000023896
Copyright © 2020 Stryker

AJNR go green

AJNR urges American Society of Neuroradiology members to reduce their environmental footprint by voluntarily suspending their print subscription.

The savings in paper, printing, transportation, and postage directly fund new electronic enhancements and expanded content.

The digital edition of *AJNR* presents the print version in its entirety, along with extra features including:

- **Publication Preview**
- **Case Collection**
- **Podcasts**
- **The *AJNR* News Digest**
- **The *AJNR* Blog**

It also reaches subscribers much faster than print. An electronic table of contents will be sent directly to your mailbox to notify you as soon as it publishes.

Readers can search, reference, and bookmark current and archived content 24 hours a day on www.ajnr.org.

ASNR members who wish to opt out of print can do so by using the AJNR Go Green link on the *AJNR* Website (http://www.ajnr.org/content/subscriber-help-and-services). Just type your name in the email form to stop print and spare our ecosystem.

Simplify
the MOC Process

Manage
your CME Credits Online

CMEgateway.org

Available to Members of Participating Societies

- American Board of Radiology (ABR)
- American College of Radiology (ACR)
- American Roentgen Ray Society (ARRS)
- American Society of Neuroradiology (ASNR)
- Commnission on Accreditation of Medical Physics Educational Programs, Inc. (CAMPEP)
- Radiological Society of North America (RSNA)
- Society of Interventional Radiology (SIR)
- SNM
- The Society for Pediatric Radiology (SPR)

It's Easy and Free!

Log on to CME Gateway to:

- View or print reports of your CME credits from multiple societies from a single access point.
- Print an aggregated report or certificate from each participating organization.
- Link to SAMs and other tools to help with maintenance of certification.

American Board of Radiology (ABR) participation!

By activating ABR in your organizational profile, your MOC–fulfilling CME and SAM credits can be transferred to your own personalized database on the ABR Web site.

Sign Up Today!

go to CMEgateway.org

We're Inside Every Great Neuroradiologist!

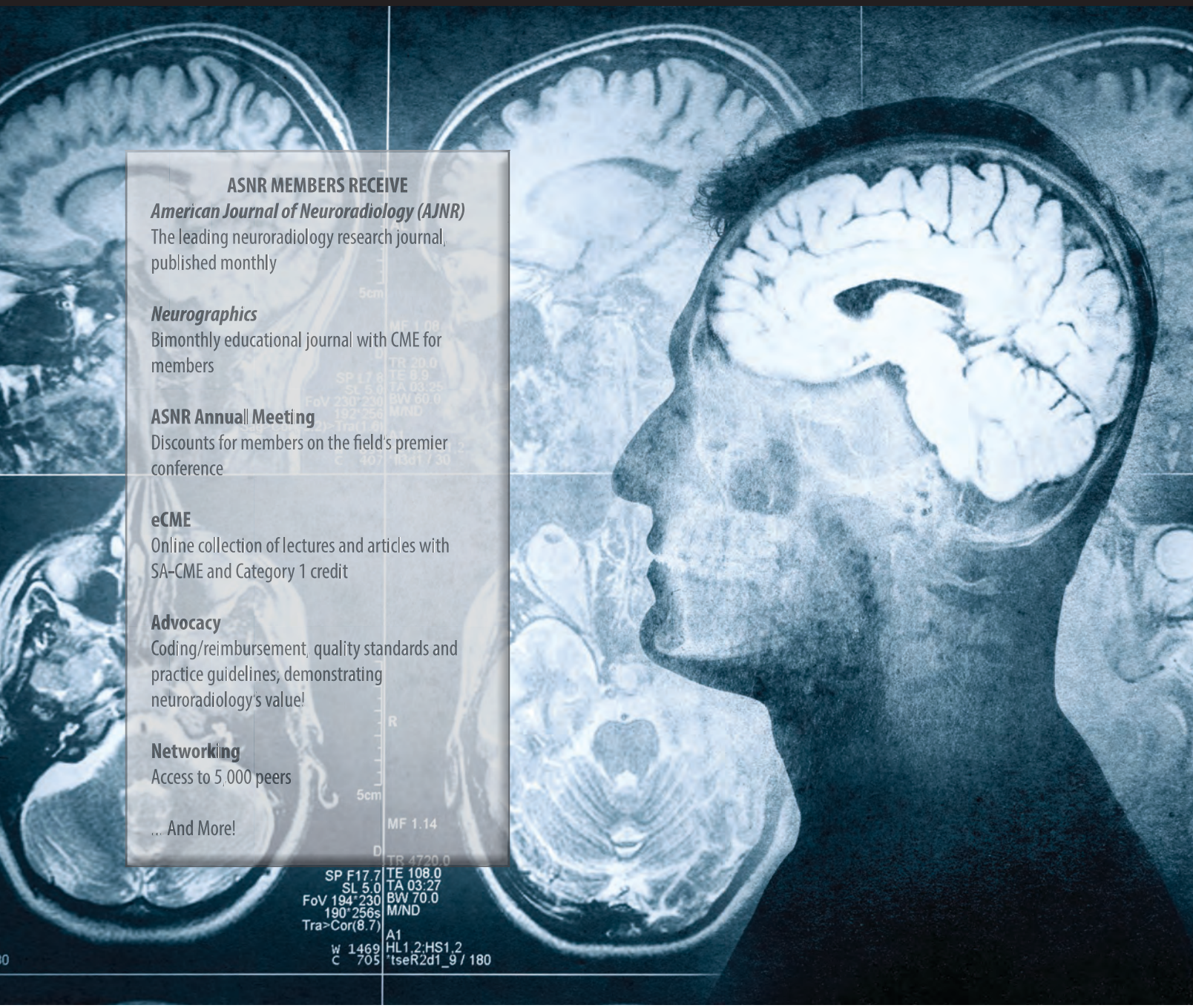

Join the leaders in neuroradiology today!
Learn more at www.asnr.org/join

ASNR
American Society of Neuroradiology

800 Enterprise Dr., Suite 205, Oak Brook, IL 60523 • (630)574-0220 • membership@asnr.org • www.asnr.org

ASNR 59th Annual Meeting

CALL FOR ABSTRACTS

Join us May 22-26, 2021, in San Francisco to present the best scientific research in Neuroradiology.

SUBMISSION DEADLINE:

Monday, November 2, 2020 (11:59 PM ET)
Submit online at asnr.org/annualmeeting

Acceptance notifications will be sent on or before January 15, 2021 upon conclusion of peer review.

ABSTRACT SUBMISSION INFORMATION

1. **IMPORTANT**: All oral presenters should be prepared to submit electronic versions of their presentations for our virtual audience, in addition to presenting to the live audience in San Francisco. Virtual presentation ability will be offered during the live meeting to those oral presenters impacted by governmental and institutional travel restrictions. For more information on ASNR21 and COVID-19 contingency planning, please visit www.asnr.org/annualmeeting.
2. Presenters of accepted abstracts **must register at their own expense** for the ASNR Annual Meeting.
3. Submission topic areas include: **Adult Brain, Spine, Head & Neck, Pediatrics, Functional/Advanced Imaging, Interventional, Health Policy, and AI/Informatics**.
4. Submit each abstract in **one** category only.
5. The *American Journal of Neuroradiology (AJNR)* encourages presenters to submit manuscripts based on their work to *AJNR* before considering other journals.
6. Maximum length: **2,500 characters, not including title, authors, images, figures**.
7. Submission site allows uploading of files into the system.
8. Changes can be made to submitted abstracts until the deadline.
9. Available awards include the Cornelius Dyke Memorial Award, Outstanding Oral Presentation Awards, and Educational Exhibit Awards.

FRED™

Flow **R**e-**D**irection
Endoluminal **D**evice

FLOW DIVERSION.

SIMPLIFIED.

MicroVention™
TERUMO

MicroVention Worldwide Innovation Center
35 Enterprise
Aliso Viejo, CA 92656 USA
PH +1 714.247.8000

MicroVention UK Limted
PH +1 44 (0) 191 258 6777

MicroVention Europe S.A.R.L.
PH +33 (1) 39 21 77 46

MicroVention Deutschland GmbH
PH +49 211 210 798-0

Web
microvention.com

FOR EACH ABSTRACT

- All authors must have disclosure on file in the submission system. Remove authors with missing disclosures prior to submitting abstracts. Email **education@asnr.org** to add authors after the submission deadline.
- At least one reference is required, and up to five references may be included. References should be formatted according to *AJNR* author instructions.
- The use of charts, tables and graphics are encouraged if relevant to the research submitted.
- Only one graphic file with a maximum of four images is permitted.
- Required graphic file resolution is 300 dpi or greater (e.g. 900 pixel width by 900 pixel height for a 3-inch by 3-inch image).
- Maximum file size of 100 megabytes.
- Only .jpg and .gif formats are accepted.

SUBMISSION CATEGORIES

ORAL PRESENTATION (With additional electronic version)

- 6-minute presentation plus shared session discussion that summarizes details of original investigative research.
- Additional electronic poster required (single PowerPoint slide, summarizing details of the oral presentation).
- Required abstract format: Purpose, Materials and Methods, Results, Conclusion.

ELECTRONIC SCIENTIFIC POSTER (Single PowerPoint Slide)

- Visual presentation summarizing details of original investigative research.
- Required abstract format: Purpose, Materials and Methods, Results, Conclusion.

ELECTRONIC EDUCATIONAL EXHIBIT (Multislide PowerPoint Presentation)

- A visually oriented educational presentation. Electronic Educational Exhibits highlight the unique didactic advantages of the computer format and focus on its interactive potential.
- Required abstract format: summary of the planned presentation and list of educational objectives. Consider use of Purpose, Materials/Methods, Results and Conclusion when appropriate.
- Live presentation time for select abstracts.

EDUCATIONAL EXHIBIT POSTER (Printed Poster; additional PDF version required for awards consideration)

- A visual presentation/display featuring cutting-edge material or instructional review of a topic.
- Required abstract format: summary of the planned presentation and list of educational objectives. Consider use of Purpose, Materials/Methods, Results and Conclusion when appropriate.
- Live presentation time for select abstracts.

Questions?
Contact the ASNR Education Department at **education@asnr.org**.

ASNR
American Society of Neuroradiology

Introducing

Eclipse 2 L

DUAL LUMEN BALLOON CATHETER

Balt's Access Portfolio Delivers Unique Solutions

Hybrid GUIDEWIRES

Magic®

FLOW-DEPENDENT MICROCATHETER SERIES

BALLAST LONG SHEATH 6F 088

Visit www.balt-usa.com to learn more

Balt USA
29 Parker, Irvine, CA 92618 • tel 949.788.1443 fax 949.788.1444 • balt-usa.com

© 2019 BALT USA MKTG – 147 Rev. A

balt
inspiring innovation

AJNR

AMERICAN JOURNAL OF NEURORADIOLOGY

Publication Preview at www.ajnr.org features articles released in advance of print. Visit www.ajnrblog.org to comment on AJNR content and chat with colleagues and AJNR's News Digest at http://ajnrdigest.org to read the stories behind the latest research in neuroimaging.

OCTOBER 2020 • VOLUME 41 • NUMBER 10 • WWW.AJNR.ORG

EDITOR-IN-CHIEF

Jeffrey S. Ross, MD
Professor of Radiology, Department of Radiology, Mayo Clinic College of Medicine, Phoenix, AZ

SENIOR EDITORS

Harry J. Cloft, MD, PhD
Professor of Radiology and Neurosurgery, Department of Radiology, Mayo Clinic College of Medicine, Rochester, MN

Christopher G. Filippi, MD
Professor and Vice Chair of Biomedical and Translational Science, Donald and Barbara Zucker School of Medicine at Hofstra/Northwell, Lenox Hill Hospital and Greenwich Village Healthplex, New York, NY

Thierry A.G.M. Huisman, MD
Radiologist-in-Chief, Texas Children's Hospital, Houston, TX

Yvonne W. Lui, MD
Associate Professor of Radiology, Chief of Neuroradiology, New York University School of Medicine, New York, NY

C.D. Phillips, MD, FACR
Professor of Radiology, Weill Cornell Medical College, Director of Head and Neck Imaging, New York-Presbyterian Hospital, New York, NY

Lubdha M. Shah, MD, MS
Professor of Radiology and Director of Spine Imaging, University of Utah Department of Radiology and Imaging Sciences, Salt Lake City, UT

STATISTICAL SENIOR EDITOR

Bryan A. Comstock, MS
Senior Biostatistician, Department of Biostatistics, University of Washington, Seattle, WA

ARTIFICIAL INTELLIGENCE DEPUTY EDITOR

Peter D. Chang, MD
Assistant Professor-in-Residence, Departments of Radiological Sciences, Computer Sciences, and Pathology, Director, Center for Artificial Intelligence in Diagnostic Medicine (CAIDM), University of California, Irvine, Irvine, CA

EDITORIAL BOARD

Ashley H. Aiken, *Atlanta, GA*
Lea M. Alhilali, *Phoenix, AZ*
Mohammed A. Almekhlafi, *Calgary, Alberta, Canada*
Joachim Berkefeld, *Frankfurt, Germany*
Aashim Bhatia, *Pittsburgh, PA*
Waleed Brinjikji, *Rochester, MN*
Judah Burns, *New York, NY*
Danielle Byrne, *Dublin, Ireland*
Federico Cagnazzo, *Montpellier, France*
J. Levi Chazen, *New York, NY*
James Y. Chen, *San Diego, CA*
Gloria C. Chiang, *New York, NY*
Daniel Chow, *Irvine, CA*
Kars C.J. Compagne, *Rotterdam, The Netherlands*
Arturo Consoli, *Suresnes, France*
Seena Dehkharghani, *New York, NY*
Nilesh K. Desai, *Houston, TX*
Yonghong Ding, *Rochester, MN*
Birgit Ertl-Wagner, *Toronto, Ontario, Canada*
Clifford J. Eskey, *Hanover, NH*
Massimo Filippi, *Milan, Italy*
Nils D. Forkert, *Calgary, Alberta, Canada*
Ana M. Franceschi, *New York, NY*
Frank Gaillard, *Melbourne, Australia*
Joseph J. Gemmete, *Ann Arbor, Michigan*
Wende N. Gibbs, *Phoenix, AZ*
Philipp Gölitz, *Erlangen, Germany*
Brent Griffith, *Detroit, MI*
Raymond Y. Huang, *Boston, MA*
Gábor Janiga, *Magdeburg, Germany*
Joseph M. Hoxworth, *Phoenix, Arizona*
Christof Karmonik, *Houston, TX*
Timothy J. Kaufmann, *Rochester, MN*
Hillary R. Kelly, *Boston, MA*
Toshibumi Kinoshita, *Akita, Japan*
Stephen F. Kralik, *Houston, TX*
Alexander W. Korutz, *Chicago, IL*
Alexander Lerner, *Los Angeles, CA*
Yinsheng Li, *Madison, WI*
Franklin A. Marden, *Chicago, IL*
Markus A. Möhlenbruch, *Heidelberg, Germany*
Kambiz Nael, *Los Angeles, CA*
Renato Hoffmann Nunes, *Sao Paulo, Brazil*
Sasan Partovi, *Cleveland, OH*
Johannes A.R. Pfaff, *Heidelberg, Germany*
Laurent Pierot, *Reims, France*
Alireza Radmanesh, *New York, NY*
Prashant Raghavan, *Baltmore, MD*
Eytan Raz, *New York, NY*
Paul M. Ruggieri, *Cleveland, OH*
Sebastian Schafer, *Madison, WI*
Maksim Shapiro, *New York, NY*
Timothy Shepherd, *New York, NY*
James Shin, *New York, NY*
Mark S. Shiroishi, *Los Angeles, CA*
Bruno P. Soares, *Baltimore, MD*
Jason F. Talbott, *San Francisco, CA*
Ruth Thiex, *Everett, Washington*
Vincent Thijs, *Melbourne, Victoria, Australia*
Fabio Triulzi, *Milan, Italy*
Anderanik Tomasian, *Los Angeles, CA*
Anja G. van der Kolk, *Utrecht, the Netherlands*
Arastoo Vossough, *Philadelphia, PA*
Elysa Widjaja, *Toronto, Ontario, Canada*
Leonard Yeo, *Singapore*
Woong Yoon, *Gwangju, South Korea*
David M. Yousem, *Evergreen, CO*
Carlos Zamora, *Chapel Hill, NC*
Chengcheng Zhu, *Seattle, WA*

EDITORIAL FELLOW

Matthew D. Alvin, *Baltimore, MD*

SPECIAL CONSULTANTS TO THE EDITOR

AJNR Blog Editor
Neil Lall, *Denver, CO*
Case of the Month Editor
Nicholas Stence, *Aurora, CO*
Case of the Week Editors
Juan Pablo Cruz, *Santiago, Chile*
Matylda Machnowska, *Toronto, Ontario, Canada*
Sapna Rawal, *Toronto, Ontario, Canada*
Classic Case Editor
Sandy Cheng-Yu Chen, *Taipei, Taiwan*
Health Care and Socioeconomics Editor
Pina C. Sanelli, *New York, NY*
Physics Editor
Greg Zaharchuk, *Stanford, CA*
Podcast Editor
Wende N. Gibbs, *Phoenix, AZ*
Twitter Editor
Roger Jordan, *Houston, TX*

Official Journal:

American Society of Neuroradiology
American Society of Functional Neuroradiology
American Society of Head and Neck Radiology
American Society of Pediatric Neuroradiology
American Society of Spine Radiology

Founding Editor
Juan M. Taveras
Editors Emeriti
Mauricio Castillo, Robert I. Grossman, Michael S. Huckman, Robert M. Quencer

Managing Editor
Karen Halm
Assistant Managing Editor
Laura Wilhelm
Editorial Assistant
Margaret B. Sabato
Executive Director, ASNR
Mary Beth Hepp

AJNR

AMERICAN JOURNAL OF NEURORADIOLOGY

OCTOBER 2020
VOLUME 41
NUMBER 10
WWW.AJNR.ORG

Publication Preview at www.ajnr.org features articles released in advance of print. Visit www.ajnrblog.org to comment on AJNR content and chat with colleagues and AJNR's News Digest at http://ajnrdigest.org to read the stories behind the latest research in neuroimaging.

1759 **PERSPECTIVES** *A. Lindqwister*

REVIEW ARTICLES

1760 **Neuroimaging in Zoonotic Outbreaks Affecting the Central Nervous System: Are We Fighting the Last War?** *G.X. Goh, et al.* — ADULT BRAIN

1768 **Stapedial Artery: From Embryology to Different Possible Adult Configurations** *S. Bonasia, et al.* — HEAD & NECK

1777 **Middle Meningeal Artery: Anatomy and Variations** *S. Bonasia, et al.* — HEAD & NECK

RADIOLOGY-PATHOLOGY CORRELATION

1786 **Exophytic Lumbar Vertebral Body Mass in an Adult with Back Pain** *J.C. Benson, et al.* — SPINE

GENERAL CONTENTS

1791 **Clinical and Neuroimaging Correlation in Patients with COVID-19** *B.C. Yoon, et al.* — ADULT BRAIN

1797 **Bilateral Basal Ganglia Hemorrhage in a Patient with Confirmed COVID-19** *R. Daci, et al.* — ADULT BRAIN

1800 **Pressing Issues in COVID-19: Probable Cause to Seize SARS-CoV-2 for Its Preferential Involvement of Posterior Circulation Manifesting as Severe Posterior Reversible Encephalopathy Syndrome and Posterior Strokes** *F. D'Amore, et al.* — ADULT BRAIN

1804 **Imaging Features of Acute Encephalopathy in Patients with COVID-19: A Case Series** *S. Kihira, et al.* — ADULT BRAIN

1809 **Perfusion Parameter Thresholds That Discriminate Ischemic Core Vary with Time from Onset in Acute Ischemic Stroke** *T. Yoshie, et al.* — ADULT BRAIN FUNCTIONAL

1816 **Presurgical Identification of Primary Central Nervous System Lymphoma with Normalized Time-Intensity Curve: A Pilot Study of a New Method to Analyze DSC-PWI** *A. Pons-Escoda, et al.* — ADULT BRAIN FUNCTIONAL

1825 **Tentorial Venous Anatomy: Variation in the Healthy Population** *J.S. Rosenblum, et al.* — ADULT BRAIN

1833 **The Variable Appearance of Third Ventricular Colloid Cysts: Correlation with Histopathology and the Risk of Obstructive Ventriculomegaly** *S.D. Khanpara, et al.* — ADULT BRAIN

AJNR (Am J Neuroradiol ISSN 0195–6108) is a journal published monthly, owned and published by the American Society of Neuroradiology (ASNR), 800 Enterprise Drive, Suite 205, Oak Brook, IL 60523. Annual dues for the ASNR include approximately 21% for a journal subscription. The journal is printed by Cadmus Journal Services, 5457 Twin Knolls Road, Suite 200, Columbia, MD 21045; Periodicals postage paid at Oak Brook, IL and additional mailing offices. Printed in the U.S.A. POSTMASTER: Please send address changes to American Journal of Neuroradiology, P.O. Box 3000, Denville, NJ 07834, U.S.A. Subscription rates: nonmember $410 ($480 foreign) print and online, $320 online only; institutions $470 ($540 foreign) print and basic online, $935 ($1000 foreign) print and extended online, $380 online only (basic), $825 online only (extended); single copies are $35 each ($40 foreign). Indexed by PubMed/MEDLINE, BIOSIS Previews, Current Contents (Clinical Medicine and Life Sciences), EMBASE, Google Scholar, HighWire Press, Q-Sensei, RefSeek, Science Citation Index, SCI Expanded, Meta/CZI, ReadCube, and Semantic Scholar. Copyright © American Society of Neuroradiology.

1841 **Transcranial MR Imaging–Guided Focused Ultrasound Interventions Using Deep Learning Synthesized CT** *P. Su, et al.* — INTERVENTIONAL FUNCTIONAL

1849 **Regional Mechanical Thrombectomy Imaging Protocol in Patients Presenting with Acute Ischemic Stroke during the COVID-19 Pandemic** *P.S. Dhillon, et al.* — INTERVENTIONAL

1856 **Antiplatelet Management for Stent-Assisted Coiling and Flow Diversion of Ruptured Intracranial Aneurysms: A DELPHI Consensus Statement** *J.M. Ospel, et al.* — INTERVENTIONAL

1863 **The Dilator-Dotter Technique: A Modified Method of Rapid Internal Carotid Artery Revascularization in Acute Ischemic Stroke** *K. Amuluru, et al.* — INTERVENTIONAL

1869 **Quantifying Intra-Arterial Verapamil Response as a Diagnostic Tool for Reversible Cerebral Vasoconstriction Syndrome** *J.M. Sequeiros, et al.* — INTERVENTIONAL

1876 **Intraprocedural Flat Panel Detector Rotational Angiography and an Image Fusion Technique for Delivery of a Microcatheter into the Targeted Shunt Pouch of a Dural Arteriovenous Fistula** *J.H. Choi, et al.* — INTERVENTIONAL

1879 **Microcatheter Originating Debris during Neuroendovascular Procedures: Mechanism of Dislodgement and Its Prevention** *I. Kan, et al.* — INTERVENTIONAL

1882 **Olfactory Bulb Signal Abnormality in Patients with COVID-19 Who Present with Neurologic Symptoms** *S.B. Strauss, et al.* — HEAD & NECK

1888 **Are Gadolinium-Enhanced MR Sequences Needed in Simultaneous ^{18}F-FDG PET/MRI for Tumor Delineation in Head and Neck Cancer?** *N. Pyatigorskaya, et al.* — HEAD & NECK

1897 **Prediction of Human Papillomavirus Status and Overall Survival in Patients with Untreated Oropharyngeal Squamous Cell Carcinoma: Development and Validation of CT-Based Radiomics** *Y. Choi, et al.* — HEAD & NECK FUNCTIONAL

1905 **COVID-19-Associated Cytotoxic Lesions of the Corpus Callosum** *P. Gaur, et al.* — PEDIATRICS

1908 **Maternal Anxiety and Depression during Late Pregnancy and Newborn Brain White Matter Development** *R.M. Graham, et al.* — PEDIATRICS

1916 **Intracranial Arterial Tortuosity in Marfan Syndrome and Loeys-Dietz Syndrome: Tortuosity Index Evaluation Is Useful in the Differential Diagnosis** *L. Spinardi, et al.* — PEDIATRICS

1923 **Fetal Intraventricular Hemorrhage in Open Neural Tube Defects: Prenatal Imaging Evaluation and Perinatal Outcomes** *R.A. Didier, et al.* — PEDIATRICS

1930 **Expanding the Neuroimaging Phenotype of Neuronal Ceroid Lipofuscinoses** *A. Biswas, et al.* — PEDIATRICS

1937 **CT-Based Measurements of Facial Parameters of Healthy Children and Adolescents in Thailand** *N. Jullabussapa, et al.* — PEDIATRICS

1943 **MRI Spectrum of Brain Involvement in Sphingosine-1-Phosphate Lyase Insufficiency Syndrome** *K.W. Martin, et al.* — PEDIATRICS

1949 **Paraspinal Myositis in Patients with COVID-19 Infection** *W.A. Mehan, et al.* — SPINE

1953 **Safety of Consecutive Bilateral Decubitus Digital Subtraction Myelography in Patients with Spontaneous Intracranial Hypotension and Occult CSF Leak** *M.C. Pope, et al.* — SPINE

1958 **Time to Resolution of Inadvertent Subdural Contrast Injection during a Myelogram: When Can the Study Be Reattempted?** *D.P. Shlapak, et al.* — SPINE

ONLINE FEATURES

LETTERS

E85 **Recanalized Aneurysms: Is Rupture Further Preventable?** *T. Kimura*

BOOK REVIEWS *R.M. Quencer, Section Editor*

Please visit www.ajnrblog.org to read and comment on Book Reviews.

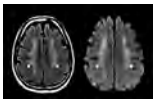

Brain MRI of a 60-year-old man with COVID-19 who presented with disorientation and decreased alertness. FLAIR image demonstrates diffuse confluent WM hyperintensity with sparing of the subcortical U-fibers while the DWI shows corresponding restricted diffusion throughout the involved WM.

Indicates Editor's Choices selection
Indicates Fellows' Journal Club selection
Indicates open access to non-subscribers at www.ajnr.org
Indicates article with supplemental on-line table
Indicates article with supplemental on-line photo
Indicates article with supplemental on-line video
Evidence-Based Medicine Level 1
Evidence-Based Medicine Level 2

Title: Dx: Dermoid Cyst. The future of radiology will be profoundly augmented by artificial intelligence; as imaging specialists, it is imperative that we understand how these techniques will enhance our ability to draw meaningful conclusions from studies. As a medical student interested in neuroimaging and machine learning, I came across multiple visually appealing cases. I used a neural network style transfer technique to apply the stylistic motifs of pre-existing art with the cases I read. The rendered image is a sagittal T1 view of a ruptured dermoid cyst merged, with permission from the artist, with *Cat Lover #3* by Marlina Vera.

Alex Lindqwister, Geisel School of Medicine at Dartmouth, Hanover, New Hampshire

Neuroimaging in Zoonotic Outbreaks Affecting the Central Nervous System: Are We Fighting the Last War?

G.X. Goh, K. Tan, B.S.P. Ang, L.-F. Wang, and C.C. Tchoyoson Lim

History doesn't repeat itself, but it often rhymes.
Mark Twain

ABSTRACT

SUMMARY: When preparing for the coronavirus disease 2019 pandemic and its effects on the CNS, radiologists should be familiar with neuroimaging appearances in past zoonotic infectious disease outbreaks. Organisms that have crossed the species barrier from animals to humans include viruses such as Hendra, Nipah, Severe Acute Respiratory Syndrome, and influenza, as well as bacteria and others. Brain CT and MR imaging findings have included cortical abnormalities, microinfarction in the white matter, large-vessel occlusion, and features of meningitis. In particular, the high sensitivity of diffusion-weighted MR imaging in detecting intracranial abnormalities has been helpful in outbreaks. Although the coronaviruses causing the previous Severe Acute Respiratory Syndrome outbreak and the current coronavirus disease 19 pandemic are related, it is important to be aware of their similarities as well as potential differences. This review describes the neuroimaging appearances of selected zoonotic outbreaks so that neuroradiologists can better understand the current pandemic and potential future outbreaks.

ABBREVIATIONS: COVID-19 = coronavirus disease 2019; HeV = Hendra virus; MERS-CoV = Middle East respiratory syndrome coronavirus; NiV = Nipah virus; SARS-CoV-2 = Severe Acute Respiratory Syndrome coronavirus 2

Currently, the coronavirus disease 2019 (COVID-19) pandemic is sweeping across the world, caused by the emerging novel zoonotic virus Severe Acute Respiratory Syndrome coronavirus 2 (SARS-CoV-2).[1] First detected in Wuhan, China, in late 2019, COVID-19 (the clinical syndrome caused by the virus) has resulted in high mortality and morbidity, overwhelming the health services as well as causing severe disruption to the economy in many parts of the world.[1,2] In the past 20 years, there have been increasing epidemic outbreaks of zoonotic diseases, including coronaviruses and various other pathogens.[3,4] Zoonoses often present with neurologic symptoms and imaging changes on CT and MR imaging; hence, it is important for neuroradiologists to be familiar with the imaging findings in past outbreaks in addition to obtaining up-to-date information on the current one.[5,6] This review is based on a literature review and the authors' ongoing research and introduces the zoonotic infections and associated neuroimaging appearances in past outbreaks that have affected the CNS, to improve our understanding of the current pandemic and future zoonotic disease outbreaks.

Received May 19, 2020; accepted after revision June 15.

From the Emerging Infectious Diseases Programme (G.X.G., L.-F.W.), Duke-NUS Medical School, Singapore; Departments of Neurology (K.T.) and Neuroradiology (C.C.T.L.), National Neuroscience Institute and Duke-NUS Medical School, Singapore; Department of Infectious Diseases and Infection Prevention and Control (B.S.P.A.), Tan Tock Seng Hospital, Singapore.

Please address correspondence to C.C. Tchoyoson Lim, MBBS, FRCR (UK), MMed (Diagostic Radiology), Department of Neuroradiology, National Neuroscience Institute, 11 Jalan Tan Tock Seng, Singapore 308433, Republic of Singapore; e-mail: tchoyoson.lim@singhealth.com.sg

Indicates open access to non-subscribers at www.ajnr.org

http://dx.doi.org/10.3174/ajnr.A6727

Emerging Zoonotic Diseases and the CNS

A zoonotic disease is defined as an infectious agent leaping from an animal reservoir to humans, often caused by mutations that permit accessibility through receptor or immune barriers of the novel host.[7] In the broadest sense, zoonoses encompass both direct spread from a vertebrate animal to humans, as well as vector-borne diseases that use intermediate arthropod vectors (typically mosquitos, ticks, sand flies, and so on), resulting in indirect spread to humans. Additionally, zoonotic pathogens range from viruses, bacteria, parasites, and fungi to prions.[8] The global burden of animal-to-human disease transmission is increasing, and up to 76% of emerging infectious disease events in recent years have been zoonotic in nature.[9] Historically, the 3 pandemics of greatest significance—the Plague (or "Black Death"), the 1918 Spanish flu, and HIV/AIDS—were all caused by zoonoses or vector-borne diseases, leading to hundreds of millions of deaths worldwide.[10]

In recent decades, bats have emerged as mammalian hosts serving as reservoirs for pathogens of high mortality. Although historically known to transmit rabies virus alongside the order

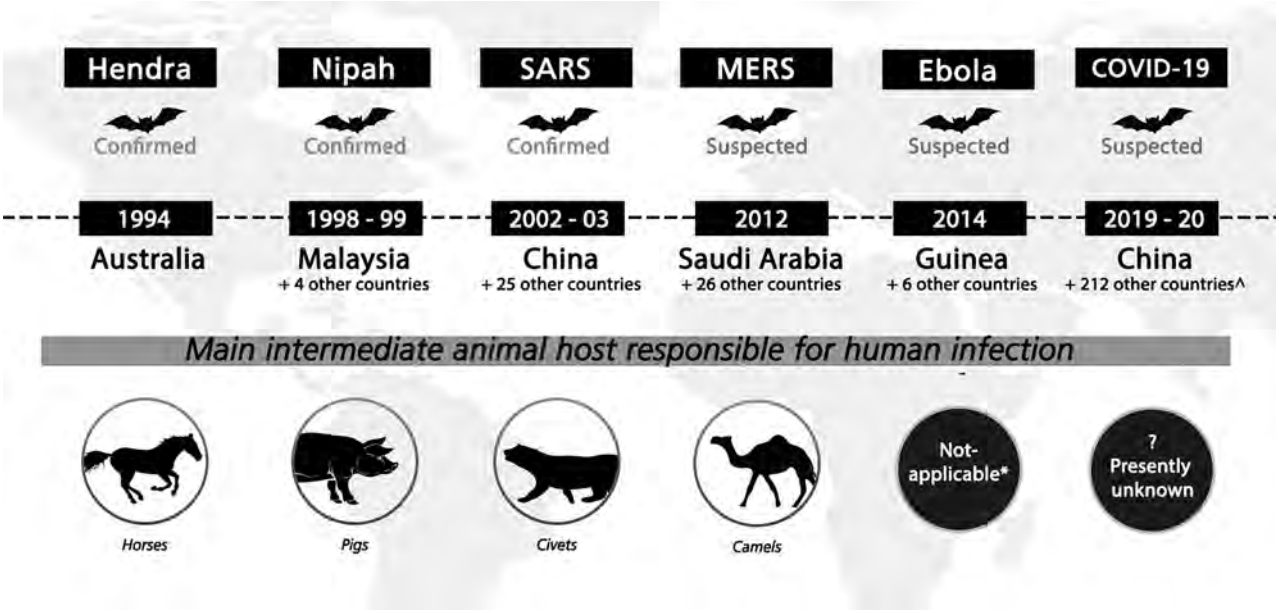

FIG 1. Summary of major emerging zoonotic outbreaks related to bats, 1994–2019. Confirmed bat-borne viruses include Hendra, Nipah, and SARS-CoV-1 viruses; bats are also suspected to be viral reservoirs for MERS, Ebola, and SARS-CoV-2 (cause of the current COVID-19 pandemic) viruses. Years when outbreaks occurred and confirmed or suspected intermediate hosts involved in virus spillover are also shown. * indicates that although the 2014 Ebola outbreak was believed to have started with direct bat-to-human transmission, nonhuman primates have been implicated in previous Ebola outbreaks. ^Data accurate as of May 11, 2020. Reprinted with permission of Duke-NUS Medical School.

Carnivora, bats have now been shown to carry assorted viruses from different families, including zoonotic viruses such as Coronaviridae, Filoviridae, and Paramyxoviridae, among others.[11] Bats are also a well-recognized reservoir for Lyssaviruses, including the rabies virus and Australian bat lyssavirus, which classically result in encephalitic or paralytic rabies.[12] Critically, bat-borne viruses cause regular and cyclical outbreaks via zoonotic transmission and spillover into secondary mammalian hosts. Increasing recognition of bats as animal reservoirs of zoonotic pathogens began with the Hendra virus (HeV) outbreak in 1994 and has only since accelerated up to the current COVID-19 pandemic.[13,14] Other important examples of novel zoonotic virus emergence linked to bats include the 1998 Nipah virus (NiV) disease in pigs in Malaysia, Severe Acute Respiratory Syndrome coronavirus 1 (SARS-CoV) in China in 2002, Middle East respiratory syndrome coronavirus (MERS-CoV) in Saudi Arabia starting in 2012, and devastating outbreaks of filoviruses from 1967 through 2018 (Fig 1).[15,16]

Table 1 shows examples of zoonotic diseases that have been associated with CNS manifestations. Zoonotic diseases with other animal hosts include the 2009 outbreak of zoonotic "swine flu" influenza H1N1 strain and sporadic human cases of avian influenza subtypes H5N1 and H9N2.[17] Within rodent reservoirs in Europe, the Americas, and Asia, hantaviruses have been found to spill over into humans and may also present with pulmonary and neurologic symptoms.[18] A large number of CNS infections are vector-borne diseases, notably arthropod-borne Alphaviruses and Flaviviruses. Key examples include the mosquito-borne Japanese encephalitis virus and West Nile virus, dengue, Chikungunya, Zika (responsible for an outbreak in 2015–2016 that caused fetal MR imaging changes),[19] and tick-borne viruses. A review of vector-borne CNS diseases is outside the scope of this article, which focuses on zoonotic outbreaks directly from animals to humans. Notably, most recent zoonotic outbreaks reaching regional or global significance appear to be viral in nature.

Table 1: Key zoonotic diseases with CNS manifestations

Pathogen Type	Animal Reservoir	Zoonotic Species or Agent
Viral	Bats	Rabies virus (RABV)
		Australian bat lyssavirus (ABLV)
		Hendra virus (HeV)
		Nipah virus (NiV)
		SARS-CoV, MERS-CoV, SARS-CoV-2
	Bats, primates, duikers	Ebola virus (EBOV)
		Marburg virus (MARV)
	Primates	Herpes B virus
	Rodents	Hantavirus
	Poultry, swine	Influenza A virus (H1N1, H1N2, H3N2, H5N1, H7N9)
Bacterial	Ruminants	*Brucella* species
		Leptospira interrogans
		Coxiella burnetii
	Rabbits, rodents	*Francisella tularensis*
	Poultry	*Chlamydia psittaci*
	Fish	*Streptococcus iniae*
Parasitic	Felines	*Toxoplasma gondii*
	Swine	*Taenia solium*
	Sheep, cattle	*Echinococcus* species
Fungal	Bats, birds, various mammals	*Histoplasma capsulatum*
		Cryptococcus neoformans, *Cryptococcus gattii*

Neuroimaging in Recent Zoonotic Infectious Outbreaks Affecting the CNS

Zoonotic Bat-Borne Henipaviruses: Hendra and Nipah Viruses. A separate genus of Henipavirus within the Paramyxoviridae family was created after the discovery of 2 new viruses causing zoonotic outbreaks, which were named after the HeV and NiV. HeV (initially named equine morbillivirus) was isolated during 2 outbreaks in 1994 at a stable in Hendra, a suburb of Brisbane, Australia, causing the deaths of 16 horses, a trainer, and another animal handler.[20] Ongoing HeV outbreaks in Australia have been reported, with a total of 94 equine disease cases, 7 human cases, and 4 deaths as of 2015, typically in veterinarians or animal handlers, with a fatality rate of 80% in horses and 57% in humans.[21,22] The virus presents with an acute febrile respiratory disease and neurologic symptoms (eg, confusion, ataxia, and seizures) in humans. Brain MR imaging showed widespread cortical lesions with sparing of the subcortical white matter on T2-weighted images, similar in appearance to subacute sclerosing panencephalitis caused by measles, the prototypic paramyxovirus.[21,23]

NiV, named after the village where the virus was first isolated, caused a larger pig-borne outbreak of fatal encephalitis and pneumonia in 1998. A total of 265 cases of acute NiV encephalitis with 105 deaths were recorded in Malaysia.[24] The virus crossed the border to neighboring Singapore, which imported live pigs for slaughter, and spread to 11 slaughterhouse workers, of whom 1 died.[25,26] Patients typically presented with fever, vomiting, headache, and dizziness, which developed into severe encephalitis with altered consciousness, brain stem dysfunction, seizures, and myoclonic jerks.[26,27] Neurologic involvement was diverse, including aseptic meningitis, diffuse encephalitis, and focal brain stem and cerebellar involvement. Some early cases were initially ascribed to Japanese encephalitis virus, which had previously caused pig-associated outbreaks in Malaysia, but there were many clinical, epidemiologic, and radiologic red flags that helped to differentiate between the diseases.

As transmission was from bats to pigs and subsequently pigs to humans, pig farms were shut and pigs culled in Malaysia. All importation of live pigs and pork products to Singapore from Malaysia was banned, and slaughterhouses closed, ending the outbreak in 1999. Starting in 2001, multiple NiV outbreaks were reported in West Bengal, India, and multiple locations in Bangladesh, with local epidemics spreading as far southward and westward as Kerala.[24] These outbreaks were caused by direct transmission from bats to humans (via consumption of fresh date palm sap or fruit contaminated by bat secretions or from contact with infected animals) and human-to-human spread of infection (including health care workers).[28] NiV outbreaks mainly caused encephalitis, but respiratory symptoms have been reported in from 29% to two-thirds of cases in different outbreaks.[29] More recent reports of outbreaks in Mindanao, the Philippines (fatal human encephalitis, influenza-like disease, and meningitis) were spread by diseased horses.[30]

MR imaging among Singaporean patients infected with NiV showed multifocal, bilateral tiny (<1 cm in maximum diameter) abnormalities, more within the subcortical and deep white matter (Fig 2) than the cortex, brain stem, or corpus callosum. Most

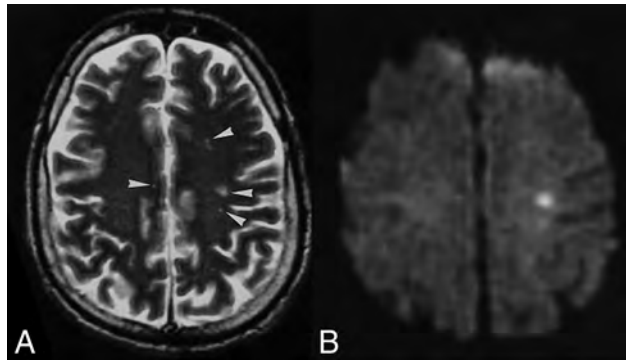

FIG 2. Patient with Nipah virus infection: initial infection. *A*, Multiple punctate white matter lesions (arrowheads) are visible on T2-weighted FSE MR image. *B*, The largest lesion is more prominent on corresponding DWI. Images reprinted from Lim et al.[31]

were prominently detected by DWI compared with T2-weighted images, and some lesions enhanced after contrast media injection.[31,32] In a follow-up MR imaging study among patients in Singapore, multiple small T1-weighted hyperintensities in the cerebral cortex, similar in appearance to laminar cortical necrosis, were noted 1 month after the outbreak, but there were no clinical or radiologic relapse or subacute sclerosing panencephalitis features. These tiny T1-weighted abnormalities also disappeared on later MR imaging studies at 6 months and later (Fig 3). Among a cohort of asymptomatic-but-seropositive Singapore slaughterhouse workers who were exposed to pigs, delayed MR imaging revealed discrete tiny lesions in the brain (but without DWI abnormalities at the late time of acquisition) similar to those detected in symptomatic patients with encephalitis.[33] In the patients in Singapore who were followed-up, 1 patient developed myelopathic symptoms from a cervical spinal cord lesion; a proportion developed psychiatric features, including depression, personality changes, and deficits in attention and memory.

In contrast, follow-up of patients in Malaysia showed a different neuroimaging pattern of extensive patchy and confluent involvement of the cortex, temporal lobe, and pons on T2-weighted images.[34] In a series of 160 Malaysian survivors of Nipah encephalitis, 12 patients had relapses, and 3 had late-onset encephalitis.[35-37] Malaysian patients may have been more severely affected than those in Singapore, perhaps because of the nature of their exposure to the virus.[29] The Singapore MR imaging pattern of tiny DWI abnormalities followed by transient T1 hyperintensities was distinctly different from the characteristic features of herpesvirus and Japanese encephalitis virus and was more consistent with virus-associated microangiopathy and ischemic microinfarction. Postmortem studies performed on Malaysian patients showed both direct neuronal invasion and disseminated microinfarction from vasculitis-induced thrombosis. Small and medium-sized blood vessels in other organs also had similar vasculitic lesions, resulting in endothelial multinucleated syncytia and fibrinoid necrosis.[24,38] In addition, postmortem examination of 2 fatal cases of HeV infections in Australia showed similar findings, which suggested that the pathologic mechanisms might be similar in HeV and NiV and supporting ischemic microinfarction as a partial explanation for MR imaging findings.[39,40]

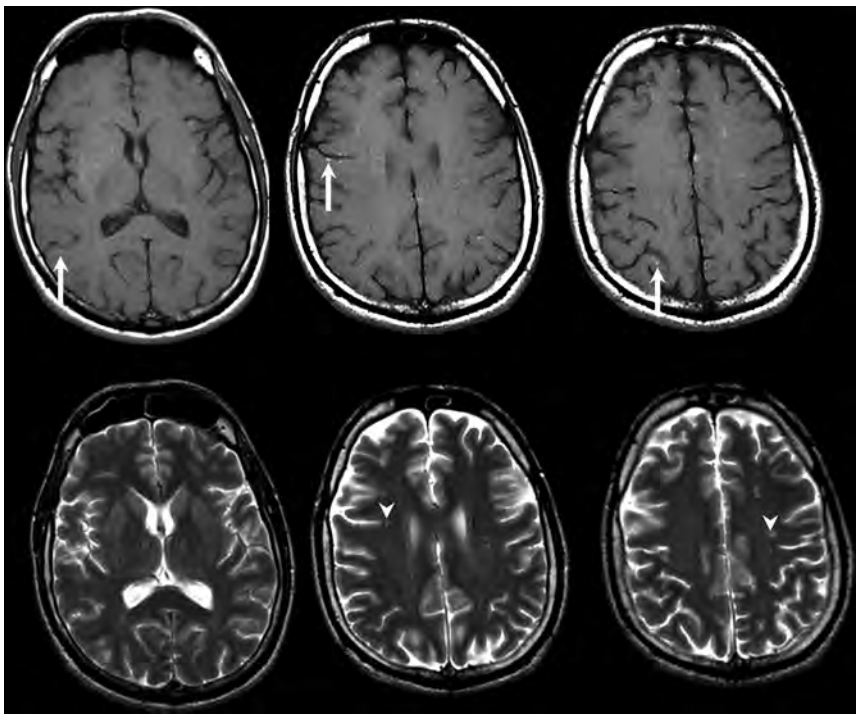

FIG 3. Patient with Nipah virus infection 1 month after infection. Selected axial T1-weighted images (*upper row*) show multifocal punctate high signal intensity on the cortical surfaces (*arrows*) as well as in the white matter. These did not enhance after contrast injection and disappeared on 6-month and subsequent follow-up MR imaging (not shown). Selected T2-weighted images (*lower row*) show noncorresponding multiple tiny focal increased signal intensity (*arrowheads*) in the white matter. These also became smaller or disappeared on follow-up MR imaging (not shown).

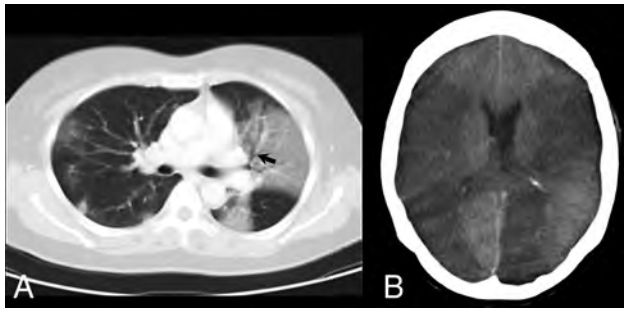

FIG 4. Patient with SARS infection. *A,* Axial 10-mm-section portable chest CT scan shows multifocal and confluent ground-glass opacities bilaterally with air bronchogram (*arrow*) in the left upper lobe. *B,* Axial CT scan of the head shows extensive low-attenuation cerebral infarction involving bilateral middle cerebral and left posterior cerebral artery territories.

Zoonotic Bat-Borne Coronavirus: SARS-CoV and MERS-CoV

SARS-CoV and MERS-CoV are 2 newly discovered β-coronaviruses and have much more aggressive behavior than the 4 endemic α-coronaviruses and discovered β-coronaviruses, which are known causes of the common cold.[41] Severe Acute Respiratory Syndrome (SARS) emerged in 2002 in Guangdong province, China, most probably spread via civet cats as intermediate hosts. Human-to-human transmission and global travel rapidly caused the outbreak to spread to a total of 33 nations. SARS was predominantly an atypical pneumonia with lower respiratory tract infection with limited transmissibility as a rule, yet punctuated by a few superspreading events, and affected 8096 people with 774 deaths.[42] The SARS outbreak ended in 2003, and although a small number of cases have occurred as a result of laboratory accidents or through animal-to-human transmission, there have been no large-scale SARS outbreaks since.[43]

CNS manifestations were noted in several seriously ill patients with multiple complications.[44] Of the 238 patients with SARS in Singapore, 5 had CNS complications, 4 patients were critically ill, and 3 died.[45] CT performed in 4 patients showed cerebral infarction involving the large-artery territories (Fig 4), including the middle cerebral artery in all 4 (bilateral in 1) and posterior cerebral artery in 2; hemorrhagic conversion was noted in 1 patient.[45] An increased incidence of pulmonary embolism and deep venous thrombosis was also noted, especially among critically ill patients treated with intravenous immunoglobulin, raising the possibility of a prothrombotic effect. Hence, the role of hypercoagulable state, iatrogenic measures, systemic hypotension, and cardiac dysfunction in seriously ill patients with SARS has been proposed to explain these findings; increased vigilance against stroke and other thrombotic complications in future outbreaks has been recommended.[45]

MERS coronavirus, with camels as intermediate hosts, emerged in 2012 in the Middle East and spread to 26 other nations.[15] A total of 2121 patients were affected in Saudi Arabia, the epicenter of the initial outbreak, and 2519 total cases and 866 deaths have occurred globally since then, with a high case fatality ratio around 35%.[46] MERS-CoV presents similar to SARS-CoV in the form of severe respiratory distress, which may progress to shock, acute kidney injury, and coagulopathy. MERS outbreaks in most countries have subsided after infection-control measures but are still simmering with sporadic cases, necessitating maintained hospital vigilance and travel-history screening.[46] In 1 patient interpreted as having acute disseminated encephalomyelitis, brain MR imaging on day 28 of illness revealed widespread, bilateral, nonenhancing hyperintense lesions on DWI and T2-weighted imaging within the frontal, temporal, and parietal subcortical white matter and corpus callosum (Fig 5); other findings included 1 patient with bilateral anterior cerebral artery infarction and another with intracranial hemorrhage.[47,48] Four of 23 patients affected by the 2015 outbreak in Korea had neurologic symptoms during or after MERS-CoV treatment. These included Bickerstaff encephalitis overlapping with Guillain-Barré

syndrome and critical illness neuropathy and myopathy; abnormal MR imaging findings were not reported.[49]

Zoonotic Viruses from Putative Bat Hosts and Other Animal Reservoirs

Both Ebola virus and Marburg virus are members of the Filoviridae family, several of which cause severe hemorrhagic fevers.[50,51] Extensive surveillance studies have identified bats as a primary reservoir and nonhuman primates as intermediate hosts, with human consumption of bushmeat implicated in localized outbreaks.[16] Since their discovery, at least 28 Ebola virus outbreaks and 13 Marburg virus outbreaks have occurred in sub-Saharan Africa, often complicated by armed conflict and hostility to medical support teams; hence, neuroimaging is poorly described.[51] Patients with Ebola virus typically have bleeding complications, and CNS involvement includes a case report of meningoencephalitis in a seriously ill patient with multiple organ failure. DWI showed multiple punctate lesions in the corpus callosum, cerebral white matter, and spinal cord, reported as consistent with microvascular occlusion and ischemia. There were no hemorrhagic lesions, and results of Ebola virus polymerase chain reaction testing on CSF were negative.[52]

Apart from bat-borne zoonotic viruses, novel influenza A viruses, including those that normally circulate in pigs (H1N1, H1N2, H3N2), and the highly virulent avian H5N1 and H7N9 viruses, are always threatening to trigger the next pandemic.[53] However, the recent 2009 influenza A H1N1 pandemic did not result in widespread CNS abnormalities, though a few reports have described brain CT or MR imaging findings. Notably, several reports described bilateral thalamic lesions, some with DWI high signal and focal hemorrhage, consistent with acute necrotizing encephalopathy (Fig 6), as well as patients with meningeal enhancement.[54,55] New-onset seizures and encephalopathy were found to commonly occur in patients with underlying neurologic disorders, with swelling of bilateral basal ganglia and thalami and cerebral edema and tonsillar herniation noted on MR imaging.[56] Overall, viruses remain the most likely class of organisms resulting in zoonotic outbreaks affecting the CNS.

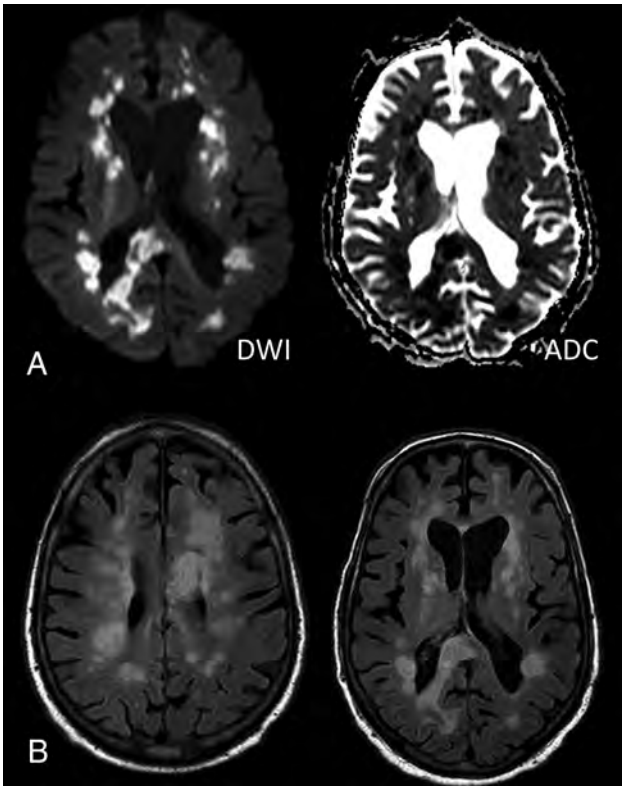

FIG 5. Patient with MERS-CoV infection (on day 28). *A,* DWI and ADC mapping show diffusion restriction of the multiple white matter lesions. *B,* Axial FLAIR images show multiple hyperintense lesions in the subcortical areas and deep white matter of the frontal, temporal, and parietal lobes bilaterally as well as in the corpus callosum. Images reprinted from Arabi et al.[47]

Zoonotic Outbreak from Contaminated Raw Fish: Group B Streptococcus ST283

Group B streptococcus bacteria are common gastrointestinal and genitourinary commensal organisms in humans, and they can cause bacteremia and meningitis in neonates and pregnant women. Invasive group B streptococcus infection is rare in healthy adults, but among patients with chronic underlying comorbidities,[57] it can cause urinary tract and soft-tissue infection, osteomyelitis, infective endocarditis, and pneumonia, but rarely meningitis.[58] In 2015, there was an outbreak of 238 cases of group B streptococcus infections in a foodborne outbreak associated with consumption of Chinese-style raw freshwater fish[59]; 29 patients had meningoencephalitis, fever, meningism, headache, encephalopathy, focal neurologic deficits, and/or seizures.

The invasive serotype III sequence type 283 (ST283) *Streptococcus agalactiae* was identified as the causative organism, with the same strain identified among farmed freshwater fish used for food preparation.[60-62] The outbreak stopped after affected fish imports into Singapore were banned and stricter

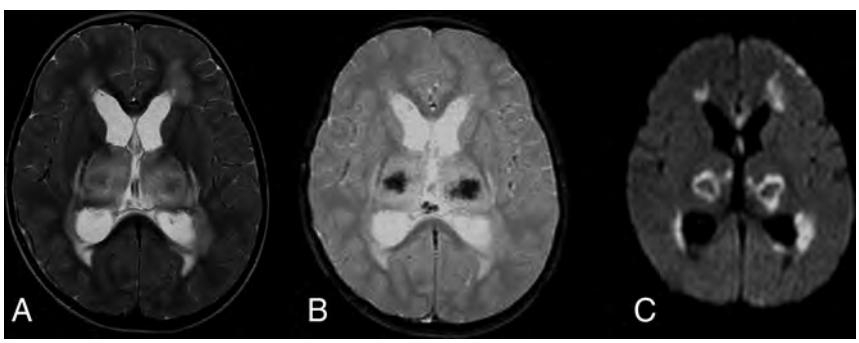

FIG 6. Patient with influenza A H1N1 infection. *A,* Axial T2-weighted image shows symmetric increased signal intensity in the thalami and supratentorial frontal white matter. *B,* T2-weighted gradient-echo image reveals decreased signal intensity in the central portion of the thalami, indicating hemorrhagic necrosis. *C,* Axial DWI reveals restricted diffusion, with a concentric pattern, symmetrically involving the thalami. Images reprinted from Ormitti et al.[54]

rules were established governing raw fish dishes.[60] However, there have been other, smaller outbreaks of human meningitis in Hong Kong and Southeast Asia involving the ST283 strain, suggesting a potential public health threat of this foodborne zoonosis in Asia.[63] Other bacteria have caused smaller zoonotic outbreaks in the past, including meningitis from infected unpasteurized dairy products, but the ST283 outbreak demonstrates the need for vigilance and a broader perspective of CNS involvement in zoonotic disease.[64]

DWI showed single or multiple tiny hyperintensities in the subarachnoid space or ventricles, consistent with small amounts of pus (Fig 7).[62,65] Eight of 14 patients also had DWI lesions in the basal ganglia, corona radiata, thalamus, midbrain, cerebral peduncle and corpus callosum, posterior limb of the internal capsule, frontal and parietal cortex, and white matter; 5 had cerebellar involvement.[65] Hyperintense pus detected by DWI in the subarachnoid space is nonspecific; many bacteria, tuberculosis, or fungi can be responsible. Meningitis may also cause additional MR imaging features such as meningeal enhancement, abscess formation, or hydrocephalus.[66] However, DWI demonstrated high sensitivity, and tiny subtle abnormalities were either less conspicuous or not visualized on T1- or T2-weighted images, suggesting cerebral infarction as a possible mechanism for some of the unusual brain parenchymal involvement.[65]

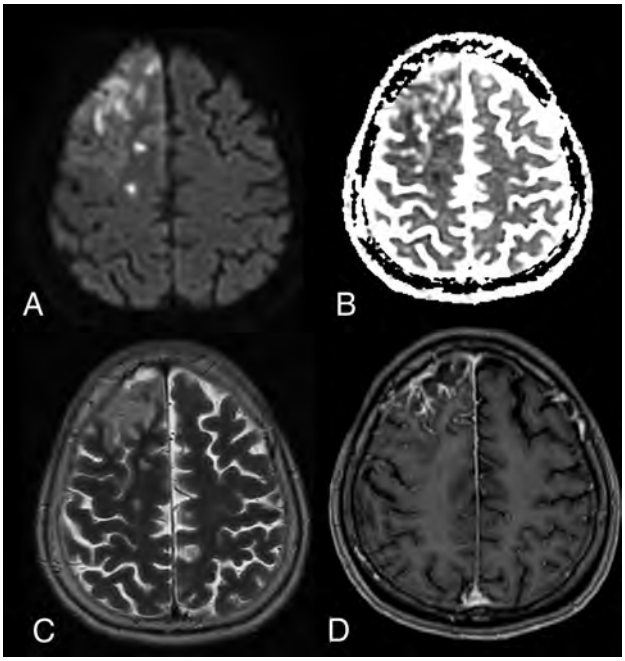

FIG 7. Patient with group B Streptococcus ST283 meningitis. *A,* Axial DWI shows multifocal high signal intensity in the cortex, white matter, and subarachnoid space of the right frontal lobe. *B,* ADC map shows corresponding low ADC. *C,* T2-weighted images show increased signal. *D,* After contrast injection, T1-weighted images show leptomeningeal enhancement, typical of meningitis.

Observations and Lessons Learned from Past Zoonotic Outbreaks

Zoonotic and nonzoonotic infections can affect the CNS by different mechanisms, and neuroradiologists may observe 3 broad patterns of changes on CNS imaging in serious infections. First, there may be direct injury to nervous tissue, entering via hematogenous or neuronal invasion and causing damage to the brain and meninges (eg, herpes virus and Streptococcus).[41] The causative bacterium or virus is usually isolated from the CSF, as has been described in HeV and NiV outbreaks; however, in many case reports for SARS-CoV/SARS-CoV-2, MERS-CoV, and the Ebola virus, the causative viruses were not successfully isolated.[45,47] Second, an immune-mediated response may be responsible for some MR imaging findings, including an early excessive innate immune response such as "cytokine storm" (eg, acute necrotizing encephalopathy similar to cases described in H1N1)[67] and a late immune response, typically taking place some days or weeks after an acute infection (eg, acute disseminated encephalomyelitis and Guillain-Barré syndrome in the peripheral nervous system).[68] Finally, CT and MR imaging manifestations may be the result of cerebrovascular complications, pre-existing comorbidities, or iatrogenic effects; these are often seen in critically ill patients in the intensive care unit. Thus, the imaging findings may not be easily categorized or definitively explained because individual patients may sustain CNS damage from multiple mechanisms.[6]

Neuroradiologists must be aware of CNS imaging features of past zoonotic infections to be prepared for current and future pandemics. In this review, we have highlighted CNS imaging in several past zoonotic infectious outbreaks, summarized in Table 2. The patterns of brain abnormalities include widespread cortical or

Table 2: Key brain neuroimaging findings in zoonotic outbreaks

Zoonotic Pathogen	Brain Neuroimaging Abnormalities
Hendra virus (HeV)	Widespread cortex[21]
Nipah virus (NiV)	Multifocal tiny white matter and others[27,31a] Widespread cortex[27,34,36]
SARS-CoV	Large arterial territory infarction (with hemorrhage)[45]
MERS-CoV	Multifocal white matter and others[47a] Large arterial territory infarction[47a] Intracranial hemorrhage[48]
Ebola virus (EBOV)	Multifocal tiny white matter and others[52a]
Influenza A H1N1 virus	Bilateral thalamus (with hemorrhage) and others[54a] Meningeal enhancement[55]
Streptococcus agalactiae ST283	Multifocal subarachnoid space and others[65a] Meningeal enhancement[65]

[a] Denotes detected on DWI.

multifocal white matter lesions, large arterial territory infarction, hemorrhage, and meningeal enhancement. Some may be relevant to the current COVID-19 pandemic, and some may eventually turn out not to be relevant or even misleading. Knowledge of typical MR imaging features of bacterial meningitis enabled authors to identify tiny amounts of pus in the subarachnoid space and ventricles in the ST283 group B Streptococcus outbreak with high sensitivity, and knowledge of Japanese encephalitis virus features enabled researchers to eliminate it during the NiV outbreak. Being open to the possibility of vasculitis-induced and coagulopathic effects of infection enabled the observations in NiV and SARS. DWI is extremely sensitive to small lesions, though it is challenging to distinguish between ischemic and infective brain damage; however, in an outbreak of infectious disease, the challenges of transportation and acquiring MR imaging in severely ill and intubated patients may mean that CT may be more appropriately used in these situations.[45,69] Finally, newer MR imaging pulse sequences such as susceptibility-weighted imaging and perfusion MR imaging may contribute to the original research literature on COVID-19, which is still being written.

CONCLUSIONS

In military history, generals and commanders are cautioned against "fighting the last war" by using outdated equipment, tactics, and concepts and failing to realize that their enemies and situations have changed. Martial language is often used to describe the current pandemic as a war, with troops, frontlines, and victories. Although Mark Twain famously said that history may not repeat itself (in exactly the same manner), it certainly has many common features. Neuroradiologists should recognize the MR imaging and CT imaging features of past zoonotic outbreaks but be prepared to recognize new imaging manifestations as data emerge. As health care professionals worldwide labor to suppress the COVID-19 pandemic, neuroradiologists should not be fighting the last war; we should instead unite and learn together in this unprecedented shared struggle.[5,70]

ACKNOWLEDGMENTS

The authors thank Ms Qianhui Cheng, Mr Shawn Teo Yi En, Dr T. Umapathi, and Dr Ng Yuen Li for their kind contributions.

Disclosures: Lin-Fa Wang—*RELATED: Grant:* National Research Foundation, *Comments*: Grants for research from 2013 to 2019.* *Money paid to the institution.

REFERENCES

1. Wu F, Zhao S, Yu B, et al. **A new coronavirus associated with human respiratory disease in China.** *Nature* 2020;579:265–69 CrossRef Medline
2. Mao L, Jin H, Wang M, et al. **Neurologic manifestations of hospitalized patients with coronavirus disease 2019 in Wuhan, China.** *JAMA Neurol* 2020;77:683 CrossRef Medline
3. Mackenzie JS. **Emerging zoonotic encephalitis viruses: lessons from Southeast Asia and Oceania.** *J Neurovirol* 2005;11:434–40 CrossRef Medline
4. Munoz LS, Garcia MA, Gordon-Lipkin E, et al. **Emerging viral infections and their impact on the global burden of neurological disease.** *Semin Neurol* 2018;38:163–75 CrossRef Medline
5. Mahajan A, Hirsch JA. **Novel coronavirus: what neuroradiologists as citizens of the world need to know.** *AJNR Am J Neuroradiol* 2020;41:552–54 CrossRef Medline
6. Morris M, Zohrabian VM. **Neuroradiologists, be mindful of the neuroinvasive potential of COVID-19.** *AJNR Am J Neuroradiol* 2020;41:E37–E39 CrossRef Medline
7. Parrish CR, Holmes EC, Morens DM, et al. **Cross-species virus transmission and the emergence of new epidemic diseases.** *Microbiol Mol Biol Rev* 2008;72:457–70 CrossRef Medline
8. Daszak P, Cunningham AA, Hyatt AD. **Emerging infectious diseases of wildlife—threats to biodiversity and human health.** *Science* 2000;287:443–49 CrossRef Medline
9. Jones KE, Patel NG, Levy MA, et al. **Global trends in emerging infectious diseases.** *Nature* 2008;451:990–93 CrossRef Medline
10. Prentice MB, Rahalison L. **Plague.** *Lancet* 2007;369:1196–207 CrossRef Medline
11. Wang LF, Cowled C. *Bats and Viruses: A New Frontier of Emerging Infectious Diseases*. 2015. Hoboken, NJ: Wiley
12. Hemachudha T, Laothamatas J, Rupprecht CE. **Human rabies: a disease of complex neuropathogenetic mechanisms and diagnostic challenges.** *Lancet Neurol* 2002;1:101–09 CrossRef Medline
13. Field HE. **Bats and emerging zoonoses: henipaviruses and SARS.** *Zoonoses Public Health* 2009;56:278–84 CrossRef Medline
14. Wang L, Anderson DE, Mackenzie JS, et al. **From Hendra to Wuhan: what has been learned in responding to emerging zoonotic viruses.** *Lancet* 2020;6736:1–2 CrossRef Medline
15. De Wit E, Van Doremalen N, Falzarano D, et al. **SARS and MERS: recent insights into emerging coronaviruses.** *Nat Rev Microbiol* 2016;14:523–34 CrossRef Medline
16. Wang LF, Anderson DE. **Viruses in bats and potential spillover to animals and humans.** *Curr Opin Virol* 2019;34:79–89 CrossRef Medline
17. Medina RA, García-Sastre A. **Influenza A viruses: new research developments.** *Nat Rev Microbiol* 2011;9:590–603 CrossRef Medline
18. Hautala T, Mähönen S-M, Sironen T, et al. **Central nervous system-related symptoms and findings are common in acute Puumala hantavirus infection.** *Ann Med* 2010;42:344–51 CrossRef Medline
19. Hygino da Cruz LC, Nascimento OJM, Lopes F, et al. **Neuroimaging findings of Zika virus–associated neurologic complications in adults.** *AJNR Am J Neuroradiol* 2018;39:1967–74 CrossRef Medline
20. Murray K, Rogers R, Selvey L, et al. **A novel morbillivirus pneumonia of horses and its transmission to humans.** *Emerg Infect Dis* 1995;1:31–33 CrossRef Medline
21. O'Sullivan JD, Allworth AM, Paterson DL, et al. **Fatal encephalitis due to novel paramyxovirus transmitted from horses.** *Lancet* 1997;349:93–95 CrossRef Medline
22. Eaton BT, Broder CC, Middleton D, et al. **Hendra and Nipah viruses: different and dangerous.** *Nat Rev Microbiol* 2006;4:23–35 CrossRef Medline
23. Öztürk A, Gürses C, Baykan B, et al. **Subacute sclerosing panencephalitis: clinical and magnetic resonance imaging evaluation of 36 patients.** *J Child Neurol* 2002;17:25–29 CrossRef Medline
24. Chua KB, Goh KJ, Wong KT, et al. **Fatal encephalitis due to Nipah virus among pig-farmers in Malaysia.** *Lancet* 1999;354:1–3 CrossRef Medline
25. Paton NI, Leo YS, Zaki SR, et al. **Outbreak of Nipah-virus infection among abattoir workers in Singapore.** *Lancet* 1999;354:1253–56 CrossRef Medline
26. Lee KE, Umapathi T, Tan CB, et al. **The neurological manifestations of Nipah virus encephalitis, a novel paramyxovirus.** *Ann Neurol* 1999;46:428–32 CrossRef Medline
27. Goh KJ, Tan CT, Chew NK, et al. **Clinical features of Nipah virus encephalitis among pig farmers in Malaysia.** *N Engl J Med* 2000;342:1229–35 CrossRef Medline
28. Rahman MA, Hossain MJ, Sultana S, et al. **Date palm sap linked to Nipah virus outbreak in Bangladesh, 2008.** *Vector-Borne Zoonotic Dis* 2012;12:65–72 CrossRef Medline

29. Ang BSP, Lim TCC, Wang L. **Nipah virus infection.** *J Clin Microbiol* 2018;56:e01875-17 CrossRef Medline
30. Ching PK, de Los Reyes VC, Sucaldito MN, et al. **Outbreak of henipavirus infection, Philippines, 2014.** *Emerg Infect Dis* 2015;21:328–31 CrossRef Medline
31. Lim CCT, Sitoh YY, Hui F, et al. **Nipah viral encephalitis or Japanese encephalitis? MR findings in a new zoonotic disease.** *AJNR Am J Neuroradiol* 2000;21:455–61 Medline
32. Lim CC, Sitoh YY, Lee KE, et al. **Meningoencephalitis caused by a novel paramyxovirus: an advanced MRI case report in an emerging disease.** *Singapore Med J* 1999;40:356–58 Medline
33. Lim CC, Lee WL, Leo YS, et al. **Late clinical and magnetic resonance imaging follow up of Nipah virus infection.** *J Neurol Neurosurg Psychiatry* 2003;74:131–33 CrossRef Medline
34. Sarji SA, Abdullah BJJ, Goh KJ, et al. **MR imaging features of Nipah encephalitis.** *AJR Am J Roentgenol* 2000;175:437–42 CrossRef Medline
35. Tan CT, Goh KJ, Wong KT, et al. **Relapsed and late-onset Nipah encephalitis.** *Ann Neurol* 2002;51:703–08 CrossRef Medline
36. Sejvar JJ, Hossain J, Saha SK, et al. **Long-term neurological and functional outcome in Nipah virus infection.** *Ann Neurol* 2007;62:235–42 CrossRef Medline
37. Abdullah S, Chang LY, Rahmat K, et al. **Late-onset Nipah virus encephalitis 11 years after the initial outbreak: a case report.** *Neurol Asia* 2012;17:71–74
38. Chua KB, Bellini WJ, Rota PA, et al. **Nipah virus: a recently emergent deadly paramyxovirus.** *Science* 2000;288:1432–35 CrossRef Medline
39. Wong KT, Robertson T, Ong BB, et al. **Human Hendra virus infection causes acute and relapsing encephalitis.** *Neuropathol Appl Neurobiol* 2009;35:296–305 CrossRef Medline
40. Wong KT, Shieh WJ, Kumar S, et al. **Nipah virus infection: pathology and pathogenesis of an emerging paramyxoviral zoonosis.** *Am J Pathol* 2002;161:2153–67 CrossRef Medline
41. Matías-Guiu J, Gomez-Pinedo U, Montero-Escribano P, et al. **Should we expect neurological symptoms in the SARS-CoV-2 epidemic?** *Neurologia* 2020;35:170–75 CrossRef Medline
42. Ruan S. **Likelihood of survival of coronavirus disease 2019.** *Lancet Infect Dis* 2020;20:630–31 CrossRef Medline
43. Wong TW. "**Will the SARS epidemic recur?" A retrospective analysis of the experts' opinions.** *J Epidemiol Community Health* 2006;60:87 Medline
44. Lau K, Yu W, Chu C, et al. **Possible central nervous system infection by SARS coronavirus.** *Emerg Infect Dis* 2004;10:2–4 CrossRef Medline
45. Umapathi T, Kor AC, Venketasubramanian N, et al. **Large artery ischaemic stroke in severe acute respiratory syndrome (SARS).** *J Neurol* 2004;251:1227–31 CrossRef Medline
46. World Health Organization. **MERS situation update.** 2020. https://applications.emro.who.int/docs/EMCSR254E.pdf?ua=1&ua=1. Accessed May 12, 2020
47. Arabi YM, Harthi A, Hussein J, et al. **Severe neurologic syndrome associated with Middle East respiratory syndrome corona virus (MERS-CoV).** *Infection* 2015;43:495–501 CrossRef Medline
48. Algahtani H, Subahi A, Shirah B. **Neurological complications of Middle East respiratory syndrome coronavirus: a report of two cases and review of the literature.** *Case Rep Neurol Med* 2016;2016:1–6 CrossRef Medline
49. Kim JE, Heo JH, Kim HO, et al. **Neurological complications during treatment of Middle East respiratory syndrome.** *J Clin Neurol* 2017;13:227–33 CrossRef Medline
50. Brauburger K, Hume AJ, Mühlberger E, et al. **Forty-five years of Marburg virus research.** *Viruses* 2012;4:1878–927 CrossRef Medline
51. Malvy D, McElroy AK, de Clerck H, et al. **Ebola virus disease.** *Lancet* 2019;393:936–48 CrossRef Medline
52. Chertow DS, Nath A, Suffredini AF, et al. **Severe meningoencephalitis in a case of Ebola virus disease: a case report.** *Ann Intern Med* 2016;165:301–04 CrossRef Medline
53. Neumann G, Kawaoka Y. **Predicting the next influenza pandemics.** *J Infect Dis* 2019;219:S14–20 CrossRef Medline
54. Ormitti F, Ventura E, Summa A, et al. **Acute necrotizing encephalopathy in a child during the 2009 influenza A(H1N1) pandemia: MR imaging in diagnosis and follow-up.** *AJNR Am J Neuroradiol* 2010;31:396–400 CrossRef Medline
55. Zeng H, Quinet S, Huang W, et al. **Clinical and MRI features of neurological complications after influenza A (H1N1) infection in critically ill children.** *Pediatr Radiol* 2013;43:1182–89 CrossRef Medline
56. Prerna A, Lim JY, Tan NW, et al. **Neurology of the H1N1 pandemic in Singapore: a nationwide case series of children and adults.** *J Neurovirol* 2015;21:491–99 CrossRef Medline
57. Skoff TH, Farley MM, Petit S, et al. **Increasing burden of invasive group B streptococcal disease in nonpregnant adults, 1990–2007.** *Clin Infect Dis* 2009;49:85–92 CrossRef Medline
58. Oyanguren B, Esteban L, Guillán M, et al. **Central nervous system involvement in adult patients with invasive infection caused by Streptococcus agalactiae.** *Neurologia* 2015;30:158–62 CrossRef Medline
59. Tan S, Lin Y, Foo K, et al. **Group B streptococcus serotype III sequence type 283 bacteremia associated with consumption of raw fish, Singapore.** *Emerg Infect Dis* 2016;22:1970–73 CrossRef Medline
60. Chau ML, Chen SL, Yap M, et al. **Group B Streptococcus infections caused by improper sourcing and handling of fish for raw consumption, Singapore, 2015.** *Emerg Infect Dis* 2017;23:1982–90 CrossRef Medline
61. Wang R, Li L, Huang YY, et al. **Pathogenicity of human ST23 Streptococcus agalactiae to fish and genomic comparison of pathogenic and non-pathogenic isolates.** *Front Microbiol* 2017;8:1–11 CrossRef Medline
62. Kalimuddin S, Chen SL, Lim CTK, et al. **2015 epidemic of severe streptococcus agalactiae sequence type 283 infections in Singapore associated with the consumption of raw freshwater fish: a detailed analysis of clinical, epidemiological, and bacterial sequencing data.** *Clin Infect Dis* 2017;64:S145–52 CrossRef Medline
63. Ip M, Cheuk ESC, Tsui MHY, et al. **Identification of a Streptococcus agalactiae serotype III subtype 4 clone in association with adult invasive disease in Hong Kong.** *J Clin Microbiol* 2006;44:4252–54 CrossRef Medline
64. van Samkar A, Brouwer MC, van der Ende A, et al. **Zoonotic bacterial meningitis in human adults.** *Neurology* 2016;87:1171–79 CrossRef Medline
65. Tan K, Wijaya L, Chiew H-J, et al. **Diffusion-weighted MRI abnormalities in an outbreak of Streptococcus agalactiae serotype III, multilocus sequence type 283 meningitis.** *J Magn Reson Imaging* 2017;45:507–14 CrossRef Medline
66. Kawaguchi T, Sakurai K, Hara M, et al. **Clinico-radiological features of subarachnoid hyperintensity on diffusion-weighted images in patients with meningitis.** *Clin Radiol* 2012;67:306–12 CrossRef Medline
67. Poyiadji N, Shahin G, Noujaim D, et al. **COVID-19–associated acute hemorrhagic necrotizing encephalopathy: CT and MRI features.** *Radiology* 2020;296:E119–20 CrossRef Medline
68. Tchoyoson LCC. **Neuroimaging in postinfectious demyelination and nutritional disorders of the central nervous system.** *Neuroimaging Clin North Am* 2011;21:843–58 CrossRef Medline
69. Schaefer PW, Grant PE, Gonzalez RG. **Diffusion-weighted MR imaging of the brain.** *Radiology* 2000;217:331–45 CrossRef Medline
70. Lim CCT, Tsuchiya K. "No Man is an Island" John Donne. *AJNR Am J Neuroradiol* 2020;349:6544 CrossRef Medline

Stapedial Artery: From Embryology to Different Possible Adult Configurations

S. Bonasia, S. Smajda, G. Ciccio, and T. Robert

ABSTRACT

SUMMARY: The stapedial artery is an embryonic artery that represents the precursor of some orbital, dural, and maxillary branches. Although its embryologic development and transformations are very complex, it is mandatory to understand the numerous anatomic variations of the middle meningeal artery. Thus, in the first part of this review, we describe in detail the hyostapedial system development with its variants, referring also to some critical points of ICA, ophthalmic artery, trigeminal artery, and inferolateral trunk embryology. This basis will allow the understanding of the anatomic variants of the middle meningeal artery, which we address in the second part of the review.

ABBREVIATIONS: MMA = middle meningeal artery; OA = ophthalmic artery; SA = stapedial artery

The stapedial artery (SA) is an embryologic artery that allows the development of orbital and dural arteries, and also of the maxillary branches. Its complex embryologic development explains numerous anatomic variations of the middle meningeal artery (MMA) and orbital arteries. Few anatomists[1-7] have dissected a human middle ear that bore a persistent SA and described the origin and course of this artery. Ear, nose, and throat surgeons reported cases discovered during middle ear surgeries, which explains the technical difficulties of the surgery in the presence of a persistent SA.[8-20] More recently, neuroradiologists have paid particular attention to this anatomic variant.[21-26] These studies, associated with the comparative anatomy,[27-29] allow the understanding of the persistence of the SA. In this article, after a quick refresh concerning hyostapedial, carotid, and ophthalmic systems, the anatomic variations, including the SA, are presented and explained.

History

The first cadaveric case of persistent SA was described by Hyrtl[30] in 1836, who called attention to an artery that runs across the obturator of the stapes in a human cadaver, with some similarities with a vessel found in hibernating animals. In the first half of the 20th century, the phenomenal publication by Padget,[31] based on the dissections of 22 human embryos of the Carnegie collection, provided a great deal of information about the embryologic development of the craniofacial arteries and, in particular, of the hyostapedial system. In the same period, Altmann[32] furnished a comprehensive explanation of the development of the aortic arches and of the carotid system variants. However, not until the 1960s, do we find the first angiographic demonstration of MMA variations and, in particular, the persistence of an SA.[33,34] At the end of the 1970s, Lasjaunias was able to give a comprehensive explanation of all variations that implicate the SA.[23,24] This group's more famous articles[23-25,35-38] were published between 1975 and 1990 and are summarized in their textbook.[39] Diamond[5,27,28] also published some articles based on the comparative anatomy, principally with the great apes, that increased our understanding of the stapedial system. In these past 3 decades, a few case reports of interesting anatomic variations that implicate the SA were published.[17,40-47]

Comparative Anatomy

The studies of comparative anatomy were fundamental in the understanding of the embryologic development of the SA. At the beginning of the 20th century, Tandler,[48] when studying the SA development in rats, explained the SA regression and the role of the external carotid artery in the formation of the MMA. Rats differed from human embryos because the supraorbital branch of the SA is primarily dependent on the first aortic arch (mandibular branch). Fuchs,[49] in the rabbit, also showed that the first 2

Received April 17, 2020; accepted after revision May 18.

From the Department of Neurosurgery (S.B., T.R.), Neurocenter of the Southern Switzerland, Lugano, Switzerland; Department of Interventional Neuroradiology (S.S., G.C.), Rothschild Foundation Hospital, Paris, France; and University of Southern Switzerland (T.R.), Lugano, Switzerland.

Please address correspondence to Thomas Robert, MD, Department of Neurosurgery, Neurocenter of the Southern Switzerland, Regional Hospital of Lugano, Via Tesserete 46, CH-6903 Lugano, Switzerland; e-mail: thomas.robert43@gmail.com

Indicates open access to non-subscribers at www.ajnr.org

http://dx.doi.org/10.3174/ajnr.A6738

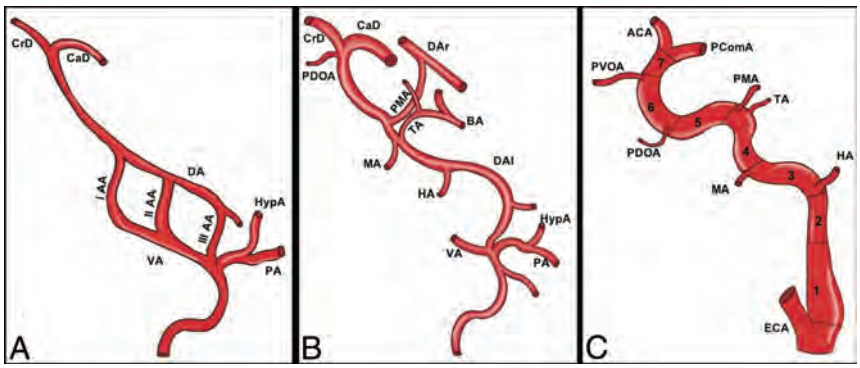

FIG 1. Embryologic segments of the ICA. Consecutive stages of ICA embryologic development. The first stages of development (*A*) are characterized by the presence of 3 aortic arches that link the ventral aorta (VA) and the dorsal aorta (DA). The VA regresses together with the ventral part of the aortic arches. The dorsal remnants of the aortic arches persist as embryonic arteries. These embryonic arteries divide the ICA into 7 embryologic segments: 1) the cervical segment: it derives from the remnant of the third aortic arch (III AA); 2) the ascending intrapetrous segment: it is the remnant of the DA between the second (II AA) and third (III AA) aortic arches; the division point between segments 2 and 3 is at the point of origin of the hyoid artery (HA), that is, the dorsal remnant of the second aortic arch (II AA); 3) the horizontal intrapetrous segment: it is the remnant of the DA between the first (I AA) and second (II AA) aortic arches; the division point is at the point of origin of the mandibular artery (MA), which corresponds to the dorsal remnant of the first aortic arch (I AA); 4) the intracavernous ascending segment: it originates from the DA between the first aortic arch (I AA) and the primitive maxillary artery (PMA), which connects the DA of the 2 sides (dorsal aorta left [DAl]; dorsal aorta right [DAr]). The trigeminal artery origins at the junction between the segment 4 and 5 of the ICA; this latter represents a primitive connection between the cavernous ICA and the basilar artery (BA); 5) the horizontal intracavernous segment: it derives from the DA between the PMA and the primitive dorsal OA (PDOA); 6) the clinoid segment: it corresponds to the DA between the PDOA and the primitive ventral OA; and 7) the terminal segment: the terminal ICA between primitive ventral OA and the primitive ICA bifurcation into the future anterior cerebral artery (ACA) and the future posterior communicating artery (PComA). The figure also shows the hypoglossal artery (HypA) and the proatlantal artery (PA), which originate proximal to the third aortic arch and will contribute to the formation of the external carotid artery (ECA) branches.

aortic arches participate in the formation of the external carotid artery as in human embryos. More recently, Diamond[28] and Falk[29] compared the development of the SA between human and great ape embryos and highlighted some analogies.

Embryology

The development and regression of the SA is strictly related to some embryonic systems. In this part of our article, we summarize the main steps of the ICA and ophthalmic artery (OA) development. We present a more-detailed description of the hyostapedial system to understand the different possible adult variations related to this artery.

The Carotid System. Because a detailed description of the ICA embryologic development is beyond the scope of this article, we focused only on the understanding of the "aberrant flow of the ICA." It consists of an intratympanic course of the ICA and could be associated with a persistent SA and consequent variation in the origin of the MMA. The principal steps of ICA development are summarized in Fig 1.

In the first stage of Padget (4–5 mm embryos), the first 2 aortic arches initiate their natural regression, which allows the ICA to be individualized. The embryologich segments of the ICA are derived from the third aortic arch and from the dorsal aorta cranial to the third aortic arch.[31,32,39] The dorsal aorta also regresses at the same time between the third and fourth aortic arches. In terms of embryology, the ICA was divided by Lasjaunias and Santoyo-Vazquez[50] into 7 different segments. The first segment corresponds to the third aortic arch from the origin of the ventral pharyngeal artery (the future external carotid artery) to the junction between the third aortic arch and the dorsal aorta. The second segment is the dorsal aorta between the second and third aortic arch. The third segment is the dorsal aorta between the first and second aortic arch. The fourth segment is the dorsal aorta between the first aortic arch and the origin of the trigeminal artery (and the primitive maxillary artery). The fifth segment is the dorsal aorta between the origin of the trigeminal artery (and the primitive maxillary artery) and the origin of the primitive dorsal OA (the future inferolateral trunk). The sixth segment is between the origin of the primitive dorsal OA and the origin of the primitive ventral OA. The seventh segment is between the primitive ventral OA and the primitive carotid bifurcation.[23,24,31,39]

It is important to note that the carotid bulb does not have the same embryologic origin as the other segments of the ICA. It originates from the pharyngo-occipital system, which easily explains variations in origin of the ascending pharyngeal and occipital arteries. Agenesis or abnormal regression of ≥1 segment of the ICA explains an intratympanic course of the ICA[12] (by pharyngo-carotid anastomosis) and also the different type of "reperfusion" in the case of ICA agenesis.[32] The intratympanic course of the ICA, also named as an "aberrant flow of the ICA," is the consequence of the abnormal regression of the first and second segments, with anastomosis between the inferior tympanic artery (from the ascending pharyngeal artery) and the caroticotympanic artery (from the carotid artery) that distally infuses the ICA. The pseudo-ICA, consequently, has an intratympanic course without passing through the stapes.[12,39,51]

Hyostapedial System. "Hyostapedial artery" is the term used to describe the complete embryologic development of the second aortic arch. The SA, which develops from the hyoid artery and takes its name after passing through the crus of the stapes, is an embryonic artery present between Padget[31] stages III and VI (9–24 mm). This is an important embryologic system from which numerous dural, orbital, and facial arteries develop. The steps of SA development are summarized in Table 1.

Table 1: Major embryologic changes in the formation of the SA

Stage	Embryo size (mm)	Major evolutions	Graphic Illustration
I	4-5	- Regression of the second aortic arch - Hyoid artery (HA) formation (dorsal remnant of the 2nd aortic arch)	
II	5-6	- Elongation of the hyoid artery (HA) - Annexation of the mandibular artery (MA) territory (1st aortic arch) by the hyoid artery (2nd aortic arch)	
III/ IV	7-12 12-14	- Cranial growing of the hyoid artery (stapedial artery) passing into the middle ear (crus of the stapes) - Extension of the two branches of the stapedial artery: Supraorbital (SOA) and Maxillomandibular (MxMA)	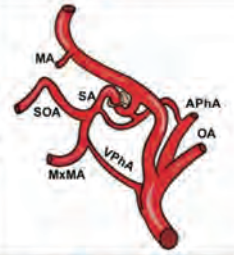
V	16-18	- Maximal development of the stapedial artery - Annexation of the supraorbital branch (SOA) by the ophthalmic artery (PDOA, PVOA) - Regression of the trans-osseous (superior orbital fissure) segment of the supraorbital branch	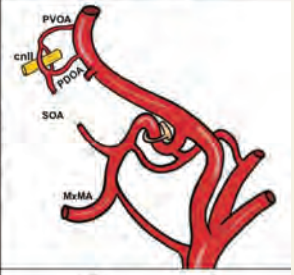
VI	20-24	- Annexation of the maxillomandibular branch by the ventral pharyngeal artery - Regression of the intratympanic segment of the stapedial artery	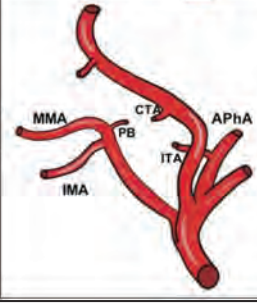

The hyoid artery is the dorsal remnant of the second aortic arch, which regresses early in the embryologic development (4-5 mm, Padget[31] stage I).[2,12] After this arch regression, at approximately the 5–6-mm stage (Padget[31] stage II), the hyoid artery presents a rapid lateral elongation between the beginning of the 7th and 19th weeks of gestation, when it gives an anastomosis to the mandibular artery (remnant of the first aortic arch).[31] During Padget[31] stage III (7–12-mm embryos), the hyoid artery is prominent and grows cranially, passing, as the SA, through the crus of the stapes. In contrast, the mandibular artery is short and difficult to identify. During this stage, the initial forms of the 2 main branches of the SA (supraorbital and maxillomandibular divisions) are visible, even if they are definitively established only in Padget[31] stage IV (12–14 mm).

At the 16–18-mm stage (Padget[31] stage V), the SA continues its elongation to the gasserian region, passing into the future tympanic cavity and, particularly, through the crus of the stapes, reaching its maximum development.[23,31,32] The supraorbital artery, which follows the ophthalmic root of the trigeminal nerve, allows the development of orbital branches (supraorbital,

Table 2: Summary of embryologic steps of the stapedial and ophthalmic systems

Stapedial System	Embryo Size (mm)	Ophthalmic System
Regression of the second aortic arch; hyoid artery formation (dorsal remnant of the second aortic arch)	4–5	Primitive maxillary artery as temporary branch; primitive dorsal OA appearance
Elongation of the hyoid artery; annexation of the mandibular artery (first aortic arch) by the hyoid artery (second aortic arch)	5–6	Primitive hyaloid artery = plexiform channels; primitive ventral OA appearance
Cranial growing of the hyoid artery (SA) passing into the middle ear (crus of the stapes)	7–14	Formation of primitive hyaloid and common ciliary arteries
Maximum development of the SA; extension of the 2 branches of the SA, supraorbital and maxillomandibular	16–19	Migration in origin of the primitive ventral OA; regression of the primitive dorsal OA; formation of the anastomotic ring
Regression of the transosseous (superior orbital fissure) segment of the supraorbital branch	20–24	Ventral interruption of the anastomotic ring; annexation of the supraorbital branch by the OA

lacrimal, ethmoids, and frontal arteries) and also of the MMA.[39] The maxillomandibular artery exits the cranial cavity through the foramen spinosum and, extracranially, gives its 2 branches: infraorbital and mandibular arteries (the future infraorbital and inferior alveolar arteries). After this maximum development of the SA, 2 annexations and 2 regressions occur to give the adult configuration of the MMA. Intracranially, the orbital branches are annexed by the primitive OA and the trans-sphenoidal segment of the supraorbital branch regresses, leaving an anastomotic artery between the anterior branch of the MMA and the lacrimal artery (the sphenoidal artery), which penetrates the orbit through the superior orbital fissure. Extracranially, the ventral pharyngeal artery annexes the maxillomandibular artery of the SA, forming the proximal stem of the MMA and becoming the external carotid artery. Consequently, by flow reversal into the SA, its tympanic portion regresses and leaves, as remnants, the caroticotympanic artery (from the ICA) and the superior tympanic artery (from the petrous branch of the MMA). These annexations and regressions with regard to the SA happen during Padget[31] stage VI (20–24-mm embryos).[31,39]

OA. The embryogenesis of the primitive OA is related in some phases to the hyostapedial systems. These phases are summarized and related to the concomitant SA steps of development presented in Table 2. The formation of the OA depends on 2 different arteries during the 4–18-mm stages; the primitive dorsal OA and the primitive ventral OA. The primitive dorsal OA develops from the cavernous segment of the primitive ICA and the primitive ventral OA develops from the anterior division of the primitive ICA. The primitive dorsal OA penetrates the orbit through the superior orbital fissure and the primitive ventral OA penetrates through the optic canal.

Next, 2 major anastomoses between these 2 arteries are formed. The first one is an intraorbital plexiform anastomosis supplied by the 2 arteries around the optic nerve (the future second segment of the OA). The second anastomosis is intradural between the primitive ventral OA and the primitive ICA to form the definitive supraclinoidal origin of the OA. The proximal portion of the primitive ventral OA (between its origin on the ACA and its anastomosis with the ICA), then regresses to give the adult stem of the OA.

In the following step, the proximal part of the primitive dorsal OA regresses and its remnant becomes the inferolateral trunk of the primitive ICA. Concomitantly, in 7- and 24-mm embryos (stages III–VI of Padget), the SA arises from the primitive hyoid arch of the petrous ICA. As described above, its supraorbital artery enters the orbit to give orbital branches. It divides into 2 different branches: the ethmoidonasal and lacrimal arteries. The ethmoidonasal artery anastomoses with the primitive OA at the arterial ring around the optic nerve, as previously described. The trans-sphenoidal part of the supraorbital artery then regresses, and its orbital branches are annexed by the primitive OA to give the adult conformation.

Trigeminal Artery. The trigeminal artery represents one of the carotid-basilar anastomoses, which appears in 4–5-mm embryos (Padget[31] stage I) and disappears in 12-mm embryos (Padget[31] stage III). It origins from the basilar artery, between the superior and the anteroinferior cerebellar arteries, passes medial to the gasserian ganglion, and follows the trigeminal nerve to the primitive ICA at the level of the junction between the fourth and fifth segments of the ICA. The trigeminal artery has a common origin on the ICA with the primitive maxillary artery. The carotid remnant of these 2 primitive arteries will be the future meningohypophyseal trunk, from which the lateral clival, marginal tentorial, and inferior hypophyseal arteries will originate.[31,32] The basilar remnant of the trigeminal artery could be considered responsible for MMA possible origin from the basilar artery. In fact, when this trigeminal remnant anastomoses with a persistent SA, the final MMA will arise from the BA. The details of this variant are explained in Part 2 of our article.

Formation of the Inferolateral Trunk. As supported by the theory of Lasjaunias,[23,24,39] with regard to the embryology of the OA, the inferolateral trunk is the carotid remnant of the primitive dorsal OA. The primitive dorsal OA develops from the cavernous segment of the primitive ICA and penetrates the orbit through the superior orbital fissure. In 40-mm embryos, the proximal part of the primitive dorsal OA regresses, and its remnant becomes the inferolateral trunk. At the adult configuration, the inferolateral trunk is composed of 4 branches: 1) superior branch, which supplies the roof of the cavernous sinus; 2) anteromedial branch,

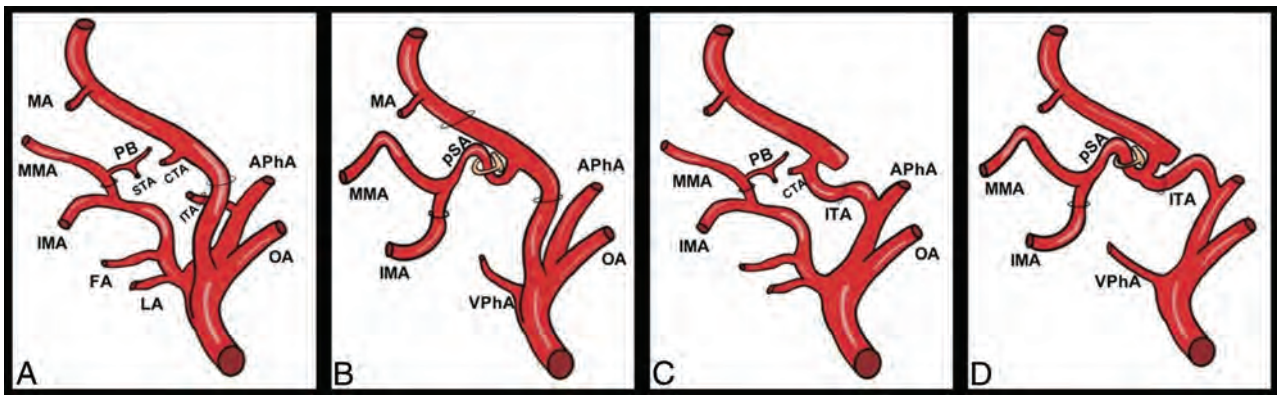

FIG 2. Persistent SA and intratympanic flow of the ICA. *A*, The normal regression process of the hyostapedial system. After the SA proximal regression, its proximal remnant originates from the ICA as the carotico-tympanic artery (CTA). Its distal part is annexed by the ventral pharyngeal artery, the future external carotid artery, to give the internal maxillary artery its first and major branch, the middle meningeal artery (MMA). The MMA side of the SA persists as the petrosal branch (PB), which gives birth to the superior tympanic artery (STA). The anastomotic branch to the hyostapedial system from the ascendant pharyngeal artery (APhA) persists as the inferior tympanic artery (ITA). The CTA, STA, and ITA contribute to the adult vascularization of the middle ear. *B*, Persistent SA. In the case of complete SA persistency, this artery originates from the petrous ICA and gives, intracranially, the MMA, and the internal maxillary artery exits the middle fossa skull base through the foramen spinosum as the extracranial branch. This variant is due to the lack of annexation of the maxillary-mandibular branch by the ventral pharyngeal artery. *C*, Pseudopetrous or aberrant intratympanic ICA. This variant is due to the agenesis of the cervical ICA (third aortic arch). The cervical ICA agenesis is bypassed through a hypertrophic inferior tympanic artery, which courses from the APhA through the inferior tympanic canal and reaches the CTA. The intratympanic ICA flow is called "aberrant" because the artery does not course into its usual canal but into an enlarged inferior tympanic canal. *D*, Pseudopetrous ICA with or without SA persistency. This variant is due to 2 phenomena: the agenesis of the cervical ICA and SA persistency. In this case, the ITA does not reach the CTA but the persistent SA (pSA).

which passes into the superior orbital fissure; 3) anterolateral branch, which runs into the foramen rotundum; and 4) posterior branch, which passes medial to the gasserian ganglion. These branches present numerous anastomoses in the cavernous region, which correspond to the remnants of the primitive trigeminal artery, OA, SA, and maxillary artery.[15]

Persistence of the SA

Changes in the events previously described can determine different adult configurations of the arteries related to the hyostapedial system, such as the persistence of the SA. The incidence of this variant is estimated to be 0.48% after a series of >1000 temporal bone dissections.[6] The possible variants related to the persistence of the SA are illustrated in Fig 2, including the rarer association of SA persistence with the so-called pseudopetrous ICA.

Complete Persistence of the SA

The complete persistence of the SA is a very rare variant, and only 2 cases were published in the context of an ICA aneurysm[25] or PHACE (posterior fossa malformations, hemangioma, arterial anomalies, coarctation of the aorta/cardiac defects, and eye abnormalities) syndrome.[39] In these cases, the SA could be seen as in the embryo, taking its origin from the petrous ICA, passing through the middle ear, and giving its 2 branches: one intracranial, which corresponds to the MMA, and the other extracranial, leaving the cranial cavity through the foramen spinosum. Consequently, the foramen spinosum is enlarged, the cochlear promontory is eroded, and the internal maxillary artery arises from the SA instead of the external carotid artery. Such an anatomic variant could easily be explained by the embryology and, particularly, by the absence of annexation of the maxillomandibular branch (of the SA) by the ventral pharyngeal artery. Consequently, in the absence of reversion of the arterial flow into the SA, its proximal (intratympanic) stem could not regress.[39]

Partial Persistence of the SA

The partial persistence of the SA is more frequent[1,7,21-24,26,32,52,53] and, in this case, only the intracranial branch of the SA keeps its origins from the petrous ICA. The foramen spinosum is absent (an orifice does not exist without its contents) or reduced in size and the MMA arises from the SA instead of the internal maxillary artery. This variant is explained by the regression of the proximal part of the maxillomandibular artery instead of the proximal part of the SA.[39] A rare case of a bilateral partial persistent SA is illustrated in Fig 3. We note that it is surprising that the complete persistence of the SA is much rarer than its partial persistence. The reasons of this phenomenon are still unknown, and are probably related to some unknown phases of the annexation of the maxillomandibulary branch by the ventral pharingeal artery.

Persistence of the SA Associated with Aberrant Flow of the ICA (Pseudo-Petrous ICA)

In rare cases,[12,21,23,24,54,55] the persistence of the SA is associated with an intratympanic course of the ICA (also known as "aberrant flow of the ICA"). This association of vascular variants with regard to both carotid and hyostapedial systems was described anatomically and angiographically.[32,39] In these cases, the ICA enters the skull base through an enlarged inferior tympanic canal (narrowing of the vessel on DSA), passes into the tympanic cavity to bend anteriorly, and reaches its normal carotid canal. The MMA arises from the ICA in its tympanic segment and passes through the stapes to have the same course described in the previous paragraph. The exocranial orifice of the carotid canal,

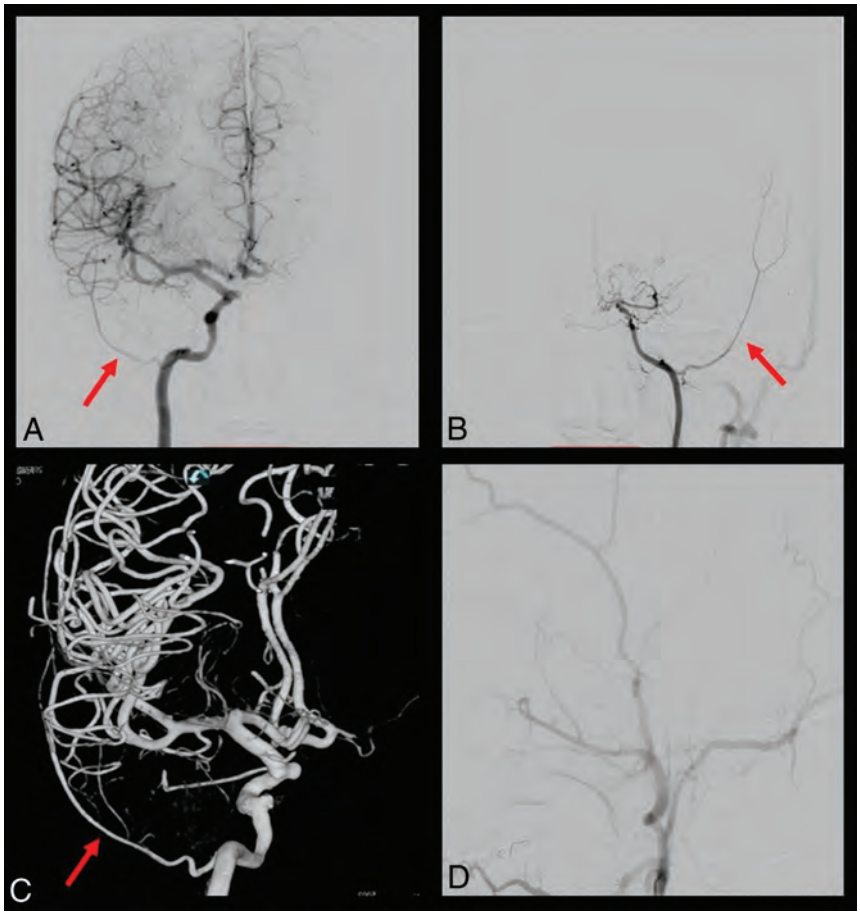

FIG 3. DSA with a bilateral partial persistent SA in a patient with Moyamoya disease. *A* and *B*, show the right and left ICA injection, respectively, with the MMA (*red arrow*) arising from the petrous ICA. This phenomenon is possible because of bilateral SA persistency. *B*, The ICA is narrowed and stopped at the level of the OA due to Moyamoya disease. *C*, A 3D reconstruction of the right ICA from which the MMA originates (*red arrow*). *D*, The left external carotid artery injection without the MMA enhancement because of its absence.

therefore, is absent in these cases.[23,24] The intratympanic course of the ICA is explained by the agenesis of the first 2 segments of the primitive ICA. The cervical segment, in fact, is the ascending pharyngeal artery with a hypertrophied inferior tympanic artery that maintains its anastomosis with the caroticotympanic artery (the branch of the ICA) into the tympanic cavity. The correct term for this aberrant flow of the ICA, in reality, is a tympano-caroticotympanic variant.[39] It bypasses the absence of the cervical ICA and provides a collateral circulation to the remainder of the ICA. Therefore, the cervical and intratympanic segments of this artery do not derivate from the carotid system but from the pharyngo-occipital and hyostapedial systems (pseudo-ICA).[23,24,39] The agenesis of the first 2 segments of the ICA could be partial, and the ICA seems duplicated.[54]

Pharyngo-Tympano-SA

This very rare variant was first described by Lasjaunias et al,[23] in 1977, in their original publication. The same case served as an illustration in the textbook, *Surgical Neuroangiography*,[39] and only 1 similar case was published by Baltsavias et al.[42] The MMA arises from the cervical portion of the ICA, ascends along the cervical ICA, enters into the tympanic cavity through the inferior tympanic canal, and follows the usual course of the SA. The 2 cases described were presented as "partial" persistence of the SA, with only the MMA arising from the SA, and the absence of the foramen spinosum. In this variant, an annexation of the SA by the inferior tympanic artery (the branch of the ascending pharyngeal artery), with regression of the proximal part of the SA explains this vascular configuration. Therefore, the SA arises from the cervical instead of the petrous segment of the ICA.

MMA Origin of the OA

The first description of orbital branches arising from the MMA was published in 1872 by Curnow.[56] He already noted in his case dissection that all orbital branches were supplied by the MMA except the central retinal artery, which kept its origin from the supracavernous ICA. Twenty years after this first description, Musgrove[57] presented another case of an MMA origin of the OA, also where the central retinal artery was supplied by the MMA and the ICA does not give any orbital artery, thus the orbit is vascularized by the MMA. After other isolated cases found during cerebral or orbital dissections,[1,27,58,59] Hayreh and Dass[60] reported 6 cases among their 170 orbital dissections in which the MMA participated completely (2 cases) or partially (4 cases) in the orbital supply. Moret et al[36] and Lasjaunias et al[23] described with precision the contribution of the MMA to the orbital vascularization and gave us a more comprehensive explanation of this anatomic variation.

The incidence of OA that arises from the MMA and penetrates the orbit through the superior orbital fissure is estimated as between 1.4 and 2.5%.[60] In this anatomic variation, orbital arteries are supplied by the anterior division of the MMA passing through the superior orbital fissure or through the spheno-orbital foramen. The central retinal artery generally keeps its vascular supply from the supracavernous ICA, but, in a few cases, the central retinal artery is also supplied by the MMA without ICA participation.[61] A case of a complete supply of the orbital arteries by the MMA is illustrated in Fig 4.

As explained before, during the embryogenesis, the SA gives the supraorbital branch, which allows the development of the lacrimal artery and anastomoses with the OA around the optic nerve

(participation of the perioptic circle). The proximal part of the supraorbital branch then normally regresses and the lacrimal artery is annexed by the OA.[39] The persistence of MMA branches (or, in extremis, the MMA origin of the OA) could be explained by 2 different phenomena: the absence of an anastomosis between the supraorbital branch and the OA, with a consequent persistence of a dual supply of the orbital arteries, or the persistence of the proximal stem of the supraorbital branch of the SA, with regression of the primitive OA (complete MMA origin of the OA). Although the supraorbital branch bifurcates (lacrimal artery laterally and ethmoido-nasal medially) usually inside the orbit, in 30% of cases, it can divide outside the orbit in the middle cranial fossa. In such cases, the ethmoido-nasal artery passes through the superior orbital fissure, but the lacrimal artery penetrates the orbit through its own canal, the spheno-orbital foramen (canal of Hyrtl, lacrimal foramen, sinus canal). The medial branch, passing through the superior orbital fissure, is named the recurrent meningeal artery in its intraorbital segment and sphenoidal artery in its intracranial segment.[23,31,39,60]

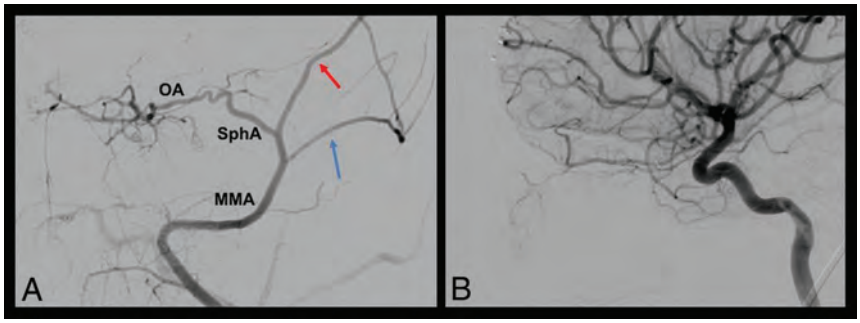

FIG 4. The MMA origin of the OA: a case of a complete OA origin from the MMA. The selective injection of the MMA in the anteroposterior projection (*A*) shows that the sphenoidal artery (SphA) arises from the MMA after its bifurcation into the anterior (*red arrow*) and posterior division (*blue arrow*). It courses along the inner surface of the temporal and sphenoidal bone and enters the orbit through the superior orbital fissure (SOF) to give rise to the OA. *B*, An oblique ICA injection, highlighting the absence of the OA.

CONCLUSIONS

All the anatomic variations linked to the development of the SA, summarized in Table 3, could have a clinical impact. Because each vascular segment that regresses during embryologic life usually persists as an anastomosis between 2 arteries, the knowledge of the embryology and the presence of these anastomoses is of paramount importance in case of external carotid branch embolization. Each residual anastomosis represents a potential undesired leak of liquid embolic agent, with possible clinical implications. Knowledge of the embryologic variants described in this article represents the basis to understand the different possible adult configurations of the MMA and their clinical implications. The most common pathologies, whose treatment requires a detailed knowledge of MMA embryology and variants, are dural AVFs, meningeal tumors, and chronic subdural hematomas. Our purpose, therefore, is to give a detailed description of these variants and their clinical implications in the second part of our article.

Table 3: Anatomic variations implicating the SA

Anatomic Variations			Embryologic Implications	
Type	Incidence	Direct and Indirect Signs	Embryologic Explanation	Embryo Size (mm)
Complete persistence of the SA	2 cases	Petrous ICA origin of the MMA; petrous ICA origin of the internal maxillary artery; enlarged foramen spinosum; eroded cochlear promontory	Lack of annexation of the maxillomandibular branch by the ventral pharyngeal artery; persistence of the tympanic segment of the SA	24
Partial persistence of the SA	0.4%	Petrous ICA origin of the MMA; absent foramen spinosum; enlarged facial canal	Regression of the proximal segment of the maxillomandibular branch; persistence of the tympanic segment of the SA	24
Tympano-carotico-tympanic variant; aberrant flow of the ICA plus persistent SA	5 cases	Intratympanic course of the ICA; petrous ICA origin of the MMA; enlarged inferior tympanic canal; absent exocranial carotid canal	Regression of the proximal segment of the maxillomandibular branch; persistence of the tympanic segment of the SA; agenesis of the first 2 segments of the ICA; anastomosis between inferior tympanic artery and caroticotympanic artery	24; 4–5
Pharyngo-tympano-stapedial variant	2 cases	Cervical ICA origin of the MMA; absent foramen spinosum	Regression of the proximal segment of the maxillomandibular branch; persistence of the tympanic segment of the SA; anastomosis between the inferior tympanic artery and the caroticotympanic artery	24
MMA origin of the OA	n = 2%	MMA origin of the OA; no OA from the ICA or only the central retinal artery	Lack of annexation of the supraorbital branch by the OA; persistence of the sphenoidal part of the supraorbital branch	24

REFERENCES

1. Fisher AG. **A case of complete absence of both internal carotid arteries, with a preliminary note on the developmental history of the stapedial artery.** *J Anat Physiol* 1913;48(pt 1):37–46 Medline
2. Kelemen G. **Arteria stapedia, in bilateral persistence.** *AMA Arch Otolaryngol* 1958;67:668–77 CrossRef Medline
3. Sando I, Baker B, Black FO, et al. **Persistence of stapedial artery in trisomy 13-15 syndrome.** *Arch Otolaryngol* 1972;96:441–47 CrossRef Medline
4. Marano GD, Horton JA, Gabriele OF. **Persistent embryologic vascular loop of the internal carotid, middle meningeal, and ophthalmic arteries.** *Radiology* 1981;141:409–10 CrossRef Medline
5. Diamond MK. **Unusual example of a persistent stapedial artery in a human.** *Anat Rec* 1987;218:345–54 CrossRef Medline
6. Moreano EH, Paparella MM, Zelterman D, et al. **Prevalence of facial canal dehiscence and of persistent stapedial artery in the human middle ear: a report of 1000 temporal bones.** *Laryngoscope* 1994;104:309–20 CrossRef Medline
7. Kawai K, Yoshinaga K, Koizumi M, et al. **A middle meningeal artery which arises from the internal carotid artery in which the first branchial artery participates.** *Ann Anat* 2006;188:33–38 CrossRef Medline
8. Baron SH. **Persistent stapedial artery, necrosis of the incus, and other problems which have influenced the choice of technique in stapes replacement surgery in otosclerosis.** *Laryngoscope* 1963;73:769–82 CrossRef Medline
9. House HP, Patterson ME. **Persistent stapedial artery: report of two cases.** *Trans Am Acad Ophthalmol Otolaryngol* 1964;68:644–46 Medline
10. Maran AG. **Persistent stapedial artery.** *J Laryngol Otol* 1965;79:971–75 CrossRef Medline
11. Davies DG. **Persistent stapedial artery: a temporal bone report.** *J Laryngol Otol* 1967;81:649–60 CrossRef Medline
12. Steffen TN. **Vascular anomalites of the middle ear.** *Laryngoscope* 1968;78:171–97 CrossRef Medline
13. Marion M, Hinojosa R, Khan AA. **Persistence of the stapedial artery: a histopathologic study.** *Otolaryngol Head Neck Surg* 1985;93:298–312 CrossRef Medline
14. Boscia R, Knox RD, Adkins WY, et al. **Persistent stapedial artery supplying a glomus tympanicum tumor.** *Arch Otolaryngol Head Neck Surg* 1990;116:852–54 CrossRef Medline
15. Pahor AL, Hussain SS. **Persistent stapedial artery.** *J Laryngol Otol* 1992;106:254–57 CrossRef Medline
16. Govaerts PJ, Marquet TF, Cremers WR, et al. **Persistent stapedial artery: does it prevent successful surgery?** *Ann Otol Rhinol Laryngol* 1993;102:724–72 CrossRef Medline
17. Wardrop P, Kerr AI, Moussa SA. **Persistent stapedial artery preventing successful cochlear implantation: a case report.** *Ann Otol Rhinol Laryngol Suppl* 1995;166:443–45 Medline
18. Jain R, Gandhi D, Gujar S, et al. **Case 67: persistent stapedial artery.** *Radiology* 2004;230:413–16 CrossRef Medline
19. Yamamoto E, Hirono Y. **Persistent stapedial artery associated with otosclerosis.** *ORL J Otorhinolaryngol Relat Spec* 1988;50:382–84 CrossRef Medline
20. Hogg ID, Stephens CB, Arnold GE. **Theoretical anomalies of the stapedial artery.** *Ann Otol Rhinol Laryngol* 1972;81:860–70 CrossRef Medline
21. Guinto FC Jr, Garrabrant EC, Radcliffe WB. **Radiology of the persistent stapedial artery.** *Radiology* 1972;105:365–69 CrossRef Medline
22. Teal JS, Rumbaugh CL, Bergeron RT, et al. **Congenital absence of the internal carotid artery associated with cerebral hemiatrophy, absence of the external carotid artery, and persistence of the stapedial artery.** *Am J Roentgenol Radium Ther Nucl Med* 1973;118:534–45 CrossRef Medline
23. Lasjaunias P, Moret J, Manelfe C, et al. **Arterial anomalies at the base of the skull.** *Neuroradiology* 1977;13:267–72 CrossRef Medline
24. Lasjaunias P, Moret J. **Normal and non-pathological variations in the angiographic aspects of the arteries of the middle ear.** *Neuroradiology* 1978;15:213–19 CrossRef Medline
25. Rodesch G, Choi IS, Lasjaunias P. **Complete persistence of the hyoido-stapedial artery in man. Case report. Intra-petrous origin of the maxillary artery from ICA.** *Surg Radiol Anat* 1991;13:63–65 CrossRef Medline
26. Sheikh BY, Coates R, Siqueira EB. **Stapedial artery supplying sphenoid wing meningioma: case report.** *Neuroradiology* 1993;35:537–38 CrossRef Medline
27. Diamond MK. **Homologies of the meningeal-orbital arteries of humans: a reappraisal.** *J Anat* 1991;178:223–41 Medline
28. Diamond MK. **Homologies of the stapedial artery in humans, with a reconstruction of the primitive stapedial artery configuration of Euprimates.** *Am J Phys Anthropol* 1991;84:433–62 CrossRef Medline
29. Falk D. **Meningeal arterial patterns in great apes: implications for hominid vascular evolution.** *Am J Phys Anthropol* 1993;92:81–97 CrossRef Medline
30. Hyrtl J. **Several human analogies of of the artery Otto discovered running through the stapes in several hibernators. New observations from the field of human and comparative anatomy.** *Neue beobachtungen aus dem gebieteder menschlichen und vergleichenden anatomie* 1836:457–66. In: states MJdö, ed.
31. Padget DH. **The development of cranial arteries in the human embryo.** *Contrib Embryol Carneg Instn* 1948;32:205–61
32. Altmann F. **Anomalies of the internal carotid artery and its branches; their embryological and comparative anatomical significance; report of a new case of persistent stapedial artery in man.** *Laryngoscope* 1947;57:313–39 Medline
33. Gabriele OF, Bell D. **Ophthalmic origin of the middle meningeal artery.** *Radiology* 1967;89:841–44 CrossRef Medline
34. Salamon G, Guerinel G, Demard F. **Radioanatomical study of the external carotid artery.** *Ann Radiol (Paris)* 1968;11:199–215 Medline
35. Seeger JF, Hemmer JF. **Persistent basilar/middle meningeal artery anastomosis.** *Radiology* 1976;118:367–70 CrossRef Medline
36. Moret J, Lasjaunias P, Theron J, et al. **The middle meningeal artery. Its contribution to the vascularisation of the orbit.** *J Neuroradiol* 1977;4:225–48 Medline
37. Merland JJ, Théron J, Lasjaunias P, et al. **Meningeal blood supply of the convexity.** *J Neuroradiol* 1977;4:129–74 Medline
38. Moret J, Lasjaunias P, Vignaud J, et al. **The middle meningeal blood supply to the posterior fossa (author's transl).** *Neuroradiology* 1978;16:306–07 CrossRef Medline
39. Lasjaunias P, Bereinstein A, ter Brugge K. *Surgical Neuroangiography.* Berlin: Springer-Verlag; 2001
40. Maiuri F, Donzelli R, de Divitiis O, et al. **Anomalous meningeal branches of the ophthalmic artery feeding meningiomas of the brain convexity.** *Surg Radiol Anat* 1998;20:279–84 CrossRef Medline
41. Shah QA, Hurst RW. **Anomalous origin of the middle meningeal artery from the basilar artery: a case report.** *J Neuroimaging* 2007;17:261–63 CrossRef Medline
42. Baltsavias G, Kumar R, Valavanis A. **The pharyngo-tympano-stapedial variant of the middle meningeal artery. A case report.** *Interv Neuroradiol* 2012;18:255–58 CrossRef Medline
43. Kumar S, Mishra NK. **Middle meningeal artery arising from the basilar artery: report of a case and its probable embryological mechanism.** *J Neurointerv Surg* 2012;4:43–44 CrossRef Medline
44. Plas B, Bonneville F, Dupuy M, et al. **Bilateral ophthalmic origin of the middle meningeal artery.** *Neurochirurgie* 2013;59:183–86 CrossRef Medline
45. Cvetko E, Bosnjak R. **Unilateral absence of foramen spinosum with bilateral ophthalmic origin of the middle meningeal artery: case report and review of the literature.** *Folia Morphol (Warsz)* 2014;73:87–91 CrossRef Medline
46. Salem MM, Fusco MR, Dolati P, et al. **Middle meningeal artery arising from the basilar artery.** *J Cerebrovasc Endovasc Neurosurg* 2014;16:364–67 CrossRef Medline

47. Kimball D, Kimball H, Tubbs RS, et al. **Variant middle meningeal artery origin from the ophthalmic artery: a case report.** *Surg Radiol Anat* 2015;37:105–08 CrossRef Medline
48. Tandler J. **Zur Entwickelungsgeschichte der Kopfarterien bei den Mammalia. 1902. Morphol.** *Jahrbuch, Bd. 30, S* 275–373, Taf. 3-5
49. Fuchs H. **Zur Entwicklungsgeschichte des Wirbeltierauges. I. Über die Entwicklung der Augengefässe des Kaninchens.** *Anat Hefte* 1905;28:1–251
50. Lasjaunias P, Santoyo-Vazquez A. **Segmental agenesis of the internal carotid artery: angiographic aspects with embryological discussion.** *Anat Clin* 1984;6:133–41 CrossRef Medline
51. Margolis MT, Newton TH. **Collateral pathways between the cavernous portion of the internal carotid and external carotid arteries.** *Radiology* 1969;93:834–36 CrossRef Medline
52. McLennan JE, Rosenbaum AE, Haughton VM. **Internal carotid origins of the middle meningeal artery. The ophthalmic-middle meningeal and stapedial-middle meningeal arteries.** *Neuroradiology* 1974;7:265–75 CrossRef Medline
53. Martins C, Yasuda A, Campero A, et al. **Microsurgical anatomy of the dural arteries.** *Neurosurgery* 2005;56(suppl):211–51; discussion 211–51 CrossRef Medline
54. Koenigsberg RA, Zito JL, Patel M, et al. **Fenestration of the internal carotid artery: a rare mass of the hypotympanum associated with persistence of the stapedial artery.** *AJNR Am J Neuroradiol* 1995;16 (suppl):908–10 Medline
55. Silbergleit R, Quint DJ, Mehta BA, et al. **The persistent stapedial artery.** *AJNR Am J Neuroradiol* 2000;21:572–77 Medline
56. Curnow J. **Two instances of irregular ophthalmic and middle meningeal arteries.** *J Anat Physiol* 1873;8:155–56 Medline
57. Musgrove J. **Origin of ophthalmic artery from middle meningeal.** *J Anat Physiol* 1893;27:279–81 Medline
58. Chanmugan PK. **Note on an unusual ophthalmic artery associated with other abnormalities.** *J Anat* 1936;70(pt 4):580–82 Medline
59. Bossi R, Pisani C. **Collateral cerebral circulation through the ophthalmic artery and its efficiency in internal carotid occlusion.** *Br J Radiol* 1955;28:462–69 CrossRef Medline
60. Hayreh SS, Dass R. **The ophthalmic artery: I. Origin and intra-cranial and intra-canalicular course.** *Br J Ophthalmol* 1962;46:65–98 CrossRef Medline
61. Louw L. **Different ophthalmic artery origins: embryology and clinical significance.** *Clin Anat* 2015;28:576–83 CrossRef Medline

Middle Meningeal Artery: Anatomy and Variations

S. Bonasia, S. Smajda, G. Ciccio, and T. Robert

ABSTRACT

SUMMARY: The middle meningeal artery is the major human dural artery. Its origin and course can vary a great deal in relation, not only with the embryologic development of the hyostapedial system, but also because of the relationship of this system with the ICA, ophthalmic artery, trigeminal artery, and inferolateral trunk. After summarizing these systems in the first part our review, our purpose is to describe, in this second part, the anatomy, the possible origins, and courses of the middle meningeal artery. This review is enriched by the correlation of each variant to the related embryologic explanation as well as by some clinical cases shown in the figures. We discuss, in conclusion, some clinical conditions that require detailed knowledge of possible variants of the middle meningeal artery.

ABBREVIATIONS: IMA = internal maxillary artery; MMA = middle meningeal artery; OA = ophthalmic artery; SA = stapedial artery

The middle meningeal artery (MMA) is one of the largest branches of the external carotid artery and the most important dural artery because it supplies more than two-thirds of the cranial dura.[1] However, the most interesting aspects of this artery are not its size or its clinical importance but its embryologic development and its numerous anatomic variations. An understanding of the anatomy and variants of the MMA provides a good knowledge and understanding of the hyostapedial system and of the vascular anatomy of the middle ear. The aim of this article is to summarize, through a narrative review based on the literature and clinical examples, the possible anatomic variations of the MMA. Each variant will be related to its embryologic explication, which we treated in detail in part 1 of this article. The knowledge of these variants is important especially for neuroradiologists to treat dural pathologies and also for surgeons who approach the middle ear pathologies.

Origin of the Artery

In almost all cases, the MMA arises from the internal maxillary artery (IMA), but it could also originate from the ICA or, more surprisingly, from the basilar artery. Possible origins of the MMA are listed in Table 1, with their respective embryologic explanation. The detailed description of the MMA embryologic development was analyzed in part 1 of our article.

IMA Origin. The classic origin of the MMA is usually described on the first segment of the IMA into the infratemporal fossa, just behind the condylar process of the mandible.[1,2] The MMA is the largest and usually the first ascending branch of the IMA,[2] but it could also have a common trunk with the accessory meningeal artery, depending on the position of the IMA course with regard to the external pterygoid muscle.[3] When the IMA passes superficially to the muscle, the MMA and accessory meningeal artery have a common origin from the IMA, and the inferior dental and posterior deep temporal arteries have a separate origin. On the contrary, when the IMA passes deep to the external pterygoid muscle, the MMA, and the accessory meningeal artery have distinct origins from the IMA, and the inferior dental and the posterior deep temporal arteries share a common trunk.[2]

Low[4] described an interesting cadaveric case of distal (third segment) IMA origin of the MMA. In his study, he inspected the osseous grooves of the skull and noted that, associated with the absence of the foramen spinosum, the osseous grooves of the MMA converge to the superior orbital fissure.[4] He concluded that the MMA takes its origin in the pterygoid fossa from the distal IMA and passes through the inferior and superior orbital fissures.[4] Probably, in his description, he misinterpreted an ophthalmic artery (OA) origin of the MMA, not already known at its publication.[3]

Received April 17, 2020; accepted after revision May 20.

From the Department of Neurosurgery (S.B., T.R.), Neurocenter of the Southern Switzerland, Lugano, Switzerland; Department of Interventional Neuroradiology (S.S., G.C.), Rothschild Foundation Hospital, Paris, France; and University of Southern Switzerland (T.R.), Lugano, Switzerland.

Please address correspondence to Thomas Robert, MD, Department of Neurosurgery, Regional Hospital of Lugano, Neurocenter of the Southern Switzerland, Via Tesserete 46, CH-6903 Lugano, Switzerland; e-mail: thomas.robert43@gmail.com

Indicates open access to non-subscribers at www.ajnr.org

http://dx.doi.org/10.3174/ajnr.A6739

Table 1: Different origin of the MMA with modifications associated and embryologic explanation

Variations in the Origin of the MMA		Embryologic Implications	
Type	Associated Changes	Embryologic Explanation	Embryo Size (mm)
IMA origin	Normal anatomy	Normal embryology	
Basilar artery origin	Absence foramen spinosum	Anastomosis between SA and trigeminal artery; anastomosis between SA and lateral pontine artery	12
Cavernous ICA origin	Absence foramen spinosum	Anastomosis between inferolateral trunk and SA	16
Partial persistent SA	Absence foramen spinosum; enlargement of the facial canal	Regression of the proximal part of the maxillomandibular branch; persistence of the intratympanic segment of the SA	24
Complete persistent SA	Enlargement of the facial canal	Lack of annexation of the maxillomandibular branch by the ventral pharyngeal artery; persistence of the intratympanic segment of the SA	24
Pseudopetrous ICA origin	Absence foramen spinosum; enlargement of the facial canal; absence of the exocranial opening of the carotid canal	Agenesis of the first and second segments of the ICA; intratympanic anastomosis between inferior tympanic and caroticotympanic arteries; persistence of the intratympanic segment of the SA	4–5; 24
Cervical ICA origin	Absence foramen spinosum; enlargement of the facial canal	Intratympanic anastomosis between inferior and superior tympanic arteries; regression of the proximal part of the maxillomandibular branch; persistence of the intratympanic segment of the SA	16; 24
Occipital artery origin	Absence foramen spinosum; enlargement of the facial canal	No clear explanation	
Distal petrous ICA origin	Absence foramen spinosum	Lack of annexation of the mandibular artery (first aortic arch) by the SA (second aortic arch)	9

Basilar Artery Origin. Altmann[5] was the first investigator to describe a case of basilar artery origin of the MMA in his monumental article about anomalies of the carotid system but failed to give clear embryologic explanation of the anatomic variation. Surprisingly, he described the origin of the artery between the AICA and PICA, and its course as "accompanying the acoustic-facial nerve," passing through the internal acoustic canal to reach the superior branch of the stapedial artery (SA). After this initial description, <10 cases of basilar artery origin of the MMA were successively published.[6-12] Usually, the MMA originates from the distal third of the basilar artery between the superior cerebellar artery and the AICA. It courses anteriorly along the trigeminal nerve to reach the gasserian region, where it anastomoses with the petrosal branch of the MMA. Usually, only the posterior (parieto-occipital) branch of the MMA arises from the basilar artery and the anterior (frontal) branch keeps its normal origin from the IMA[6,9-11,13]; however, in a few cases,[6,8,12] the complete territory of the MMA had a basilar artery origin.

Two distinct embryologic explanations are postulated by investigators to explain this anatomic variation. Seeger and Hemmer[6] and Lasjaunias et al[3,7] explained it by an anastomosis in the gasserian region between the basilar remnant of the trigeminal artery and the persistent SA. Consequently, after regression of the proximal stem of the SA at the level of the stapes, the MMA takes its origin from the basilar artery. Other investigators postulated that an enlarged lateral pontine artery develops during the embryologic life and anastomoses with the SA.[8,9,14] A rare case of MMA origin from an enlarged pontine artery is presented in Fig 1. Kuruvilla et al[10] described a particular case in which the MMA arose directly from the PICA and not from the basilar artery. No embryologic explanation was found to explain such an origin.

OA Origin. The MMA could also originate from the OA instead of the IMA. The incidence of this vascular variation is estimated to be 0.5% by Dilenge and Ascherl,[15] based on a large angiographic series. Few cases of MMA that arose from the OA are described in the literature.[7,16-24] The first case was presented by Curnow[25] and, in the same period, Meyer[26] also cited 4 cadaveric cases originally described by Zuckerkandl in 1876,[27] during a congress presentation. This vascular anomaly is considered as the consequence of 2 different embryologic processes.[7] The first is the failure of the supraorbital branch (SA) to regress. The second is the absence of anastomosis between the maxillomandibular branch of the SA and the IMA.[28] Consequently, the MMA origins from the OA passing through the lateral part of the superior orbital fissure and the foramen spinosum are usually absent.

Maiuri et al[29] proposed 3 different types of this vascular variation, as highlighted in Table 2. The first type is the complete MMA territory taken over by the OA through the superficial recurrent OA. The second type is only the anterior branch of the MMA with an OA origin; the posterior branch of the MMA keeps its origin from the IMA. The third type is not really an OA origin of the MMA but an anastomosis between the OA and the accessory meningeal artery (through the deep recurrent OA), and, consequently, the anterior meningeal territory is supplied by both the MMA and the OA, without any communication. Two cases of complete and

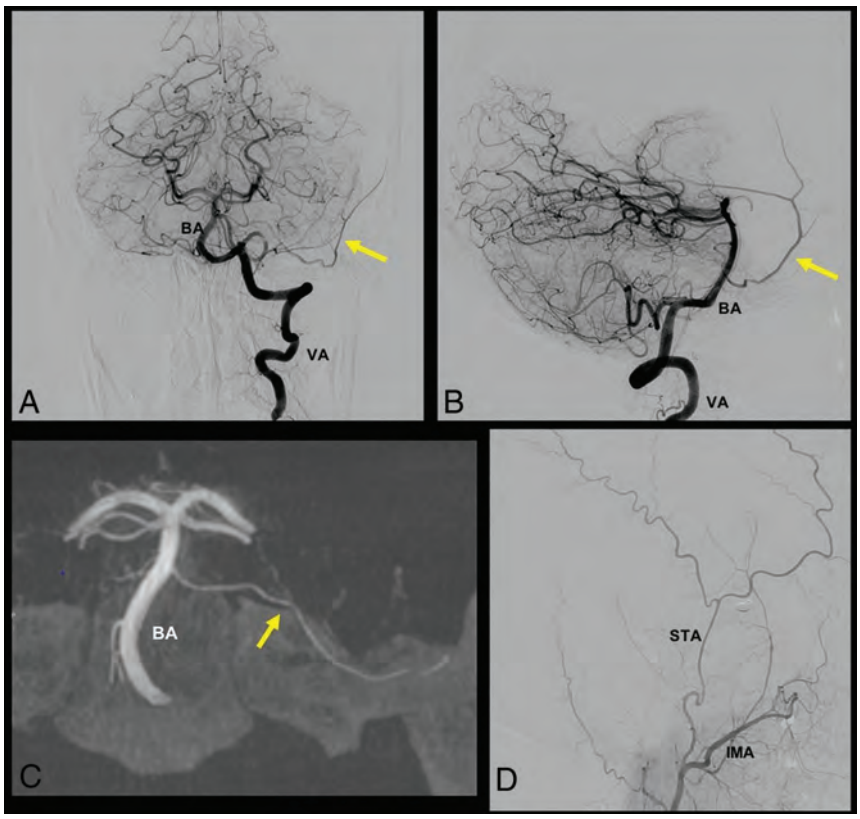

FIG 1. A case of MMA origin from basilar artery (BA) pontine perforating branch. In this case, the MMA originates from a pontine branch of the BA, as indicated by the *yellow arrow* in *A*, *B*, and *C*. *A* and *B*, A frontal and lateral view of left vertebral artery (VA) injection, respectively. *C*, A frontal XperCT (Philips Healthcare) reconstruction with the same MMA origin. *D*, A distal external carotid artery injection, where the superficial temporal artery (STA) and the IMA are visible, without the typical MMA origin from the IMA.

Table 2: Different types of OA origin of the MMA[a]

Type	Vascular Anatomy	Foramen Spinosum
I	Complete OA origin of the MMA	Absence
II	Partial OA origin of the MMA; anterior division from the OA; posterior division from the IMA	Reduced in size
III	OA origin of the accessory meningeal artery	Normal

[a] From Ref.[28]

partial origins of the MMA from the OA are reported in Fig 2. It is still a matter of debate if the MMA originates from the OA directly or from the proximal part of the lacrimal artery.[28]

Cavernous ICA Origin. The lone case of a cavernous ICA origin of the MMA was described by Lasjaunias et al[7] in one of their most famous articles that summarized distinct vascular anomalies encountered at the base of the skull. They published, at another time, the same case in their textbook[3] to illustrate this very rare anatomic variant. In this case, all branches of the MMA were filled during ICA injection, and its origin arose from the horizontal portion of the cavernous ICA. Lasjaunias et al[7] elegantly explained this variation by the anastomosis during embryologic life between the posterior branch of the inferolateral trunk and the SA; consequently, the proximal stem of the MMA regressed (or was not formed) and the foramen spinosum was absent.

Petrous ICA Origin (Complete and Partial Persistence of the SA). The complete persistence of the SA is a very rare variant, only 2 cases were published in the context of an ICA aneurysm[30] or PHACE (posterior fossa malformations, hemangioma, arterial anomalies, coarctation of the aorta/cardiac defects, and eye abnormalities) syndrome.[3] In these cases, the SA keeps its embryonic origin from the petrous ICA, passes through the middle ear, and gives it 2 branches: one intracranial, which corresponds to the MMA, and the other extracranial, which leaves the cranial cavity through the foramen spinosum. Consequently, the foramen spinosum is enlarged, the cochlear promontory is eroded, and the IMA arises from the SA instead of the external carotid artery. Such an anatomic variant could easily be explained by the absence of an embryologic annexation of the maxillomandibular branch (of the SA) by the ventral pharyngeal artery, details of which are described in part 1 of our article.

The partial persistence of the SA is more frequent,[1,5,7,28,31-36] and, in this case, only the intracranial branch of the SA keeps its origin from the petrous ICA. The foramen spinosum is absent or reduced in size and the MMA arises from the SA instead of the IMA. This variant is explained by the regression of the proximal part of the maxillomandibular artery instead of the proximal part of the SA.[3]

Pseudopetrous ICA Origin (Persistence of the SA Associated with Aberrant Flow of the ICA). In rare cases, the persistence of the SA and the consequent origin of the MMA from the petrous ICA are associated with an intratympanic course of the ICA (also known as "aberrant flow of the ICA").[7,14,28,32,37,38] The intratympanic course of the ICA is explained by the agenesis of the first 2 segments of the primitive carotid artery, with a hypertrophied inferior tympanic artery that maintains the anastomosis between the ascendant pharyngeal artery and the caroticotympanic artery (a branch of the ICA) into the tympanic cavity. Therefore, the cervical and intratympanic segments of this artery do not derivate from the carotid system but from the pharyngo-occipital and

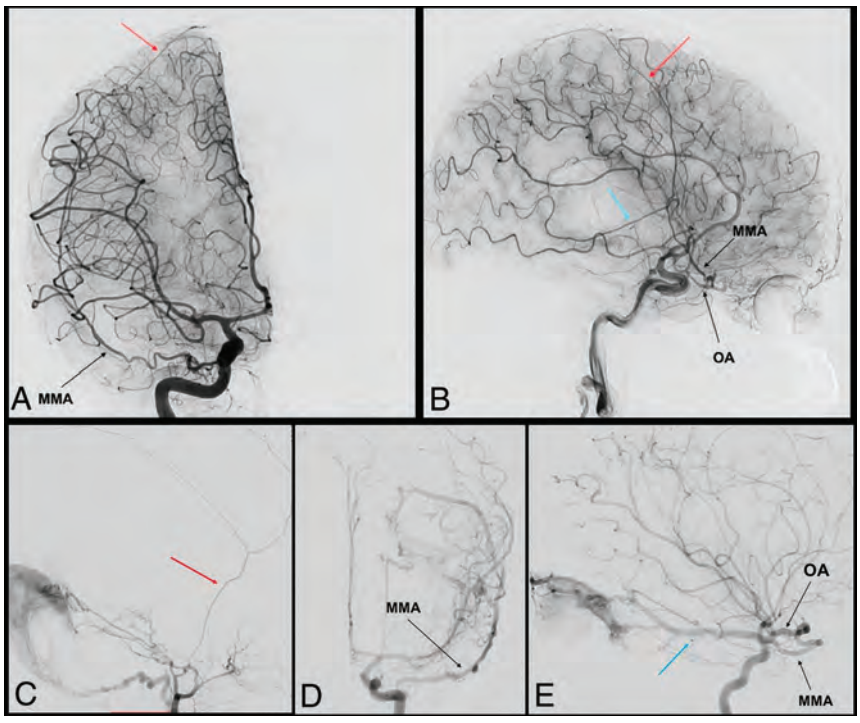

FIG 2. Complete and partial MMA origin from OA. The anteroposterior and lateral view angiograms (*A* and *B* respectively) show a rare case of a complete MMA origin from the OA. The OA, through the superficial recurrent OA, gives origin to the MMA, that passes through the lateral part of the superior orbital fissure, and bifurcates into its anterior (*red arrow*) and posterior division (*blue arrow*). In the angiograms *C*, *D*, and *E*, a rare case of a partial origin of the MMA from the OA is shown. *D* and *E*, Angiograms of a left ICA injection in the frontal and lateral views, where the posterior branch of the MMA (*blue arrow*) originates at the OA and feeds a tentorial AVF. After the external carotid artery injection (*C*), only the anterior branch of the MMA is enhanced (*red arrow*).

hyostapedial systems (pseudo-ICA).[3,7,28] In these cases, the MMA arises from the ICA in its tympanic segment and passes through the stapes to have the same course described in the previous paragraph. This variant is described in detail in part 1 of our article.

Cervical ICA Origin (Pharyngotympanostapedial Artery). The MMA could also arise from the cervical segment of the ICA. This very rare variant was first described by Lasjaunias et al[7] in their original publication. The same case served as an illustration in the textbook "*Surgical Neuroangiography*"[3] and only 1 similar case was published by Baltsavias et al.[39] The MMA arises from the cervical portion of the ICA, ascends along the cervical ICA, enters into the tympanic cavity through the inferior tympanic canal, and follows the usual course of the SA. The 2 cases described were presented as "partial" persistence of the SA, with only the MMA arising from the SA and the absence of the foramen spinosum. In this variant, an annexation of the SA by the inferior tympanic artery (the branch of the ascending pharyngeal artery), with regression of the proximal part of the SA explains this vascular configuration. Therefore, the SA arises from the cervical instead of the petrous segment of the ICA.

Occipital Artery Origin. Diamond[40] described a remarkable case of partial persistent SA found during a temporal bone dissection. The peculiarity of this case was that the SA arose from the occipital artery instead of the petrous ICA passing through a "special foramen" to enter into the petrous part of the temporal bone between the styloid process and the carotid canal. After passing through the posterior wall of the tympanic cavity and through the stapes, the SA entered the facial canal to reach the petrous apex and to give rise to the future branches of the MMA. In this article, Diamond[40] did not give a clear embryonic explanation or a hypothesis of the variant he found.

Distal Petrous ICA Origin (Mandibular Artery Origin). Lasjaunias et al[3] were the only investigators to show a case of a distal petrous ICA origin of the MMA near the normal origin of the vidian artery. In this case, the MMA did not follow an intratympanic course.[3] The investigators explained this variant by the absence of annexation of the first aortic arch by the second aortic arch (the SA); therefore, the mandibular artery retains its primary territory, which is the MMA territory.[3]

Course of the Artery

The first extracranial segment of the MMA is from its origin to its entry into the foramen spinosum. The more anterior the origin of the MMA is, the more oblique backward is the extracranial segment. At the level of the foramen spinosum, the artery bends anteriorly and laterally to follow the temporal fossa. This bend is responsible for the characteristic aspect of the MMA on DSA. After its entry into the cranial cavity, the MMA has a lateral course grooving the greater sphenoid wing. Merland et al[2] described 3 intracranial segments of the MMA. The first is the temporobasal segment, where the artery follows the temporal fossa and curves upward, where it becomes the second or temporopterional segment. After passing the pterional region, the artery enters in its coronal segment where the artery follows the coronal suture to end at the region of the bregma. Martins et al[1] considered the course of the artery shorter and simpler. They described the termination of the MMA, where it divides into anterior and posterior divisions at the pterional region. The anterior division of the MMA is classically the coronal segment previously described by Merland et al.[2]

Branches of the Artery

The 2 most precise and complete publications that describe the branches of the MMA were published by Merland et al[2] and Martins et al.[1] One description is based on cerebral angiographies; the other is based on cadaveric dissections. Before these publications, Salamon et al[41,42] paid particular attention to correlate the anatomy with the angiographic images. As noted in the previous

Table 3: Different branches of the MMA with their respective anastomosis

MMA Branches	Origin from the MMA	Territory (Dural and Neural)	Possible Anastomosis
Petrosal branch	Foramen spinosum	Trigeminal ganglion and nerves; posteromedial floor of the middle fossa; insertion of tentorium (medial half); superior petrosal sinus	Ascending pharyngeal artery (carotid branch); medial and lateral tentorial arteries (ICA)
Superior tympanic artery	Petrosal branch	Greater superficial petrosal nerve; geniculate ganglion; tympanic cavity (superior part)	Inferior tympanic artery (ascending pharyngeal artery); caroticotympanic artery (ICA); anterior tympanic artery (IMA); stylomastoid artery (posterior auricular artery)
Cavernous branch	Petrosal branch	Lateral wall of the cavernous sinus	Accessory meningeal artery; inferolateral trunk (ICA)
Anterior division or frontal branch	Pterional region	Frontal and anterior parietal convexity; superior sagittal sinus; anterior and middle fossa (lateral part)	Anterior and posterior ethmoidal arteries (OA); contralateral MMA
Falcine arteries	Anterior and posterior division	Falx cerebri	Anterior falcine artery (OA); anterior cerebral artery; posterior meningeal artery (vertebral artery)
Medial branch or sphenoidal branch	Anterior division	Lesser sphenoid wing; superior orbital fissure; peri-orbital (lateral)	Recurrent meningeal branches (OA); inferolateral trunk (ICA)
Petrosquamosal branch	Posterior division	Posterolateral floor of the middle fossa; insertion of tentorium (lateral half); superior petrosal sinus; transverse and sigmoid sinuses; dura of the posterior fossa (superior part)	Ascending pharyngeal artery (jugular branch); lateral tentorial artery (ICA); occipital artery (mastoid branch)
Parieto-occipital branch	Posterior division	Temporosquamous dura; parieto-occipital convexity; superior sagittal sinus	Posterior meningeal artery (vertebral artery)

paragraph, these 2 investigators (Merland and Martins) used a different naming of the branches, even if the terminology used by Martins et al[1] seems to be the most comprehensive. Different branches of the MMA with the dural territory associated and possible anastomosis with other dural arteries are shown in Table 3.[41]

The course and branches of MMA are indicated on the DSA, shown in Fig 3. The MMA divides, at the pterional region, into 2 divisions: anterior and posterior. Before its bifurcation, the MMA gives 2 branches that supply the dura of the temporal fossa.[2,19,28] The first is the petrosal branch, which courses on the petrous apex and supplies the dura of this region (including the gasserian ganglion) and also the superior part of the tympanic cavity via the superior tympanic artery passing through the facial canal. The second basal branch of the MMA is the cavernous branch, which supply the lateral wall of the cavernous sinus and anastomoses with branches of the inferolateral trunk.

The anterior division of the MMA is in the dura of the convexity and follows the coronal suture until the bregma. This anterior division of the MMA has 2 types of terminal branches: 1) falcine arteries, which anastomose with branches of the anterior falcine artery, and 2) contralateral branches, which cross the midline to anastomose with branches of the contralateral MMA. Near the pterional region, the anterior division gives a medial branch that runs under the lesser sphenoid wing that supplies the dura of anterior part of the temporal fossa, the superior orbital fissure, and could anastomose with the recurrent meningeal branches of the OA.[1,2] The posterior division of the MMA also supplies the dura of the convexity and gives 2 principal branches: the petrosquamosal branch and the parieto-occipital branch.[1] These 2 branches participate in the vascularization of the parieto-temporo-occipital dura, the transverse sinuses, and also the posterior two-thirds of the tentorium.[43] Branches of the posterior division of the MMA anastomose with dural branches of the occipital, ascending pharyngeal, subarcuate, and vertebral arteries.[41,43]

Dural Territory

The MMA supplies most of the dura of the cranial convexity via its anterior and posterior divisions, and usually participates in the vascularization of the superficial half of the falx cerebri. The frontomedial dura and the occipitomedial dura, on the contrary, are usually supplied by the anterior meningeal artery from the OA and by the posterior meningeal artery from the vertebral artery, respectively.[1] The supra-tentorial dural territory of the convexity is in balance among these 3 arteries; therefore, the territory of the MMA could be variable.[1,2,41] The dura of the superior sagittal sinus is also supplied by branches of the MMA but also branches of the anterior meningeal artery (anterior part) and branches of the posterior meningeal artery (posterior part).[7] The MMA could also supply the torcular region via its posterior division.[1]

At the skull base, it supplies the middle cranial fossa and the lateral part of the anterior cranial fossa[41] and also the inferior part of the lateral wall of the cavernous sinus via its cavernous branch. Its participation in the vascularization of the tentorium is limited to the insertion of the tentorium and to the superior sagittal sinus.[44] The anterior division of the MMA through its medial branch supplies the dura of the lesser sphenoid wing and the superior orbital fissure region.[2] These branches also participate in the vascularization of the lateral wall of the periorbita and could also participate in the vascularization of orbital branches by anastomoses with the lacrimal artery (through the deep recurrent meningeal artery of the OA).[19]

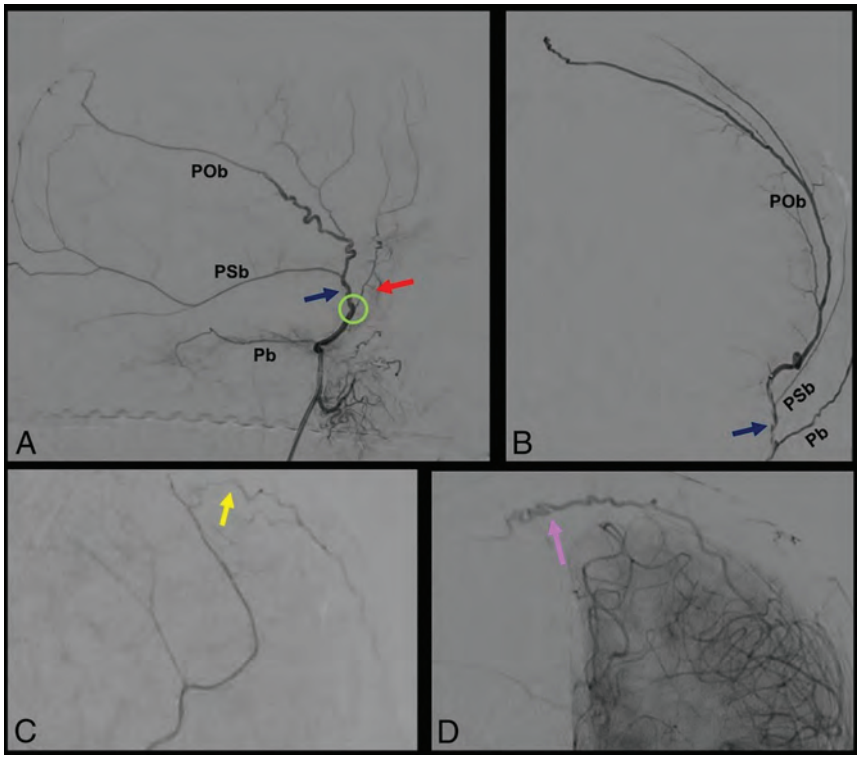

FIG 3. DSA, showing segments and branches of the MMA. *A* and *B*, show selective MMA injection from a lateral (*A*) and frontal (*B*) view. The MMA bifurcates at the pterional region (*green circle*) into 2: an anterior (*red arrow*) and posterior (*blue arrow*) division. Before its bifurcation, the MMA gives the petrosal branch (Pb), which courses on the petrous apex. The posterior division gives 2 principal branches: the petrosquamosal branch (PSb) and the parieto-occipital branch (POb). The anterior division ends with 2 kinds of terminal branches, visible after common carotid artery injection: the falcine arteries (*yellow arrow*) (*C*), which anastomose with branches of the anterior falcine artery from the OA, and contralateral branches (*purple arrow*) (*D*) that cross the midline to anastomose with a contralateral MMA.

Through its posterior division, the MMA also gives branches destined to the dura of the superolateral part of the cerebellar fossa. Moret et al[43] showed the importance of the MMA in the vascularization of the posterior fossa dura, always in balance with branches of the ascending pharyngeal and occipital arteries. The MMA also partially supplies the trigeminal and facial nerves.[1-3] Indeed, the petrosal branch gives branches to the gasserian ganglion and to the maxillary and mandibular divisions of the trigeminal nerve in their cavernous portion. The greater superficial petrosal nerve and the geniculate ganglion of the facial nerve also receive branches from the petrosal branch of the MMA.[1] Also, the superior tympanic artery, which is the petrosal remnant of the SA and, therefore, a branch of the petrosal branch, supplies the superior part of the tympanic cavity.[42]

Possible Anastomoses

The dural vascular territory of the MMA is in balance between numerous arteries coming from ICA, external carotid artery, and also from the vertebrobasilar system. Therefore, the MMA presents a lot of anastomoses with branches arising from the other arteries. The 3 major anatomic regions of vascular anastomoses are the following: the peri- and the cavernous region, the frontomedial region, and the posterior fossa (Fig 4).[1]

On the skull base,[45] its petrosal branch anastomoses with the accessory meningeal artery, the ascending pharyngeal artery (via its carotid branch), the inferolateral trunk, the meningohypophyseal trunk, and the recurrent meningeal artery of the OA.[19,41] At the frontal region, the anterior division of the MMA anastomoses principally with the dural branches of the OA: the anterior and posterior ethmoidal arteries and also the anterior falcine artery.[15,41] In the posterior fossa, it anastomoses, principally with the posterior meningeal artery and with the mastoid branch of the occipital artery.[43] The last natural anastomosis to be noted is between the MMAs of both sides on the midline.[1]

Clinical Implications

The understanding of the vascular anatomy of the dura mater has a major importance both for neuroradiologists and neurosurgeons because this artery is involved in many diseases.

Chronic Subdural Hematomas. During the past 5 years, the MMA has been of interest to neuroradiologists and neurosurgeons in the treatment of recurrent chronic subdural hematomas. Mostly in patients > 65 years old, under anticoagulant and antiplatelet therapy, and with mild head trauma bridging vein injury can cause chronic subdural hematoma.[46] Traditional treatment consists of burr-hole evacuations, with a high rate of recurrence (2–37%).[46,47] This trend is attributed to the inflammatory response caused by residual blood, which causes the formation of membranes around the hematoma. Membranes are also stimulated by angiogenic factors to neoangiogenesis, which results in the formation of fragile microcapillaries, with a high recurrent bleeding risk. In this context, some investigators, for example, Link et al,[46] proposed the management of recurrent chronic subdural hematoma through endovascular MMA embolization. The MMA represents the principal blood supply of the bleeding membranes; thus, its occlusion allows the collection to be resorbed.[46-48] These investigators described a recurrence rate similar to surgical evacuation but with a less-invasive procedure.[46-48] Thus, this technique could represent an alternative treatment option, especially for elderly patients with recurrent chronic subdural hematoma.

Meningeal Tumors. Meningiomas are the most common benign intracranial tumors, mostly located at the skull vault or at the skull base. Because MMA is the major dural artery, most cranial meningiomas receive its supply. Surgery represents the first-line treatment for symptomatic meningiomas, but preoperative MMA

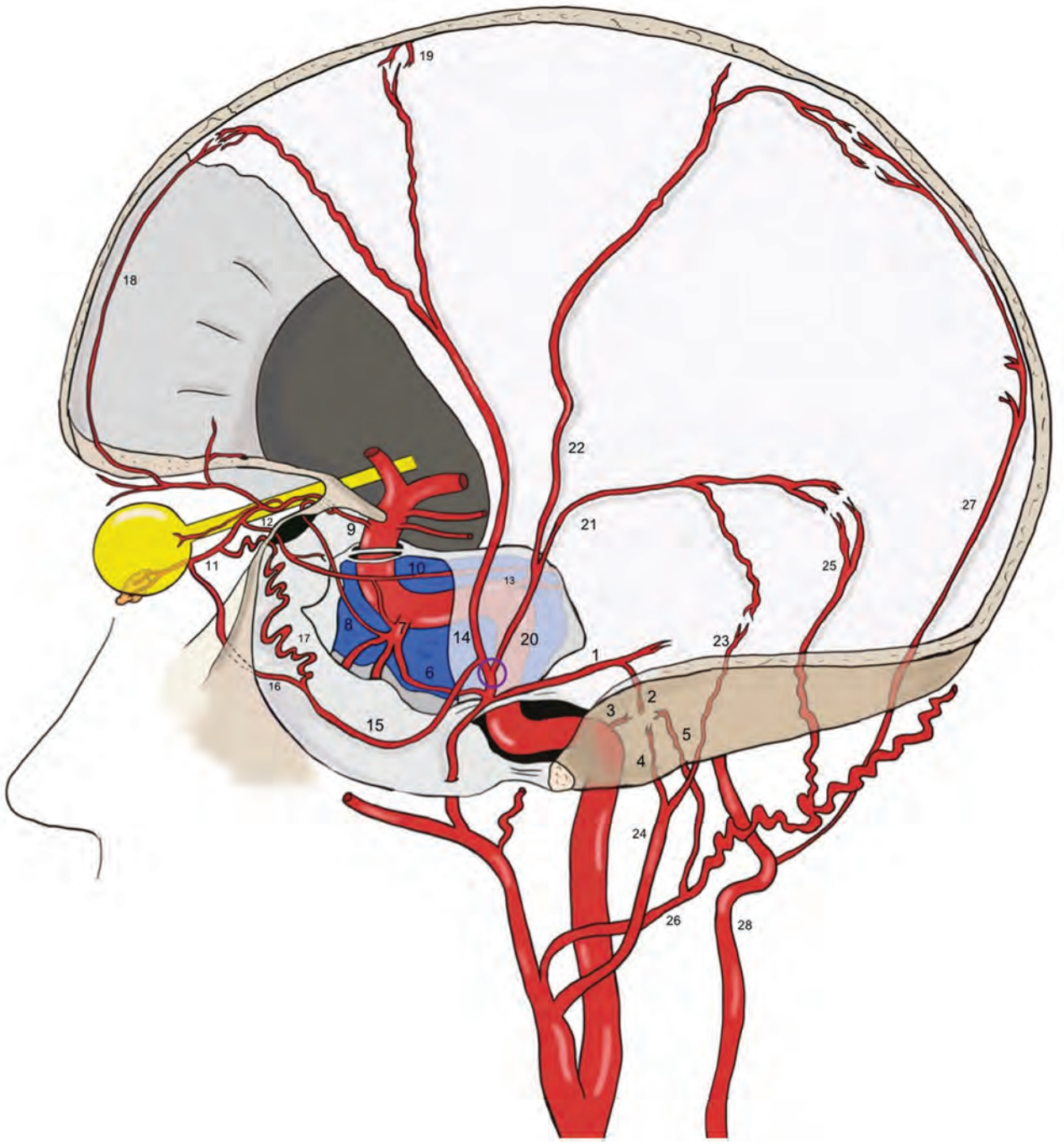

FIG 4. Anastomoses of the MMA. Before the MMA bifurcation (*purple circle*), the petrous branch (*1*), from which the superior tympanic artery (*2*) originates, anastomoses into the middle ear with the caroticotympanic artery (*3*, from the ICA), and with the inferior tympanic artery (*4*, from the ascending pharyngeal artery), with the posterior tympanic artery (*5*, from the occipital artery). The cavernous branch of the MMA (*6*) on the other side anastomoses with the inferolateral trunk (ILT) (*7*), which is itself connected to the OA (*9*) through the deep recurrent OA (*8*). The ILT, the MMA, and the OA are also linked to each other through the marginal tentorial artery (*10*), whose origin can vary from the lacrimal artery (*11*), via superficial recurrent OA (*12*), to the meningohypophyseal trunk (*13*). After the MMA bifurcation at the pterion, its frontal division (*14*) gives a medial branch (*15*), which can bifurcate intracranially into a lateral meningolacrimal artery (*16*), and a medial sphenoidal artery (*17*). Both branches reach the lacrimal artery, even if the meningolacrimal artery more distal than the sphenoidal artery. The anastomoses with the OA and the ILT represent the most dangerous connections in the case of MMA transarterial embolization because of the risk of particle embolism into these arteries. The frontal division of the MMA reaches the convexity, following the coronal suture and anastomoses with the anterior falcine artery (*18*, OA–anterior ethmoidal artery) and with branches of the contralateral MMA (*19*). The posterior division of the MMA (*20*) divides into a petrosquamosal branch (*21*) and a parieto-occipital branch (*22*). The former anastomoses with the jugular branch (*23*) of the ascending pharyngeal artery (*24*) and with the mastoid branch (*25*) of the occipital artery (*26*). The latter is linked to the posterior meningeal artery (*27*), from the vertebral artery (*28*) at the border areas.

embolization could be used to reduce the blood supply of the meningioma to limit the blood loss during resection. Meningiomas, depending on their locations, can be supplied by ICA dural branches, external carotid artery dural branches, or a combination of these. Richter and Schachenmayr[49] classified meningiomas into 4 types, depending on their vascular supply: type I, with exclusive external carotid artery vascularization; type II, with a mixed ICA–external carotid artery blood supply with external carotid artery prevalence; type III, with a mixed supply with an ICA prevalence; and type IV, with an exclusive ICA supply. Usually, anterior cranial fossa meningiomas are supplied by the MMA and anterior falcine artery from the OA; middle cranial fossa meningiomas are fed by MMA and dural branches of petrous and cavernous ICA.

However, posterior fossa meningiomas are rarely supplied by the MMA but from the posterior meningeal artery from the vertebral artery and from other external carotid artery branches. For these reasons, MMA embolization should be reserved for meningiomas type I or II of the Richter classification, with typical DSA blush, for middle cranial fossa and selective cases of anterior cranial fossa lesions.[50] During the procedure, the neuroradiologist should keep in mind the possible anastomoses between MMA and ICA branches to avoid complications. After MMA embolization, surgery can be performed with very variable timing (from 0 to 30 days after the procedure).[51] Also, the neurosurgeon has to keep in mind the general organization of the dural vascularization, which gives important help for meningioma surgery and other meningeal tumors.[15]

Dural AVF. The principal dural pathology treated by neuroradiologists is the dural AVF. Also, for these procedures, a good knowledge of the precise anatomy of the MMA, of its variations, and its vascular anastomoses, helps in the avoidance of complications.[3] Transarterial embolization through MMA has been described as a successful option for dural AVF treatment.[52-54] According to Griessenauer et al,[52] a robust MMA supply is the best predictor for successful embolization. Other factors that make the MMA a favorable way to perform transarterial embolization are its long straight course, which facilitates the penetration of Onyx, (Covidien) its quite large diameter, which allows the introduction of catheters, and its large dural territory, which often reaches dural AVFs in various locations. As already noted, the presence of an SA also has an important impact on the technical difficulty for performing a stapedectomy.[49,55] The middle ear surgeon could avoid excessive blood loss by knowing the presence of such a vascular variation during the surgical planning.

REFERENCES

1. Martins C, Yasuda A, Campero A, et al. **Microsurgical anatomy of the dural arteries.** *Neurosurgery* 2005;56:211–51; discussion 211–51 CrossRef Medline
2. Merland JJ, Theron J, Lasjaunias P, et al. **Meningeal blood supply of the convexity.** *J Neuroradiol* 1977;4:129–74 Medline
3. Lasjaunias P, Bereinstein A, ter Brugge K. *Surgical Neuroangiography KG.* Berlin: Springer-Verlag; 2001
4. Low FN. **An anomalous middle meningeal artery.** *Anat Rec* 1946;95:347–51 CrossRef Medline
5. Altmann F. **Anomalies of the internal carotid artery and its branches; their embryological and comparative anatomical significance; report of a new case of persistent stapedial artery in man.** *Laryngoscope* 1947;57:313–39 CrossRef Medline
6. Seeger JF, Hemmer JF. **Persistent basilar/middle meningeal artery anastomosis.** *Radiology* 1976;118:367–70 CrossRef Medline
7. Lasjaunias P, Moret J, Manelfe C, et al. **Arterial anomalies at the base of the skull.** *Neuroradiology* 1977;13:267–72 CrossRef Medline
8. Katz M, Wisoff HS, Zimmerman RD. **Basilar-middle meningeal artery anastomoses associated with a cerebral aneurysm. Case report.** *J Neurosurg* 1981;54:677–80 CrossRef Medline
9. Shah QA, Hurst RW. **Anomalous origin of the middle meningeal artery from the basilar artery: a case report.** *J Neuroimaging* 2007;17:261–63 CrossRef Medline
10. Kuruvilla A, Aguwa AN, Lee AW, et al. **Anomalous origin of the middle meningeal artery from the posterior inferior cerebellar artery.** *J Neuroimaging* 2011;21:269–72 CrossRef Medline
11. Kumar S, Mishra NK. **Middle meningeal artery arising from the basilar artery: report of a case and its probable embryological mechanism.** *J Neurointerv Surg* 2012;4:43–44 CrossRef Medline
12. Salem MM, Fusco MR, Dolati P, et al. **Middle meningeal artery arising from the basilar artery.** *J Cerebrovasc Endovasc Neurosurg* 2014;16:364–67 CrossRef Medline
13. Waga S, Okada M, Yamamoto Y. **Basilar-middle meningeal arterial anastomosis. Case report.** *J Neurosurg* 1978;49:450–52 CrossRef Medline
14. Steffen TN. **Vascular anomalites of the middle ear.** *Laryngoscope* 1968;78:171–97 CrossRef Medline
15. Dilenge D, Ascherl GF Jr. **Variations of the ophthalmic and middle meningeal arteries: relation to the embryonic stapedial artery.** *AJNR Am J Neuroradiol* 1980;1:45–54 Medline
16. Gabriele OF, Bell D. **Ophthalmic origin of the middle meningeal artery.** *Radiology* 1967;89:841–44 CrossRef Medline
17. Brucher J. **Origin of the ophthalmic artery from the middle meningeal artery.** *Radiology* 1969;93:51–52 CrossRef Medline
18. Royle G, Motson R. **An anomalous origin of the middle meningeal artery.** *J Neurol Neurosurg Psychiatry* 1973;36:874–76 CrossRef Medline
19. Moret J, Lasjaunias P, Théron J, et al. **The middle meningeal artery. Its contribution to the vascularisation of the orbit.** *J Neuroradiol* 1977;4:225–48 Medline
20. Diamond MK. **Homologies of the meningeal-orbital arteries of humans: a reappraisal.** *J Anat* 1991;178:223–41 Medline
21. Liu Q, Rhoton AL Jr. **Middle meningeal origin of the ophthalmic artery.** *Neurosurgery* 2001;49:401–06; discussion 406-07 CrossRef Medline
22. Plas B, Bonneville F, Dupuy M, et al. **Bilateral ophthalmic origin of the middle meningeal artery.** *Neurochirurgie* 2013;59:183–86 CrossRef Medline
23. Cvetko E, Bosnjak R. **Unilateral absence of foramen spinosum with bilateral ophthalmic origin of the middle meningeal artery: case report and review of the literature.** *Folia Morphol (Warsz)* 2014;73:87–91 CrossRef Medline
24. Kimball D, Kimball H, Tubbs RS, et al. **Variant middle meningeal artery origin from the ophthalmic artery: a case report.** *Surg Radiol Anat* 2015;37:105–08 CrossRef Medline
25. Curnow J. **Two instances of irregular ophthalmic and middle meningeal arteries.** *J Anat Physiol* 1873;8(pt 1):155–56 Medline
26. Meyer F. **About the anatomy of orbital arteries.** *Morph Jahr* 1887;12:414–58
27. Zuckerkandl E. **Zur Anatomie der Orbita Arterien.** *Med Jahr* 1876:343
28. Lasjaunias P, Moret J. **Normal and non-pathological variations in the angiographic aspects of the arteries of the middle ear.** *Neuroradiology* 1978;15:213–19 CrossRef Medline
29. Maiuri F, Donzelli R, de Divitiis O, et al. **Anomalous meningeal branches of the ophthalmic artery feeding meningiomas of the brain convexity.** *Surg Radiol Anat* 1998;20:279–84 CrossRef Medline
30. Rodesch G, Choi IS, Lasjaunias P. **Complete persistence of the hyoido-stapedial artery in man. Case report. Intra-petrous origin**

of the maxillary artery from ICA. *Surg Radiol Anat* 1991;13:63–65 CrossRef Medline
31. Fisher AG. **A case of complete absence of both internal carotid arteries, with a preliminary note on the developmental history of the stapedial artery.** *J Anat Physiol* 1913;48(pt 1):37–46 Medline
32. Guinto FC Jr, Garrabrant EC, Radcliffe WB. **Radiology of the persistent stapedial artery.** *Radiology* 1972;105:365–69 CrossRef Medline
33. Teal JS, Rumbaugh CL, Bergeron RT, et al. **Congenital absence of the internal carotid artery associated with cerebral hemiatrophy, absence of the external carotid artery, and persistence of the stapedial artery.** *Am J Roentgenol Radium Ther Nucl Med* 1973;118:534–45 CrossRef Medline
34. McLennan JE, Rosenbaum AE, Haughton VM. **Internal carotid origins of the middle meningeal artery. The ophthalmic-middle meningeal and stapedial-middle meningeal arteries.** *Neuroradiology* 1974;7:265–75 CrossRef Medline
35. Sheikh BY, Coates R, Siqueira EB. **Stapedial artery supplying sphenoid wing meningioma: case report.** *Neuroradiology* 1993;35:537–38 CrossRef Medline
36. Kawai K, Yoshinaga K, Koizumi M, et al. **A middle meningeal artery which arises from the internal carotid artery in which the first branchial artery participates.** *Ann Anat* 2006;188:33–38 CrossRef Medline
37. Koenigsberg RA, Zito JL, Patel M, et al. **Fenestration of the internal carotid artery: a rare mass of the hypotympanum associated with persistence of the stapedial artery.** *AJNR Am J Neuroradiol* 1995;16 (suppl):908–10 Medline
38. Silbergleit R, Quint DJ, Mehta BA, et al. **The persistent stapedial artery.** *AJNR Am J Neuroradiol* 2000;21:572–77 Medline
39. Baltsavias G, Kumar R, Valavanis A. **The pharyngo-tympano-stapedial variant of the middle meningeal artery. A case report.** *Interv Neuroradiol* 2012;18:255–58 CrossRef Medline
40. Diamond MK. **Unusual example of a persistent stapedial artery in a human.** *Anat Rec* 1987;218:345–54 CrossRef Medline
41. Salamon G, Grisoli J, Paillas JE, et al. **Arteriographic study of the meningeal arteries. (role of selective injections, of subtraction and of radio-anatomical correlations).** *Neurochirurgia (Stuttg)* 1967;10:1–19 CrossRef Medline
42. Salamon G, Guérinel G, Demard F. **Radioanatomical study of the external carotid artery.** *Ann Radiol (Paris)* 1968;11:199–215 Medline
43. Moret J, Lasjaunias P, Vignaud J, et al. **The middle meningeal blood supply to the posterior fossa (author's transl).** *Neuroradiology* 1978;16:306–07 CrossRef Medline
44. Silvela J, Zamarron MA. **Tentorial arteries arising from the external carotid artery.** *Neuroradiology* 1978;14:267–69 CrossRef Medline
45. Margolis MT, Newton TH. **Collateral pathways between the cavernous portion of the internal carotid and external carotid arteries.** *Radiology* 1969;93:834–36 CrossRef Medline
46. Link TW, Boddu S, Marcus J, et al. **Middle meningeal artery embolization as treatment for chronic subdural hematoma: a case series.** *Oper Neurosurg (Hagerstown)* 2018;14:556–62 CrossRef Medline
47. Fiorella D, Arthur AS. **Middle meningeal artery embolization for the management of chronic subdural hematoma.** *J Neurointerv Surg* 2019;11:912–15 CrossRef Medline
48. Haldrup M, Ketharanathan B, Debrabant B, et al. **Embolization of the middle meningeal artery in patients with chronic subdural hematoma-a systematic review and meta-analysis.** *Acta Neurochir (Wien)* 2020;162:777–84 CrossRef Medline
49. Richter HP, Schachenmayr W. **Preoperative embolization of intracranial meningiomas.** *Neurosurgery* 1983;13:261–68 CrossRef Medline
50. Dubel GJ, Ahn SH, Soares GM. **Contemporary endovascular embolotherapy for meningioma.** *Semin Intervent Radiol* 2013;30:263–77 CrossRef Medline
51. Shah A, Choudhri O, Jung H, et al. **Preoperative endovascular embolization of meningiomas: update on therapeutic options.** *Neurosurg Focus* 2015;38:E7 CrossRef Medline
52. Griessenauer CJ, He L, Salem M, et al. **Middle meningeal artery: gateway for effective transarterial Onyx embolization of dural arteriovenous fistulas.** *Clin Anat* 2016;29:718–28 CrossRef Medline
53. Hayashi K, Ohmoro Y, KY, et al. **Non-sinus-type dural arteriovenous fistula cured by transarterial embolization from middle meningeal artery: two case reports.** *J Neuro Endovasc Ther* 2018;12:542–45 Medline
54. Hlavica M, Ineichen BV, Fathi AR, et al. **Parasagittal dural arteriovenous fistula treated with embozene microspheres.** *J Endovasc Ther* 2015;22:952–55 CrossRef Medline
55. Maran AG. **Persistent stapedial artery.** *J Laryngol Otol* 1965;79:971–75 CrossRef Medline

Exophytic Lumbar Vertebral Body Mass in an Adult with Back Pain

J.C. Benson, M.A. Vizcaino, D.K. Kim, C. Carr, P. Rose, L. Eckel, and F. Diehn

ABSTRACT

SUMMARY: Chordomas are rare primary bone malignancies derived from notochord remnants. The tumors often are slow-growing and often present with indolent, nonspecific symptoms. Nevertheless, chordomas are locally aggressive and highly prone to local recurrence, necessitating precise planning before biopsy and/or surgical resection. Familiarity with the imaging features of chordomas is, therefore, essential. This case highlights the typical imaging and pathologic features of a spinal chordoma as well as the surgical approach and the patient's subsequent outcome.

In brief, this case involves a 70-year-old man presented with a 1-month history of low-back and bilateral thigh pain that was unresponsive to physical therapy or chiropractic care. His symptoms were exacerbated by standing and walking and affected his left leg more than the right one. He had no known malignancy; his medical history was unremarkable except for atrial fibrillation. The patient had undergone MR imaging at an outside institution that had shown a mass in his lumbar spine. He subsequently presented to our institution for further care.

Imaging

An initial lumbar spine radiograph demonstrated a destructive lesion in the L3 vertebral body with endplate deformities (not shown). Subsequent MR imaging confirmed the presence of a large left-eccentric exophytic mass arising from L3 (Fig 1). Although some internal heterogeneity was noted, the tumor was predominantly hypointense on T1WI and markedly hyperintense on T2WI. The mass demonstrated heterogeneous areas of solid and linear enhancements, some corresponding to T2-hypointense intratumoral septations. The moderately enhancing tumor extended into the adjacent soft tissues, displacing the left psoas muscle and narrowing the left L3–4 foramen, with pushing rather than infiltrative-appearing margins. CT, too, showed a large destructive mass arising from the L3 vertebral body. No intralesional calcifications were noted within the lytic tumor. A whole-body nuclear medicine bone scan (not shown) showed neither convincing activity nor photopenia in the corresponding region, nor were metastases seen elsewhere.

The marked T2 hyperintensity of the tumor, internal T2-hypointense septations, and large extraosseous components were suggestive of a chordoma. Chondrosarcoma was considered, though classic "rings and arcs" were not observed. Giant cell tumors are found much more commonly in the sacrum, but they share many similar imaging characteristics with chordomas when seen in the mobile spine. Plasmacytomas typically remain within the bone and often have a "minibrain" or "soap bubble" intratumoral appearance.[1] Finally, a solitary metastasis, though possible, was thought unlikely given the appearance of the mass and the lack of known primary malignancy.

The likelihood of a chondroma or chondrosarcoma had implications for immediate management. A contemplated biopsy, for example, should be carefully planned and well-documented because the entire biopsy track is often resected or radiated in cases of chordoma or sarcoma to prevent local recurrence. Some surgeons even prefer the entry site of any percutaneous biopsy to be marked to facilitate the subsequent resection of the track.

Operative Report and Follow-Up

The patient's surgical resection was performed in a staged, en bloc fashion (Fig 2). On the first day, the patient underwent an anterior, transperitoneal approach to mobilize the visceral and vascular structures away from the tumor. Additionally, because the extraosseous tumor extended above the L2–3 and below the L3–4 disc spaces laterally and endplate fractures had allowed tumor entry into the disc spaces, osteotomies cut through the lower portion of the L2 vertebral body and the upper portion of the L4 vertebral body to allow removal of the specimen without inadvertent entry into the tumor.

Received May 4, 2020; accepted after revision June 2.

From the Departments of Radiology (J.C.B., D.K.K., C.C., L.E., F.D.), Pathology (M.A.V.), and Orthopedic Surgery (P.R.), Mayo Clinic, Rochester, Minnesota.

Please address correspondence to John C. Benson, MD, 200 1st St. SW, Department of Radiology, Mayo Clinic, Rochester, MN 55905; e-mail: benson.john3@mayo.edu

http://dx.doi.org/10.3174/ajnr.A6749

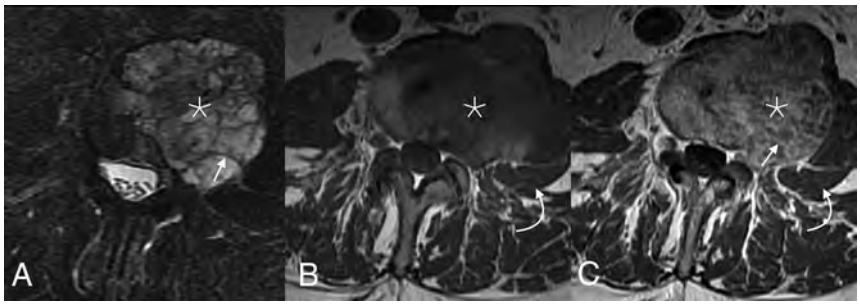

FIG 1. Axial MR imaging of the mass. T2 fat-saturated (*A*), T1 precontrast (*B*), and postcontrast (*C*) sequences show a mass centered within the mid and left aspects of the L3 vertebral body (*asterisk*). Most of the tumor demonstrates substantial T2 prolongation, which is particularly evident with fat saturation. Internal T2-hypointense septations are noted, which enhance with moderate avidity (*straight arrows*), while the fluid-filled regions lack enhancement. The tumor extends out of the left vertebral body into the adjacent soft tissues, displacing but not invading the left psoas muscle laterally (*curved arrows*).

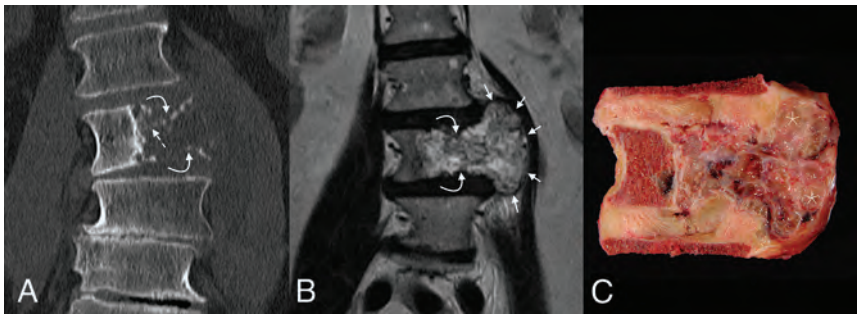

FIG 2. Coronal imaging and corresponding gross pathology of the tumor. On CT (*A*), the mass is destructive, with faint small foci of high attenuation, either representing amorphous calcifications or residual/partially destroyed vertebral body trabeculae (*dashed arrow*). Both the superior and inferior endplates are fractured (*curved arrows*). The degree of extraosseous extension is best seen on T2 MR imaging (*B*), where the soft-tissue components are seen to mushroom out along the adjacent intervertebral discs (*between the short arrows*), with pushing-type margins. The gross pathology specimen (*C*) confirms the presence of numerous high-water-content loculations (*asterisk*) separated by small septations, corresponding with areas of T2 hyperintensity.

The patient returned to surgery 48 hours later for posterior tumor delivery and an instrumented spinal reconstruction. This involved laminectomies from the lower portion of L2 through the upper portion of L4 for exposure of the dural tube, sacrifice of the bilateral L2 and L3 nerve roots, and completion of osteotomies through L2 and L4 for en bloc tumor delivery. Reconstruction was performed with a combination of posterior pedicle screw instrumentation, bone autograft, and an anterior titanium cage.

Three years after the patient's en-bloc L3 vertebrectomy with tumoral resection, he was diagnosed with a recurrent lesion in his L4 vertebral body and adjacent paraspinal soft tissues, seen on both PET and MR imaging. This was treated with cryoablation. Imaging performed during the subsequent 18 months demonstrated no other recurrences or metastases. The remainder of the patient's follow-up course was completed at an outside institution. He ultimately died 6 years postoperatively from complications related to Parkinson disease and had asymptomatic local recurrence at the time of his death.

Pathology

Histologic sections demonstrated a neoplasm arranged in nests and cords within a prominent myxoid mucoid matrix (Fig 3). Most of the tumor cells were large, round-to-oval, with central nuclei and abundant eosinophilic cytoplasm with mild vacuolation. Scattered physaliphorous cells with multivacuolation and a foamy appearance were also present. Only rare mitoses were identified. Immunohistochemistry performed on paraffin-embedded tissue demonstrated nuclear brachyury and cytoplasmic keratin CAM 5.2 expression in the neoplastic cells (Figs 3*C*, -*D*). The tumor was also immunoreactive for vimentin, while S-100 protein was negative.

Despite chondrosarcoma in the differential diagnosis of chordoma, the lack of chondroid differentiation in this case along with the presence of physaliphorous cells favored the diagnosis of chordoma. Given the growth pattern and myxoid background of this neoplasm in addition to keratin immune expression, metastatic carcinoma was another diagnostic consideration. Nonetheless, brachyury is a highly sensitive and specific marker expressed in chordoma and negative in chondrosarcoma and carcinoma. On the basis of the morphologic and immunophenotypic findings, the diagnosis of chordoma was rendered.

Diagnosis: Chordoma

Discussion. Chordomas are primary bone malignancies that typically occur in adults older than 40 years of age and affect men more than women.[2,3] The tumors are rare, with an incidence of 0.08 per 100,000 individuals, accounting for 1%–8% of primary bone tumors.[4] However, they do represent up to 20% of primary bone tumors of the spine.[5] The tumors arise from vestigial notochord remnants, which typically involute during the tenth week of gestation.[5] This embryologic origin likely explains the observed anatomic proclivity for the clivus, spine, and sacrum.[6] The distribution among these sites is relatively evenly split, with roughly one-third of chordomas arising from each site, though vertebral bodies are typically described as the least commonly involved.[7] Within the spine, however, cervical segments are most often involved, particularly C2. The pathogenesis of chordomas also explains the tumoral predilection for midline or paramedian locations because notochordal remnants evolve into the nucleus pulposus.

On imaging, chordomas usually appear as destructive osseous masses with involvement of the adjacent soft tissues.[8] Many tumors are large at the time of diagnosis, owing to their indolent

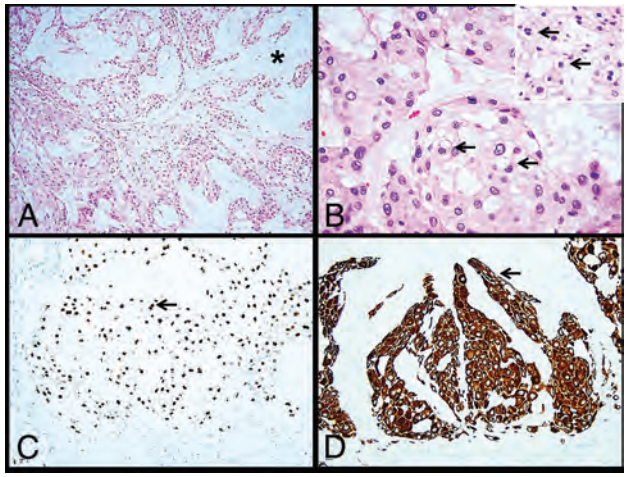

FIG 3. Histology images. The tumor consists of cells arranged in nests and cords (*A*) within an abundant mucoid matrix (*A*, *asterisk*). Most of the tumor cells are large with central nuclei and mildly vacuolated eosinophilic cytoplasm (*B*, *arrows*). Scattered physaliphorous cells are also present (*B* inset, *arrows*). Immunohistochemistry demonstrates nuclear brachyury (C, *arrow*) and cytoplasmic keratin CAM 5.2 (*D*, *arrow*) expression in tumor cells.

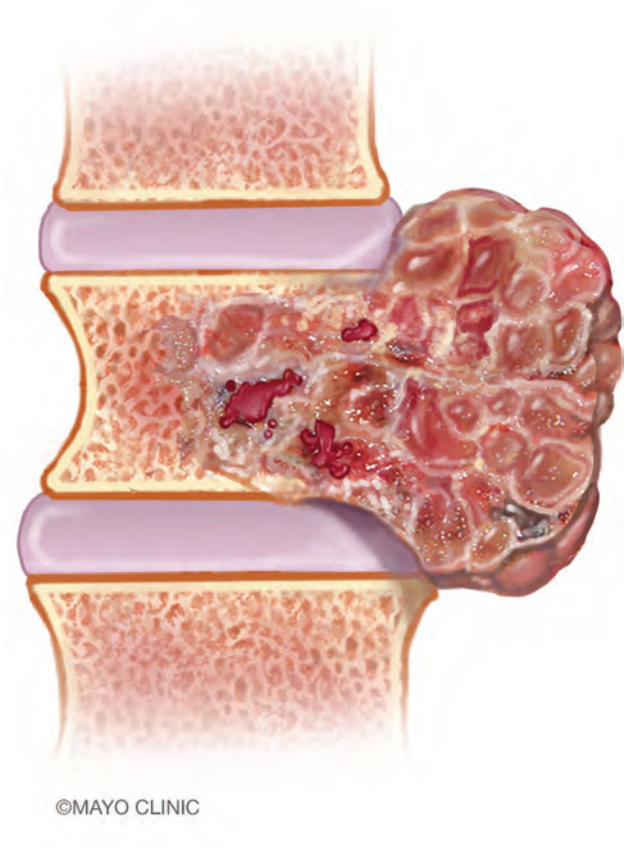

FIG 4. An artist's illustration of a spinal chordoma. The tumors are generally sizable at the time of diagnosis. Extraosseous components are often larger than those within the vertebral bodies and extend along the adjacent spinal segments, compatible with the classically described dumbbell appearance. Image used with permission of Mayo Foundation for Medical Education and Research. All rights reserved.

growth. The appearance exhibited is often that of a "dumbbell" or "mushroom" configuration, in which the exophytic component is more expansile than the vertebral body from which the tumor originates.[9] Due to the indolent growth of the malignancy, the margins of the tumor tend to displace adjacent tissue rather than invade it. The paraspinal component can extend along the margins of ≥1 adjacent vertebral body but typically spares the intervertebral disc (Fig 4). Infrequently, tumors may spread into the paraspinal soft tissues via the neural foramina, simulating the appearance of a schwannoma.[10]

On CT, chordomas tend to be lobulated, osteolytic, expansile, and exophytic. Intratumoral attenuation is low due to the presence of myxoid-type tissue. Punctate calcifications and/or flecks of residual or destroyed bone are often present.[11] These calcifications appear amorphous and are found in higher concentrations near the tumor margins.[12] On MR imaging, the most notable feature is that of striking intratumoral T2 prolongation due to high internal water content. Although not pathognomonic, markedly elevated T2 signal within a lobulated midline spinal mass is highly suggestive of a chordoma. Areas of intrinsic T1 hyperintensity are often present, representing hemorrhage or mucinous material. Varying degrees of enhancement can be seen. The fibrous septa separating the T2 bright mucinous regions of the tumor tend to be T2 hypointense and enhancing.[13] However, a minority of chordomas may not enhance, and this subset may have a lower risk of posttreatment recurrence in a skull base location.[14] Finally, diffusion-weighted imaging may have diagnostic and prognostic value: Lower ADC values both favor chondroma over chondrosarcoma and predict chordoma tumor progression.[15,16]

The imaging findings in this case fit many of the classic descriptors of a chordoma. The tumor was large, osteolytic, exophytic, and demonstrated striking intratumoral T2 signal separated by more hypointense septations. Its dumbbell shape—owing to a large extraosseous component that had well-defined rather than infiltrating margins that extended along the spine—was particularly distinctive. Chondrosarcomas share many of these features but typically have an intratumoral chondroid matrix (Table). Giant cell tumors lack the internal T2 hyperintensity seen in this tumor and typically occur in younger patients. Plasmacytoma was thought less likely because of the prominent intratumoral septations. A solitary metastasis, though possible, was considered lower on the differential, given the patient's lack of a primary malignancy.

Histologically, chordomas also have several characteristic features. Macroscopically, the tumors are made up of lobulated gelatinous gray tissue that may appear encapsulated. Chordomas are formed by large vacuolated cells forming nests and strands within a myxoid mucoid matrix.[17] Cellularity can be variable, and some tumors may show solid areas. Physaliphorous cells are round-to-oval with central nuclei and abundant cytoplasm with prominent perinuclear vacuolation. Although classic in chordomas, these cells may be sparse-to-rare in some cases. Mitotic activity is generally low. Chordomas may exhibit foci of chondroid differentiation, particularly those arising in the spheno-occipital region.[18] In rare cases, a spindle cell component with features of malignant fibrous histiocytoma can be noted; such tumors are designated as dedifferentiated chordomas.[19] Immunohistochemically, chordomas demonstrate

Comparison of various demographic, location, and imaging features of chordomas with those of the most common imaging differential diagnoses

	Chordoma	GCT	Chondrosarcoma	Plasmacytoma
Age at diagnosis (range) (peak yr)	40–60	20–30	30–70	30–60
Most common location in mobile spine	Cervical	Lumbar (sacrum much more common)	Lumbar	Thoracic
Commonly involves posterior elements	–	+	+	+
Intratumoral calcification	Amorphous	–	Rings and arcs	–
T2WI	↑↑	↓→	↑	↑
Extraosseous extension	+	+	+	–
Characteristic feature	Dumbbell or mushroom shape	Lytic lesion without sclerotic rim; fluid-fluid levels	Intratumoral chondroid matrix	Minibrain, soap bubble

Note:—GCT indicates Giant cell tumor; –, features absent; +, features present; ↓→, hypo- to iso-intense intralesional signal; ↑, hyperintense intralesional signal.

nuclear positivity for brachyury, which is highly sensitive and specific for this tumor. It can also express keratin CAM 5.2, epithelial membrane antigen, vimentin, and S-100 protein.[20] The differential diagnosis of chordoma includes chondrosarcoma and metastatic carcinoma. Even though chondrosarcomas can mimic chordomas morphologically (especially if the latter shows extensive chondroid differentiation), chondrosarcoma is negative for brachyury by immunohistochemistry and has frequent *isocitrate dehydrogenase 1* and *2* (*IDH1/IDH2*) gene mutations. In contrast, chordoma is consistently immunoreactive for brachyury and does not show *IDH1/IDH2* mutations.[21] Metastatic carcinomas are also immunoreactive for keratins. However, they are also positive for other organ-specific markers and do not express brachyury.

Although slow-growing, chordomas are locally aggressive malignancies, often displacing adjacent structures.[22] Overall, the prognosis of chordomas is poor, with a median survival of 6.3–7.7 years, and a 5-year survival rate of 68%–72%.[23,24] Resected tumors often recur locally and are thought to be seeded by the pseudocapsule at the tumor margins.[24] Thus, achieving negative margins during surgery is paramount in the treatment of such tumors. Recurrences have poor prognoses, with substantially worsened 5- and 10-year survival than primary tumors.[25] Radiation treatment has also been shown to improve local control and overall survival, and cryoablation and laser interstitial thermal therapies have been reported for treatment of recurrences.[26-28] Large tumor size, intratumoral necrosis, and advanced age are also associated with worse outcomes.[10] Metastases, conversely, are rare, even in the setting of large tumors. When present, metastases usually occur late in the disease course.[29]

Case Summary

- Chordomas of the mobile spine classically have a mushroom or dumbbell shape and striking intratumoral T2 hyperintensity, with T2-hypointense septations.
- Diagnostic considerations include chondrosarcoma, giant cell tumor, plasmacytoma, and solitary metastasis.
- Suspicion of a chordoma should be communicated to ensure careful planning of any future biopsy and/or surgical resection.
- Brachyury immunohistochemistry is very helpful to distinguish chordoma from other mimics.
- Resection with wide surgical margins is essential to prevent local recurrences.

Disclosures: Peter Rose—*UNRELATED*: *Consultancy*: K2M, *Comments*: prior preliminary design contract to develop spine oncology implants: total ~$5000, all donated to charity; *Travel/Accommodations/Meeting Expenses Unrelated to Activities Listed:* Depuy Spine, *Comments*: prior expense reimbursement while chairing a spine tumor educational course; donated to charity.

REFERENCES

1. Major NM, Helms CA, Richardson WJ. **The "mini brain": plasmacytoma in a vertebral body on MR imaging.** *AJR Am J Roentgenol* 2000;175:261–63 CrossRef Medline
2. Pendharkar AV, Ho AL, Sussman ES, et al. **Surgical management of sacral chordomas: illustrative cases and current management paradigms.** *Cureus* 2015;7:e301 CrossRef Medline
3. Zhou Y, Hu B, Wu Z, et al. **A giant lumbar chordoma: a case report.** *Medicine (Baltimore)* 2018;97:e11128 CrossRef Medline
4. Smoll NR, Gautschi OP, Radovanovic I, et al. **Incidence and relative survival of chordomas: the standardized mortality ratio and the impact of chordomas on a population.** *Cancer* 2013;119:2029–37 CrossRef Medline
5. Muneer M, Badran S, Al-Hetmi T. **A rare presentation of axial chordoma and the approach to management.** *Am J Case Rep* 2019;20:773–75 CrossRef Medline
6. Godkin O, Elkhwad H, McCabe J. **Large chordoma of the sacrum.** *BMJ Case Rep* 2017;2017:bcr2017221293 CrossRef Medline
7. Frezza AM, Botta L, Trama A, et al. **Chordoma: update on disease, epidemiology, biology and medical therapies.** *Curr Opin Oncol* 2019;31:114–20 CrossRef Medline
8. Farsad K, Kattapuram SV, Sacknoff R, et al. **Sacral chordoma.** *Radiographics* 2009;29:1525–30 CrossRef Medline
9. Smolders D, Wang X, Drevelengas A, et al. **Value of MRI in the diagnosis of non-clival, non-sacral chordoma.** *Skeletal Radiol* 2003;32:343–50 CrossRef Medline
10. Noor A, Bindal P, Ramirez M, et al. **Chordoma: a case report and review of literature.** *Am J Case Rep* 2020;21:e918927 CrossRef Medline
11. Murphey MD, Andrews CL, Flemming DJ, et al. **From the archives of the AFIP: primary tumors of the spine—radiologic pathologic correlation.** *Radiographics* 1996;16:1131–58 CrossRefMedline
12. Krol G, Sundaresan N, Deck M. **Computed tomography of axial chordomas.** *J Comput Assist Tomogr* 1983;7:286–89 CrossRef Medline
13. Rodallec MH, Feydy A, Larousserie F, et al. **Diagnostic imaging of solitary tumors of the spine: what to do and say.** *Radiographics* 2008;28:1019–41 CrossRef Medline
14. Lin E, Scognamiglio T, Zhao Y, et al. **Prognostic implications of gadolinium enhancement of skull base chordomas.** *AJNR Am J Neuroradiol* 2018;39:1509–14 CrossRef Medline

15. Yeom KW, Lober RM, Mobley BC, et al. **Diffusion-weighted MRI: distinction of skull base chordoma from chondrosarcoma.** *AJNR Am J Neuroradiol* 2013;34:1056–61.S1 CrossRef Medline
16. Sasaki T, Moritani T, Belay A, et al. **Role of the apparent diffusion coefficient as a predictor of tumor progression in patients with chordoma.** *AJNR Am J Neuroradiol* 2018;39:1316–21 CrossRef Medline
17. MacLean FM, Soo MY, Ng T. **Chordoma: radiological–pathological correlation.** *Australas Radiol* 2005;49:261–68 CrossRef Medline
18. Wasserman JK, Gravel D, Purgina B. **Chordoma of the head and neck: a review.** *Head Neck Pathol* 2018;12:261–68 CrossRef Medline
19. Shih AR, Cote GM, Chebib I, et al. **Clinicopathologic characteristics of poorly differentiated chordoma.** *Mod Pathol* 2018;31:1237–45 CrossRef Medline
20. Oakley GJ, Fuhrer K, Seethala RR. **Brachyury, SOX-9, and podoplanin, new markers in the skull base chordoma vs chondrosarcoma differential: a tissue microarray-based comparative analysis.** *Mod Pathol* 2008;21:1461–69 CrossRef Medline
21. Arai M, Nobusawa S, Ikota H, et al. **Frequent IDH1/2 mutations in intracranial chondrosarcoma: a possible diagnostic clue for its differentiation from chordoma.** *Brain Tumor Pathol* 2012;29:201–06 CrossRef Medline
22. Phang ZH, Saw XY, Nor N, et al. **Rare case of neglected large sacral chordoma in a young female treated by wide en bloc resection and sacrectomy.** *BMC Cancer* 2018;18:1112 CrossRef Medline
23. McMaster ML, Goldstein AM, Bromley CM, et al. **Chordoma: incidence and survival patterns in the United States, 1973–1995.** *Cancer Causes Control* 2001;12:1–11 CrossRef Medline
24. Pillai S, Govender S. **Sacral chordoma: a review of literature.** *J Orthop* 2018;15:679–84 CrossRef Medline
25. Ailon T, Torabi R, Fisher CG, et al. **Management of locally recurrent chordoma of the mobile spine and sacrum.** *(Phila Pa 1976)* 2016;41:S193–98 CrossRef Medline
26. Indelicato DJ, Rotondo RL, Begosh-Mayne D, et al. **A prospective outcomes study of proton therapy for chordomas and chondrosarcomas of the spine.** *Int J Radiat Oncol Biol Phys* 2016;95:297–303 CrossRef Medline
27. Williams BJ, Karas PJ, Rao G, et al. **Laser interstitial thermal therapy for palliative ablation of a chordoma metastasis to the spine: case report.** *J Neurosurg Spine* 2017;26:722–24 CrossRef Medline
28. Kurup AN, Woodrum DA, Morris JM, et al. **Cryoablation of recurrent sacrococcygeal tumors.** *J Vasc Interv Radiol* 2012;23:1070–75 CrossRef Medline
29. Fourney DR, Gokaslan ZL. **Current management of sacral chordoma.** *Neurosurg Focus* 2003;15:1–5 CrossRef Medline

Clinical and Neuroimaging Correlation in Patients with COVID-19

B.C. Yoon, K. Buch, M. Lang, B.P. Applewhite, M.D. Li, W.A. Mehan, Jr, T.M. Leslie-Mazwi, and S.P. Rincon

ABSTRACT

BACKGROUND AND PURPOSE: Coronavirus disease 2019 (COVID-19) is increasingly being recognized for its multiorgan involvement, including various neurological manifestations. We examined the frequency of acute intracranial abnormalities seen on CT and/or MR imaging in patients with COVID-19 and investigated possible associations between these findings and clinical parameters, including length of hospital stay, requirement for intubation, and development of acute kidney injury.

MATERIALS AND METHODS: This was a retrospective study performed at a large academic hospital in the United States. A total of 641 patients presented to our institution between March 3, 2020, and May 6, 2020, for treatment of coronavirus disease 2019, of whom, 150 underwent CT and/or MR imaging of the brain. CT and/or MR imaging examinations were evaluated for the presence of hemorrhage, infarction, and leukoencephalopathy. The frequency of these findings was correlated with clinical variables, including body mass index, length of hospital stay, requirement for intubation, and development of acute kidney injury as documented in the electronic medical record.

RESULTS: Of the 150 patients, 26 (17%) had abnormal CT and/or MR imaging findings, with hemorrhage in 11 of the patients (42%), infarction in 13 of the patients (50%), and leukoencephalopathy in 7 of the patients (27%). Significant associations were seen between abnormal CT/MR imaging findings and intensive care unit admission ($P = .039$), intubation ($P = .004$), and acute kidney injury ($P = .030$).

CONCLUSIONS: A spectrum of acute neuroimaging abnormalities was seen in our cohort of patients with coronavirus disease 2019, including hemorrhage, infarction, and leukoencephalopathy. Significant associations between abnormal neuroimaging studies and markers of disease severity (intensive care unit admission, intubation, and acute kidney injury) suggest that patients with severe forms of coronavirus disease 2019 may have higher rates of neuroimaging abnormalities.

ABBREVIATIONS: COVID-19 = coronavirus disease 2019; SARS-CoV-2 = Severe Acute Respiratory Syndrome coronavirus 2

Severe Acute Respiratory Syndrome coronavirus 2 (SARS-CoV-2) infection, which causes coronavirus disease 2019 (COVID-19), has been shown to have multiorgan manifestations, with involvement of the lungs, heart, kidneys, liver, and CNS.[1-10] Emerging small cohort studies have demonstrated myriad neuroimaging manifestations related to COVID-19, including stroke, hemorrhagic necrotizing encephalitis, and leukoencephalopathy.[6,9-12] A previous study by Mao et al[5] demonstrated a high rate of neurologic symptoms in patients with COVID-19 and severe respiratory disease. A recent study by Jain et al[13] also described a spectrum of neuroimaging findings associated with COVID-19 and found that patients with acute strokes had a higher mortality risk.

However, it remains unknown exactly which clinical parameters are associated with intracranial abnormalities, in part, because patients with COVID-19 can present with a wide spectrum of laboratory and clinical findings of varying severity. Our aim was to evaluate the frequency of neuroimaging findings in patients with COVID-19, define the types of abnormality present, and investigate possible associations between neuroimaging abnormalities and different clinical parameters. Our hypothesis was that the presence of intracranial abnormalities, such as intracranial hemorrhage, infarction, and leukoencephalopathy, would be associated with clinical parameters suggestive of more severe disease, such as length of hospital stay, intensive care unit admission, and

Received May 29, 2020; accepted after revision June 16.

From the Departments of Radiology (B.C.Y., K.B., M.L., B.P.A., M.D.L., W.A.M., Jr., S.P.R.) and Neurosurgery and Neurology (T.M.L.-M.), Massachusetts General Hospital, Harvard Medical School, Boston, Massachusetts.

Please address correspondence to Byung C. Yoon, MD, Department of Radiology, Massachusetts General Hospital, 55 Fruit St, Boston, MA 02114; e-mail: byoon@mgh.harvard.edu; @MghNeuroRad

Indicates open access to non-subscribers at www.ajnr.org

http://dx.doi.org/10.3174/ajnr.A6717

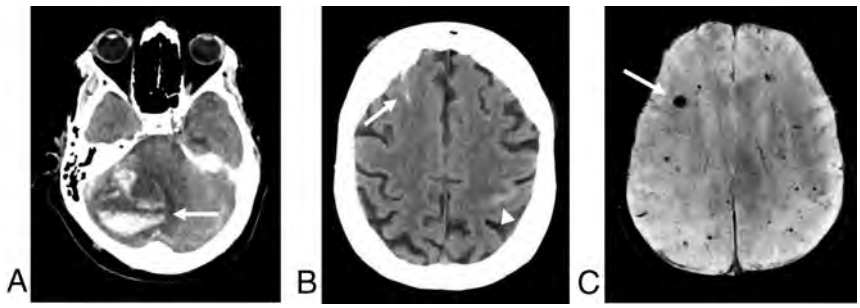

FIG 1. Examples of intracranial hemorrhages in patients with COVID-19. *A*, An axial noncontrast CT of a 42-year-old man demonstrates an acute intraparenchymal hematoma in the right cerebellar hemisphere, with severe mass effect and effacement of the fourth ventricle; multiple areas of layering hemorrhage are seen within the hematoma (*arrow*), suggestive of an underlying coagulopathy. *B*, Noncontrast CT of an 84-year-old woman after a fall shows scattered, curvilinear hyperdensities along the right superior frontal sulcus and left central sulcus, most consistent with acute subarachnoid hemorrhage. *C*, SWI of a 41-year-old man demonstrates scattered foci of susceptibility effect in the bilateral frontal and parietal lobes (*arrow*), most consistent with microhemorrhages.

intubation. Given that acute kidney injury in patients with COVID-19 has been reported to be associated with vascular injury (thrombi and endothelial damage),[14] we also hypothesized that the presence of acute kidney injury may be associated with a higher incidence of cerebrovascular abnormalities.

MATERIALS AND METHODS

Study Cohort

This was a retrospective institutional review board–approved study performed at a large academic hospital in the United States. Between March 3, 2020, and May 6, 2020, a total of 641 patients received medical care at our hospital for COVID-19. Included in our study were all patients at our hospital with documented SARS-CoV-2 infection diagnosed by reverse transcriptase–polymerase chain reaction and who underwent CT and/or MR imaging for the evaluation of neurologic symptoms. Exclusion criteria included patients with suspected COVID-19 who ultimately proved to be COVID-19–negative by the combination of negative reverse transcriptase–polymerase chain reaction results with negative clinical and thoracic imaging criteria, and patients with COVID-19 who underwent CT and MR imaging with substantial artifact, precluding diagnostic assessment.

Clinical Data

Basic demographic information, including age, sex, and body mass index, was obtained from the electronic medical record and recorded for each patient. Clinical data, including length of hospital stay, need for intensive care unit admission, need for intubation, clinical diagnosis of acute kidney injury, and death, were recorded for each patient. The indication for neuroimaging evaluation was recorded for each patient. The length of stay was recorded up to May 19, 2020.

Imaging Technique

All CT examinations were obtained on 64-section multidetector row CT scanners with protocols that included noncontrast CT of the head and CT angiograms of the head and neck. CT examinations were performed on either a Revolution CT (GE Healthcare) or a Force CT (Siemens) scanner. Noncontrast CT studies of the head were axially acquired (120-kV/auto-mAs) at 5-mm- and 1.25-mm-thick slices, and imaging was obtained from the level of the skull base to the vertex. Soft tissue and bone algorithms were available for review with 1.5–2-mm-thick/interval coronal and sagittal reconstructions.

CT angiogram images of the neck were obtained from the level of the aortic arch through the superior orbital rim with 0.625–1.25-mm-thick slices (120-kVp/auto-mAs), after a dose of 80-100 mL of iohexol (Omnipaque; GE Healthcare) or iopamidol (Isovue; Bracco), 370 mg/mL administered by a power injector at a rate of 4-5 mL/s. Coronal and sagittal reformats with 2-mm-thick slices were reconstructed. MR imaging examinations of the brain were obtained on either a 1.5T Signa scanner (GE Healthcare) or a 3T Skyra scanner (Siemens).

MR imaging sequences performed included axial DWI, axial T2 FLAIR, axial T2WI, axial SWI (susceptibility-weighted imaging), and sagittal T1WI. Intravenous contrast was used in a subset of studies.

Image Evaluation

All CT and MR imaging examinations obtained during the hospitalization of patients for COVID-19 were reviewed by 2 neuroradiologists. Intracranial abnormalities, including the presence of hemorrhage, acute or subacute infarction, and/or leukoencephalopathy (Figs 1 and 2) were recorded. For intracranial hemorrhages, the compartment of intracranial hemorrhage (SAH, subdural, epidural, intraventricular, or parenchymal) was defined. The relative size of parenchymal hemorrhage was recorded (microhemorrhage versus lobar hemorrhage). Microhemorrhages were defined as foci of susceptibility effect that were not evident on other sequences such as T1WI or T2WI. The imaging studies were also evaluated for the presence of acute or subacute infarctions with the location and vascular territory of the infarct recorded. The presence of acute WM injury and/or leukoencephalopathy was also recorded, defined as restricted diffusion with corresponding T2 FLAIR hyperintensity within the WM.[15,16]

Data Analysis

A Fisher exact test was performed to evaluate for potential associations between the frequency of recorded neuroimaging abnormalities and clinical parameters, including the length of hospital stay, intubation status, and acute kidney injury. A 2-tailed *t* test was performed to evaluate for significant differences in patient age and body mass index for patients with negative versus positive neuroimaging studies. $P < .05$ was considered statistically

significant. GraphPad Prism (GraphPad Software) was used for statistical analysis.

RESULTS

A total of 150 patients with COVID-19 diagnosed by reverse transcriptase–polymerase chain reaction underwent neuroimaging at our institution. Among these, 141 patients had a CT scan, 21 patients had an MRI, and 31 patients had both CT and MR examinations. None of the patients was excluded from the study for suboptimal imaging. One of the patients had an MR examination that was motion degraded, but the imaging quality was deemed adequate to rule out acute intracranial abnormalities. The same patient had a follow-up MR imaging 16 days after the motion-degraded, initial MR study, which also did not demonstrate any acute or subacute intracranial abnormalities. Twenty-six patients (17%) had an abnormal neuroimaging study; the remaining 124 patients (83%) had no acute intracranial abnormality. The mean age (+/− standard deviation) of our cohort was 63.6 ± 16 years, with a range of 22–96 years. There were 98 men and 52 women enrolled in the study (Table 1).

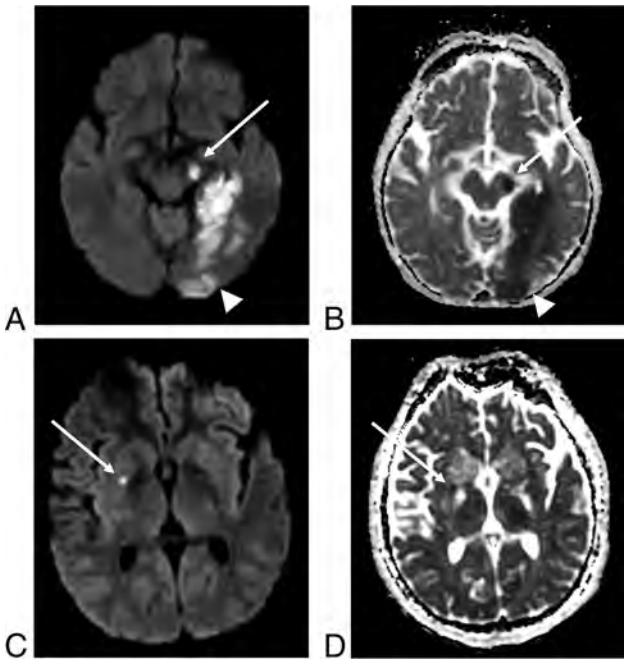

FIG 2. Examples of acute infarcts in patients with COVID-19. Axial DWI (*A*) and corresponding apparent diffusion coefficient map (*B*) of a 50-year-old woman demonstrate restricted diffusion related to an acute left posterior cerebral artery territory infarction. The left temporo-occipital region (*arrowhead*), left hippocampus, and the left cerebral peduncle (*arrow*) are involved. Axial DWI (*C*) and ADC (*D*) images of a 24-year-old man shows a small, subtle focus of restricted diffusion in the right putamen (*arrow*), most consistent with an acute infarct.

Table 2: Summary of clinical presentation, imaging indications, and findings

Clinical Presentation	*n/N* (%)
Respiratory symptoms[a]	21/26 (81)
Fever	7/26 (27)
Headache	2/26 (8)
Fall	2/26 (8)
Stroke symptoms	2/26 (8)
Multiple concerns	12/26 (46)
Imaging indications	
Altered mental status	14/26 (54)
Concern for infarct	8/26 (31)
Concern for intracranial hemorrhage	1/26 (4)
Hypoxia	1/26 (4)
Seizure	1/26 (4)
Headache	1/26 (4)
Imaging findings	
Intracranial hemorrhage	11/26 (42)
SAH	2/11 (18)
Intraparenchymal hemorrhage	2/11 (18)
Microhemorrhage	7/11 (64)
Infarction	13/26 (50)
ACA territory infarction	0/13 (0)
MCA territory infarction	5/13 (38)
PCA territory infarction	2/13 (15)
PICA territory infarction	1/13 (8)
Borderzone infarction	1/13 (8)
Multiterritorial infarction	2/13 (15)
Leukoencephalopathy	7/26 (27)
Multiple abnormalities (infarction + hemorrhage)	4/26 (15)

Note:—SAH indicates subarachnoid hemorrahge; ACA, anterior cerebral artery; MCA, middle cerebral artery; PCA, posterior cerebral artery; PICA, posterior inferior cerebellar artery.

[a]Including shortness of breath, respiratory distress, respiratory failure, and hypoxia.

Table 1: Comparison between patients with coronavirus disease 2019 with and without intracranial abnormalities

	Acute Intracranial Abnormalities	No Acute Intracranial Abnormalities	Statistical Significance (*P* Value)
Patients, *n*	26	124	
Men/women, *n*	16/10	82/42	–
Mean age, mean ± SD, y	63.6 ± 16	64 ± 16.5	ns ($P = .896$)
Age range, y	24–87	22–96	–
Body mass index ± SD, kg/m^2	27.9 ± 5.3	28.5 ± 7.7	ns ($P = .655$)
Length of stay ± SD (days)	24.9 ± 12.8	23.4 ± 16.9	ns ($P = .091$)
Intensive care unit admission, % (*n*)	81.5 (22)	62.1 (77)	($P = .039$)[a]
Intubation rate, % (*n*)	77.8 (21)	49.2 (61)	($P = .004$)[b]
Acute kidney injury rate, % (*n*)	76.9 (20)	53.2 (66)	($P = .030$)[a]
Mortality rate, % (*n*)	23.1 (6)	12.1 (15)	ns ($P = .209$)

Note:—SD indicates standard deviation; ns, not significant; y, years.

[a] $P < 0.05$.

[b] $P < 0.01$.

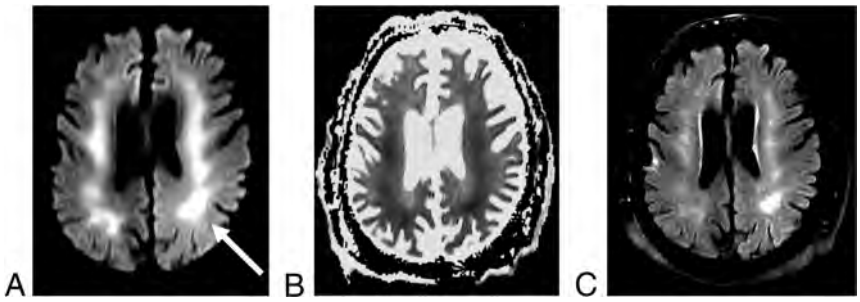

FIG 3. Leukoencephalopathy in a 61-year-old man with COVID-19. Axial DWI (*A*) and apparent diffusion coefficient map (*B*) sequences are notable for extensive, confluent areas of restricted diffusion (*arrow*) that involve the bilateral centrum semiovale and corona radiata. (*C*) Corresponding T2 FLAIR hyperintensity is also seen.

For patients with intracranial abnormalities, the most common symptoms on presentation were respiratory (21/26 patients [81%]), including shortness of breath, respiratory distress, respiratory failure, and hypoxia (Table 2). This was followed by fever (7/26 patients [27%]), headache (2/26 patients [8%]), fall (2/26 patients [8%]), and stroke symptoms (2/26 patients [8%]). Twelve of 26 patients (46%) presented with multiple symptoms (Table 2). The indications for undergoing neuroimaging most commonly included altered mental status (14/26 patients [54%]) and clinical findings consistent with stroke (8/26 patients [31%]) (Table 2).

In the patients with positive neuroimaging studies, intracranial hemorrhage was seen in 11 patients (42%) of the cohort (Table 2, Fig 1). Most of the patients with intracranial hemorrhage had microhemorrhages (7/11 patients [64%]). Two patients (18%) had SAH, and 2 had intraparenchymal hematomas. Acute or subacute infarctions were seen in 13 patients (50%), with the most frequent territory of involvement being the MCA territory (38%) (Table 2, Fig 2). A smaller subset of patients had infarcts in other territories, including posterior cerebral artery (2/13 patients [15%]), posterior inferior cerebellar artery (1/13 patients [8%]), and watershed (1/13 patients [8%]) infarcts. Two of the patients (15%) had multiterritorial infarction. Four of the patients (15%) had both infarction and intracranial hemorrhage. A leukoencephalopathy pattern was identified in 7 patients (27%) of the cohort (Fig 3). None of the patients with leukoencephalopathy had intracranial hemorrhage or infarction. Similar frequencies of respiratory symptoms were noted between the groups of patients with intracranial hemorrhage and/or infarction (17/20 patients [85%]) compared with those with leukoencephalopathy (6/7 patients [86%]). One of the 2 patients who presented after a fall had SAH (Fig 1*B*). The other patient who presented after a fall had acute infarction but no intracranial hemorrhage.

Statistically significant associations were found between the patients with positive neuroimaging studies and the requirement for intensive care unit admission ($P = .039$), need for intubation ($P = .004$), and development of acute kidney injury ($P = .030$) (Table 1). There was no statistically significant difference in patient age, body mass index, length of stay, and mortality in patients with positive versus negative neuroimaging studies (Table 1). Comparable numbers of patients remained hospitalized as of May 19, 2020, with 52 patients (42%) without intracranial abnormalities and 12 patients (46%) with intracranial abnormalities still in the hospital.

DISCUSSION

The results of this study highlight a spectrum of neuroimaging findings associated with COVID-19, including intracranial hemorrhage, infarction, and leukoencephalopathy, in a 150-patient cohort. In our cohort, 26 of the patients (17%) were found to have intracranial abnormalities, of which most were related to infarction (50%) and intracranial hemorrhage (42%). Leukoencephalopathy was seen in 27% of the patients. Four patients (15%) had both infarction and intracranial hemorrhage. The incidence of intracranial abnormalities in patients who underwent neuroimaging was lower than the 47% rate reported from Italy by Mahammedi et al.[9] The frequency of infarctions and intracranial hemorrhages was higher in our patient cohort than the previously reported rates (31% infarction and 6% hemorrhage), with a lower rate of leukoencephalopathy than the 35% in the study by Mahammedi et al.[9] The difference in the incidence rates is likely due to various factors, among them the inclusion of spine imaging by Mahammedi et al,[9] the different geographies and, therefore, populations, and possible differences in criteria used to categorize intracranial abnormalities.

Microhemorrhages have various etiologies, including cerebral amyloid angiopathy and trauma. Two of the patients had imaging studies that predated the COVID-19 pandemic, one from 2007 and the other from 2017. The patient with the more recent, 2017, previous study was 87 years old and had evidence of cerebral amyloid angiopathy on that study. However, this patient had an acute infarct on the neuroimaging obtained during admission for COVID-19. The other patient was 69 years old and had a solitary focus of microhemorrhage in 2007, with a marked increase in the number of microhemorrhages on the 2020 COVID-19–related study. The remaining 5 patients had no previous neuroimaging studies. These 5 patients spanned an age range of 41 to 60 years. Given that cerebral amyloid angiopathy is less common in this age group, we doubt that cerebral amyloid angiopathy was the cause of the hemorrhages observed in these patients with severe COVID-19 infection. The distribution of the microhemorrhages was also not specific for other causes, for example, trauma. By contrast, 1 of the patients with SAH on imaging presented after a fall, with trauma clearly acting as a confounder for the potential cause of the hemorrhage.

A significant association was demonstrated between the presence of acute abnormalities on neuroimaging studies and the severity of disease as indicated by the requirement for intensive care unit admission, the need for intubation, and development of acute kidney injury. These associations have not been previously described in the literature; however, Mao et al[5] noted an association between abnormal neuroimaging studies and patients with

severe COVID-19 lung manifestations. These data add to the growing body of literature that indicates the multisystem nature of the SARS-CoV-2 infection and its imaging manifestations. A common mechanism for multiorgan dysfunction in the disease has not yet been identified, though viral mechanisms of cellular entry and replication through exploitation of the angiotensin-converting enzyme 2 receptor are now defined. The angiotensin-converting enzyme 2 receptor is widely distributed.[17] Viral invasion of endothelial cells, and an immune response to this, has been reported in diverse vascular beds in patients with COVID-19.[18] The SARS-CoV-2 virus has been identified in postmortem human brains, which suggests the possibility of viral tropism to cerebral vascular beds. Microvascular thrombosis and prothrombotic complications are recognized as crucial aspects of disease progression.[19,20] The correlation that we describe between acute kidney injury and neuroimaging findings may indeed reflect the involvement of vascular beds in different organs, with viral or immune-mediated disruption of the neurovascular unit[21] underpinning the diverse range of neuroimaging findings in these patients. These mechanisms are speculative and in need of additional study.

Previous studies on patients with COVID-19 infection have demonstrated an association between obesity and higher rates of hospitalization and mortality.[22-25] We investigated the possible relationship between a higher body mass index and the development of acute neurologic abnormalities in our cohort but found no significant association. One of the hypotheses for increased severity of COVID-19 infection in patients who are obese is the impediment of diaphragmatic excursion due to obesity.[25] The lack of a significant association between obesity and intracranial abnormalities in our cohort may be related, in part, to this physical mechanism, as opposed to a direct, tissue-based pathologic link.

There are several limitations to this study, beyond the single-center, retrospective nature of it. First, we elected to use broad and intuitive measures of disease severity (intensive care unit admission, the need for intubation, acute kidney injury, and mortality) over the narrow range of reported inflammatory cytokines (D-dimer, interleukin 2, interleukin 6, etc) and other biomarkers that have been observed in patients with COVID-19 who were admitted to intensive care units.[26] This decision was based on the ongoing uncertainty about the implications of these markers on disease progression and outcome. The measures that we apply are, in turn, readily applied clinically, but there may be additional associations between acute neuroimaging manifestations of COVID-19 and other organ system involvement, which are not explored here. Second, our patient cohort is relatively small, and it is possible that nonstatistically significant differences in clinical parameters, such as the mortality rate and length of stay, may achieve statistical significance with the inclusion of more patients. However, much of the literature on COVID-19 infection and associated neuroimaging findings has been in the form of case series and small cohort studies, and there is a responsibility to report observed findings at these early stages of the COVID-19 experience to guide future research directions. It is also possible that the true incidence of intracranial abnormalities is higher, given that most of the patients only had CT imaging, which is less sensitive than MR imaging to assess for subtle intracranial abnormalities, including leukoencephalopathy and low-volume infarctions. These possibilities are speculative. Third, we report findings from a defined and narrow time period in patients who were hospitalized and subsequently imaged for neurologic symptoms. The true burden of acute neuroimaging findings in the total hospitalized and nonhospitalized COVID-19 patient population, therefore, remains unknown.

CONCLUSIONS

The results of this study describe the spectrum of acute neuroimaging abnormalities observed in patients with COVID-19 that occurred at a higher frequency than reported in other cohort series. In addition, a correlation was found between acute neuro-imaging abnormalities and several clinical parameters that reflect disease severity. Clinicians treating patients with COVID-19 who develop worsened systemic disease, including acute kidney injury, with any neurologic signs or symptoms should be aware of these findings and obtain neuroimaging studies based on this association and the therapeutic implications of acute intracranial disease.

Disclosures: William A. Mehan, Jr.—*UNRELATED: Consultancy:* Kura Oncology, *Comments:* Independent reviewer of head and neck cancer imaging studies for a clinical trial; *Expert Testimony:* CRICO and other medical insurance companies, *Comments:* Expert opinion on medicolegal cases involving neuroimaging. Thabele Leslie-Mazwi—*UNRELATED: Employment:* Massachusetts General Hospital.

REFERENCES

1. Wang W, Tang J, Wei F. **Updated understanding of the outbreak of 2019 novel coronavirus (2019-nCoV) in Wuhan, China.** *J Med Virol* 2020;92:441–47 CrossRef Medline
2. Simpson S, Kay FU, Abbara S, et al. **Radiological Society of North America expert consensus statement on reporting chest CT findings related to COVID-19. Endorsed by the Society of Thoracic Radiology, the American College of Radiology, and RSNA.** *Radiol Cardiothorac Imaging* 2020;2:e200152 CrossRef
3. Ng M-Y, Lee EY, Yang J, et al. **Imaging profile of the COVID-19 infection: radiologic findings and literature review.** *Radiol Cardiothorac Imaging* 2020;2:e200034 CrossRef
4. Pan L, Mu M, Yang P, et al. **Clinical characteristics of COVID-19 patients with digestive symptoms in Hubei, China: a descriptive, cross-sectional, multicenter study.** *Am J Gastroenterol* 2020;115:766–73 CrossRef Medline
5. Mao L, Jin H, Wang M, et al. **Neurologic manifestations of hospitalized patients with coronavirus disease 2019 in Wuhan, China.** *JAMA Neurol* 2020;77:1–9 CrossRef Medline
6. Poyiadji N, Shahin G, Noujaim D, et al. **COVID-19–associated acute hemorrhagic necrotizing encephalopathy: CT and MRI features.** *Radiology* 2020;296:E119–E120 CrossRef Medline
7. Ye M, Ren Y, Lv T. **Encephalitis as a clinical manifestation of COVID-19.** *Brain Behav Immun* 2020;88:945–46 CrossRef Medline
8. Moriguchi T, Harii N, Goto J, et al. **A first case of meningitis/encephalitis associated with SARS-coronavirus-2.** *Int J Infect Dis* 2020;94:55–58 CrossRef Medline
9. Mahammedi A, Saba L, Vagal A, et al. **Imaging in neurological disease of hospitalized COVID-19 patients: an Italian multicenter retrospective observational study.** *Radiology* 2020 May 21. [Epub ahead of print] CrossRef Medline
10. Franceschi AM, Ahmed O, Giliberto L, et al. **Hemorrhagic posterior reversible encephalopathy syndrome as a manifestation of COVID-19 infection.** *AJNR Am J Neuroradiol* 2020;41:1173–76 CrossRef Medline

11. Radmanesh A, Derman A, Lui YW, et al. **COVID-19–associated diffuse leukoencephalopathy and microhemorrhages.** *Radiology* 2020 May 21. [Epub ahead of print] CrossRef Medline
12. Sachs JR, Gibbs KW, Swor DE, et al. **COVID-19-associated leukoencephalopathy.** *Radiology* 2020;296:E184–E185 CrossRef Medline
13. Jain R, Young M, Dogra S, et al. **COVID-19 related neuroimaging findings: a signal of thromboembolic complications and a strong prognostic marker of poor patient outcome.** *J Neurol Sci* 2020; 414:116923 CrossRef Medline
14. Su H, Yang M, Wan C, et al. **Renal histopathological analysis of 26 postmortem findings of patients with COVID-19 in China.** *Kidney Int* 2020;98:219–27 CrossRef Medline
15. Okumura A, Kidokoro H, Tsuji T, et al. **Differences of clinical manifestations according to the patterns of brain lesions in acute encephalopathy with reduced diffusion in the bilateral hemispheres.** *AJNR Am J Neuroradiol* 2009;30:825–30 CrossRef Medline
16. McKinney AM, Kieffer SA, Paylor RT, et al. **Acute toxic leukoencephalopathy: potential for reversibility clinically and on MRI with diffusion-weighted and FLAIR imaging.** *AJR Am J Roentgenol* 2009;193:192–206 CrossRef Medline
17. Hamming I, Timens W, Bulthuis MLC, et al. **Tissue distribution of ACE2 protein, the functional receptor for SARS coronavirus. A first step in understanding SARS pathogenesis.** *J Pathol* 2004; 203:631–37 CrossRef Medline
18. Varga Z, Flammer AJ, Steiger P, et al. **Endothelial cell infection and endotheliitis in COVID-19.** *Lancet* 2020;395:1417–18 CrossRef Medline
19. Wang J, Hajizadeh N, Moore EE, et al. **Tissue plasminogen activator (tPA) treatment for COVID-19 associated acute respiratory distress syndrome (ARDS): a case series.** *J Thromb Haemost* 2020;18: 1752–55 CrossRef Medline
20. Oudkerk M, Büller HR, Kuijpers D, et al. **Diagnosis, prevention, and treatment of thromboembolic complications in COVID-19: report of the National Institute for Public Health of the Netherlands.** *Radiology* 2020 Apr 23. [Epub ahead of print] CrossRef Medline
21. Lo EH, Broderick JP, Moskowitz MA. **tPA and proteolysis in the neurovascular unit.** *Stroke* 2004;35:354–56 CrossRef Medline
22. Zhang F, Xiong Y, Wei Y, et al. **Obesity predisposes to the risk of higher mortality in young COVID-19 patients.** *J Med Virol* 2020 May 21. [Epub ahead of print] CrossRef Medline
23. Palaiodimos L, Kokkinidis DG, Li W, et al. **Severe obesity is associated with higher in-hospital mortality in a cohort of patients with COVID-19 in the Bronx, New York.** *Metabolism* 2020;108:154262 CrossRef Medline
24. Caussy C, Pattou F, Wallet F, et al. **Prevalence of obesity among adult inpatients with COVID-19 in France.** *Lancet Diabetes Endocrinol* 2020;8:562–64 CrossRef Medline
25. Kass DA, Duggal P, Cingolani O. **Obesity could shift severe COVID-19 disease to younger ages.** *Lancet* 2020;395:1544–45 CrossRef Medline
26. Chen G, Wu D, Guo W, et al. **Clinical and immunologic features in severe and moderate coronavirus disease.** *J Clin Invest* 2020; 130:2620–29 CrossRef Medline

Bilateral Basal Ganglia Hemorrhage in a Patient with Confirmed COVID-19

R. Daci, M. Kennelly, A. Ferris, M.U. Azeem, M.D. Johnson, F. Hamzei-Sichani, A.H. Jun-O'Connell, and S.K. Natarajan

ABSTRACT

SUMMARY: Bilateral basal ganglia hemorrhage is exceedingly rare. To our knowledge, our patient is the first reported case of a confirmed coronavirus disease 2019 (COVID-19) patient who had bilateral basal ganglia hemorrhage. In the absence of other risk factors for bilateral deep cerebral involvement, we suspect that COVID-19 may be contributing to these rare pathologies. Most published data represent a correlation between COVID-19 and neurologic complications, and more research is still needed to prove causation.

ABBREVIATIONS: COVID-19 = coronavirus disease 2019; SARS-CoV-2 = Severe Acute Respiratory Syndrome coronavirus 2

COVID-19 is a highly communicable disease caused by Severe Acute Respiratory Syndrome coronavirus 2 (SARS-CoV-2). The highest viral load for SARS-CoV-2 can be found in the lungs, nasopharynx, and oropharynx, and lower levels are detected in the brain, kidneys, liver, and blood.[1] Neurologic manifestations may occur in up to 50% of patients with coronavirus disease 2019 (COVID-19) and may include encephalopathy, anosmia, ageusia, headache, dizziness, seizure, stroke, increased intracranial pressure, SARS-CoV-2 meningitis, and necrotizing encephalitis.[2-4] There have been cases of ischemic and hemorrhage strokes in patients with COVID-19.[5] Bilateral basal ganglia hemorrhages per se are exceedingly rare, with 1 study indicating less than 30 reported cases worldwide.[6] Here we report a case of a patient with COVID-19 who presented with acute, bilateral basal ganglia hemorrhage.

CASE PRESENTATION

A woman in her 60s with past medical history of obstructive sleep apnea, gastrointestinal reflux, asthma, and migraines presented to our hospital with severe frontal headache, cough, and fatigue. Initial CT of the head was normal (Fig 1, left). Her sputum tested positive for SARS-CoV-2 RNA and she was sent home to quarantine. Two days later, the patient was found unresponsive at her home. She was normotensive. A CT of the head revealed bilateral basal ganglia acute parenchymal hematomas with surrounding edema and partial effacement of both lateral ventricles (Fig 1, right). The patient was intubated for airway protection.

CTA and CTV were negative for intracranial aneurysms, vascular malformations, vasospasm, or cerebral venous thrombosis. MR imaging revealed hyperintense lesions on T1, hypointense on T2, high signal on susceptibility-weighted imaging, and no diffusion restriction indicating acute basal ganglia hematomas (Fig 2). MRA and MRV revealed normal flow voids with no evidence of venous occlusion. The carboxyhemoglobin level was 2.7. Ethylene glycol testing was negative. The CSF was not tested for SARS-CoV-2 due to hospital pandemic restrictions. A urine drug screen was positive for prescribed amphetamines and marijuana.

Nine days after admission, the patient was extubated. A CT of the head revealed resolving hematomas. After extubation, the patient remained tachypneic, febrile, and required supplemental oxygen therapy. She developed leukocytosis, thrombocytosis, and lactic acidosis, concerning for either COVID-19 pulmonary manifestations and/or superimposed bacterial infection. Her C-reactive protein was 124.2; erythrocyte sedimentation rate, 99; D-dimer, 2.18; and fibrinogen, 436. The family decided to initiate comfort measures and the patient died 2 days later due to cardiorespiratory failure.

DISCUSSION

There have been other reports suggesting involvement of bilateral deep cerebral structures in COVID-19 (Table). There has been 1 previous case reported in the literature of bilateral basal ganglia involvement in a patient with presumed COVID-19 infection; however, that patient's nasopharyngeal SARS-CoV-2 polymerase chain reaction was negative (Table).[4] Poyiadji et al[7] reported a case of a

Received May 29, 2020; accepted after revision June 11.

From the Departments of Neurological Surgery (R.D., M.K., M.D.J., F.H-S., S.K.N.), and Neurology (A.F., M.U.A., A.H.J.-O.), University of Massachusetts Medical School, UMass Memorial Health Care, Worcester, Massachusetts.

Please address correspondence to Sabareesh K. Natarajan, MD, MS, 55 Lake Ave North, Worcester, MA 01655; e-mail: sabareesh.natarajan@umassmemorial.org; @UMassNeuroSurg

Indicates open access to non-subscribers at www.ajnr.org

http://dx.doi.org/10.3174/ajnr.A6712

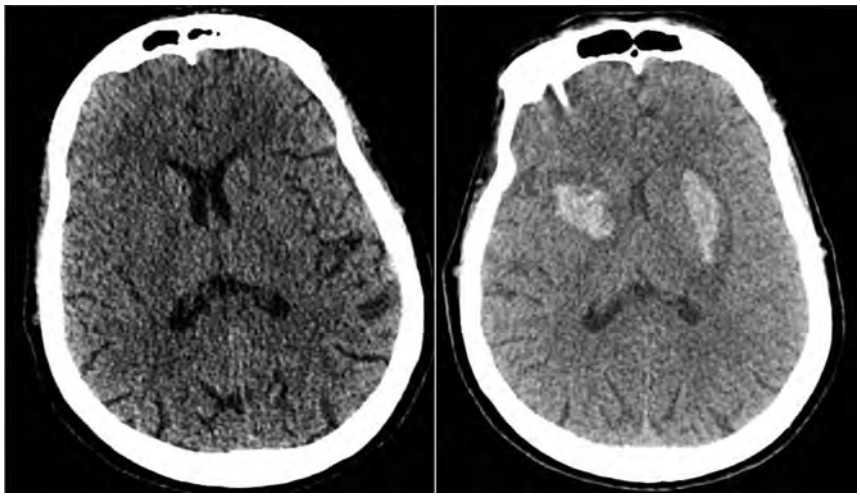

FIG 1. CT of the head obtained on day 1 of presentation (normal head CT, *left*). Two days later, a CT of the head was obtained because of worsening neurologic status (*right*). CT of the head revealed bilateral basal ganglia acute parenchymal hematomas measuring 2.7 cm × 1.9 cm × 1.4 cm (*right*) and 3.8 cm × 1.6 cm × 2.6 cm (*left*) with surrounding edema and partial effacement of bilateral lateral ventricles.

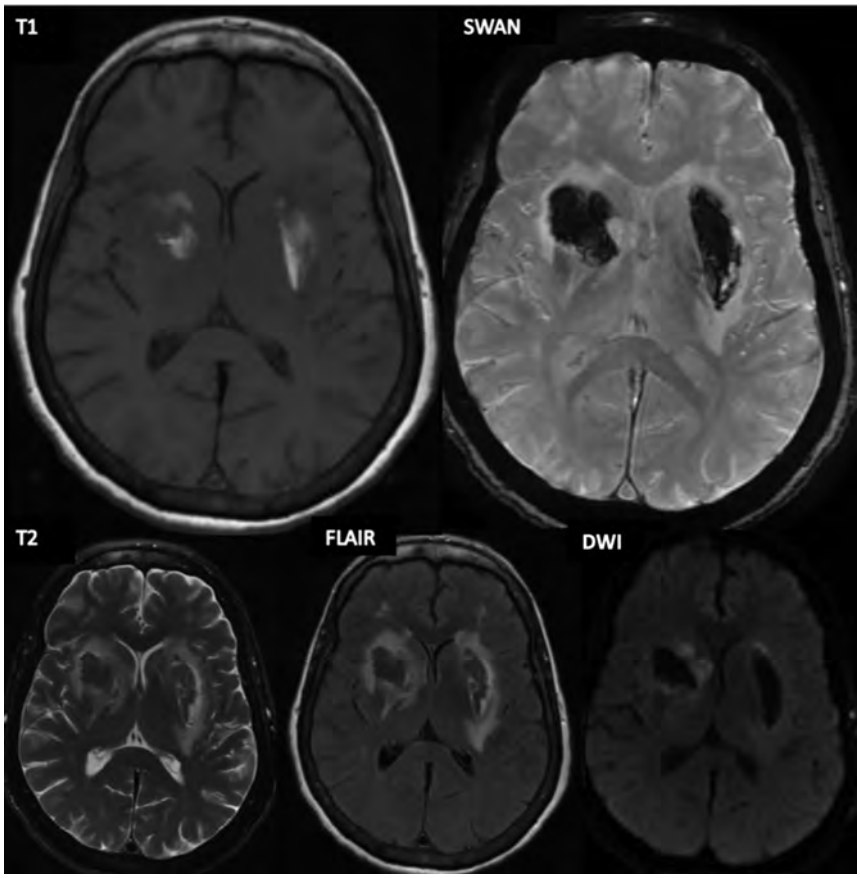

FIG 2. MR imaging of the brain revealing T1 hyperintense lesions (*upper right*) and high signal intensity on susceptibility-weighted imaging (SWAN, *upper left*). The lesions are hypointense on T2-weighted images (*bottom right*), exhibit surrounding edema on FLAIR images (*bottom middle*), and there is no diffusion restriction (DWI, *bottom left*).

woman with COVID-19 who was found to have hemorrhagic rim-enhancing lesions within the bilateral thalami and medial temporal lobes.

The basal ganglia and thalami are highly metabolic brain regions, predisposing them to hypoxic-ischemic injury, toxic poisoning (carbon monoxide, methanol, cyanide), metabolic abnormalities (liver disease, Leigh disease, Wilson disease, hypoglycemia, and osmotic myelinolysis), and neurodegeneration.[8] Focal flavivirus infection, toxoplasmosis, and primary CNS lymphoma can also attack the bilateral basal ganglia or thalami.[8] The basal ganglia are supplied by small medial and lateral lenticulostriate arteries of the anterior and middle cerebral arteries, making them susceptible to hypertensive disease. However, basal ganglia hemorrhage in hypertensive disease is unilateral in most cases.[6,9] Our patient was normotensive on presentation, making hypertensive hemorrhage less likely.

Because the venous drainage of the bilateral basal ganglia is into the great cerebral vein, bilateral basal ganglia hemorrhage could theoretically be explained by great cerebral vein thrombosis. There have been 6 reported cases of cerebral venous thrombosis in patients with COVID-19 in the literature.[10] Although our patient's MR venogram was negative, it is possible that the patient developed a cerebral venous thrombosis of her galenic venous system and had spontaneous lysis of her clot before imaging.

Traumatic bilateral basal ganglia hemorrhage has rarely been reported.[11] Although our patient was found unconscious, she did not have any external signs of cranial trauma. Amphetamines in our patient's urine may predispose to ischemia or hemorrhage, however her CTA and MRA were negative for vasospasm. The lesions did not exhibit restricted diffusion, as observed in several hypoxic-ischemic, toxic, or metabolic etiologies. Additionally, testing for carbon monoxide and ethylene glycol was negative.

It has been postulated that SARS-CoV-2 can be neurotropic via the transcribiform route or

Hemorrhagic involvement of bilateral deep cerebral structures in patients with COVID-19

	Patient 1	Patient 2	Our Patient
Age	50s	50s	60s
Sex	F	F	F
Anatomic location	Bilateral thalami, bilateral medial temporal lobes	Bilateral basal ganglia	Bilateral basal ganglia
SARS-CoV-2 PCR nasopharyngeal specimen	Positive	Negative	Positive
Medical history	Unknown	Diabetes, hypertension, lumbar fusion	Obstructive sleep apnea, gastrointestinal reflux, asthma, and migraines
Presenting symptom	Altered mental status	Loss of consciousness	Headache
COVID-19 symptoms	Cough, fever	Cough, fever	Cough, sore throat, fatigue
Presenting blood pressure	Unknown	150/100	134/70
Chest CT findings	Unknown	Bilateral ground glass opacities	Bilateral ground glass opacities
Outcome status	Unknown	Recovered and discharged from the hospital	Death
CSF	Negative for herpes simplex virus	Not obtained	Not obtained

Note:—PCR indicates polymerase chain reaction.

the hematogenous circulatory system.[2] It is unclear why COVID-19 would predispose to bilateral basal ganglia hemorrhage. COVID-19 has been reported to predispose to a hypercoagulable state, increasing the likelihood of cerebrovascular disease and ischemic stroke.[12] We speculate that the pathology of COVID-19, whether by direct viral invasion or via systemic inflammatory responses, may contribute to bilateral basal ganglia hemorrhage and to other neurologic complications.

Disclosures: Farid Hamzei-Sichani—*UNRELATED: Employment:* University of Massachusetts Medical School.

REFERENCES

1. Puelles VG, Lutgehetmann M, Lindenmeyer MT, et al. **Multiorgan and renal tropism of SARS-CoV-2.** *N Engl J Med* 2020. [Epub ahead of Print] CrossRef Medline
2. Baig AM, Khaleeq A, Ali U, et al. **Evidence of the COVID-19 virus targeting the CNS: tissue distribution, host-virus interaction, and proposed neurotropic mechanisms.** *ACS Chem Neurosci* 2020;11:995–98 CrossRef Medline
3. Asadi-Pooya AA, Simani L. **Central nervous system manifestations of COVID-19: a systematic review.** *J Neurol Sci* 2020;413:116832 CrossRef Medline
4. Haddadi KG, Shafizad M. **Basal ganglia involvement and altered mental status: a unique neurological manifestation of coronavirus disease 2019.** *Cureus* 2020;12:e7869 CrossRef Medline
5. Tunc A, Unlubas Y, Alemdar M, et al. **Coexistence of COVID-19 and acute ischemic stroke report of four cases.** *J Clin Neurosci* 2020;77:227–29 CrossRef Medline
6. Yang Z, Chen J, Mu J. **Simultaneous bilateral basal ganglia hemorrhage.** *Curr Drug Deliv* 2017;14:807–15 CrossRef Medline
7. Poyiadji N, Shahin G, Noujaim D, et al. **COVID-19-associated acute hemorrhagic necrotizing encephalopathy: CT and MRI features.** *Radiology* 2020;296:e119–20 CrossRef Medline
8. Hegde AN, Mohan S, Lath N, et al. **Differential diagnosis for bilateral abnormalities of the basal ganglia and thalamus.** *Radiographics* 2011;31:5–30 CrossRef Medline
9. Zhao J, Chen Z, Wang Z, et al. **Simultaneous bilateral hypertensive basal ganglia hemorrhage.** *Neurol Neurochir Pol* 2016;50:275–79 CrossRef Medline
10. Poillon G, Obadia M, Perrin M, et al. **Cerebral venous thrombosis associated with COVID-19 infection: causality or coincidence?** *J Neuroradiol* 2020 May 11. [Epub ahead of Print] CrossRef Medline
11. Kankane VK, Gupta TK, Jaiswal G. **Traumatic bilateral basal ganglia bleed: a report of rare two cases and review of the literature.** *Asian J Neurosurg* 2016;11:457 CrossRef Medline
12. Goldberg MF, Goldberg MF, Cerejo R, et al. **Cerebrovascular disease in COVID-19.** *AJNR Am J Neuroradiol* 2020;41:1170–72 CrossRef Medline

Pressing Issues in COVID-19: Probable Cause to Seize SARS-CoV-2 for Its Preferential Involvement of Posterior Circulation Manifesting as Severe Posterior Reversible Encephalopathy Syndrome and Posterior Strokes

F. D'Amore, G. Vinacci, E. Agosti, L.P. Cariddi, A.V. Terrana, F.A. Vizzari, M. Mauri, and A. Giorgianni

ABSTRACT

SUMMARY: Since December 2019, a novel Severe Acute Respiratory Syndrome coronavirus 2 from China has rapidly spread worldwide. Although respiratory involvement is the mainstay of coronavirus disease 2019 (COVID-19), systemic involvement has recently drawn more attention. In particular, a number of recent articles have shed light on the nervous system as one of the possible targets. At our institution, we observed 15 patients with acute brain vascular manifestations; most interesting, we had a higher prevalence of the posterior circulation acute impairment. In our series, 7 patients had acute posterior cerebral injury: 1, hemorrhagic posterior reversible encephalopathy syndrome; 5, posterior circulation ischemic stroke; and 1, parieto-occipital hemorrhagic stroke. On the basis of our evidence and previous basic science reports, we believe a common etiopathogenetic thread may connect ischemic/hemorrhagic events of the posterior circulation and posterior reversible encephalopathy syndrome in the setting of COVID-19.

ABBREVIATIONS: COVID-19 = coronavirus disease 2019; PRES = posterior reversible encephalopathy syndrome; SARS-CoV-2 = Severe Acute Respiratory Syndrome coronavirus 2

Last December, the first cases of a novel viral coronavirus disease 2019 (COVID-19) caused by the Severe Acute Respiratory Syndrome coronavirus 2 (SARS-CoV-2) were identified in China. Since then, the virus has spread so quickly worldwide that the World Health Organization declared COVID-19 a pandemic on March 11, 2020.[1] Italy first faced the largest outbreak besides Asia, with Lombardy outnumbering all other regions in Italy in terms of COVID-19 infections and deaths. As of May 21, >5 million SARS-CoV-2 infections have been confirmed worldwide, with the highest number of cases (>1.5 million) and deaths (almost 100,000) registered in the United States.[2] From the beginning of this medical emergency, our hospital has admitted >1100 patients who tested positive for SARS-CoV-2.[3] Although it is well-known that SARS-CoV-2 has a preferential pulmonary and gastrointestinal tropism, current evidence points to multiorgan involvement. A growing number of studies have reported SARS-CoV-2 involvement of the CNS, showing a wide variety of neurologic symptoms.[4] According to a Chinese study, the incidence of neurologic symptoms was about 36% in a cohort of patients with COVID-19.[5]

Case Series

From February 21 to the submission of this article, we collected patients positive for SARS-CoV-2 presenting with neurologic impairment who underwent CT and CTA and/or MR imaging (On-line Table). Demographic, clinical, and anamnestic data (age, sex, and clinical data) were obtained from clinical records. All imaging examinations were separately reviewed by 3 board-certified Neuroradiologists (F.D., A.V.T., A.G., with, respectively, 7, 6, and 10 years of experience in neuroimaging).

A total of 27 patients satisfied the inclusion criteria. Among these, 15 (7 men, 8 women; mean age, 68 years; range, 21–88 years) had acute imaging findings (On-line Table), of whom, 7 patients had acute posterior circulation ischemic-hemorrhagic events. The remainder showed miscellaneous findings: 1 case with supratentorial posttraumatic SAH, 2 cases with spontaneous acute or chronic convexities subdural hemorrhage, 1 posttraumatic, 2 with spontaneous intraparenchymal supratentorial hemorrhage (with negative findings on CTA), 1 with multicompartmental

Received May 21, 2020; accepted after revision June 3.

From the Departments of Neuroradiology (F.D., A.V.T., F.A.V., A.G.) and Neurology and Stroke Unit (L.P.C., M.M.), Hospital of Circolo and Macchi Foundation, Varese, Lombardia, Italy; Departments of Radiology (G.V.) and Neurosurgery (E.A.), University of Insubria, Hospital of Circolo and Macchi Foundation, Varese, Lombardia, Italy; and Clinical and Experimental Medical Humanities (L.P.C.), Center of Research in Medical Pharmacology, Univeristy of Insubria, Varese, Italy.

Please address correspondence to Gabriele Vinacci, MD, University of Insubria, Department of Radiology, Hospital of Circolo and Macchi Foundation, Viale Luigi Borri, 57, Varese, 21100, Italy; e-mail: gabriele_vinacci@libero.it

Indicates open access to non-subscribers at www.ajnr.org
Indicates article with supplemental on-line table.

http://dx.doi.org/10.3174/ajnr.A6679

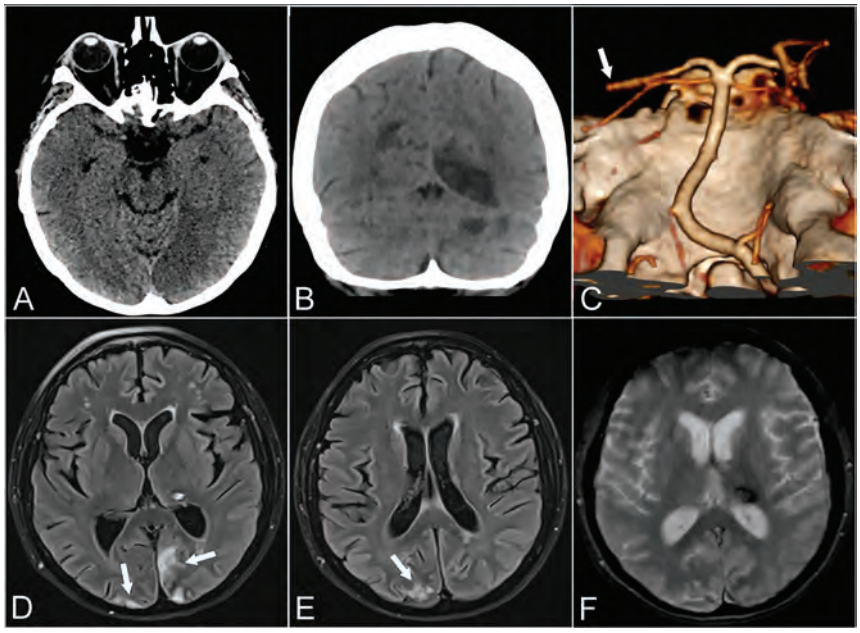

FIG 1. Patient 1. A 57-year-old woman with psychomotor retardation, left gaze deviation, and right superior and inferior limb paresis. Axial CT at baseline shows medial occipital loss of gray-white differentiation consistent with acute ischemia (*A*). Ten days later, coronal CT shows additional well-defined left cerebellar and right parieto-occipital hypoattenuating areas in keeping with subacute ischemia (*B*). Left distal posterior cerebral artery occlusion on CTA VR (Volume Rendering) reformats from the same day (*white arrow*, *C*). Axial T2 FLAIR (*D* and *E*) and axial T2* gradient recalled-echo (*F*) 6 weeks later show focal left thalamic signal drop-out, consistent with hemorrhage. Early chronic ischemic changes are also noted in the parieto-occipital lobes (*white arrows*, *D* and *E*).

bleeding of unknown etiology, and 1 patient who developed clinical and imaging findings in keeping with encephalitis. CT did not show any acute findings in 12 cases. In all patients with a baseline brain CT scan positive for acute changes, 6 underwent CTA, and MR imaging was available in 4 cases; all had CT follow-up, except those who died.

The subgroup of posterior circulation acute events comprised 7 patients (3 men, 4 women; mean age, 72 years, range, 57–88 years) representing 47% (7/15) of the total positive cases (On-line Table). In 5 patients, acute ischemic changes were found (Fig 1), of which 2 cases evolved into hemorrhagic transformation. One patient showed right parieto-occipital hemorrhagic stroke at baseline; subsequent CTA ruled out vascular malformations or acute thrombosis. In the other patient, imaging at baseline revealed extensive bilateral subcortical edema with multifocal hemorrhages, predominantly in the occipital lobes. Follow-up imaging showed progressive resorption of edema and hemorrhages, in keeping with posterior reversible encephalopathy syndrome (PRES) (Fig 2).

DISCUSSION

Our series shows a high prevalence of posterior circulation vascular events, not directly referable to a secondary cause as opposed to the heterogeneous etiology in the remaining cases. We speculate that SARS-CoV-2 may have played a role leading to acute brain injury, with a preferential involvement of the posterior circulation, which may be more susceptible to the SARS-CoV-2 infection effects.

Although SARS-CoV-2 targets primarily the lung parenchyma, earlier evidence in the literature highlighted its neurotrophic and neuroinvasive tendencies.[6] SARS-CoV-2 invades the CNS through different pathways, from peripheral nerves, especially via the olfactory nerves, through the bloodstream by infecting endothelial cells and altering the BBB, by lymphatic pathways, and, last, by the disruption of the gastrointestinal environment, which may indirectly alter BBB integrity.[7] SARS-CoV-2 can interact with host cells through the angiotensin-converting enzyme 2 cell membrane receptor expressed in a wide variety of cells such as airway epithelia, lung parenchyma, kidney cells, small intestine cells, as well as neurons and vascular endothelia.[6] Once it binds to neuronal angiotensin-converting enzyme 2 receptors, it is able to activate a self-reinforcing inflammatory response through a cytokine storm, which ultimately results in irreversible neuronal damage.[8] Angiotensin-converting enzyme 2 receptors are expressed in cerebral endothelial cells that take part in hormone formation, the sympathoadrenal system, and vascular autoregulation.[9] Endothelial disruption as a consequence of endotheliitis induced by SARS-CoV-2 can contribute to the pathophysiology of brain damage.[6] Infective lymphocytic endotheliitis has been proved by postmortem analysis.[10] The neuroinvasive potential is also supported by clinical experience as reported by several recent studies. For example, a Chinese study[5] reported various manifestations of CNS involvement in 53 patients with COVID-19 in a sample of 214 patients. In another study, SARS-CoV-2 was found in the CSF in a patient diagnosed with encephalitis, therefore confirming its direct CNS invasion.[11] Other studies have also highlighted imaging features of COVID-19 brain involvement.[12-15]

As recently described, ischemic stroke is a known complication in patients with COVID-19. In our series, we found 5 ischemic strokes of the posterior circulation in line with other studies. Mao et al[5] described 4 cases of acute stroke, while others described the onset of acute ischemic stroke in 5 younger patients.[15] Beyrouti et al[12] described 6 cases of acute stroke, 4 of which were posterior strokes. Goldberg and Goldberg[16] recently showed a case of ischemic stroke with occlusion of the MCA and bilateral anterior cerebral arteries.

Ischemic stroke could be related both to the endotheliitis process[10] and hypercoagulability status, which can evolve to embolism.[17] Endothelium inflammation may shift vascular equilibrium toward vasoconstriction, leading to ischemia.[18] We

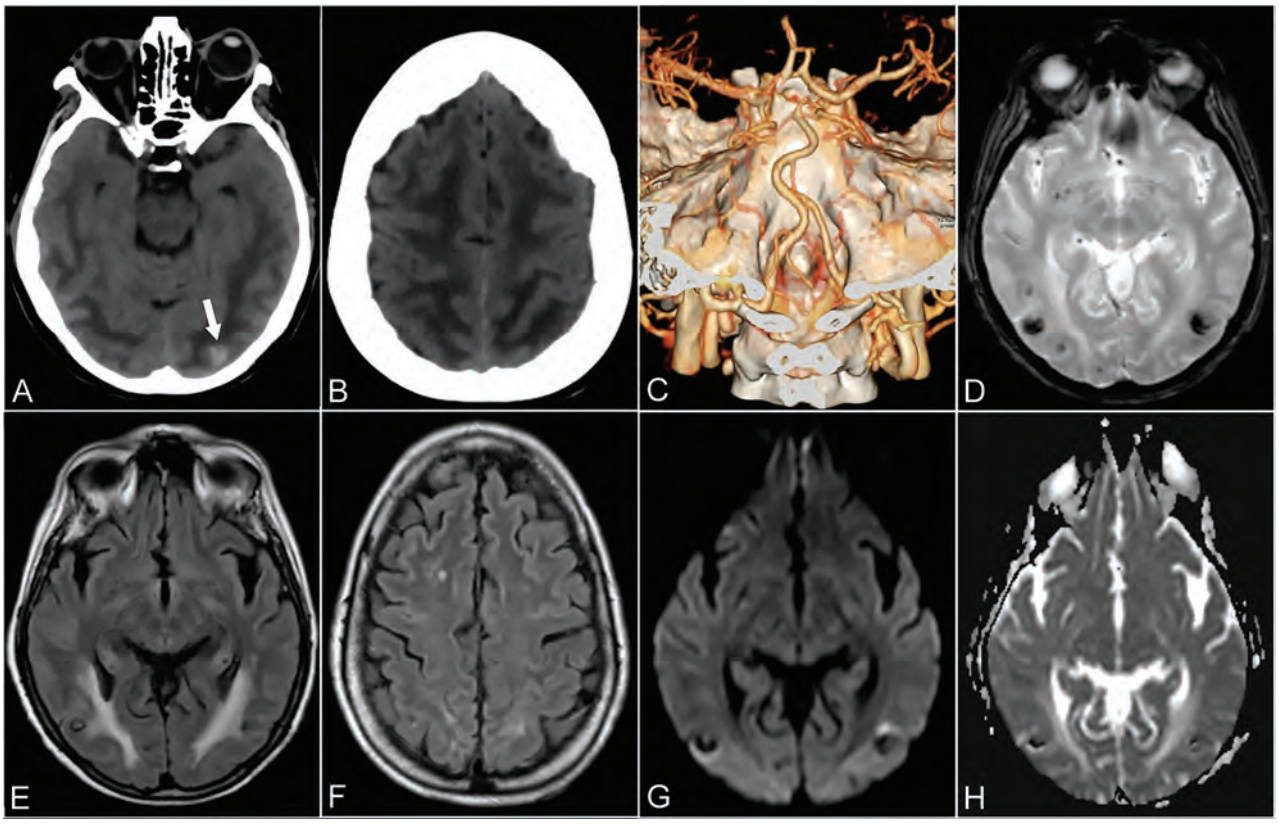

FIG 2. Patient 6. A 64-year-old woman presenting with drowsiness and reduction in visual acuity. Baseline axial CT shows ill-defined, bilateral hemispheric, white matter hypoattenuation, sparing the adjacent cortex, tapering off in the polar aspect of the frontal lobes, consistent with vasogenic edema (*A* and *B*). A small hyperattenuating lesion is noted in the left occipital lobe, suggestive of focal bleeding (*arrow*, *A*). CTA VR reformatted imaging was unremarkable in appearance (*C*). Three weeks later axial T2* gradient recalled-echo (*D*), axial T2 FLAIR (*E* and *F*), DWI (*G*), and an ADC map (*H*) demonstrate a partial resorption of edema and the presence of bilateral focal predominantly hypointense lesions (*E*) characterized by blooming (*D*) and signal blackout (*G* and *H*) in keeping with focal hemorrhage.

also reported 1 parieto-occipital hemorrhage, 1 case of complicated hemorrhagic PRES, and the hemorrhagic transformation of 2 ischemic strokes. Intracranial hemorrhage in patients with COVID-19 has already been reported.[5,19] In our series, we also noted 4 hemorrhagic strokes involving the anterior circulation.

One patient in our cohort presented with clinical and imaging features of a severe form of PRES. A recent case report has shown 2 cases of hemorrhagic PRES.[20] Our patient presented with extensive edema on a baseline CT scan with the presence of hemorrhagic lesions which is a severe and rare manifastation of PRES (Fig 2).[21] PRES is a multifactorial clinical-radiologic entity characterized by reversible subcortical vasogenic edema. Although not completely elucidated, several pathogenetic theories entailing rapid increase of arterial blood pressure beyond the autoregulatory potential, the release of vasoconstrictors, and endogenous or exogenous stimulants in addition to T-cell-derived cytokine release converge to an abnormal activation and consequent disruption of endothelial cell homeostasis.[22,23] Moreover, infective agents promote polymorphonuclear leukocyte activation and lead to additional release of mediators, resulting in increased vessel permeability, which leads to the development of interstitial edema.[23] Most interesting, the well-known frequent association of PRES with posterior circulation involvement has been ascribed to its lack of sympathetic innervation in contrast to the anterior circulation.[22,24] We ruled out other potential PRES mimickers, such as hypoxic-ischemic encephalopathy, meningoencephalitis, and acute toxic leukoencephalopathy in light of clinical and laboratory data and imaging follow-up. The improvement of pneumonia and laboratory parameters as well as the negative results on subsequent nasopharyngeal swabs paralleled by neurologic symptom resolution may strengthen the hypothesis of SARS-CoV-2 as a primary causative agent. Therefore, endothelial dysfunction, possibly at the capillary level, set off by SARS-CoV-2 infection, may be the etiopathogenesis of PRES.

In our cohort, we found that the posterior circulation was the most common primary site of acute vascular injury. The endothelial disruption related to SARS-CoV-2 could be a common feature acting as a promoting and synergistic agent underlying the preferential involvement of the posterior circulation, presumably due to its intrinsic hemodynamic weakness compared with the anterior circulation. Further studies with larger sample sizes are needed to support our hypothesis.

REFERENCES

1. **WHO Director-General's opening remarks at the media briefing on COVID-19, March 18, 2020.** https://www.who.int/dg/speeches/

detail/who- director-general-s- opening-remarks-at-the-media-briefing-on-covid-19—11-march-2020. Accessed May 21, 2020
2. **COVID-19 Map: Johns Hopkins Coronavirus Resource Center.** https://coronavirus.jhu.edu/map.html. Accessed May 21, 2020
3. Oltre millecento pazienti accolti nelle strutture dedicate all'emergenza Covid-19 dell'ASST Sette Laghi - asstsettelaghi. https://www.asst-settelaghi.it/contenuto-web/-/asset_publisher/shmOK1pliUE0/content/oltre-millecento-pazienti-accolti-nelle-strutture-dedicate-all-emergenza-covid-19-dell-asst-sette-laghi. Accessed May 21, 2020
4. Ahmad I, Rathore FA. **Neurological manifestations and complications of COVID-19: a literature review.** *J Clin Neurosci* 2020;77:8–12 CrossRef Medline
5. Mao L, Jin H, Wang M, et al. **Neurologic manifestations of hospitalized patients with coronavirus disease 2019 in Wuhan, China.** *JAMA Neurol* 2020 Apr 10. [Epub ahead of Print] CrossRef Medline
6. Baig AM, Khaleeq A, Ali U, et al. **Evidence of the COVID-19 virus targeting the CNS: tissue distribution, host–virus interaction, and proposed neurotropic mechanisms.** *ACS Chem Neurosci* 2020;11:995–98 CrossRef Medline
7. Li Z, Liu T, Yang N, et al. **Neurological manifestations of patients with COVID-19: potential routes of SARS-CoV-2 neuroinvasion from the periphery to the brain.** *Front Med* 2020 May 4. [Epub ahead of Print] CrossRef Medline
8. Mehta P, McAuley DF, Brown M, et al; HLH Across Speciality Collaboration, UK. **COVID-19: consider cytokine storm syndromes and immunosuppression.** *Lancet* 2020;395:1033–34 CrossRef Medline
9. Saavedra JM. **Brain angiotensin II: new developments, unanswered questions and therapeutic opportunities.** *Cell Mol Neurobiol* 2005;25:485–512 CrossRef Medline
10. Varga Z, Flammer AJ, Steiger P, et al. **Endothelial cell infection and endotheliitis in COVID-19.** *Lancet* 2020;395:1417–18 CrossRef Medline
11. Moriguchi T, Harii N, Goto J, et al. **A first case of meningitis/encephalitis associated with SARS-Coronavirus-2.** *Int J Infect Dis* 2020; 94:55–58 CrossRef
12. Beyrouti R, Adams ME, Benjamin L, et al. **Characteristics of ischaemic stroke associated with COVID-19.** *J Neurol Neurosurg Psychiatry* 2020 Apr 30. [Epub ahead of Print] CrossRef Medline
13. Helms J, Kremer S, Merdji H, et al. **Neurologic features in severe SARS-CoV-2 infection.** *N Engl J Med* 2020;382:2268–62 CrossRef Medline
14. Giorgianni A, Vinacci G, Agosti E, et al. **Neuroradiological features in COVID-19 patients: first evidence in a complex scenario.** *J Neuroradiol* 2020 May 15. [Epub ahead of Print] CrossRef Medline
15. Oxley TJ, Mocco J, Majidi S, et al. **Large-vessel stroke as a presenting feature of Covid-19 in the young.** *N Engl J Med* 2020;382:e60 CrossRef
16. Goldberg MF, Goldberg MF. **Cerebrovascular disease in COVID-19.** *AJNR Am J Neuroradiol* 2020 May 14. [Epub ahead of Print] CrossRef Medline
17. Marietta M, Ageno W, Artoni A, et al. **COVID-19 and haemostasis: a position paper from Italian Society on Thrombosis and Haemostasis (SISET).** *Blood Transfus* 2020;18:167–69 CrossRef Medline
18. Bonetti PO, Lerman LO, Lerman A. **Endothelial dysfunction: a marker of atherosclerotic risk.** *Arterioscler Thromb Vasc Biol* 2003;23:168–75 CrossRef Medline
19. Sharifi-Razavi A, Karimi N, Rouhani N. **COVID-19 and intracerebral haemorrhage: causative or coincidental?** *New Microbes New Infect* 2020;35:100669 CrossRef Medline
20. Franceschi AM, Ahmed O, Giliberto L. **Hemorrhagic posterior reversible encephalopathy syndrome as a manifestation of COVID-19 infection** *AJNR Am J Neuroradiol* 2020 May 21. [Epub ahead of Print] CrossRef Medline
21. Hugonnet E, Da Ines D, Boby H, et al. **Posterior reversible encephalopathy syndrome (PRES): features on CT and MR imaging.** *Diagn Interv Imaging* 2013;94:45–52 CrossRef Medline
22. Hinduja A. **Posterior reversible encephalopathy syndrome: clinical features and outcome.** *Front Neurol* 2020;11:71 CrossRef Medline
23. Fugate JE, Rabinstein AA. **Posterior reversible encephalopathy syndrome: clinical and radiological manifestations, pathophysiology, and outstanding questions.** *Lancet Neurol* 2015;14:914–25 CrossRef Medline
24. Gao B, Lyu C, Lerner A, et al. **Controversy of posterior reversible encephalopathy syndrome: what have we learnt in the last 20 years?** *J Neurol Neurosurg Psychiatry* 2018;89:14–20 CrossRef Medline

Imaging Features of Acute Encephalopathy in Patients with COVID-19: A Case Series

S. Kihira, B.N. Delman, P. Belani, L. Stein, A. Aggarwal, B. Rigney, J. Schefflein, A.H. Doshi, and P.S. Pawha

ABSTRACT

SUMMARY: Coronavirus disease 2019 was declared a global pandemic by the World Health Organization on March 11, 2020. There is a scarcity of data on coronavirus disease 2019–related brain imaging features. We present 5 cases that illustrate varying imaging presentations of acute encephalopathy in patients with coronavirus disease 2019. MR features include leukoencephalopathy, diffusion restriction that involves the GM and WM, microhemorrhages, and leptomeningitis. We believe it is important for radiologists to be familiar with the neuroradiologic imaging spectrum of acute encephalopathy in the coronavirus disease 2019 population.

ABBREVIATIONS: COVID-19 = coronavirus disease 2019; SARS-CoV = Severe Acute Respiratory Syndrome coronavirus

Coronavirus disease 2019 (COVID-19) is a clinical manifestation of Severe Acute Respiratory Syndrome coronavirus (SARS-CoV) 2 infection. This virus was first detected in Wuhan, China, in December 2019,[1] and, by March 11, 2020, it had been declared a global pandemic by the World Health Organization.[2] Recent studies have demonstrated encephalopathic symptoms in up to 36% of hospitalized patients with COVID-19, including altered mental status, confusion, and headaches.[3]

There is a scarcity of data on COVID-19–related brain MR features. Poyiadji et al[4] suggested a possible link between COVID-19 infection and acute necrotizing encephalopathy, and subsequent case reports described encephalitis in patients with COVID-19.[5-7] A recent study from Turkey included a range of neuroimaging findings in patients with COVID-19 in the intensive care unit, with cortical signal abnormality and diffusion restriction predominating.[8] Recently, Radmanesh et al[9] reported 2 neuroimaging findings, diffuse leukoencephalopathy and WM microhemorrhages, in patients with COVID-19. Respiratory distress is seen in up to 25% of patients with COVID-19,[10] and hypoxia itself can result in leukoencephalopathy and microhemorrhages in certain settings.[11,12] However, the current literature is limited on whether these MR findings in patients with COVID-19 are due to primary pathology or secondary complications from hypoxia.

We have encountered MR findings of encephalopathy among 5 patients with COVID-19 during the surge of disease in New York City from late March to late April 2020. As COVID-19 continues to grow on a global scale, it is important for radiologists to be familiar with varying presentations of acute encephalopathy that may be encountered in patients with COVID-19 (On-line Table).

CASE 1

A 59-year-old woman with no known medical history presented with respiratory distress (40% on room air and required intubation in the emergency department, and, subsequently, was found to be positive for COVID-19 on reverse transcriptase–polymerase chain reaction nasal swab test result. Her family confirmed acute disorientation on the day of presentation. Her hospital stay was complicated by non-ST-elevation myocardial infarction and focal seizures. A CT of the head was unremarkable; however, subsequent MR imaging of the brain (Fig 1) on day 7 of intubation demonstrated patchy and confluent areas of restricted diffusion and FLAIR hyperintensity that involved the cerebral cortices and WM (Fig 1*A*), with involvement of the basal ganglia, splenium of corpus callosum (Fig 1*B*, -*C*), and pons (Fig 1*D*). A small amount of scattered predominantly frontoparietal leptomeningeal FLAIR hyperintensity was present (Fig 1*A*). A few small subcortical and corpus callosum microhemorrhages were noted as well as trace intraventricular hemorrhage. CSF bacterial culture showed no growth over 5 days. There was no elevation of leukocytes or protein in the CSF. The COVID-19 viral load was not detected on CSF analysis. Other etiologies, such as *E coli*, *H Haemophilus*,

Received May 13, 2020; accepted after revision June 15.

From the Departments of Diagnostic, Molecular and Interventional Radiology (S.K., B.N.D., P.B., A.A., B.R., J.S., A.H.D., P.S.P.), and Neurology (L.S.), Icahn School of Medicine at Mount Sinai, New York, New York.

Please address correspondence to Puneet S. Pawha, MD, Department of Diagnostic, Molecular and Interventional Radiology, Icahn School of Medicine at Mount Sinai and The Mount Sinai Hospital, One Gustave L. Levy Pl, Box 1234, New York, NY 10029; e-mail: puneet.pawha@mountsinai.org

Indicates open access to non-subscribers at www.ajnr.org

Indicates article with supplemental on-line table.

http://dx.doi.org/10.3174/ajnr.A6715

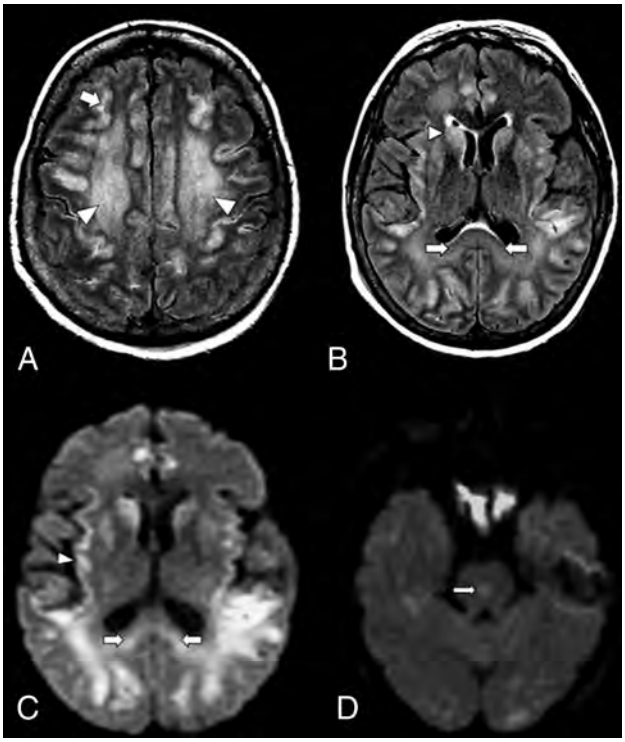

FIG 1. An axial MR image of a 59-year-old woman with COVID-19 who presented with respiratory distress and acute disorientation (case 1). *A*, FLAIR image demonstrates confluent FLAIR hyperintensity that involves cerebral WM (*arrowheads*) and patchy involvement of cerebral cortices; a small amount of scattered frontoparietal leptomeningeal FLAIR hyperintensity is noted (*arrow*). *B*, FLAIR image shows hyperintensity that involves the splenium (*arrows*) and basal ganglia (*arrowhead*). *C*, DWI demonstrates restricted diffusion that involves the splenium of the corpus callosum (*arrows*) and the cortex (*arrowhead*). *D*, DWI shows a diffusion-restricting focus in the pons (*arrow*).

N Neisseria, CMV Cytomegalovirus, HSV1 and 2 Herpes simplex virus 1 and 2, and West Nile virus, were not detected on CSF analysis. No oligoclonal bands were present. There was no status epilepticus, discrete anoxic episode, or known toxic and/or metabolic abnormality to account for the imaging findings. The patient is currently undergoing plasma exchange for concern for presumed COVID-19–related autoimmune encephalitis, though hypoxia may also be a contributing factor.

CASE 2

A 60-year-old man with hypertension and diabetes mellitus type 2 presented with fever, cough, altered mental status, and dyspnea for 2 weeks, and was determined to be positive for COVID-19 on reverse transcriptase–polymerase chain reaction nasal swab test result. The presenting O_2 saturation was 92% on room air. The patient was encephalopathic on presentation, with disorientation and decreased alertness. His hospital stay was complicated by hypoxic respiratory failure, which required intubation and was further complicated by cardiogenic shock attributed to Takotsubo cardiomyopathy. He also developed acute renal failure, which required multiple cycles of dialysis. Although his altered mental status was initially attributed to uremic encephalopathy, he continued to remain altered despite dialysis. A CT of the head was unremarkable except for chronic basal ganglia calcification. Video EEG demonstrated diffuse theta slowing, but no epileptiform discharges. A brain MR imaging (2 weeks after intubation) (Fig 2) demonstrated confluent FLAIR hyperintensity and diffusion restriction throughout the cerebral WM, with sparing of subcortical U-fibers. Subsequent CSF analysis was unremarkable and without COVID-19 viral load detection. MR findings and clinical history would be compatible with post–hypoxic leukoencephalopathy; however, because encephalopathy preceded respiratory distress, a component of COVID-19–related leukoencephalitis is also considered.

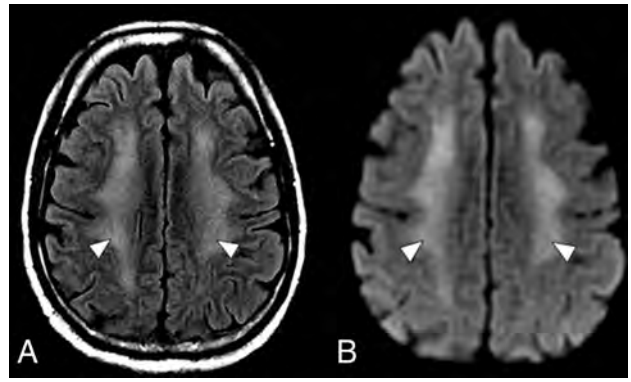

FIG 2. An axial MR imaging of the brain of a 60-year-old man with COVID-19 who presented with disorientation and decreased alertness (case 2). *A*, A FLAIR image demonstrates diffuse confluent WM hyperintensity with sparing of the subcortical U-fibers (*arrowheads*). *B*, DWI shows corresponding restricted diffusion throughout the involved WM (*arrowheads*).

CASE 3

A 35-year-old woman at 28 weeks' gestation and diagnosed with pyelonephritis 2 weeks earlier presented with abdominal pain, fever, cough, and decreased alertness, and was positive for COVID-19 on reverse transcriptase–polymerase chain reaction nasal swab test result. O_2 saturation was 90% on room air at presentation. She was being worked up for encephalopathy; however, her hospital stay was complicated by hypoxic respiratory failure, which required intubation, and cardiac arrest a few days later, which required cardiopulmonary resuscitation. After the return of spontaneous circulation, the patient was taken for emergent caesarean section. Her mental status remained poor. A CT of the head was unremarkable. EEG showed generalized slowing compatible with encephalopathy but no electrographic seizures.

MR imaging of the brain 4 days later (day 8 of intubation) (Fig 3*A*,-*B*) demonstrated numerous small foci of susceptibility within the peripheral cerebral subcortical WM and throughout the corpus callosum, most pronounced at the splenium, favored to reflect microhemorrhages. Some foci were linear, which raised the additional but less likely consideration of venous microthrombi. Splenial confluent FLAIR hyperintensity was seen, consistent with edema (Fig 3*C*); however, no other parenchymal edema was noted. Diffuse prominent sulcal FLAIR hyperintensity was present; however, this is often artifactual in the setting of the

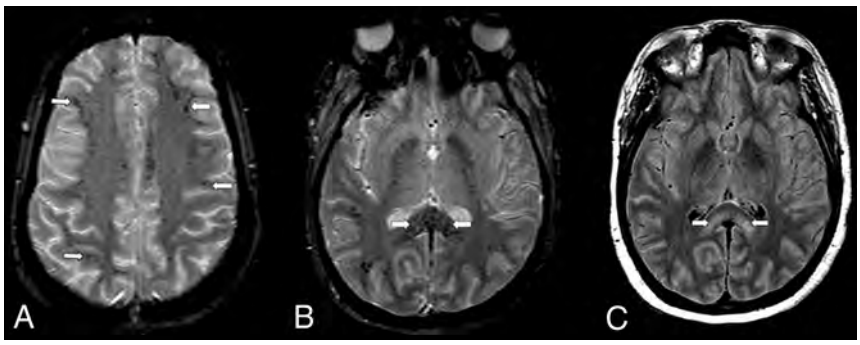

FIG 3. An axial MR imaging of the brain of a 35-year-old woman with COVID-19 who presented with decreased alertness (case 3). *A*, A gradient recalled-echo (GRE) image demonstrates numerous small foci of susceptibility in the peripheral subcortical WM (*arrows*). *B*, A more inferior GRE image shows numerous small foci of susceptibility throughout the corpus callosum, particularly the splenium (*arrows*). *C*, A FLAIR image demonstrates confluent bilateral hyperintensity that involves the splenium (*arrows*).

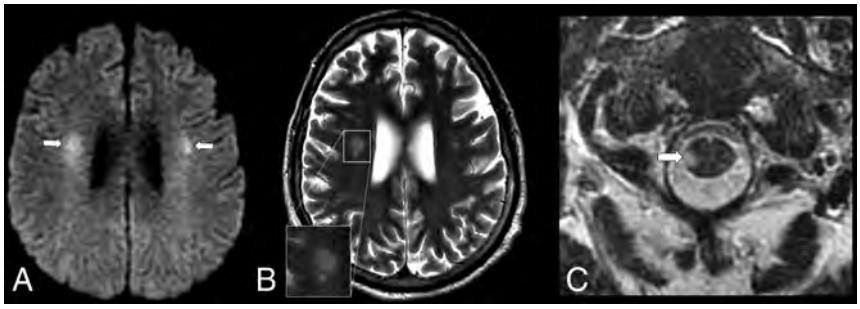

FIG 4. An axial MR imaging of the brain of a 48-year-old man with COVID-19 and with acute flaccid paralysis of the bilateral lower extremities (case 4). *A*, DWI demonstrates multiple diffusion-restricting foci in the WM, including right greater than left corona radiata (*arrows*). *B*, A T2 FSE image shows a "halo" appearance of a dominant right corona radiata lesion (*inset*), suggestive of demyelination. *C*, A T2 FSE image demonstrates a focal lesion in the right lateral column of the spinal cord at C1 (*arrow*), which corresponds to a diffusion-restricting focus on MR imaging of the brain.

patient receiving high oxygen fraction, which can confound assessment for meningitis. CSF bacterial culture showed no growth for 4 days. There was no elevation of leukocytes or protein in the CSF. Other etiologies, such as *E coli*, *H Haemophilus*, *N Neisseria*, CMV Cytomegalovirus, HSV1 and 2 Herpes simplex virus 1 and 2, and West Nile virus were undetected on CSF analysis. Autoimmune antibodies and oligoclonal bands were also not detected. Testing for the presence of SARS-CoV-2 in the CSF was unable to be performed. A working diagnosis was a hemorrhagic leukoencephalopathy in the setting of active viral infection.

CASE 4

A 48-year-old man with no known medical history initially presented with nausea, vomiting, and cough, and was found to have COVID-19 on reverse transcriptase–polymerase chain reaction nasal swab test result. His presenting oxygen saturation was 100% on room air. The first 2 inpatient weeks were complicated by acute respiratory distress syndrome, which required intubation, and acute kidney injury, which required peritoneal dialysis. The patient subsequently became altered, with flaccid paralysis of bilateral lower extremities activating a code stroke. A CT of the head and a CTA were unremarkable, with an ASPECTS of 10.

MR imaging of the brain the following day (week 3 of intubation) (Fig 4*A*) showed multiple diffusion-restricting and FLAIR hyperintense foci within the WM, specifically in the right centrum semiovale and bilateral corona radiata, left temporal lobe, and left medullary pyramid, and in the spinal cord at C1. T2 FSE imaging (Fig 4*B*) showed a halo-like appearance of the dominant lesion in the corona radiata and another, smaller lesion, which favored a demyelinating/inflammatory etiology over infarct. Concurrent MR imaging of the spine (Fig 4*C*) showed focal T2 hyperintense lesions within the right lateral cord at C1 (which corresponded to the focal restricted diffusion seen on the MR imaging of the brain) and T5 levels as well as a third lesion in the left lateral column at T5. CSF protein and glucose were elevated to 132 mg/dL and 105 mg/dL, respectively. There was no oligoclonal band, and the cytopathology result was negative. Given the findings of multiple diffusion restricting lesions limited to WM structures of the brain and cord in the setting of recent COVID-19 infection, a postviral autoimmune demyelinating encephalomyelitis was favored.

CASE 5

A 41-year-old man with morbid obesity who had previously undergone a gastric sleeve procedure presented with nonproductive cough, shortness of breath, and subjective chills for 4 days. At presentation, oxygen saturation was 95% on room air. He was found to have COVID-19 on reverse transcriptase–polymerase chain reaction nasal swab test result and associated pneumonia. The hospital course was complicated by hypoxic respiratory failure, which required intubation, and acute kidney injury, which required dialysis. The patient was on ventilation for 3 weeks and was found to be disoriented and decreased in alertness after extubation, which persisted despite several cycles of hemodialysis. A CT of the head performed 4 weeks after intubation was unremarkable, but the subsequent MR imaging demonstrated FLAIR hyperintensity of the globi pallidi and more extensively throughout the cerebral WM, with subcortical U-fiber sparing (Fig 5), with corresponding moderately restricted diffusion. The leading consideration was de-layed post–hypoxic leukoencephalopathy; however, basal ganglia involvement also prompted consideration of encephalitis and metabolic encephalopathy. Postviral demyelination is less likely given the diffuse symmetric MR findings.

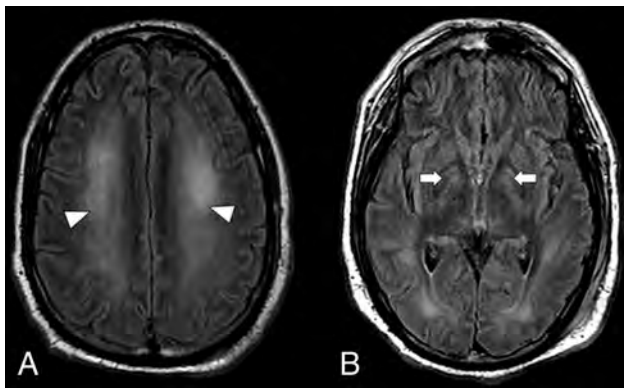

FIG 5. An axial MR imaging of the brain of 41-year-old man with COVID-19 and with persistent disorientation and decreased alertness 1 week after extubation (case 5). *A*, A FLAIR image demonstrates hyperintensity throughout the cerebral WM (*arrowheads*). *B*, A more-inferior FLAIR image demonstrates hyperintensity of the globi pallidi bilaterally (*arrows*).

DISCUSSION

The 5 cases presented illustrate varying imaging presentations of acute encephalopathy in patients with COVID-19. There is a scarcity of data on COVID-19–related MR findings of encephalopathy. Differential considerations in all cases included potential complications of the SARS-CoV-2 virus. All 5 patients demonstrate WM signal abnormalities and areas of diffusion restriction. Three of 5 patients demonstrated large confluent and symmetric diffusion restriction in the cerebral WM, with sparing of subcortical U-fibers. This pattern can be seen with delayed post–hypoxic leukoencephalopathy, which is a leading consideration in 2 patients in whom MR imaging was obtained 1–4 weeks after hypoxic events; however, encephalopathy was noted even before hypoxia in 2 of 3 patients with this confluent WM abnormality. Clinically significant hypoxic burden is reported with 5%–25% of patients with COVID-19 and who require ventilation,[10,13] and even more are presumed to have silent hypoxia before presentation.[14] This is a confounding variable because hypoxia can result in varying MR findings, for example, those seen in delayed post–hypoxic leukoencephalopathy[12] and high-altitude cerebral edema.[11] Given the clinically significant hypoxia encountered in patients with COVID-19, we believe that the MR findings in some cases are multifactorial, with a likely frequent component of post–hypoxic leukoencephalopathy.[10]

Results of a few recent studies have suggested COVID-19–related neuroimaging findings in patient with encephalopathy.[8,9,15] Our findings differed from those of Kandemirli et al,[8] which showed GM involvement in most cases. Radmanesh et al[9] reported findings of diffuse leukoencephalopathy and microhemorrhages, which are also present in our series. In addition, there are several important novel findings in our study that may help to understand the broad spectrum of COVID-19–related MR imaging findings. Basal ganglia 2 patients) and pontine (1 patient) involvement of edema and diffusion restriction have not been described in association with COVID-19 in previous studies. In addition, COVID-19–related postviral demyelination of the brain and spinal cord is a novel finding.

Viral encephalitis is a sequela of direct viral neuroinvasion and is typically dictated by the receptor binding domain of the virus. Studies in SARS-CoV, whose genomic sequence closely resembles SARS-CoV-2 of COVID-19,[16] suggest that the pathology involves a cytokine cascade through angiotensin-converting enzyme 2 receptor binding, which leads to blood-brain barrier breakdown.[17] Angiotensin-converting enzyme 2 is widely expressed in the glial cells and in the brain stem nuclei regulating the cardiorespiratory systems.[18] Moreover, this cytokine cascade and the direct cytopathic damage by the virus was proposed to cause neurologic disease, such as encephalitis, in susceptible individuals[19] and was recently described in a subset of patients with COVID-19.[20] Viral entry into the CNS may result from either hematogenous dissemination or retrograde peripheral nerve propagation within the brain, with the latter appealing for the explanation of anosmia in the COVID-19 population.[21]

Two patients in this case series demonstrated splenial edema, which has also been previously reported in Middle East Respiratory Syndrome coronavirus encephalitis.[22] The patients in our cases also demonstrated microhemorrhages within subcortical regions and corpus callosum, one extensive and the other mild. This distribution has been described in high-altitude cerebral edema and also in patients who are critically ill[11,12] and was also described by Radmanesh et al[9] as a potential COVID-19–related finding. Additional consideration for this appearance includes hemorrhagic leukoencephalitis, possibly even a forme fruste of acute hemorrhagic leukoencephalitis, the autoimmune process that typically has a more fulminant course. In addition, cytokine cascade has been shown to lead to thromboembolic phenomena as a result of a hypercoagulable state,[23] which could then cause small vessel thromboses and microhemorrhages within the brain. Hemorrhagic foci are also seen in acute necrotizing encephalopathy; however, the patients in our cases show the absence of necrosis and dissimilar distribution. CSF analysis was unremarkable in all cases of suspected possible viral encephalitis in this case study, perhaps not surprising given the low utility of the viral analysis in CSF where levels are typically very low.[24] However, a negative viral assay does not rule out the diagnosis.

A case of suspected postviral demyelination is included in this case series, presumed to be related to recent COVID-19 infection. Postviral encephalomyelitis or acute disseminated encephalomyelitis is an immune-mediated inflammatory demyelinating disorder that occurs within days to weeks of viral infection. The age of onset remains young in the adult population, with a mean age in the 40s.[25] Acute disseminated encephalomyelitis is not the result of tissue invasion by the microbes themselves, unlike in viral encephalitis. Demyelination is often in the cerebral WM and spinal cord, although it may also involve the GM. CSF analysis is nonspecific in patients with acute disseminated encephalomyelitis and may be normal in up to one-third of patients.[26] Although this series includes the presumptive first report of postviral demyelinating encephalomyelitis from COVID-19, MR imaging features are typical of this entity, and this mechanism would parallel other coronavirus subtypes in which acute disseminated encephalomyelitis has also been described.[27]

A comprehensive delineation of post–hypoxic leukoencephalopathy, postviral autoimmune encephalitis, and infectious

leukoencephalitis is not possible given our small sample size. Symmetric confluent leukoencephalopathy favors a component of post–hypoxic leukoencephalopathy, and more focal WM lesions (particularly if the spinal cord or the posterior fossa is involved) may suggest postviral autoimmune demyelination. Basal ganglia involvement can raise suspicion for encephalitis in the absence of known causative factors. In addition, we acknowledge that silent hypoxia is associated with COVID-19 infection and would be difficult to measure because the patient would be asymptomatic and not seek medical attention at the time. However, only 1 patient had clinically significantly low oxygen saturation (<90%) at the time of presentation, which suggests that encephalopathy may have preceded hypoxia.

Whether these imaging appearances are the sequelae of direct infectious encephalitis, postviral encephalitis, hypoxia, or simply critical illness–related encephalopathy remains under investigation. In some patients with COVID-19, encephalopathy may be multifactorial. This case series serves to raise awareness of varying presentations of presumed encephalitis that may be seen in patients with COVID-19. Knowledge of these neuroimaging features may aid in the detection and early management of neurologic complications in this patient population.

Disclosures: Bradley Delman—*UNRELATED: Payment for Lectures Including Service on Speakers Bureaus:* Bayer Healthcare, Comments: Internal lectures (no more than 1 per year).

REFERENCES

1. Huang C, Wang Y, Li X, et al. **Clinical features of patients infected with 2019 novel coronavirus in Wuhan, China.** *Lancet* 2020;395:497–06 CrossRef Medline
2. WHO Director-General's opening remarks at the media briefing on COVID-19 - 11. March 2020
3. Weiss P, Murdoch DR. **Clinical course and mortality risk of severe COVID-19.** *Lancet* 2020;395:1014–15 CrossRef Medline
4. Poyiadji N, Shahin G, Noujaim D, et al. **COVID-19–associated acute hemorrhagic necrotizing encephalopathy: CT and MRI features.** *Radiology* 2020;296:E119–E120 CrossRef Medline
5. Moriguchi T, Harii N, Goto J, et al. **A first case of meningitis/encephalitis associated with SARS-Coronavirus-2.** *Int J Infect Dis* 2020;94:55–58 CrossRef Medline
6. Sohal S, Mossammat M. **COVID-19 presenting with seizures.** *IDCases* 2020;20:e00782 CrossRef Medline
7. Ye M, Ren Y, Lv T. **Encephalitis as a clinical manifestation of COVID-19.** *Brain Behav Immun* 2020;88;945–46 CrossRef Medline
8. Kandemirli SG, Dogan L, Sarikaya ZT, et al. **Brain MRI findings in patients in the intensive care unit with COVID-19 infection.** *Radiology* 2020 May 8. [Epub ahead of Print] CrossRef Medline
9. Radmanesh A, Derman A, Lui YW, et al. **COVID-19 –associated diffuse leukoencephalopathy and microhemorrhages.** *Radiology* 2020 May 21. [Epub ahead of Print] CrossRef Medline
10. Greenland JR, Michelow MD, Wang L, et al. **COVID-19 infection: implications for perioperative and critical care physicians.** *Anesthesiology* 2020;132:1346–61 CrossRef Medline
11. Hackett PH, Yarnell PR, Hill R, et al. **High-altitude cerebral edema evaluated with magnetic resonance imaging: clinical correlation and pathophysiology.** *JAMA* 1998;280:1920–25 CrossRef Medline
12. Fanou EM, Coutinho JM, Shannon P, et al. **Critical illness-associated cerebral microbleeds.** *Stroke* 2017;48:1085–87 CrossRef Medline
13. Möhlenkamp S, Thiele H. **Ventilation of COVID-19 patients in intensive care units.** *Herz* 2020;45:329–31 CrossRef Medline
14. Xie J, Tong Z, Guan X, et al. **Critical care crisis and some recommendations during the COVID-19 epidemic in China.** *Intensive Care Med* 2020;46:837–40 CrossRef Medline
15. Helms J, Kremer S, Merdji H, et al. **Neurologic features in severe SARS-CoV-2 infection.** *N Engl J Med* 2020;382:2268–70 CrossRef Medline
16. Lu R, Zhao X, Li J, et al. **Genomic characterisation and epidemiology of 2019 novel coronavirus: implications for virus origins and receptor binding.** *Lancet* 2020;395:565–74 CrossRef Medline
17. Zhou P, Yang X-L, Wang X-G, et al. **A pneumonia outbreak associated with a new coronavirus of probable bat origin.** *Nature* 2020; 579:270–73 CrossRef Medline
18. Xia H, Lazartigues E. **Angiotensin-converting enzyme 2 in the brain: properties and future directions.** *J Neurochem* 2008;107:1482–94 CrossRef Medline
19. Mehta P, McAuley DF, Brown M, et al. HLH Across Specialty Collaboration, UK. **COVID-19: consider cytokine storm syndromes and immunosuppression.** *Lancet* 2020;395:1033–34 CrossRef Medline
20. Wu Y, Xu X, Chen Z, et al. **Nervous system involvement after infection with COVID-19 and other coronaviruses.** *Brain Behav Immun* 2020;87:18–22 CrossRef Medline
21. Dubé M, Le Coupanec A, Wong AHM, et al. **Axonal transport enables neuron-to-neuron propagation of human coronavirus OC_{43}.** *J Virol* 2018;92:e00404 CrossRef Medline
22. Arabi YM, Harthi A, Hussein J, et al. **Severe neurologic syndrome associated with Middle East respiratory syndrome corona virus (MERS-CoV).** *Infection* 2015;43:495–501 CrossRef Medline
23. Ma J, Xia P, Zhou Y, et al. **Potential effect of blood purification therapy in reducing cytokine storm as a late complication of critically ill COVID-19.** *Clin Immunol* 2020;214:108408 CrossRef Medline
24. Debiasi RL, Tyler KL. **Molecular methods for diagnosis of viral encephalitis.** *Clin Microbiol Rev* 2004;17:903–25 CrossRef Medline
25. Sonneville R, Demeret S, Klein I, et al. **Acute disseminated encephalomyelitis in the intensive care unit: clinical features and outcome of 20 adults.** *Intensive Care Med* 2008;34:528–32 CrossRef Medline
26. Schwarz S, Mohr A, Knauth M, et al. **Acute disseminated encephalomyelitis: A follow-up study of 40 adult patients.** *Neurology* 2001;56:1313–18 CrossRef Medline
27. Yeh EA, Collins A, Cohen ME, et al. **Detection of coronavirus in the central nervous system of a child with acute disseminated encephalomyelitis.** *Pediatrics* 2004;113(pt 1):e73–76 CrossRef Medline

Perfusion Parameter Thresholds That Discriminate Ischemic Core Vary with Time from Onset in Acute Ischemic Stroke

T. Yoshie, Y. Yu, H. Jiang, T. Honda, H. Trieu, F. Scalzo, J.L. Saver, and D.S. Liebeskind, on behalf of the UCLA Reperfusion Therapy Investigators

ABSTRACT

BACKGROUND AND PURPOSE: When mapping the ischemic core and penumbra in patients with acute ischemic stroke using perfusion imaging, the core is currently delineated by applying the same threshold value for relative CBF at all time points from onset to imaging. We investigated whether the degree of perfusion abnormality and optimal perfusion parameter thresholds for defining ischemic core vary with time from onset to imaging.

MATERIALS AND METHODS: In a prospectively maintained registry, consecutive patients were analyzed who had ICA or M1 occlusion, baseline perfusion and diffusion MR imaging, treatment with IV tPA and/or endovascular thrombectomy, and a witnessed, well-documented time of onset. Ten superficial and deep MCA ROIs were analyzed in ADC and perfusion-weighted images.

RESULTS: Among the 66 patients meeting entry criteria, onset-to-imaging time was 162 minutes (range, 94–326 minutes). Of the 660 ROIs analyzed, 164 (24.8%) showed severely or moderately reduced ADC (ADC $\leq$ 620, ischemic core), and 496 (75.2%), mildly reduced or normal ADC (ADC $>$ 620). In ischemic core ADC regions, longer onset-to-imaging times were associated with more highly abnormal perfusion parameters–relative CBF: Spearman correlation, $r = -0.22$, $P = .005$; relative CBV: $r = -0.41$, $P < .001$; MTT: $-r = -0.29$, $P < .001$; and time-to-maximum: $r = 0.35$, $P < .001$. As onset-to-imaging times increased, the best cutoff values for relative CBF and relative CBV to discriminate core from noncore tissue became progressively lower and overall accuracy of the core tissue definition increased.

CONCLUSIONS: Perfusion abnormalities in ischemic core regions become progressively more abnormal with longer intervals from onset to imaging. Perfusion parameter value thresholds that best delineate ischemic core are more severely abnormal and have higher accuracy with longer onset-to-imaging times.

ABBREVIATIONS: AUC = area under the ROC curve; OTI = onset to imaging; rCBF = relative cerebral blood flow; rCBV = relative cerebral blood volume; ROC = receiver operating characteristic; Tmax = time-to-maximum

Imaging of the mismatch between ischemic core and penumbra is now a proved means to identify late-presenting patients with acute ischemic stroke who will benefit from intravenous thrombolysis 4.5–9 hours after onset[1] and endovascular thrombectomy 6–24 hours after onset.[2,3] A favorable mismatch profile is a small ischemic core of irreversibly infarcted tissue and a large penumbra of threatened-but-salvageable tissue. Conversely, large ischemic core volume on DWI or CT perfusion imaging and a small volume of salvageable penumbral tissue on multimodal MR imaging or CT are associated with unfavorable clinical outcomes.[4-6]

When DWI is used to define the ischemic core, the volume and degree of ADC change directly reflect the total duration and intensity of ischemia experienced from stroke onset until the moment of imaging. Accordingly, the volume of tissue with low ADC values reflects both the time from stroke onset to imaging (OTI) and the varying degrees of hypoperfusion during this interval.[7,8]

However, when perfusion imaging is used to define the ischemic core, the situation is very different. Perfusion imaging primarily provides a physiologic snapshot of 1 moment in time, indexing the physiologic conditions present at the time of imaging rather than integrating total ischemia time and intensity until

Received March 22, 2020; accepted after revision June 29.

From the Department of Neurology (T.Y., Y.Y., H.J., T.H., H.T., F.S., J.L.S., D.S.L.), David Geffen School of Medicine at University of California, Los Angeles, Los Angeles, California; Department of Neurology and Neuro Endovascular Therapy (T.Y.), St. Marianna University Toyoko Hospital, Kanagawa, Japan; Department of Neurology (H.J.), the First Affiliated Hospital of Harbin Medical University, Harbin, Heilongjiang, China.

Paper previously presented, in part, at Annual Meeting of the International Stroke Conference, Honolulu, Hawaii 2019; February 6–8.

Please address correspondence to Tomohide Yoshie, MD, PhD, Department of Neurology and Neuro Endovascular Therapy, St. Marianna University Toyoko Hospital, 3-435, Kosugimachi, Nakaharaku, Kawasaki, Kanagawa, 211-0063, Japan; e-mail: tomohide.yoshie.1215@marianna-u.ac.jp

Indicates article with supplemental on-line tables.

Indicates article with supplemental on-line photos.

http://dx.doi.org/10.3174/ajnr.A6744

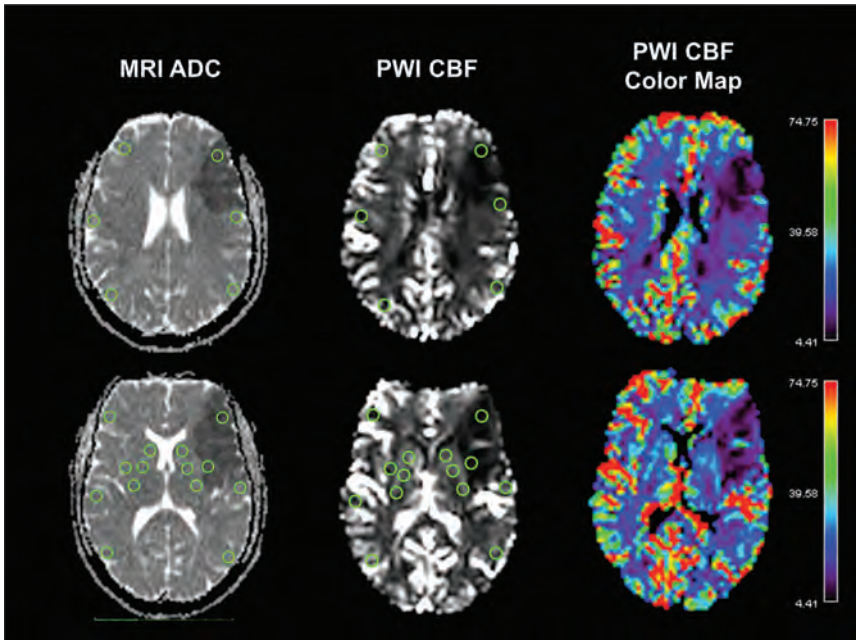

FIG 1. ROI placement. ROIs are shown as *green circles* on the ADC map (left) and black and white CBF map (middle). The color-coded CBF map is shown on the right. In addition to these maps, identical ROIs were placed on CBV, MTT, and Tmax maps.

imaging. Preclinical studies in stroke animal models have found that the degree of cerebral blood flow impairment worsens with time in infarct core regions,[9,10] suggesting that perfusion parameters used to distinguish core from noncore may vary as OTI time intervals vary. Studies in patients with acute ischemic stroke have not elucidated well whether the perfusion value thresholds that best demarcate irreversible infarcted core from salvageable penumbra tissue are time-invariant or time-dependent.

Studies of perfusion imaging strategies for identifying infarct core have found that when comparing different perfusion parameters, the degree of relative cerebral blood flow (rCBF) reduction is the best variable to use.[11] Commonly, the threshold of rCBF of $<$30% is used for detecting ischemic core. This perfusion threshold has been defined regardless of time from onset.

The purpose of this study was to evaluate whether optimal perfusion thresholds for ischemic core vary with OTI time.

MATERIALS AND METHODS

Subjects

In a prospectively maintained registry, we identified consecutive patients with acute ischemic stroke between July 2011 and October 2016 meeting the following eligibility criteria: 1) treatment with IV tPA and/or endovascular thrombectomy, 2) both DWI and PWI performed before reperfusion therapy, 3) occlusion of the ICA or MCA M1 segment on initial MR angiography, and 4) witnessed onset while awake permitting reliable assessment of clinical onset time. Patients who received IV tPA from an outside hospital and were then transferred to our center were included if the initial MR angiography showed ICA or M1 occlusion. The study was approved by the institutional review board in David Geffen School of Medicine at University of California Los Angeles for conduction under a waiver of consent for a minimal-risk study analyzing clinically collected data.

Image Acquisition and Processing

During this study, standard care at our institution included using MR imaging as the initial technique for assessment of patients with acute ischemic stroke whenever possible. If a patient had a contraindication to MR imaging, such as a pacemaker or cardiorespiratory instability, CT was instead performed. MR imaging studies were performed on a 1.5-T (Magnetom Vision+, Sonata or Symphony) or 3-T (Magnetom Trio) MRI (Siemens Medical Systems, Erlangen, Germany). The standard stroke MR imaging protocol included DWI, gradient recalled-echo, FLAIR, PWI, and MR angiography of the cervical and intracranial vessels. MR imaging without PWI was performed if the patient was not eligible for contrast, such as having contrast allergy or renal dysfunction. DWI was obtained with 2 levels of diffusion sensitization (b values = 0 and 1000 s/mm^2, 5- to 7-mm section thickness, and no gap). PWI was performed using an axial dynamic gradient-echo echo-planar perfusion-weighted se-quence. If indicated, tPA was started in the scanner after the DWI and gradient recalled-echo sequences and before the remaining acquisitions, to expedite therapy initiation.

PWI data were postprocessed using Olea Sphere (Olea Medical). The arterial input function in each patient was automatically selected, with the selection reviewed by the imaging analyst. If the automatically selected arterial input function was not in an appropriate location, another arterial input function was selected manually in the proximal segment of the MCA contralateral to the occlusion side. The Oscillation Singular Value Decomposition (oSVD) technique was used as a deconvolution method, and the deconvoluted perfusion parameters (CBF, CBV, MTT, and time-to-maximum [Tmax]) were calculated.

Quantitative Analysis

For quantitative analysis, a vascular neurologist (T.Y.) who was blinded to clinical data and other images including FLAIR images, assessed the imaging data. Quantitative measurement of ADC and perfusion values was performed with imaging software (Horos, Version 3.1.2; Horos Project; https://horosproject.org/), using small circular ROIs with areas of 50 mm^2. First, 10 ROIs were placed on ADC images in anatomically defined regions over the MCA territory, similar to those defined by the ASPECTS, at 2 section levels, 1 at the level of the thalamus and basal ganglia and 1 just rostral to the ganglionic structures. The 10 ROIs were located at the caudate, lentiform, internal capsule, insular ribbon, inferior anterior MCA cortex (M1), MCA cortex lateral to the insular ribbon (M2), inferior posterior MCA cortex (M3), superior anterior

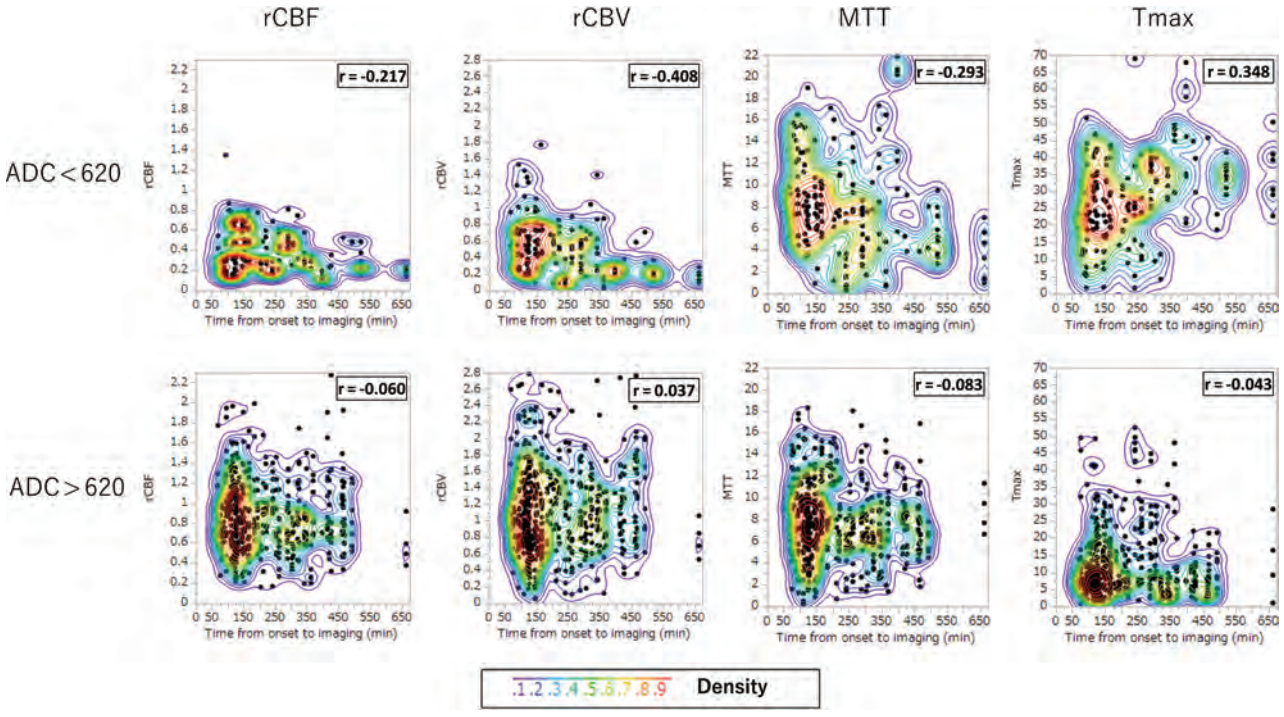

FIG 2. Scatterplot of ROI perfusion parameter values and onset-to-imaging time for 660 ROIs, separately for severely-moderately reduced ADC (ADC ≤ 620, upper row) and mildly reduced–normal ADC (ADC > 620, lower row). Colors indicate the density of points, increasing from blue to green to yellow to red.

MCA cortex (M4), superior lateral MCA cortex (M5), and superior posterior MCA cortex (M6) (Fig 1). Then ROIs of the same size and location were placed on the PWI maps, including CBF, CBV, MTT, and Tmax images. If an ROI placement included pixels of large vessels or artifacts, the ROI was moved manually, avoiding these elements at the discretion of the operator's visual analysis, using a maximum CBF threshold value of 70 or 80 mL/100 × g. We used rCBF for the CBF evaluation because previous studies have shown that rCBF is superior for assessing ischemic lesions to absolute CBF[11] and rCBF is more widely used in the clinical care of patients with acute stroke. rCBF was calculated as ipsilateral CBF/contralateral CBF; and contralateral CBF was measured in the mirrored region. Relative CBV (rCBV) was similarly calculated and used for CBV evaluation. Finally, we used rCBF, rCBV, MTT, and Tmax for analysis as perfusion values.

Statistical Analysis

All ROIs were categorized between 2 groups according to ADC values; ROIs with ADC < 620 were assigned to the moderate-to-severely reduced ADC group, and ADC ≥ 620, to the normal-to-mildly reduced ADC group. The χ^2 test for categoric variables and a Wilcoxon rank sum test for continuous variables were used to compare the study characteristics associated with the ADC categories. To assess the relationship between PWI values and time from onset to MR imaging, we performed a Spearman correlation coefficient analysis between each PWI value and the OTI time. Because multiple ROIs were included for a patient, Huber-White standard errors clustered on patient identifiers were used to account for within-person correlations. In addition, patients were divided into 3 groups according to the OTI time: <180 minutes, 180–360 minutes, and >360 minutes. A Wilcoxon rank sum test was performed to compare PWI values between each time group. To evaluate whether accuracy and optimal thresholds for defining ischemic core are dependent on time, receiver operating characteristic (ROC) curve analysis for ADC < 620 was performed in each time group. The area under the ROC curve (AUC), sensitivity, and specificity were calculated for each PWI value. The best cutoff points were calculated using the Youden Index, assigning equal weights to specificity and sensitivity. We used χ^2 statistics to compare the AUC between each OTI time group. Statistical analysis was performed using JMP Pro 13.0.0 statistical software (SAS Institute) and STATA 15.1 (StataCorp). $P < .05$ indicated a significant difference.

RESULTS

During the study period, 472 patients were treated with IV tPA and/or endovascular thrombectomy, among whom 228 had acute ICA or M1 occlusion. Of these, 74 underwent CT rather than MR imaging, 37 had MR imaging but without PWI sequences, 8 had poor-quality MR imaging acquisitions due to body movement or artifacts, and 43 had unclear onset times. Accordingly, 66 patients met the full study inclusion criteria, and 660 ROIs were analyzed. A flow diagram for inclusion in this study is shown in On-line Fig 1.

The median age of patients was 74 years (interquartile range, 64.5–83 years). Forty patients (60.6%) were women. Occlusion location was the ICA in 30 patients (45.4%), the proximal M1 in 15 patients (22.7%), and the distal M1 in 21 patients (31.8%). Laterality was left-sided occlusion in 34 (51.5%) and right-sided in 32 patients (48.5%). The mean baseline NIHSS score was 15.4 ± 8.2. Atrial fibrillation was present in 42 (63.6%) patients. The median time from onset to DWI was 162 minutes (interquartile range, 94–325.5 minutes; range, 69–664 minutes).

ROIs with Low and Normal ADCs

Of 660 ROIs, 164 (24.8%) were categorized to severely-moderately reduced ADC, and 496 (75.2%), to mildly reduced–normal, with characteristics shown in On-line Table 1. Severely-moderately reduced ADC regions were characterized by more frequent left-brain laterality and more frequent involvement of lentiform, internal capsule, and insular ribbon regions and less frequent involvement of the posterior MCA cortex regions, lower rCBF, lower rCBV, and higher Tmax. Time from onset to imaging did not differ among the ADC groups.

Relationship Between Each PWI Value and Time from Onset to MR Imaging

Figure 2 shows the relation between OTI time and perfusion parameters. In ROIs with severely-moderately reduced ADC, longer OTI time was associated with more greatly reduced rCBF (Spearman correlation, $r = -0.217$, $P = .005$), rCBV ($r = -0.408$, $P < .001$), and MTT ($r = -0.293$, $P < .001$), and more greatly prolonged Tmax ($r = 0.348$, $P < .001$) (On-line Table 2). Huber-White standard errors clustered on patient identifiers showed the same correlation in rCBF ($P = .029$), rCBV ($P = .006$), and Tmax ($P = .001$); however, there was no significant correlation in MTT ($P = .231$). In contrast, no significant relationship was noted in both a Spearman correlation coefficient analysis and Huber-White standard errors between OTI and perfusion parameters in mildly reduced–normal ADC areas.

To evaluate broad regional effects, we clustered ROIs into an MCA cortical group (M1–M6) and a deep group (caudate, lentiform, internal capsule, insular ribbon). The association of OTI and perfusion parameters was present for all 4 perfusion parameters for the deep group and 3 of 4 perfusion parameters for the MCA cortical group (rCBV, MTT, and Tmax, but not rCBF; On-line Table 2 and On-line Fig 2).

Considering the 3 OTI categories (<180 minutes, 180–360 minutes, >360 minutes), similar patterns were seen in the continuous analysis of OTI. Longer OTI time windows were associated with lower rCBF, rCBV, and MTT and higher Tmax in regions with severely-moderately reduced ADC (Fig 3).

ROC Curve Analysis

In ROC analysis, perfusion parameter ability to identify ROIs with ADC < 620, rCBF, rCBV, and Tmax all performed comparably with AUC of 0.89 (95% CI, 0.86–0.91), 0.85 (95% CI, 0.81–0.88), and 0.85 (95% CI, 0.81–0.88) (Table). In contrast, the MTT did not reach statistical significance. With regard to the relation between OTI time, both the predictive performance and the best threshold values for rCBF, rCBV, and Tmax changed across the 3 OTI time windows. The predictive accuracy of the parameters improved; for example, the AUCs of rCBF for <180 minutes, 180–360 minutes, and >360 minutes were 0.85 (95% CI, 0.79–0.89), 0.90 (95% CI, 0.85–0.93), and 0.97 (95% CI, 0.93–0.98). In addition, for rCBF and rCBV, the best threshold increased to more severely abnormal values with longer OTI times. For example, for rCBF, the best thresholds for <180 minutes, 180–360 minutes, and >360 minutes were reductions of 72%, 60%, and 48%. In contrast, for Tmax, the best thresholds were similar for <180 minutes (the best thresholds 18.6) and >360 minutes (18.7) and higher for 180–360 minutes (22.2).

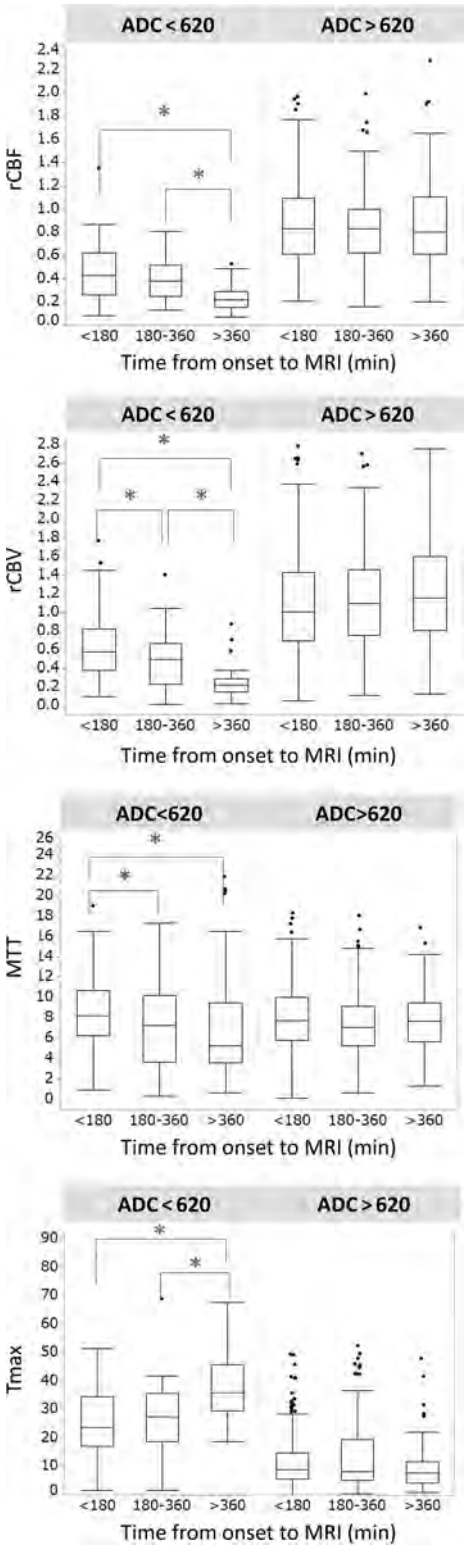

FIG 3. Boxplots of perfusion parameters according to categoric time from onset to imaging, <180 minutes ($n = 33$), 180–360 minutes ($n = 21$), and >360 minutes ($n = 12$). The *asterisk* indicates statistical significance ($P < .05$) in a Wilcoxon rank sum test between each onset-to-imaging time group.

ROC curve analysis for ischemic core regions (ADC ≤ 620)

	All	Onset-to-Imaging Time		
		<180 Min (n = 33)	180–360 Min (n = 21)	>360 Min (n = 12)
rCBF				
AUC (95% CI)	0.89 (0.86–0.91)	0.85 (0.79–0.89)[a]	0.90 (0.85–0.93)[a]	0.97 (0.93–0.98)
Best thresholds	0.60	0.72	0.60	0.48
Sensitivity	0.84	0.91	0.92	0.97
Specificity	0.78	0.62	0.79	0.88
rCBV				
AUC (95% CI)	0.85 (0.81–0.88)	0.76 (0.70–0.81)[a,b]	0.87 (0.82–0.91)[a]	0.97 (0.92–0.99)
Best thresholds	0.74	0.74	0.77	0.37
Sensitivity	0.82	0.72	0.90	0.91
Specificity	0.75	0.72	0.75	0.97
MTT				
AUC (95% CI)	0.49 (0.43–0.54)	0.55 (0.47–0.62)	0.53 (0.43–0.62)	0.62 (0.48–0.74)
Best thresholds	NS	NS	NS	NS
Sensitivity	NS	NS	NS	NS
Specificity	NS	NS	NS	NS
Tmax				
AUC (95% CI)	0.85 (0.81–0.88)	0.82 (0.76–0.87)[a]	0.79 (0.72–0.85)[a]	0.97 (0.92–0.98)
Best thresholds	18.6	18.6	22.2	18.7
Sensitivity	0.80	0.74	0.72	1.00
Specificity	0.82	0.84	0.80	0.89

Note:—NS indicates not significant.

[a] Statistical significance ($P < .05$), compared with the AUC for >360 minutes.

[b] Statistical significance compared with the AUC for 180–360 minutes.

DISCUSSION

This study of patients with acute ischemic stroke imaged between 1 hour 9 minutes to 11 hours 4 minutes from the defined onset time had 3 notable findings regarding the relation between OTI time and cerebral perfusion parameters: First, in regions that had progressed to irreversible infarction (ADC < 620), perfusion parameter values varied with OTI time, with long OTI times associated with more severely reduced rCBF and rCBV and more severely prolonged Tmax, as well as a shorter MTT. In contrast, perfusion parameters did not vary with time to imaging in regions with relatively preserved tissue bioenergetics. Second, the accuracy with which rCBF, rCBV, and Tmax perfusion parameters could define the ischemic core improved with longer OTI times. Third, the best thresholds to apply to these perfusion parameters to distinguish infarct core from tissue with relatively preserved ADC were increasingly abnormal values with longer OTI times.

These findings were achieved, in part, by the use in the current study of MR perfusion imaging to investigate the ability of perfusion parameters to delineate ischemic core. Most prior studies of perfusion-defined core have focused on CT perfusion imaging, which lacks the more direct assessment of infarct core afforded by diffusion MR images.[12–14] By evaluating perfusion parameters with MR imaging instead of CT acquisitions, we were able to compare perfusion findings with concurrently obtained diffusion MR images. In contrast, CT studies must use follow-up imaging after successful reperfusion to distinguish retroactively tissues that were core versus noncore, an approach with greater noise arising from incomplete reperfusion in many cases and from further progression of infarct during the interval between initial perfusion imaging and therapeutic reperfusion. As a result, most CT perfusion studies evaluating the temporal influence on CT perfusion thresholds for infarct core have focused on variations in the time interval from imaging to reperfusion, rather than the time interval from onset to imaging.

Several prior MR imaging studies have evaluated the aspects of the relationship between diffusion and perfusion findings on initial imaging but did not study the variation with OTI. For example, studies have found the following: Low ADC values are associated with low PWI CBF values;[15] PWI measures of ischemia severity can differentiate ischemic core from penumbra with good accuracy;[16] and rCBF is a well-performing perfusion parameter for assessing infarct core.[11] Our non-OTI-related findings that showed that rCBF had the highest AUC for infarct core are consonant with these prior investigations. In previous studies using CT perfusion and DWI, the best rCBF thresholds to distinguish ischemic core ranged widely, from 16%[17] to 50%.[18] Our finding that the best threshold value varies with OTI helps to explain these discrepancies. The optimal cutoff point of rCBF values for identifying infarct core in our study tended to be less severely abnormal than those in previous reports. Several reasons could explain this difference. Most prior studies obtained CT perfusion first, followed by DWI, so the identified parameter cutoffs reflect not only infarct core present at the time of perfusion imaging but also infarct core evolving in the interim. Varied trajectories of infarct growth during this interval would improve cerebral blood flow so that cerebral ischemia infarct progression could transpire between the imaging timepoints.

Some prior studies determined thresholds discriminating tissue status at the individual voxel level while we evaluated discrimination of 10 distinct ROIs within the MCA territory. Averaging of perfusion values arising from individual voxels with ADC values higher than the rest of the ROIs would tend to increase threshold values. Some previous studies derived rCBF and rCBV values using automatically selected ROIs in the contralateral hemisphere that were not manually reviewed and revised

to avoid inclusion of voxels within large vessels. Intravascular contralateral voxels would cause contralateral CBF and CBV values to be artifactually high and thereby cause rCBF and rCBV values to be artifactually low.

The worsening of perfusion parameters in infarct core regions with longer times since onset likely reflects several physiologic processes. The progressive extent of infarction within infarct core regions, including loss of islands of bioenergetically preserved tissue, leads to reduced metabolic demand for blood flow. Progressive ischemic injury to vascular endothelial tissues within infarct core regions leads to greater compromise of cerebral flow autoregulation, as well as capillary-arteriolar swelling with loss of vessel lumen and increased vascular resistance to flow. In addition, in some patients, progressive collateral failure arises because patients with mild cardiomyopathy are unable to sustain indefinitely increased cardiac output as a component of the stress response to the acute physiologic alteration. Our findings in human patients are consistent with preclinical animal stroke model studies also showing that CBF declines with longer time from onset.[9,10] Our results showed that the stronger association of OTI and CBF was found in the basal ganglia rather than the cortical region. There was a tendency of CBF to decline with longer time from onset in cortical regions, but it was not statistically significant. A previous animal study also showed a significant decrease with time of the CBF in the caudate and putamen, whereas the cortex showed no significant decline.[9] Because CBF depends on some factors such as leptomeningeal collaterals, these results indicate that the CBF decline in basal ganglia core regions directly reflects these physiologic processes.

The findings of this study have potential implications for clinical practice. In patients with acute ischemic stroke in whom ischemic core is being defined by perfusion rather than diffusion parameters, most commonly with CT imaging, the accuracy of the ischemic core definition will increase with longer OTI times. Clinicians should recognize that maps of the ischemic core in patients imaged early after onset will be less reliable. In addition, because the best perfusion parameter threshold values for delineating ischemic core vary with time from onset, CT perfusion imaging protocols may be optimized using cutoff values specific to each patient's time from the definite or best-estimated clinical onset time. In addition, our findings have potential applicability for MR imaging strategies as well. In patients with undocumented onset time, when regions with low ADC values still have relatively high rCBF and rCBV values, it is likely that the actual time of onset was recent.

This study has strengths and limitations. Strengths include rater review and revision of the placement of small circular ROIs for matched analysis of DWI and PWI. These small ROIs permitted sampling of defined anatomic regions, avoidance of overlap with other ROIs, and exclusion of large vessels and artifacts, avoiding confounds that can arise from unsupervised automatic ROI placement. A limitation is that this was a retrospective study for prospectively collected consecutive patients and single-reader-evaluated images. The reader was well-trained for MR imaging and perfusion imaging and blinded to clinical data; however, this feature may be a limitation of this study. Another limitation is that the ROIs included both gray and white matter. Although superficial and deep lesion sites could be analyzed separately, analysis of pure gray matter and pure white matter voxels was not possible. An additional limitation is that most OTI times analyzed were in the first 8 hours after onset. This is the time when most patients eligible for reperfusion therapy present, but exploration of temporal effects in later time periods 8–24 hours after onset was limited. In addition, the ADC threshold of 620 used to distinguish ischemic core from noncore is known to not perfectly discriminate these regions. This threshold was selected because multiple studies have demonstrated that it is among the best-performing ADC cutoff points and it is the threshold most widely used for MR core imaging in routine clinical practice.

CONCLUSIONS

We showed relationships between perfusion and time from onset. Perfusion values in normal-to-mildly reduced ADC areas have no relationship with the time from onset. In contrast, each perfusion value in a low ADC area depends on time. The accuracy and optimal thresholds for ischemic core in perfusion images depend on time. Thus, time from onset should be considered for evaluating the ischemic core using perfusion imaging modalities.

ACKNOWLEDGMENTS

We thank the patients who participated in this research and their families as well as Yasuyuki Kaga (EPS Corp) for advice with statistical analysis.

Disclosures: Yannan Yu—*UNRELATED*: *Employment*: Stanford University; *Grants/Grants Pending*: Stanford University. David S. Liebeskind—*UNRELATED*: *Consultancy*: Cerenovus, Genentech, Medtronic, Stryker, Vesalio, *Comments*: Imaging Core Lab.

REFERENCES

1. Campbell BC, Ma H, Ringleb PA, et al; EXTEND, ECASS-4, and EPITHET Investigators. **Extending thrombolysis to 4.5-9 h and wake-up stroke using perfusion imaging: a systematic review and meta-analysis of individual patient data.** *Lancet* 2019;394:139–47 CrossRef Medline
2. Nogueira RG, Jadhav AP, Haussen DC, et al; DAWN Trial Investigators. **Thrombectomy 6 to 24 hours after stroke with a mismatch between deficit and infarct.** *N Engl J Med* 2018;378:11–21 CrossRef Medline
3. Albers GW, Marks MP, Kemp S, et al; DEFUSE 3 Investigators. **Thrombectomy for stroke at 6 to 16 hours with selection by perfusion imaging.** *N Engl J Med* 2018;378:708–18 CrossRef Medline
4. Albers GW, Goyal M, Jahan R, et al. **Ischemic core and hypoperfusion volumes predict infarct size in SWIFT PRIME.** *Ann Neurol* 2016;79:76–89 CrossRef Medline
5. Wannamaker R, Guinand T, Menon BK, et al. **Computed tomographic perfusion predicts poor outcomes in a randomized trial of endovascular therapy.** *Stroke* 2018;49:1426–33 CrossRef Medline
6. Olivot JM, Mosimann PJ, Labreuche J, et al. **Impact of diffusion-weighted imaging lesion volume on the success of endovascular reperfusion therapy.** *Stroke* 2013;44:2205–11 CrossRef Medline
7. Lin W, Lee JM, Lee YZ, et al. **Temporal relationship between apparent diffusion coefficient and absolute measurements of cerebral blood flow in acute stroke patients.** *Stroke* 2003;34:64–70 CrossRef Medline
8. Baird AE, Benfield A, Schlaug G, et al. **Enlargement of human cerebral ischemic lesion volumes measured by diffusion-weighted magnetic resonance imaging.** *Ann Neurol* 1997;41:581–89 CrossRef Medline

9. Rohl L, Sakoh M, Simonsen CZ, et al. **Time evolution of cerebral perfusion and apparent diffusion coefficient measured by magnetic resonance imaging in a porcine stroke model.** *J Magn Reson Imaging* 2002;15:123–29 CrossRef Medline
10. Kohno K, Hoehn-Berlage M, Mies G, et al. **Relationship between diffusion-weighted MR images, cerebral blood flow, and energy state in experimental brain infarction.** *Magn Reson Imaging* 1995;13:73–80 CrossRef Medline
11. Campbell BC, Christensen S, Levi CR, et al. **Cerebral blood flow is the optimal CT perfusion parameter for assessing infarct core.** *Stroke* 2011;42:3435–40 CrossRef Medline
12. Bivard A, Kleinig T, Miteff F, et al. **Ischemic core thresholds change with time to reperfusion: a case control study.** *Ann Neurol* 2017;82:995–1003 CrossRef Medline
13. d'Esterre CD, Boesen ME, Ahn SH, et al. **Time-dependent computed tomographic perfusion thresholds for patients with acute ischemic stroke.** *Stroke* 2015;46:3390–97 CrossRef Medline
14. Qiao Y, Zhu G, Patrie J, et al. **Optimal perfusion computed tomographic thresholds for ischemic core and penumbra are not time dependent in the clinically relevant time window.** *Stroke* 2014;45:1355–62 CrossRef Medline
15. Thijs VN, Adami A, Neumann-Haefelin T, et al. **Clinical and radiological correlates of reduced cerebral blood flow measured using magnetic resonance imaging.** *Arch Neurol* 2002;59:233–38 CrossRef Medline
16. Shih LC, Saver JL, Alger JR, et al. **Perfusion-weighted magnetic resonance imaging thresholds identifying core, irreversibly infarcted tissue.** *Stroke* 2003;34:1425–30 CrossRef Medline
17. Kamalian S, Kamalian S, Maas MB, et al. **CT cerebral blood flow maps optimally correlate with admission diffusion-weighted imaging in acute stroke but thresholds vary by postprocessing platform.** *Stroke* 2011;42:1923–28 CrossRef Medline
18. Bivard A, Levi C, Krishnamurthy V, et al. **Defining acute ischemic stroke tissue pathophysiology with whole brain CT perfusion.** *J Neuroradiol* 2014;41:307–15 CrossRef Medline

Presurgical Identification of Primary Central Nervous System Lymphoma with Normalized Time-Intensity Curve: A Pilot Study of a New Method to Analyze DSC-PWI

A. Pons-Escoda, A. Garcia-Ruiz, P. Naval-Baudin, M. Cos, N. Vidal, G. Plans, J. Bruna, R. Perez-Lopez, and C. Majos

ABSTRACT

BACKGROUND AND PURPOSE: DSC-PWI has demonstrated promising results in the presurgical diagnosis of brain tumors. While most studies analyze specific parameters derived from time-intensity curves, very few have directly analyzed the whole curves. The aims of this study were the following: 1) to design a new method of postprocessing time-intensity curves, which renders normalized curves, and 2) to test its feasibility and performance on the diagnosis of primary central nervous system lymphoma.

MATERIALS AND METHODS: Diagnostic MR imaging of patients with histologically confirmed primary central nervous system lymphoma were retrospectively reviewed. Correlative cases of glioblastoma, anaplastic astrocytoma, metastasis, and meningioma, matched by date and number, were retrieved for comparison. Time-intensity curves of enhancing tumor and normal-appearing white matter were obtained for each case. Enhancing tumor curves were normalized relative to normal-appearing white matter. We performed pair-wise comparisons for primary central nervous system lymphoma against the other tumor type. The best discriminatory time points of the curves were obtained through a stepwise selection. Logistic binary regression was applied to obtain prediction models. The generated algorithms were applied in a test subset.

RESULTS: A total of 233 patients were included in the study: 47 primary central nervous system lymphomas, 48 glioblastomas, 39 anaplastic astrocytomas, 49 metastases, and 50 meningiomas. The classifiers satisfactorily performed all bilateral comparisons in the test subset (primary central nervous system lymphoma versus glioblastoma, area under the curve = 0.96 and accuracy = 93%; versus anaplastic astrocytoma, 0.83 and 71%; versus metastases, 0.95 and 93%; versus meningioma, 0.93 and 96%).

CONCLUSIONS: The proposed method for DSC-PWI time-intensity curve normalization renders comparable curves beyond technical and patient variability. Normalized time-intensity curves performed satisfactorily for the presurgical identification of primary central nervous system lymphoma.

ABBREVIATIONS: AUC = area under the curve; NAWM = normal-appearing white matter; nTIC = normalized time-intensity curve; MSID = maximal signal intensity drop; PCNSL = primary central nervous system lymphoma; PSR = percentage of signal recovery; TIC = time-intensity curve; CE-TIWI = contrast-enhanced TIWI; TTA = time-to-arrival; rCBV = relative cerebral blood volume

The presurgical diagnosis of brain tumors is highly relevant to patient management. Although histopathology remains the criterion standard, a presurgical suggestion of particular tumor types, such as primary central nervous system lymphoma (PCNSL) or metastasis, may greatly influence further procedures.[1-4]

MR imaging plays a pivotal role in the presurgical identification of brain tumors. Conventional MR imaging findings have been widely described; nevertheless, their performance is limited.[5-11] Given this limitation, an increasing number of studies have focused on monitoring physiologic and metabolic characteristics. In this sense, parameters derived from DSC-PWI have shown promising results in the diagnosis of brain tumors, and especially PCNSL.[12-20] DSC-PWI generates time-intensity curves (TICs) from dynamic monitoring of T2* signal intensity changes during contrast administration. Specific well-known parameters such as relative cerebral blood volume (rCBV) and percentage of

Received May 5, 2020; accepted after revision July 3.

From the Radiology Department (A.P.-E., P.N.-B., M.C., C.M.), Institut de Diagnòstic per la Imatge, Pathology Department (N.V.), Neurosurgery Department (G.P.), Neurology Department (J.B.), and Neurooncology Unit (A.P.-E., N.V., G.P., J.B., C.M.), Insitut Català d'Oncologia, Institut d'Investigació Biomèdica de Bellvitge, Hospital Universitari de Bellvitge, L'Hospitalet de Llobregat, Barcelona, Spain; and Radiomics Group (A.G.-R., R.P.-L.), Vall d'Hebron Institut d'Oncologia, Barcelona, Spain.

Please address correspondence to Albert Pons-Escoda, MD, Radiology Department, Institut de Diagnòstic per la Imatge (IDI), Hospital Universitari de Bellvitge. C/Feixa Llarga SN, L'Hospitalet de Llobregat, 08907, Barcelona, Spain; e-mail: albert.pons.idi @gencat.cat; @PonsEscoda

Indicates article with supplemental on-line tables.

Indicates article with supplemental on-line photo.

http://dx.doi.org/10.3174/ajnr.A6761

signal recovery (PSR) are extracted from these TICs. Although visual evaluation of the entire TICs has been suggested by some authors,[21] to the best of our knowledge, there are no previous studies that have quantitatively evaluated the whole range of points that form the TIC altogether. This is probably because technical variability and patient physiologic characteristics hinder direct point-by-point comparisons.[22-24]

Constructing normalized TICs (nTICs) would minimize the influence of physiologic and some technical parameters (especially regarding the timing of dynamics) on the TIC, offering interesting advantages: 1) It enables the possibility of performing a direct comparison of the entire nTIC between tumor types on a point-by-point basis, not limited to concrete parameters such as rCBV or PSR; and 2) it enhances the construction of user-friendly classifiers based on quantitative and visual comparison of particular cases to a data set of brain tumors.

The present article has 2 aims: first, to design an applicable method of processing TICs from DSC-PWI that allows obtaining normalized and comparable curves beyond technical and patient variability; and second, to test the applicability of this method by evaluating its diagnostic performance in a large series of patients with PCNSL.

MATERIALS AND METHODS

This article has been revised for publication by the research ethics committee of our tertiary hospital (Hospital Universitari de Bellvitge). The patient data were anonymized for this analysis. The confidential information of the patients was protected in accordance with national and European norms. Unspecific informed consent to participate in research projects was obtained from all patients. A waiver of a specific informed consent was provided by the ethics committee for this retrospective study.

Patients

Newly diagnosed patients with histologically confirmed PCNSL (2006–2019) were retrieved from our center database. Correlative cases by date and number, of glioblastoma, anaplastic astrocytoma, metastasis, and meningioma were retrieved from the same database for comparison.

Patients without PCNSL were selected to achieve the same number of patients with PCNSL, matched by year of acquisition. The rationale was to equalize the influence of technical differences of MR imaging sequences during such a long period (2006–2019) among tumor types. Inclusion criteria for the study were as follows: 1) confirmed tumor diagnosis by histology according to The World Health Organization 2007 or 2016 criteria, 2) an available diagnostic MR imaging examination including DSC-PWI and axial contrast-enhanced T1WI (CE-T1WI), 3) absence of previous oncospecific treatment at the time of the MR imaging examination, and 4) enhancing tumor on CE-T1WI with a shortest diameter of at least 10 mm. The flow diagram of study participants is shown in the On-line Figure.

Imaging

All the MR imaging examinations included in the study were acquired in the same tertiary hospital with 1 of 3 different scanners: Ingenia 3T with a 32-channel head coil, Ingenia or Intera 1.5T with a 16-channel head coil (Philips Healthcare). Acquisition parameters for DSC-PWI sequences (all gradient-echo) are summarized in On-line Tables 1 and 2. The intravenous contrast (gadobutrol; 1 mmol/mL, 0.1 mmol/kg) injection protocol was as follows: 18- or 20-ga peripheral intravenous access. No preload was performed. Baseline acquisition was on the order of 10 points. The start of the automatic injection (power injector at 4–5 mL/s) was by a manual setting. A final bolus of saline (25–50 mL) was injected at the same speed. The time and number of dynamics ranged from 1.26 to 3.55 seconds and 30 to 60, respectively.

The quality of the sequences was evaluated by visual inspection by 2 neuroradiologists (A.P.-E. and C.M.) with 5 years of experience in MR imaging of brain tumors. The examinations were labeled as poor quality and excluded from the study under the following circumstances: 1) artifacts prevented enhancing tumor segmentation on CE-T1WI or coregistration of CE-T1WI and DSC-PWI, or 2) an obvious low signal-to-noise ratio was observed in the raw TICs.

Postprocessing

Supervised semiautomatic volumetric segmentations (histogram thresholding and morphologic operations) of the enhancing tumor and normal-appearing white matter (NAWM) were performed on CE-T1WI and coregistered with DSC-PWI. Necrosis and nonenhancing components of the tumors were excluded from the segmentation. Semiautomatic volumetric segmentation of the whole enhancing lesion instead of partial, manual, or single-section ROI selection methods was chosen to minimize operator-dependency as well as to include all the intrinsic heterogeneity of the tumors in the analysis. 3D Slicer, Version 4.10 (http://www.slicer.org) was used for segmentation,[25] and the BRAINSFit module of 3D Slicer, for coregistering.[26]

Two TICs for each case, 1 of the enhancing tumor and 1 of the NAWM, were obtained by averaging the TICs for all voxels within the segmented area. Baseline and the initial point of the descending curve were aligned. Signal intensity values (SI_i) of the enhancing tumor TIC were normalized by dividing by the maximal signal intensity drop (MSID) of the NAWM ($SI_i/MSID_{NAWM}$). Time values (T_i) were normalized as relative to the period of the descending curve on NAWM, which is the subtraction of time-to-peak (TTP) minus time-to-arrival (TTA) [T_i / (TTP_{NAWM} – TTA_{NAWM})]. We used TTP-TTA instead of TTP to normalize time values to avoid the potential human operator variability of TTA, mainly due to differences in the coordination between contrast infusion and sequence start. Finally, the same constant time points (0.2 TTP-TTA fractions from 0 to a total of 5, resulting in 26 constant time points) were extrapolated for all the curves (Fig 1). To detect the initial point of the descending curve necessary for alignment and TTA calculation, we calculated the average slope and SD of the 4 points before and after the MSID, and the first point where the curve slope became greater than the average minus the SD was established as the initial descending point.

The TICs were processed using Python 3.6 software (https://www.python.org/downloads/release/python-360/).

As a secondary subanalysis, to compare our method with conventional rCBV and PSR measures, we obtained mean rCBV and

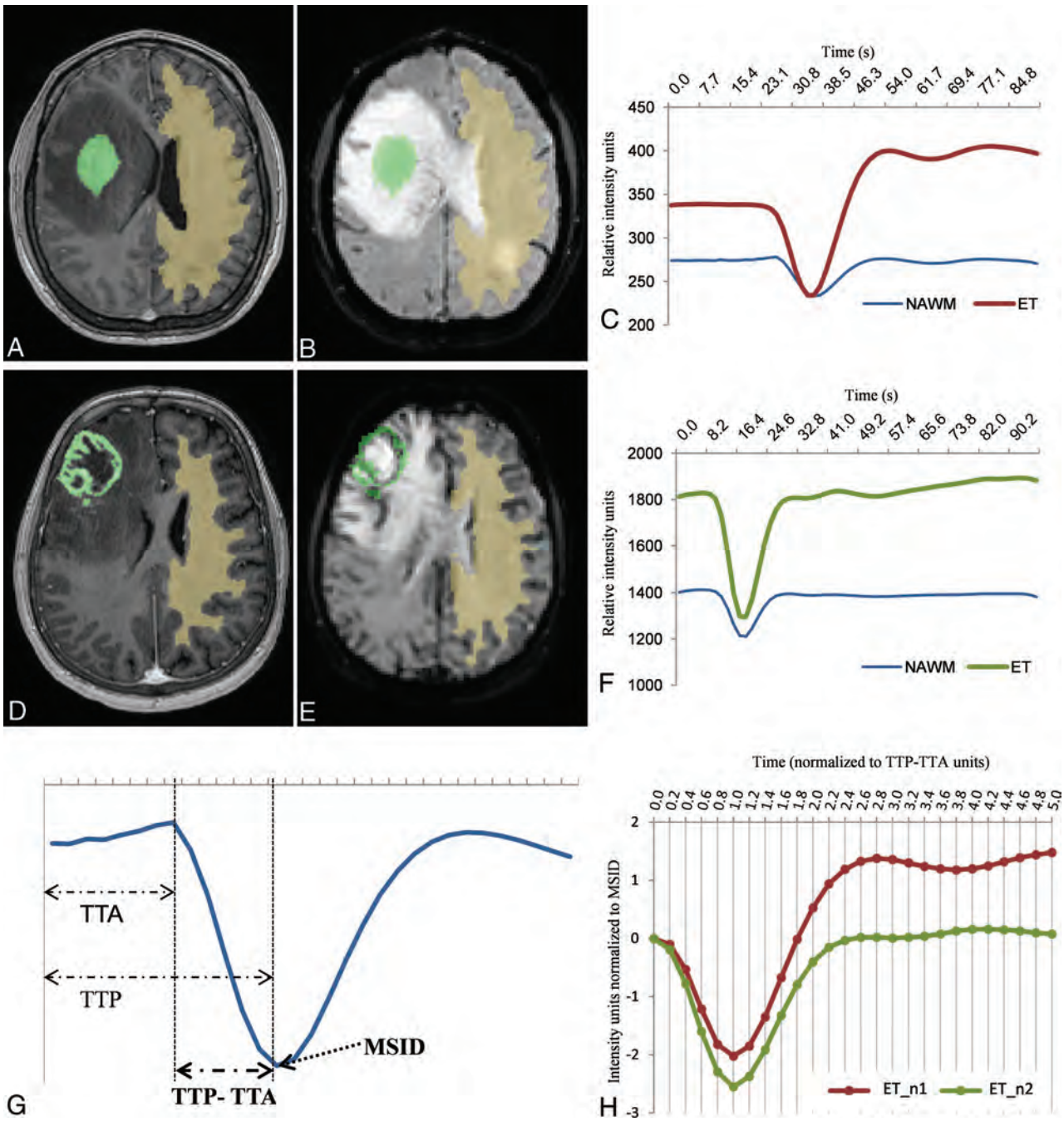

FIG 1. Solid (*A* and *B*) and necrotic (*D* and *E*) tumors and respective NAWM segmentations on axial CE-T1WI (*A* and *D*) and coregistered on DSC-PWI (*B* and *E*). Resultant raw curves by averaging the TIC for each voxel within the segmented areas (*C* and *F*), noncomparable due to differences in time, intensity, baseline, or initial point of the descending curve. Exemplification of the parameters used to normalize the curves, MSID, and TTP-TTA, relative to NAWM (*G*). Resultant normalized tumor curves, superimposable and comparable point by point (*H*). Curves with the exact same number of time-matching points and sharing common units of time (relative to TTP-TTA of the NAWM) and intensity (relative to MSID of the NAWM).

PSR values. rCBV was obtained with leakage correction[27] and normalized to the NAWM; PSR was obtained as described by Cha et al.[28] Both parameters were calculated using the same volumetric segmentation and coregistration as in the main analysis.

Statistics

The study sample was split into training (70%) and test (30%) subsets, which were balanced by the date of examination to minimize the impact of quality and technical differences between TICs of the more distant-in-time examinations. For the statistical analysis, pair-wise comparisons between PCNSL and each of the other tumor types were made. First, a stepwise selection was run in the training set, which rendered the 5 best discriminatory points per comparison pair. Stepwise selection is an unsupervised automatic procedure for variable selection, which can be used in cases of a large number of potential explanatory variables but

with no underlying theory on which to base the model. Subsequently, predictive models were trained using logistic binary regression in each pair of the training set. Finally, the constructed classifiers based on the algorithms from the training set were applied to the test set.

All the statistical computations were performed with R statistical and computing software, Version 3.5.1 (http://www.r-project.org).[29]

RESULTS

Patients

Fifty PCNSLs fulfilled the inclusion criteria and were included in the study. An additional 50 glioblastomas, 45 anaplastic astrocytomas, 50 metastases, and 50 meningiomas balanced with PCNSLs by date were included for comparison. The entire initial dataset included 245 patients (133 men; mean age, 59 years; range, 18–85 years). Demographics of the study sample are summarized in On-line Table 3.

Anaplastic astrocytoma was the only tumor type whose number of cases could not match the total of PCNSLs. Although the prevalence of anaplastic astrocytoma was higher than that of PCNSL, this was because only 45 cases fulfilled inclusion criterion number 4, "Enhancing tumor on CE-T1WI with a shortest diameter of at least 10 mm."

A total of 3 PCNSLs, 2 glioblastomas, 6 anaplastic astrocytomas, and 1 metastasis were ruled out by the quality filter. As a result, 47 PCNSLs, 48 glioblastomas, 39 anaplastic astrocytomas, 49 metastases, and 50 meningiomas were included in the final dataset (total $n = 233$). The patient dataset was split into training (70%) and test (30%) subsets balanced by the date of examination (training: 33 PCNSLs, 35 glioblastomas, 29 anaplastic astrocytomas, 36 metastases, and 36 meningiomas; test: 14 PCNSLs, 13 glioblastomas, 10 anaplastic astrocytomas, 13 metastases, and 14 meningiomas) (On-line Figure).

Normalized Curve Analysis and Pair-Wise Comparisons with PCNSL

Mean nTICs obtained from the training subset for each tumor type are shown in Fig 2. These mean curves are superimposable and comparable in a single graph due to the applied normalization method. This format provides a user-friendly tool for visual comparisons of nTICs. In this sense, notable differences were found between tumor-type nTICs on a first visual assessment, the most obvious around the MSID and the signal recovery segments. It is remarkable that all the curves in Fig 2 have the same number of time-matching points as well as sharing common units of time (relative to TTP-TTA of the NAWM) and intensity (relative to MSID of the NAWM). These features enable point-by-point absolute quantification of differences.

The 5 best discriminatory time points per pair of tumors achieved by stepwise selection are represented in Fig 2. The classifier algorithms, based on the logistic binary regression with the intercept and the relative power (coefficient) for each stepwise selected time point, are shown in On-line Tables 4 and 5.

Satisfactory results were obtained to enable segregating tumor types in all pair-wise comparisons in the training set. In summary, the area under the curve (AUC) values for all bilateral comparisons ranged between 0.86 (PCNSL versus anaplastic astrocytoma) and 1.00 (PCNSL versus meningioma), while the classification accuracies ranged between 74% (PCNSL versus anaplastic astrocytoma) and 97% (PCNSL versus meningioma). The same algorithms were applied to the test subset of tumors, confirming satisfactory classifications with AUC values between 0.83 (PCNSL versus anaplastic astrocytoma) and 0.96 (PCNSL versus glioblastoma) and accuracies between 71% (PCNSL versus anaplastic astrocytoma) and 96% (PCNSL versus meningioma) (Table).

The discriminating threshold of the constructed predictive model was set to zero to calculate the exposed results. Zero value corresponds to the point of maximum accuracy in binary logistic regressions. Nevertheless, this threshold can be easily modified, allowing the algorithm to be adapted to different clinical scenarios requiring specific sensitivity or specificity profiles.

Figures 3 and 4 are real clinical examples of the classifier user-friendly applicability. The nTIC curves of particular "problem" cases are overlapped on mean nTIC curves of each tumor type to visually assess similarities. The values after running the algorithm on the "problem" cases are depicted in a scatterplot to visually assess the likelihood of a particular diagnosis.

Regarding the rCBV and PSR subanalyses, the performance of these parameters is summarized in On-line Tables 6 and 7. In a general sense, mean rCBV and PSR showed inferior diagnostic performance to nTICs, with the only accuracies being slightly superior for PSR in PCNSL versus anaplastic astrocytoma and PCNSL versus metastasis in the test subgroups.

DISCUSSION

In this study, we have reported the design of an innovative method to obtain normalized TICs from DSC-PWI beyond patient and technical differences, which allows the following: 1) constructing mean curves for visual analysis, 2) performing point-by-point statistical comparisons between curves, and 3) building classifiers. We have tested its applicability in the presurgical identification of PCNSL and obtained satisfactory results.

DSC-PWI is an MR imaging technique that can be performed on most MR imaging units currently and provides noninvasive in vivo assessment of microvascular systems. It consists of a dynamic temporal acquisition during the vascular first pass of a contrast bolus. The injection of gadolinium results in an initial reduction in T2 signal intensity of tissues and subsequent signal recovery during contrast washout. TICs can be generated from this process. Well-studied parameters such as rCBV and PSR are extracted from these curves. The rCBV corresponds to the AUC, is usually measured relative to the NAWM, and has been related to histologic measurements of tumor vascularization.[22,24,30] The PSR is measured relative to the TIC baseline and may quantify the predominant T1 (signal recovery above baseline) or T2 (signal recovery below baseline) effects. These effects represent different leakage phenomena, which are explained by a complex combination of blood-brain barrier permeability, vascular volume fraction and vessel size, and tumor cell size and density.[22,30,31] The extraction of rCBV or PSR from TICs may represent an oversimplification of the information contained in the entire TIC. In fact, the curves have many other points that

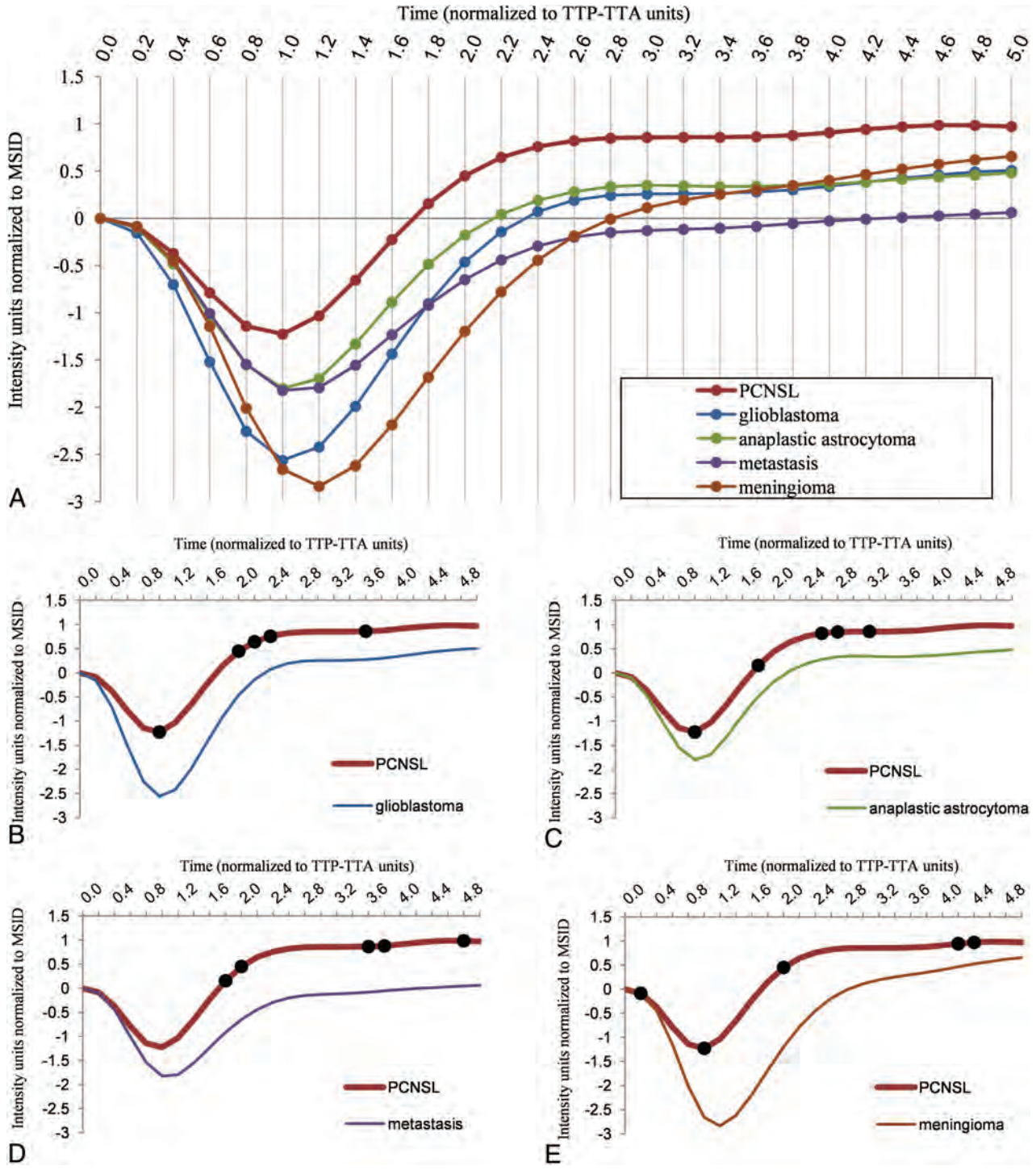

FIG 2. Normalized mean tumor curves for each type (PCNSL, glioblastoma, anaplastic astrocytoma, metastasis, and meningioma) obtained in the training subset (*A*). The curves are superimposable and comparable in a single graphic. This format provides a user-friendly tool for visual comparison of curves. Paired comparisons of normalized mean tumor curves for PCNSL against glioblastoma (*B*), anaplastic astrocytoma (*C*), metastasis (*D*), and meningioma (*E*), as well as representation of the 5 stepwise selected discriminatory TTP-TTA time points per pair (*black dots*).

remain excluded from these parameters. Along this line, some studies have suggested analyzing the whole curve to obtain improved information. Unfortunately, the proposed analysis was qualitative and limited to the visual pattern evaluation of the curve.[21] Quantitative assessment of the entire curve has not been accomplished to date, to our knowledge. This could be due to differences in the acquisition technique (including operator-dependency on some parameters) and patient physiologic features, which produce noncomparable TICs between different examinations or patients.[22,23] For example, there may be differences in

the number and time of dynamics, in contrast injection start point and speed, or in patient heart rate preventing TICs from being comparable.[16,22-24]

With these considerations in mind, we have developed a novel method for obtaining standardized, normalized, and comparable TICs independent of some technical and patient variability. We considered 2 parameters to be normalized to obtain comparable curves: time and intensity signal. Time was normalized as constant proportions of TTP-TTA from NAWM, and the time axis was re-dimensioned from seconds to fractions of 0.2 TTP-TTA units. Signal intensity was normalized to the MSID in NAWM. This normalization approach provided superimposable curves that could be visually analyzed and a list of point values that could be statistically compared among cases. Indeed, after normalization, mean curves for each tumor group could be constructed, allowing visual comparisons; the best discriminatory points with their optimal weighting for discrimination could be statistically determined, enabling the construction of classifiers; and particular cases could be displayed on scatterplots, providing visual representations of the likelihood of the diagnostic classification. Accordingly, we consider that this methodology could be further applied to construct user-friendly classifiers for the diagnosis of brain tumors. Examples of this potential application are shown in Figs 3 and 4.

We tested the performance of our method in the presurgical identification of PCNSL.

Reliable presurgical identification of PCNSL is vital because its management greatly differs from that of the other most prevalent enhancing brain tumors.[1-3,32] Maximal PCNSL resection is not recommended, and early stereotactic biopsy before

Summary of the results in training and test subsets

	AUC	Accuracy	Sensitivity	Specificity
PCNSL vs GB				
Training	0.96	88% (60/68)	88% (29/33)	89% (31/35)
Test	0.96	93% (25/27)	93% (13/14)	92% (12/13)
PCNSL vs AA				
Training	0.86	74% (46/62)	76% (25/33)	72% (21/29)
Test	0.83	71% (17/24)	93% (13/14)	60% (6/10)
PCNSL vs MET				
Training	0.92	81% (56/69)	81% (26/32)	81% (30/37)
Test	0.95	93% (25/27)	100% (14/14)	85% (11/13)
PCNSL vs MEN				
Training	1.00	97% (67/69)	97% (32/33)	97% (35/36)
Test	0.93	96% (27/28)	100% (14/14)	93% (13/14)

Note:—GB indicates glioblastoma; AA, anaplastic astrocytoma; MET, metastasis; MEN, meningioma.

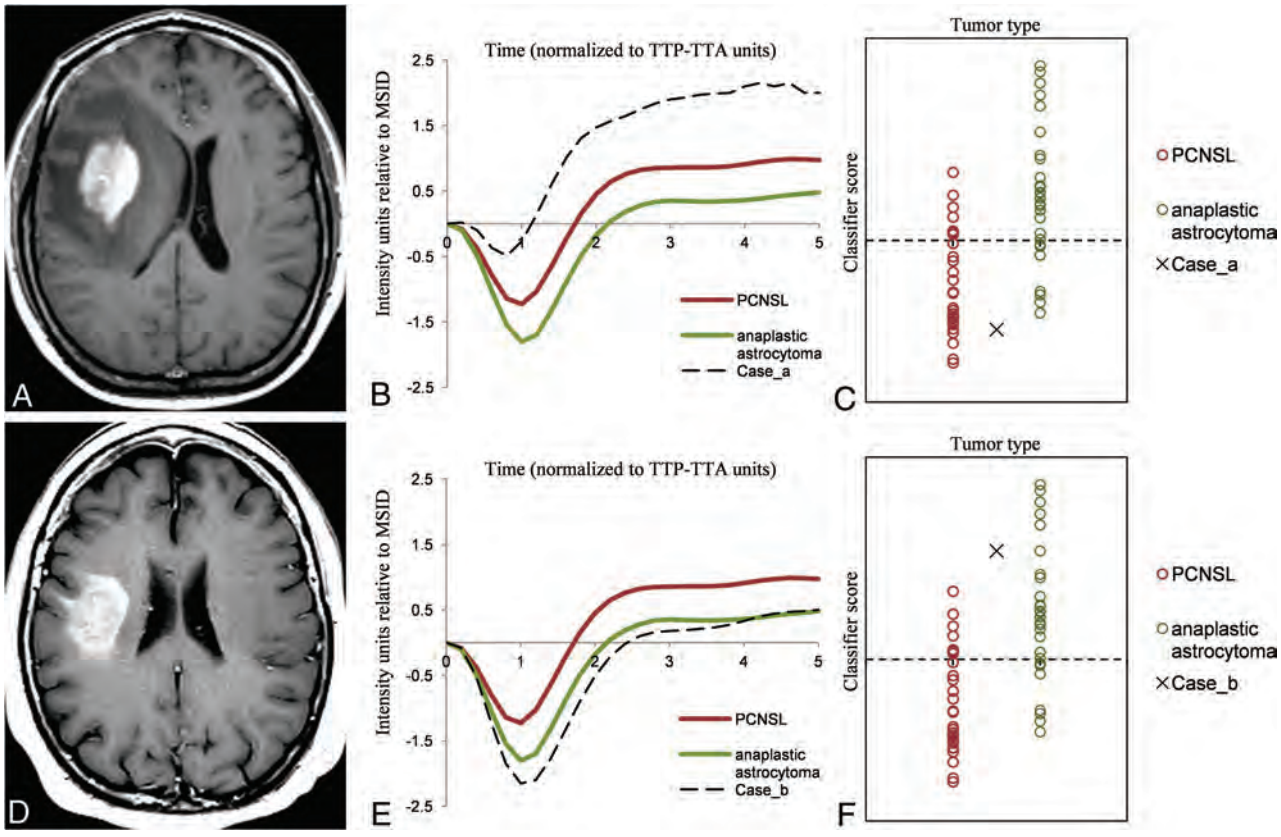

FIG 3. Example of clinical applicability on a "real" problem case. Axial CE-T1WI of 2 different patients (*A* and *D*) depicting 2 subcortical right frontal, solid enhancing tumors. PCNSL and anaplastic astrocytoma may be diagnostic possibilities to consider. Tumor normalized curves of each case overlapped to PCNSL, and anaplastic astrocytoma mean curves for visual assessment (*B* and *E*) show that the case in the upper row has similarities with PCNSL while in contrast, the case in the lower row has similarities with anaplastic astrocytoma. Representation of the classifier results on a scatterplot (*C* and *F*) demonstrates that the case in the upper row remains on the inferior side and may likely be a PCNSL, while the case in the lower row is more likely to be an anaplastic astrocytoma. We pathologically confirmed both diagnoses: case in the upper row, PCNSL; case in the lower row, anaplastic astrocytoma.

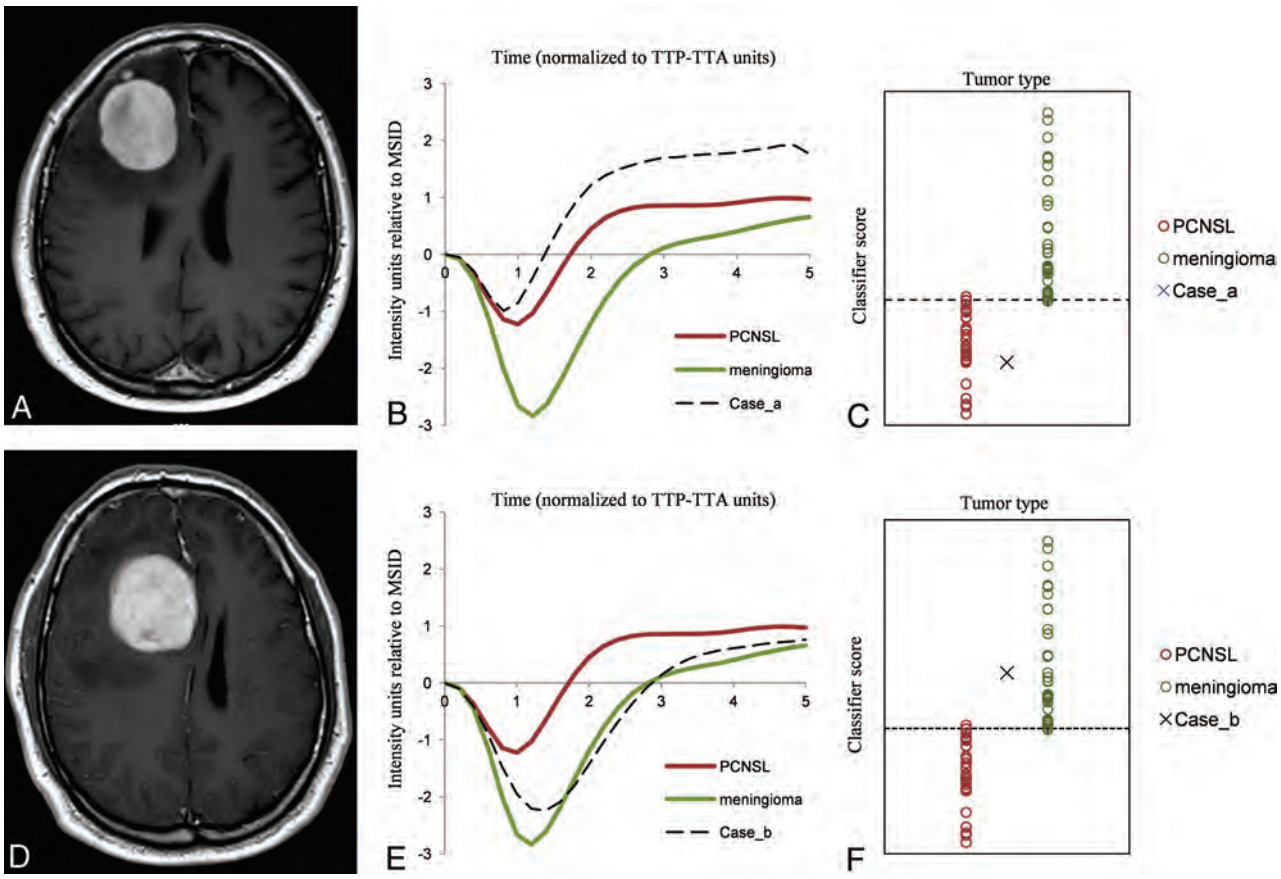

FIG 4. Example of clinical applicability on a "real" problem case. Axial CE-T1WI of 2 different patients with similar tumors (*A* and *D*): well defined, solid, avidly enhancing and right frontal peripherally located. PCNSL and meningioma were the 2 main diagnostic options considered. The tumor normalized curve of each case overlapping with PCNSL and meningioma mean curves (*B* and *E*) show that the case in the upper row is similar to PCNSL while the case in the lower row is close to meningioma. Representation of the classifier results on the scatterplot (*C* and *F*) suggests that the cases are likely to be PCNSL and meningioma, respectively. We pathologically confirmed both diagnoses: case in the upper row, PCNSL, case in the lower row, meningioma.

corticosteroid administration is mandatory when it is suspected from imaging.[32-35] Conventional MR imaging in PCNSL has been widely analyzed and may be useful for guiding initial management.[5-7] Nevertheless, these features may vary between patients and may overlap with other tumors.[8-11] Thus, radiologic diagnosis of PCNSL remains a challenge, and additional advanced imaging techniques such as DSC-PWI are increasingly being evaluated. Many articles have evaluated the potential of DSC-PWI for differentiating PCNSL from other tumors with excellent results. These studies focus on rCBV and PSR quantifications. Basically, PCNSL shows low rCBV and high PSR.[12-20] Some authors recently reported an additional parameter directly extracted from TICs termed "peak height," which has shown promising results.[12,15] However, the lack of technique standardization, which causes variability in the identification of the best discriminating parameter and its relevant thresholds between different studies, as well as the lack of a user-friendly way to depict the results, impedes the widespread clinical application of these perfusion parameters.[16,22-24]

We obtained satisfactory accuracy values in the comparisons between PCNSL and glioblastoma, anaplastic astrocytoma, metastasis, and meningioma in the test subset. Accuracies ranged between 71% (versus anaplastic astrocytoma) and 96% (versus meningioma). Moreover, the performance of the new method is overall superior compared with the analysis of conventional rCBV or PSR measures in our dataset (On-line Tables 6 and 7). Visual differences between the standardized nTICs of the different tumors were noted, especially in the segments around the MSID and the return to baseline (Fig 2). Statistical analysis confirmed that the best discriminatory points were situated around those segments of the curves that may somehow be related to the traditional rCBV, peak height, and PSR, which can be evaluated on conventional raw TICs. Indeed, we hypothesize that our method evaluates a mixture of these known relevant values along with other potentially discriminatory and otherwise hidden values of the curve, all together in a single step. Additionally, the method enables a user-friendly representation of the results (Figs 3 and 4). For this, we used a pair-wise model that takes advantage of the radiologist's interaction by narrowing the most probable diagnoses. Then, the classifier is used as a support tool for diagnosis and not as an independent reader.

The variety of DSC pulse sequence parameters included in this retrospective study deserves special attention. Differences on these parameters (flip angle, TE, TR) affect the curve morphology and indeed seem to partially justify the variability in values and thresholds found in the literature regarding both rCBV and

PSR.[31] In this sense, an overall predominantly high T1-weighting of the sequences in our study (On-line Table 1) seems to be carrying higher PSR values if compared with some prior studies.[20]

Several limitations of our study must be considered. The single-site and retrospective character of the study may affect reproducibility. Nevertheless, the single-site origin may confer homogeneity that could be useful for this pilot study. At any rate, multicentric and prospective studies in new real clinical scenarios are needed for validation. The inclusion of a wide range of MR imaging examination dates and consequent technical differences may have affected the consistency of results. Some of them, such as the timing of dynamics or little heterogeneities in technical parameters, may be considered positive for the study by demonstrating the robustness of the method. Other parameters, such as variations in TE, TR, or flip angle, may be considered potentially confusing. In particular, higher T1-weighting of older sequences in our study may overestimate PSR values.[20,31] Balancing of cases between tumor types and training and test cohorts was an attempt to minimize its impact on the results. Finally, we did not stratify subtypes of tumors or DSC sequence parameters used to avoid excessive fragmentation of the dataset.

On the other hand, our study has several strong points. First, a large sample of PCNSL was included, which provides a robust method and very high accuracy rates despite heterogeneity. Second, a wide-but-logical differential diagnosis was considered in the comparisons, which emphasizes the clinical usefulness of the results. Third, there is the semiautomatization of the image segmentation and coregistration as well as the TIC processing, which minimized operator-dependency in favor of reproducibility. Last, the method allowed including all the nTIC point values in the analysis without supervision, which provides an objective approach to the classification process.

CONCLUSIONS

The novel proposed method of assessing DSC-PWI renders normalized point-by-point comparable TICs beyond technique and patient variability, enables the construction of classifiers that can be presented in user-friendly interfaces, and shows good performance when tested, with excellent results in the presurgical identification of PCNSL.

ACKNOWLEDGMENTS

We want to thank Marcel Vidal for assistance with statistics in an earlier version of the article.

Disclosures: Raquel Perez-Lopez—*UNRELATED*: *Employment*: Vall d'Hebron Institute of Oncology; *Expert Testimony*: Roche; *Grants/Grants Pending*: Astra Zeneca, CRIS Foundation, Prostate Cancer Foundation, FERO Foundation, Carlos III Research Institute*; *Payment for Lectures Including Service on Speakers Bureaus*: Roche. *Money paid to the institution.

REFERENCES

1. Chiavazza C, Pellerino A, Ferrio F, et al. **Primary CNS lymphomas: challenges in diagnosis and monitoring.** *Biomed Res Int* 2018; 2018:3606970 CrossRef Medline
2. Altwairgi AK, Raja S, Manzoor M, et al. **Management and treatment recommendations for World Health Organization grade III and IV gliomas.** *Int J Health Sci (Qassim)* 2017;11:54–62 Medline
3. Enrique GV, Irving SR, Ricardo BI, et al. **Diagnosis and management of brain metastases: an updated review from a radiation oncology perspective.** *J Cancer Metastasis Treat* 2019;5:54 CrossRef
4. Euskirchen P, Peyre M. **Management of meningioma.** *Presse Med* 2018;47:e245–52 CrossRef Medline
5. Tang YZ, Booth TC, Bhogal P, et al. **Imaging of primary central nervous system lymphoma.** *Clin Radiol* 2011;66:768–77 CrossRef Medline
6. Giannini C, Dogan A, Salomão DR. et al. **CNS lymphoma.** *J Neuropathol Exp Neurol* 2014;73:478–94 CrossRef Medline
7. Bühring U, Herrlinger U, Krings T, et al. **MRI features of primary central nervous system lymphomas at presentation.** *Neurology* 2001;57:393–96 CrossRef Medline
8. Upadhyay N, Waldman AD. **Conventional MRI evaluation of gliomas.** *Br J Radiol* 2011;84:84 Spec No 2(Spec Iss 2);S107–11 CrossRef
9. Fink K, Fink J. **Imaging of brain metastases.** *Surg Neurol Int* 2013;4:209 CrossRef
10. Watts J, Box G, Galvin A, et al. **Magnetic resonance imaging of meningiomas: a pictorial review.** *Insights Imaging* 2014;5:113–22 CrossRef Medline
11. Huang RY, Bi WL, Griffith B, et al; International Consortium on Meningiomas. **Imaging and diagnostic advances for intracranial meningiomas.** *Neuro Oncol* 2019;21:i44–61 CrossRef Medline
12. Lee MD, Baird GL, Bell LC, et al. **Utility of percentage signal recovery and baseline signal in DSC-MRI optimized for relative CBV measurement for differentiating glioblastoma, lymphoma, metastasis, and meningioma.** *AJNR Am J Neuroradiol* 2019;40:1145–50 CrossRef Medline
13. Xing Z, You RX, Li J, et al. **Differentiation of primary central nervous system lymphomas from high-grade gliomas by rCBV and percentage of signal intensity recovery derived from dynamic susceptibility-weighted contrast-enhanced perfusion MR imaging.** *Clin Neuroradiol* 2014;24:329–36 CrossRef Medline
14. Liang R, Li M, Wang X, et al. **Role of rCBV values derived from dynamic susceptibility contrast-enhanced magnetic resonance imaging in differentiating CNS lymphoma from high grade glioma: a meta-analysis.** *Int J Clin Exp Med* 2014;7:5573–77 Medline
15. Neska-Matuszewska M, Bladowska J, Saôsiadek M, et al. **Differentiation of glioblastoma multiforme, metastases and primary central nervous system lymphomas using multiparametric perfusion and diffusion MR imaging of a tumor core and a peritumoral zone: searching for a practical approach.** *PLoS One* 2018;13: e0191341 CrossRef Medline
16. Xu W, Wang Q, Shao A, et al. **The performance of MR perfusion-weighted imaging for the differentiation of high-grade glioma from primary central nervous system lymphoma: a systematic review and meta-analysis.** *PLoS One* 2017;12:e0173430 CrossRef Medline
17. Wang S, Kim S, Chawla S, et al. **Differentiation between glioblastomas, solitary brain metastases, and primary cerebral lymphomas using diffusion tensor and dynamic susceptibility contrast-enhanced MR imaging.** *AJNR Am J Neuroradiol* 2011;32:507–14 CrossRef Medline
18. Lee IH, Kim ST, Kim HJ, et al. **Analysis of perfusion weighted image of CNS lymphoma.** *Eur J Radiol* 2010;76:48–51 CrossRef Medline
19. Calli C, Kitis O, Yunten N, et al. **Perfusion and diffusion MR imaging in enhancing malignant cerebral tumors.** *Eur J Radiol* 2006; 58:394–403 CrossRef Medline
20. Mangla R, Kolar B, Zhu T, et al. **Percentage signal recovery derived from MR dynamic susceptibility contrast imaging is useful to differentiate common enhancing malignant lesions of the brain.** *AJNR Am J Neuroradiol* 2011;32:1004–10 CrossRef Medline
21. Chinchure S, Thomas B, Wangju S, et al. **Mean intensity curve on dynamic contrast-enhanced susceptibility-weighted perfusion MR**

imaging: review of a new parameter to differentiate intracranial tumors. *J Neuroradiol* 2011;38:199–206 CrossRef Medline

22. Welker K, Boxerman J, Kalnin A, et al; American Society of Functional Neuroradiology MR Perfusion Standards and Practice Subcommittee of the ASFNR Clinical Practice Committee. **ASFNR Recommendations for Clinical Performance of MR Dynamic Susceptibility Contrast Perfusion Imaging of the Brain.** *AJNR Am J Neuroradiol* 2015;36:E41–51 CrossRef Medline
23. Willats L, Calamante F. **The 39 steps: evading error and deciphering the secrets for accurate dynamic susceptibility contrast MRI.** *NMR Biomed* 2013;26:913–31 CrossRef Medline
24. Paulson ES, Schmainda KM. **Comparison of dynamic susceptibility-weighted contrast-enhanced MR methods: recommendations for measuring relative cerebral blood volume in brain tumors.** *Radiology* 2008;249:601–13 CrossRef Medline
25. Fedorov A, Beichel R, Kalpathy-Cramer J, et al. **3D Slicer as an image computing platform for the Quantitative Imaging Network.** *Magn Reson Imaging* 2012;30:1323–41 CrossRef Medline
26. Johnson H, Harris G, Williams K. **BRAINSFit: mutual information rigid registrations of whole-brain 3D images, using the insight toolkit.** 2009. https://www.nitrc.org/docman/view.php/52/639/BRAINSFit.pdf. Accessed October 1, 2019
27. Hu LS, Baxter LC, Pinnaduwage DS, et al. **Optimized preload leakage-correction methods to improve the diagnostic accuracy of dynamic susceptibility-weighted contrast-enhanced perfusion MR imaging in posttreatment gliomas.** *AJNR Am J Neuroradiol* 2010; 31:40–48 CrossRef Medline
28. Cha S, Lupo JM, Chen MH, et al. **Differentiation of glioblastoma multiforme and single brain metastasis by peak height and percentage of signal intensity recovery derived from dynamic susceptibility-weighted contrast-enhanced perfusion MR imaging.** *AJNR Am J Neuroradiol* 2007;28:1078–84 CrossRef Medline
29. R Foundation. **R: A language and environment for statistical computing.** 2020. http://www.r-project.org/. Accessed October 15, 2019
30. Korfiatis P, Erickson B. **The basics of diffusion and perfusion imaging in brain tumors.** *Appl Radiol* 2014;43:22–29 Medline
31. Boxerman JL, Paulson ES, Prah MA, et al. **The effect of pulse sequence parameters and contrast agent dose on percentage signal recovery in DSC-MRI: implications for clinical applications.** *AJNR Am J Neuroradiol* 2013;34:1364–69 CrossRef Medline
32. Qian L, Tomuleasa C, Florian I-A, et al. **Advances in the treatment of newly diagnosed primary central nervous system lymphomas.** *Blood Res* 2017;52:159–66 CrossRef Medline
33. Hoang-Xuan K, Bessell E, Bromberg J, et al; European Association for Neuro-Oncology Task Force on Primary CNS Lymphoma. **Diagnosis and treatment of primary CNS lymphoma in immunocompetent patients: guidelines from the European Association for Neuro-Oncology.** *Lancet Oncol* 2015;16:e322–32 CrossRef Medline
34. Önder E, Arıkök AT, Önder S, et al. **Corticosteroid pre-treated primary CNS lymphoma: a detailed analysis of stereotactic biopsy findings and consideration of interobserver variability.** *Int J Clin Exp Pathol* 2015;8:7798–808 Medline
35. Weller M, Martus P, Roth P, et al; German PCNSL Study Group. **Surgery for primary CNS lymphoma? Challenging a paradigm.** *Neuro Oncol* 2012;14:1481–84 CrossRef Medline

Tentorial Venous Anatomy: Variation in the Healthy Population

J.S. Rosenblum, J.M. Tunacao, V. Chandrashekhar, A. Jha, M. Neto, C. Weiss, J. Smirniotopoulos, B.R. Rosenblum, and J.D. Heiss

ABSTRACT

BACKGROUND AND PURPOSE: A new transtentorial venous system consisting of medial, intermediate, and lateral tentorial veins, connecting infra- and supratentorial compartments, was recently shown in 2 cadaver dissections and 2 patient scans. We sought to characterize the venous patterns within the tentorium and their relation to measures of skull development in a cohort of healthy adults.

MATERIALS AND METHODS: We retrospectively reviewed tentorial venous anatomy of the head using CTA/CTV performed for routine care or research purposes in 238 patients. Included studies had adequate contrast opacification of venous structures and a section thickness of ≤2 mm; we excluded cases with space-occupying lesions and vascular pathologies. Tentorial angle, dural sinus configurations, and measures of skull base development were assessed as predictors of tentorial venous anatomy variation via Cramér V association, the binary encoded Pearson correlation, and nearest-point algorithm with the Euclidean distance metric for clustering.

RESULTS: Tentorial vein development was related to the ringed configuration of the tentorial sinuses ($P < .005$). There were 3 configurations. Groups 1A and 1B ($n = 50/238$) had ringed configuration, while group 2 did not ($n = 188/238$). Group 1A ($n = 38/50$) had a medialized ringed configuration, and group 1B had a lateralized ringed configuration ($n = 12/50$). Measurements of skull base development were predictive of these groups. The ringed configuration of group 1 was related to the presence of a split confluens, which correlated with a decreased internal auditory canal–petroclival fissure angle. Configuration 1A was related to the degree of petrous apex pneumatization (P value = .010).

CONCLUSIONS: Variations in the transtentorial venous system directly correlate with cranial development.

ABBREVIATIONS: CC-JB = carotid canal–jugular bulb; IAC-PCF = internal auditory canal–petroclival fissure; ITV = intermediate tentorial vein; LTS = lateral tentorial sinus; LTV = lateral tentorial vein; MTS = medial tentorial sinus; MTV = medial tentorial vein; RC = ringed configuration

Neuroradiologists are critical in presurgical planning, particularly for complex surgical approaches to the skull base such as anterior petrosectomy, combined presigmoid/retrosigmoid approaches, and supracerebellar-transtentorial approach to the mesial temporal lobe.[1-5] The safety of these surgical approaches has been framed around incising avascular regions of the tentorium. However, tentorial sectioning may still produce unexplained adverse consequences.[6,7] Several cadaveric and radiographic studies previously demonstrated the anatomic patterns of bridging veins to the tentorium and medial and lateral venous sinuses within the tentorium.[8-11] A recent study found a relationship between the anatomy of the tentorial sinuses at the transverse-sigmoid junction and cranial morphometrics.[12] However, several studies of veins within the tentorium have demonstrated a wide variation inconsistent

Received April 2, 2020; accepted after revision July 2.

From the Surgical Neurology Branch (J.S.R., J.D.H.), National Institute of Neurological Disorders and Stroke, National Institutes of Health, Bethesda, Maryland; Neuro-Oncology Branch (J.S.R.), National Cancer Institute, National Institutes of Health, Bethesda, Maryland; Department of Radiology and Radiological Science (J.M.T., C.W.), The Johns Hopkins University School of Medicine, Baltimore, Maryland; SmartSulis LLC (V.C.), Trabuco Canyon, California; Section on Medical Neuroendocrinology (A.J.), Eunice Kennedy Shriver National Institute of Child Health and Human Development, National Institutes of Health, Bethesda, Maryland; Department of Neurosurgery (M.N.), Hospital Beneficência Portuguesa de São Paulo, Institute of Neurological Science of São Paulo Bela Vista, São Paulo, Brazil; Department of Radiology (J.S.), George Washington University, Washington, DC; MedPix (J.S.), National Library of Medicine, Bethesda, Maryland; and Department of Neurosurgery (B.R.R.), Riverview Medical Center, Red Bank, New Jersey.

Paper previously presented as an E-poster and abstract at: Annual Meeting of the American Association of Neurological Surgeons, April 25-29, 2020; Boston, Massachusetts.

This study was supported, in part, by the Intramural Research Programs of the National Institute of Neurological Disorders and Stroke and National Cancer Institute at the National Institutes of Health.

Please address correspondence to Jared S. Rosenblum, MD, Building 35, Room 2B203, Neuro-Oncology Branch, Center for Cancer Research, National Cancer Institute, Bethesda, MD 20892; e-mail: Jared.rosenblum@nih.gov; @JaredRosenblum

Indicates open access to non-subscribers at www.ajnr.org
Indicates article with supplemental on-line appendix and tables.
Indicates article with supplemental on-line photos.

http://dx.doi.org/10.3174/ajnr.A6775

with direct drainage of the bridging veins into the tentorial sinuses.[13-16] Intimate knowledge of the normal variations of the tentorial venous anatomy is of critical importance for neuroradiologists guiding neurosurgeons in presurgical planning and understanding postoperative complications.

Recently, a transtentorial venous system comprising the tentorial sinuses and veins connecting the anterior, middle, and posterior fossae was identified in 2 cadavers without intracranial pathology and 2 patients with disparate outcomes: 1) remote cerebellar infarct and hemorrhagic conversion due to compromise of the transtentorial venous system, and 2) tolerance of bilateral transverse sinus thrombosis because of collateral drainage through the tentorial veins.[17] Thus, the tentorial veins, remnants of the embryologic venous drainage system,[18-20] appeared to retain pathologic and physiologic relevance.[17]

The transtentorial network comprises 3 main veins and 2 main tentorial sinuses. The medial and lateral tentorial sinuses (MTS and LTS) may be distinct or connected, described previously as the ringed configuration (RC).[14,15] The medial tentorial vein (MTV) courses within the free edge of the tentorium, originating from the straight sinus and draining to the cavernous sinus. The intermediate tentorial vein (ITV) courses within the tentorium from the straight sinus to the superior petrosal sinus. The lateral tentorial vein (LTV) originates from the MTS or the RC of the tentorial sinuses and drains to the superior petrosal sinus. Plexiform anastomoses connect the tentorial veins and sinuses at various points.[17]

Herein, we aimed to define normal variations in the tentorial venous anatomy within the general population. Further, we hypothesized that the variations in tentorial sinus and vein anatomy were related to and could be predicted by the extent of skull base development, as measured by cranial morphometrics.

MATERIALS AND METHODS

Study Criteria

Tentorial venous anatomy of the head was evaluated on CTA and CTV performed for routine care or for research during 1 year at a single institution (The Johns Hopkins Hospital). Patients underwent vascular imaging either for research protocol, stroke evaluation, or follow-up of known lesions.

Studies were reviewed by expert neuroradiologists and the study team. Patients with known space-occupying lesions or vascular pathologies including acute dural venous sinus stenosis or thrombosis, AVM/AVF, new aneurysms or those enlarging on follow-up, cavernous malformations, developmental venous anomalies, intracranial hemorrhage, or infarction were excluded. Patients with stable aneurysms ($n = 9$; $3 > 4$ mm) with a long duration of follow-up were included; no change in intracranial vascular anatomy was seen longitudinally in these patients. We included studies with adequate contrast opacification of the venous structures and section thicknesses of $\leq$2 mm.

The study protocol for retrospective chart review was approved by the institutional review board.

Radiologic Measures

Measurements of the Skull Base. Scans were performed on 64-section multidetector CT (Definition 64 AS Section; Siemens) with 120 kV, 175 mA, 64 × 0.6 mm collimation, after IV nonionic contrast (Omnipaque 350 [iohexol]or Visipaque 320 [iodixanol]; GE Healthcare). Axial 0.75-mm slices at increments of 0.5 mm were reconstructed using a 512 × 512 matrix, with a standard kernel.

Bony measurements were performed on CT to assess skull base development, as follows. The petrosagittal angle was measured at the intersection of a midsagittal line from the nasal septum to the internal occipital protuberance and a line on each side from the spheno-occipital synchondrosis to the stylomastoid foramen.[21] The angle between the internal auditory canal and the petroclival fissure (IAC-PCF angle) was also measured.[22] The distance between the carotid canal and jugular bulb (CC-JB distance) was measured 1 section before the turn of the petrous segment of the internal carotid artery.[22] Development of the petrous apex was assessed as petrous apex pneumatization.[22] The tentorial angle was measured between a line extending from the nasion through the tuberculum sella and a second line through the straight sinus in the midsagittal plane.[23] Sample measurements are shown in On-line Fig 1. Measurements were performed by the study team on OsiriX DICOM Viewer (https://www.osirix-viewer.com/).

Definition of Dural Sinuses, Tentorial Sinus, and Tentorial Vein Anatomy. The transverse sinuses were assessed for patency and congenital stenosis. The cavernous sinuses were also assessed for patency or developmental anomalies. Congenital anomaly was distinguished from new stenosis by reviewing longitudinal imaging when available or by correlating with clinical findings—such as papilledema or elevated intracranial pressure; these cases were excluded. The presence of a split confluens sinuum was also noted. The tentorial sinuses were defined medial or lateral along the tentorium and by their presence and respective origins.[8] The MTS either originates from the straight sinus or the medial portion of the transverse sinus.[8] The LTS, when present, originates from either the lateral portion of the transverse sinus or the transverse–sigmoid sinus junction.[8,11] The RC of the tentorial sinuses was defined as a continuity of the MTS and LTS.[13,15] The MTV, ITV, and LTV were defined as previously described.[17]

Volumetric Reconstruction of CT Venography

Volume-rendered 3D images were generated using SkyScan CT-Vox software. DICOM study files were imported into CTVox in DICOM 8-bit format (https://www.bruker.com/products/microtomography/micro-ct-software/3dsuite.html). The preview function in CTVox was used to select an appropriate section with the contrast-enhanced structures of interest, eg, tentorial veins. For the patient shown in Figure 1, this was coronal section IM-021–074; DICOM files are available in the Supplementary DICOM Data (https://gin.g-node.org/JaredRosenblum/Rosenblum_AJNR_2020_Supplemental_DICOM_Data_and_Transfer_Function). The initial suggested dynamic range for this study in the 8-bit data converter was 1034–1134 HU with a minimum of 0 and a maximum of 65,535 HU. The highest intensity pixel value of the chosen section for this scan was 2580 HU.

The import histogram was restricted to exclude parenchyma, saturate contrast within the tentorial veins, and to lessen saturation of bone. The lower bound was set to 1075 HU to exclude parenchyma, which was approximately 40 HU. The upper bound was set to 3580 HU, which was 1000 HU above the maximum value

of bone. The opacity was adjusted to show a limited view of the surrounding soft tissues and highlight vessels with contrast. This was saved as a preset transfer function that can be loaded into CTVox (Supplementary Transfer Function). Lighting was adjusted to optimize visualization of the render; 18% shadows, 0% specular, and 100% diffuse settings were applied.

Statistical Analysis

Determining Variable Relationships. Categories of dural sinuses and tentorial veins were defined on the basis of the definitions of the anatomy above. Cramér V association estimator (https://github.com/shakedzy/dython/blob/master/dython/nominal.py), which depends on χ^2 comparisons, was used to measure the association strength among categoric variables based on the above definitions, holding values between 0 and 1.[24] This determines whether there is a significant difference between expected and observed frequencies in the categories. The equation for strength of association is

$$V = \sqrt{\frac{x^2/n}{\min(c-1, r-1)}},$$

where n = sum total of observations, c = number of columns, and r = number of rows.

Preliminary categories were made on the basis of observations in the patient population. To incorporate all variables into the Cramér V estimation and validate categories, we binned numeric variables into ranges. These included all bony angular and distance measurements and the tentorial angle.

Related variables (categories) were clustered and then linked using the nearest-point algorithm,[25,26] which computes the minimum (min), two elements, one in each cluster, that are closest to each other, distances (dist) using the following equation:

$$d(u, v) = \min[\mathrm{dist}(u[i], v[j])],$$

for all points i in cluster u and j in cluster v. The distance metric used was the Euclidean distance,[27,28] which arranges all points as m n-dimensional vectors. Agglomerated variables were highlighted through a dendrogram heat map, which represents both the strength of relationships and variable relationship clusters. To validate relationship clusters, we performed uncertainty coefficient analysis (Thiel's U association measure), which is derived from the conditional entropy between 2 variables.[29]

To perform correlation analysis and determine the directionality of relationships across all variables, we binarily encoded categoric variables into dummy variables. Each categoric value was assigned a new column, assigning a 1 or 0 to each sample, depending on the presence or absence of that specific value.

To measure the direction of linear relationship between numeric variables, we used the Pearson correlation.[28] The equation is

$$\rho = \frac{\mathrm{cov}(X, Y)}{\sigma_x \sigma_y},$$

and is calculated in a sample population as

$$r = \frac{\sum_{i=1}^{n}(x_i - \bar{x})(y_i - \bar{y})}{\sqrt{\sum_{i=1}^{n}(x_i - \bar{x})^2 (y_i - \bar{y})^2}}.$$

The Pearson correlation coefficient holds values between −1 and 1. Negative values imply an inverse linear relationship; positive values imply a positive linear correlation. Variables were clustered and linked using the nearest-point algorithm, with Euclidean distance as the distance metric. Correlated and clustered variable outcomes were highlighted through a dendrogram heat map. Observation distributions were plotted for all variables. The kernel density estimate and histograms were used to visualize probability distributions.

RESULTS

Of the available radiologic imaging of the head at our institution, 238 CTA/CTV studies were included in the investigation based on the criteria defined in the study criteria section of the Materials and Methods. Patient data are available in the On-line Supplementary Data. Patients ranged in age from 19 to 100 years, with a mean age of 58 ± 18 years; this is summarized in the On-line Summary Statistics file. Delayed-phase CTA or CTV was optimal for evaluating the tentorial veins and was also used for 3D reconstruction and visualization (Fig 1). The tentorial sinuses were observed in their known variations, including the RC. We confirmed the common presence of the MTV, ITV, and LTV and found variations (Fig 2). The MTV was always present in the expected location along the tentorial free edge. The ITV and LTV had variable configurations.

Preliminary categories of these variations were defined (On-line Table 1) for statistical analysis. Detailed patient characteristics and category distribution are provided in On-line Fig 2. The ITV and LTV were categorized according to their interruption and drainage patterns. The baseline category (variation 0) was a continuous and uninterrupted LTV, as previously described.[17] The ITV was further categorized into 4 variations. Variation 1 was interrupted by the MTS, draining from the straight sinus to the superior petrosal sinus. Variation 2 was interrupted by the LTS, draining from the straight sinus to the superior petrosal sinus. Variation 3 was interrupted by a plexiform anastomosis, draining from the straight sinus to the MTV. Variation 4 was interrupted by the RC, draining to the superior petrosal sinus. The LTV was similarly categorized as follows. In variation 1, the LTV was interrupted by the LTS, draining from the transverse sinus to the superior petrosal sinus. In variation 2, the LTV was interrupted by a lateralized RC, draining from the transverse sinus to the RC. In variation 3, the LTV was interrupted by a medialized RC, draining from the RC to the superior petrosal sinus.

The Cramér V association clustered heat map showed 2 intercorrelated variable groupings (Fig 3). The first group consisted of the following variables: the origin of the MTS, the presence or absence of the RC of the tentorial sinuses, and the configurations of the ITV and LTV. The second group consisted of the cavernous sinus patency or congenital anomaly, transverse sinus patency or congenital stenosis, origin of the LTS, and the presence of the MTV. The uncertainty coefficient (Thiel's U) confirmed the clustering groups and provided directionality to the associations (On-line Fig 3).

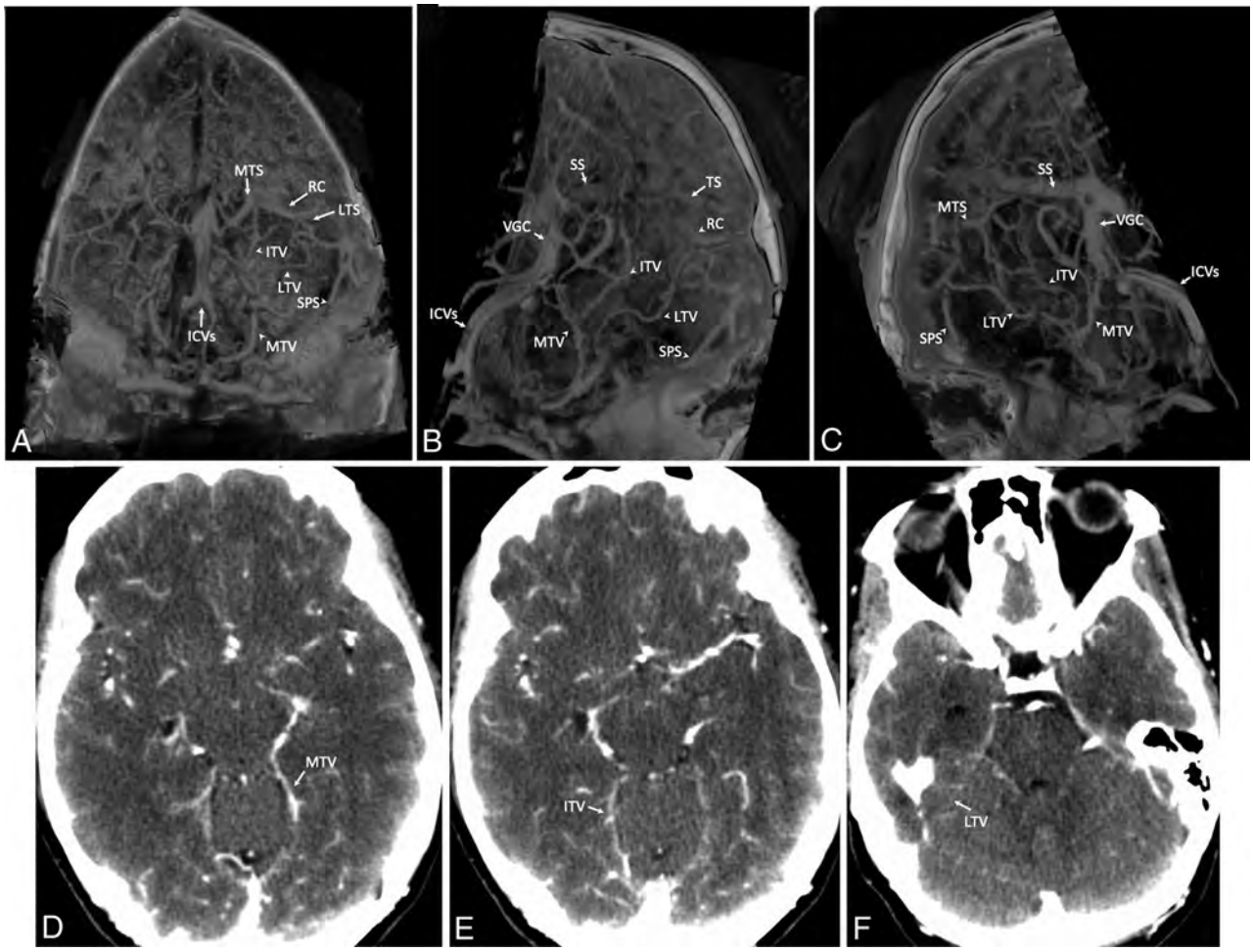

FIG 1. Transtentorial veins. *A–C*, 3D volumetric reconstruction of delayed-phase CTA of the head and neck; parenchyma (0–40 HU) has been segmented out, leaving the intracranial vessels filled with contrast. *A*, Reconstructed volume of the head is shown from the anteroposterior view with a 30° downward rotation to show the plane of the tentorium. *B*, The same reconstruction as in *A* is rotated to show the left side. *C*, The same reconstruction rotated to show the right side, which is symmetric. *D–F,* Source axial images for the volumetric reconstruction of this scan are shown; MTV, ITV, and LTV are labeled. ICV indicates the internal cerebral vein; SS, straight sinus; SPS, superior petrosal sinus; VGC, vein of Galen confluens; TS, transverse sinus; MTV, medial tentorial sinus.

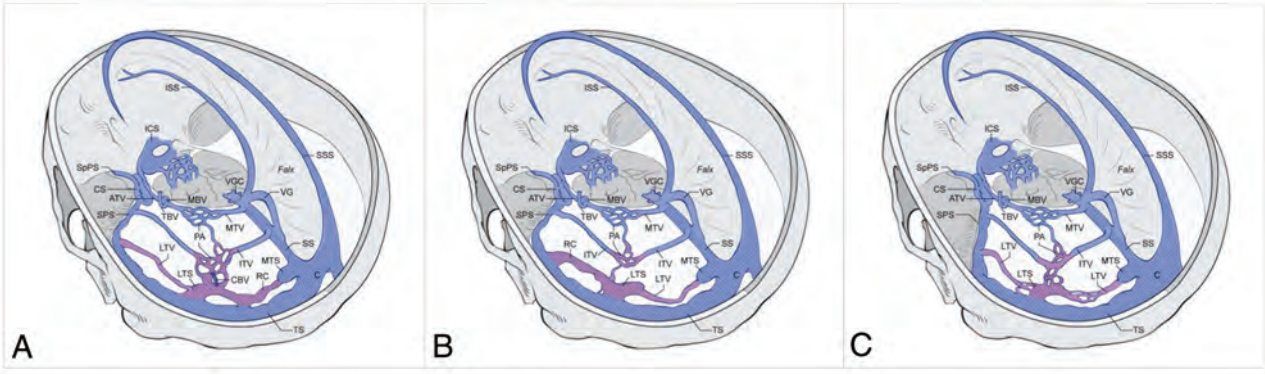

FIG 2. Schematic representation of 3 transtentorial vein configurations. The 2 groups of tentorial sinus configurations are shown; group 1, which is subdivided, has an RC, while group 2 does not. Regions of variation are shaded in purple, *cross-hatching* denotes sinuses, and veins are blue. The split confluens is shown for groups 1A and 1B. The degree of petrous apex pneumatization for each group is also shown. *A*, Configuration 1A has a medialized RC, and the ITV is interrupted by plexiform anastomosis to the RC or LTS. *B*, Configuration 1B has a lateralized RC, and the ITV is uninterrupted. *C*, In configuration 2, the RC is absent; the LTV connects the MTS to the LTS and the LTS to the superior petrosal sinus. Relevant draining sinuses are also shown. CS indicates cavernous sinus; ATV, apical tentorial vein; CBV, cerebellar bridging vein; ICS, intercavernous sinus; ISS, inferior sagittal sinus; MBV, mesencephalic bridging vein; PA, plexiform anastomosis; SpPS, sphenoparietal sinus; SS, straight sinus; SSS, superior sagittal sinus; VGC, vein of Galen confluens; VG, vein of Galen; TS, transverse sinus; SPS, superior petrosal sinus; C, confluens; TBV, tentorial bridging vein; ICV, internal cerebral vein.

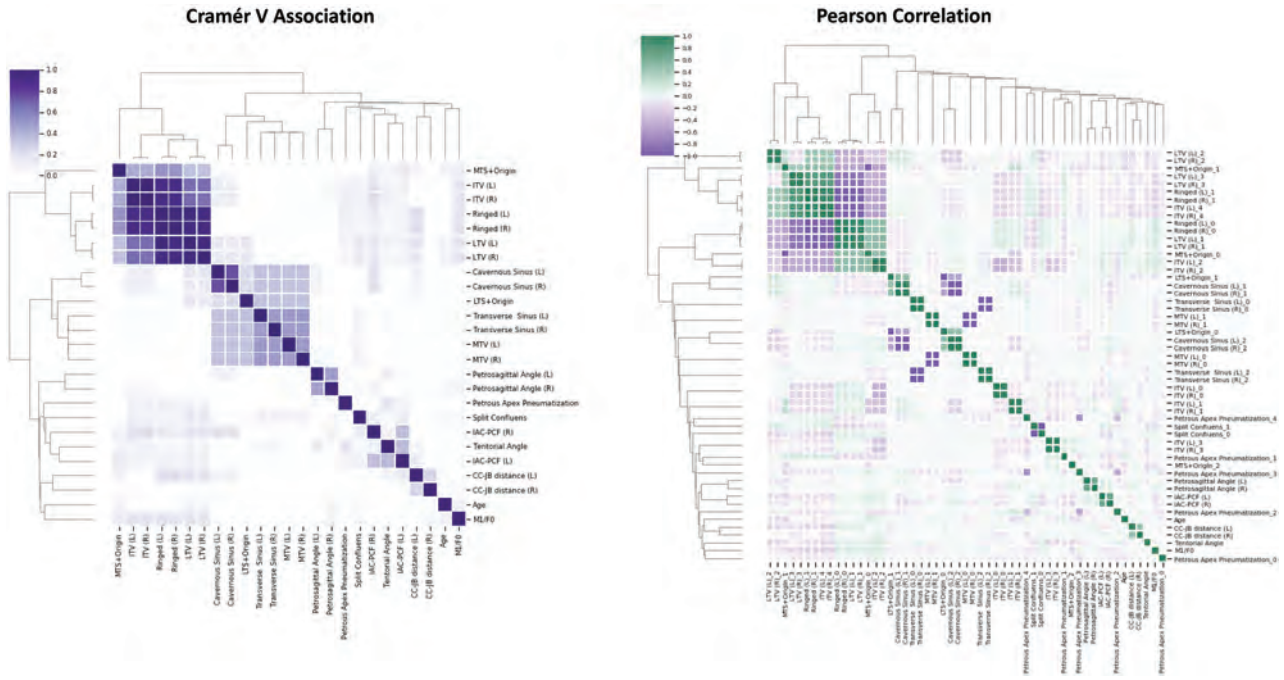

FIG 3. Association and correlation with clustering highlights common tentorial vein configurations. *Left,* Cramér V association heat map, a symmetric measure of associations among categoric variables, presents 2 intercorrelated variable groupings. The first shows a high-to-perfect association among the MTS origin, RC, ITV, and LTV. The second shows a moderate-to-high association among the cavernous sinus, LTS origin, transverse sinus, and MTV. *Right,* The Pearson correlation heat map reveals 2 primary configurations, one of which also has an alternate configuration based on the presence or absence of the ring connection of the MTS and LTS. In the first configuration, the RC is medialized. Due to the presence of the medialized RC originating from the MTS at the straight sinus, the tentorial veins have the following connections: The ITV is interrupted by the RC, and the LTV is lateralized, draining to the superior petrosal sinus. An alternate and slightly less common configuration comprises a lateralized RC and resultant medialized LTV. The second primary configuration has no RC, the ITV is interrupted by the LTS, and the LTV is also interrupted by the LTS. In this configuration, the MTS may be present or absent. IAC-PCF (*left*) and (*right*) (degrees); petrosagittal angle (*left*) and (*right*) (degrees); CC-JB distance (*left*) and (*right*) (millimeters); remaining variables are categoric. The ITV was categorized as 0 through 4 as per the result of preliminary categorization. LTV was categorized as 1 through 3 per results of preliminary categorization. female = 0; M1, male = 1.

The Pearson correlation clustered heat map for all variables (Fig 3) performed to further assess the directionality of relationship between the correlated variables showed 2 primary groups based on the presence or absence of the RC of the tentorial sinuses (*P* values shown in On-line Tables 2 and 3). The first group was further divided into subgroups based on the location of the RC. Groups 1A and 1B ($n = 50/238$) had RC, while group 2 was defined by its absence ($n = 188/238$). Configuration 1A ($n = 38/50$) had a medialized RC tentorial sinus, while it was lateralized in configuration 1B ($n = 12/50$). Further, measures of skull base development were predictive of these configurations (Fig 4). The RC of group 1 was related to the presence of a split confluens, which was predicted by a decreased IAC-PCF angle (Fig 5). Configuration 1A was related to the degree of petrous apex pneumatization.

DISCUSSION

This study evaluated the anatomy of the tentorial sinuses and veins in a large healthy population using CTA/CTV ($n = 238$) and thus identified patterns of variation of the tentorial veins. Further, we evaluated the relationships among cranial morphometrics, dural and tentorial sinuses anatomy, and tentorial venous anatomy. Using statistical analyses, we identified bony measurements that can predict the configurations of tentorial veins, including the IAC-PCF angle and the degree of petrous apex pneumatization that can be made on CT/CTA/CTV. In addition, we developed a semiautomated process of volumetric reconstruction of dural and tentorial venous anatomy used in this study. Together, our study provides information for radiographic evaluation of intracranial venous anatomy critical for surgical planning and avoidance of complications that may arise as a consequence of sacrifice of tentorial veins.[6,17] Further, our study may aid in determining which patients with postoperative venous sinus thrombosis remain asymptomatic or resolve spontaneously versus which require intervention.[7] Knowledge of the transtentorial venous system is critical to neuroradiologists guiding neurosurgeons in surgical planning of skull base approaches. Further, this anatomy will enable prompt neuroradiologic recognition of surgical complications.

Although we did not perform a head-to-head comparison, the MR imaging, MRA, and MRV studies available at our institution were excluded from analysis because of poor visualization of the structures of interest. This was either due to larger section thickness, lack of contrast opacification of small-caliber vessels, or noncontrast (time-of-flight) measurement, which did not adequately demonstrate tentorial veins. Thus, this study included only CTA/CTV with a section thickness of 0.75 mm. From these studies, we identified 2 primary groups of tentorial venous anatomy in this population. These groups were correlated to the RC of the tentorial sinuses. Group 1A, which was characterized by a

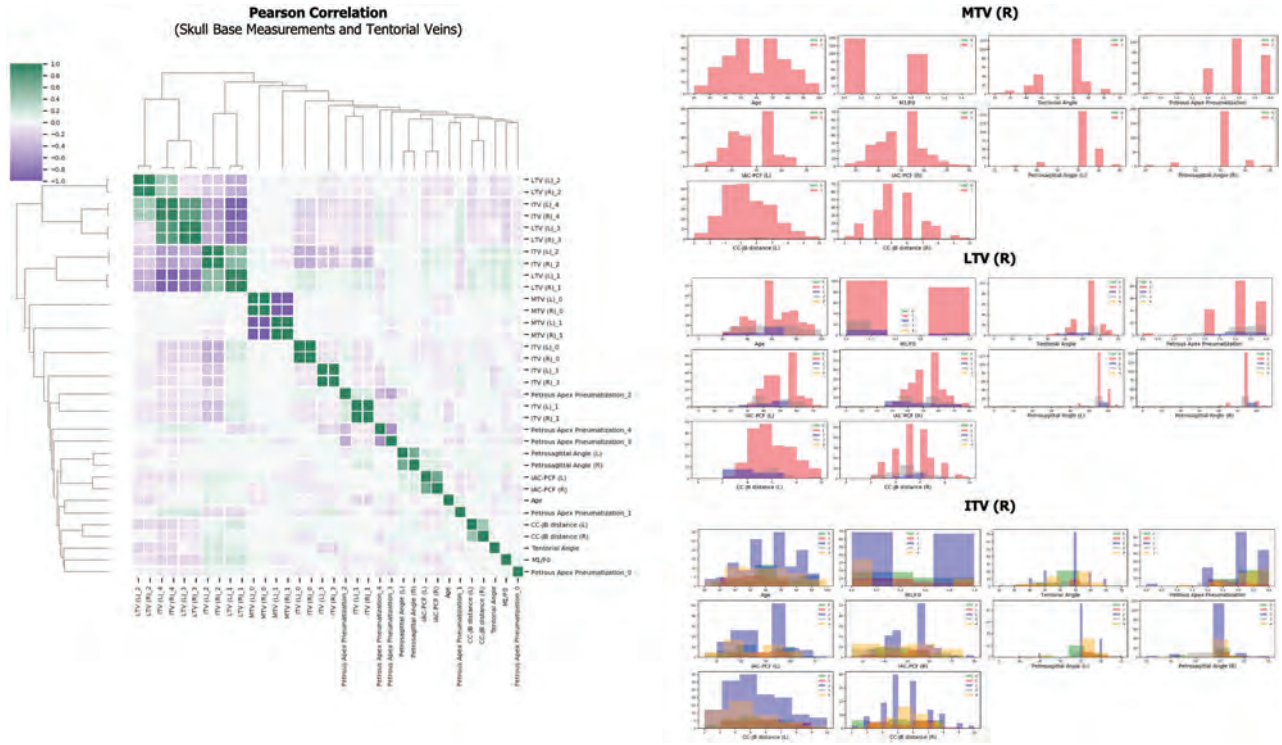

FIG 4. Tentorial vein and skull base measurement subset correlation with clustering and distribution plots. *Left*, The Pearson correlation heat map further characterizes the medialized RC with the ITV and LTV. This characterization confirms that when the RC of the MTS and LTS is present and medialized, the ITV and LTV originate from this connection and are lateralized (group 1A). The strongest associated configuration comprises this; the lateralized RC is confirmed (group 1B). The configuration with the absent RC between the tentorial sinuses is also again confirmed (group 2). This configuration appears related to the CC-JB distance and the tentorial angle in the heat map. *Right*, Y-axes in all charts are patient numbers. Probability density functions and kernel density estimates for skull base measurements, grouped by tentorial vein categories, reveal additional relationships. The distribution plots are shown for the right side of the tentorium only because symmetry is upheld as shown in the heat map. The probability density functions for LTV 3 and ITV 4 (configuration 1A) are nearly identical; this is inversely related to male sex, CC-JB distance, and petrous apex pneumatization 0 (less complete). This group is positively correlated to petrous apex pneumatization 1 (more complete). Group 1B has no correlation with petrous apex pneumatization; however, it is distinguished from group 2 by oppositional correlation to the IAC-PCF. The probability density functions and kernel density estimates of ITV 2 and LTV 1 (group 2) are very similar. IAC-PCF (*left*) and (*right*) (degrees); petrosagittal angle (*left*) and (*right*) (degrees); CC-JB distance (*left*) and (*right*) (millimeters); the remaining variables are categoric. ITV was categorized as 0 through 4 per the results of preliminary categorization. LTV was categorized as 1 through 3 per the results of preliminary categorization. F0 indicates female = 0; M1, male = 1; R, right; L, left.

medialized RC, and group 1B, which was characterized by a lateralized RC, were correlated to the presence of a split confluens, a proposed sign of incomplete late development of the dural sinuses.[30] Conversely, group 2 (characterized by the absence of the RC) was correlated with complete development of the confluens. Further, these groups were predicted by bony measures of skull base development, such as the degree of petrous apex pneumatization or the IAC-PCF angle. Thus, the cranial morphometrics performed predicted specific intracranial venous configurations.

These findings are consistent with previous investigations of venous development. First, tentorial drainage of the midbrain veins is critical during development.[17,30] Second, at this time, when the jugular foramen is narrowed by the developing petrous pyramid, retrograde venous flow dilates the transverse sinuses.[30] The dilation of the transverse and sigmoid sinuses results in the their pouching into the tentorium and subsequent development of the medial and lateral tentorial sinuses and cortical veins, including the vein of Labbé, which may drain into these.[30] Extracranial drainage of these sinuses, including the mastoid, anterior condylar, and posterior condylar emissary veins, also develops during the dilation phase and most often originates from the sigmoid sinus.[30] Third, joining of the 2 transverse sinuses into the confluens is the last part of development of the dural sinuses.[18,30] The transverse sinuses, petrosal sinuses, and cavernous sinuses develop from the lateral head vein on each side.[31] We hypothesized on the basis of this information that the tentorial venous drainage pattern would depend on the extent of development of the skull base.

Grouping our observations in this patient population by categories such as bony measures, dural sinuses, and tentorial veins generated preliminary categoric relationships via the Cramér V association measure. For example, without tentorial sinuses in the RC, both the ITV and LTV can originate from the straight sinus. However, in the presence of a medialized RC, such as in group 1A, the LTV, and less often the ITV, may originate from the RC. These relationships were grouped into putative anatomic configurations of venous drainage via an agglomerative clustering algorithm and dendrogram heat maps. These intercorrelated variable groupings were confirmed by the Thiel's U association. Because the uncertainty coefficient is not a symmetric analysis, it allows understanding of the conditionality behind relationships. For example,

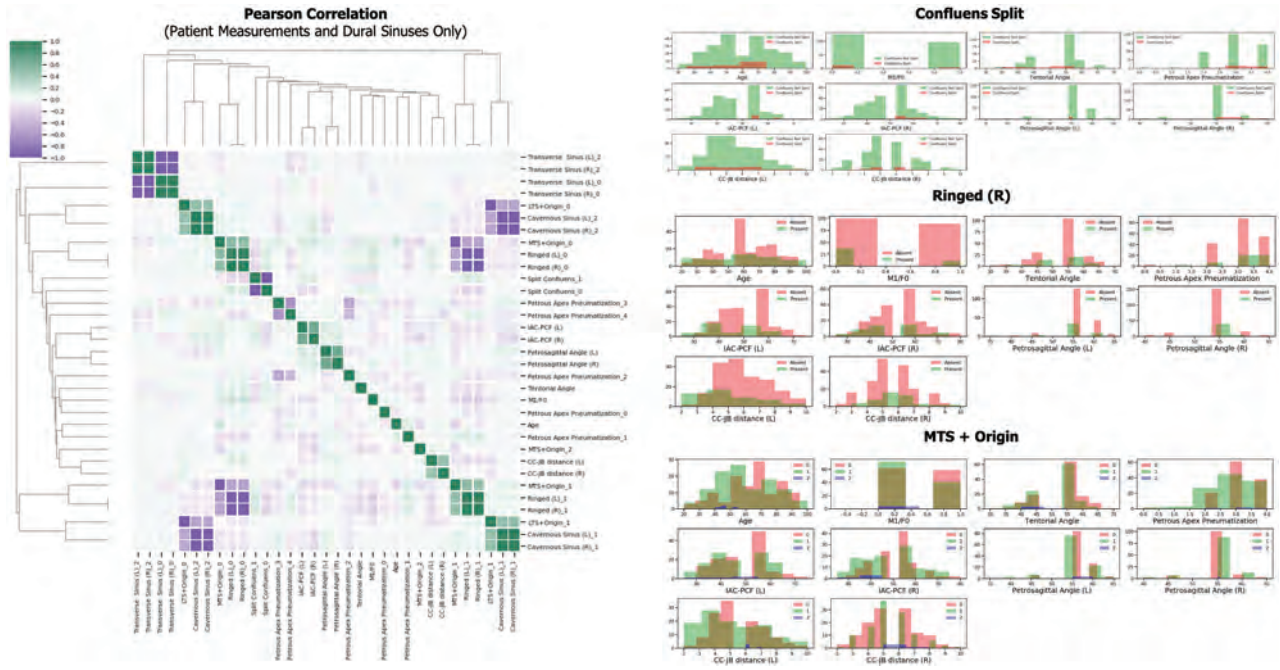

FIG 5. Dural sinus and skull base measurement subset correlation with clustering and distribution plots. *Left*, The Pearson correlation heat map further characterizes the relationship among the dural sinuses, cavernous sinuses, and skull base measurements. This confirms that an LTS originating in the transverse sinus is linked with a patent cavernous sinus. As a corollary, an LTS originating in the transverse sinus–sigmoid sinus junction is linked with a diminutive cavernous sinus. The clustering also reiterates the relationship between the RC presence and the location of the origin of the MTS. *Right,* Y-axes in all charts are patient numbers. Probability density functions and kernel density estimates for skull base measurements, grouped by dural sinus categories, provide additional support for the determined anatomic configurations. The distribution plots are shown for the right side of the RC only because symmetry was upheld as shown in the heat map. The probability density functions for LTS originating from the transverse sinus (LTS origin 0) and patent cavernous sinus (cavernous sinus 2) are similar; these show a weak positive correlation with the absent RC (configuration 2). Conversely, the probability density functions for LTS originating at the transverse sinus–sigmoid sinus junction (LTS origin 1) and a congenitally diminutive cavernous sinus (cavernous sinus 1) are similar, showing a weak positive correlation with the RC (configuration family 1). IAC-PCF (left) and (*right*) (degrees); petrosagittal angle (*left*) and (*right*) (degrees); CC-JB distance (*left*) and (*right*) (millimeters); the remaining variables are categoric. The ITV was categorized as 0 through 4 per the results of preliminary categorization. The LTV was categorized as 1 through 3 per the results of preliminary categorization. F0 indicates female = 0; M1, male = 1; R, right; L, left.

knowing the RC status allows strong prediction of the ITV and LTV configurations; however, conversely, knowing the ITV category is a weaker predictor of RC status.

Subsequent binary encoding of variables, the Pearson correlation, and clustering confirmed and further defined the putative anatomic configurations. For example, the most common cluster in the putative groups comprised the following variables: the presence or absence of RC, origin of the MTS, ITV configuration, and LTV configuration. These held true for the Pearson correlation, which provided further detail and clarified the 3 groups defined above: groups 1A, 1B, and 2.

The statistical analyses performed in this study not only allowed the confirmation of the presence of the transtentorial venous system but also identified the relationship between completed development of the skull base and the configurations of this venous drainage. Knowledge of the venous anatomy of the tentorium is critical for surgical planning of approaches involving manipulation or sectioning of the tentorium or veins bridging to it. Further, this transtentorial venous system may explain certain phenomena, including remote cerebellar infarction and asymptomatic spontaneous or postoperative transverse sinus thrombosis.

While this study did not evaluate patients undergoing surgical intervention, previous studies have described or hypothesized venous configurations that may lead to adverse outcomes such as remote cerebellar infarct.[11,17] Our analysis supports the importance of avoiding these complications by preserving both the MTV and LTS and their sole venous drainage of remote parenchyma. We hypothesize that configurations with greater anastomoses between tentorial veins, such as Group 1A found in this study, would be less prone to complications of sectioning the tentorium. However, the tentorial venous drainage must be considered in the context of the intracranial venous drainage, such as a narrowed transverse sinus or jugular bulb, as previously shown to lead to complication.[17] Further study of the clinical and surgical relevance of this transtentorial venous system is needed.

CONCLUSIONS

The analysis of 238 patients identified 3 variations of the transtentorial venous system in a large healthy population and identified bony measures of skull base development associated with each variation. Knowledge of this anatomy is critical for neuroradiologists and neurosurgeons in surgical planning, reducing the risk of interventions, and explaining the mechanism of surgical complications arising from compromise of the tentorial venous system.

ACKNOWLEDGMENT

The authors would like to acknowledge the National Institutes of Health Medical Arts Department, specifically Erina He, for the schematic representation in Fig 2.

REFERENCES

1. Kawase T, Shiobara R, Toya S. **Middle fossa transpetrosal-transtentorial approaches for petroclival meningiomas. Selective pyramid resection and radicality.** *Acta Neurochir (Wien)* 1994;129:113–20 CrossRef Medline
2. Al-Mefty O, Ayoubi S, Smith RR. **The petrosal approach: indications, technique, and results.** *Acta Neurochir Suppl (Wien)* 1991;53:166–70 CrossRef Medline
3. Malis LI. Surgical resection of tumors of the skull base. In: Wilkins RH, Rengachary SS, eds. *Neurosurgery*. Vol 1. McGraw-Hill; 1985:1011–21
4. Türe U, Harput MV, Kaya AH, et al. **The paramedian supracerebellar-transtentorial approach to the entire length of the mediobasal temporal region: an anatomic and clinical study: laboratory investigation.** *J Neurosurg* 2012;116:773–79 CrossRef Medline
5. de Oliveira JG, Párraga RG, Chaddad-Neto F, et al. **Supracerebellar transtentorial approach—resection of the tentorium instead of an opening—to provide broad exposure of the mediobasal temporal lobe: anatomical aspects and surgical implications.** *J Neurosurg* 2012;116:764–72 CrossRef Medline
6. Amini A, Osborn AG, McCall TD, et al. **Remote cerebellar hemorrhage.** *AJNR Am J Neuroradiol* 2006;27:387–90 Medline
7. Benjamin CG, Sen RD, Golfinos JG, et al. **Postoperative cerebral venous sinus thrombosis in the setting of surgery adjacent to the major dural venous sinuses.** *J Neurosurg* 2018 Oct 1. [Epub ahead of print] CrossRef Medline
8. Matsushima T, Suzuki SO, Fukui M, et al. **Microsurgical anatomy of the tentorial sinuses.** *J Neurosurg* 1989;71:923–28 CrossRef Medline
9. Oka K, Rhoton AL Jr, Barry M, et al. **Microsurgical anatomy of the superficial veins of the cerebrum.** *Neurosurgery* 1985;17:711–48 CrossRef Medline
10. Ueyama T, Al-Mefty O, Tamaki N. **Bridging veins on the tentorial surface of the cerebellum: a microsurgical anatomic study and operative considerations.** *Neurosurgery* 1998;43:1137–45 CrossRef Medline
11. Miabi Z, Midia R, Rohrer SE, et al. **Delineation of lateral tentorial sinus with contrast-enhanced MR imaging and its surgical implications.** *AJNR Am J Neuroradiol* 2004;25:1181–88 Medline
12. Vatansever A, Mut M, Ergun KM, et al. **The anatomy of the sigmoid-transverse junction according to the tentorial angle.** *J Craniofac Surg* 2019;30:2280–84 CrossRef Medline
13. Browder K, Kaplan HA, Krieger AJ. **Venous channels in the tentorium cerebelli: surgical significance.** *Surg Neurol* 1975;3:37–39 Medline
14. Browder J, Kaplan HA, Krieger AJ. **Anatomical features of the straight sinus and its tributaries: clinical correlations.** *J Neurosurg* 1976;44:55–61 CrossRef Medline
15. Kaplan HA, Browder J, Krieger AJ. **Venous channels within the intracranial dural partitions.** *Radiology* 1975;115:641–45 CrossRef Medline
16. Chung JI, Weon YC. **Anatomic variations of the deep cerebral veins, tributaries of basal vein of Rosenthal: embryologic aspects of the regressed embryonic tentorial sinus.** *Interv Neuroradiol* 2005;11:123–30 CrossRef Medline
17. Rosenblum JS, Neto M, Essayed WI, et al. **Tentorial venous anatomy: cadaveric and radiographic study with discussion of origin and surgical significance.** *World Neurosurg* 2019;131:e38–45 CrossRef Medline
18. Padget DH. **The cranial venous system in man in reference to development, adult configuration, and relation to arteries.** *Am J Anat* 1956;98:307–55 CrossRef Medline
19. Streeter GL. The developmental alterations in the vascular system of the brain of the human embryo. In: *Contributions to Embryology Carnegie Institution No. 24*. Carnegie Institution of Washington; 1921
20. Velut S. **Embryology of the cerebral veins** [in French]. *Neurochirurgie* 1987;33:258–63 Medline
21. Schulter FP. **A comparative study of the temporal bone in three populations of man.** *Am J Phys Anthropol* 1976;44:453–68 CrossRef Medline
22. Lee DH, Kim MJ, Lee S, et al. **Anatomical factors influencing pneumatization of the petrous apex.** *Clin Exp Otorhinolaryngol* 2015;8:339–44 CrossRef Medline
23. Kao SC, Waziri MH, Smith WL, et al. **MR imaging of the craniovertebral junction, cranium, and brain in children with achondroplasia.** *AJR Am J Roentgenol* 1989;153:565–69 CrossRef Medline
24. Cramér H. *Mathematical Methods of Statistics*. Princeton University Press; 1946:282
25. Hastie T, Tibshirani R, Friedman J. Hierarchical clustering. In: Hastie T, Tibshirani R, Friedman J, eds. *The Elements of Statistical Learning*, 2nd ed. Springer-Verlag 2009:520–28
26. Hierarchical Clustering. https://docs.scipy.org/doc/scipy/reference/cluster.hierarchy.html#module-scipy.cluster.hierarchy. Accessed November 3, 2019
27. Rokach L, Maimon O. Clustering methods. In: Maimon O, Rokach L, eds. *Data Mining and Knowledge Discovery Handbook*. Springer-Verlag; 2005:321–52
28. scipy.spatial.distance.pdist. https://docs.scipy.org/doc/scipy/reference/generated/scipy.spatial.distance.pdist.html. Accessed November 3, 2019
29. Press WH, Flannery BP, Teukolsky SA, et al. Information-theoretic properties of distributions. In: Press WH, Teukolsky SA, Vetterling WT, et al, eds. *Numeric Recipes: The Art of Scientific Computing*. 3rd ed. Cambridge University Press; 1992
30. Okudera T, Huang YP, Ohta T, et al. **Development of the posterior fossa dural sinuses, emissary veins, and jugular bulb: morphological and radiologic study.** *AJNR Am J Neuroradiol* 1994;15:1871–83 Medline
31. Mitsuhashi Y, Hayasak K, Kawakami T, et al. **Dural venous system in the cavernous sinus: a literature review and embryological, functional, and endovascular clinical considerations.** *Neurol Med Chir (Tokyo)* 2016;56:326–39 CrossRef Medline

The Variable Appearance of Third Ventricular Colloid Cysts: Correlation with Histopathology and the Risk of Obstructive Ventriculomegaly

S.D. Khanpara, A.L. Day, M.B. Bhattacharjee, R.F. Riascos, J.P. Fernelius, and K.D. Westmark

ABSTRACT

BACKGROUND AND PURPOSE: While third ventricular colloid cysts may present as an incidental finding, they also harbor the potential to cause ventricular obstruction and sudden death. Herein we analyze the relationship between imaging appearance and the risk of obstructive ventriculomegaly.

MATERIALS AND METHODS: This is a retrospective review of the MR imaging appearance of 64 patients with colloid cysts, 46 of whom also had a CT scan, obtained by a tertiary hospital imaging report data base search over a 10-year period. Cysts were categorized by appearance on T2-FLAIR and correlated with patient age, cyst size, and the risk of obstructive ventriculomegaly. Histopathologic correlation was available for 28 cases.

RESULTS: The 64-patient cohort was 52% female, median age 50 years (range 10 to 99 years). Cysts hyperintense on T2-FLAIR (53.1%) were larger ($P < .001$), occurred in younger patients ($P = .01$), and had a higher risk of obstructive ventriculomegaly than homogeneously hypointense cysts (relative risk 6.18, 95% CI [2.04, 18.67]). Three patterns of T2 hyperintensity were identified: homogeneously hyperintense, hyperintense rim, and cysts with "dot sign." Although "dot sign" cysts were larger ($P < .001$), there was no significant difference in patient age or the risk of ventricular obstruction among T2 hyperintense cysts. Cyst wall histopathology did not vary with imaging appearance.

CONCLUSIONS: Hyperintensity on T2-FLAIR, whether homogeneous, rim, or "dot sign," is associated with larger cyst size and younger patient age, and is an imaging risk factor for obstructive ventriculomegaly. The hyperintense rim does not represent a thickened cyst wall.

ABBREVIATIONS: CC = colloid cyst; CCRS = colloid cyst risk score; PAS = periodic acid-Schiff; EMA = epithelial membrane antigen; *CDX2* = *Caudal Type Homeobox 2*; AUC = area under the curve

Colloid cysts (CCs) are benign neoplasms accounting for 0.1% to 1% of all intracranial tumors.[1] Previously thought to be a paraphyseal remnant,[2,3] more recent histochemical and ultrastructural analyses support an endodermal origin.[4-7] Although congenital lesions, CCs rarely present in the pediatric population and typically come to attention in the 4th and 5th decades.[8] CCs occur almost exclusively within the third ventricle near the foramen of Monro where they may obstruct CSF flow resulting in sudden neurologic deterioration and death.[9] A CC risk score (CCRS) has been proposed in the neurosurgical literature that, in addition to patient age <65 years and presence of a headache, incorporates the following imaging variables: risk zone (location in the third ventricle near the foramen of Monro or aqueduct of Sylvius), cyst size ≥7 mm, and hyperintensity on T2-FLAIR imaging.[10] This paper further expands on the imaging appearance of CCs on T2-FLAIR and correlates it with histopathology, cyst size, patient age, and the occurrence of obstructive ventriculomegaly.

MATERIALS AND METHODS

The study is institutional review board approved and compliant with the Health Insurance Portability and Accountability Act guidelines. This is a retrospective study of 64 patients identified by a tertiary hospital imaging report data base search (Primordial) for "colloid cyst," limited to imaging of the brain. Patients who had a

Received March 4, 2020; accepted after revision June 16.

From the Departments of Diagnostic and Interventional Imaging (S.D.K., R.F.R., K.D.W.), Neurosurgery (A.L.D.), and Pathology (M.B.B.), McGovern Medical School, The University of Texas Health Science Center at Houston, Houston, Texas; Department of Quality and Outcomes Management (J.P.F.), Texas Children's Hospital, Houston, Texas.

Previously presented, in part, at: Annual Meeting of the American Society of Neuroradiology, June 2-7, 2018, Vancouver, British Columbia, Canada.

Please address correspondence to Roy F. Riascos, MD, Professor and Chief of Neuroradiology, Department of Diagnostic and Interventional Imaging, The University of Texas Health Science Center at Houston, Suite MSB 2.130B, 6431 Fannin St, Houston, TX 77030; e-mail: Roy.F.Riascos@uth.tmc.edu

http://dx.doi.org/10.3174/ajnr.A6722

Demographic and imaging characteristics of 64 colloid cyst

Signal Intensity on T2-FLAIR	Hyperintense ($n = 34$)			Hypointense ($n = 30$)	Total
	Homogeneously Hyperintense	"Dot Sign"	Hyperintense Rim		
Number of patients	12	6	16	30	64
Sex (Male)	6 (50%)	3 (50%)	9 (56.2%)	13 (43.3%)	31 (48%)
Patient age (years)					
Mean (+/− SD)	37.0 (23.4%)	37.5 (15.6%)	52.1 (22%)	55.2 (14.7%)	49.8 (19.8%)
Median	25.5	31.5	49.5	53	50
Cyst size (mm)					
Mean	10.6	16.8	11.1	6.8	9.6
Median	11.0	15.0	12.5	6.3	9.0
Obstructive ventriculomegaly	8 (67%)	5 (83.3%)	8 (50%)	3 (10%)	24 (37.5%)
CT[a] (hyperattenuated/ iso-hypoattenuated)	4/4	0/5	14/0	20/0	38/9
T1 signal (hyper-/iso-/ hypointense)	1/5/6	5/1/0	10/5/1	16/14/0	32/25/7
Zone II	3	0	2	6	11
Histopathology available for review	8	3	10	7	28

[a] CT was not available in all cases.

missing sequence (T1, T2, or T2-FLAIR), did not have a confirmed diagnosis of CC on review of the MR imaging, or had significant artifacts that precluded evaluation were excluded. Patients with cysts measuring less than 4 mm were excluded as characterization in these cases was difficult. Noncontrast MR imaging was available for all 64 patients with postcontrast T1WI in 38 patients. CT images were available for 47 patients.

Imaging Evaluation

MR imaging scans were performed on 1.5 and 3T MR imaging machines (Ingenia 3T, Achieva 3T, Intera 1.5T, Philips Healthcare; HDXT 3T and Excite 1.5T, GE Healthcare). For this retrospective study, no specific imaging protocol was used. All noncontrast MRI of the brain had axial T1, T2, and T2-FLAIR, sagittal T1, DWI, and axial T2* (GRE or SWI) sequences. Postcontrast, T1 fat-suppressed imaging was performed in 3 orthogonal planes after administration of MultiHance (0.1 mmol/kg body weight; Bracco Diagnostics). All CT scans were performed as routine brain on 64- and 128-section scanners with 3 orthogonal planes available for interpretation.

The imaging was reviewed by a senior neuroradiologist (27 years of experience) and a neuroradiology fellow. The following imaging features were recorded: cyst size (greatest axial dimension), risk zone location as described by Beaumont et al,[10] enhancement pattern, diffusion restriction, calcification, hemorrhage, and presence or absence of a hyperintense rim, "black hole," or an intracystic nodule ("dot sign").[10-12] Signal intensity on T1, T2, and T2-FLAIR imaging was recorded relative to that of adjacent gray matter. Obstructive ventriculomegaly was recorded if there was disproportionate dilation of the lateral ventricles relative to the sulci without enlargement of the third ventricle. Attenuation on CT was recorded relative to adjacent gray matter.

Based on the T2-FLAIR sequence, the CCs were divided into 2 groups: hyperintense and hypointense cysts. Hyperintense cysts were further subdivided into 3 categories: 1) homogeneously hyperintense; 2) hyperintense with a "dot sign"; 3) thin hyperintense rim with a much larger iso- to hypointense core. These groups were correlated with patient age, cyst size, and the presence of obstructive ventriculomegaly. Blinded review of the pathology was undertaken by a senior neuropathologist with 35 years of experience. Histopathology was correlated with the imaging appearance of the cyst.

Statistical Methods

The independent *t* test was used to compare differences in median age and cyst size for the overall hyperintense and hypointense cohorts. Nonparametric Wilcoxon rank-sum and Fisher exact tests were then used to conduct a further subgroup analysis of continuous variables (ie, age and cyst size) and the presence of obstructive ventriculomegaly, respectively. The distribution and normality were assessed by using standard graphic methods and kurtosis values. Level of significance was set at $P < .05$. Statistical analysis was performed by using STATA for Windows (version 15.0, StataCorp).

Pathologic Correlation

Histopathology was available for review in 28 cases. Cysts were examined by using H&E, supplemented with special stains: periodic acid-Schiff (PAS), mucicarmine, and Masson trichrome stains, and immunohistochemistry analysis with antibodies for Pan-keratin, CAM 5.2, CK-7, Keratin 20, epithelial membrane antigen (EMA), *Caudal Type Homeobox 2* (*CDX2*), and glial fibrillary acidic protein. Not all cysts were examined as specimens sometimes contained cyst contents only, without the cyst wall.

RESULTS

The 64-patient cohort had an median age of 50 years (range = 10 to 99 years) and 52% were female. Median cyst size was 9.0 mm. Most of cysts were located in risk zone I, 17.1% were in zone II, and none were in zone III as defined by Beaumont et al.[10] Obstructive ventriculomegaly was present in 37.5% (24/64) of patients. All cysts with associated obstructive ventriculomegaly were in zone I (Table).

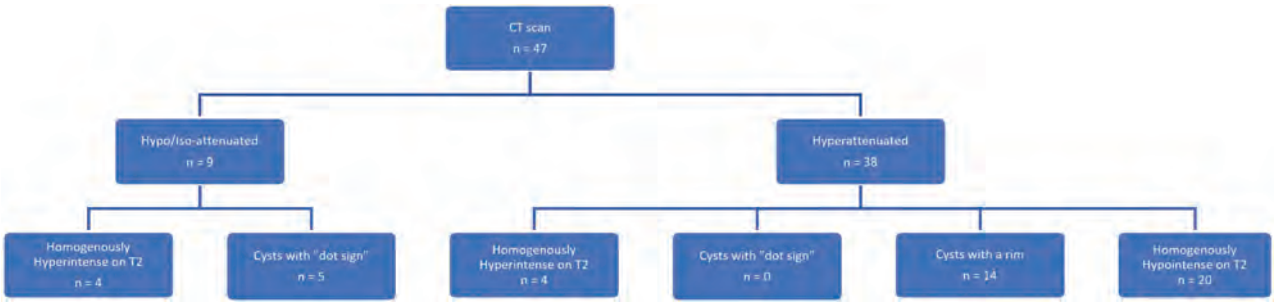

FIG 1. An overview of the imaging appearance of third ventricular colloid cyst on CT and corresponding MR imaging characteristics.

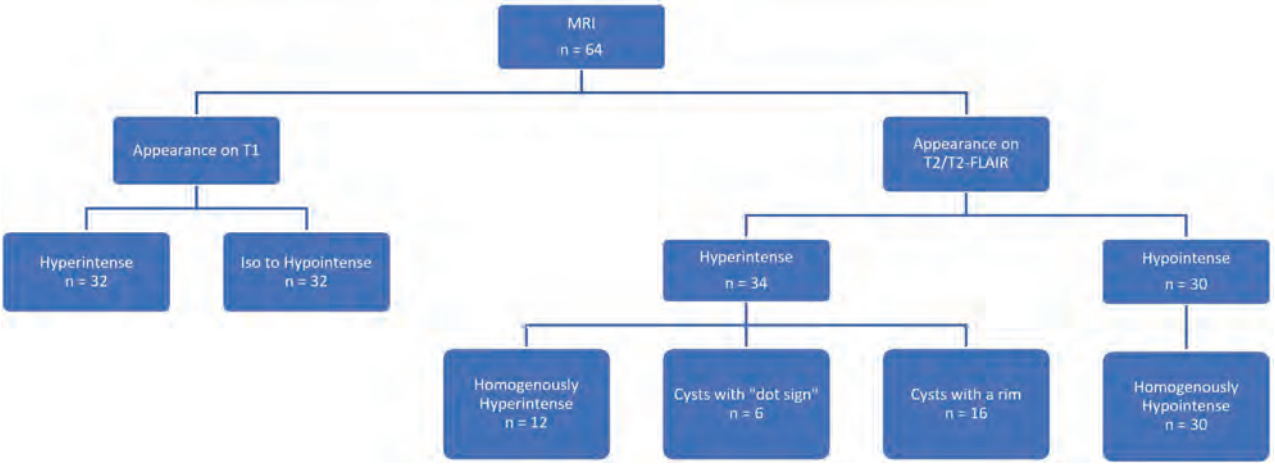

FIG 2. An overview of the imaging appearance of third ventricular colloid cyst on MR imaging.

CT

CT was available for 47 patients (Fig 1). Most colloid cysts (81%) were hyperattenuated with 7 iso-attenuated and 2 hypoattenuated relative to adjacent gray matter. In no case was a cyst iso-attenuated with CSF. Calcification was not identified within any cyst or cyst wall.

MRI

All 64 patients had an MR imaging, with postcontrast imaging available for 38 patients. Half of the cysts were hyperintense on the T1WI. No cyst was isointense to CSF on the T1WI. Although some cysts showed minimal, discontinuous enhancement along the wall it was likely due to adjacent vessels rather than true enhancement, no thick rimlike or nodular enhancement was seen. None of the cysts showed evidence of restricted diffusion, nor was there susceptibility artifact suggesting recent or remote hemorrhage.

Based on the appearance on T2-FLAIR, CCs were divided into hyperintense (34 patients) and hypointense groups (30 patients) (Fig 2). Median age was significantly lower (43.5 versus 53 years, $P = .01$), median cyst size was larger (12 versus 6.3 mm, $P < .0001$), and the risk of obstructive ventriculomegaly was higher (relative risk 6.18, 95% CI [2.04, 18.67]) in the hyperintense group. Hyperintensity on T2-FLAIR appeared in 3 different patterns: homogeneously hyperintense, cysts with rim, and cysts with "dot sign." Homogeneously hypointense cysts had no internal variability in signal. Relationship of demographics, obstructive ventricfulomegaly, and appearance of colloid cysts on CT and MR imaging is summarized in the Table.

Homogeneously Hypointense Cysts ($n = 30$)

These cysts were uniformly hypointense on T2 and T2-FLAIR sequences and constituted the most common appearance in our study. These cysts did not have an apparent rim or varying signal intensity core. There was no evidence of susceptibility artifact to account for the low signal. All cysts in this category were uniformly hyperattenuated and well-circumscribed on CT. The median age at presentation in this group of patients was 53 years with a median cyst diameter of 6.3 mm (range: 4 mm to 12 mm). Only 10% of these patients presented with ventriculomegaly ($P < .001$).

Homogeneously Hyperintense Cysts ($n = 12$)

These cysts were uniformly hyperintense on T2 and T2-FLAIR sequences (Fig 3). They were associated with a significantly higher risk of obstructive ventriculomegaly (67% patients, $P < .001$) in comparison to homogeneously hypointense cysts, but had a similar risk in comparison with other hyperintense cysts. The median cyst size in this group was significantly higher than homogeneously hypointense cysts (11 versus 6.3 mm, $P < .001$). Median age of presentation was lower than in patients with homogeneously hypointense cysts (25.5 years versus 53 years,

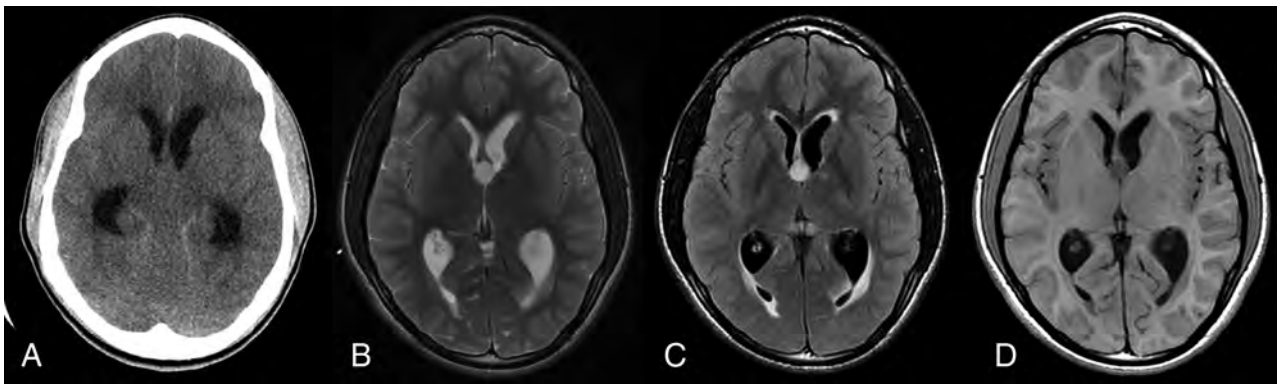

FIG 3. Homogeneously hyperintense cyst: 13-year-old boy found unconscious after complaining of headache for 2 days. Initial CT demonstrates dilation of the lateral ventricles. However, the colloid cyst was difficult to detect as it was isointense relative to the adjacent brain. Subsequent MR imaging showed a colloid cyst homogeneously hyperintense on T2 (*B*) and T2-FLAIR weighted images (*C*) and hypointense on T1-weighted axial image (*D*). Also, note the presence of periventricular edema associated with ventriculomegaly.

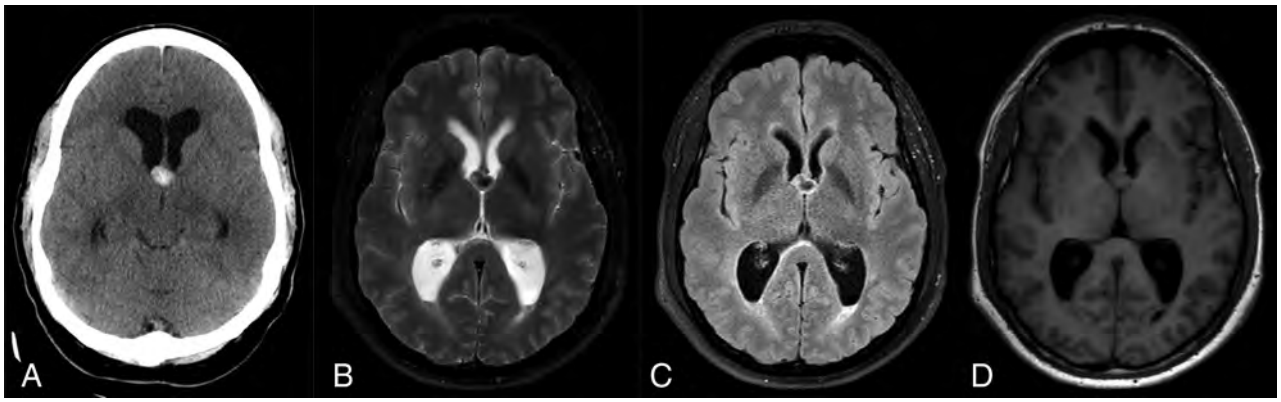

FIG 4. Cyst with rim: 55-year-old woman with a 6-week history of headache. Non-contrast CT (*A*) shows a hyperattenuated colloid cyst measuring 13 mm at the roof of third ventricle. On T2WI (*B*), the colloid cyst has a hypointense core with a thin hyperintense rim, which is more pronounced on T2-FLAIR (*C*). The cyst is mildly heterogeneous and isointense centrally on T1-weighted image (*D*). There was no evidence of hemorrhage on the GRE sequence (image not shown). There is associated enlargement of the lateral ventricles with periventricular edema.

$P = .01$). Half of the cysts were uniformly hypoattenuated and half uniformly hyperattenuated on CT.

Cysts with "Dot Sign" (n = 6)

These cysts were almost entirely hyperintense on T2WI and T2-FLAIR with a tiny, <5 mm, internal hypointense nodule that has been previously described in the imaging literature as the "dot sign." These "dots" were significantly smaller than the hypointense "cores" described in the "cysts with rim." Five out of 6 cysts with the dot sign were hyperintense on the T1WI; therefore, the nodule was not visualized on T1WI. Obstructive ventriculomegaly was significantly more common than in homogeneously hypointense cysts (83.3% versus 10%, $P < .001$). These cysts were significantly larger than both homogeneously hypointense cysts (median diameter of 15 mm versus 6.3 mm, $P < .001$) and other hyperintense cysts ($P = .007$ and $P = .03$ for homogeneously hyperintense and cysts with rim, respectively). The median age at presentation was significantly lower than in patients with homogeneously hypointense cysts (31.5 versus 53 years, $P < .001$) but similar to those with other hyperintense cysts. These cysts were iso- to hypoattenuated on CT with a punctate area of hyperattenuation corresponding to the intracystic nodule identified in 1 case.

Cysts with Rim (n = 16)

These cysts had a hyperintense rim and an iso- to hypointense central core that occupied at least 50% of the total cyst on T2WI and T2-FLAIR (Fig 4). Cysts with markedly hypointense cores have been previously termed as having a "black hole" appearance. Correlating the MR imaging appearance with CT revealed that the hypointense cores were hyperattenuated on CT (Fig 1). Cysts with hyperintense rims were larger than the homogeneously hypointense cysts (median diameter of 12.5 versus 6.3, $P < .001$). Obstructive ventriculomegaly occurred in 50% of these patients which was significantly higher than in the homogeneously hypointense group ($P = .02$), but similar to those with other hyperintense cysts.

Histopathology

The contents of colloid cysts, available for histopathologic examination in 28 cases, consisted of amorphous, proteinaceous, and acellular gelatinous material. Histopathology was available for 3/6 cysts with "dot sign" on imaging. The hypointense "dot" corresponded to an intracystic nodule in 1 case and was described grossly as a gelatinous papillary protrusion. The nodule was not

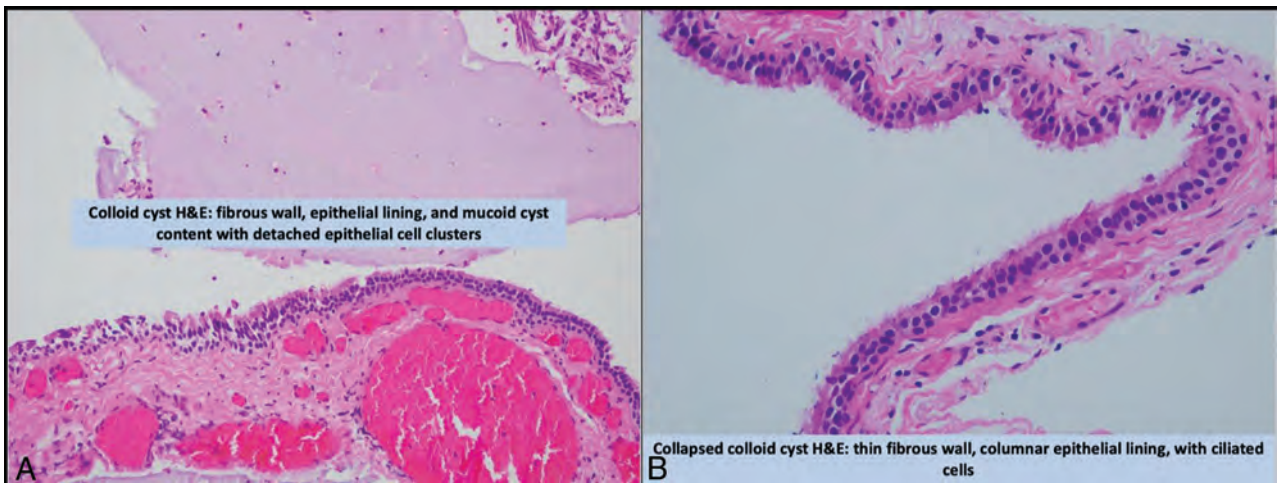

FIG 5. Hematoxylin and Eosin staining of a typical homogeneously hyperintense cyst on T2 and T2-FLAIR images. The cyst wall is composed of columnar, ciliated epithelial cells. The wall was not thickened and there was not an abnormal increase in goblet cells or any cellular atypia. Contents of the cysts consisted of a mucoid material with detached epithelial clusters of cells.

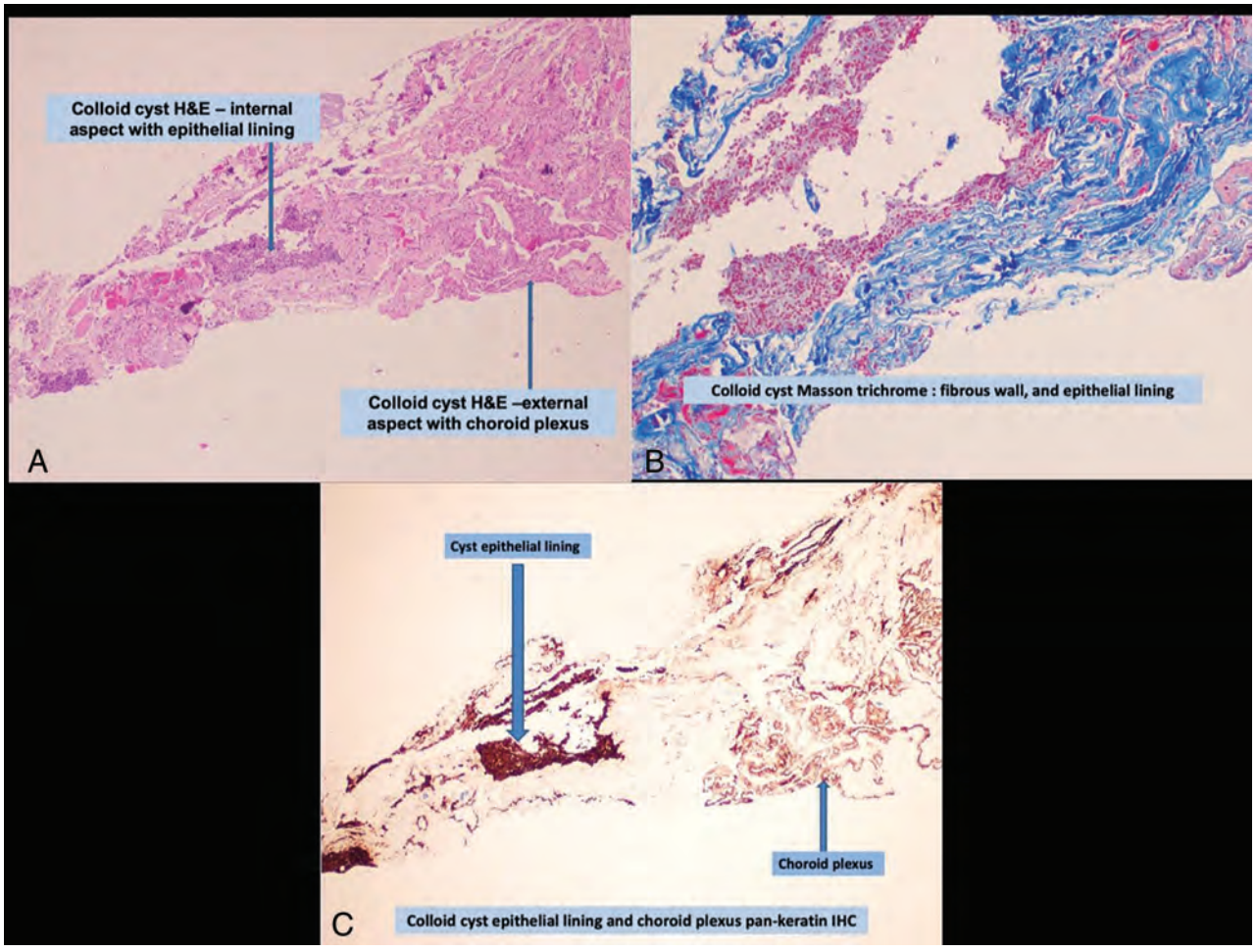

FIG 6. Pathologic examination of a cyst that had the "cysts with rim" appearance revealed a viscous plug of colloid material which was PAS-positive. The cyst wall consisted of a thin fibrous capsule and a lining of partly ciliated cuboidal to columnar epithelium (*A*). The fibrous wall, and the associated choroid plexus stroma are highlighted by the Masson trichrome stain (*B*). The cyst epithelium is positive for CAM 5.2, pankeratin (*C*), EMA, and CK7; it is negative for CDX2. The peripheral cyst wall was not unusually thickened and was approximately 1–3 microns thick, and therefore would not have been visible on MR imaging.

separately described in the examination of the other 2 cysts that were received in fragments.

Despite the varied MR imaging appearance on histopathological examination, the appearance of colloid cysts was monotonous with a very thin fibrous wall lined by a single to pseudostratified layer of columnar-cuboidal, partially ciliated epithelium with goblet cells infrequently seen (Figs 5 and 6). The cyst wall was not significantly thicker in cysts with rim. Choroid plexus was identified in 4 specimens. Calcification was present in 1 cyst wall that was not visible, even retrospectively, on GRE-T2*WI. There was evidence of prior hemorrhage in the wall of 1 "dot sign" cyst that was not visible on imaging.

DISCUSSION

Although increasingly diagnosed as an incidental finding, third ventricular colloid cysts are well known for their potential to become symptomatic by creating ventricular obstruction often with serious outcome.[13,14] Various clinical and imaging characteristics have been studied in hopes of determining which cysts are most likely to become symptomatic. Prior neurosurgical literature has noted an increased incidence of symptoms and rapid deterioration in pediatric patients with "watery cysts," hyperintense on T2-weighted and T2-FLAIR imaging.[15,16]

A relationship between cyst signal intensity and symptomatology was first demonstrated in the adult population by Pollock et al,[17] who observed that hyperintensity on T2WI, in addition to cyst size, patient age, ventriculomegaly, and headache, was significantly associated with symptomatic cysts. Although MR imaging was available for only one-third of patients and there was no comment regarding cyst appearance on T2-FLAIR, they found a 5-fold increase in hyperintense signal on T2WI in patients who were symptomatic. Interestingly, 71% of their hyperintense cysts were large, measuring ≥10 mm.[17]

Variables thought to be predictive of symptomatic status were further explored by Beaumont et al,[10] who combined demographic, clinical, and imaging factors to form the CCRS which is a system for use by neurosurgeons to attempt to identify patients at highest risk of having a symptomatic cyst and to stratify the risk of hydrocephalus. In the CCRS, a point is awarded for: age <65; cyst diameter ≥7 mm; presence of a headache at presentation; risk zone location; and the presence of hyperintensity on T2-FLAIR. On a 0- to 5-point scale, a score of ≤2 is considered low risk, whereas a score of ≥4 is associated with a high risk of symptoms and obstructive hydrocephalus. A score of 3 represents an intermediate risk. Cysts with T2-FLAIR hyperintensity were significantly more likely to be symptomatic (relative risk = 2.4) and to present with hydrocephalus (relative risk = 5.1) than those without hyperintensity. Remarkably, they reported that all but 1 cyst with associated obstructive hydrocephalus (96.6%) were hyperintense on the T2-FLAIR sequence. Although hyperintensity on T2WI was not significant for symptomatic cysts, it was significantly associated, but to a lesser degree than FLAIR, with hydrocephalus. The discrepancy in the recording of a cyst as hyperintense on T2-FLAIR, but not on T2-weighted imaging, may be due to increased conspicuity of this hyperintensity when surrounding CSF is suppressed. This would most likely be a factor in cysts with rim or smaller cysts. It is also possible that T1-shortening may also play a role even though there was no relationship between hyperintensity on the T1-weighted images and cysts being symptomatic in our study and the work of others.[10,17] Further, in our study, there was no association between cyst hyperintensity on T2-FLAIR and T1-shortening evidenced on the T1WI, likely due to the dominant effect of T2-shortening on T2-weighted imaging including the T2-FLAIR sequence. Beaumont et al[10] speculated that a "protein doping" effect within the cyst secondary to an osmotic phenomenon was responsible for the hyperintensity on FLAIR that was more conspicuous relative to T2-weighted images.

The CCRS has recently been externally validated as having excellent discriminatory capacity for symptomatic (area under the curve [AUC] = 0.914) and obstructive hydrocephalus (AUC = 0.943). In this validation study, cyst appearance was reported only for the T2-FLAIR sequence and not precisely defined, but was available for all 156 patients.[18] The presence of hyperintensity on T2-FLAIR was significantly associated with symptomatic status (OR = 6.4) and obstructive hydrocephalus (OR = 5.72). Hyperintensity was identified in 53% of symptomatic cysts and 56% of those creating obstructive hydrocephalus but was found in only 18% of those that were asymptomatic. Cyst size, presence of a headache, and risk zone location were also significant factors.

Our observation that T2-FLAIR signal hyperintensity is associated with ventricular obstruction in patients with CCs supports the findings of these prior studies. We observed that patients with hyperintense cysts were likely to present at a younger age and have larger cysts. A plausible justification for increased risk of ventriculomegaly in hyperintense cysts may to some extent be due to their larger size. A hypothetical explanation for association of T2-FLAIR hyperintensity and cyst symptomatology has been suggested by Beaumont et al[10] and Melhem et al[19]; higher protein concentration within the cyst is associated with hyperintensity on T2-FLAIR sequence. A higher concentration of protein may create an osmotically driven influx of free water resulting in cyst enlargement, subsequent obstruction of the foramen of Monro, and ventriculomegaly. A lowering of protein concentration and increased free water would lead to T2 prolongation. Thus, the cysts that are hyperintense on T2-FLAIR are more likely to enlarge and become symptomatic. We found that hyperintensity on T2-FLAIR manifests in one of three main patterns, homogeneously hyperintense, hyperintense rim, and "dot sign;" all of which are associated with larger cyst size, younger patient age, and a higher risk of obstructive ventriculomegaly in comparison to homogeneously hypointense cysts. Of the hyperintense cysts, those with the "dot sign" were significantly larger but were otherwise similar to other hyperintense cysts.

The histopathologic appearance of the cyst wall was monotonous and did not substantially vary despite significant differences in the appearance of the cysts on imaging (Figs 5 and 6). We postulate that the hyperintense rim represents a peripheral hydration layer, which accounts for the increase in T2 and T2-FLAIR signal around a hypointense, viscous central core. The CT appearance of cysts with rim is also in agreement as, on close examination, the hyperattenuated central core is surrounded by a subtle lower attenuation periphery, with an ill-defined border between the regions of differing attenuation. In prior radiologic-pathologic

correlation reports regarding the "black hole" appearance, the center has been found to be highly viscous (like "motor oil") or even described as solid, whereas the high signal rim has been described as liquid and consisting of amorphous material with cellular debris, erythrocytes, and cholesterol clefts.[20,21] Lack of susceptibility artifact on the SWI and diffusion-weighted imaging, within the center of the black hole cysts supports prior investigations, which have stated that neither paramagnetic metals nor hemorrhage account for the T2-shortening seen within the black hole cysts.[11]

In keeping with the literature, most of our cysts were hyperattenuated on CT.[10,16,17] In general, higher attenuation on CT corresponded to lower signal on the T2WI; both believed to indicate higher viscosity which correlates with difficult aspiration in the surgical literature.[5,22]

Half of the cysts were hyperintense on the T1-weighted images. This T1-shortening, as reported in prior literature, is likely related to higher protein and cholesterol content and is not due to calcium, metal, or blood products.[11,23] Interestingly, cysts with the "dot sign" were high in signal intensity not only on both T2 and T2-FLAIR, but also on T1-weighted imaging indicating a higher protein and/or cholesterol content. In vitro studies of protein solutions have shown that T1 hyperintensity is seen with protein concentrations exceeding 9 g/dL.[24] At extremely high concentrations, greater than 17 g/dL, in vitro solutions of protein remained high in signal on the T1-weighted images but T2-shortening effects predominated so that the solutions became dark on T2WI. We did not observe any association between the CT attenuation or T1 hyperintensity with symptomatic clinical presentation, which is in keeping with the existing imaging literature.[10,17]

Calcification has rarely been reported in the walls of colloid cysts, but was not seen in any of our cases.[25] On histopathologic examination, our specimens often contained choroid plexus, as it is closely juxtaposed to the cyst wall. In some of these cases, it seems likely that calcification in psammoma bodies, which are intrinsic to the choroid plexus, may be mistakenly attributed to the colloid cyst wall (Fig 6). Although we did not discover any element of hemorrhage within our colloid cysts, hemorrhagic cysts are well reported in the literature and may be a cause of abrupt neurologic decline.[26]

The limitations of our study include the retrospective design and relatively small sample size in the subgrouping of hyperintense cysts. The lack of a uniform imaging protocol due to retrospective nature of the study is another limitation. Pathologic examination was often limited because the specimen sometimes lacked the cyst wall. We used obstructive ventriculomegaly as an "end point" and did not address the degree of ventriculomegaly due to the complex interdependence of many variables including ventricular compliance, intermittent obstruction scenarios, lack of recognition of subtle, or early, ventricular dilation as well as the marked variation in the time from symptom onset to imaging.

CONCLUSIONS

Three different imaging subtypes of T2-FLAIR hyperintense cysts are observed: homogeneously hyperintense; cysts with rim; and cysts with "dot sign." These T2-FLAIR hyperintense CCs are associated with younger patient age, larger cyst size, and a greater occurrence of obstructive ventriculomegaly than cysts with no hyperintensity. No association was observed between CT attenuation or T1 hyperintensity and obstructive ventriculomegaly. The hyperintense rim of a "black hole" cyst does not represent a thickened cyst wall.

REFERENCES

1. McLendon RE, Rosenblum MK, Bigner DD. *Russell & Rubinstein's Pathology of Tumors of the Nervous System* 3rd ed. CRC Press; 2006
2. Kappers JA. **The development of the paraphysis cerebri in man with comments on its relationship to the intercolumnar tubercle and its significance for the origin of cystic tumors in the third ventricle.** *J Comp Neurol* 1955;102:425–509 CrossRef Medline
3. Shuangshoti S, Roberts MP, Netsky MG. **Neuroepithelial (colloid) cysts: pathogenesis and relation to choroid plexus and ependyma.** *Arch Pathol* 1965;80:214–24 Medline
4. Tsuchida T, Hruban RH, Carson BS, et al. **Colloid cysts of the third ventricle: immunohistochemical evidence for nonneuroepithelial differentiation.** *Hum Pathol* 1992;23:811–16 CrossRef Medline
5. Kondziolka D, Lunsford LD. **Stereotactic management of colloid cysts: factors predicting success.** *J Neurosurg* 1991;75:45–51 CrossRef Medline
6. Ho KL, Garcia JH. **Colloid cysts of the third ventricle: ultrastructural features are compatible with endodermal derivation.** *Acta Neuropathol* 1992;83:605–12 CrossRef Medline
7. Graziani N, Dufour H, Figarella-Branger D, et al. **Do the suprasellar neurenteric cyst, the Rathke cleft cyst and the colloid cyst constitute a same entity?** *Acta Neurochir (Wien)* 1995;133:174–80 CrossRef Medline
8. Macdonald RL, Humphreys RP, Rutka JT, et al. **Colloid cysts in children.** *Pediatr Neurosurg* 1994;20:169–77 CrossRef Medline
9. de Witt Hamer PC, Verstegen MJT, De Haan RJ, et al. **High risk of acute deterioration in patients harboring symptomatic colloid cysts of the third ventricle.** *J Neurosurg* 2002;96:1041–45 CrossRef Medline
10. Beaumont TL, Limbrick DD, Rich KM, et al. **Natural history of colloid cysts of the third ventricle.** *JNS* 2016;125:1420–30 CrossRef Medline
11. Maeder PP, Holtås SL, Basibüyük LN, et al. **Colloid cysts of the third ventricle: correlation of MR and CT findings with histology and chemical analysis.** *AJR Am J Roentgenol* 1990;155:135–41 CrossRef Medline
12. Osborn AG, Hedlund GL, Salzman KL. Introduction to neoplasms, cysts and tumor-like lesions. *Osborne's Brain,* 2nd ed. 2018 Elsevier Health Sciences
13. Little JR, MacCarty CS. **Colloid cysts of the third ventricle.** *J Neurosurg* 1974;40:230–35 CrossRef Medline
14. Mathiesen T, Grane P, Lindgren L, et al. **Third ventricle colloid cysts: a consecutive 12-year series.** *J Neurosurg* 1997;86:5–12 CrossRef Medline
15. Kumar V, Behari S, Kumar Singh R, et al. **Pediatric colloid cysts of the third ventricle: management considerations.** *Acta Neurochir (Wien)* 2010;152:451–61 CrossRef Medline
16. Alnaghmoosh N, Alkhani A. **Colloid cysts in children, a clinical and radiological study.** *Childs Nerv Syst* 2006;22:514–16 CrossRef Medline
17. Pollock BE, Schreiner SA, Huston J. **A theory on the natural history of colloid cysts of the third ventricle.** *Neurosurgery* 2000;46:1077–83 CrossRef Medline
18. Alford EN, Rotman LE, Shank CD, et al. **Independent validation of the colloid cyst risk score to predict symptoms and hydrocephalus in patients with colloid cysts of the third ventricle.** *World Neurosurg* 2020;134:e747–53 CrossRef Medline
19. Melhem ER, Jara H, Eustace S. **Fluid-attenuated inversion recovery MR imaging: identification of protein concentration thresholds for**

CSF hyperintensity. *AJR Am J Roentgenol* 1997;169:859–62 CrossRef Medline
20. Urso JA, Ross GJ, Parker RK, et al. **Colloid cyst of the third ventricle: radiologic-pathologic correlation.** *J Comput Assist Tomogr* 1998;22:524–27 CrossRef Medline
21. Wilms V, Marchal L, Hecke L, et al. **Colloid cysts of the third ventricle: MR findings.** *J Comput Assist Tomogr* 1990;14:527–31 CrossRef Medline
22. Khoury CE, Brugières P, Decq P, et al. **Colloid cysts of the third ventricle: are MR imaging patterns predictive of difficulty with percutaneous treatment?** *AJNR Am J Neuroradiol* 2000;21:489–92 Medline
23. Armao D, Castillo M, Chen H, et al. **Colloid cyst of the third ventricle: imaging-pathologic correlation.** *AJNR Am J Neuroradiol* 2000;21:1470–77 Medline
24. Ahmadi J, Destian S, Apuzzo ML, et al. **Cystic fluid in craniopharyngiomas: MR imaging and quantitative analysis.** *Radiology* 1992;182:783–85 CrossRef Medline
25. Türe U, Hiçdönmez T, Elmaci I, et al. **Solid-calcified colloid cyst of the third ventricle.** *Clin Neurol Neurosurg* 2001;103:51–55 CrossRef Medline
26. Beems T, Menovsky T, Lammens M. **Hemorrhagic colloid cyst.** *Surg Neurol* 2006;65:84–86 CrossRef Medline

Transcranial MR Imaging–Guided Focused Ultrasound Interventions Using Deep Learning Synthesized CT

P. Su, S. Guo, S. Roys, F. Maier, H. Bhat, E.R. Melhem, D. Gandhi, R. Gullapalli, and J. Zhuo

ABSTRACT

BACKGROUND AND PURPOSE: Transcranial MR imaging–guided focused ultrasound is a promising novel technique to treat multiple disorders and diseases. Planning for transcranial MR imaging–guided focused ultrasound requires both a CT scan for skull density estimation and treatment-planning simulation and an MR imaging for target identification. It is desirable to simplify the clinical workflow of transcranial MR imaging–guided focused ultrasound treatment planning. The purpose of this study was to examine the feasibility of deep learning techniques to convert MR imaging ultrashort TE images directly to synthetic CT of the skull images for use in transcranial MR imaging–guided focused ultrasound treatment planning.

MATERIALS AND METHODS: The U-Net neural network was trained and tested on data obtained from 41 subjects (mean age, 66.4 ± 11.0 years; 15 women). The derived neural network model was evaluated using a k-fold cross-validation method. Derived acoustic properties were verified by comparing the whole skull-density ratio from deep learning synthesized CT of the skull with the reference CT of the skull. In addition, acoustic and temperature simulations were performed using the deep learning CT to predict the target temperature rise during transcranial MR imaging–guided focused ultrasound.

RESULTS: The derived deep learning model generates synthetic CT of the skull images that are highly comparable with the true CT of the skull images. Their intensities in Hounsfield units have a spatial correlation coefficient of 0.80 ± 0.08, a mean absolute error of 104.57 ± 21.33 HU, and a subject-wise correlation coefficient of 0.91. Furthermore, deep learning CT of the skull is reliable in the skull-density ratio estimation ($r = 0.96$). A simulation study showed that both the peak target temperatures and temperature distribution from deep learning CT are comparable with those of the reference CT.

CONCLUSIONS: The deep learning method can be used to simplify workflow associated with transcranial MR imaging–guided focused ultrasound.

ABBREVIATIONS: DL = deep learning; MAE = mean absolute error; SDR = skull-density ratio; tcMRgFUS = transcranial MR imaging–guided focused ultrasound; UTE = ultrashort TE

Transcranial MR imaging–guided focused ultrasound (tcMRgFUS) is a promising novel technique for treating multiple disorders and diseases, including essential tremor,[1] neuropathic pain,[2] and Parkinson disease.[3] During tcMRgFUS treatment, ultrasound energy is deposited from multiple ultrasound elements to a specific location in the brain to increase tissue temperature and ablate the targeted tissue. tcMRgFUS treatment-planning is usually performed in 3 steps: 1) CT images are acquired to estimate regional skull density and skull geometry and to estimate ultrasound attenuation during ultrasound wave propagation,[1] 2) MR images are acquired to identify the ablation target in the brain,[1] and 3) the CT and MR images are fused to facilitate treatment-planning. Minimizing the steps involved to get to actual treatment can have a positive impact on clinical workflow. Here, we focus on the implications of minimizing patient burden by eliminating CT imaging (hence no radiation) and replacing it with synthesized CT of the skull based on ultrashort TE (UTE) images.

UTE MR imaging is an important technique for imaging short-T2 tissue components such as bone. A previous study has

Received March 30, 2020; accepted after revision July 5.

From the Department of Diagnostic Radiology and Nuclear Medicine (P.S., S.G., S.R., E.R.M., D.G., R.G., J.Z.), University of Maryland School of Medicine, Baltimore, Maryland; Siemens Medical Solutions USA (P.S., H.B.), Malvern, Pennsylvania; Center for Metabolic Imaging and Therapeutics (S.G., S.R., R.G., J.Z.), University of Maryland Medical Center, Baltimore, Maryland; and Siemens Healthcare GmbH (F.M.), Erlangen, Germany.

P. Su and S. Guo contributed equally to this work.

Please address correspondence to Jiachen Zhuo, PhD, Department of Diagnostic Radiology and Nuclear Medicine, University of Maryland School of Medicine, 670 W Baltimore St, Baltimore, MD, 21201; e-mail: jzhuo@umm.edu

Indicates article with supplemental on-line photo.

http://dx.doi.org/10.3174/ajnr.A6758

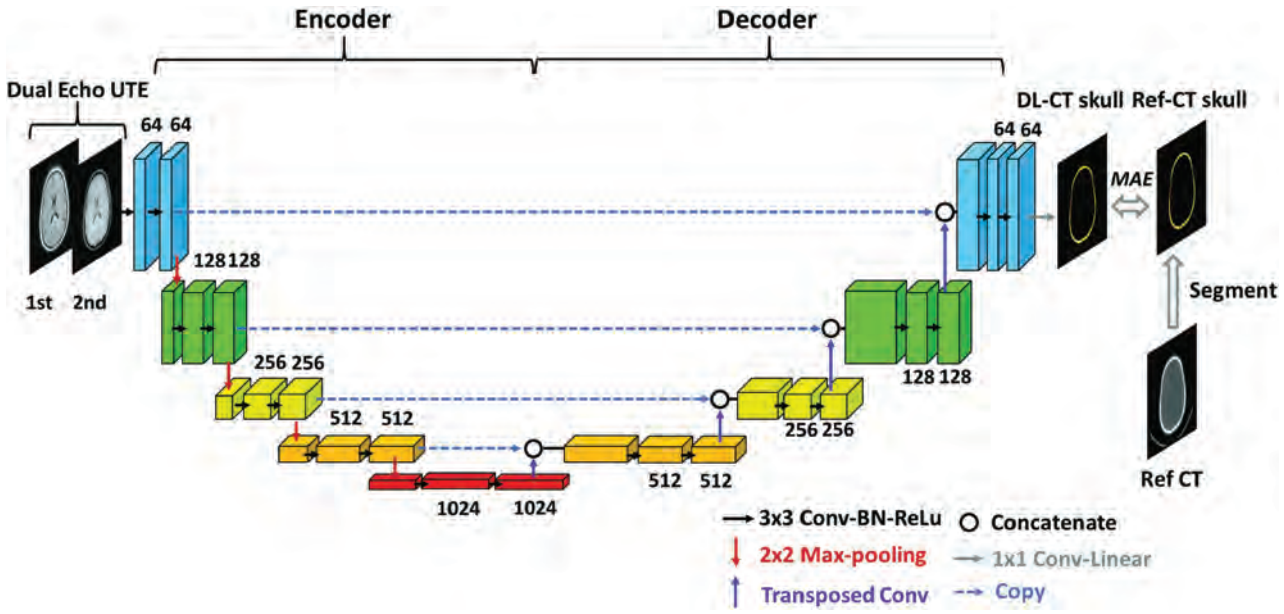

FIG 1. Schema of the employed deep learning architecture based on the widely used U-Net convolutional neural network consisting of encoding and decoding pathways. Dual-echo UTE images were used as the input for the network. Reference CT of the skull was segmented from the reference CT and was used as the predication target. The difference between output of the network, DL synthetic CT of the skull, and reference CT of the skull was minimized using MAE loss function. Drop-out regularization (rate = 0.5) was applied connecting the encoder and decoder. BN indicates batch normalization; ReLu, rectified linear unit; Conv, convolutional layer; Ref-CT, reference CT.

shown the feasibility of using UTE MR images for tcMRgFUS planning.[4] The conversion of UTE MR images to CT intensity (also termed "synthetic CT") is based on the inverse-log relationship between UTE and CT signal intensity.[4,5]

Deep learning (DL) with a convolutional neural network has recently led to breakthroughs in medical imaging fields such as image segmentation[6] and computer-aided diagnosis.[7] Domain transfer (eg, MR imaging to CT) is one of the fields in which DL has been applied recently with high accuracy and precision.[8-12] DL-based methods synthesize CT images either by classifying MR images into components (eg, tissue, air, and bone)[10,12] or by directly converting MR imaging intensities into CT Hounsfield units.[8,9,11] The established applications include MR imaging–based attenuation correction in MR imaging/PET[10-12] and treatment-planning for MR imaging–guided radiation therapy procedures.[9] However, to our knowledge, DL methods have not been applied in the context of tcMRgFUS. In tcMRgFUS, our focus is skull CT intensity rather than the whole head as in the above procedures. By narrowing the focus area, we can potentially achieve higher accuracy in obtaining synthetic skull CT images from MR imaging.

The purpose of this study was to examine the feasibility of DL techniques to convert MR imaging dual-echo UTE images directly to synthetic CT of the skull images and assess its suitability for tcMRgFUS treatment-planning procedures.

MATERIALS AND METHODS

Study Participants

We retrospectively evaluated data obtained from 41 subjects (mean age, 66.4 ± 11.0 years; 15 women) who underwent the tcMRgFUS procedure and for whom both dual-echo UTE MR imaging and CT data were available. The study was approved by the institutional review board (University of Maryland at Baltimore).

Image Acquisition and Data Preprocessing

MR brain images were acquired on a 3T system (Magnetom Trio; Siemens) using a 12-channel head coil. A prototype 3D radial UTE sequence with 2 TEs was acquired in all subjects.[13] Imaging parameters were the following: 60,000 radial views, TE1/TE2 = 0.07/4 ms, TR= 5 ms, flip angle = 5°, matrix size = 192 × 192 × 192, spatial resolution = 1.3 × 1.3 × 1.3 mm^3, scan time = 5 minutes.[13,14] CT images at 120 kV were acquired using a 64-section CT scanner (Brilliance 64; Philips Healthcare), with a reconstructed matrix size = 512 × 512 and resolution = 0.48 × 0.48 × 1 mm^3. A C-filter (Philips Healthcare), a Hounsfield unit–preserving sharp ramp filter, was applied to all images.

UTE images were corrected for signal inhomogeneity with nonparametric nonuniform intensity normalization bias correction using Medical Image Processing, Analysis, and Visualization (National Institutes of Health).[15] Both UTE volumes (TE1 and TE2) for each subject were normalized by the tissue signal of the TE1 image to account for signal variation across subjects. CT images from each subject were registered and resampled to the corresponding UTE images using the FMRIB Linear Image Registration Tool (FLIRT; https://fsl.fmrib.ox.ac.uk/fsl/fslwiki/FLIRT) using a normalized mutual information cost function.[16] Finally, CT of the skull images were derived by segmenting the registered CT images using automatic image thresholding with the Otsu method.[17] The same threshold value was applied to the DL synthetic CT (DL-CT) data. Only the skull from the superior slices relevant for the tcMRgFUS procedure from both UTE and CT was included. CT-UTE registration results were evaluated by visual inspection. One subject was

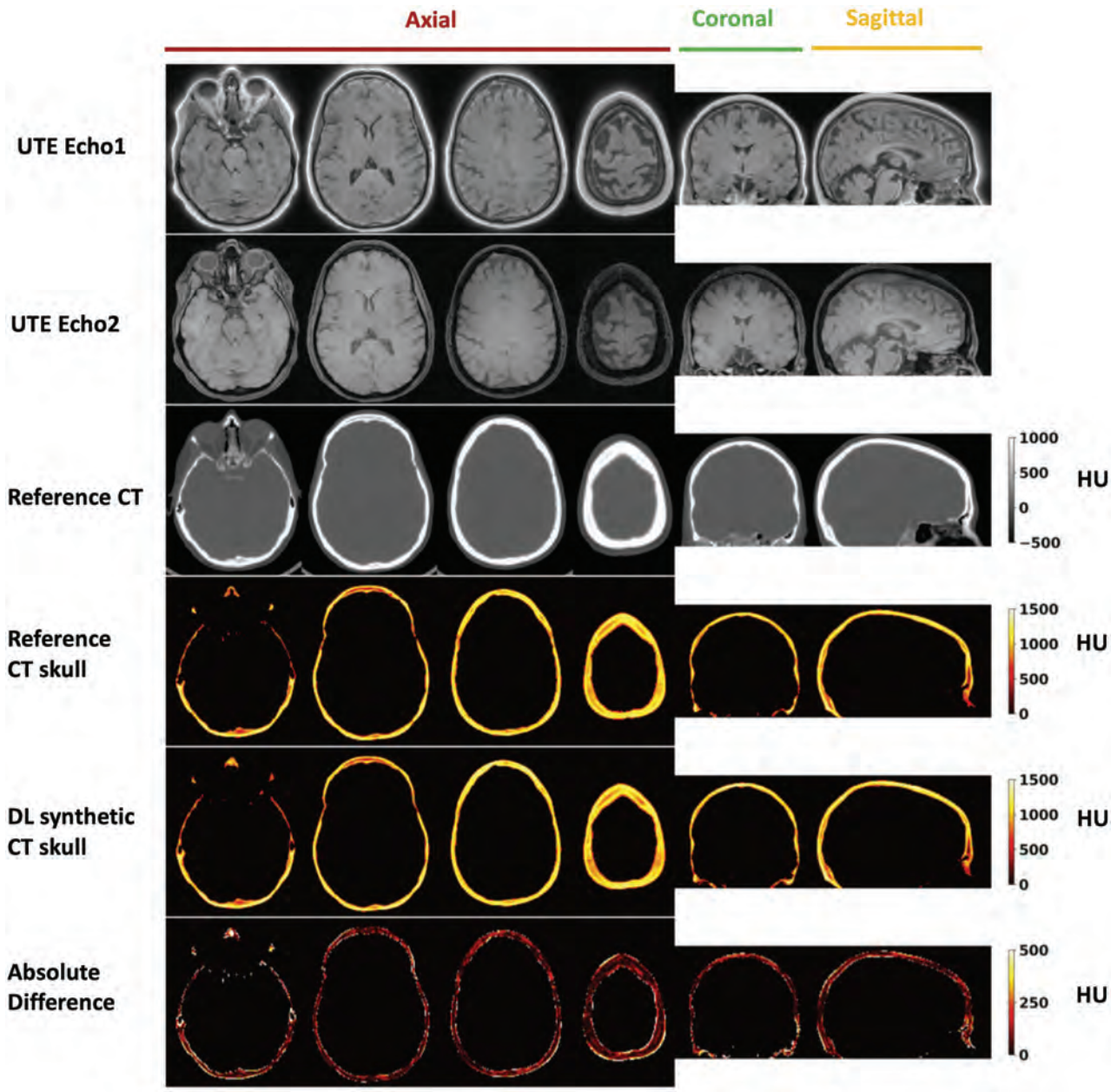

FIG 2. Deep learning results from 1 representative testing subject (55 years of age, female). From top to bottom: UTE echo 1 and echo 2 images, reference CT, segmented reference CT of the skull, DL synthetic CT of the skull, and the absolute difference between the 2. For this subject, the Dice coefficient for skull masks between DL synthetic CT and the reference CT is 0.92, and the mean absolute difference is 96.27 HU.

excluded due to failed registration, leading to 40 subjects in total (mean age, 66.5 ± 11.2 years; 15 women).

Deep Learning Model and Neural Network Training

A schematic diagram of the deep learning model architecture based on U-Net convolutional neural network (https://lmb.informatik.uni-freiburg.de/people/ronneber/u-net/)[18] is illustrated in Fig 1. It consists of 2 pathways in opposite directions: encoding and decoding. The encoding pathway extracts features of the input images, while the decoding pathway has the opposite direction, restoring these features.

Dual-echo UTE images were used as the input to the neural network, with each echo as a separate input channel to the network. Reference CT of the skull images was used as the prediction target. Output of the network is the DL-CT of the skull.

UTE-CT image pairs from 32 subjects were selected as the training dataset, and the other 8, as the testing dataset. The neural network was defined, trained, and tested using Keras with Tensorflow backend (https://www.tensorflow.org) with a Tesla K40C GPU (memory of 12GB). Mean absolute error (MAE) between DL-CT of the skull and the reference CT of the skull was minimized using the ADAM algorithm, derived from adaptive moment estimation.[19] The training was performed with 100 epochs, and the learning rate was 0.001. Training of the model took approximately 6 hours.

Evaluation of Model Performance

The performance of the neural network model was evaluated using the 5-fold cross-validation method. The 40 subjects were randomly divided into 5 groups, each with 8 subjects. Each time 1 group was held as a testing dataset, the other 4 served as the training datasets; thus, the model was trained 5 separate times. Testing results from all 40 subjects were used to evaluate the performance of the model. The following 4 metrics were used to compare the DL-CT from the testing datasets with the reference CT of the skull images: 1) Dice coefficient to evaluate the similarity between the 2 sets of images; 2) a voxelwise spatial correlation coefficient between the 2 methods considering all the voxel intensities (in Hounsfield units); 3) average of absolute differences between the 2 methods for voxels within skull region; and 4) global CT Hounsfield unit values for each subject by averaging all the voxels within the skull region. Metrics using a conventional method[4] were also derived to enable comparison with the DL method. Note that only testing datasets ($n = 40$) from cross-validation results were used for evaluation and the following validation/simulation.

Skull Density Ratio Validation

To further evaluate the accuracy of DL-CT-derived skull properties, we also calculated the regional skull thickness and the skull-density ratio (SDR) based on each of the 1024 ultrasound rays on 40 subjects. We validated our model by comparing the whole SDR from DL-CT of the skulls with reference CT of the skulls. The SDR is calculated as the ratio of the minimum over the maximum intensity (Hounsfield unit) along the skull path of ultrasonic waves from each of the 1024 transducers, and the whole-skull SDR is the average of all SDRs. Whole-skull SDR > 0.45 is the eligibility criterion for tcMRgFUS treatment for efficient sonication.[20]

Acoustic and Temperature Simulation

A key aspect of the tcMRgFUS is the guidance obtained from MR thermometry maps during the procedure, eg, to predict the target temperature rise. We therefore compared acoustic and temperature fields from the simulation using both CT and DL-CT images on 8 test subjects. The acoustic fields within the head were simulated using a 3D finite-difference algorithm, which aims to solve the full Westervelt equation.[21] The acoustic properties of the skull were derived from CT images of the subjects. Temperature rise was estimated using the inhomogeneous Pennes equation[22] of heat conduction with the calculated acoustic intensity field as input. Both acoustic and temperature simulations were performed with the target at the center of the anterior/posterior commissure line for each subject at a spatial resolution of UTE scans. Temperature elevations at the focal spots caused by a 16-second, 1000-W sonication were simulated for both reference CT and DL-CT images, assuming that the base temperature of the brain was 37°C.

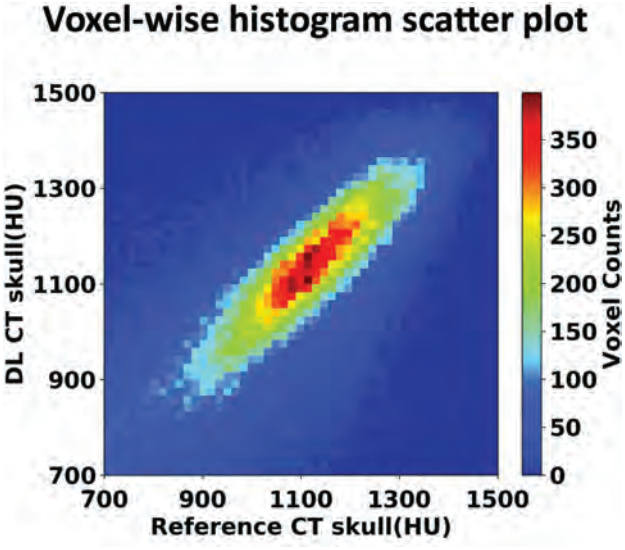

FIG 3. Voxelwise 2D histogram scatterplot between the reference skull CT intensity and the DL synthetic skull CT signal intensity in Hounsfield units within skull. The correlation coefficient is $r = 0.80$ (same testing subject as in Fig 2). *Color bar* represents the voxel count.

RESULTS

Figure 2 shows the DL-CT of the skull images in comparison with the reference CT of the skull images from a representative test subject. The difference images show minimal discrepancy, demonstrating that the trained DL network has successfully learned the mapping from dual-echo UTE images to CT of the skull-intensity images. The On-line Figure shows the DL model loss (MAE) as a function of the epoch number for both the training and testing datasets from a representative cross-validation run.

The signal intensities between the 2 CT scans are highly correlated ($r = 0.80$) as shown in the voxelwise 2D histogram (Fig 3), demonstrating that DL can accurately predict the spatial variation across regions within the skull. The Table summarizes various metrics estimating the performance of the DL model from all 5 runs of the cross-validation process, along with the average from all 40 testing datasets. As shown in the Table, model performance is comparable between different runs in the cross-validation process. As a comparison, the MAE and spatial correlation coefficient from the conventional method[4] were 0.37 ± 0.09 and 432.19 ± 46.61 HU, performances significantly poorer than our proposed deep learning method.

Various metrics (mean ± standard deviation) showing the performance of the deep learning model from all 5 runs of the cross-validation process[a]

	Run 1	Run 2	Run 3	Run 4	Run 5	Average
Dice coefficient	0.91 ± 0.03	0.92 ± 0.03	0.91 ± 0.03	0.91 ± 0.02	0.92 ± 0.03	0.91 ± 0.03
Spatial correlation coefficient	0.84 ± 0.05	0.77 ± 0.10	0.81 ± 0.07	0.78 ± 0.08	0.81 ± 0.08	0.80 ± 0.08
MAE (HU)	89.32 ± 12.29	109.18 ± 23.49	98.95 ± 13.75	105.10 ± 17.62	120.29 ± 26.91	104.57 ± 21.33

[a] Averaged metrics from all 40 testing datasets are also included.

Subject-wise scatterplots of average CT values and SDR values are shown in Fig 4. A strong correlation between the DL-CT and the reference CT Hounsfield unit values ($r = 0.91$, $P < .001$) was observed, demonstrating that the derived model can predict the global intensity of the skull accurately. The high whole-skull SDR correlation ($r = 0.96$, $P < .001$) between DL-CT and the reference CT suggests a strong potential for the use of DL-CT images for treatment-planning in tcMRgFUS.

Figure 5 shows averaged regional skull thickness maps Fig 5*A*, -*B* and averaged regional SDR maps (Figure 5*D*, -*E*) based on the reference CT and DL-CT images from all 40 test subjects. The errors in skull thickness measurement at any given entry were <0.2 mm (2%), averaged at 0.03 mm (0.3%) (Fig 5*C*). The maximum error for SDR calculation across the 1024 entries was found to be about 0.03 (4%) and averaged less than 0.01 (1.3%) (Fig 5*F*).

Comparisons between calculated bone density and the simulated temperature rise results are shown in Fig 6 for 8 representative test subjects. The estimated voxelwise average bone density difference within the skull for all subjects was 50 kg/m^3, indicating less than an average of 2.3% error for UTE-derived acoustic properties compared with the reference CT images (columns 1 and 2). Simulated temperature patterns are very similar for all 8 cases (columns 3 and 4), indicating that the skull shape and thickness of DL-CT are highly comparable with the reference CT. The differences of simulated peak temperature rise based on original and DL synthetic CT images for all 8 subjects are well within the errors that one might expect from the simulation.

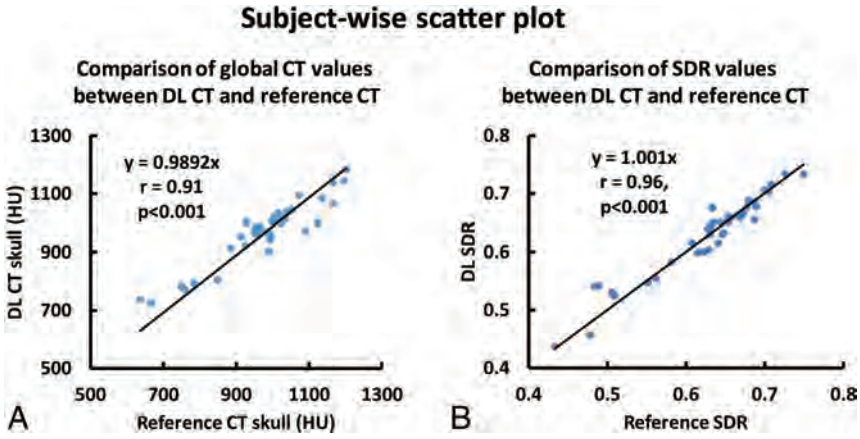

FIG 4. *A*, Association of average CT Hounsfield unit values between the DL synthetic CT of the skull and the reference CT of the skull for all 40 testing subjects from cross-validation. Each *dot* represents 1 subject. *B*, The relationship between SDR values determined from the reference CT and DL synthetic CT from all 40 subjects. Each *dot* represents 1 subject.

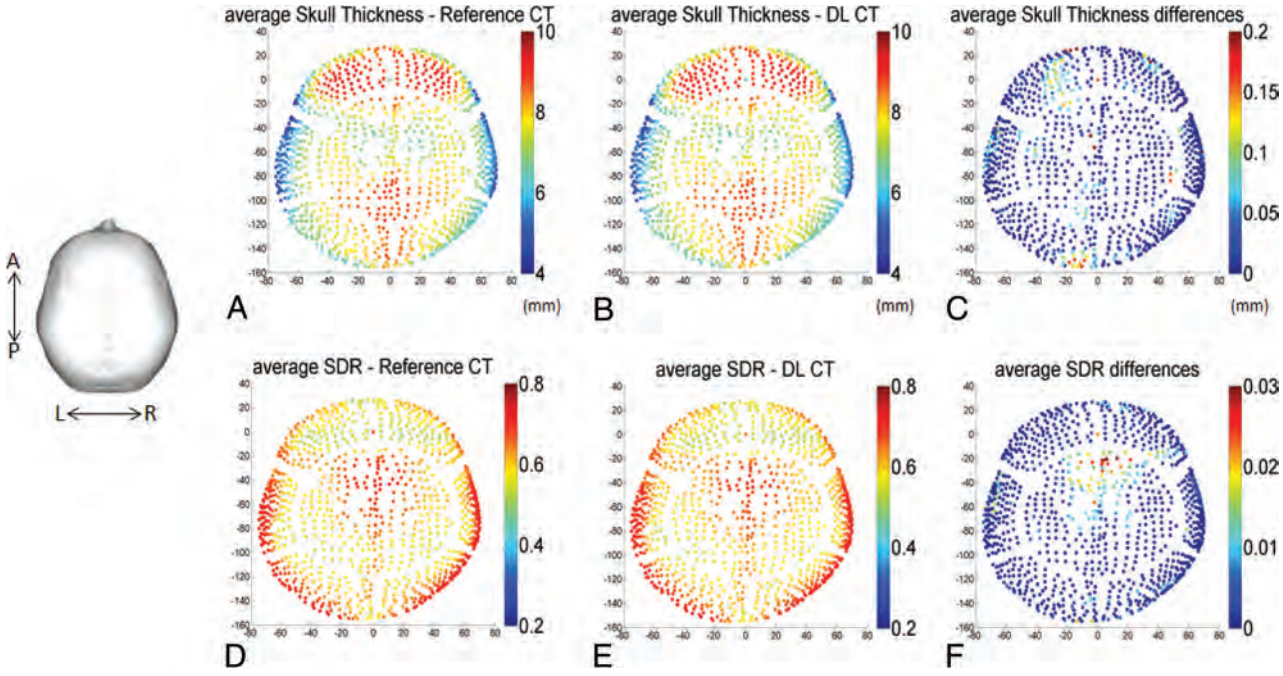

FIG 5. *A* and *B*, The calculated average skull thickness map from the reference CT and the DL synthetic CT images, respectively, from all 40 testing subjects. *C*, The differences between *A* and *B* with a maximum thickness difference of 0.2 mm (2% error) and the average error of 0.03 mm (0.3%). Note that regional maps are based on the entries of the 1024 ultrasound beams from the ExAblate system (InSightec). *D* and *E*, The calculated average SDR map based on the reference CT and DL synthetic CT images from all 40 subjects. *F*, The differences between *D* and *E* with a maximum SDR difference of 0.03 (4% error) and the average error of 1024 entries was <0.01 (1.3%).

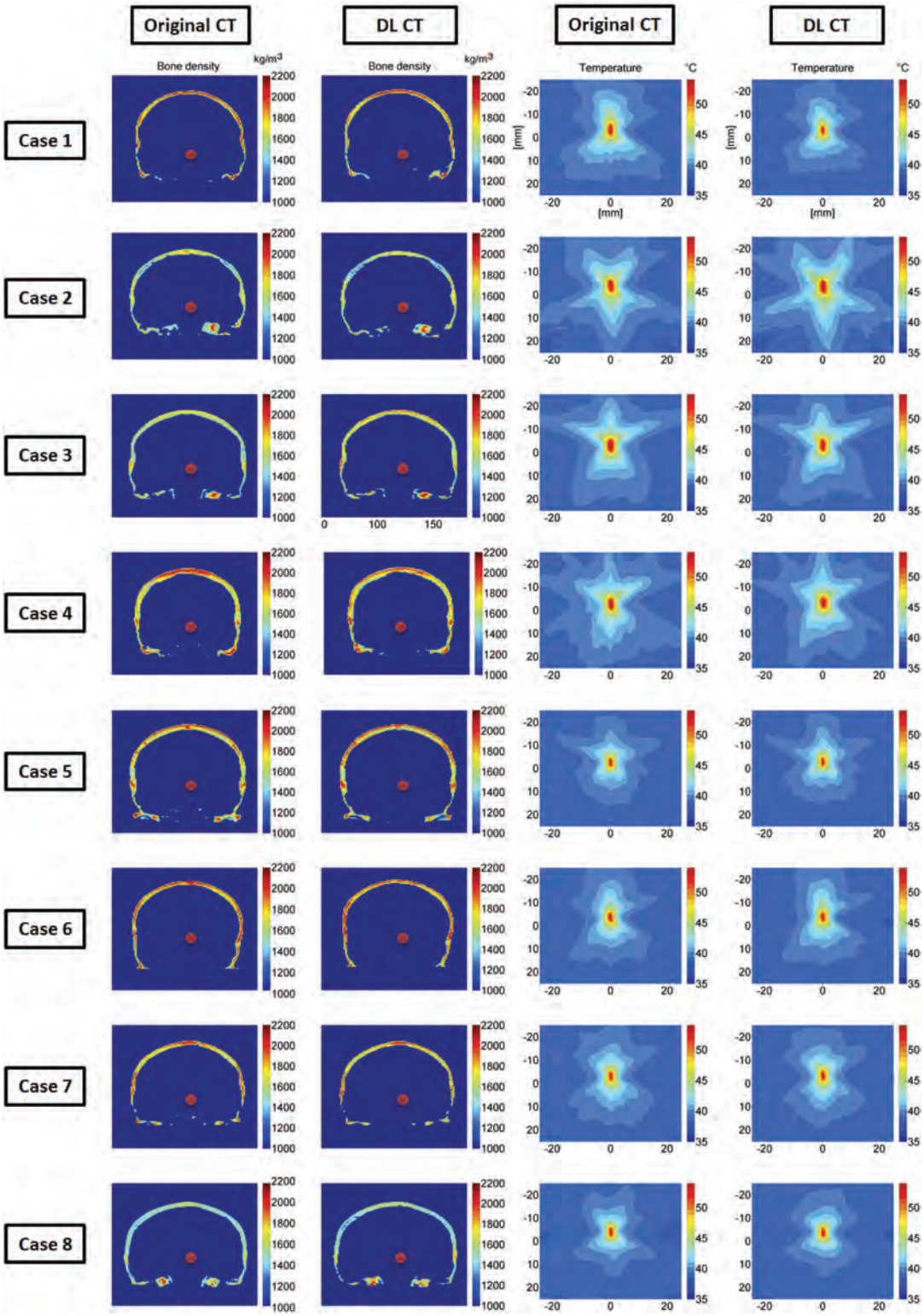

FIG 6. Comparison of calculated bone density and the simulated temperature rise. The *first and second columns* show the calculated bone density map using the reference CT and DL synthetic CT images on 8 representative testing cases, in which the *red dots* are the assigned focal targets. In the *third and fourth columns*, the simulated temperature elevations at the focal spots caused by a 16-second, 1000-W sonication are compared between reference CT and DL synthetic CT on a base brain temperature of 37°C. The simulated peak temperature rise values based on original and DL synthetic CT images for all 8 subjects are the following: case 1: 55.3°C and 54.2°C (6.0% error on temperature rise), case 2: 59.0°C and 58.9°C (0.5% error), case 3: 57.6°C and 55.9°C (8.2% error), case 4: 57.5°C and 59.1°C (7.8% error), case 5: 54.3°C and 54.6°C (0.6% error), case 6: 55.5°C and 56.0°C (0.9% error), case 7: 54.5°C and 55.1°C (1.1% error), case 8: 53.5°C and 54.5°C (1.9% error), respectively. These errors are well within the errors that one might expect from the simulation.

DISCUSSION

In this study, we examined the feasibility of leveraging deep learning techniques to convert MR imaging dual-echo UTE images directly to CT of the skull images and to assess the applicability of such derived images to replace real CT of the skull images during tcMRgFUS procedures. The proposed neural network is capable of accurately predicting Hounsfield unit intensity values within the skull. Various metrics were used to validate the DL model, and they all demonstrated excellent correspondence between DL-CT of the skull images and the reference CT of the skull images. Furthermore, the acoustic properties as measured using the SDR and temperature simulation suggest that DL-CT images can be used to predict target temperature rise. Our proposed DL model has the potential to eliminate CT during tcMRgFUS planning, thereby simplifying clinical workflow and reducing the number of patient visits and overall procedural costs, while eliminating patient exposure to ionizing radiation. To our knowledge, this is the first study to apply deep learning in synthesizing CT of the skull images with MR imaging UTE images for tcMRgFUS treatment planning.

Several previous studies have reported methods to derive CT information from MR imaging.[9-12,23] Multiple DL-based CT synthesis studies have reported CT bone segmentation with Dice coefficient values ranging from 0.80 to 0.88.[9-12,23] In our study, the proposed model shows excellent performance in estimating CT-equivalent skull with a Dice score of 0.91 ± 0.03 for all 40 testing datasets. The moderately higher level of performance over other previous methods may be because only a limited amount of the skull was taken into consideration due to its relevance for tcMRgFUS, whereas previous methods also included brain tissue.[15-21] Furthermore, our model predicted CT intensity with a high voxelwise correlation (0.80 ± 0.08) and low MAE (104.57 ± 21.33 HU) for all 40 subjects compared with the reference CT of the skull. One study[4] reported an MAE between the reference CT and UTE-generated synthetic CT of 202 HU in the context of tcMRgFUS. Applying this method[4] to our dataset, we observed a higher MAE of 432.19 ± 46.61 HU. The discrepancy may be due to differences of the subject cohort and skull mask delineation. Another study reported an MAE of 174 ± 29 HU within the skull.[9] Compared with these studies, our results represent a marked improvement over existing methods.

While this is the first report demonstrating the feasibility of applying deep learning in tcMRgFUS, our proposed framework can be further improved in a few ways: First, the DL field is rapidly evolving, and newer state-of-the-art techniques continue to emerge. The inputs to the implemented 2D U-Net neural network in our case were individual 2D dual-echo UTE images to generate 2D CT of the skull images as output. It is highly possible that a 2.5D or 3D U-Net may further minimize these errors because these approaches use context information for training. However, note that the 3D U-Net requires significantly more memory resources than the 2D U-Net. Additionally, alternative loss formulations or combinations may be considered (eg, an adversarial component to the loss function to maximize the realistic appearance of the generated output). Given the relatively small dataset and the fact that the MR imaging-to-CT mapping task does not require full-FOV MR imaging, an alternative approach may be to train a patch-wise classifier (same encoder-decoder architecture, simply smaller). Not only will the model be more compact, it will likely be more regularized and more generalizable to edge cases (eg, craniotomy).

This study has several limitations. One limitation is that the average age of our patient cohort is relatively high (66.5 ± 11.2 years of age). This might limit the usage of our model in younger cohorts or pediatric populations due to bone density variations. Incorporating data from younger subjects into our training data can address this issue. Another limitation is our relatively small sample size for the deep learning study and the lack of an independent test dataset. More datasets will certainly improve the performance of the model and allow better generalization of our model. Additionally, our CT of the skull synthesis was based on MR imaging UTE images, which have relatively low spatial resolution compared with CT (1.33 versus 0.44 mm in-plane resolution). This resolution discrepancy might affect the accuracy of our model in predicting the skull mask and Hounsfield unit values. To address this issue, high-resolution UTE 3D images are needed using advanced parallel imaging, compressed sensing, or even DL-based undersampling/reconstruction to further reduce the scan time while preserving enough information for CT synthesis. Finally, we will investigate the effect of data augmentation on larger datasets in detail and use an advanced deep learning model such as the Generative Adversarial Network (https://github.com/goodfeli/adversarial) to further improve our model in a future study.

CONCLUSIONS

We examined the feasibility of using DL-based models to automatically convert dual-echo UTE images to synthetic CT of the skull images. Validation of our model was performed using various metrics (Dice coefficient, voxelwise correlation, MAE, global CT value) and by comparing both global and regional SDRs derived from DL and the reference CT. Additionally, temperature simulation results suggest that DL-CT images can be used to predict target temperature rise. Our proposed DL model shows promise for replacing the CT scan with UTE images during tcMRgFUS planning, thereby simplifying workflow.

Disclosures: Pan Su—*RELATED*: *Other*: employment: Siemens Healthineers. Florian Maier—*UNRELATED*: *Employment*: Siemens Healthcare GmbH; *Stock/Stock Options*: Siemens Healthineers AG, *Comments*: I am a shareholder. Himanshu Bhat—*RELATED*: *Other*: Siemens Healthineers, *Comments*: employment. Dheeraj Gandhi—*UNRELATED*: *Board Membership*: Insightec*; *Grants/Grants Pending*: MicroVention, Focused Ultrasound Foundation*; *Royalties*: Cambridge Press. *Money paid to the institution.

REFERENCES

1. Elias WJ, Huss D, Voss T, et al. **A pilot study of focused ultrasound thalamotomy for essential tremor.** *N Engl J Med* 2013;369:640–48 CrossRef Medline
2. Jeanmonod D, Werner B, Morel A, et al. **Transcranial magnetic resonance imaging-guided focused ultrasound: noninvasive central lateral thalamotomy for chronic neuropathic pain.** *Neurosurg Focus* 2012;32:E1 CrossRef Medline
3. Monteith S, Sheehan J, Medel R, et al. **Potential intracranial applications of magnetic resonance-guided focused ultrasound surgery.** *J Neurosurg* 2013;118:215–21 CrossRef Medline
4. Guo S, Zhuo J, Li G, et al. **Feasibility of ultrashort echo time images using full-wave acoustic and thermal modeling for transcranial**

MRI-guided focused ultrasound (tcMRgFUS) planning. *Phys Med Biol* 2019;64:095008 CrossRef Medline
5. Wiesinger F, Sacolick LI, Menini A, et al. **Zero TE MR bone imaging in the head.** *Magn Reson Med* 2016;75:107–14 CrossRef Medline
6. Akkus Z, Galimzianova A, Hoogi A, et al. **Deep learning for brain MRI segmentation: state of the art and future directions.** *J Digit Imaging* 2017;30:449–59 CrossRef Medline
7. Litjens G, Sanchez CI, Timofeeva N, et al. **Deep learning as a tool for increased accuracy and efficiency of histopathological diagnosis.** *Sci Rep* 2016;6:26286 CrossRef Medline
8. Han X. **MR-based synthetic CT generation using a deep convolutional neural network method.** *Med Phys* 2017;44:1408–19 CrossRef Medline
9. Dinkla AM, Wolterink JM, Maspero M, et al. **MR-only brain radiation therapy: dosimetric evaluation of synthetic CTs generated by a dilated convolutional neural network.** *Int J Radiat Oncol Biol Phys* 2018;102:801–12 CrossRef Medline
10. Gong K, Yang J, Kim K, et al. **Attenuation correction for brain PET imaging using deep neural network based on Dixon and ZTE MR images.** *Phys Med Biol* 2018;63:125011 CrossRef Medline
11. Jang H, Liu F, Zhao G, et al. **Technical note: deep learning based MRAC using rapid ultrashort echo time imaging.** *Med Phys* 2018 May 15. [Epub ahead of print] CrossRef Medline
12. Liu F, Jang H, Kijowski R, et al. **Deep learning MR imaging-based attenuation correction for PET/MR imaging.** *Radiology* 2018;286:676–84 CrossRef Medline
13. Speier P, Trautwein F. **Robust radial imaging with predetermined isotropic gradient delay correction.** In: *Proceedings of the Annual Meeting of the International Society of Magnetic Resonance in Medicine,* Seattle, Washington. May 6-13, 2006; 2379
14. Robson MD, Gatehouse PD, Bydder M, et al. **Magnetic resonance: an introduction to ultrashort TE (UTE) imaging.** *J Comput Assist Tomogr* 2003;27:825–46 CrossRef Medline
15. Sled JG, Zijdenbos AP, Evans AC. **A nonparametric method for automatic correction of intensity nonuniformity in MRI data.** *IEEE Trans Med Imaging* 1998;17:87–97 CrossRef Medline
16. Jenkinson M, Smith S. **A global optimisation method for robust affine registration of brain images.** *Med Image Anal* 2001;5:143–56 CrossRef Medline
17. Otsu N. **A threshold selection method from gray-level histograms.** *IEEE Trans Syst Man Cybern* 1979;9:62–66 CrossRef
18. Ronneberger O, Fischer P, Brox T. **U-net: Convolutional networks for biomedical image segmentation.** In: *International Conference on Medical Image Computing and Computer-Assisted Intervention Cham,* Switzerland: Springer; 2015; 234–41
19. Kingma DP, Ba JL. **Adam: a method for stochastic optimization.** *arXiv.org* 2014 https://arxiv.org/abs/1412.6980. Accessed September 1, 2019
20. D'Souza M, Chen KS, Rosenberg J, et al. **Impact of skull density ratio on efficacy and safety of magnetic resonance-guided focused ultrasound treatment of essential tremor.** *J Neurosurg* 2018 April 26. [Epub ahead of print] CrossRef Medline
21. Hamilton MF, Blackstock DT. *Nonlinear Acoustics*. Academic Press; 1988
22. Pennes HH. **Analysis of tissue and arterial blood temperatures in the resting human forearm.** *J Appl Physiol* 1998;85:5–34 CrossRef Medline
23. Liu F, Yadav P, Baschnagel AM, et al. **MR-based treatment planning in radiation therapy using a deep learning approach.** *J Appl Clin Med Phys* 2019;20:105–14 CrossRef Medline

Regional Mechanical Thrombectomy Imaging Protocol in Patients Presenting with Acute Ischemic Stroke during the COVID-19 Pandemic

P.S. Dhillon, K. Pointon, R. Lenthall, S. Nair, G. Subramanian, N. McConachie, and W. Izzath

ABSTRACT

BACKGROUND AND PURPOSE: Chest CT is a rapid, useful additional screening tool for coronavirus disease 2019 (COVID-19) in emergent procedures. We describe the feasibility and interim outcome of implementing a modified imaging algorithm for COVID-19 risk stratification across a regional network of primary stroke centers in the work-up of acute ischemic stroke referrals for time-critical mechanical thrombectomy.

MATERIALS AND METHODS: We undertook a retrospective review of 49 patients referred to the regional neuroscience unit for consideration of mechanical thrombectomy between April 14, 2020, and May 21, 2020. During this time, all referring units followed a standard imaging protocol that included a chest CT in addition to a head CT and CT angiogram to identify Severe Acute Respiratory Syndrome coronavirus 2 (SARS-CoV-2) infective pulmonary changes.

RESULTS: Overall, 2 patients had typical COVID-19 radiologic features and tested positive, while 7 patients had indeterminate imaging findings and tested negative. The others had normal or atypical changes and were not diagnosed with or suspected of having COVID-19. There was an overall sensitivity of 100%, specificity of 74.1%, negative predictive value of 100%, and positive predictive value of 22.2% when using chest CT to diagnose COVID-19 in comparison with the real-time reverse transcriptase–polymerase chain reaction test. The mean additional time and radiation dose incurred for the chest CT were 184 ± 65.5 seconds and 2.47 ± 1.03 mSv. Multiple cardiovascular and pulmonary incidental findings of clinical relevance were identified in our patient population.

CONCLUSIONS: Chest CT provides a pragmatic, rapid additional tool for COVID-19 risk stratification among patients referred for mechanical thrombectomy. Its inclusion in a standardized regional stroke imaging protocol has enabled efficient use of hospital resources with minimal compromise or delay to the overall patient treatment schedule.

ABBREVIATIONS: COVID-19 = coronavirus disease 2019; MT = mechanical thrombectomy; PPE = personal protective equipment; PSC = primary stroke centers; RT-PCR = real-time reverse transcriptase–polymerase chain reaction; SARS-CoV-2 = Severe Acute Respiratory Syndrome coronavirus 2

The coronavirus disease 2019 (COVID-19), a manifestation of the Severe Acute Respiratory Syndrome coronavirus-2 (SARS-CoV-2), was declared a pandemic by the World Health Organization on March 11, 2020.[1,2] At present, the COVID-19 incidence in the United Kingdom is one of highest in the world with 261,184 cases and 36,914 deaths, accurate as of May 25, 2020.[3] Recent reports have described neurologic manifestations of COVID-19, including acute ischemic stroke.[4-6] Some of the proposed mechanisms underlying the increased prevalence of cardiovascular disease in COVID-19 include widespread systemic inflammatory and cytokine responses, diffuse intravascular coagulation, atherosclerotic plaque rupture, and hemodynamic alterations.[7-10]

The latest publications by professional societies, including the Society of NeuroInterventional Surgery and the European Society of Minimally Invasive Neurological Therapy, stress the need for maintenance of services providing emergent mechanical thrombectomy (MT) in patients with cerebral large-vessel occlusion.[11-13] The time-critical nature of MT precludes awaiting the results of any COVID-19 reverse transcriptase–polymerase chain reaction (RT-PCR) swab test, which, at present, can take up to 24 hours and has a false-negative rate, which currently mandates retesting to confirm negative status.

Received May 29, 2020; accepted after revision July 2.

From the Interventional Neuroradiology Department (P.S.D., R.L., S.N., N.M., W.I.), Queen's Medical Centre, Nottingham University Hospitals National Health Service Trust, Nottingham, UK; Cardiothoracic Radiology Department (K.P.) and Stroke Medicine Department (G.S.), Nottingham City Hospital, Nottingham University Hospitals National Health Service Trust, Nottingham, UK.

Please address correspondence to Permesh Dhillon, MD, Interventional NeuroRadiology Department, B Floor, Queens Medical Centre, Derby Road, Nottingham University Hospitals NHS Trust, Nottingham, NG7 2UH, United Kingdom; e-mail: permesh.dhillon@nhs.net

Indicates open access to non-subscribers at www.ajnr.org
Indicates article with supplemental on-line appendix.

http://dx.doi.org/10.3174/ajnr.A6754

Table 1: COVID-19 pneumonia imaging classification according to the CT findings[a]

COVID-19 Pneumonia Imaging Classification	Rationale	CT Findings
Typical appearance	Commonly reported imaging features of greater specificity for COVID-19 pneumonia	Peripheral, bilateral GGOs with or without consolidation or visible intralobular lines (crazy-paving) Multifocal GGOs of rounded morphology with or without consolidation or visible intralobular lines (crazy-paving) Reverse halo sign or other findings of organizing pneumonia (seen later in the disease)
Indeterminate	Nonspecific imaging features of COVID-19 pneumonia	Absence of typical features AND Presence of multifocal, diffuse, perihilar, or unilateral GGO with or without consolidation lacking a specific distribution; they are nonrounded or nonperipheral Few very small GGOs with a nonrounded and nonperipheral distribution
Negative	Uncommonly or not reported features of COVID-19 pneumonia	Absence of typical or indeterminate features AND Presence of isolated lobar or segmental consolidation without GGO Discrete small nodules (centrilobular, tree-in-bud sign) Lung cavitation Smooth interlobular septal thickening with pleural effusion OR no abnormal findings

Note:—GGO indicates ground glass opacity.

[a] Adapted from the proposed Radiological Society of North America and British Society of Thoracic Imaging chest CT classification for reporting of COVID-19 pneumonia.[15,16]

Patients with SARS-Cov-2 infection may be symptomatic or asymptomatic. Patients with acute ischemic stroke may not be able to provide a reliable clinical history or screening information due to underlying dysphasia or impaired consciousness. Additionally, family members may not be present to provide corroborating histories at the point of admission due to ongoing isolation and social distancing measures.

In combination, establishing COVID-related risks in this population is challenging. MT networks have to adopt a strategy for COVID-19 risk stratification to ensure the safety of healthcare professionals and other patients at the primary stroke centres (PSC), during inter-hospital ambulance transfer and during admission at the tertiary neuroscience unit.

A similar strategy is also required to select the intra-procedural anaesthetic technique, location of post-anaesthetic recovery and determine whether step-down care should be to a dedicated COVID-19 or non-COVID-19 ward. A pragmatic and rapid initial COVID-19 screening process within the PSC assists efficient use of personal protective equipment (PPE) and direction along the appropriate care pathway.

Herein, we describe our experience in a regional neuroscience center (Nottingham University Hospitals NHS Trust) that receives MT referrals from 6 PSCs, in implementing a coordinated regional approach to screening patients for both large-vessel occlusion and imaging evidence of COVID-19. We also undertook a retrospective review of the thoracic imaging to identify pulmonary and cardiovascular findings of clinical relevance.

MATERIALS AND METHODS

Study Population

This study was registered with and approved by the audit committee of the hospital board, and individual patient consent was waived. We reviewed our prospectively collated data base of all hyperacute ischemic stroke referrals for consideration of MT between April 14, 2020 and May 21, 2020. Eligible patients were accepted for MT treatment based on local guidelines adapted from the National Institute of Clinical Excellence guidance.[14]

Following a regional protocol established before the pandemic, all hyperacute stroke referrals presenting with a suspected large-vessel occlusion within 24 hours of symptom onset routinely undergo an unenhanced CT of the head and dual-phase CT angiography from the aortic arch to the skull vertex. Following agreement with all referring PSCs, a chest CT was added to this protocol, to image the thorax. Referred patients being treated for COVID-19 during admission and those who had been tested within 48 hours before the referral did not warrant a chest CT.

Chest CT Parameters. Chest CT images were obtained on a Somatom Definition AS or AS Plus, 64- or 128-section multidetector CT system (Siemens) at our institution. The scan range was from the lung apices to the diaphragms immediately following acquisition of the dual-phase CT angiogram from the aortic arch to the skull vertex. We used the following reference acquisition parameters: tube voltage = 120 kV, tube current = 70 mAs, 0.5-second helical rotation time, and 1.2 helical pitch. The reconstructed axial CT section thickness was 1 mm, and further sections were reconstructed in the axial, coronal, and sagittal planes of 2-mm section thickness at 2-mm increments. The effective radiation dose calculated from the total dose-length product and the additional time incurred from completion of the dual-phase CT angiography to completion of the chest CT were obtained from the radiologic information system. There were variations of the scanner models and acquisition parameters across the regional hospitals.

CT Reporting

All images were reviewed by a neuroradiologist while considering the referral for MT. Chest CT findings were promptly reported by radiologists at the referring institutions to ensure optimization of detection and interpretation of findings, which may be subtle in early disease. The Radiological Society of North America and

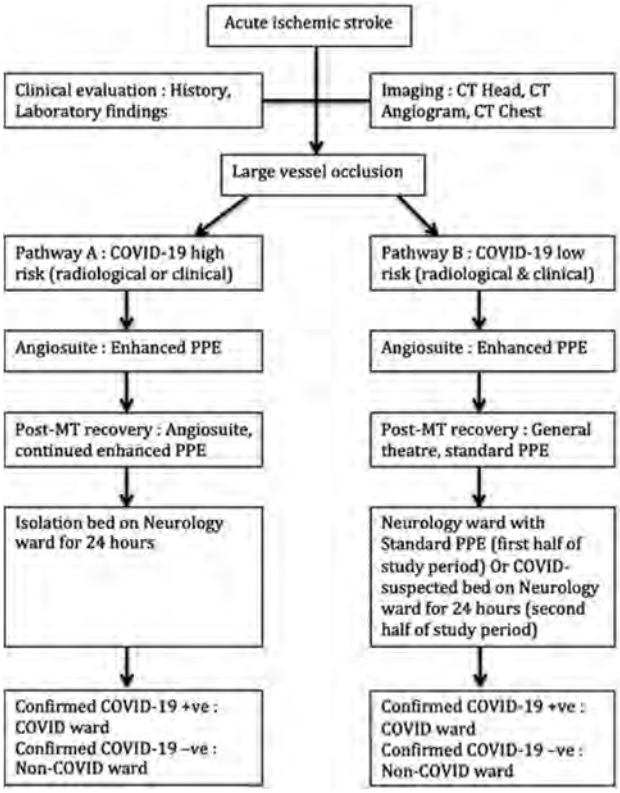

FIG 1. Comparison of the patient pathways according to the COVID-19 risk. High risk for COVID-19 on admission included typical or indeterminate pulmonary findings on the chest CT and/or any clinical suspicion. Low risk for COVID-19 included atypical or normal findings on the chest CT and no clinical suspicion. Enhanced PPE indicates filtering facepiece class 3 masks, visors, and long-sleeved fluid-repellent overalls. Standard PPE indicates fluid-resistant surgical masks, gloves, and aprons; −ve, negative; +ve, positive.

the British Society of Thoracic Imaging publications of pulmonary findings in COVID-19 were used as a guide for the reviewing radiologist (Table 1).[15,16] The thoracic imaging was then retrospectively reviewed by a cardiothoracic radiologist to audit thoracic CT findings using the British Society of Thoracic Imaging standardized evaluation to assess the presence and extent of COVID or other lung diseases. Rapid image transfer was enabled by the regional PACS network. All chest CT reports were reviewed on the local and regional PACS servers to identify the incidence of typical and indeterminate pulmonary features (deemed positive) or atypical and normal findings (deemed negative) for COVID-19. Discrepancies between the original thoracic CT reports and the retrospective review were communicated with the referring centers with further discussion planned at our local discrepancy meeting.

Patient Pathway and Management

Patients or their family members, if present and able, were asked a series of screening questions related to potential COVID-19 infection, and pertinent laboratory findings, including lymphopenia, were used while the patient was being worked-up for a potential MT (On-line Appendix). At the beginning of the study period, only patients who had any symptoms or pulmonary radiologic findings suspicious for COVID-19 underwent a nasopharyngeal or oral swab test. However, in the second half of the study period, all admitted patients underwent a swab test due to the gradually increasing availability of the test kits. The RT-PCR results were subsequently identified on the local institutions' clinical results reporting system, usually available within 24 hours. All patients accepted for MT were then transferred directly to our angiography suite for the procedure. Enhanced precautions were taken by all health care staff during the ambulance transfer and preparation of the angiography suite, peri- and intraprocedurally, particularly if any patient had suspected symptoms and/or had any typical or indeterminate radiologic findings of COVID-19 (Fig 1). Any suspicion of COVID-19 played a factor in the decision for procedures to be performed under conscious sedation or local or general anesthetic, made collaboratively by the interventional neuroradiologist and anesthetist. Intubation and extubation were performed within the negative pressure angiography suite. In view of the time pressures, the essential MT team members were locked in the angiography suite to avoid further delay associated with the mandated air exchange (between 10 and 30 minutes) after intubation. Appropriate deep cleaning and decontamination of the angiography suite were completed between cases. After MT, any patient with clinical and/or imaging features suspicious for COVID-19 was managed with additional precautions, with immediate post-general anesthetic recovery within the angiography suite as per institutional policy, which could take up to 2 hours. The patient was thereafter transferred to a dedicated COVID-19 bed according to our local protocol until he or she was fully worked-up clinically. In the latter half of the study period, separate COVID-19–proved beds and COVID-19–suspected beds were established, and patients were transferred to the appropriate beds according to their known COVID-19 status at the time.

Standard data and statistical analysis was performed using GraphPad Prism (GraphPad Software).

RESULTS

Since the implementation of the revised imaging protocol during the study period, we received 49 MT referrals and performed 13 MTs. The mean age of all patients was 73.1 ± 13.1 years, with an age range of 52–102 years, with 25 men and 24 women. Among the patients undergoing MT, none had imaging features typical of COVID-19, while 3 patients had pulmonary changes indeterminate for COVID-19 but eventually tested negative. Two further patients had only clinical suspicion for COVID-19. All 5 patients were managed according to pathway A as described in Fig 1. The remaining 8 patients had no suspicious CT features and were not diagnosed with or suspected of having COVID-19 (managed according to pathway B). Different levels of PPE (enhanced PPE in high-risk patients and standard PPE in low-risk patients) were used during postanesthetic and ward care according to the COVID-19 risk.

Of the 36 patient referrals declined for MT, 2 patients had typical COVID-19 pulmonary features and tested positive, while 4 patients had indeterminate imaging findings and subsequently tested negative (Figs 2 and 3). The others had normal or atypical changes and were not diagnosed with or suspected of having

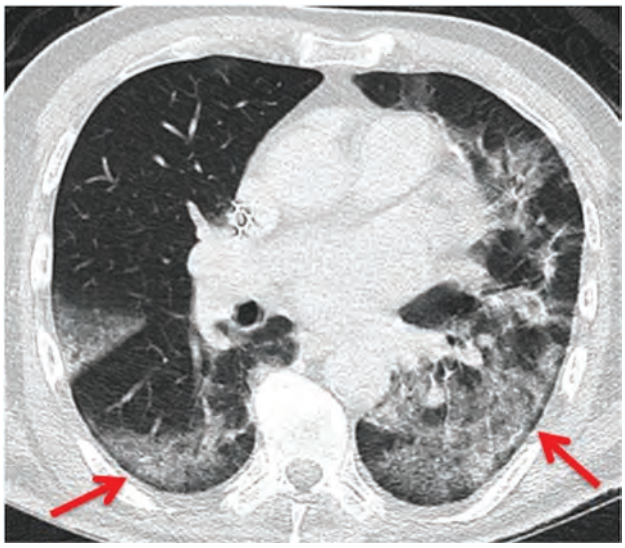

FIG 2. Typical features of COVID-19 pneumonia. Axial CT images at the level of the hilum show bilateral ground glass opacities (*arrows*) with areas of lobular sparing and sparing of the immediate subpleural area. This patient tested positive by RT-PCR analysis.

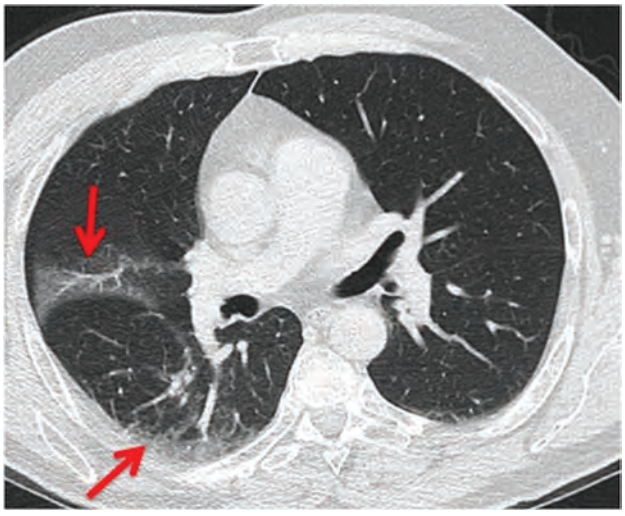

FIG 3. Indeterminate features of COVID-19 pneumonia. Axial CT images show unilateral, localized, peripheral ground glass opacities (*arrows*). This patient tested negative for COVID-19 by RT-PCR analysis.

COVID-19. Nine patients did not undergo a chest CT (tested/diagnosed negative during or just before admission).

There was an overall sensitivity of 100%, specificity of 74.1%, negative predictive value of 100%, and positive predictive value of 22.2% when using chest CT to diagnose COVID-19 in comparison with the RT-PCR test (Table 2). The mean additional time incurred for the chest CT was 184 ± 65.5 seconds (range, 45–337 seconds). The average added effective radiation dose from the extension of the chest CT was 2.47 ± 1.03 mSv.

There was good corroboration of the COVID-19 classification between general radiologists as primary reporters at the PSCs and the cardiothoracic radiologist. Only 1 case of indeterminate pulmonary features was more definitively labeled as typical, and 1 case of atypical findings was labeled as indeterminate by the cardiothoracic radiologist (Table 3). Multiple pulmonary and cardiovascular incidental findings, dichotomized according to clinical relevance, were identified following retrospective review of the thoracic imaging (Table 4).

Table 2: Correlation between chest CT features and RT-PCR swab results for the diagnosis of COVID-19 pneumonia[a]

	RT-PCR +ve	RT-PCR −ve
Chest CT +ve	2[a]/0[b]	6[a]/1[b]
Chest CT -ve	0[a]/0[b]	8[a]/1[b]

Note:—−ve indicates negative; +ve, positive.
[a] Clinical suspicion.
[b] Asymptomatic for COVID-19 pneumonia.

Table 3: Comparison of classification of COVID-19 pulmonary findings between the primary reporter (general radiologist at primary stroke centers) and secondary reviewer (cardiothoracic radiologist) according to the adapted RSNA and BSTI guidance

COVID-19 Pneumonia Imaging Classification	Primary Reporter (*n* = Patients)	Secondary Reviewer (*n* = Patients)
Typical	2	3
Indeterminate	7	7
Negative (atypical or normal)	29	28

Note:—BSTI indicates British Society of Thoracic Imaging; RSNA, Radiological Society of North America.

DISCUSSION

This study describes the feasibility and outcome of implementing a modified imaging algorithm by the inclusion of a chest CT in the work-up of hyperacute stroke referrals for MT across a network of PSCs. Incidental thoracic findings of clinical relevance were also detected in this elderly cohort of patients with cardiovascular disease.

The recent publications from professional societies and review articles have suggested the possibility of inclusion of a complete chest CT in the scanning algorithm, but none have reported the value of it in a regional MT cohort.[11-13,17,18] Kwee et al[19] reported a series of incidental COVID-19 pulmonary findings in a small mixed cohort of patients presenting with acute ischemic stroke and head trauma. However, the incurred radiation dose and time of performing the additional chest CT could not be gleaned from their study.

Yang et al[20] included chest CT in their local institution's COVID-19 screening and took enhanced precautions for COVID-19 MT patients, which resulted in overall delays of hospital arrival to puncture time in the MT cohort during the pandemic compared to a pre-pandemic period. In contrast to our study, we describe an attainable approach taken when faced with the additional challenge of implementing the revised triaging algorithm across all referring PSCs to avoid further delays on arrival at our neuroscience tertiary center.

The sensitivity, specificity, and negative predictive values reported are encouraging in our patient cohort and lend some support to findings from previous studies that have reported the

Table 4: List of incidental findings identified on review of the thoracic imaging in this cohort, summarized according to their clinical relevance

Incidental Pulmonary/CVS Findings of Substantial Clinical Relevance (n = Patients)	Incidental Pulmonary/CVS Findings of Indeterminate Clinical Relevance (n = Patients)
Lung malignancy/suspicious nodule[2]	Emphysema[4]
Pulmonary edema[4]	Lung fibrosis/pneumoconiosis[3]
Left ventricular thrombus/aneurysm[2]	Ascending aortic dilation[2]
Left atrial dilation: anterior-posterior diameter >45 mm[16]	

Note:—CVS indicates cardiovascular.

potential benefit of chest CT in identifying features of COVID-19.[21-23] The poor positive predictive value of chest CT in our study is in line with previously reported studies.[19,22] Chest CT has a high sensitivity for COVID-19 pneumonia, but its low-to-moderate specificity and positive predictive value preclude its use as a stand-alone screening tool for COVID-19 according to the recommendations by the Radiological Society of North America, the American College of Radiology, and the British Society of Thoracic Imaging.[15,24] While the aim of this study was not to assess the use of chest CT as a stand-alone screening tool for COVID-19, chest CT may provide useful additional information in the context of time-critical interventions when the available clinical history may be limited and a COVID-19 lab test result is not available. Recent reports have described the need to ration PPE usage due to a global shortage in PPE supply.[25] Furthermore, the lack of high sensitivity and specificity of the currently available tests, the extended turnaround time of obtaining these results, the lengthy postanesthesia recovery within the angiography suite, the decontamination procedure in patients with suspected COVID-19, and the shortage of critical care or isolation beds remain a challenge with a noticeable impact on health care and interventional services at our institution. Careful consideration of anesthetic choice should also be made due to the risks of airway intubation as an aerosol-generating procedure during general anesthesia, which is commonly used in MT cases.[26] Hence, the addition of a screening chest CT during the work-up for emergent procedures, such as MT, may be of benefit in risk-stratifying this cohort of patients.[27]

The mean added time incurred with the inclusion of the chest CT was approximately 3 minutes in our study, which is in line with the proposed algorithm by Nguyen et al[12] to consider chest CT if it did not incur more than a 5-minute delay to treatment. The mean radiation dose of 2.47 mSv for the chest CT reported in our study falls below the average annual radiation dose per person in the UK of 2.7 mSv/person/annum.[28] The small addition of the radiation dose and scanning time incurred may be outweighed by the potential benefits of the outreaching effects on the patient management and safety of the involved health care staff.

In our study, no patient accepted for MT had typical radiologic findings or tested positive for COVID-19, while the minority of patients who had indeterminate radiologic findings or clinical suspicion for COVID-19 and those who did not have any suspicion for COVID-19, either symptomatically or radiologically, were managed according to our locally recommended PPE usage (detailed in the Fig 1 legend). Not all asymptomatic patients with normal imaging features were subsequently tested for COVID-19, particularly if they did not demonstrate an inflammatory response in their blood profile or have symptoms during admission, due to the limited availability of testing kits at the beginning of the study period. Hence, while unlikely, we cannot completely exclude the possibility that some of the aforementioned group of patients may be carriers of the SARS-CoV-2 virus.

The low incidence of patients with COVID-19 presenting with acute ischemic stroke symptoms during the study period could be due to the inclusion of asymptomatic patients, and the geographic variation in the rates of infection across our multiple localities compared with the more densely populated and highly endemic cities where increased infection rates have been reported.[19,29] Nevertheless, the use of the suggested imaging algorithm is feasible and may be of further benefit in more endemic areas, where rapid COVID-19 testing kits are not available in the MT patient pathway. Kihira et al[29] described incidental lung apical findings in patients with suspected COVID-19 during their routine imaging work-up using CT angiograms from the aortic arch for acute stroke presentations. However, as evidenced in previous studies, there is a possibility of missing a proportion of pulmonary findings that may only be prevalent in the mid to lower lung lobes, which are not covered in the routine imaging protocol.[24,30]

Following retrospective review of the thoracic imaging, multiple incidental findings were identified, which highlight the range of comorbidities present in a cohort of elderly patients with cardiovascular disease. In particular, we identified potential cardiac causes for underlying large-vessel occlusion, such as a left ventricular thrombus, as well as left atrial enlargement, known to be strongly associated with cardiac dysfunction and atrial fibrillation.[31,32] Knowledge of these risk factors may be a factor that alters post-MT care or secondary prevention. Only half of these patients had known underlying cardiac disease such as cardiac failure, previous myocardial infarction, or atrial fibrillation. A proportion of findings also included pulmonary edema and cardiac failure, which may factor in decisions for the anesthetic choice in MT. Finally, a minority of patients had suspicious findings for underlying lung malignancy, which may have implications on their overall prognosis. There was minimal variation in the retrospective review of COVID-19 findings by the cardiothoracic radiologist and the primary reporters, which suggests satisfactory reporting of the COVID-19 classification with implications on the risk stratification across various PSCs.

Limitations of this study include its retrospective review and the inclusion of a relatively small cohort of patients. Additionally, this study only included patients referred with suspected large-vessel occlusion for potential MT and does not encompass all acute suspected stroke referrals. RT-PCR testing of oro- or nasopharyngeal swabs was deemed the criterion standard for the diagnosis of COVID-19 in this study, despite known variations in its sensitivity.[33] Also, there are limitations to the accuracy of chest CT in detecting COVID-19 in symptomatic and asymptomatic

patients. Hence, correlation with the clinical findings, blood biomarkers, and RT-PCR results, whenever available, remains essential. Furthermore, there were variations in clinical practice during the study period due to changing local availability of and guidance on the PPE use, COVID-19 testing, and intensive care or ventilated beds. The COVID-19 status and the availability of ventilated beds also impacted the decision to accept MT referrals in elderly patients (older than 70 years of age) presenting with large-vessel occlusion during the study.

CONCLUSIONS

For patients being referred for time-critical MT procedures in whom a reliable clinical history may not be available, chest CT provides a pragmatic, rapid additional tool that assists COVID-19 risk stratification, and its inclusion in a standardized stroke imaging protocol across our network of PSCs has enabled efficient use of hospital resources with minimal compromise or delay to the overall patient journey. The prevalence of incidental thoracic findings of clinical relevance in this patient cohort may be of benefit in the decision-making for future MT referrals and postprocedural care.

ACKNOWLEDGMENTS

We would like to thank the stroke, neurology, and radiology teams at the Nottingham University Hospitals National Health Service Trust, University Hospitals of Leicester National Health Service Trust, University Hospitals of Derby and Burton National Health Service Foundation Trust, Sherwood Forest Hospitals National Health Service Foundation Trust, and United Lincolnshire Hospitals National Health Service Trust.

Disclosures: Kate Pointon—*UNRELATED*: *Employment*: Nottingham University Hospital; *Expert Testimony*: legal reports; *Royalties*: chest x-ray educational book. Robert Lenthall—*UNRELATED*: *Expert Testimony*: Parliamentary Health Service Ombudsman, National Institute of Clinical Excellence, *Comments*: external advisor to the Parliamentary Health Service Ombudsman, expert advisor to National Institute of Clinical Excellence; *Payment for Development of Educational Presentations* paid to an individual: faculty member for The European Course in Minimally Invasive Neurological Therapy; *Travel/Accommodations/Meeting Expenses Unrelated to Activities Listed*: frequent recipient of expenses, *Comments*: personal expenses from many device manufacturers to support attendance at meetings during the past 2 decades, benefit from funding to professional interest groups to support such meetings; *Other*: past recipient of educational grants, *Comments*: In the past, Nottingham University Hospitals has received grants from MicroVention and Cordis Neurovascular to support an interventional neuroradiology fellowship training post, no current funding.* Norman McConachie—*UNRELATED*: *Consultancy*: MicroVention, *Comments*: for educational activity; *Payment for Lectures Including Service on Speakers Bureaus*: Stryker; *Travel/Accommodations/Meeting Expenses Unrelated to Activities Listed*: MicroVention. Wazim Izzath—*UNRELATED*: *Payment for Lectures Including Service on Speakers Bureaus*: Stryker, *Comments*: educational consultancy. *Money paid to the institution.

REFERENCES

1. Huang C, Wang Y, Li X, et al. **Clinical features of patients infected with 2019 novel coronavirus in Wuhan, China.** *Lancet* 2020;395:497–506 CrossRef Medline
2. **WHO Director-General's opening remarks at the media briefing on COVID-19 - 11 March 2020.** https://www.who.int/emergencies/diseases/novel-coronavirus-2019/interactive-timeline#event-71. Accessed May 22, 2020
3. Coronavirus (COVID-19) in the UK. https://coronavirus.data.gov.uk/ - category=regions&map=rate. Accessed May 22, 2020
4. Li Y, Wang M, Zhou Y, et al. **Acute cerebrovascular disease following COVID-19: a single center, retrospective, observational study.** *Stroke Vasc Neurol* 2020 Jul 2. [Epub ahead of Print] CrossRef Medline
5. Oxley TJ, Mocco J, Majidi S, et al. **Large-vessel stroke as a presenting feature of Covid-19 in the young.** *N Engl J Med* 2020;382:e60 CrossRef Medline
6. Goldberg MF, Goldberg MF, Cerejo R, et al. **Cerebrovascular disease in COVID-19.** *AJNR Am J Neuroradiol* 2020;41:1170–72 CrossRef Medline
7. Lillicrap D. **Disseminated intravascular coagulation in patients with 2019-nCoV pneumonia.** *J Thromb Haemost* 2020;18:786–87 CrossRef Medline
8. Klok FA, Kruip M, van der Meer NJM, et al. **Incidence of thrombotic complications in critically ill ICU patients with COVID-19.** *Thromb Res* 2020;191:145–47 CrossRef Medline
9. Smeeth L, Thomas SL, Hall AJ, et al. **Risk of myocardial infarction and stroke after acute infection or vaccination.** *N Engl J Med* 2004;351:2611–18 CrossRef Medline
10. Mehta P, McAuley DF, Brown M, et al; HLH Across Speciality Collaboration, UK. **COVID-19: consider cytokine storm syndromes and immunosuppression.** *Lancet* 2020;395:1033–34 CrossRef Medline
11. Fraser JF, Arthur AS, Chen M, et al. **Society of NeuroInterventional Surgery recommendations for the care of emergent neurointerventional patients in the setting of Covid-19.** *J Neurointerv Surg* 2020;12:539–41 CrossRef Medline
12. Nguyen TN, Abdalkader M, Jovin TG, et al. **Mechanical thrombectomy in the era of the COVID-19 pandemic: emergency preparedness for neuroscience teams: a guidance statement from the Society of Vascular and Interventional Neurology.** *Stroke* 2020;51:1896–1901 CrossRef Medline
13. Aggour M, White P, Kulcsar Z, et al. **European Society of Minimally Invasive Neurological Therapy (ESMINT) recommendations for optimal interventional neurovascular management in the COVID-19 era.** *J Neurointerv Surg* 2020;12:542–44 CrossRef Medline
14. **Stroke and transient ischaemic attack in over 16s: diagnosis and initial management 2019.** https://www.nice.org.uk/guidance/ng128. Accessed May 22, 2020
15. Simpson S, Kay FU, Abbara S, et al. **Radiological Society of North America Expert Consensus Statement on Reporting Chest CT Findings Related to COVID-19: Endorsed by the Society of Thoracic Radiology, the American College of Radiology, and RSNA.** *J Thorac Imaging* 2020;35:219–27 CrossRef Medline
16. **BSTI CT reporting proforma: COVID-19 Version 2 13.04.2020.** https://www.bsti.org.uk/media/resources/files/BSTI_COVID_CT_Proforma_v2_13.04.2020.pdf. Accessed May 22, 2020
17. Leslie-Mazwi TM, Fargen KM, Levitt M, et al. **Preserving access: a review of stroke thrombectomy during the COVID-19 pandemic.** *AJNR Am J Neuroradiol* 2020;41:1136–41 CrossRef Medline
18. Smith MS, Bonomo J, Knight WA, et al. **Endovascular therapy for patients with acute ischemic stroke during the COVID-19 pandemic: a proposed algorithm.** *Stroke* 2020;51:1902–09 CrossRef Medline
19. Kwee RM, Krdzalic J, Fasen B, et al; COVID-19 CT Investigators South-East Netherlands (CISEN) Study Group. **CT scanning in suspected stroke or head trauma: is it worth to go the extra mile and include the chest to screen for COVID-19 infection?** *AJNR Am J Neuroradiol* 2020;41:1165–69 CrossRef Medline
20. Yang B, Wang T, Chen J, et al. **Impact of the COVID-19 pandemic on the process and outcome of thrombectomy for acute ischemic stroke.** *J Neurointerv Surg* 2020;12:664–68 CrossRef Medline
21. Dangis A, Gieraerts C, Bruecker YD, et al. **Accuracy and reproducibility of low-dose submillisievert chest CT for the diagnosis of COVID-19.** *Radiology: Cardiothoracic Imaging* 2020;2:e200196 CrossRef
22. Ai T, Yang Z, Hou H, et al. **Correlation of chest CT and RT-PCR testing in coronavirus disease 2019 (COVID-19) in China: a report of 1014 cases.** *Radiology* 2020;296:E32–40 CrossRef Medline

23. Fang Y, Zhang H, Xie J, et al. **Sensitivity of chest CT for COVID-19: comparison to RT-PCR.** *Radiology* 2020;296:E115–17 CrossRef Medline
24. Kim H, Hong H, Yoon SH. **Diagnostic; performance of CT and reverse transcriptase-polymerase chain reaction for coronavirus disease 2019: a meta-analysis.** *Radiology* 2020 Apr 17. [Epub ahead of Print] CrossRef Medline
25. Emanuel EJ, Persad G, Upshur R, et al. **Fair allocation of scarce medical resources in the time of Covid-19.** *N Engl J Med* 2020;382:2049–55 CrossRef Medline
26. Flexman AM, Abcejo AS, Avitsian R, et al. **Neuroanesthesia practice during the COVID-19 pandemic: recommendations from Society for Neuroscience in Anesthesiology & Critical Care (SNACC).** *J Neurosurg Anesthesiol* 2020;32:202–09 CrossRef Medline
27. Qureshi AI, Abd-Allah F, Alsenani F, et al. **Management of acute ischemic stroke in patients with COVID-19 infection: report of an international panel.** *Int J Stroke* 2020;15:540–54 CrossRef Medline
28. Public Health England. **Ionising Radiation Exposure of the UK Population: 2010 Review.** https://www.phe-protectionservices.org.uk/cms/assets/gfx/content/resource_3595csc0e8517b1f.pdf. Accessed May 22, 2020
29. Kihira S, Schefflein J, Chung M, et al. **Incidental COVID-19 related lung apical findings on stroke CTA during the COVID-19 pandemic.** *J Neurointerv Surg* 2020;12:669–72 CrossRef Medline
30. Wong HY, Lam HY, Fong AH, et al. **Frequency and distribution of chest radiographic findings in COVID-19 positive patients.** *Radiology* 2020;296:E72–78 CrossRef Medline
31. Stolzmann P, Scheffel H, Leschka S, et al. **Reference values for quantitative left ventricular and left atrial measurements in cardiac computed tomography.** *Eur Radiology* 2008;18:1625–34 CrossRef Medline
32. Takx RA, Vliegenthart R, Schoepf UJ, et al. **Prognostic value of CT-derived left atrial and left ventricular measures in patients with acute chest pain.** *Eur J Radiol* 2017;86:163–68 CrossRef Medline
33. Winichakoon P, Chaiwarith R, Liwsrisakun C, et al. **Negative nasopharyngeal and oropharyngeal swabs do not rule out COVID-19.** *J Clin Microbiol* 2020;58:e00297-20 CrossRef Medline

Antiplatelet Management for Stent-Assisted Coiling and Flow Diversion of Ruptured Intracranial Aneurysms: A DELPHI Consensus Statement

J.M. Ospel, P. Brouwer, F. Dorn, A. Arthur, M.E. Jensen, R. Nogueira, R. Chapot, F. Albuquerque, C. Majoie, M. Jayaraman, A. Taylor, J. Liu, J. Fiehler, N. Sakai, K. Orlov, D. Kallmes, J.F. Fraser, L. Thibault, and M. Goyal

ABSTRACT

BACKGROUND AND PURPOSE: There is a paucity of data regarding antiplatelet management strategies in the setting of stent-assisted coiling/flow diversion for ruptured intracranial aneurysms. This study aimed to identify current challenges in antiplatelet management during stent-assisted coiling/flow diversion for ruptured intracranial aneurysms and to outline possible antiplatelet management strategies.

MATERIALS AND METHODS: The modified DELPHI approach with an on-line questionnaire was sent in several iterations to an international, multidisciplinary panel of 15 neurointerventionalists. The first round consisted of open-ended questions, followed by closed-ended questions in the subsequent rounds. Responses were analyzed in an anonymous fashion and summarized in the final manuscript draft. The statement received endorsement from the World Federation of Interventional and Therapeutic Neuroradiology, the Japanese Society for Neuroendovascular Therapy, and the Chinese Neurosurgical Society.

RESULTS: Data were collected from December 9, 2019, to March 13, 2020. Panel members achieved consensus that platelet function testing may not be necessary and that antiplatelet management for stent-assisted coiling and flow diversion of ruptured intracranial aneurysms can follow the same principles. Preprocedural placement of a ventricular drain was thought to be beneficial in cases with a high risk of hydrocephalus. A periprocedural dual, intravenous, antiplatelet regimen with aspirin and a glycoprotein IIb/IIIa inhibitor was preferred as a standard approach. The panel agreed that intravenous medication can be converted to oral aspirin and an oral P2Y12 inhibitor within 24 hours after the procedure.

CONCLUSIONS: More and better data on antiplatelet management of patients with ruptured intracranial aneurysms undergoing stent-assisted coiling or flow diversion are urgently needed. Panel members in this DELPHI consensus study preferred a periprocedural dual-antiplatelet regimen with aspirin and a glycoprotein IIb/IIIa inhibitor.

ABBREVIATION: GPIIb/IIIa = glycoprotein IIb/IIIa receptor

Received May 13, 2020; accepted after revision June 30.

From the Departments of Clinical Neurosciences (J.M.O., M.G.) and Diagnostic Imaging (M.G.), University of Calgary, Calgary, Alberta, Canada; Department of Radiology (J.M.O.), University Hospital of Basel, Basel, Switzerland; Department of Interventional Neuroradiology (P.B.), Karolinksa Hospital, Stockholm, Sweden; University NeuroVascular Center (P.B.), Leiden University Medical Center, Haaglanden Medical Center, Leiden, the Netherlands; Institute of Neuroradiology (F.D.), University of Bonn, Bonn, Germany; Department of Neurosurgery (A.A.), Semmes-Murphey Clinic/University of Tennessee, Memphis, Tennessee; Departments of Neurological Surgery, Radiology and Medical Imaging (M.E.J.), University of Virginia Health, Charlottesville, Virginia; Marcus Stroke & Neuroscience Center (R.N.), Grady Health System, Atlanta, Georgia; Department of Neurology (R.N.), Emory University School of Medicine, Atlanta, Georgia; Department of Neuroradiology (R.C.), Alfred Krupp Krankenhaus Essen, Essen, Germany; Department of Neurosurgery (F.A.), Barrow Neurological Institute, Phoenix, Arizona; Department of Radiology (C.M.), Academic Medical Center, Amsterdam, the Netherlands; Departments of Diagnostic Imaging, Neurology, and Neurosurgery (M.J.), Warren Alpert School of Medicine at Brown University, Providence, Rhode Island; Groote Schuur Hospital (A.T.), University of Cape Town, Cape Town, South Africa; Department of Neurosurgery (J.L.), Changhai Hospital Naval Medical University, Shanghai, China; Department of Diagnostic and Interventional Neuroradiology (J.F.), University Medical Center Hamburg-Eppendorf, Hamburg, Germany; Department of Neurosurgery (N.S.), Kobe City Medical Center General Hospital, Kobe, Japan; Meshalkin National Medical Research Center (K.O.), Novosibirsk, Russian Federation; Department of Radiology (D.K.), Mayo Clinic, Rochester, Minnesota; Departments of Neurosurgery, Neurology, Radiology, and Neuroscience (J.F.F.), University of Kentucky, Lexington, Kentucky; and Member of the Scientific Committee of the World Federation of Interventional and Therapeutic Neuroradiology (L.T.).

Please address correspondence to Mayank Goyal, MD, Departments of Radiology and Clinical Neurosciences, Foothills Medical Centre, 1403 29th St. NW, Calgary, AB, T2N2T9; e-mail: mgoyal@ucalgary.ca; @johanna_ospel; @mayank_G0

Indicates article with supplemental on-line appendix and table.

Indicates article with supplemental on-line photos.

http://dx.doi.org/10.3174/ajnr.A6814

A growing number of ruptured intracranial aneurysms are treated with endovascular techniques.[1-3] While open surgical techniques remain a viable option for treating ruptured aneurysms, the availability and dissemination of endovascular devices and techniques are increasing. Wide-neck and fusiform aneurysms often require permanent placement of either a stent (ie, stent-assisted coiling) or a flow diverter. However, the increased thrombogenicity of such devices requires dual-antiplatelet therapy. This is less problematic in patients with unruptured intracranial aneurysms; but, in patients with ruptured aneurysms, physicians must weigh the risk of thrombotic complications against the risk of rebleeding. There is a relative paucity of data on antiplatelet management for stent-assisted coiling/flow diversion of ruptured intracranial aneurysms. Antiplatelet regimens reported in the literature vary widely, both for flow diversion[4] and stent-assisted coiling,[3,5-8] and they are based on nonrandomized, retrospective single-center studies. Providing practical guidance for physicians based on the limited available data is challenging and is further complicated by the differences in availability and access to certain antiplatelet agents, dependent on the jurisdiction/region of practice.

Furthermore, platelet-function testing has recently become available in clinical routine, and it has raised hopes for individually tailored and more effective antiplatelet management strategies. Platelet function testing is increasingly used in the elective setting, but its reliability and clinical impact remain controversial.[9,10] A recent meta-analysis on patients treated with flow diversion showed that platelet-function testing is associated with worse rather than improved outcomes,[9] possibly because its results might lead to rapid and haphazard alterations in medication. Platelet-function testing would also introduce additional treatment delays. Its value in the setting of ruptured intracranial aneurysms is, therefore, uncertain.

Whether and when to place a ventricular drain when treating ruptured intracranial aneurysms is another controversial topic, for which there are no uniform recommendations.[4] Some physicians favor a low threshold for preprocedural placement of a ventricular drain because placement in the postprocedural period, after antiplatelet medication has been initiated, is associated with a higher risk of hemorrhagic complications. Others have found no association between the timing of antiplatelet medication in relation to ventricular drain placement and hemorrhagic complications.[11] Given the lack of evidence for antiplatelet management of stent-assisted coiling/flow diversion in ruptured intracranial aneurysms, most physicians extrapolate their experience from unruptured cases and base their management decisions on personal experience and the local circumstances (access to and cost of antiplatelet agents).

MATERIALS AND METHODS

Literature Search

In preparation for the DELPHI process, a MEDLINE literature search of English language articles containing the search terms "antiplatelet," "stent placement," "flow diversion," and "ruptured intracranial aneurysm" was performed for articles from January 2006 to December 2019. Bibliographies of relevant publications were screened to identify further studies of interest. Relevant articles were embedded in the respective survey questions and the full text articles distributed to the panel members. The On-line Table provides an overview of the key studies that were identified and used as a basis for the panel consensus on antiplatelet agents and dosage.

Panel Members and DELPHI Methodology

We formed a panel of 15 neurointerventionalists and used a modified DELPHI approach (https://www.rand.org/topics/delphi-method.html) as an attempt to provide a preliminary framework and practical guidance for antiplatelet management for stent-assisted coiling/flow diversion in ruptured intracranial aneurysms until more data become available that allow evidence-based recommendations. The panel members in this study were experienced neurointerventionalists with high clinical and academic expertise in aneurysm treatment (15 neurointerventionalists affiliated with interventional neuroradiology, neurosurgery, and neurology from 8 countries). A list of the panel members can be found in the On-line Appendix. In addition, a pharmacology expert (L.T.) and an additional neurointerventional consultant with long-standing expertise in endovascular aneurysm treatment (R.C.) were consulted and provided feedback.

DELPHI Methodology

The DELPHI method is a systematic, interactive forecasting method that was originally developed to predict the impact of technology on warfare during the cold war.[12] The underlying assumption is that in the absence of reliable data, forecasts or judgments from a structured, selected panel of experts are more accurate than estimates from individuals or unstructured groups. A selected group of individuals with high expertise in the area of interest undergoes a series of questionnaires with controlled-opinion feedback; the final goal is to reach a group consensus. The method has been successfully implemented in health care research and is often used to standardize patient care in areas with a relative paucity of data until reliable evidence becomes available.[13] In this study, the DELPHI technique was applied to generate a framework for antiplatelet management in the setting of stent-assisted coiling and flow diversion for unruptured intracranial aneurysms, an area in which evidence-based recommendations are not possible due to the limited body of literature. Figure 1 outlines the principal steps of the DELPHI approach as it was performed in this panel.[14]

Data Collection and Analysis

Anonymity was ensured through personalized links sent via an on-line response system (Qualtrics.com), in which panel members responded independent of each other to subsequent iterations of survey rounds. The first round contained exclusively open-ended questions. Answers from this initial round were analyzed in an affinity diagram (On-line Fig 2) and formed the basis for the following rounds, which consisted of closed-ended questions. Results from the previous DELPHI survey round were returned to the group during the next round in the form of statistical summaries, without attributing specific responses

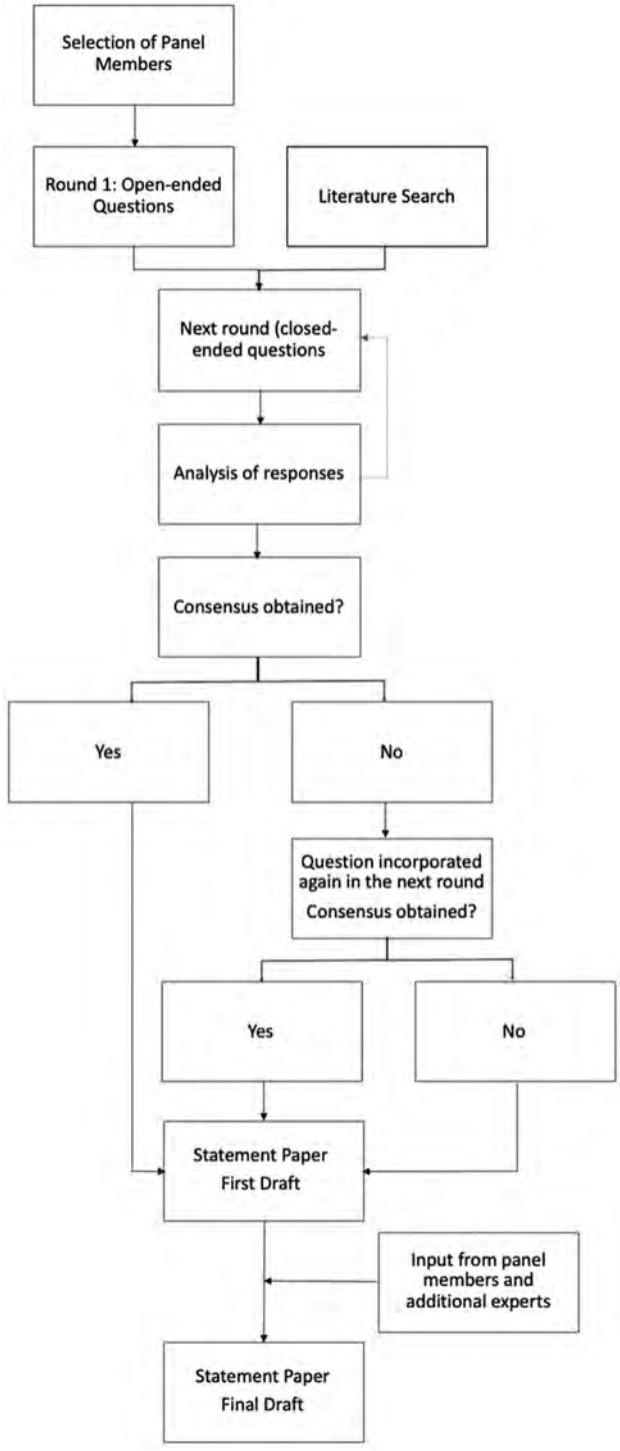

FIG 1. Flow chart of the modified DELPHI process as it was used in this study.

to individuals. At the final stage, group responses were assessed for consensus.

RESULTS

Response data were collected from December 2019 to March 2020. All 15 panel members completed a total of 6 survey rounds. The results were then summarized in a first draft, which was circulated among the panel members and the additional expert for discussion. The received feedback was incorporated in the final statement draft. The statement was endorsed by the World Federation of Interventional and Therapeutic Neuroradiology, the Japanese Society for Neuroendovascular Therapy, and the Chinese Neurosurgical Society.

Preprocedural Management: Ventricular Drains

In line with a recent meta-analysis,[15] panel members agreed that in scenarios with manifest hydrocephalus or a high risk thereof (eg, patients with subarachnoid hemorrhage World Federation of Neurosurgical Societies grade III or higher, Fisher grade 3 or higher, intraparenchymal hemorrhage, Glasgow Coma Scale of $\leq$10), it is worth considering placement of a ventricular drain before the procedure, even if the hydrocephalus is not manifest at the time of decision-making. In cases with no manifest hydrocephalus and a low risk thereof (eg, patients with subarachnoid hemorrhage World Federation of Neurosurgical Societies grade I, Fisher grade 1, Glasgow Coma Scale of 10–15), preprocedural placement of a ventricular drain might not be necessary. No consensus was achieved for cases with an intermediate risk of hydrocephalus (eg, patients with subarachnoid hemorrhage, World Federation of Neurosurgical Societies grade III, Fisher grade 4, Glasgow Coma Scale of 10–15, and small intraparenchymal hemorrhage but no hydrocephalus).

Preprocedural Management: Platelet Function Testing

There was consensus that routine platelet-function testing before the initiation of antiplatelet therapy for stent-assisted coiling/flow diversion of ruptured intracranial aneurysms may not be necessary.

Dual-Antiplatelet Regimen

The panel agreed that antiplatelet management for stent-assisted coiling and flow diversion of ruptured intracranial aneurysms can be identical, and they favored a dual-antiplatelet regimen as a standard approach. Alterations based on device coating were thought to not be necessary because currently available data on antithrombogenic device coatings[16,17] were considered insufficient to justify changes in antiplatelet therapy.

First Antiplatelet Agent

The panel agreed on intravenous aspirin being the first-line agent of choice whenever intravenous aspirin is available as a single 500-mg bolus. In case intravenous aspirin is not available, oral aspirin was thought to be a suitable alternative, with a loading dose of 75–325 mg and a daily maintenance dose of $<$100 mg. The panel members believed that oral aspirin should be administered as soon as possible to maximize the time between administration and deployment of the intravascular device. For patients with reduced levels of consciousness or intubated patients, rectal aspirin (120–300 mg) may be used as an alternative to intravenous aspirin.

Second Antiplatelet Agent

The panel members agreed on a glycoprotein IIb/IIIa receptor (GPIIb/IIIa inhibitor; abciximab, eptifibatide, tirofiban) as the second antiplatelet agent of choice. They favored a dosing scheme

Table 1: Consensus recommendations for the dosage of GPIIb/IIIa receptor inhibitors[18-26]

Agent	Tirofiban	Eptifibatide	Abciximab
Loading dose (IV or IA bolus)	12 mcg/kg for30 min[a]	180 mcg/kg for 1–2 min	0.25 mg/kg
Maintenance dose (if necessary, IV infusion for 12–24 hours)	0.1 mcg/kg/min	2 mcg/min	0.125 mcg/kg/min
Trade name	Aggrastat	Integrilin	ReoPro
Duration of antiplatelet effect	4–8 hours	4 hours	48 hours

Note:—IA indicates intra-arterial.
[a] 0.4 mcg/kg/min.

Table 2: Consensus recommendations for dosing of oral P2Y12 inhibitors in the postprocedural period[24,27]

Agent	Clopidogrel[a]	Ticagrelor	Prasugrel
Loading dose[b]	600 mg	180 mg	40–60 mg
Maintenance dose	75 mg daily	60–90 mg 2×/day	5–10 mg daily
Trade name	Plavix	Brilinta/Brilique	Effient
Onset of action	2 hours	30 min	15–30 min

[a] The panel favored clopidogrel as the oral P2Y12 inhibitor of choice in the postprocedural period after discontinuation of the GPIIb/IIIa inhibitor but acknowledged that in case of known clopidogrel resistance, an alternative P2Y12 inhibitor may be chosen and that evidence from unruptured intracranial aneurysm treatment might suggest a superior safety profile of prasugrel compared with clopidogrel in the acute phase.[28] It was thought that in cases in which ticagrelor was administered in the periprocedural period, it could be continued beyond the periprocedural period, depending on the cost and availability of different agents.
[b] If deemed necessary.

that consists of an initial bolus, followed by an infusion if necessary (see Table 1 for dosing schemes), whereby the choice of the GPIIb/IIIa inhibitor will likely depend on the local availability of certain agents. The panel also acknowledged that with increasing availability of intravenous cangrelor, the periprocedural antiplatelet regimen might change. In case GPIIb/IIIa inhibitors are not available, ticagrelor was favored as an alternative second agent, with an oral loading dose of 180 mg, followed by a twice-daily 60- to 90-mg maintenance dose.

Timing of Device Placement

Panel members agreed that intracranial devices (stents, flow diverters) can probably be placed immediately after antiplatelet therapy has been initiated. Once the intention to treat a patient with a ruptured intracranial aneurysm with stent-assisted coiling or flow diversion is clear, the antiplatelet medication can be initiated immediately. In an optimal scenario, the time gap between administration of an intravenous agent and device placement would be as long or longer than the time to onset of action of the agent. However, the panel agreed that if the time gap is shorter than the time to onset of action, it might be reasonable to proceed with the procedure; a waiting period between administration of the antiplatelet agents and device placement was not considered obligatory in such cases.

Intraprocedural Thrombotic Complications

The panel recommended that any filling defect in a vessel should raise the suspicion of a thrombotic complication and trigger treatment. Intraprocedural thrombotic complications may be managed with intra-arterial or additional intravenous infusion of GPIIb/IIIa inhibitors. At the same time, the panel members acknowledged that the occurrence of thrombotic complications will be very rare with a GPIIb/IIIa inhibitor as 1 of the 3 first-line antiplatelet agents.

Postprocedural Management: Transition to Oral Antiplatelet Agents

There was consensus that the periprocedural intravenous antiplatelet regimen can be converted to an oral regimen within 24 hours after the procedure in patients who can be clinically monitored (in intubated patients, one may consider continuing the intravenous scheme longer because the reliability of oral medication when administered via a nasogastric tube can be poor). Oral aspirin (75- to 325-mg loading dose, followed by a <100-mg daily maintenance dose) can thereby replace intravenous aspirin. The second intravenous agent may be converted to an oral P2Y12 inhibitor (see Table 2 for dosing schemes).

Postprocedural Management: Platelet-Function Testing

Panel members agreed that routine platelet-function testing after stent-assisted coiling/flow diversion for ruptured intracranial aneurysms may not be necessary.

Figure 2 summarizes the panel consensus for antiplatelet management for stent-assisted coiling/flow diversion of ruptured intracranial aneurysms.

DISCUSSION

This DELPHI consensus study identifies current challenges and suggests a possible approach to antiplatelet management for stent-assisted coiling/flow diversion in ruptured intracranial aneurysms until sufficient evidence becomes available, and it encourages further research in this regard. While the DELPHI panel in this study acknowledged the potential advantages of antiplatelet testing, panel members mostly believed that platelet-function testing in its current form may not be necessary, possibly reflecting the lack of standardization and prevailing uncertainty regarding the value of currently available platelet-function tests.[9,10] In fact, a recent meta-analysis showed that platelet-function testing before flow-diverter treatment for intracranial aneurysms in the elective setting might be associated with worse outcomes.[9] There clearly seems to be a need for faster and more standardized platelet-function tests and more reliable data on the clinical impact of the test results for the theoretic benefits to translate into clinical practice. Panel members also believed that antiplatelet management for stent-assisted coiling and flow diversion of ruptured intracranial aneurysms can follow the same principles, most likely because there are currently no studies that suggest otherwise.

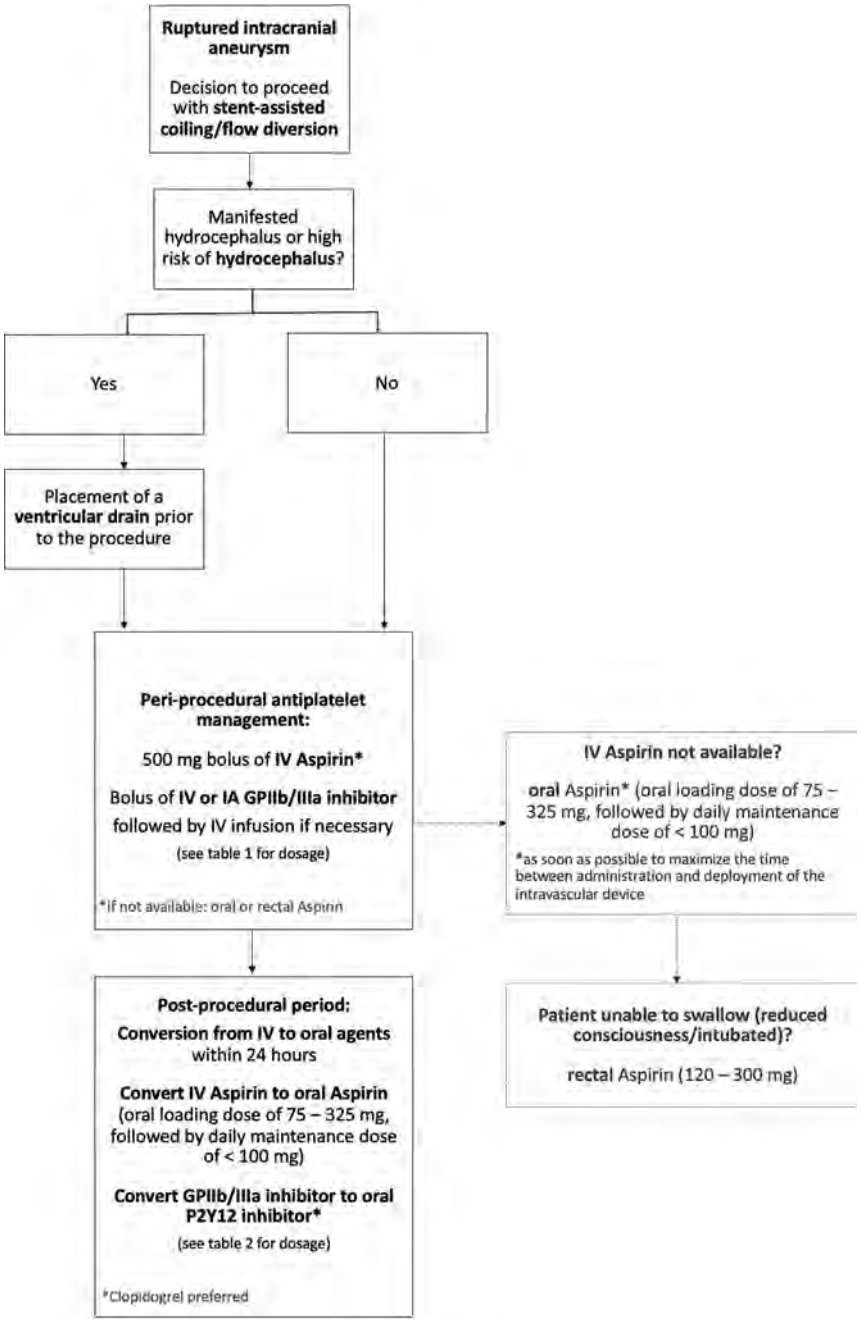

FIG 2. Summary of panel consensus for antiplatelet management for stent-assisted coiling/flow diversion of ruptured intracranial aneurysms.

The metal-coverage of flow diverters is, however, much higher compared with stents, and further research toward device-specific antiplatelet regimens as well as antithrombogenic surface coatings[16,17] should be encouraged. A periprocedural, dual, intravenous, antiplatelet regimen with aspirin and a GPIIb/IIIa inhibitor with conversion to oral aspirin and an oral P2Y12 inhibitor within 24 hours after the procedure was preferred as a standard approach. This regimen is very similar to the management of elective aneurysm treatment with stent-assisted coiling/flow diversion in many places and was probably favored by most panel members due to the lack of large, inclusive studies focusing on patients with ruptured aneurysms. In the latter, conducting studies on antiplatelet therapy is much more difficult due to the emergent nature of the condition, but it would be of high importance to reduce variability and improve safety in antiplatelet management.

Limitations

The results of this study should not be misinterpreted as advocating stent-assisted coiling or flow diversion over surgical clipping, endosaccular treatments, or conservative therapy for any particular patient, nor is it intended to compete with or replace any future evidence-based recommendations. On the contrary, the authors and panel members believe that such data are urgently needed. The relatively low number of panel members could have resulted in personal biases in the presented recommendations, and region-specific

peculiarities, such as limited or no access to certain agents, could not be taken into account. Furthermore, the considerations outlined in this perspective are a snapshot in time, as antiplatelet therapy and neurointerventional devices continue to evolve. With further advances in surface coatings of stents and flow diverters for instance, dual-antiplatelet therapy could soon become obsolete. Last, this DELPHI consensus statement focused on antiplatelet management in the acute phase; thus, considerations on the optimal timing for conversion from intravenous to oral agents were not addressed in depth nor were questions on ventricular drain removal, ventriculoperitoneal/ventriculoatrial shunts, and cases with simultaneous intraparenchymal hemorrhage.

CONCLUSIONS

Studies to determine the optimal antiplatelet regimen for stent-assisted coiling and flow diversion in the setting of ruptured intracranial aneurysms are urgently needed. Panel members in this DELPHI consensus study preferred a periprocedural dual-antiplatelet regimen with aspirin and a GPIIb/IIIa inhibitor.

Disclosures: Johanna M. Ospel—*UNRELATED*: *Grants/Grants Pending*: Julia Bangerter Rhyner Foundation, University of Basel Research Foundation, Freiwiliige Akademische Gesellschaft Basel, *Comments*: research scholarships. Patrick Brouwer—*UNRELATED*: *Consultancy*: Cerenovus; *Payment for Lectures Including Service on Speakers Bureaus*: Cerenovus. Franziska Dorn—*UNRELATED*: *Consultancy*: Cerus Endovascular, phenox, Balt; *Payment for Lectures Including Service on Speakers Bureaus*: speakers honoraria from Cerenovus and Acandis. Adam Arthur—*UNRELATED*: *Consultancy*: Balt, Cerenovus, Medtronic, MicroVention, Penumbra, Siemens, Stryker*; *Stock/Stock Options*: Bendit, Cerebrotech, EndoStream, Magneto, Marblehead Medical, Neurogami, Serenity, Synchron, Triad Medical, Vascular Simulations. Mary E. Jensen—*UNRELATED*: *Employment*: University of Virginia Health System. Raul Nogueira—*OTHER RELATIONSHIPS*: *Consulting Fees*: Anaconda, Biogen, Cerenovus, Genentech, Imperative Care, Medtronic, phenox, Prolong Pharmaceuticals, Stryker Neurovascular; *Stock/Stock Options*: advisory roles with Astrocyte Pharmaceuticals, Brainomix, Cerebrotech, Ceretrieve, Corindus Vascular Robotics, Vesalio, Viz-Ai, and Perfuze. Rene Chapot—*UNRELATED*: *Payment for Lectures Including Service on Speakers Bureaus*: Balt, Medtronic, MicroVention, Siemens, Stryker*; *Travel/Accommodations/Meeting Expenses Unrelated to Activities Listed*: Boston, Balt, MicroVention, Rapid Medical, Siemens. Charles Majoie—*UNRELATED*: *Grants/Grants Pending*: European Commission, Dutch Heart Foundation, Stryker*; *Stock/Stock Options*: Nico.lab (modest), *Comments*: a company that focuses on the use of artificial intelligence for medical imaging analysis. Mahesh Jayaraman—*UNRELATED*: *Consultancy*: Medtronic, *Comments*: speaking for stroke systems of care at ISC 2018. Allan Taylor—*UNRELATED*: *Employment*: Groote Schuur Hospital, *Comments*: full-time employment with a public hospital; *Expert Testimony:* defense and prosecuting attorneys, *Comments*: I provide expert testimony in neuromuscular cases for 1 to 2 matters per year; *Other*: private practice, *Comments*: I have a limited private practice for patients with neuromuscular disease. Jens Fiehler—*UNRELATED*: *Consultancy*: Acandis, Cerenovus, Medtronic, MicroVention, Stryker, Penumbra; *Grants/Grants Pending*: Acandis, Cerenovus, Medtronic, MicroVention, Stryker*; *Stock/Stock Options*: Tegus; *OTHER RELATIONSHIPS*: Eppdata CEO. Nobuyuki Sakai—*UNRELATED*: *Grants/Grants Pending*: Terumo, Medtronic, *Comments*: Modest*; *Payment for Lectures Including Service on Speakers Bureaus*: Biomedical Solutions, Stryker, Terumo.* Mayank Goyal—*UNRELATED*: *Consultancy*: Stryker, Medtronic, MicroVention, Mentice, *Comments*: advice on acute stroke intervention; *Grants/Grants Pending*: Medtronic, Stryker, Cerenovus, *Comments*: unrestricted research grants to University of Calgary*; *Patents (Planned, Pending or Issued)*: GE Healthcare, *Comments*: licensing agreement: Systems of Acute Stroke Diagnosis; *Royalties*: GE Healthcare. Kirill Orlov—*UNRELATED*: *Consultancy*: Medtronic, MicroVention. Justin Fraser—*UNRELATED*: *Board Membership:* Cerelux; *Consultancy*: Medtronic, Penumbra, Stream; *Grants/Grants Pending*: American Heart Association, University of Kentucky; *Stock/Stock Options*: Fawkes Biotechnology. David Kallmes—*UNRELATED*: *Grants/Grants Pending*: MicroVention, NeuroSigma, Medtronic, *Comments*: funding for preclinical research*; *Patents (Planned, Pending or Issued)*: Mayo Clinic, *Comments*: patent for protection device*; *Stock/Stock Options*: Marblehead Medical, Superior Medical Experts. *Money paid to the institution.

REFERENCES

1. Hammer A, Steiner A, Kerry G, et al. **Treatment of ruptured intracranial aneurysms yesterday and now**. *PLoS One* 2017;12:e0172837 CrossRef Medline
2. Howard BM, Frerich JM, Madaelil TP, et al. **"Plug and pipe" strategy for treatment of ruptured intracranial aneurysms**. *J Neurointerv Surg* 2019;11:43–48 CrossRef Medline
3. Zuo Q, Yang P, Lv N, et al. **Safety of coiling with stent placement for the treatment of ruptured wide-necked intracranial aneurysms: a contemporary cohort study in a high-volume center after improvement of skills and strategy**. *J Neurosurg* 2019;131:435–41 CrossRef Medline
4. Madaelil TP, Moran CJ, Cross DT 3rd, et al. **Flow diversion in ruptured intracranial aneurysms: a meta-analysis**. *AJNR Am J Neuroradiol* 2017;38:590–95 CrossRef Medline
5. Cai K, Ji Q, Cao M, et al. **Association of different stenting procedures with symptomatic thromboembolic complications in stent-assisted coiling of ruptured wide-necked intracranial aneurysms**. *World Neurosurg* 2017;104:824–30 CrossRef Medline
6. Li C, Li Y. **Stent-assisted coiling of ruptured wide-necked intracranial aneurysms**. *Interv Neuroradiol* 2013;19:283–88 CrossRef Medline
7. Liu P, Lv X, Li Y, et al. **Stent-assisted coiling of ruptured wide-necked intracranial aneurysms: a single-center experience of 218 consecutive patients**. *Neurol India* 2016;64(Suppl):S70–77 CrossRef Medline
8. Yang P, Zhao K, Zhou Y, et al. **Stent-assisted coil placement for the treatment of 211 acutely ruptured wide-necked intracranial aneurysms: a single-center 11-year experience**. *Radiology* 2015;276:545–52 CrossRef Medline
9. Brinjikji W, Lanzino G, Cloft HJ, et al. **Platelet testing is associated with worse clinical outcomes for patients treated with the Pipeline Embolization Device**. *AJNR Am J Neuroradiol* 2015;36:2090–95 CrossRef Medline
10. Comin J, Kallmes DF. **Platelet-function testing in patients undergoing neurovascular procedures: caught between a rock and a hard place**. *AJNR Am J Neuroradiol* 2013;34:730–34 CrossRef Medline
11. Hudson JS, Prout BS, Nagahama Y, et al. **External ventricular drain and hemorrhage in aneurysmal subarachnoid hemorrhage patients on dual antiplatelet therapy: a retrospective cohort study**. *Neurosurgery* 2019;84:479–84 CrossRef Medline
12. Dayé C. **How to train your oracle: the Delphi method and its turbulent youth in operations research and the policy sciences**. *Soc Stud Sci* 2018;48:846–68 CrossRef Medline
13. Steurer J. **The Delphi method: an efficient procedure to generate knowledge**. *Skeletal Radiology* 2011;40:959–61 CrossRef Medline
14. Dalkey NC, Helmer-Hirschberg O. *An Experimental Application of the Delphi Method to the Use of Experts*. Rand; 1962
15. Cagnazzo F, Di Carlo DT, Petrella G, et al. **Ventriculostomy-related hemorrhage in patients on antiplatelet therapy for endovascular treatment of acutely ruptured intracranial aneurysms: a meta-analysis**. *Neurosurg Rev* 2020;43:397–406 CrossRef Medline
16. Manning NW, Cheung A, Phillips TJ, et al. **Pipeline shield with single antiplatelet therapy in aneurysmal subarachnoid haemorrhage: multicentre experience**. *J Neurointerv Surg* 2019;11:694–98 CrossRef Medline
17. Aguilar Perez M, AlMatter M, Hellstern V, et al. **Use of the pCONus HPC as an adjunct to coil occlusion of acutely ruptured aneurysms: early clinical experience using single antiplatelet therapy**. *J Neurointerv Surg* 2020 Feb 26. [Epub ahead of print] CrossRef Medline
18. Kang HS, Kwon BJ, Roh HG, et al. **Intra-arterial tirofiban infusion for thromboembolism during endovascular treatment of intracranial aneurysms**. *Neurosurgery* 2008;63:230–37; discussion 237–38 CrossRef Medline

19. Pandya DJ, Fitzsimmons BF, Wolfe TJ, et al. **Measurement of antiplatelet inhibition during neurointerventional procedures: the effect of antithrombotic duration and loading dose**. *J Neuroimaging* 2010;20:64–69 CrossRef Medline
20. Dumont TM, Kan P, Snyder KV, et al. **Adjunctive use of eptifibatide for complication management during elective neuroendovascular procedures**. *J Neurointerv Surg* 2013;5:226–30 CrossRef Medline
21. Brinjikji W, Morales-Valero SF, Murad MH, et al. **Rescue treatment of thromboembolic complications during endovascular treatment of cerebral aneurysms: a meta-analysis**. *AJNR Am J Neuroradiol* 2015;36:121–25 CrossRef Medline
22. Choi HH, Cho YD, Han MH, et al. **Antiplatelet premedication-free stent-assisted coil embolization in acutely ruptured aneurysms**. *World Neurosurg* 2018;114:e1152–60 CrossRef Medline
23. Choi HH, Lee JJ, Cho YD, et al. **Antiplatelet premedication for stent-assisted coil embolization of intracranial aneurysms: low-dose prasugrel vs clopidogrel**. *Neurosurgery* 2018;83:981–88 CrossRef Medline
24. Kim KS, Fraser JF, Grupke S, et al. **Management of antiplatelet therapy in patients undergoing neuroendovascular procedures**. *J Neurosurg* 2018;129:890–905 CrossRef Medline
25. Samaniego EA, Gibson E, Nakagawa D, et al. **Safety of tirofiban and dual antiplatelet therapy in treating intracranial aneurysms**. *Stroke Vasc Neurol* 2019;4:36–42 CrossRef Medline
26. Tonetti DA, Jankowitz BT, Gross BA. **Antiplatelet therapy in flow diversion**. *Neurosurgery* 2020;86:S47–52 CrossRef Medline
27. Fiorella D, Thiabolt L, Albuquerque FC, et al. **Antiplatelet therapy in neuroendovascular therapeutics**. *Neurosurg Clin N Am* 2005;16:517–40, vi CrossRef Medline
28. Cagnazzo F, Perrini P, Lefevre PH, et al. **Comparison of prasugrel and clopidogrel used as antiplatelet medication for endovascular treatment of unruptured intracranial aneurysms: a meta-analysis**. *AJNR Am J Neuroradiol* 2019;40:681–86 CrossRef Medline

The Dilator-Dotter Technique: A Modified Method of Rapid Internal Carotid Artery Revascularization in Acute Ischemic Stroke

K. Amuluru, D. Sahlein, F. Al-Mufti, T. Payner, C. Kulwin, A. DeNardo, and J. Scott

ABSTRACT

BACKGROUND AND PURPOSE: Acute ischemic stroke due to tandem occlusive lesions involves high-grade ICA stenosis or occlusion with a distal intracranial occlusion. Several approaches and devices exist in the treatment of tandem occlusions; however, a consensus on the optimal technique does not exist. The Dotter technique is a method of catheter-based angioplasty to recanalize cervical ICA occlusions. We present a modified dilator-Dotter technique, which involves a polyethylene, tapered inner dilator to initially cross the occlusion, followed by guide catheterization and subsequent intracranial thrombectomy. The purpose of this study was to examine the safety and efficacy of this dilator-Dotter technique.

MATERIALS AND METHODS: We performed a retrospective review of patients with acute stroke due to tandem ICA intracranial occlusions, treated with our dilator-Dotter technique and thrombectomy between June 2018 and December 2019. We examined clinical, radiographic, and procedural data, as well as complications and outcomes.

RESULTS: Thirty-two patients were included. In 100% of cases, the dilator-Dotter technique resulted in ICA recanalization allowing successful thrombectomy. TICI 2b-3 revascularization was obtained in 31 patients (96%), within an average time of 25 minutes. The average preprocedural ICA stenosis was 98%, including 23 patients (72%) with complete occlusion. Following the dilator-Dotter technique, average ICA stenosis improved to 59%. There were no instances of death, iatrogenic dissection, emboli to new territory, or symptomatic intracranial hemorrhage.

CONCLUSIONS: The dilator-Dotter technique may be a safe and effective modification of the traditional Dotter technique in allowing rapid ICA recanalization in cases of acute ischemic stroke due to tandem occlusions.

ABBREVIATIONS: ADAPT = direct aspiration first-pass technique; AIS = acute ischemic stroke; ICH = intracranial hemorrhage; LVO = large-vessel occlusion; sICH = symptomatic intracranial hemorrhage

Acute ischemic stroke (AIS) due to tandem occlusive lesions involves acute dissection or ulcerated rupture of an unstable proximal ICA atherosclerotic plaque causing stenosis/occlusion and subsequent embolic intracranial large-vessel occlusion (LVO).[1,2] Several methods exist in the treatment of AIS due to tandem occlusions, involving various approaches (anterograde versus retrograde) and devices; however, a consensus on the optimal technique does not exist.[3,4] One of the primary issues in cases of tandem occlusions is management of the proximal ICA occlusion. Balloon angioplasty, emergent carotid stent placement, and catheter angioplasty are all options to recanalize the ICA or achieve access to the distal intracranial occlusion.

The Dotter technique is a well-known method of catheter-based angioplasty used by interventional radiologists in other parts of the body, particularly in peripheral vascular occlusive disease.[5] Neurointerventionalists have implemented the Dotter technique in cases of AIS involving cervical ICA occlusions, given its simplicity and timeliness. We describe a modification of the Dotter technique using a polyethylene dilator, which is biomechanically less traumatic compared with the traditional Dotter technique. We present a series of 32 cases of AIS due to cervical ICA occlusive disease with tandem, distal, intracranial LVOs treated with the dilator-Dotter technique, followed by intracranial

Received April 13, 2020; accepted after revision June 15.

From the Division of Neurointerventional Radiology (K.A., D.S., A.D., J.S.) and Division of Cerebrovascular Neurosurgery (T.P., C.K.), Goodman Campbell Brain and Spine, Indianapolis, Indiana; Department of Neuroendovascular Surgery and Neurocritical Care (F.A.-M.), Westchester Medical Center at New York Medical College, Valhalla, New York; and Division of Neurointerventional Radiology (K.A., D.S., A.D., J.S.) and Division of Cerebrovascular Neurosurgery (T.P., C.K.), Ascension St. Vincent's Medical Center, Indianapolis, Indiana.

Please address correspondence to Krishna Amuluru, MD, Goodman Campbell Brain and Spine, Division of Neurointerventional Radiology, 13345 Illinois St, Carmel, IN 46032; e-mail: kamuluru@goodmancampbell.com; @AmuluruKrishna

Indicates article with supplemental on-line table.

http://dx.doi.org/10.3174/ajnr.A6733

thrombectomy. We review the pathophysiology of tandem occlusions, the controversy surrounding treatment techniques, and the biomechanical benefits of dilator angioplasty. This study received institutional (St. Vincent's) review board approval.

MATERIALS AND METHODS

Patient Selection and Preprocedural Management

We performed a retrospective review of our Comprehensive Stroke Center data base of patients with AIS treated with endovascular thrombectomy between June 2018 and December 2019. Patients who demonstrated critical stenosis or occlusions of-ICA origin and tandem ipsilateral intracranial occlusions were included. Patients without clinically relevant ICA steno-occlusive disease and those with proximal disease noncontributory to the distal occlusion were excluded. Cases of AIS with proximal ICA occlusion resulting from dissection were excluded. Cases of proximal ICA occlusion treated with the "traditional" Dotter technique or balloon angioplasty were excluded. Cases of AIS due to posterior circulation pathology were excluded.

All patients with AIS presenting or transferred to our center undergo a noncontrast CT scan of the head and are evaluated by a neurologist who determines whether the patient is a candidate for intravenous tPA. Candidacy for endovascular treatment is determined according to the guidelines set forth by the American Heart Association/American Stroke Association for the Management of Patients with AIS and the Society of Neurointerventional Surgery Standards and Guidelines Committee.[6,7]

Clinical and procedural data including age, sex, NIHSS score on presentation, endovascular devices used, procedural time to definitive revascularization (TICI grade 2b–3), preprocedural severity of the stenosis and/or occlusion, procedural complications, postprocedural hemorrhage, NIHSS score at discharge, and mRS score at follow-up were recorded.

Interventional Technique

All patients in this series were treated under general anesthesia. Access via the right common femoral artery was used in most cases. In 1 case, right radial access was used due to chronic bilateral femoral arterial occlusion. A 6F, 90-cm, straight-tip Neuron MAX 088 guide catheter (Penumbra) over a 5F Berenstein catheter with a 0.035-inch Glidewire (Terumo) was used to select the common carotid artery proximal to the occlusion, and cervical and intracranial angiography was performed. In certain cases, a priori knowledge of the proximal occlusion was determined from the preprocedural CTA. The diagnostic catheter was removed, and the prepackaged Neuron MAX 088 inner dilator was inserted into the guide catheter along with the Glidewire. The proximal occlusion was then crossed with the Glidewire, and the inner dilator was subsequently tracked over the wire and across the occlusion. The Neuron MAX 088 guide catheter was then advanced over the dilator, through the occluded segment, and into the cervical ICA. The Neuron MAX 088 guide catheter was vigorously aspirated during and after removal of the dilator and wire. In most cases, contrast was gently injected through the dilator before its removal to confirm the position within the true lumen and to further define the intracranial tandem occlusion.

Attention was then turned to the intracranial thrombus, which was treated using either a combination stent retriever (Solitaire Platinum, Medtronic; or Embotrap II, Johnson & Johnson) through an aspiration catheter (SOFIA 5F or 6F, MicroVention; React 71, Medtronic; or JET 7 reperfusion catheter, Penumbra) technique or the direct aspiration first-pass technique (ADAPT) technique according to the operator's discretion. Intracranial thrombectomy was determined successful if the therapy resulted in TICI 2b–3 recanalization. Adjunctive intra-arterial tPA or antiplatelet medications were not used.

Once intracranial flow was restored, the Neuron Max 088 catheter was retracted proximal to the carotid occlusion under vigorous aspiration. In 2 cases involving particularly severe multifocal ICA calcific atherosclerotic disease, there was pre-emptive concern for possible artery-to-artery embolization with removal of the guide catheter. In these cases, the Neuron MAX 088 was retracted using an embolic protection device positioned in the ICA. The patency of the cervical ICA was re-evaluated with repeat cervical angiography (approximately 10–15 minutes) until the operator was confident that the dilator-Dotter technique would maintain patency or at least provide short-term stability until a more definitive therapy could be performed. If re-occlusion was encountered, balloon angioplasty or emergent carotid stent placement was considered on the basis of the patient's history, clinical presentation, and the risk of vessel injury and/or intracranial hemorrhage.

Postinterventional Management

Following endovascular intervention, antiplatelet therapy is typically started on postprocedural day 1 after imaging demonstrating the absence of hemorrhage. Postprocedural carotid patency is monitored by carotid Doppler and/or CTA. Depending on a patient's pre- and postprocedural functional status, clinical history, and final infarction volume, definitive carotid recanalization with endarterectomy or carotid stent placement is performed within a timeframe determined by the neurology and neurovascular services. In cases involving subacute complete re-occlusion in the absence of new or worsening clinical symptoms, definitive recanalization is avoided due to a physiologically compensatory circle of Willis.

RESULTS

Between June 2018 and December 2019, we treated 372 patients with endovascular thrombectomy for AIS at our institution. Three hundred ten patients were excluded due to absent and/or noncontributory proximal ICA disease. Seventeen patients were excluded due to proximal steno-occlusive disease treated with the "traditional" Dotter technique or balloon angioplasty before the intracranial thrombectomy. Thirteen patients were excluded due to proximal ICA dissections, determined either on the preprocedural CTA or via DSA showing classic "flame-shaped" luminal narrowing in the absence of calcific atherosclerotic disease. Thus, 32 patients were included who demonstrated critical stenosis or occlusions of the ICA origin and tandem occlusions of the ipsilateral carotid terminus or middle cerebral artery.

Of the 32 patients, 25 were men (78%) and 7 were women (22%). The mean age and NIHSS score at presentation were 63 years and 17 (range, 6–30), respectively. Eleven patients (34%) received intravenous tPA before the procedure. (On-line Table).

Procedural Results

The average time from groin access to definitive intracranial revascularization (TICI 2b–3) was 25 minutes (range, 7–88 minutes). In 18 cases, distal thrombectomy was performed using a combination of an aspiration catheter along with a stent retriever, while aspiration alone (ADAPT technique) was used in 12 cases. In 2 patients, the distal tandem occlusion resolved after a proximal Dotter-dilator technique. Definitive intracranial revascularization (TICI 2b–3) was obtained in 31 patients (97%), with 18 patients (56%) achieving full TICI 3 recanalization.

Preprocedural ICA stenosis ranged from 90% to 100% (mean, 98%), including 23 patients with complete occlusion (72%). The dilator-Dotter technique resulted in successful access to the cervical ICA and the ability to perform intracranial thrombectomy in 100% of cases. Following the dilator-Dotter technique, ICA stenosis decreased to 59% (range, 4%–100%). Twenty-four patients (75%) demonstrated a residual post-Dotter stenosis of ≤70% (range, 4%–70%; mean, 50%), which was not hemodynamically flow-limiting.

In 6 patients (19%), acute restenosis with flow limitation or re-occlusion was identified after intracranial thrombectomy and after removing the Neuron MAX guide catheter from the ICA. These 6 patients necessitated further interventions (5 stent placements and 1 balloon angioplasty, all with embolic protection devices). There were no instances of iatrogenic dissection or emboli to new territory. There were no procedural complications.

Clinical Outcomes

No patients died during the immediate inpatient hospitalization. There were no cases of postprocedural symptomatic intracranial hemorrhage (sICH). Four patients (13%) developed postprocedural hemorrhagic transformation, all of which were asymptomatic hemorrhagic infarction type 1, petechial hemorrhage. The mean NIHSS score at discharge was 6 (range, 0–20). Patient 15 presented 7 hours after acute onset of a left MCA syndrome, with an NIHSS score of 20. Despite successful recanalization and lack of hemorrhagic transformation, the patient demonstrated no meaningful clinical improvement and was discharged to home hospice care. Patient 26 required an emergent internal carotid artery stent after intracranial thrombectomy, which re-occluded on postintervention day 2, causing massive cerebral edema necessitating hemicraniectomy, and the patient died on postinfarct day 47.

In 6 patients (19%), subacute re-occlusion was discovered on follow-up carotid duplex sonography and/or CTA during the subsequent hospitalization. None demonstrated worsening or new symptoms; thus, none required further intervention.

In 20 patients (63%), no further carotid intervention was performed during the follow-up period, either due to residual stenosis <70% or subacute re-occlusion. In 7 patients, eventual definitive carotid endarterectomy was performed, within a range of 1 day to 6 months following the ictal stroke. One patient underwent carotid stent placement 2 months after the ictal stroke.

DISCUSSION

Approximately 10%–25% of patients with intracranial LVO will have a concomitant proximal extracranial occlusion, and conversely, 50% of patients with proximal extracranial occlusion will have a tandem distal intracranial LVO.[8] AIS in patients with tandem lesions has a poor prognosis, with only 2%–12% of patients achieving favorable clinical outcome after systemic thrombolysis.[4] Intravenous thrombolysis and other combined approaches have limited success in this subgroup of patients.[8,9] Accordingly, the Multicenter Randomized Clinical trial of Endovascular treatment for Acute ischemic stroke in the Netherlands (MR CLEAN), Endovascular Treatment for Small Core and Anterior Circulation Proximal Occlusion With Emphasis on Minimizing CT to Recanalization Times (ESCAPE), and Endovascular Revascularization With Solitaire Device Versus Best Medical Therapy in Anterior Circulation Stroke Within 8 Hours (REVASCAT) trials, which included 32.3%, 17%, and 18.6% of patients with acute tandem occlusions, respectively, showed treatment effect in favor of thrombectomy compared with medical management.[10-12]

In the treatment of tandem occlusions, controversy exists regarding the order in which to treat the proximal and distal lesions, and consensus on management guidelines does not exist.[2,3,13-15] Advantages of the retrograde/reverse approach include prioritizing the critical intracranial thrombectomy step, quicker restoration of cerebral blood flow, and the possibility of reducing final cerebral infarction volume.[14] On the other hand, advantages of proximal recanalization first include subsequent access to the intracranial LVO with larger guide catheters, collateral restoration, theoretic reduction of further embolization, and, in some cases, spontaneous distal recanalization.[2,3,13-16] Controversy also exists regarding balloon angioplasty alone versus carotid stent placement for the treatment of the proximal lesion. Both techniques have associated risks, including distal emboli propagation and intracerebral hemorrhage.[2,14,17,18] Although angioplasty alone may restore anterograde flow with a less-invasive procedure, disadvantages compared with stent stabilization include the possibility of "rebound" restenosis or re-occlusion, which may be as high as 16%.[19]

Percutaneous transluminal catheter angioplasty (Dotter technique) was first described in 1965 by Dr Charles Dotter, who used a coaxial system of rigid polyethylene catheters to recanalize an occluded popliteal artery, resulting in salvage of the limb.[20] The Dotter technique has since been implemented in the neurointerventional space, where simplified techniques of ICA recanalization are regarded favorably in the time-sensitive environment of AIS.[21] Woodward et al[21] described crossing and sequentially dilating ICA stenoses with a 6F diagnostic catheter, followed by advancement of a 6F Shuttle Sheath (Cook Medical, Bloomington, IN) across the stenosis. However, factors such as stenosis severity, length, eccentricity, stiffness, and vessel angulation can preclude catheter placement, resulting in technical failure. Forceful advancement of a catheter with a large size mismatch to the guidewire (step-off) across the stenosis may result in intimal dissection, flap formation, embolization, perforation, and spasm.

The Neuron MAX 088 guide catheter comes prepackaged with a 100- or 110-cm (depending on the length of the Neuron MAX 088 chosen) High-density polyethylene (HDPE) polymer inner dilator shaft, which has an inner diameter (ID) of 0.035 inches. Used mainly for femoral artery access directly through the skin, it extends 11.5 cm distal to the Neuron MAX 088 catheter tip when fully click-locked through the included cross-cut valve (Fig 1). Smooth, coaxial dilation of an occluded ICA using

the tapered dilator is not only intuitively less traumatic compared with traditional Dotter angioplasty over a wire or nontapered diagnostic catheter, but it also exerts less shear force on the arterial intimal surface and associated plaque.[22,23] Furthermore, sequentially tapered dilator angioplasty results in less longitudinal movement of the vessel compared with dilation with a sole catheter over a wire with a large size mismatch, reducing the risk of dissection, embolization, and perforation.[22] Although the risk of iatrogenic embolization exists any time an unstable stenosis is crossed, in our cohort, our technique caused zero cases of dissection, perforation, or embolization.

In our cohort, we encountered zero instances of sICH. This outcome is comparable with previous reports of the traditional Dotter technique in AIS due to tandem occlusions and is favorable compared with data on patients treated with emergent carotid stent placement.[3,21,24,25] Studies examining the complications of acute ICA stent placement in patients with AIS have shown an intracranial hemorrhage (ICH) rate as high as 25%.[3,24,25] Dorado et al[25] showed that the placement of a stent was an independent predictor of sICH in their report on acute stent placement during stroke intervention. Several theories exist on why emergent carotid stent placement and mechanical thrombectomy may increase the risk of ICH. Patients with increasingly proximal occlusions are at higher risk of established infarction of the basal ganglia, which predisposes to hemorrhagic conversion. Additionally, emergent stent placement exposes patients to hyperperfusion syndrome (re-establishment of flow dynamics that have been chronically absent), which, when combined with established infarction, can lead to an increased risk of ICH. Finally, aggressive prophylactic antiplatelet therapy, to prevent in-stent thrombosis, may further

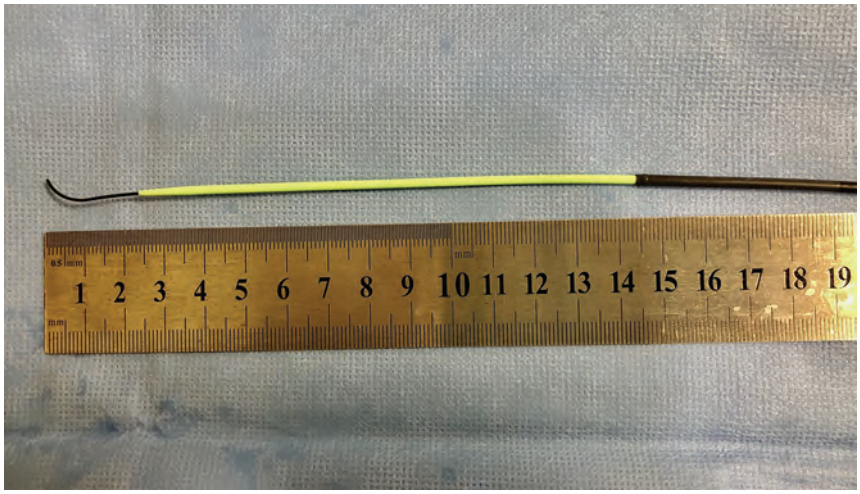

FIG 1. High-density polyethylene polymer inner dilator shaft extends 11.5-cm distal to the Neuron MAX 088 catheter tip, with a 0.035-inch Glidewire.

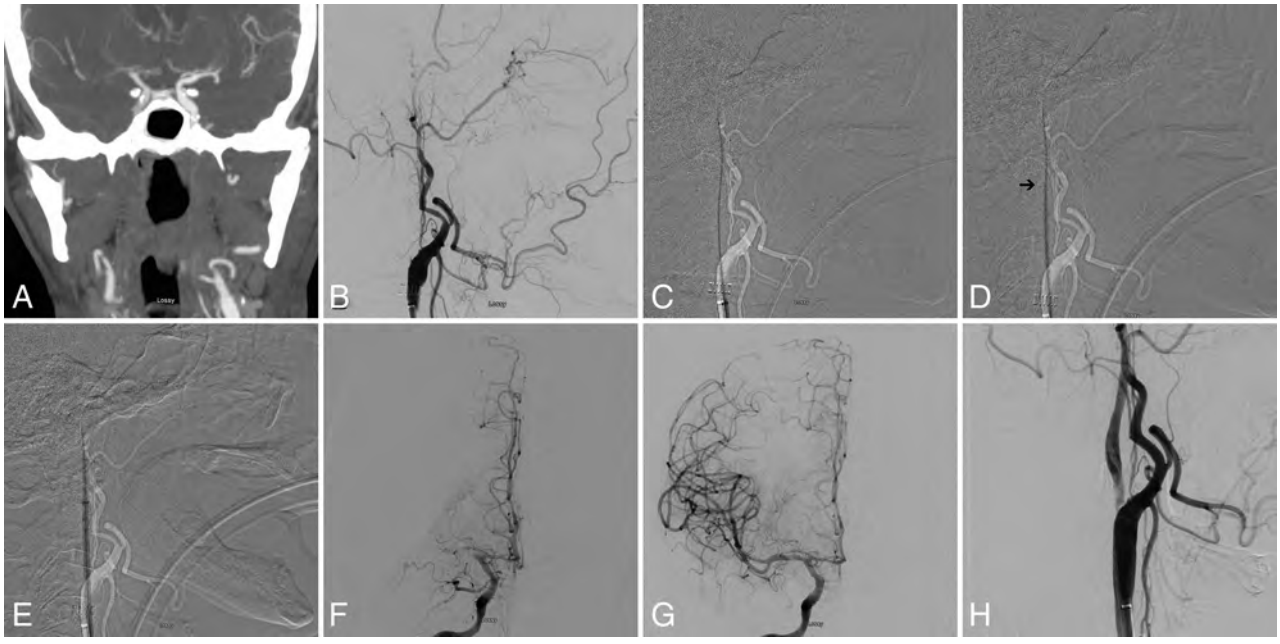

FIG 2. *A*, Preprocedural CTA showing acute occlusion of right MCA. Note nonopacification of cervical right ICA. *B*, Digital subtraction angiogram of the right common carotid artery in a lateral view shows occlusion of cervical ICA at the origin. *C*, Subtracted fluoroscopic roadmap shows crossing of the cervical ICA occlusion with a Glidewire, followed by the Neuron MAX 088 inner dilator (*D*). Despite radiolucency of the dilator, note the subtle change in Glidewire angulation indicating the dilator tip location (*arrow*). *E*, Subsequent dilator-Dotter angioplasty by crossing the ICA occlusion with the Neuron MAX 088. Note the lack of dilator-catheter "step-off." *F*, Angiogram in a frontal view shows tandem intracranial occlusion of right MCA, with subsequent successful thrombectomy (*G*) yielding a TICI 3 recanalization. *H*, The patient is left with 80% stenosis on the final postinterventional angiogram, which eventually asymptomatically reoccluded.

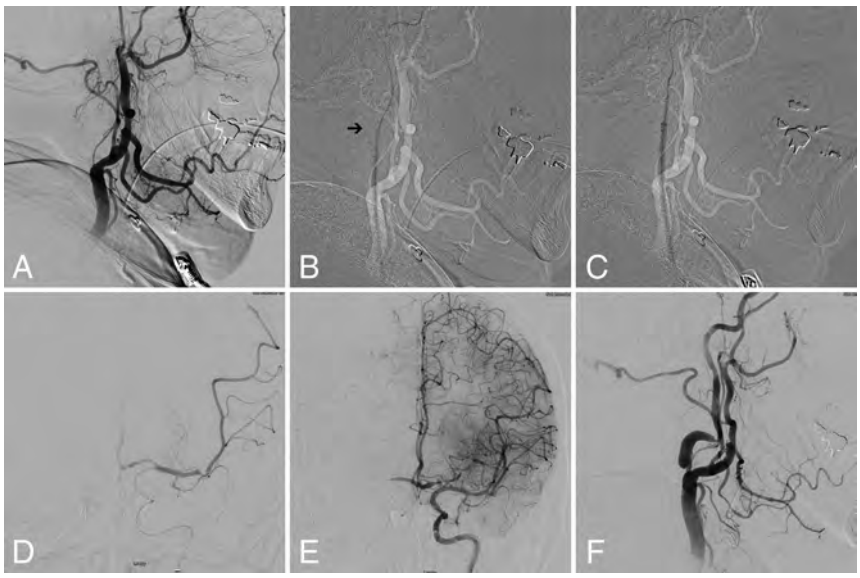

FIG 3. *A*, Digital subtraction angiogram of the left common carotid artery in a lateral view showing occlusion of cervical ICA at the origin. *B*, Subtracted fluoroscopic roadmap shows crossing of the cervical ICA occlusion with the Glidewire and Neuron MAX 088 inner dilator Note the subtle change in Glidewire angulation indicating the dilator tip location (*arrow*). *C*, Subsequent dilator-Dotter angioplasty by crossing the ICA occlusion with the Neuron MAX 088. *D*, Microcatheter angiogram in frontal view shows tandem intracranial occlusion of superior-division M2 segment of the left MCA, with subsequent successful thrombectomy (*E*) yielding TICI 3 recanalization. Note the robust crossflow across the anterior communicating artery. *F*, The patient was left with high-grade stenosis on the final postinterventional angiogram, which eventually asymptomatically re-occluded on follow-up carotid duplex sonography.

increase subsequent ICH risk.[25] These issues are only further complicated in patients who have received intravenous tPA or in whom the cerebral infarct volume is unknown.[17] Thus, any approach that can restore proximal ICA patency while obviating emergent balloon angioplasty or stent placement is a potentially powerful technique in this population.

In our cohort, we encountered a mean preprocedural stenosis rate of 98%, which improved to 58% after dilator-Dotter angioplasty. These results compare slightly favorably with those in a recent examination of the traditional Dotter technique, which examined 7 patients with a preinterventional stenosis of 88%, which improved to 61% after intervention.[21] In 6 of our patients (19%), acute rebound stenosis/occlusion necessitated further intervention with balloon angioplasty or stent placement, all of which were successful without complication. Six additional patients (23%) demonstrated subacute re-occlusion during their hospitalization, all of whom were asymptomatic, presumably due to a physiologically compensatory circle of Willis (Figs 2 and 3). While these 12 patients demonstrate the unclear long-term efficacy of the dilator-Dotter technique, the technique facilitated definitive recanalization in a timely manner (mean, 25 minutes) without the need for ancillary devices and their associated risk. Furthermore, we postulate that in addition to enabling rapid ICA access for timely thrombectomy, the intermediate recanalization achieved may be sufficient to provide short-term stability until more definitive endarterectomy or stent placement can be performed. Indeed, 8 of our patients clinically improved enough to undergo eventual carotid endarterectomy or stent placement.

The predominant risks of the dilator-Dotter technique include iatrogenic dissection, embolization, and/or perforation, though these risks are present when any unstable stenosis is crossed, regardless of the technique or device used. In several cases, once the proximal occlusion was crossed using the dilator-Dotter technique, subsequent placement of the guide catheter in the ICA resulted in flow arrest, decreasing the likelihood of iatrogenic thromboembolization during thrombectomy. Finally, the inner dilator is radiolucent, making visualization difficult. However, if the Neuron MAX 088 is visualized on fluoroscopy, appreciation of the 11.5-cm length extrusion from the Neuron MAX 088 catheter tip allows operator recognition of the tip location. Furthermore, appreciation of the change in angulation of the dilator to the Glidewire will also aid in recognition of tip location (Fig 1). Operators should be aware that all ICA occlusions in this series were in the setting of atherosclerosis; if an occlusion due to dissection is encountered, using the dilator-Dotter technique may exacerbate the dissection.

Limitations of our study include the retrospective nature as well as the small patient population. The results herein reported using the Neuron MAX inner dilator might not be generalizable to other manufacturers' dilators. Given the presence of tandem intracranial LVO, there is no way to determine whether our technique caused angiographically occult embolism due to the pre-existing distal occlusion. Despite this limitation, we encountered zero instances of embolization to new territory when comparing the preprocedural CTA with the first angiogram after the dilator-Dotter technique.

CONCLUSIONS

In this series of 32 patients with AIS due to tandem ICA intracranial occlusions, the dilator-Dotter technique resulted in rapid ICA recanalization in all cases, allowing successful thrombectomy attempts. There were no instances of death, iatrogenic dissection, emboli to new territory, or symptomatic intracranial hemorrhage. The dilator-Dotter technique may be a safe and effective modification of the traditional Dotter technique in allowing rapid ICA recanalization in cases of AIS due to tandem occlusions.

Disclosures: Daniel Sahlein—*UNRELATED*: *Consultancy*: Medtronic, MicroVention, phenox, Stryker; *Grants/Grants Pending*: MicroVention; *Payment for Lectures Including Service on Speakers Bureaus*: Medtronic, MicroVention; *Payment for Development of*

Educational Presentations: Medtronic. Fawaz Al-Mufti—*UNRELATED*: *Employment*: Westchester Medical Center at New York Medical College.

REFERENCES

1. Kim YS, Garami Z, Mikulik R, et al; CLOTBUST Collaborators. **Early recanalization rates and clinical outcomes in patients with tandem internal carotid artery/middle cerebral artery occlusion and isolated middle cerebral artery occlusion.** *Stroke* 2005;36:869–71 CrossRef Medline
2. Spiotta AM, Lena J, Vargas J, et al. **Proximal to distal approach in the treatment of tandem occlusions causing an acute stroke.** *J Neurointerv Surg* 2015;7:164–69 CrossRef Medline
3. Malik AM, Vora NA, Lin R, et al. **Endovascular treatment of tandem extracranial/intracranial anterior circulation occlusions: preliminary single-center experience.** *Stroke* 2011;42:1653–57 CrossRef Medline
4. Rubiera M, Ribo M, Delgado-Mederos R, et al. **Tandem internal carotid artery/middle cerebral artery occlusion: an independent predictor of poor outcome after systemic thrombolysis.** *Stroke* 2006;37:2301–05 CrossRef Medline
5. Brillu C, Picquet J, Villapadierna F, et al. **Percutaneous transluminal angioplasty for management of critical ischemia in arteries below the knee.** *Ann Vasc Surg* 2001;15:175–81 CrossRef Medline
6. Powers WJ, Rabinstein AA, Ackerson T, et al. **Guidelines for the early management of patients with acute ischemic stroke: 2019 update to the 2018 guidelines for the early management of acute ischemic stroke: a guideline for healthcare professionals from the American Heart Association/American Stroke Association.** *Stroke* 2019;50:e344–418 CrossRef Medline
7. Mokin M, Ansari SA, McTaggart RA, et al; Society of NeuroInterventional Surgery, **Indications for thrombectomy in acute ischemic stroke from emergent large vessel occlusion (ELVO): report of the SNIS Standards and Guidelines Committee.** *J Neurointerv Surg* 2019;11:215–20 CrossRef Medline
8. Christou I, Felberg RA, Demchuk AM, et al. **Intravenous tissue plasminogen activator and flow improvement in acute ischemic stroke patients with internal carotid artery occlusion.** *J Neuroimaging* 2002;12:119–23 CrossRef
9. Lekoubou A, Cho TH, Nighoghossian N, et al. **Combined intravenous recombinant-tissular plasminogen activator and endovascular treatment of spontaneous occlusive internal carotid dissection with tandem intracranial artery occlusion.** *Eur Neurol* 2010;63:211–14 CrossRef Medline
10. Berkhemer OA, Fransen PS, Beumer D, et al; MR CLEAN Investigators. **A randomized trial of intraarterial treatment for acute ischemic stroke.** *N Engl J Med* 2015;372:11–20 CrossRef Medline
11. Campbell BC, Mitchell PJ, Kleinig TJ, et al. **Endovascular therapy for ischemic stroke with perfusion-imaging selection.** *N Engl J Med* 2015;372:1009–18 CrossRef
12. Jovin TG, Chamorro A, Cobo E, et al; REVASCAT Trial Investigators. **Thrombectomy within 8 hours after symptom onset in ischemic stroke.** *N Engl J Med* 2015;372:2296–2306 CrossRef Medline
13. Mpotsaris A, Bussmeyer M, Buchner H, et al. **Clinical outcome of neurointerventional emergency treatment of extra- or intracranial tandem occlusions in acute major stroke: antegrade approach with Wallstent and Solitaire stent retriever.** *Clin Neuroradiol* 2013;23:207–15 CrossRef Medline
14. Rangel-Castilla L, Rajah GB, Shakir HJ, et al. **Management of acute ischemic stroke due to tandem occlusion: should endovascular recanalization of the extracranial or intracranial occlusive lesion be done first?** *Neurosurg Focus* 2017;42:E16 CrossRef Medline
15. Al-Mufti F, Amuluru K, Manning NW, et al. **Emergent carotid stenting and intra-arterial abciximab in acute ischemic stroke due to tandem occlusion.** *Br J Neurosurg* 2017;31:573–77 CrossRef Medline
16. Amuluru K, Al-Mufti F, Romero CE. **Acute ischemic stroke due to common carotid ostial disease with tandem intracranial occlusions treated with thrombectomy and staged retrograde stenting.** *Interv Neurol* 2018;7:445–51 CrossRef Medline
17. Behme D, Molina CA, Selim MH, et al. **Emergent carotid stenting after thrombectomy in patients with tandem lesions.** *Stroke* 2017;48:1126–28 CrossRef Medline
18. Stampfl S, Ringleb PA, Mohlenbruch M, et al. **Emergency cervical internal carotid artery stenting in combination with intracranial thrombectomy in acute stroke.** *AJNR Am J Neuroradiol* 2014;35:741–46 CrossRef Medline
19. McCabe DJ, Pereira AC, Clifton A, et al; CAVATAS Investigators. **Restenosis after carotid angioplasty, stenting, or endarterectomy in the Carotid and Vertebral Artery Transluminal Angioplasty Study (CAVATAS).** *Stroke* 2005;36:281–86 CrossRef Medline
20. Dotter CT, Judkins MP. **Percutaneous transluminal treatment of arteriosclerotic obstruction.** *Radiology* 1965;84:631–43 CrossRef Medline
21. Woodward K, Wegryn S, Staruk C, et al. **The Dotter method revisited: early experience with a novel method of rapid internal carotid artery revascularization in the setting of acute ischemic stroke.** *J Neurointerv Surg* 2016;8:360–66 CrossRef Medline
22. Kinney TB, Chin AK, Rurik GW, et al. **Transluminal angioplasty: a mechanical-pathophysiological correlation of its physical mechanisms.** *Radiology* 1984;153:85–89 CrossRef Medline
23. Kinney TB, Fan M, Chin AK, et al. **Shear force in angioplasty: its relation to catheter design and function.** *AJR Am J Roentgenol* 1985;144:115–22 CrossRef Medline
24. Cohen JE, Gomori JM, Rajz G, et al. **Extracranial carotid artery stenting followed by intracranial stent-based thrombectomy for acute tandem occlusive disease.** *J Neurointerv Surg* 2015;7:412–17 CrossRef Medline
25. Dorado L, Castano C, Millan M, et al. **Hemorrhagic risk of emergent endovascular treatment plus stenting in patients with acute ischemic stroke.** *J Stroke Cerebrovasc Dis* 2013;22:1326–31 CrossRef Medline

Quantifying Intra-Arterial Verapamil Response as a Diagnostic Tool for Reversible Cerebral Vasoconstriction Syndrome

J.M. Sequeiros, J.A. Roa, R.P. Sabotin, S. Dandapat, S. Ortega-Gutierrez, E.C. Leira, C.P. Derdeyn, G. Bathla, D.M. Hasan, and E.A. Samaniego

ABSTRACT

BACKGROUND AND PURPOSE: There is mounting evidence supporting the benefit of intra-arterial administration of vasodilators in diagnosing reversible cerebral vasoconstriction syndrome. We prospectively quantified the degree of luminal diameter dilation after intra-arterial administration of verapamil and its accuracy in diagnosing reversible cerebral vasoconstriction syndrome.

MATERIALS AND METHODS: Patients suspected of having intracranial arteriopathy on noninvasive imaging and referred for digital subtraction angiography were enrolled in a prospective registry. Intra-arterial verapamil was administered in vascular territories with segmental irregularities. The caliber difference ($Caliber_{post} - Caliber_{pre}$) and the proportion of caliber change ($[(Caliber_{post} - Caliber_{pre})/Caliber_{pre}] \times 100\%$) were used to determine the response to verapamil. The diagnosis of reversible cerebral vasoconstriction syndrome was made on the basis of clinical and imaging features at a follow-up appointment, independent of the reversibility of verapamil. Receiver operating characteristic curve analysis was performed to determine the best threshold.

RESULTS: Twenty-six patients were included, and 9 (34.6%) were diagnosed with reversible cerebral vasoconstriction syndrome. A total of 213 vascular segments were assessed on diagnostic angiography. Every patient with a final diagnosis of reversible cerebral vasoconstriction syndrome responded to intra-arterial verapamil. The maximal proportion of change ($P < .001$), mean proportion of change ($P = .002$), maximal caliber difference ($P = .004$), and mean caliber difference ($P = .001$) were statistically different between patients with reversible cerebral vasoconstriction syndrome and other vasculopathies. A maximal proportion of change ≥32% showed a sensitivity of 100% and a specificity of 88.2% to detect reversible cerebral vasoconstriction syndrome (area under the curve = 0.951). The Reversible Cerebral Vasoconstriction Syndrome-2 score of ≥5 points achieved a lower area under the curve (0.908), with a sensitivity of 77.8% and a specificity of 94.1%.

CONCLUSIONS: Objective measurement of the change in the arterial calibers after intra-arterial verapamil is accurate in distinguishing reversible cerebral vasoconstriction syndrome from other vasculopathies. A proportion of change ≥32% has the best diagnostic performance.

ABBREVIATIONS: AUC = area under the curve; CD = caliber difference; IA = intra-arterial; ICAD = intracranial atherosclerotic disease; DSA = digital subtraction angiography; PACNS = primary angiitis of the central nervous system; PC = proportion of change; RCVS = reversible cerebral vasoconstriction syndrome; ROC = receiver operating characteristic; TCH = thunderclap headache

Reversible cerebral vasoconstriction syndrome (RCVS) comprises a group of disorders characterized by prolonged-but-reversible vasoconstriction of the cerebral arteries. It is usually characterized by self-limited and reversible multifocal narrowing, which is associated with acute-onset, severe, recurrent headaches with or without additional neurologic deficits.[1] Vasoconstriction often involves distal cerebral arteries, develops in the first 4–5 days after symptom onset, and persists for >3 weeks.[2] Due to the lack of specific criteria, the presumptive diagnosis needs to be confirmed with reversibility of angiographic abnormalities within 12 weeks of clinical onset.[3,4] Other intracranial stenotic arteriopathies such as primary angiitis of the central nervous system (PACNS), Moyamoya disease, or intracranial atherosclerotic disease (ICAD) present with similar findings on initial noninvasive

Received May 29, 2020; accepted after revision July 4.

From the Departments of Neurology (J.M.S., J.A.R., R.P.S., S.D., S.O.-G., E.C.L., E.A.S.), Neurosurgery (J.A.R., S.O.-G., D.M.H., E.A.S.), and Radiology (S.O.-G., C.P.D., G.B., E.A.S.), University of Iowa Hospitals and Clinics, Iowa City, Iowa.

This work was supported by the 2019 Brain Aneurysm Research Grant from The Bee Foundation and by a Pilot Research Grant from the Society of Vascular and Interventional Neurology, both granted to Edgar Samaniego.

Please address correspondence to Edgar A. Samaniego, MD, MS, 200 Hawkins Dr, Iowa City, IA 52246; e-mail: edgarsama@gmail.com; @esamaniego

Indicates article with supplemental on-line tables.

Indicates article with supplemental on-line photos.

http://dx.doi.org/10.3174/ajnr.A6772

imaging.[5,6] Distinguishing these conditions early in their course is crucial because treatment options are different, have potential adverse effects, and may affect clinical outcomes.[7] Clinical and radiologic differences between RCVS and PACNS have been described;[8] however, a prompt and accurate diagnosis remains challenging in patients with atypical presentation.[9]

Calcium channel blockers have been used to challenge vasoconstrictive changes in patients with suspected RCVS.[10-18] However, other arteriopathies may have reversible changes with time, and it is unclear whether calcium channel blockers can be used reliably to diagnose RCVS. We evaluated the degree of response to intra-arterial (IA) infusion of verapamil as a diagnostic tool in distinguishing RCVS from other intracranial vasculopathies.

MATERIALS AND METHODS

After institutional review board approval, patients were enrolled in a prospective registry for patients with intracranial vasculopathy between September 2017 and January 2020. As part of the clinical protocol at our institution, patients with possible underlying vasculopathy are routinely referred for digital subtraction angiography (DSA). IA verapamil challenge was performed as part of the diagnostic DSA. Demographic, clinical, laboratory, and radiologic data were collected from electronic medical charts at discharge and last follow-up.

Diagnosis of RCVS

The final diagnosis of RCVS was adjudicated after the last outpatient follow-up and was based on the criteria proposed by Calabrese et al.[1] The adjudication was independent of the reversibility of vascular changes after IA verapamil. The criteria proposed by Calabrese et al include the following: 1) severe, acute headache with or without neurologic signs or symptoms, 2) normal or near-normal CSF analysis findings (protein level <80 mg%; leukocyte count < 10 mm^3; and normal glucose level), 3) angiography documenting multifocal segmental cerebral artery vasoconstriction, 4) no evidence of aneurysmal SAH, and 5) reversibility of angiographic abnormalities within 12 weeks after onset.

IA Verapamil Challenge

DSA was performed with selective catheterization of the internal carotid and vertebral arteries. Subtracted images were reviewed, and if there was evidence of irregularities suggestive of an underlying vasculopathy, 5 mg of IA verapamil was slowly administered for 10 minutes in the most affected vascular territory. Blood pressure was closely monitored to avoid a drop of >5 mm Hg in mean arterial pressure during the IA administration of verapamil. If the patient experienced any substantial drop in blood pressure, the IA infusion was stopped and resumed only once the blood pressure was back to baseline. A total of 5 mg of verapamil was diluted in saline to a final concentration of 0.5 mg/mL and manually infused at a continuous rate of 1 mL/min through the side port of a 3-way valve connected to the diagnostic catheter and to a continuous heparinized saline infusion. A repeat angiogram of the same vascular territory was obtained 10 minutes following the IA administration of verapamil.

Radiologic Assessment

Qualitative and quantitative assessment was performed using PACS software. To achieve accurate measurements before and after verapamil injections, we used the same projection angle, source-to-object distance (x-ray tube to patient), and patient-to-detector distance in both angiograms. We used 2× magnification for imaging assessment in all cases. The qualitative assessment of reversibility was performed blindly, comparing pre- and post-verapamil angiograms that were provided by the Department of Radiology without any identifiers (name, time, or order). Anterior-posterior, lateral, and oblique projections were evaluated by 2 experienced neurointerventionalists (E.A.S. and S.D.). Both reviewers were blinded to clinical data and did not know the sequence of pre- and post-verapamil angiograms. Score sheets to determine arterial involvement, vascular territory affected, and morphologic changes between both angiograms were collected (On-line Figs 1 and 2). Vascular territories were divided as follows: 1) proximal branches: A1, M1, P1, vertebral artery, and basilar artery; 2) middle branches: A2, M2, P2, superior cerebellar artery, anterior-inferior cerebellar artery, posterior-inferior cerebellar artery; and 3) distal branches: A3, M3–M4, P3, and any other more distal branch. Morphologic changes were reported as the following: 1) concentric, smooth tapering ("sausaging"); 2) eccentric narrowing, irregular/notched; and 3) segmental dilation, using the same description by Singhal et al.[8] The response to IA verapamil was graded as a dichotomous variable (yes/no).

A quantitative assessment was performed by measuring the caliber of different arterial segments on pre- and post-verapamil angiograms.[19] The diameter of proximal, middle, and distal arterial branches was measured in millimeters. For each patient, the intracranial artery located in the most affected vascular territory was identified; this artery usually showed multiple irregularities suggestive of a vasculopathy process. The area of maximal narrowing of each vascular segment was measured on pre- and post-verapamil angiograms. After visual inspection, areas that appeared more stenotic in each segment were measured; the reviewer registered only the shortest caliber in each segment and used the same area for assessing the patient's second angiogram. Measurements were performed by the same reviewers in a different session at least 4 weeks from the initial subjective assessment. Again, reviewers were blinded to clinical data and the order of the angiograms. Two objective measurements of change (reversibility) were statistically tested as predictors of RCVS:

$$1)\ \text{Caliber Difference} = \text{Caliber}_{\text{post}} - \text{Caliber}_{\text{pre}}$$

$$2)\ \text{Proportion of Change} = \left[\frac{(\text{Caliber}_{\text{post}} - \text{Caliber}_{\text{pre}})}{\text{Caliber}_{\text{pre}}}\right] \times 100\%.$$

For each equation, mean and maximal values were used (a total of 4 measurements per arterial segment). Changes in diameter were analyzed with a receiver operating characteristic (ROC) curve to determine the best threshold in diagnosing RCVS.

The performance of the RCVS-2 score was compared with the objective radiologic determination of reversibility. The RCVS-2

Table 1: Baseline, clinical course, and work-up among patients with and without RCVS

Variable	RCVS ($n = 9$)	No RCVS ($n = 17$)	P[a]
Age (mean) (yr)	44.9	55.7	.06
Women (%)	8 (88.9)	10 (58.8)	.19
Race			
White (%)	8 (88.9)	12 (70.6)	.39
African American (%)	1 (11.1)	2 (11.8)	
Other (%)	0 (0)	3 (17.7)	
Medical history			
Migraine (%)	4 (44.4)	0 (0)	.008
Depression/anxiety (%)	8 (88.9)	3 (17.6)	.001
Hypertension (%)	2 (22.2)	14 (82.4)	.009
Trigger/associated condition	7 (77.8)	2 (11.8)	.002
Vasoconstrictive drugs			
SSRI (%)	6 (66.7)	1 (5.9)	.002
Illicit drugs (%)	0 (0)	1 (5.9)	.65
Postpartum (%)	2 (22.2)	0 (0)	.11
Clinical presentation			
Thunderclap headache (%)	5 (55.6)	1 (5.9)	.01
Other headaches (%)	2 (22.2)	5 (29.4)	.54
Focal neurologic signs			
Hemiparesis/aphasia (%)	5 (55.6)	10 (58.8)	.99
Visual symptoms (%)	3 (33.3)	1 (5.9)	.10
Seizures (%)	2 (22.0)	1 (5.9)	.27
Diagnostic work-up			
ESR (mean) (mm/h)	22.5	43.9	.31
CRP (mean) (mg/L)	3.0	1.9	.61
Normal CSF[b] (%)	2/5 (40.0)	4/9 (44.4)	.99
Brain biopsy (%)	1 (11.1)	1 (5.9)	.58
Abnormal neuroimaging findings (%)			
Infarct (%)	3 (33.3)	13 (76.5)	.046
Multiple (%)	2/3 (66.7)	12/13 (92.3)	.35
Borderzone territory (%)	2/3 (66.7)	1/13 (7.7)	.08
IPH (%)	0 (0)	4 (23.5)	.26
SAH in convexity (%)	5 (55.6)	2 (11.8)	.03
CTA/MRA with vasculopathy			
CTA [$n = 14$][c] (%)	2/5 (40)	5/9 (55.6)	.99
MRA [$n = 16$][c] (%)	2/6 (33.3)	10/10 (100)	.008
Patients with intracranial vasculopathy on DSA not detected by CTA and/or MRA ($n = 26$) (%)	6/9 (66.7)	3/17 (17.6)	.028
RCVS-2 score of ≥ 5	5 (55.6)	1 (5.9)	.01

Note:—CRP indicates C-reactive protein; ESR, erythrocyte sedimentation rate; IPH, intraparenchymal hemorrhage; SSRI, selective serotonin reuptake inhibitor.

[a] P value calculated using a t test, χ^2 test, or Fisher test as appropriate.

[b] Normal CSF if <5 cells and <50 mg/dL.

[c] Number of examinations performed including both groups.

score is a semiquantitative scoring system developed as a bedside diagnostic algorithm. This grading system adjudicates points to different categories as follows: single or recurrent thunderclap headache (TCH) = +5 points, involvement of the intracranial carotid artery = −2 points, a vasoconstrictive trigger = +3 points, female sex = +1 point, and the presence of subarachnoid hemorrhage = +1 point. A score ≥5 has a high sensitivity and specificity in diagnosing RCVS.[9]

Statistical Analysis

Continuous variables are presented as mean ± SD, and categoric variables are presented as frequency and percentage. Distributions of values for mean and maximal measurements of reversibility (caliber difference [CD] and proportion of change [PC]) were tested for normality using the Shapiro-Wilk method. For normally distributed variables, Student t tests were used to compare means. For nonparametric variables, Mann-Whitney U tests were used to compare the medians between the size groups. For categoric values, χ^2 or Fisher tests were applied as appropriate. An ROC analysis using the Youden index was performed to establish the best cutoffs for measurements of reversibility (CD and PC) to diagnose RCVS. The RCVS-2 score was also compared with our objective assessments of reversibility in pre- and post-verapamil angiograms using the DeLong test. A 2-sided P value < .05 was considered significant. All statistical analyses were performed with SPSS Statistics 25.0 (IBM).

RESULTS

Twenty-six patients with intracranial vasculopathy and suspected RCVS were included in the study. Nine patients had a confirmed clinical diagnosis of RCVS (34.6%); 8 with ICAD; 7 with undetermined intracranial vasculopathy; and 2 with PACNS (Table 1).

Qualitative Assessment

Both reviewers reported an angiographic response to IA verapamil in 88.9% (8/9) of patients in the RCVS group versus 41.2% (reviewer 1) and 47.1% (reviewer 2) in the no-RCVS group (On-line Table 1). The Cohen κ analysis demonstrated poor intraobserver agreement to subjectively detect RCVS by comparing pre- and post-verapamil DSAs (reviewer 1: $\kappa = 0.41$, $P = .019$; reviewer 2: $\kappa = 0.35$, $P = .037$). Also, the interrater reliability to detect overall vascular changes was very poor ($\kappa = 0.28$, $P = .149$).

Quantitative Assessment

Two hundred thirteen vascular segments were assessed on DSA, and 87 (40.5%) had post-IA verapamil changes. The statistical analysis showed significant differences in all measurements of reversibility for patients with RCVS, including maximal PC ($P < .001$), mean PC ($P = .002$), maximal CD ($P = .004$), and mean CD ($P = .001$) compared with patients without RCVS (Table 2 and On-line Table 2). The Cohen κ analysis demonstrated substantial interobserver agreement for objective vessel diameter measurements ($\kappa = 0.86$).

CD and PC as Predictors of RCVS

ROC curve analysis was performed to establish the best PC and CD thresholds in diagnosing RCVS (Fig 1). Maximal PC ≥32% had a sensitivity of 100% and a specificity of 88.2% to detect RCVS, with an excellent area under the curve (AUC) of 0.951. However, an RCVS-2 score of ≥5 points had a sensitivity of 77.8% and a specificity of 94.1%, achieving a nonstatistically significant lower AUC in the analysis (0.908) ($P = .47$). Mean PC and mean CD performed similarly in the analysis (AUC = 0.886 and 0.882, respectively), whereas maximal CD performed the worst (AUC = 0.840) (Table 3).

DISCUSSION

Reversibility of intracranial vasoconstriction is the key to diagnosing RCVS. In this study, the objective assessment of caliber changes in affected arteries after the IA infusion of verapamil was accurate and reliable in distinguishing RCVS from other intracranial arteriopathies. The degree of response to IA verapamil quantified as improvement in the caliber of each vascular segment had an excellent performance as a predictor of RCVS. A maximal proportion of change ≥32% in post-verapamil angiograms showed better diagnostic performance than the RCVS-2 score. The subjective assessment of vessel caliber before and after IA administration of verapamil was poor and should not be used routinely as the only marker of reversibility on RCVS.

Patients with typical RCVS symptoms who present with TCH have a well-known trigger and a mild evolution with angiographic changes that generally resolve in 12 weeks.[4] However, the clinical presentation of RCVS is variable, and patients may present without TCH in up to 15% of cases.[20] Patients without TCH may experience severe forms of RCVS, present with coma or confusion due to stroke or posterior reversible encephalopathy syndrome, or have fulminant RCVS. The clinical spectrum of RCVS varies among different populations, and the diagnosis of atypical cases can be challenging.[21] Moreover, the classic "string of beads" appearance of vasoconstriction has been described in only 12%–81% of patients with RCVS.[4]

Previous reports have suggested the benefit of calcium channel blockers (nicardipine, verapamil, and nimodipine) and phosphodiesterase inhibitors (milrinone) in diagnosing and treating RCVS (On-line Table 3).[11-18,22-24] Diagnosis entails the IA infusion of these drugs to determine the improvement in the caliber of the affected vascular segment. Other vasculopathies such as ICAD and PACNS usually do not improve after these challenges or have a milder response, perhaps suggesting some degree of overlap between these conditions. Ospel et al[18] used verapamil in diagnosing RCVS by documenting the reversibility of vascular changes in 11 patients. Luminal narrowing was classified as mild = <30% of normal caliber, moderate = 30%–60% of normal caliber, and severe =

Table 2: Reversibility measurements among patients with and without RCVS

Reversibility Measurement[a]	RCVS ($n = 9$)	No RCVS ($n = 17$)	P Value[b]
Maximal PC (%)	50.6 ± 13.6	21.7 ± 12.5	<.001
Mean PC (%)	20.4 ± 9.8	6.2 ± 6.0	.002
Maximal CD (mm)	0.54 ± 0.27	0.25 ± 0.17	.004
Mean CD (mm)	0.23 ± 0.13	0.07 ± 0.08	.001

[a] Reversibility measurements shown as mean ± SD.
[b] P value was calculated using the Mann-Whitney U test, given a nonparametric distribution of data.

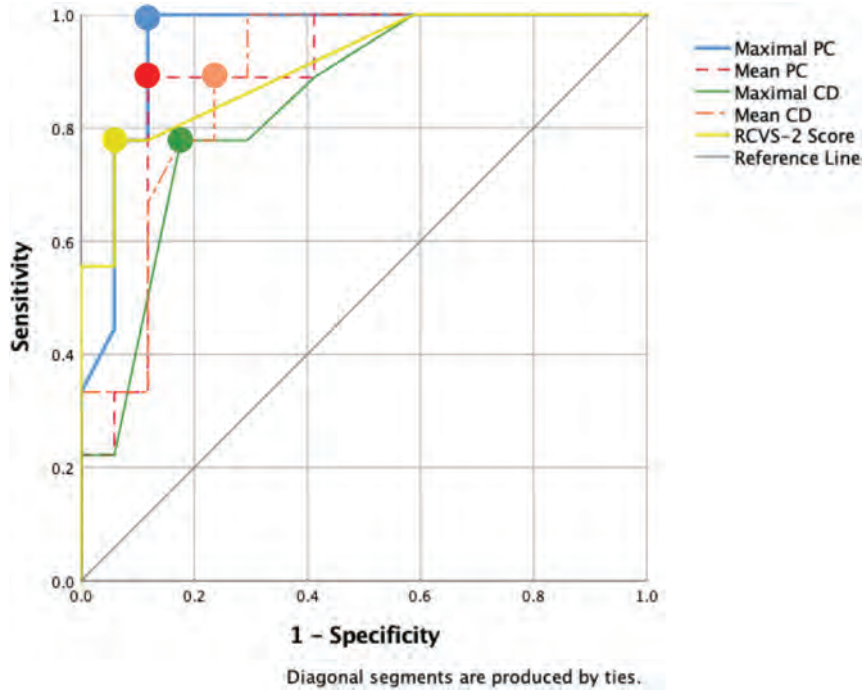

FIG 1. ROC analysis to predict RCVS using objective reversibility measurements and RCVS-2 scores. *Circles* identify best coordinates (cutoffs) for each curve.

Table 3: Cutoffs, AUC, sensitivity, specificity, and positive and negative predictive values of different reversibility measurements

Reversibility Measurement	Cutoff	AUC	95% CI	Sen	Spe	PPV	NPV
Maximal PC (%)	≥32	0.951	0.87–1.00	100	88.2	81.8	100
Mean PC (%)	≥14.4	0.886	0.76–1.00	88.9	88.2	80	93.8
Maximal CD (mm)	≥0.45	0.840	0.68–0.99	77.8	82.4	70	87.5
Mean CD (mm)	≥0.125	0.882	0.75–1.00	88.9	76.5	66.7	92.8
RCVS-2 score (points)	≥5.0	0.908	0.79–1.00	77.8	94.1	87.5	88.9

Note:—NPV indicates negative predictive value; PPV, positive predictive value; Sen, sensitivity; Spe, specificity.

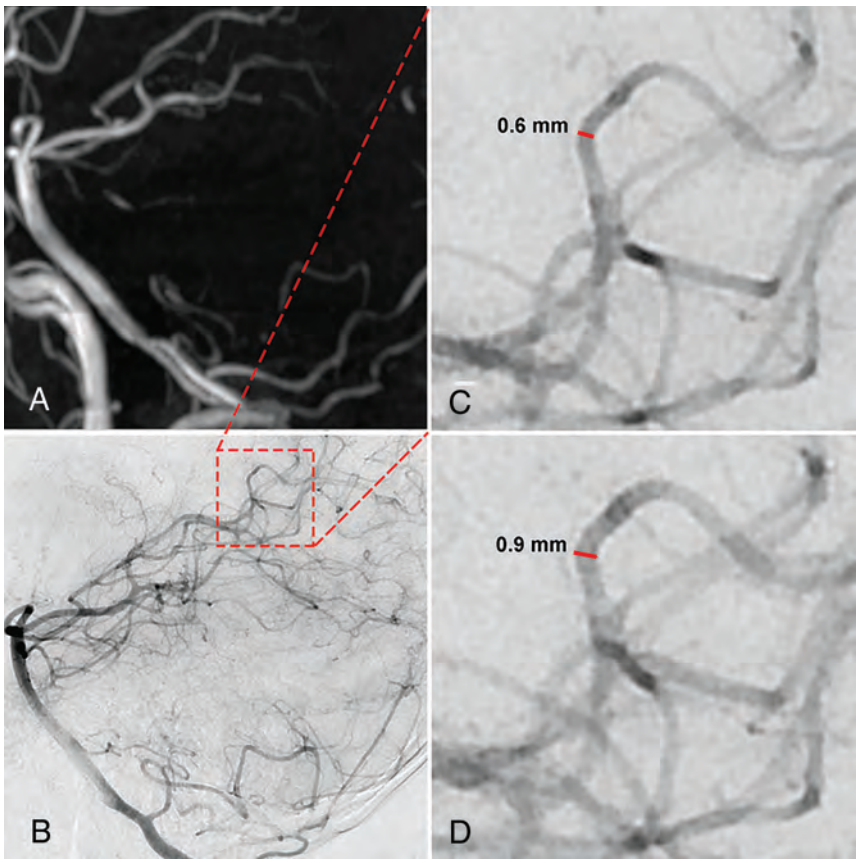

FIG 2. *A*, Contrast-enhanced MRA of a patient with atypical RCVS. The posterior cerebral artery branches appear unremarkable. *B*, Lateral angiogram with areas of segmental narrowing in the posterior circulation. *C*, Pre-verapamil infusion DSA shows the caliber of a P3 branch = 0.6 mm. *D*, Post-verapamil infusion DSA shows a 0.3-mm CD (0.9 − 0.6 mm, 50% PC) in the P3 branch at the same level. These subtle changes in distal branches were not diagnosed in subjective assessments.

>60% of normal caliber. We have objectively documented that a maximal proportion of change of 32% in the lumen diameter after the administration of IA verapamil had a sensitivity of 100% and a specificity of 82% in diagnosing RCVS. All the RCVS cases included in our series were confirmed as RCVS on follow-up using strict diagnostic criteria.

The sensitivity and specificity of DSA in diagnosing RCVS has not been assessed in blinded studies.[4] However, the sensitivity of indirect methods of angiography such as CTA and/or MRA is about 70% compared with DSA.[25] Furthermore, patients may have normal findings on the first DSA if performed early. Thus, subsequent angiograms may be required 1 week after the onset of symptoms to document changes.[26] Our subjective assessment showed poor intra- and interobserver agreement when determining caliber changes in the middle and distal branches. In our cohort, these vascular regions are involved in approximately 89% and 72% of cases, respectively. Singhal et al[8] also reported 92% and 86% of changes affecting the middle and distal branches, respectively. The accuracy of CTA/MRA in detecting mild changes in the distal branches is lower than that of DSA due to their inferior spatial resolution (Fig 2).[2,27,28] The sensitivity of CTA and MRA in detecting small (<3-mm) aneurysms is inferior to that of DSA.[29] The accuracy of these noninvasive imaging modalities in determining <1-mm caliber changes in the middle and distal branches is insufficient compared with DSA. The objective DSA quantification of changes in the diameter of vascular segments after the administration of IA verapamil demonstrated high accuracy in detecting RCVS (Fig 3). Therefore, objective rather than subjective quantification of subtle changes in pre- and post-IA verapamil angiograms should be routinely performed to ascertain the correct diagnosis.

The role of DSA in RCVS has been criticized for its invasiveness, radiation exposure, use of contrast, and lack of scope for intervention.[30] Moreover, the IA administration of vasoactive drugs has been questioned due to the risk of iatrogenic hypotension, reperfusion injury, and theoretic disruption of the blood-brain barrier.[31] While most patients with RCVS have a good outcome, a considerable number of patients will experience a more fulminant course that results in permanent disability or death. This occurs most prominently in patients with atypical clinical presentations whose diagnosis and subsequent treatment are delayed.[31] There is growing evidence that IA administration of vasoactive drugs can be done safely and that DSA may be therapeutic in addition to its valuable diagnostic capabilities.[10,13] It is also possible that the verapamil-induced vasodilation shortens the course of the illness and lowers the chances of subsequent ischemic complications. We recommend DSA with IA verapamil challenge for patients with atypical RCVS presentations (without TCH or classical triggers), slow disease evolution, or an alternative diagnosis being entertained. DSA is particularly helpful if there is an intracranial lesion (ischemic or hemorrhagic) and normal indirect angiographic findings (CTA/MRA) in the setting of a suspected intracranial vasculopathy like RCVS.

This study is limited by the small number of patients. RCVS is a rare condition, and a more thorough assessment would require a prospective multicenter study. Another limitation is the intrinsic selection bias favoring recruitment of sicker patients. Every patient had abnormal imaging findings with evidence of an ischemic stroke and/or hemorrhage at presentation, but almost half did not have the typical TCH. Milder cases of RCVS with typical presentation were not referred for DSA. Therefore, the reversibility of vasoconstriction and the diagnostic accuracy of the IA verapamil challenge are yet to be proved in most cases of RCVS. An ideal statistical comparison between the 2 diagnostic tools became difficult due to few patients with atypical

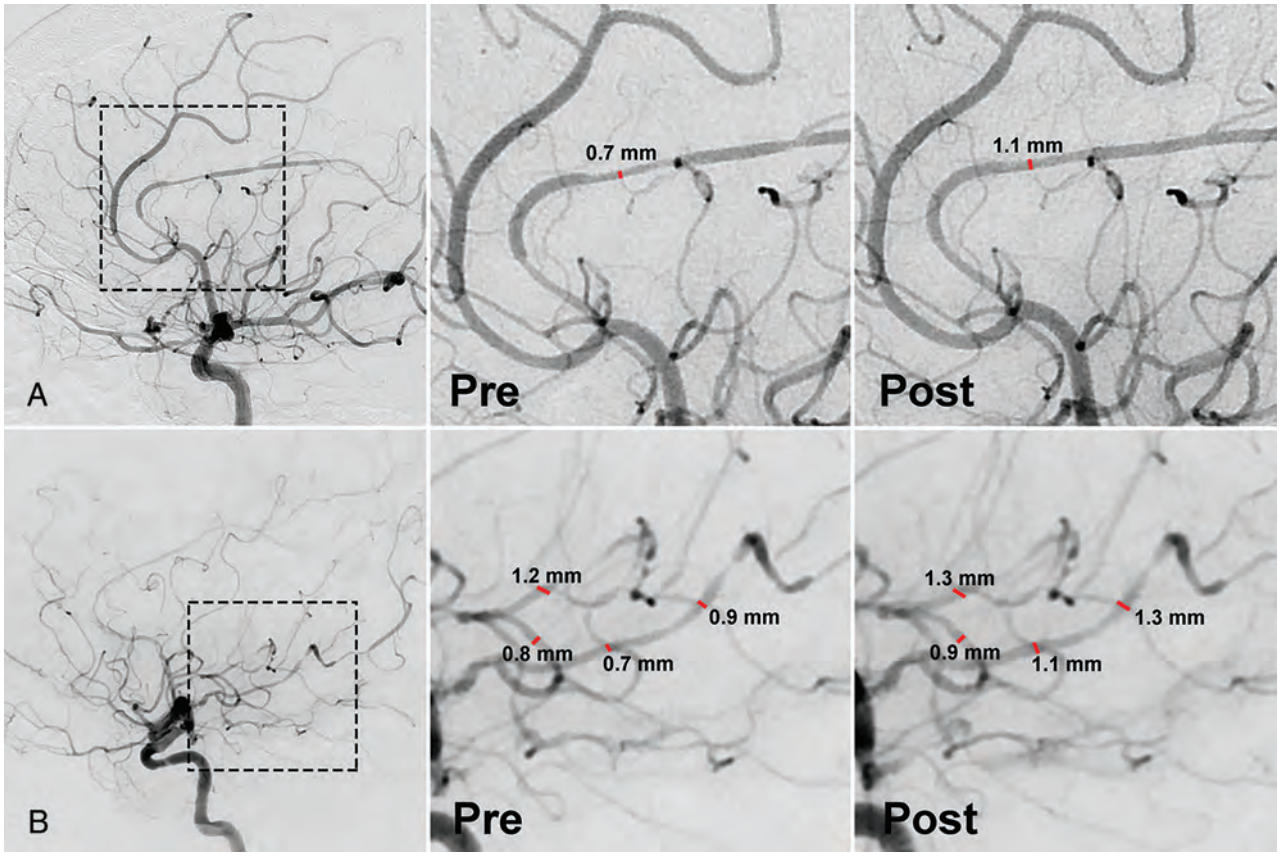

FIG 3. *A*, Patient with RCVS in the right anterior cerebral artery territory. *B*, Patient with RCVS in the right posterior cerebral artery territory. Note the classic string of beads pattern of the affected branches. The *square* delineates zoomed-in areas of the angiogram that were blindly analyzed by 2 readers. These measurements were later labeled as pre- and post-IA verapamil.

presentations of RCVS, even at a high-volume stroke center. The method used for objective vessel-caliber assessment in this study might seem laborious, but for a vascular neuroimaging–trained physician, it would take only a few additional minutes at the workstation. With the recent overwhelming advances in neuroradiology using artificial intelligence,[32] an automated assessment tool might be feasible in the near future.

CONCLUSIONS

Objective quantification of the caliber of affected arterial segments on pre- and post- IA verapamil angiograms has a high diagnostic yield in patients with atypical RCVS. A maximal proportion of change ≥32% had the best performance as a diagnostic tool and was superior to both subjective assessment of reversibility and the clinical RCVS-2 score.

Data are available on reasonable request. Additional unpublished data will be made available by the corresponding author with an appropriate request.

Disclosures: Santiago Ortega-Gutierrez—*UNRELATED*: *Consultancy*: Stryker and Medtronic proctor; * Colin P. Derdeyn—*UNRELATED*: *Consultancy*: Penumbra, Genae, NoNo, *Comments*: Data and Safety Monitoring Boards for clinical trials*; *Employment*: University of Iowa Hospitals and Clinics; *Stock/Stock Options*: Pulse Therapeutics. *Money paid to the institution.

REFERENCES

1. Calabrese LH, Dodick DW, Schwedt TJ, et al. **Narrative review: reversible cerebral vasoconstriction syndromes**. *Ann Intern Med* 2007;146:34–44 CrossRef Medline
2. Miller TR, Shivashankar R, Mossa-Basha M, et al. **Reversible cerebral vasoconstriction syndrome, Part 2: diagnostic work-up, imaging evaluation, and differential diagnosis**. *AJNR Am J Neuroradiol* 2015;36:1580–88 CrossRef Medline
3. Singhal AB, Hajj-Ali RA, Topcuoglu MA, et al. **Reversible cerebral vasoconstriction syndromes: analysis of 139 cases**. *Arch Neurol* 2011;68:1005–12 CrossRef Medline
4. Ducros A. **Reversible cerebral vasoconstriction syndrome**. *Lancet Neurol* 2012;11:906–17 CrossRef Medline
5. Ducros A, Boukobza M, Porcher R, et al. **The clinical and radiological spectrum of reversible cerebral vasoconstriction syndrome: a prospective series of 67 patients**. *Brain* 2007;130:3091–101 CrossRef Medline
6. Kadkhodayan Y, Alreshaid A, Moran CJ, et al. **Primary angiitis of the central nervous system at conventional angiography**. *Radiology* 2004;233:878–82 CrossRef Medline
7. Singhal AB, Topcuoglu MA. **Glucocorticoid-associated worsening in reversible cerebral vasoconstriction syndrome**. *Neurology* 2017;88:228–36 CrossRef Medline
8. Singhal AB, Topcuoglu MA, Fok JW, et al. **Reversible cerebral vasoconstriction syndromes and primary angiitis of the central nervous system: clinical, imaging, and angiographic comparison**. *Ann Neurol* 2016;79:882–94 CrossRef Medline
9. Rocha EA, Topcuoglu MA, Silva GS, et al. **RCVS2 score and diagnostic approach for reversible cerebral vasoconstriction syndrome**. *Neurology* 2019;92:e639–47 CrossRef Medline

10. Crockett MT, Di Loreto M, Philips TJ. **Severe reversible cerebral vasoconstriction syndrome in a postpartum patient treated successfully with direct instillation of intra-arterial verapamil during cerebral angiography**. *J Vasc Interv Neurol* 2017;9:43–44 Medline
11. Elstner M, Linn J, Muller-Schunk S, et al. **Reversible cerebral vasoconstriction syndrome: a complicated clinical course treated with intra-arterial application of nimodipine**. *Cephalalgia* 2009;29:677–82 CrossRef Medline
12. Farid H, Tatum JK, Wong C, et al. **Reversible cerebral vasoconstriction syndrome: treatment with combined intra-arterial verapamil infusion and intracranial angioplasty**. *AJNR Am J Neuroradiol* 2011;32:E184–87 CrossRef Medline
13. French KF, Hoesch RE, Allred J, et al. **Repetitive use of intra-arterial verapamil in the treatment of reversible cerebral vasoconstriction syndrome**. *J Clin Neurosci* 2012;19:174–76 CrossRef Medline
14. Ioannidis I, Nasis N, Agianniotaki A, et al. **Reversible cerebral vasoconstriction syndrome: treatment with multiple sessions of intra-arterial nimodipine and angioplasty**. *Interv Neuroradiol* 2012;18:297–302 CrossRef Medline
15. John S, Donnelly M, Uchino K. **Catastrophic reversible cerebral vasoconstriction syndrome associated with serotonin syndrome**. *Headache* 2013;53:1482–87 CrossRef Medline
16. Kass-Hout T, Kass-Hout O, Sun CH, et al. **A novel approach to diagnose reversible cerebral vasoconstriction syndrome: a case series**. *J Stroke Cerebrovasc Dis* 2015;24:e31–37 CrossRef Medline
17. Linn J, Fesl G, Ottomeyer C, et al. **Intra-arterial application of nimodipine in reversible cerebral vasoconstriction syndrome: a diagnostic tool in select cases?** *Cephalalgia* 2011;31:1074–81 CrossRef Medline
18. Ospel JM, Wright CH, Jung R, et al. **Intra-arterial verapamil treatment in oral therapy-refractory reversible cerebral vasoconstriction syndrome**. *AJNR Am J Neuroradiol* 2020;41:293–99 CrossRef Medline
19. Milburn JM, Moran CJ, Cross DT, et al. **Increase in diameters of vasospastic intracranial arteries by intraarterial papaverine administration**. *J Neurosurg* 1998;88:38–42 CrossRef Medline
20. Wolff V, Ducros A. **Reversible cerebral vasoconstriction syndrome without typical thunderclap headache**. *Headache* 2016;56:674–87 CrossRef Medline
21. Caria F, Zedde M, Gamba M, et al; Italian Project on Stroke at Young Age (IPSYS) Investigators. **The clinical spectrum of reversible cerebral vasoconstriction syndrome: the Italian Project on Stroke at Young Age (IPSYS)**. *Cephalalgia* 2019;39:1267–76 CrossRef Medline
22. Al-Mufti F, Dodson V, Wajswol E, et al. **Chemical angioplasty for medically refractory reversible cerebral vasoconstriction syndrome**. *Br J Neurosurg* 2018;32:431–35 CrossRef Medline
23. Bouchard M, Verreault S, Gariepy JL, et al. **Intra-arterial milrinone for reversible cerebral vasoconstriction syndrome**. *Headache* 2009;49:142–45 CrossRef Medline
24. Laneuville M, Ding J, Shamy M, et al. **Intra-arterial milrinone may differentiate fulminant RCVS from vasculitis**. *Neurology* 2017;89:1093–94 CrossRef Medline
25. Ducros A, Bousser MG. **Reversible cerebral vasoconstriction syndrome**. *Pract Neurol* 2009;9:256–67 CrossRef Medline
26. Ghia D, Cuganesan R, Cappelen-Smith C. **Delayed angiographic changes in postpartum cerebral angiopathy**. *J Clin Neurosci* 2011;18:435–36 CrossRef Medline
27. Ducros A, Wolff V. **The typical thunderclap headache of reversible cerebral vasoconstriction syndrome and its various triggers**. *Headache* 2016;56:657–73 CrossRef Medline
28. Hartung MP, Grist TM, François CJ. **Magnetic resonance angiography: current status and future directions**. *J Cardiovasc Magn Reson* 2011;13:19 CrossRef Medline
29. Turan N, Heider RA, Roy AK, et al. **Current perspectives in imaging modalities for the assessment of unruptured intracranial aneurysms: a comparative analysis and review**. *World Neurosurg* 2018;113:280–92 CrossRef Medline
30. Tan LH, Flower O. **Reversible cerebral vasoconstriction syndrome: an important cause of acute severe headache**. *Emerg Med Int* 2012;2012:303152 CrossRef Medline
31. Miller TR, Shivashankar R, Mossa-Basha M, et al. **Reversible cerebral vasoconstriction syndrome, Part 1: epidemiology, pathogenesis, and clinical course**. *AJNR Am J Neuroradiol* 2015;36:1392–99 CrossRef Medline
32. Hosny A, Parmar C, Quackenbush J, et al. **Artificial intellience in radiology**. *Nat Rev Cancer* 2018;18:500–10 CrossRef Medline

Intraprocedural Flat Panel Detector Rotational Angiography and an Image Fusion Technique for Delivery of a Microcatheter into the Targeted Shunt Pouch of a Dural Arteriovenous Fistula

J.H. Choi, D.Y. Cho, Y.S. Shin, and B.-S. Kim

ABSTRACT

SUMMARY: The accurate and safe delivery of a microcatheter to a targeted shunt pouch is essential for successful transvenous embolization of intracranial dural arteriovenous fistulas. However, complex anatomy and variations in head and neck veins and occluded sinuses can hinder intraprocedural microcatheter delivery. In this study, we introduce an intraprocedural flat panel detector rotational angiography and image fusion technique to aid precise navigation inside the veins and proper placement of the microcatheter in the targeted shunt pouch.

ABBREVIATIONS: ACC = anterior condylar confluence; DAVF = dural arteriovenous fistula; FPCTRA = flat panel CT rotational angiography; IF = image fusion; TVE = transvenous embolization

For the successful treatment of intracranial dural arteriovenous fistulas (DAVFs), precise evaluation of the angioarchitecture using pretherapeutic DSA is important. However, identification of detailed angioarchitectures of some DAVFs using conventional 2D-DSA or 3D rotational angiography images is difficult because of overlapping vessels.[1,2] With the evolution of angiography equipment and 3D postprocessing technology, performing a flat panel CT rotational angiography and image fusion (FPCTRA and IF) technique to obtain a fusion image using 2 different rotational angiographic images is feasible. This technique enables physicians to gain better pretherapeutic knowledge for establishing an appropriate treatment plan.[1-3] However, to our knowledge, no research has focused mainly on the value of the intraprocedural FPCTRA and IF technique. Especially, for transvenous embolization (TVE), the most important factor for successful occlusion is the accurate and safe delivery of a microcatheter to the shunt pouch. Complex anatomy and variations in head and neck veins,[4] especially those located in the skull base,[5] and sinus occlusion[6,7] can hinder intraprocedural microcatheter delivery. In this study, we introduce an intraprocedural FPCTRA and IF technique to aid the navigation of a microcatheter inside veins and confirm the placement of the microcatheter in the targeted pouch.

Received April 3, 2020; accepted after revision June 3.

From the Departments of Neurosurgery (J.H.C., Y.S.S.) and Radiology (B.-S.K.), Seoul St. Mary's Hospital, The Catholic University of Korea College of Medicine, Seoul, Republic of Korea; Department of Neurosurgery (D.Y.C.), Ewha Womans University Seoul Hospital, College of Medicine, Ewha Womans University, Seoul, Republic of Korea.

Please address correspondence to Bum-Soo Kim, MD, PhD, Department of Radiology, Seoul St. Mary's Hospital, The Catholic University of Korea, 222 Banpodaero, Seochogu, Seoul, 06591, Republic of Korea; e-mail: bumrad@catholic.ac.kr

Indicates article with supplemental on-line appendix and table.

Indicates article with supplemental on-line photos.

http://dx.doi.org/10.3174/ajnr.A6724

Technique

For treating all DAVFs and image processing, we used Artis Zee biplane angiography equipment (Siemens). All procedures were conducted with the patient under general anesthesia. Systemic heparin (2000- to 3000-IU bolus) was routinely administrated after placement of a femoral sheath. Antiplatelet agents were not routinely administrated. We placed a 5F angiocatheter in the main feeding artery and a 7F guiding catheter in the internal jugular vein or the retromandibular vein according to the access route. Thereafter, we performed 3D dual rotation angiography with contrast injection to obtain subtraction (vessel only), mask (bone only), and native fill (vessel with bone) images as a baseline. We named this series DSA24, which irradiated at 0.24 μGy/frame and took 30 frame/s for 5 seconds. The rotational angle was 200° with 1.5° increments, resulting in 133 projections and a rotation velocity of 40°/s. For contrast, we infused iodixanol (Visipaque 270; GE Healthcare) via the external carotid artery with an injector at a rate of 2–3 mL/s for 5 seconds with a 1- to 2-second acquisition delay according to vessel diameter and shunt flow. Acquired data were sent to the workstation (syngo 3D workplace; Siemens), and 3D reconstruction was performed with the following parameters: kernel type, Hounsfield unit; image characteristics, normal; reconstruction mode, dual volume; section matrix, 512 × 512; and voxel size, 0.47 mm. A size 18

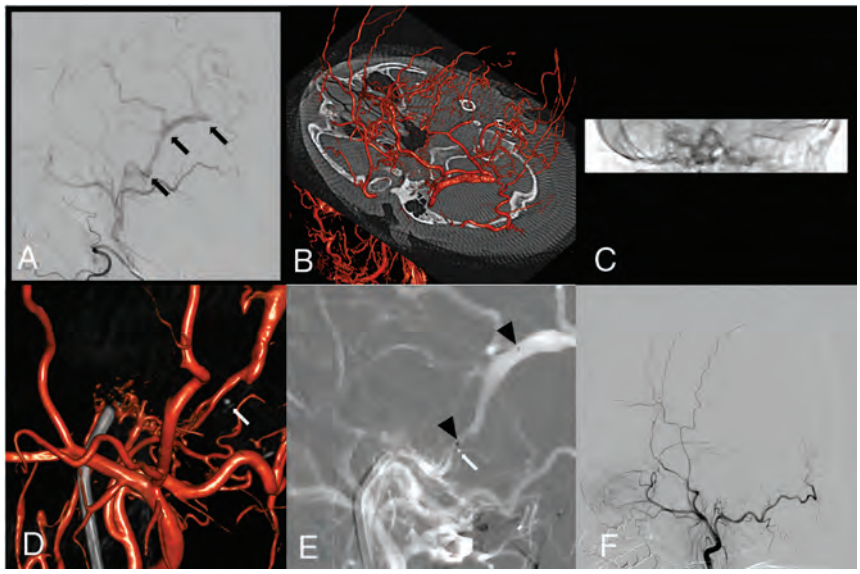

FIGURE. Case 1. A 61-year-old female patient presenting with intracranial hemorrhage. *A*, Initial right external carotid angiography shows a transverse sigmoid dural AVF with an isolated sinus (*black arrow*) and pial reflux. *B*, Intraprocedural 0.24-μG/frame FPCTRA (DSA24) is performed to obtain subtraction and mask images as a control. *C*, During the microcatheter navigation, we perform low-dose FPCTRA with a reduced FOV (DRcare). *D*, We found that the microcatheter was placed in the wrong direction (*white arrow*) by fusion of the initial DSA24 and follow-up DRcare images. *E*, After we pulled back the microcatheter (*white arrow*), we directed it the right way and placed the microcatheter in the target shunt (*black arrowhead*). *F*, Successful coil embolization is performed.

microcatheter (Excelsior 1018, Stryker) and a 0.014-inch microwire (Transend; Stryker) were usually used for navigation. During navigation, if needed, we performed 3D single-rotation angiography with a reduced FOV without contrast injection while keeping the microwire and microcatheter inside the vein and fused with the initial subtraction image to identify the microcatheter going in the right direction. This series was named DRcare, which was performed with a single rotation for 5 seconds and irradiated 0.10 μGy/frame. In the workstation, we performed 3D reconstruction: kernel type, EE; image characteristics, normal; reconstruction mode, native. Two different image datasets (DSA24 and DRcare) were fused by a mapping application syngo iDentify (Syngo 3D workplace, Siemens AG, Erlangern, Germany), which superimposes the spatial coordinate system of the initial dataset onto that of the second dataset. We used landmark-based automatic registration to avoid misalignment.[8] When the microcatheter accessed the shunt pouch, we also checked DRcare and fused images to confirm the exact placement of the microcatheter in the target. Thereafter, we inserted the coil until the shunt disappeared.

Clinical Results

Details of the study population and outcome assessment are presented in the On-line Appendix. We used the FPCTRA and IF technique in 18 of 58 DAVFs treated with TVE between January 2009 and March 2020. Among them, 11 had ipsilateral sinus occlusion (8 in the cavernous sinus, 2 in the anterior condylar confluence [ACC], and 1 in the transverse-sigmoid sinus). We approached the shunt pouch through the occluded sinus by blinded navigation ($n = 6$) or through alternative venous routes (the facial or superficial temporal vein, $n = 5$). Seven DAVFs were located in the ACCs. The complete or near-complete occlusion rate and symptom-free or improved rate were 94.4% and 100%, respectively. There was no catheter-related vessel injury with or without using this technique. We could access the shunt via the transfemoral route in all cases treated using this technique (On-line Table). In contrast, we failed to reach the shunt pouch via the transfemoral approach in 5 cases without this technique. Therefore, surgical cannulation of the target sinus or the direct ophthalmic vein approach was additionally performed to reach the shunt. Illustrative cases are presented in the Figure and On-line Figs 1 and 2.

DISCUSSION

In this study, we described an intraprocedural FPCTRA and IF technique and demonstrated its usefulness during the TVE. The transvenous approach may have technical difficulties for various reasons. In cases with an occluded accessing route due to thrombosis or hypoplasia, TVE can be more challenging. Breaching the occluded sinus by blinded navigation can be attempted. However, breaching the occluded route is not always feasible, and serious complications, including vessel perforation, can occur.[7] In addition, delivery of the microcatheter in the wrong direction can occur because breaching the occluded route is always performed by blinded navigation. Moreover, the complexity of head and neck veins that have numerous tributaries and confluences may prevent the microguidewire and microcatheter from advancing in the right direction to the shunt pouch.[4] Especially, a DAVF involving the ACC can be challenging for navigation of the microcatheter because of complex venous anatomy around the hypoglossal canal.[5] Additionally, roadmap images during TVE may have low image quality and efficacy due to an overlap of vessels on 2D-DSA. Therefore, blinded microcatheter navigation may be needed, and the microcatheter position for coil insertion can be inappropriately placed. These might lead to unexpected complications or incomplete occlusion. In this study, we used the FPCTRA and IF technique to overcome these obstacles. MPR or a partial MIP image was mainly used for identification of the microcatheter tip with bony landmarks during the blinded navigation. To confirm appropriate microcatheter placement, we used mainly 3D volume-rendering or MPR fusion images.

This study has some limitations. The retrospective nature and small sample size may not be enough to draw definite conclusions. Moreover, our technique was mainly used in DAVFs involving an ACC or with sinus occlusion needing blinded

navigation. Other typical lesions could be successfully treated using conventional techniques. Therefore, we do not advocate our technique as a first-line use. Finally, our technique may require more radiation exposure. However, minimizing additional radiation exposure can be accomplished using low-dose protocols. Further large-volume data should be evaluated to confirm the efficacy and safety of our technique.

Intraprocedural use of FPCTRA and IF for TVE might be an effective and safe method to navigate the microcatheter into the targeted shunt pouch, especially in cases that require blinded microcatheter navigation.

REFERENCES

1. Tanoue S, Kiyosue H, Mori H, et al. **Fusion imaging using subtracted and unsubtracted rotational angiography for pretherapeutic evaluation of dural arteriovenous fistulas.** *Jpn J Radiol* 2014;32:600–07 CrossRef Medline
2. Li H, Wan F, Li J, et al. **Flat detector computed tomography-based "dual vessel fusion" technique for diagnosis and surgical planning in the management of dural arteriovenous fistula.** *World Neurosurg* 2015;84:520–27 CrossRef Medline
3. Fukuda K, Higashi T, Okawa M, et al. **Fusion technique using three-dimensional digital subtraction angiography in the evaluation of complex cerebral and spinal vascular malformations.** *World Neurosurg* 2016;85:353–58 CrossRef Medline
4. Choi JH, Shin YS, Kim BS. **Making microguidewire loop facilitates navigation through tortuous or abruptly angulated head and neck veins to access cavernous sinus dural arteriovenous fistulas.** *World Neurosurg* 2019;129:e561–65 CrossRef Medline
5. Spittau B, Millán DS, El-Sherifi S, et al. **Dural arteriovenous fistulas of the hypoglossal canal: systematic review on imaging anatomy, clinical findings, and endovascular management.** *J Neurosurg* 2015;122:883–903 CrossRef Medline
6. Biondi A, Milea D, Cognard C, et al. **Cavernous sinus dural fistulae treated by transvenous approach through the facial vein: report of seven cases and review of the literature.** *AJNR Am J Neuroradiol* 2003;24:1240–46 Medline
7. Cho YD, Rhim JK, Yoo DH, et al. **Transvenous microguidewire looping technique for breach of ipsilateral inferior petrosal sinus occlusions en route to cavernous sinus dural arteriovenous fistulas.** *Interv Neuroradiol* 2016;22:590–95 CrossRef Medline
8. Yuki I, Ishibashi T, Dahmani C, et al. **Combination of high-resolution cone beam computed tomography and metal artefact reduction software: a new image fusion technique for evaluating intracranial stent apposition after aneurysm treatment.** *BMJ Case Rep* 2019;12:e230687 CrossRef Medline

Microcatheter Originating Debris during Neuroendovascular Procedures: Mechanism of Dislodgement and Its Prevention

I. Kan, K. Karagiozov, S. Ito, S. Sato, and Y. Murayama

ABSTRACT

SUMMARY: Embolic material dislodgement from microcatheters can potentially induce subclinical brain damage as evidenced by a delayed enhanced or other type of lesions. Some of the most frequently used microcatheters were investigated in vitro in different setups and combinations with different port insertions and rotating hemostatic valves. It was found that side port application increases injury to the catheter surface and debris dislodgement by conflicting with internal ledges in rotating hemostatic valves. This initial observation suggests the need for measures to remove the produced debris during such procedures.

ABBREVIATIONS: DEL = delayed enhanced lesion; FTIR = Fourier-transform infrared; RHV = rotating hemostatic valve

Intraprocedural embolization by coating material particles from medical devices, especially stent devices,[1,2] and nickel allergy reaction to these particles,[3,4] have been presumed to be the potential cause of delayed enhanced lesions (DELs) after endovascular surgery, but these have also been reported after the double-catheter technique[5] and balloon-assisted coil embolization[6] with multiple-microcatheter usage. Therefore, an in vitro setup of dual-microcatheter access via 2 single-port, rotating hemostatic valves (RHVs) connected one to the other via the side port was investigated for debris dislodgement.

MATERIALS AND METHODS

Microcatheters and Devices

The Excelsior SL-10 microcathter (Stryker) was evaluated by in vitro simulation of its application in different device configurations during endovascular procedures, by comparing it with 3 similar types of microcatheters and between 2 similar RHV devices.

For hydrophilic coating–integrity study before and after interactions with the RHV, the Excelsior SL-10 was stained with a 0.1% aqueous solution of Congo red for 60 minutes and dried for 24 hours,[7] and the Headway 17 (Terumo) and Echelon 10 (Medtronic) microcatheters were stained with a 0.1% aqueous solution of Toluidine blue.

Two single-port RHVs (Abbott 0.096-inch model 23242 RHV; Abbott Vascular) (AbbottRHV) were connected in series, via the side port (On-line Fig 1). Sequentially, we tested an SL-10 insertion (with a CHIKAI 14 guidewire; Asahi Intecc) separately through the attached RHV straight port or the side ports; 2 microcatheters under the same conditions, a Headway 21 (Terumo) or Prowler 21 (Codman & Shurtleff) microcatheter through the straight port and the SL-10 through the side port; and finally an SL-10 without a guidewire (Table). Next a combination of Headway 17 and Echelon 10 were tested. Finally, a Gateway Advantage Y Adaptor model H74904482012 (Boston Scientific) (BostonRHV) was compared with the Abbott model.

The inside of the RHV was flushed with saline as during routine surgical procedures on a single insertion and extraction through the available port, and the skived material from microcatheters was collected from the flush fluid in a 0.45-μm filter. Three neurointerventionalists including the first author independently assessed the amount of debris, rating it semiquantitatively in 3 grades: –, none; +, any identifiable; and ++, substantial amount/bulk of debris (On-line Fig 2*B*).

After extraction from the RHV, the length of the stained microcatheter from the tip to 1000 mm proximally was photographed using a stereomicroscope. For microscopic testing, the debris from an unstained microcatheter was collected in saline and sent to the pathology department, where Papanicolaou and hematoxylin-eosin stains were applied.

The samples collected in the 0.45-μm filters were directly analyzed using Fourier-transform infrared (FTIR) spectroscopy with

Received April 15, 2020; accepted after revision June 15.

From the Departments of Neurosurgery (I.K., K.K., Y.M.) and Pathology (S.I., S.S.), The Jikei University Hospital, Tokyo, Japan.

This work was supported by an educational research grant to our department from Stryker.

Please address correspondence to Issei Kan, MD, Department of Neurosurgery, The Jikei University Hospital, 3-25-8 Nishi-Shinbashi, Minato-ku, 105-8461 Tokyo, Japan; e-mail: isseikan@gmail.com

Indicates article with supplemental on-line photos.

http://dx.doi.org/10.3174/ajnr.A6723

Microcatheter combinations investigated and the amount of debris they produced

Step	Side Port	Straight Port	RHV	Amount of Debris	
				Insertion	Extraction
1 SL-10 Evaluation	None	SL-10	Abbott	–	–
	SL-10	None	Abbott	+	++
	SL-10[a,b]	Headway 21	Abbott	+	++
	SL-10	Prowler 21	Abbott	+	++
	SL-10 without guidewire	Prowler 21	Abbott	–	–
2 Microcatheter comparison	Headway 17[a]	Headway 21	Abbott	+	++
(similar MC to SL-10)	Echelon 10[a]	Headway 21	Abbott	+	++
3 RHV comparison (other RHV)	SL-10[b]	Headway 21	Boston Scientific	–	+

Note:—MC indicates microcatheter; – for amount of debris, none; +, identifiable; ++, substantial, "None" under Side Port and Straight Port, absence of device use.
[a] Microcatheter comparison.
[b] RHV comparison.

a Thermo-Nicolet 6700 FTIR spectrometer (attenuated total reflection mode; Thermo Electron) and a germanium crystal with a typical penetration depth of ~1 μm. The analytic spot size was approximately 100 x 100 μm. OMNIC Series Software (ThermoFisher) was used for the data analysis.

The pulling resistance force for SL-10 was evaluated with and without a guidewire through the 2 different types of RHVs using Digital Force Gauge DS2-20N (Imada, Aichi, Japan).

Both RHVs were imaged using a MicroCT Scanner NSI X25 (GE Healthcare) for cross-sectional views (14.7- μm voxel). High-resolution conebeam DynaCT RHV images (Artis Q biplane; Siemens) with the microcatheter inserted were acquired to measure the curvature radius of the microcatheter and the angle between the RHV side and straight ports.

RESULTS

All single-test combinations with side port SL-10 use (alone or through Headway 21 or Prowler 21) yielded some amount of debris at insertion and much more at extraction. The straight port SL-10 insertion and the SL-10 without a guidewire or together with the Prowler 21 did not produce debris.

The double-microcatheter application (Headway17/Headway21, Echelon10/Headway21) produced smaller amounts of debris at insertion and more significant amounts at extraction.

On a single experiment performed, the AbbottRHV produced more debris than the BostonRHV both on insertion and extraction.

All microcatheters inserted through the additional side port RHV (with and without a microcatheter in the main port) demonstrated damaged or skived coating 110 mm from the microcatheter tip (On-line Figs 1*A* and 2*A*), and microscopically stained debris resembled the microcatheter coating.

FTIR debris analysis from the Excelsior SL-10 detected polyvinylpyrrolidone and a sulfonate salt similar to sodium lignosulfonate, and from the Headway 17, an organic acid salt similar to sodium alginate with trace of silicone species. Similar substances were detected for the Echelon 10 microcatheter. These results were all indicative of chemical structural components of catheter coating materials, mentioned in the corresponding documents accompanying the devices.

AbbottRHV produced 16-gram-force resistance with the guidewire and 3-gram-force without it, while for BostonRHV these values were 4 gram-force and 1 gram-force respectively, 3 to 4 times difference between RHVs and with/without the guidewire.

The CT scans of both AbbottRHV and BostonRHV showed a small ledge (protrusion) at the junction of the side and straight ports (On-line Fig 1*C*). The microcatheter inserted through the side port has to follow a tighter turn that requires direct firm contact with the ledge.

DISCUSSION

This in vitro study confirms that coating skiving of several types of stained-in-advance microcatheters will release debris when inserted through the side ports of RHVs. Some authors already have suggested that concurrent use of multiple microcatheters may cause DEL, blaming intracatheter friction and skiving of the microcatheter coating.[1,5,8]

We selected the widely applied method of multiple-microcatheter use and explored its course through the RHV to find more severe coating damage with the AbbottRHV. It can be assumed that differences in geometries between RHVs with the presence of a ledge inside creating friction resistance are probably the reason for this observation.

Biopsy-proved existence of foreign body emboli after endovascular treatment of intracranial aneurysms has already been reported, and pathologic findings have shown foreign body granuloma reaction with inflammatory cell infiltration.[1,6,9] In the center of the granuloma, blue-gray nonpolarized material was frequently observed with H&E staining, and it appeared to be polyvinylpyrrolidone catheter coating.[1,10]

Most articles reporting DELs (cerebral leptomeningeal enhancement with perilesional edema seen after endovascular treatment of cerebral aneurysms) refer to the use of stent-assisted coil embolization or flow diverters.[1-4] Speculated potential causes were polyglycolic lactic acid polymer,[11] hydrophilic coating,[1,12-14] and nickel allergy.[3] However, DEL occurrence following coil embolization as well as balloon-assisted coil embolization have also been reported.[2,5,6,15]

A continuous skiving of all microcatheter coating after staining was observed from 110 to 1000 mm from the tip, and the obtained debris was similar to that in previous reports.[1,10] The microcatheter distal tip is more flexible than its proximal sections, and that feature may be the cause for not observing skived

coating most distally as impact is reduced. Insertion with the guidewire reduced microcatheter flexibility and increased the debris amount.

On the basis of this study, removing the guidewire before microcatheter extraction and aspiration of the guiding catheter content at the time of microcatheter extraction to reduce coating debris discharge into the circulation are suggested because the constant infusion through the port will inject debris into the circulation. Internal lumen modification of RHVs to reduce the mechanical conflict of side port channels could be helpful.

As a preliminary investigation, this study inherently contains limitations. First, currently, it is not confirmed that skived coating causes DEL. Next, there is no evidence for or against changes induced by the dyes used on the catheter coating, and finally, there are many different brands and models of RHVs and microcatheters currently available in different clinical settings; therefore, further investigation of these devices is warranted.

CONCLUSIONS

This preliminary study shows that a microcatheter insertion through an RHV side port may induce coating damage and debris dislodgement. Further investigation is warranted into dual-microcatheter access using different device combinations, and redesigning to minimize microcatheter coating damage and debris release. Measures to counteract this issue are necessary.

ACKNOWLEDGMENTS

We are very grateful for the contribution of Dr. Toshihiro Ishibashi and Dr. Tomonobu Kodama for the independent blind assessment of the amount of debris produced. Stryker provided the methodology and performed the FTIR and MicroCT investigations, with the catheter staining/debris collection technique in this study.

Disclosures: Yuichi Murayama—*UNRELATED*: *Consultancy*: Stryker, Kaneka Medix, Tokai Medical Products; *Grants/Grants Pending*: Stryker, *Comments*: An educational research grant to our department from Stryker was used, in part, to support this study.* *Money paid to the institution.

REFERENCES

1. Shapiro M, Ollenschleger MD, Baccin C, et al. **Foreign body emboli following cerebrovascular interventions: clinical, radiographic, and histopathologic features.** *AJNR Am J Neuroradiol* 2015;36:2121–26 CrossRef Medline
2. Cruz JP, Marotta T, O'Kelly C, et al. **Enhancing brain lesions after endovascular treatment of aneurysms.** *AJNR Am J Neuroradiol* 2014;35:1954–58 CrossRef Medline
3. Park HS, Nakagawa I, Yokoyama S, et al. **Nickel-associated delayed multiple white matter lesions after stent-assisted coil embolization of intracranial unruptured aneurysm.** *J Neurointerv Surg* 2018;10:e1 CrossRef Medline
4. Tsang AC, Nicholson P, Pereira VM. **Nickel-related adverse reactions in the treatment of cerebral aneurysms: a literature review.** *World Neurosurg* 2018;115:147–53 CrossRef Medline
5. Oh SW, Shin NY, Lee HJ, et al. **Delayed enhancing lesions after coil embolization of aneurysms: clinical experience and benchtop analyses.** *J Neurointerv Surg* 2017;9:1243–47 CrossRef Medline
6. Shotar E, Law-Ye B, Baronnet-Chauvet F, et al. **Non-ischemic cerebral enhancing lesions secondary to endovascular aneurysm therapy: nickel allergy or foreign body reaction? Case series and review of the literature.** *Neuroradiology* 2016;58:877–85 CrossRef Medline
7. Babcock DE, Hergenrother RW, Craig DA, et al. **In vivo distribution of particulate matter from coated angioplasty balloon catheters.** *Biomaterials* 2013;34:3196–205 CrossRef Medline
8. Ikemura A, Ishibashi T, Otani K, et al. **Delayed leukoencephalopathy: a rare complication after coiling of cerebral aneurysms.** *AJNR Am J Neuroradiol* 2020;41:286–92 CrossRef Medline
9. Hu YC, Deshmukh VR, Albuquerque FC, et al. **Histopathological assessment of fatal ipsilateral intraparenchymal hemorrhages after the treatment of supraclinoid aneurysms with the Pipeline Embolization Device.** *J Neurosurg* 2014;120:365–74 CrossRef Medline
10. Fealey ME, Edwards WD, Giannini C, et al. **Complications of endovascular polymers associated with vascular introducer sheaths and metallic coils in 3 patients, with literature review.** *Am J Surg Pathol* 2008;32:1310–16 CrossRef Medline
11. Mehta RI, Mehta RI, Fishbein MC, et al. **Intravascular polymer material after coil embolization of a giant cerebral aneurysm.** *Hum Pathol* 2009;40:1803–07 CrossRef Medline
12. Mehta RI, Mehta RI. **Hydrophilic polymer embolism: an update for physicians.** *Am J Med* 2017;130:e287–90 CrossRef Medline
13. Stanley JRL, Tzafriri AR, Regan K, et al. **Particulates from hydrophilic-coated guiding sheaths embolise to the brain.** *Eurointervention* 2016;11:1435–41 CrossRef Medline
14. Mehta RI, Mehta RI, Solis OE, et al. **Hydrophilic polymer emboli: an under-recognized iatrogenic cause of ischemia and infarct.** *Mod Pathol* 2010;23:921–30 CrossRef Medline
15. Skolarus LE, Gemmete JJ, Braley T, et al. **Abnormal white matter changes after cerebral aneurysm treatment with polyglycolic-polylactic acid coils.** *World Neurosurg* 2010;74:640–44 CrossRef Medline

Olfactory Bulb Signal Abnormality in Patients with COVID-19 Who Present with Neurologic Symptoms

S.B. Strauss, J.E. Lantos, L.A. Heier, D.R. Shatzkes, and C.D. Phillips

ABSTRACT

BACKGROUND AND PURPOSE: Unique among the acute neurologic manifestations of Severe Acute Respiratory Syndrome coronavirus 2, the virus responsible for the coronavirus disease 2019 (COVID-19) pandemic, is chemosensory dysfunction (anosmia or dysgeusia), which can be seen in patients who are otherwise oligosymptomatic or even asymptomatic. The purpose of this study was to determine if there is imaging evidence of olfactory apparatus pathology in patients with COVID-19 and neurologic symptoms.

MATERIALS AND METHODS: A retrospective case-control study compared the olfactory bulb and olfactory tract signal intensity on thin-section T2WI and postcontrast 3D T2 FLAIR images in patients with COVID-19 and neurologic symptoms, and age-matched controls imaged for olfactory dysfunction.

RESULTS: There was a significant difference in normalized olfactory bulb T2 FLAIR signal intensity between the patients with COVID-19 and the controls with anosmia ($P = .003$). Four of 12 patients with COVID-19 demonstrated intraneural T2 signal hyperintensity on postcontrast 3D T2 FLAIR compared with none of the 12 patients among the controls with anosmia ($P = .028$).

CONCLUSIONS: Olfactory bulb 3D T2 FLAIR signal intensity was greater in the patients with COVID-19 and neurologic symptoms compared with an age-matched control group with olfactory dysfunction, and this was qualitatively apparent in 4 of 12 patients with COVID-19. Analysis of these preliminary finding suggests that olfactory apparatus vulnerability to COVID-19 might be supported on conventional neuroimaging and may serve as a noninvasive biomarker of infection.

ABBREVIATIONS: COVID-19 = coronavirus disease 2019; OB = olfactory bulb; SARS-CoV-2 = Severe Acute Respiratory Syndrome coronavirus 2

Severe Acute Respiratory Syndrome coronavirus 2 (SARS-CoV-2), the virus responsible for the coronavirus disease 2019 (COVID-19) pandemic, may produce a broad range of acute neurologic symptoms that involve both the CNS and the peripheral nervous system, including stroke,[1] meningitis, encephalitis, Guillain-Barré syndrome, and acute necrotizing hemorrhagic encephalopathy.[2] Unique among these acute neurologic manifestations is chemosensory dysfunction (anosmia or dysgeusia), which can be seen in patients who are otherwise oligosymptomatic or even asymptomatic. A single-institution report from the United States that involved 1480 patients with COVID-19 testing showed that loss of smell and taste was reported in 68% of patients who tested positive for COVID 19, of whom, 26% did not recover.[3] The reported incidence of anosmia varies internationally: as low as 30% in South Korea, where there is widespread testing, and as high as 88% in Europe, where testing practices might be less uniform.[4-11] Chemosensory symptoms may present as viral prodromes or be concomitant with the development of other disease symptoms.[12] Although olfactory dysfunction can be seen with rhinoviruses, parainfluenza, Epstein-Barr virus, and other coronaviruses, this symptom is typically linked with rhinorrhea and nasal obstruction, whereas there is accumulating evidence that SARS-CoV-2 associated olfactory dysfunction is seen independent of nasal congestion.[2,6] Anosmia in the absence of other symptoms is reported in as many as 1 of 6 individuals with SARS-CoV-2 infection.[10]

The olfactory bulbs (OBs) are easily identified on conventional MR imaging and are located immediately beneath the olfactory sulci within the anterior cranial fossa, above the cribriform plate. The normal imaging appearance of the adult OB is well described[13-15] and should appear oval- or j-shaped in morphology and demonstrate uniform T2 signal intensity from the center to

Received May 26, 2020; accepted after revision June 30.

From the Department of Radiology (S.B.S., J.E.L., L.A.H., C.D.P.), Weill Cornell Medical College, New York-Presbyterian, New York, New York; and Department of Radiology (D.R.S.), Zucker School of Medicine at Hofstra/Northwell, Lenox Hill Hospital and The New York Head and Neck Institute, New York, New York.

Please address correspondence to C. Douglas Phillips, MD, Weill Cornell Imaging at New York-Presbyterian, 1305, York Ave 3rd Floor, New York, NY 10021; e-mail: cdp2001@med.cornell.edu; @CDP_Rad

Indicates open access to non-subscribers at www.ajnr.org

http://dx.doi.org/10.3174/ajnr.A6751

the periphery.[15] The olfactory neural network includes first-order projections to the piriform cortex and amygdala as well as secondary projections, including the orbitofrontal cortex, thalamus, and insula.[16] Morphologic changes in the OB and associated areas have been shown in various other disease states, including chronic rhinosinusitis, post–viral anosmia, and neurodegenerative disease.[17-19] Moreover, both central and peripheral components of the olfactory system seem to have distinct functional roles in olfactory perception.[20]

Although much remains unknown with regard to the pathophysiology of anosmia in the setting of COVID-19, given that chemosensory dysfunction is reported as the first symptom of disease in up to 27% of patients,[21] imaging-detected OB pathology might serve as a noninvasive biomarker for infection. To our knowledge, there are no studies that systematically evaluated patients with COVID-19 for radiologic evidence of OB, tract, and olfactory association area abnormalities. The purpose of this study was to determine if there is imaging evidence of olfactory apparatus pathology in patients with COVID-19 and neurologic symptoms. We hypothesize that individuals with COVID-19 will show evidence of OB pathology manifesting as OB signal abnormality.

MATERIALS AND METHODS

Subject Enrollment

This was a Health Insurance Portability and Accountability Act retrospective, case-control study performed with approval of the institutional review board at Weill Cornell Medical Center. A radiology report data base query was performed to identify all patients with suspected or confirmed COVID-19 and MR imaging of the brain performed as part of standard of care between April 4, 2020, and May 4, 2020. Inclusion criteria for subjects included positive SARS-CoV-2 reverse transcription–polymerase chain reaction result from nasopharyngeal specimen, MR imaging examination, including thin-section coronal T2WI of the OB (2 mm) and high-resolution 3D T2 FLAIR images of the whole brain. An age-matched control group was scanned for olfactory dysfunction with previous MR imaging of the brain that included thin-section coronal T2WI and high-resolution 3D T2 FLAIR.

Imaging Acquisition

MR images were acquired by using a 3T MR imaging system on several in- and outpatient scanners at our institution: Signa Architect (GE Healthcare; 6 cases, 3 controls), Discovery 750W (GE Healthcare; 6 cases), Skyra (Siemens; 9 controls) by using a 48-channel head coil. Coronal T2WIs of the OB were acquired with the following parameters: repetition time/echo time, 2744.0/108.3 ms; field of view, 180.0 × 180.0 mm; and section thickness, 2.0 mm. Sagittal 3D T2 FLAIR images were acquired after the administration of Gadavist (gadobutrol) 0.1 mmol/kg (Bayer Schering Pharma) intravenous contrast with the following parameters: repetition time/echo time 6002.0/126.9 ms; inversion time, 1681.0 ms; field of view, 215.3 × 108.7 mm; and section thickness, 1.0 mm (with 3-mm coronal and axial reconstructed images).

Imaging Data Analysis

Evaluation of the patients and the controls was done via consensus review by 2 neuroradiologists (L.A.H. [with 34 years of imaging experience], J.L. [with 10 years of imaging experience]); a third neuroradiologist (C.D.P. [with 30 years of imaging experience]) adjudicated the differences when consensus was not reached. All the reviewers were blinded to patient category. Consensus review was performed for the following measures: Kennedy staging for paranasal sinus disease (0–IV), mucosal disease that involves the olfactory recess, loss of OB volume (coronal T2 of the OB), OB and olfactory tract signal abnormality (coronal T2 of the OB), OB and olfactory tract signal abnormality (3D T2 FLAIR), the presence of abnormality in the piriform cortex and amygdala, the presence of signal abnormality in the orbitofrontal cortex, and evaluation for other relevant imaging findings (the presence of acute stroke; chronic microvascular disease graded as mild, moderate, severe). Paranasal sinus disease was assessed by using the Kennedy staging,[22] as outlined in Table 1. The OB volume loss was a qualitative determination based on loss of the normal oval- or J-shaped morphology, or loss of volume compared with the contralateral OB.[15] The OB and olfactory tract signal intensity was assessed relative to the trigeminal nerve; OB and olfactory tract hyperintense to the trigeminal nerve was classified as abnormal. Quantitative assessment of the OB signal intensity was also performed. For each patient, an ROI was drawn at the mid segment of the OB as well as in the left superior frontal WM to calculate normalized values (Fig 1).

Patients were excluded if coronal T2WI of the OB was not performed (n = 19), high-resolution 3D T2 FLAIR was not

Table 1: Kennedy staging

Stage	Description
0	Normal
I	Anatomic abnormalities, unilateral sinus disease, bilateral disease limited to ethmoid sinuses
II	Bilateral ethmoid disease with involvement of 1 dependent sinus
III	Bilateral ethmoidal disease with involvement of 2 or more dependent sinuses on each side
IV	Diffuse sinonasal polyposis

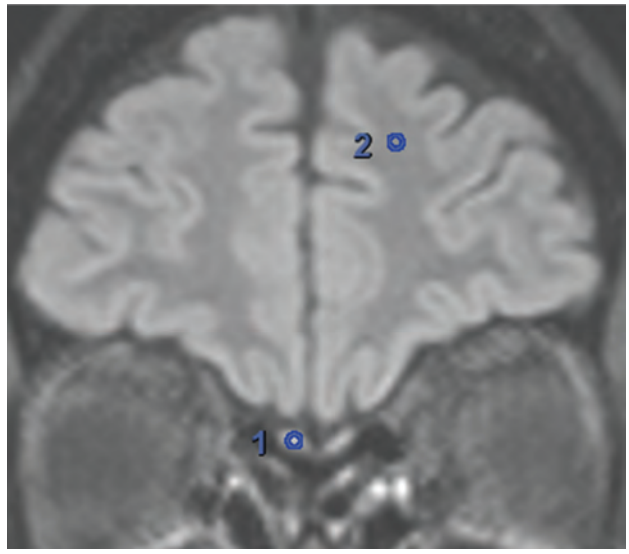

FIG 1. Quantitative assessment of OB signal intensity. For each patient, the ROI is drawn at the mid segment of the OB and within the left superior frontal WM to calculate normalized values.

Table 2: Demographic and clinical characteristics of patients and controls

Characteristic	Patients (n = 12)	Controls (n = 12)
Age, mean ± standard deviation, y	58.25 ± 14.852	58.00 ± 13.824
Sex at birth	6 women, 6 men	9 women, 3 men
Indication for study (n/N)	Altered mental status (9/12); ataxia, dysarthria (1/12); status epilepticus (1/12); paresthesia, anosmia (1/12)	Anosmia (7); phantosmia (2); hyposmia (3)
Kennedy staging score, n/N		
0	3	7
I	4	2
II	0	0
III	2	0
IV	3	3
Olfactory recess involvement, n/N	0	1

performed ($n = 10$), if motion degradation precluded satisfactory evaluation ($n = 1$), or if the final SARS-CoV-2 reverse transcription–polymerase chain reaction result was negative ($n = 3$) . One patient underwent 2 examinations; therefore, only the first study was included. The remaining 12 patients with a history of COVID-19 infection and sequences of interest were included in the study. Demographic data (age, sex at birth), date of positive SARS-CoV-2 reverse transcription–polymerase chain reaction result, and date of examination were recorded. A total of 12 age-matched controls who underwent MR imaging of the brain with an olfactory protocol were also included.

Statistical Analyses

Statistical analyses were performed by using SPSS (version 26; IBM). The χ^2 test of independence was used to assess significant differences between patients with COVID-19 and the anosmia control group in OB T2 FLAIR hyperintensity. The independent 2-sample t test was performed to test for significance of difference in age and the Kennedy staging score between patients with COVID-19 and the controls with anosmia, and normalized OB T2 FLAIR signal intensity between patients with COVID-19 and the controls with anosmia. The Spearman rank correlation analysis was used to test for significance of association between age and normalized OB T2 FLAIR signal intensity.

RESULTS

Demographic and clinical characteristics of the patients and the controls are shown in Table 2. There was no significant difference in age between the 2 groups ($P = .966$). There were significantly more women in the anosmia control group (9 women, 3 men) compared with patients with COVID-19 (6 women, 6 men) ($P < .001$). All the subjects included within the COVID-19 group had laboratory confirmation of SARS-Cov-2 infection. The average latency between the COVID-19 diagnosis and the MR imaging examination was 14.17 days (range, 0–32 days). There was no significant difference between the patients with COVID-19 and the controls with anosmia, and the grading of paranasal sinus mucosal disease ($P = .346$). There was a range of disease severity among the patients with COVID-19: five patients required intubation and 5 patients presented with purely neurologic and/or psychiatric symptoms in the absence of pulmonary manifestations of the infection. Among the 11 patients with COVID-19 who presented and required hospitalization, the length of stay ranged from 4 to 71 days (mean, 27 days). Seven of 12 patients with COVID-19 received hydroxychloroquine over the course of their treatment.

There was a significant difference in a normalized OB T2 FLAIR signal intensity between the patients with COVID-19 (mean normalized signal intensity, 1.85 [range, 0.74–1.85]) and the controls with anosmia (mean normalized signal intensity, 1.27 [range, 0.99–3.13]) ($P = .003$) (Fig 2). There was no correlation between age and a normalized OB signal intensity ($R = -0.128$, $P = .552$). The patients with COVID-19 and the controls with anosmia did not demonstrate OB volume loss or signal abnormality based on thin-section T2WI of the OB. However, 4 of 12 patients with COVID-19 demonstrated intraneural T2 signal hyperintensity on 3D T2 FLAIR (Figs 3 and 4) compared with none of the 12 patients (Fig 5) among the controls with anosmia ($P = .028$). Of the patients in the COVID-19 group, there was no significant difference between those with and those without OB and olfactory tract neuritis, and the number of days between the COVID-19 diagnosis and the MR imaging examination ($P = .882$) or severity of paranasal sinus disease ($P = .080$). Olfactory recess disease was seen in a single control with anosmia but not in any of the patients with COVID-19. A single patient with COVID-19 demonstrated an increased T2 signal in the entorhinal cortex and the orbitofrontal cortex; this individual was admitted for delirium and lethargy in the setting of *Escherichia coli* urinary tract infection, with persistent altered mental status despite resolution of the infection.

In terms of additional imaging findings on the performed examinations, there was a significant difference in distribution among categories of chronic microvascular ischemic disease (none, mild, moderate, severe) between the patients and the controls, as shown in Table 3 ($P \leq .001$). Additional notable findings included posterior reversible encephalopathy syndrome (2 patients with COVID-19, neither of whom demonstrated qualitatively increased OB and olfactory tract signal intensity on 3D T2 FLAIR) and acute infarction (2 patients with COVID-19, 1 of whom demonstrated qualitatively increased OB and olfactory tract signal intensity on 3D T2 FLAIR). Anosmia data were available for only 1 of the 12 patients with COVID-19. This individual presented with right arm numbness, paresthesia, and loss of sense of smell, and was found to have increased T2 signal in the OB and olfactory tract on 3D T2 FLAIR.

DISCUSSION

In this retrospective case-control study that examined imaging correlates to COVID-19, we found that the patients with acute-to-subacute COVID-19 were more likely to demonstrate

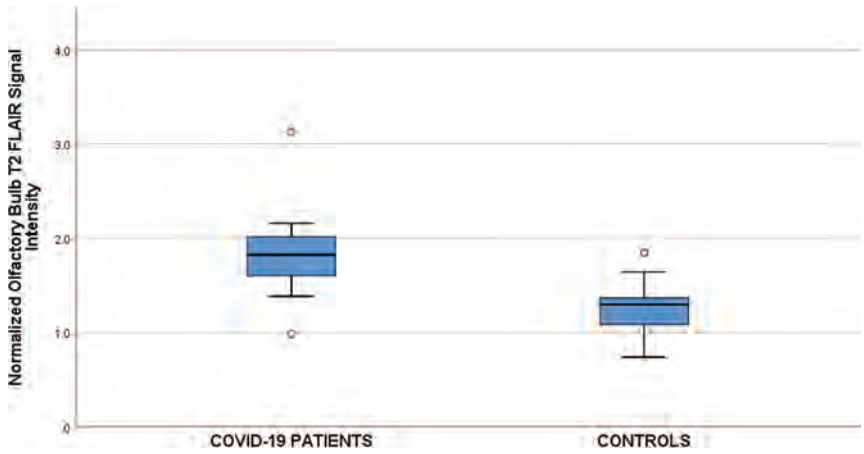

FIG 2. Normalized OB T2 FLAIR signal intensity in patients and controls. Box-and-whisker plots show median and interquartile ranges for each group. There was a significant difference in mean signal intensity between the patients and the controls (P = .003). Findings remain significant even with the exclusion of the COVID-19 high outlier depicted at a mean normalized OB T2 FLAIR signal intensity of 3.1.

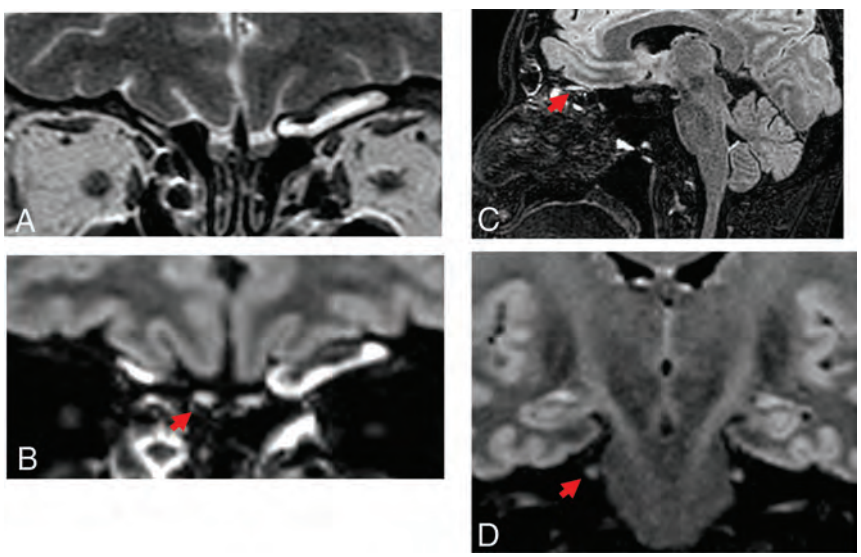

FIG 3. A 48-year-old woman positive for COVID-19 who presented with weakness and unsteady gait of 1 week's duration. Neurologic examination was significant for truncal ataxia, dysarthria, and left-sided dysmetria. *A*, Coronal high-resolution T2WI demonstrates normal OB morphology and signal intensity. *B*, Coronal and (*C*) sagittal postcontrast T2 FLAIR images demonstrate an increased T2 signal within the OB (*red arrows*). Note relative increased signal compared with (*D*) coronal T2WI at the level of the intracisternal segment of the trigeminal nerve (*red arrow*).

increased intraneural T2 signal abnormality on 3D T2 FLAIR in the OB compared with the controls with anosmia and not infected, which may represent enhancement or intrinsic T2 prolongation. There was a group-wise difference in normalized T2 FLAIR signal intensity between the patients with COVID-19 and the controls with anosmia. This difference was evident in 4 of 12 patients with COVID-19 on consensus review. These findings were independent of the presence of olfactory recess or paranasal sinus disease. We did not find signal abnormality in other structures related to the olfactory apparatus, including the orbitofrontal and entorhinal (piriform and amygdala) regions. These preliminary findings have important implications in terms of establishing biomarkers for acute infection, understanding the potential neurotropism of SARS-Cov-2, and identifying a subset of patients who might require longitudinal clinical and imaging follow-up to assess for neurologic changes.

A report by Galougahi et al[23] demonstrated no signal abnormality or morphologic changes in a patient with sudden-onset anosmia and positive SARS-CoV-2 polymerase chain reaction result during the acute phase of the illness. Similarly, we did not detect signal abnormality on coronal T2WI; rather, signal abnormality was detected on 3D-T2 FLAIR sequences, defined as hyperintense relative to the trigeminal nerve. An additional case report on acute onset anosmia in a patient with COVID-19 demonstrated complete olfactory cleft obstruction[24]; in contrast, we did not find olfactory recess disease in any of our patients with COVID-19. However, given the characteristic imaging appearance, it is possible that the previously reported case represents respiratory epithelial adenomatoid hamartoma rather than pathology related to COVID-19.[24]

Olfactory neuritis observed in our study might be a secondary effect of olfactory dysfunction and might reflect a phenomenon similar to post–infectious olfactory loss seen in the setting of other upper respiratory infections. Although the neuroinvasive potential of SARS-COV-2 remains to be established, direct CNS inoculation due to viral neurotropism is also plausible. The anatomy of the olfactory recess and the relationship among the nasal epithelium, OB, and CNS allows for a natural pathway for virus spread via neuronal transport.[25] Trans-synaptic transfer of virus is described in SARS-CoV[26] and Middle East respiratory syndrome coronavirus,[27] betacoronaviruses homologous to SARS-CoV-2 and responsible for previous epidemics. Preclinical experiments in transgenic mice demonstrated that the intranasal introduction of these viruses resulted in CNS inoculation, with neuronal loss in areas of viral expression. Therefore, it has been postulated that the neuroinvasive potential of SARS-COV-2 might similarly occur via a trans-synaptic route. Angiotensin-converting enzyme 2 protein expression is present

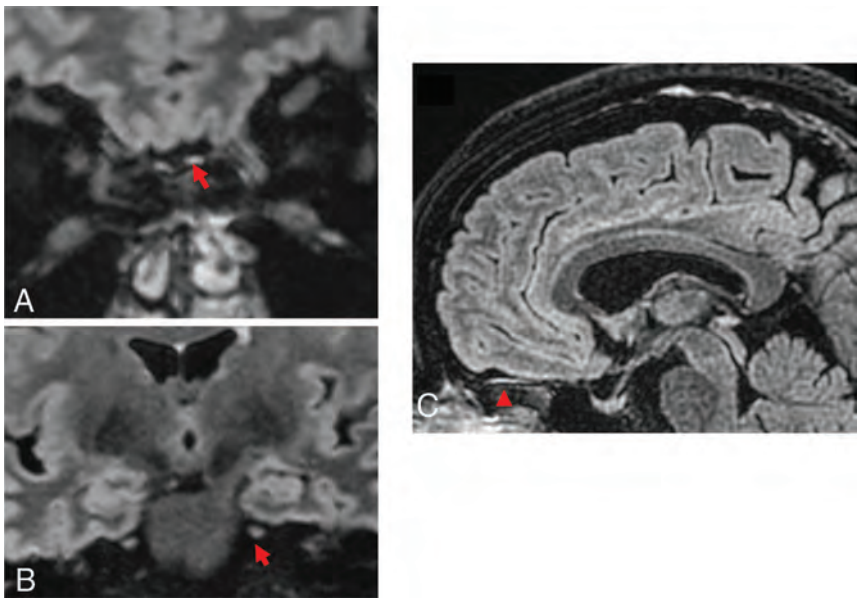

FIG 4. A 52-year-old woman positive for COVID-19 and with a history of major depressive disorder, was found to be catatonic. *A*, Coronal and (*B*) sagittal postcontrast 3D T2 FLAIR demonstrates increased intraneural signal within the OBs (*red arrows*) relative to (*C*) coronal postcontrast 3D T2 FLAIR images of the trigeminal nerve (*red arrow*).

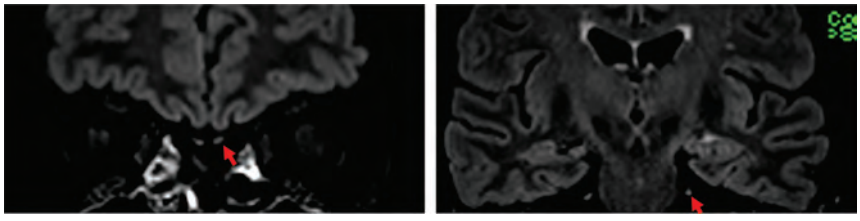

FIG 5. A 74-year-old woman (in the control group) with decreased sense of smell of several months' duration. Coronal postcontrast 3D T2 FLAIR of (*A*) the OB (*red arrow*) and (*B*) the trigeminal nerve (*red arrow*) demonstrate isointense signal.

Table 3: Severity of chronic microvascular ischemic disease in patients and controls

Subjects	None	Mild	Moderate	Severe
Patients with COVID-19	0.50	0.25	0.167	0.83
Controls with anosmia	0.333	0.417	0.25	0.00

in sustentacular and olfactory stem cells and may serve as a putative target for SARS-CoV-2 infection of olfactory epithelium.[25] Alternatively, viral binding to angiotensin-converting enzyme 2 receptors expressed in CNS capillary endothelium might result in endothelial damage, which enables spike protein binding to neuronal angiotensin-converting enzyme 2 receptors and subsequent CNS infection.[28] Another possibility is that hematogenous spread may occur via the blood supply shared by olfactory sensory neurons and the OB.

Imaging correlates to anosmia on conventional MR imaging have been shown in the setting of other disease status causing olfactory dysfunction. For instance, OB volume loss has been demonstrated in patients with migraine headache,[29] chronic rhinosinusitis,[30] trauma,[30,31] and subsequent to upper respiratory tract infection.[30,32] Morphologic changes in the OB have also been demonstrated in neurodegenerative diseases, including Parkinson disease[18] and Alzheimer disease.[19] Chung et al[33] evaluated OB volume and signal intensity in patients with a reported history of olfactory deficit due to chronic rhinosinusitis, trauma, prior viral infection, and idiopathic etiologies, and found that OB volume loss was more common in patients with olfactory dysfunction than in those with normosmia. However, there was no significant difference between the 2 groups in terms of T2 signal abnormality ($P = .395$).[33] The investigators attributed their findings to the chronicity of olfactory deficits because patients in the cohort experienced olfactory deficits for >2 months.[33]

The presence of an increased T2 signal observed in our study might reflect the acuity of the time course; it is possible that, if these individuals were imaged at longer-term follow-up, we would observe volume loss in the absence of signal abnormality. For instance, studies have demonstrated a negative correlation between the duration of anosmia and OB volume loss. Yao et al[17] demonstrated OB volume loss in individuals with anosmia of 0.5–8.7 years' duration and that the volume negatively correlated with the duration of olfactory loss. In addition, Yao et al[17] reported orbitofrontal cortex volume loss. In our study, a single patient with COVID-19 demonstrated increased entorhinal and orbitofrontal signal abnormality; however, the clinical significance of this isolated finding is uncertain.

There are several limitations to this study. Patients included were those who underwent MR imaging of the brain as part of standard of care during the COVID-19 pandemic. As such, our findings do not necessarily reflect patients on the milder end of the spectrum who might not have undergone imaging due to regulatory constraints or those on the more severe end of the spectrum who may have been too clinically unstable to undergo MR imaging. Although quantitative measures for the OB T2 FLAIR signal intensity were normalized to superior frontal WM, a large proportion of patients with COVID-19 underwent examinations on inpatient scanning systems versus outpatient scanning systems, and, therefore, it is possible that technical factors contributed to the differences observed between the 2 groups. Although all the patients included in the study demonstrated neurologic manifestations of disease, the presence of anosmia was not documented for all the subjects in this small-sample, retrospective study. Three of the 24 patients included in this study underwent noncontrast 3D T2 FLAIR, which might have decreased sensitivity for detection of

signal abnormality. On consensus review, we found increased T2 signal within the OBs in 33% of patients with COVID-19, similar to some estimates of acute-onset anosmia in patients with COVID-19.[11] A larger, prospective study with both self-reported and objective data[34,35] on olfaction with imaging performed at uniform chronology could potentially validate these preliminary results that suggest the possibility of OB signal intensity as a noninvasive biomarker of disease in COVID-19.

CONCLUSIONS

OB 3D T2 FLAIR signal intensity was greater in patients with COVID-19 and neurologic symptoms compared with an age-matched control group with olfactory dysfunction, and was qualitatively apparent in 4 of 12 patients with COVID-19. Analysis of these preliminary findings suggests that olfactory apparatus vulnerability to COVID-19 might be supported on conventional neuroimaging. Future prospective studies that examine the relationship between imaging findings and objective chemosensory assessment are warranted.

REFERENCES

1. Oxley TJ, Mocco J, Majidi S, et al. **Large-vessel stroke as a presenting feature of Covid-19 in the young.** *N Engl J Med* 2020;382:e60 CrossRef Medline
2. Nath A. **Neurologic complications of coronavirus infections.** *Neurology* 2020;94:809–10 CrossRef Medline
3. Wölfel R, Corman VM, Guggemos W, et al. **Virological assessment of hospitalized patients with COVID-2019.** *Nature* 2020;581:465–69 CrossRef Medline
4. Bagheri SH, Asghari A, Farhadi M, et al. **Coincidence of COVID-19 epidemic and olfactory dysfunction outbreak in Iran.** *Medical Journal of The Islamic Republic of Iran (MJIRI)* 2020;34:446–52 CrossRef
5. Mao L, Jin H, Wang M, et al. **Neurologic manifestations of hospitalized patients with coronavirus disease 2019 in Wuhan, China.** *JAMA Neurol* 2020;77:1–9 CrossRef Medline
6. Lechien JR, Chiesa-Estomba CM, De Siati DR, et al. **Olfactory and gustatory dysfunctions as a clinical presentation of mild-to-moderate forms of the coronavirus disease (COVID-19): a multicenter European study.** *Eur Arch Otorhinolaryngol* 2020;277;2251–61 CrossRef Medline
7. Menni C, Valdes AM, Freidin MB, et al. **Real-time tracking of self-reported symptoms to predict potential COVID-19.** *Nature medicine* 2020;26:1037–40 CrossRef Medline
8. Gautier J-F, Ravussin Y. **A new symptom of COVID-19: loss of taste and smell.** *Obesity (Silver Spring)* 2020;28:848 CrossRef Medline
9. Yan CH, Faraji F, Prajapati DP, et al. **Association of chemosensory dysfunction and Covid-19 in patients presenting with influenza-like symptoms.** *Int Forum Allergy Rhinol* 2020;10:806–13 CrossRef Medline
10. Hopkins C, Surda P, Kumar N. **Presentation of new onset anosmia during the COVID-19 pandemic.** *Rhinology* 2020;58:295–98 CrossRef Medline
11. Giacomelli A, Pezzati L, Conti F, et al. **Self-reported olfactory and taste disorders in patients with severe acute respiratory coronavirus 2 infection: a cross-sectional study.** *Clinical Infectious Diseases* 2020;71:889–90 CrossRef Medline
12. Sedaghat AR, Gengler I, Speth MM. **Olfactory dysfunction: a highly prevalent symptom of COVID-19 with public health significance.** *Otolaryngol Head Neck Surg* 2020;163:12–15 CrossRef Medline
13. Suzuki M, Takashima T, Kadoya M, et al. **MR imaging of olfactory bulbs and tracts.** *AJNR Am J Neuroradiol* 1989;10:955–57 Medline
14. Yousem DM, Geckle RJ, Bilker WB, et al. **Olfactory bulb and tract and temporal lobe volumes: normative data across decades.** *Ann N Y Acad Sci* 1998;855:546–55 CrossRef Medline
15. Schneider JF, Floemer F. **Maturation of the olfactory bulbs: MR imaging findings.** *AJNR Am J Neuroradiol* 2009;30:1149–52 CrossRef Medline
16. Yousem DM, Oguz KK, Li C. **Imaging of the olfactory system.** *Semin Ultrasound CT MR* 2001;22:456–72 CrossRef Medline
17. Yao L, Yi X, Pinto JM, et al. **Olfactory cortex and olfactory bulb volume alterations in patients with post-infectious olfactory loss.** *Brain Imaging Behav* 2018;12:1355–62 CrossRef Medline
18. Wang J, You H, Liu J-F, et al. **Association of olfactory bulb volume and olfactory sulcus depth with olfactory function in patients with Parkinson disease.** *AJNR Am J Neuroradiol* 2011;32:677–81 CrossRef Medline
19. Wilson RS, Arnold SE, Schneider JA, et al. **Olfactory impairment in presymptomatic Alzheimer's disease.** *Ann N Y Acad Sci* 2009; 1170:730–35 CrossRef Medline
20. Seubert J, Freiherr J, Frasnelli J, et al. **Orbitofrontal cortex and olfactory bulb volume predict distinct aspects of olfactory performance in healthy subjects.** *Cereb Cortex* 2013;23:2448–56 CrossRef Medline
21. Kaye R, Chang CWD, Kazahaya K, et al. **COVID-19 anosmia reporting tool: initial findings.** *Otolaryngol Head Neck Surg* 2020;163:132–34 CrossRef Medline
22. Lund VJ, Kennedy DW. **Staging for rhinosinusitis.** *Otolaryngol Head Neck Surg* 1997;117(pt 2):S35–40 CrossRef Medline
23. Galougahi MK, Ghorbani J, Bakhshayeshkaram M, et al. **Olfactory bulb magnetic resonance imaging in SARS-CoV-2-induced anosmia: the first report.** *Acad Radiol* 2020;27:892–93 CrossRef Medline
24. Eliezer M, Hautefort C, Hamel A-L, et al. **Sudden and complete olfactory loss function as a possible symptom of COVID-19.** *JAMA otolaryngology-head & neck surgery* 2020;146:674–75 CrossRef Medline
25. Brann DH, Tsukahara T, Weinreb C, et al. **Non-neuronal expression of SARS-CoV-2 entry genes in the olfaory system suggests mechanisms underlying COVID-19-associated anosmia.** *Science Advances* 2020;6:eabc5801 CrossRef
26. Netland J, Meyerholz DK, Moore S, et al. **Severe acute respiratory syndrome coronavirus infection causes neuronal death in the absence of encephalitis in mice transgenic for human ACE2.** *J Virol* 2008;82:7264–75 CrossRef Medline
27. Li K, Wohlford-Lenane C, Perlman S, et al. **Middle East respiratory syndrome coronavirus causes multiple organ damage and lethal disease in mice transgenic for human dipeptidyl peptidase 4.** *J Infect Dis* 2016;213:712–22 CrossRef Medline
28. Baig AM, Khaleeq A, Ali U, et al. **Evidence of the COVID-19 virus targeting the CNS: tissue distribution, host–virus interaction, and proposed neurotropic mechanisms.** *ACS Chem Neurosci* 2020;11: 995–98 CrossRef Medline
29. Aktürk T, Tanık N, Serin Hİ, et al. **Olfactory bulb atrophy in migraine patients.** *Neurol Sci* 2019;40:127–32 CrossRef Medline
30. Hummel T, Urbig A, Huart C, et al. **Volume of olfactory bulb and depth of olfactory sulcus in 378 consecutive patients with olfactory loss.** *J Neurol* 2015;262:1046–51 CrossRef Medline
31. Yousem DM, Geckle RJ, Bilker WB, et al. **Posttraumatic smell loss: relationship of psychophysical tests and volumes of the olfactory bulbs and tracts and the temporal lobes.** *Acad Radiol* 1999;6:264–72 CrossRef
32. Rombaux P, Mouraux A, Bertrand B, et al. **Olfactory function and olfactory bulb volume in patients with postinfectious olfactory loss.** *Laryngoscope* 2006;116:436–39 CrossRef Medline
33. Chung MS, Choi WR, Jeong H-Y, et al. **MR imaging–based evaluations of olfactory bulb atrophy in patients with olfactory dysfunction.** *AJNR Am J Neuroradiol* 2018;39:532–37 CrossRef Medline
34. Hummel T, Sekinger B, Wolf SR, et al. **'Sniffin'sticks': olfactory performance assessed by the combined testing of odor identification, odor discrimination and olfactory threshold.** *Chem Senses* 1997;22: 39–52 CrossRef Medline
35. Doty RL, Shaman P, Kimmelman CP, et al. **University of Pennsylvania Smell Identification Test: a rapid quantitative olfactory function test for the clinic.** *Laryngoscope* 1984;94(pt 1):176–78 CrossRef Medline

Are Gadolinium-Enhanced MR Sequences Needed in Simultaneous ^{18}F-FDG-PET/MRI for Tumor Delineation in Head and Neck Cancer?

N. Pyatigorskaya, R. De Laroche, G. Bera, A. Giron, C. Bertolus, G. Herve, E. Chambenois, S. Bergeret, D. Dormont, M. Amor-Sahli, and A. Kas

ABSTRACT

BACKGROUND AND PURPOSE: PET/MRI with ^{18}F-FDG has demonstrated the advantages of simultaneous PET and MR imaging in head and neck cancer imaging, MRI allowing excellent soft-tissue contrast, while PET provides metabolic information. The aim of this study was to evaluate the added value of gadolinium contrast–enhanced sequences in the tumor delineation of head and neck cancers on ^{18}F-FDG-PET/MR imaging.

MATERIALS AND METHODS: Consecutive patients who underwent simultaneous head and neck ^{18}F-FDG-PET/MR imaging staging or restaging followed by surgery were retrospectively included. Local tumor invasion and lymph node extension were assessed in 45 head and neck anatomic regions using ^{18}F-FDG-PET/MR imaging by 2 rater groups (each one including a radiologist and a nuclear medicine physician). Two reading sessions were performed, one without contrast-enhanced sequences (using only T1WI, T2WI, and PET images) and a second with additional T1WI postcontrast sequences. The results were compared with the detailed histopathologic analysis, used as reference standard. The κ concordance coefficient between the reading sessions and sensitivity and specificity for each region were calculated.

RESULTS: Thirty patients were included. There was excellent agreement between the contrast-free and postgadolinium reading sessions in delineating precise tumor extension in the 45 anatomic regions studied (Cohen $\kappa = 0.96$, 95% CI = [0.94–0.97], $P < .001$). The diagnostic accuracy did not differ between contrast-free and postgadolinium reading sessions, being 0.97 for both groups and both reading sessions. For the 2 rater groups, there was good sensitivity for both contrast-free (0.83 and 0.85) and postgadolinium reading sessions (0.88 and 0.90, respectively). Moreover, there was excellent specificity (0.98) for both groups and reading sessions.

CONCLUSIONS: Gadolinium chelate contrast administration showed no added value for accurate characterization of head and neck primary tumor extension and could possibly be avoided in the PET/MR imaging head and neck workflow.

ABBREVIATIONS: HNC = head and neck cancer; IDEAL = iterative decomposition of water and fat with least-square estimation; SUV_{max} = maximum standardized uptake value; PNS = perineural spread

Integrated PET/MR imaging systems are increasingly used in clinical practice. PET/MR imaging with ^{18}F-FDG has demonstrated the advantages of simultaneous PET and MR imaging, with MR imaging allowing excellent soft tissue contrast and PET providing metabolic information.[1,2] This multimodality imaging may improve the diagnostic accuracy in complex anatomic regions.

Head and neck cancer (HNC) is a frequent pathology with high morbidity and mortality rates.[3] Precise clinical and imaging delineation of tumor expansion is challenging in the complex head and neck anatomic area. Nevertheless, accurate tumor delineation by imaging is essential for therapeutic decision making and for performing complete tumor resection while preserving healthy functional surrounding tissue.

In simultaneously acquired PET/MR imaging, MR images are the most time-consuming. PET/MR imaging in a clinical setting should be time-efficient for maintaining sufficient patient workflow and because the increase in acquisition time is a source of

Received July 10, 2019; accepted after revision June 21, 2020.

From Assistance Publique Hôpitaux de Paris Neuroradiology Department (N.P., E.C., D.D., M.A.-S.), and Nuclear Medicine Department (G.B., S.B., A.K.), Pitié-Salpêtrière-Charles Foix Hospital, Paris, France; Sorbonne University (N.P., D.D.), Pierre and Marie Faculty of Medicine, Paris, France; Nuclear Medicine Department (R.D.L.), Morvan Hospital, Brest, France; Sorbonne University (A.G., A.K.), Laboratoire d'Imagerie Biomédicale, Paris, France; Sorbonne University, Maxillo-Facial Surgery Department (C.B.), and Pathology Department (G.H.), Pitié Salpêtrière–Charles Foix Hospital, Assistance Publique Hôpitaux de Paris, Paris, France; and CIMI Sorbonne University UPMC (C.B.), Paris, France.

Please address correspondence to Nadya Pyatigorskaya, Service de Neuroradiologie, Hôpital Pitié-Salpêtrière, 47-83 Boulevard de l'Hôpital, 75651 Paris Cedex 13, France, e-mail: nadya.pyatigorskaya@gmail.com

Indicates article with supplemental on-line table.

Indicates article with supplemental on-line photos.

http://dx.doi.org/10.3174/ajnr.A6764

motion artifacts and patient discomfort. Still, protocol optimization should not lead to the degradation of imaging quality and diagnostic accuracy. PET/MR imaging acquisition commonly includes a head and neck MR imaging protocol usually performed in clinical practice[4,5] and PET acquisition. However, in clinical context, each MR image should provide additional information to that provided by ^{18}F-FDG-PET. Consequently, the utility of each MR image in this combined examination should be questioned and justified.

Gadolinium contrast–enhanced sequences are useful in the detection and delineation of head and neck tumors.[6] However, these sequences are time-consuming, and gadolinium administration can cause potential side effects such as nephrogenic systemic sclerosis[7,8] or gadolinium chelate brain accumulation.[9]

Thus, before including a contrast-enhanced MR image in the protocol of simultaneous PET/MR imaging for head and neck examination, it is important to first examine whether gadolinium-enhanced sequences provide any additional information of value compared with ^{18}F-FDG-PET/MR imaging including only nonenhanced morphologic MR images.[10] Indeed, although gadolinium contrast–enhanced sequences are known to have an important place in MR imaging examination, there is currently no evidence concerning their usefulness in simultaneous head and neck ^{18}F-FDG-PET/MR imaging acquisition.[11] Only 1 study on a pediatric population investigated whether gadolinium contrast enhancement added any information in PET/MR imaging, finding no notable difference in the diagnostic accuracy between the enhanced and unenhanced images.[12] Another study, which investigated the added value of MR imaging sequences compared with PET/CT, suggested that PET/MR imaging could be a legitimate alternative to PET/CT in patients with HNC.[11] To the best of our knowledge, no study has yet systematically investigated whether gadolinium contrast–enhanced sequences provide any additional information compared with contrast-free simultaneous ^{18}F-FDG-PET/MR imaging for assessing precise local and regional invasion in HNC.

The aim of this study was to evaluate the added value of gadolinium contrast–enhanced sequences for HNC tumor delineation using ^{18}F-FDG-PET/MR imaging to examine the usefulness of this sequence in HNC PET/MR imaging protocols.

MATERIALS AND METHODS

Patients

Thirty consecutive patients with histopathologically confirmed HNC examined in our institution between November 2015 and June 2016 were retrospectively included. The inclusion criteria were available simultaneous ^{18}F-FDG-PET/MR imaging scan performed in the context of staging or restaging the histopathologically confirmed HNC, which included the sequences with and without contrast administration, and head and neck surgery performed within 4 weeks after the PET/MR imaging examination with available detailed pathologic analysis of precise tumor extension. None of the patients were undergoing any therapy at the time of imaging or in the interval between the imaging and the resection. The restaging examination was performed at least 4 weeks after the surgery and 12 weeks after radiation therapy, as previously recommended for posttreatment evaluation in HNC.[13,14]

The data for this study were extracted from the local data base of PET/MR imaging examinations, which was approved by the French authority for the protection of privacy and personal data in clinical research (CNIL, approval No. 2111722). This study was performed according to the principles of the Declaration of Helsinki.

Imaging Protocol

All the images were acquired simultaneously with an integrated PET/MR imaging system (Signa 3T, GE Healthcare) using the same protocol, 60 minutes after IV injection of 3.7 MBq/kg ^{18}F-FDG. No patients had blood glucose level >11 mmol/L, and all had been fasting for 6 hours or more before the ^{18}F-FDG injection. Contraindications for MR imaging were respected.

Simultaneous PET/MR imaging acquisition was performed in the head and neck region using a 40-channel head and neck receiver coil; the duration time was approximately 20 min. The protocol included a 2-point Dixon MR imaging sequence for the attenuation correction (which resulted in in-phase T1WI, out-of-phase T1WI, water-only, and fat-only images); an axial FSE T1WI, iterative decomposition of water and fat with least-square estimation (IDEAL) FSE axial T2WI sequence; and a 3D contrast-enhanced FSE T1WI acquired immediately after the injection of gadoterate meglumine (Dotarem 0.2 mL/kg, Guerbet). The simultaneous PET acquisition, which lasted 16 minutes, was followed by a whole-body simultaneous PET/MR imaging acquisition from the neck to the proximal femur, including 4 bed-PET/MR imaging position scans. Finally, an axial postcontrast-injection IDEAL FSE T1WI, a coronal IDEAL FSE T2WI, and an axial DWI centered on the head and neck region were acquired during about 8 minutes. The total duration of PET/MR imaging examination was 45–50 minutes.

PET data were reconstructed iteratively using the ordered subsets expectation maximization algorithm, integrating TOF, point spread function modeling, and attenuation, truncation, and scatter corrections with a matrix size of 256 × 256, 4 iterations and 28 subsets, and a filter cutoff of 3 mm for head and neck scans, resulting in voxel size of 1.17 × 1.17 × 2.78 mm. For photon attenuation correction, a 2-point Dixon MR imaging was used.

Image Analysis

PET/MR images were analyzed by 2 rater groups, each comprising an experienced radiologist (M.A.-S. or N.P.) and an experienced nuclear medicine physician (A.K. or G.B.) with at least 11 years of practice. The raters performing the PET/MR imaging readings were blinded to previous medical history, suspected diagnosis, pathologic findings, and other imaging technique results. Whole-body PET/MR imaging and DWI were unavailable to the raters during the reading. The images were analyzed using an Advantage Workstation 4.6 (AW4.6, GE Healthcare).

For the first reading session (referred to as "contrast free"), only PET images and contrast-free spin-echo T1WI and IDEAL T2WI were available for simultaneous interpretation. For each of the 45 specific anatomic regions

Table 1: Lesion characteristics

	Total Number of Subjects (%)	Number of Subjects with T1–T2 Lesions (%)
Histologic type		
Squamous cell carcinoma	23 (77%)	8 (80%)
Adenoid cystic carcinoma	4 (13%)	1 (10%)
Adenocarcinoma	1 (3%)	1 (10%)
Sarcoma	1 (3%)	
Melanoma metastasis	1 (3%)	
Tumor stage		
pT1	4 (13%)	4 (40%)
pT2	6 (20%)	6 (60%)
pT3	1 (3%)	
pT4	16 (53%)	
Lymph node stage		
pN0	12 (38%)	
pN1	5 (17%)	
pN2a	1 (3%)	
pN2b	6 (20%)	
pN2c	1 (3%)	
pN3	0	
Initial tumor location		
Base of tongue	1 (3%)	
Tongue	6 (20%)	2 (20%)
Floor of mouth	4 (13%)	3 (30%)
Vestibule or lip	2 (7%)	
Maxillary	2 (7%)	
Palate	3 (10%)	
Mandibular	8 (27%)	
Amygdala	1 (3%)	3 (30%)
Salivary glands	3 (10%)	2 (20%)
Staging		
Initial diagnosis	23 (77%)	6 (60%)
Recurrence	7 (23%)	4 (40%)

determined together with the pathologists (On-line Table), the raters had to specify the presence or absence of tumor invasion. All areas of focal uptake were identified and correlated to the corresponding MR images. Analyses of the PET/MR imaging data included qualitative and quantitative assessment. Areas of focal ^{18}F-FDG-uptakes were classified as probably malignant or as probably benign based on visual analysis, focused on the pattern and asymmetry of FDG distribution as well as contrast to background uptake, especially in anatomic structures with physiologic uptake (eg, palatine tonsils or salivary glands). The semiquantitative standardized uptake value (SUV_{max}) was used as a tool to supplement visual interpretation. SUV_{max} values were measured in tissues or nodes with increased ^{18}F-FDG uptake using a volume of interest based on a 40% isocontour threshold with an AW4.6 workstation.[15,16] The morphologic criteria for tumor malignancy included a masslike lesion with irregular borders, low T1-weighted signal, and usually iso or high T2-weighted signal. The combination of the most relevant findings (morphologic and metabolic) was considered for the PET/MR imaging classification. The lesions were classified by consensus using a qualitative 2-point scale as follows: 1 represented malignant tumor invasion of the anatomic region, and 0 represented the absence of suspicious invasion. The same reading was performed for the assessment of lymph node involvement. Lymph nodes with suspected malignant invasion were reported in each anatomic region. The size, shape, homogeneity, capsular disruption, and intensity of ^{18}F-FDG uptake were taken into consideration.

The second interpretation session (referred to as "postgadolinium") followed the same method of analysis, which additionally included gadolinium-enhanced images and the assessment of contrast enhancement in each region. The time interval between the 2 reading sessions was at least 8 weeks.

Histopathologic Analysis

All the lesions were analyzed by an experienced senior anatomopathologist with 14 years of experience (G.H.). Each of the included patients had a histopathologic confirmation of the lesion nature. Histopathologic tumor grade, surgical margin invasion by the tumor, and invasion of each of the 45 systematically examined anatomic regions (On-line Table) were determined. The histopathologic results were considered as standard of reference for this study. Only lymph nodes with available pathology analysis were considered.

Statistical Analysis

Statistical analysis was performed using JMP Pro 14 (SAS Institute). The interrater agreement and the agreement between contrast-free and postgadolinium sessions were estimated using the Cohen κ coefficient for each region and for each reading session. The sensitivity, specificity, and diagnostic accuracy were also calculated for each region for each reading session. Additionally, the overall diagnostic accuracy was estimated. The values between 0.9 and 1 were considered "excellent," between 0.80 and 0.90 as "good," and between 0.70 and 0.80 as "fair." These values were also determined for a subgroup analysis ($n = 10$) of small-sized tumors (stage T1 and T2 according to the American Joint Committee on Cancer *Cancer Staging Manual* 7th edition, being applicable at the time of the study) because these lesions are considered to be more difficult to detect and explore.[17]

RESULTS

Patients and Lesions

Thirty consecutive patients (61.6 ± 16.8 years old, 12 women) were retrospectively included. Histopathologic tumor types included squamous cell carcinomas ($n = 23$), adenoid cystic

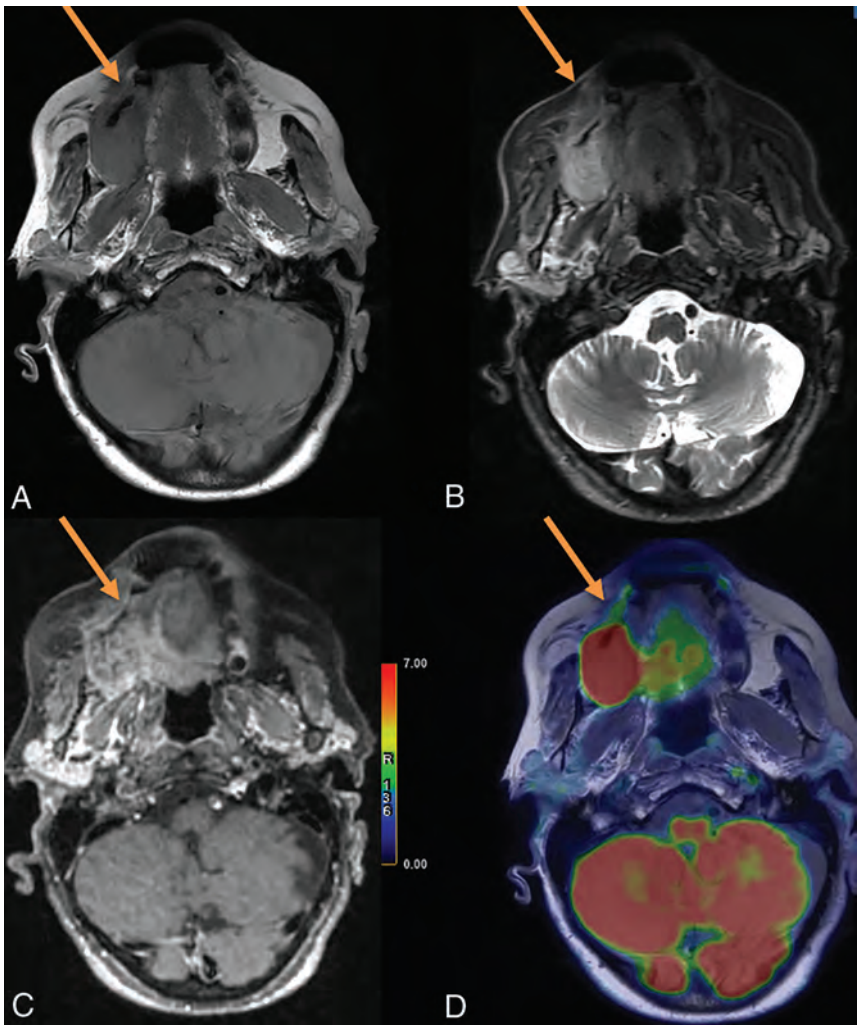

FIG 1. Initial staging of a right maxillary squamous cell carcinoma in an 84-year-old woman. *A*, Axial T1-weighted spin-echo (SE) sequence. *B*, Axial T1-weighted fat-saturated sequence. *C*, Fusion between axial T1WSE sequence. *C*, 3D T1-weighted fat-saturated SE postcontrast sequence, axial plane. *D*, Fusion between axial T1-weighted SE sequence and ^{18}F-FDG-PET. Both T1-weighted FDG-PET/MR imaging with and without gadolinium showed right hard palate invasion. The anterior tumor margin (*arrow*) was difficult to define on both contrast-free and postcontrast T1WI (*B* and *D*). PET imaging allowed clarification of the lesion margins (*A* and *C*).

carcinomas ($n = 4$), adenocarcinoma ($n = 1$), sarcoma ($n = 1$), and melanoma metastasis ($n = 1$). Twenty-five patients (83%) underwent cervical lymph node resection; in 19 (76%) patients, the resection was unilateral, and in 6 (24%) patients, it was bilateral. A total of 142 cervical lymph nodes were analyzed. The head and neck surgery was performed within 25.8 ±13.2 (range, 2–29) days after the PET/MR imaging examination. The lesion characteristics are shown in Table 1, Figs 1-3, and On-line Figs 1 and 2.

Agreement between Evaluations

There was excellent agreement between the contrast-free and postgadolinium reading sessions for the precise assessment of tumor extension (Cohen $\kappa = 0.96$, 95% CI = [0.94–0.97], $P < .001$). Good interrater agreement was also found for the contrast-free session ($\kappa = 0.78$, 95% CI = [0.74–0.81], $P < .001$) and for the postgadolinium session ($\kappa = 0.78$, 95% CI = [0.73–0.83], $P < .001$). The data for each region are detailed in the On-line Table.

Diagnostic Accuracy

The diagnostic accuracy did not differ between the contrast-free and postgadolinium reading sessions (0.97 for both groups and both reading sessions). For the first group (A.K. and M.A.-S.), there was good sensitivity for both contrast-free and postgadolinium reading sessions (0.83 and 0.85, respectively), and there was excellent specificity (0.98 for each reading session). For the second raters group (G.B. and N. P.), there was also good sensitivity (0.88 and 0.9, respectively), and there was excellent specificity (0.98 for each reading session). The data regarding the sensitivity and specificity for the assessment of tumor invasion for each of the 45 anatomic regions are detailed in Table 2.

Lymph Node Analysis

The agreement between the contrast-free and postgadolinium sessions was good (Cohen $\kappa = 0.90$, 95% CI = [0.78–0.95], $P < .001$). For both contrast-free and postgadolinium reading sessions, there was good sensitivity (0.85), and there was excellent specificity (0.97 and 0.98, respectively).

Subgroup Analysis

For small-sized tumor lesions (T1–T2 stages), there was also excellent intrarater agreement for tumor extension assessment between the contrast-free and postgadolinium reading sessions (Cohen $\kappa = 0.91$, 95% CI = [0.85– 0.96], $P < .001$). The diagnostic accuracy for T1–T2 lesions did not differ from the overall accuracy (0.97 for both groups and both reading sessions). For the first rater group, there was good sensitivity (0.79 for both contrast-free and postgadolinium sessions), and there was excellent specificity (0.98 for both reading sessions). For the second rater group, the sensitivity was good (0.89 and 0.79, respectively), and specificity was excellent (0.99 for both reading sessions).

DISCUSSION

We observed excellent diagnostic accuracy of simultaneous ^{18}F-FDG-PET/MR imaging for the assessment of locoregional extension of HNC with or without gadolinium contrast administration. There was excellent agreement between the contrast-free and postgadolinium reading sessions, and there were good sensitivity and

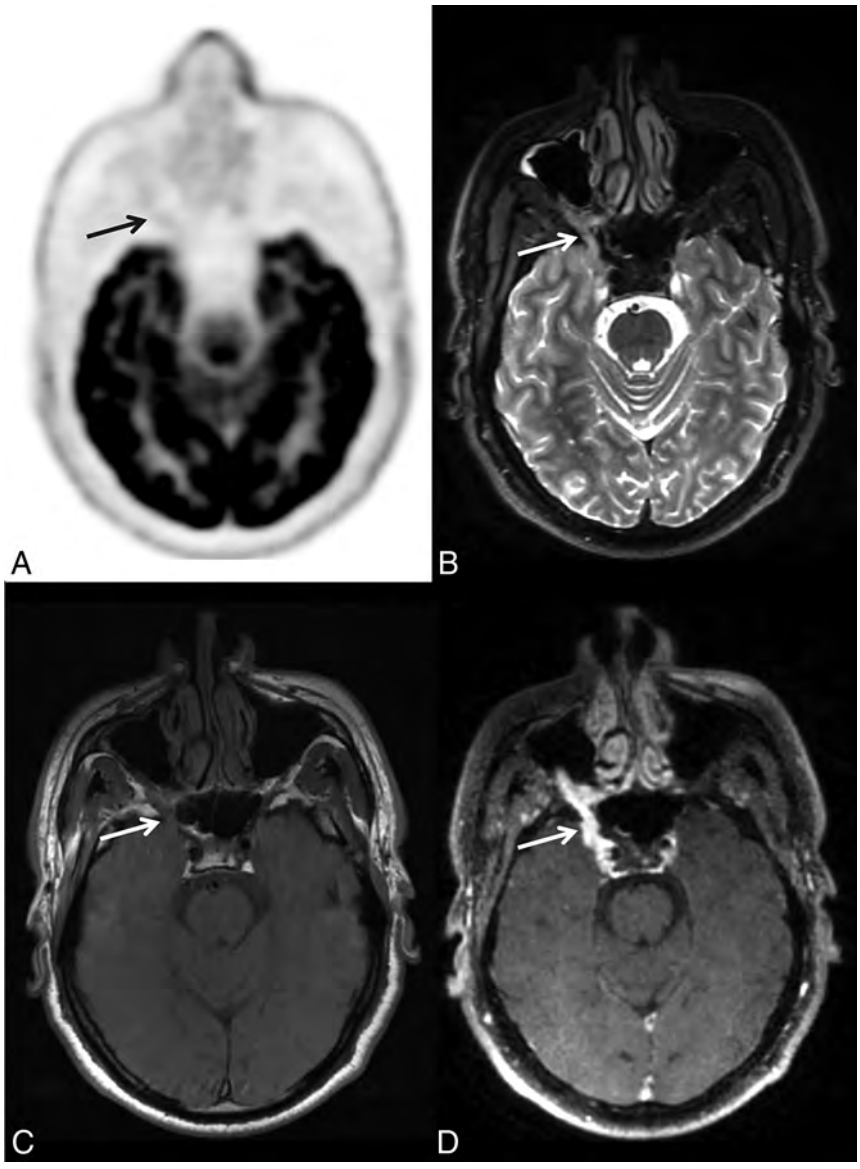

FIG 2. Initial staging of right adenoid cystic carcinoma of a minor salivary gland (palate) in a 55-year-old man. *A*, Axial FDG-PET. *B*, Axial T2-weighted spin-echo (SE) sequence. *C*, Axial T1-weighted SE sequence. *D*, 3D T1-weighted fat-saturated SE postcontrast sequence. On both T1-weighted and T2-weighted MR imaging (*B* and *C*), thickening of the trigeminal nerve is present, with a loss of signal of the fatty tissue in the pterygopalatine fossa, strongly suggestive of perineural spread of the tumor. On the T1-weighted postgadolinium sequence (*D*), high enhancement of the trigeminal nerve is visible (*arrow*). There is no significant perineural ^{18}F-FDG uptake (*A*); only slight uptake is discernable when guided by MR imaging findings.

excellent specificity for the assessment of local tumor extension as well as for the evaluation of lymph node involvement, similarly with and without gadolinium injection.

To the best of our knowledge, this is the first simultaneous PET/MR imaging study investigating the added value of gadolinium-enhanced sequences in adults and the first study of the head and neck region.

To this day, several studies have debated on the added value of PET/MR imaging compared with PET/CT in HNC evaluation. Although some studies found no advantages of PET/MR imaging in terms of diagnostic performance,[16,18-20] others showed it to be advantageous in terms of overall diagnostic accuracy[21] or of tumor delineation,[22] which is particularly relevant in the head and neck region, where anatomic landmarks are complex and mobile because of patients positioning differences between examinations.[23] Additionally, coregistration procedures between PET/CT and MR imaging are usually performed in studies conducted for research purposes, being less feasible in clinical practice using routine algorithms. Consequently, several studies have demonstrated the superiority of PET/MR imaging versus PET/CT[24] and versus the association of PET/CT and MR imaging.[25,26]

The main drawback of PET/MR imaging is its long acquisition time.[27] However, although the duration of PET/MR imaging is longer than that of PET/CT, it should be pointed out that acquiring simultaneous PET/MR imaging data reduces the overall examination time compared with sequential PET/CT and MR examinations. PET/MR imaging should still be as short as possible for clinical workflow optimization, especially in patients with HNC, who often have swallowing or breathing difficulties.

In PET/MR workflow considerations, the limiting factor for reducing the acquisition time is the MR imaging and not the PET acquisition. Indeed, transaxial PET data for a 25-cm fields of view are acquired within $\leq$10 min, whereas simultaneously acquired MR pulse sequences require much longer imaging times.

In the context of workflow optimization, one should question the relevance of each MR image. Furthermore, the information provided by PET and MR modalities should be as complementary as possible, any redundancy being avoided.

Avoiding contrast injection is also preferable in patients with severe renal failure, who are at risk of developing nephrogenic systemic sclerosis,[7,8] especially in the case of repeated injections and if the linear-structured gadolinium-chelated molecules are used.[28] Moreover, gadolinium chelate deposition in the brain was recently reported,[9] especially in patients undergoing repeated injections, as would be the case for

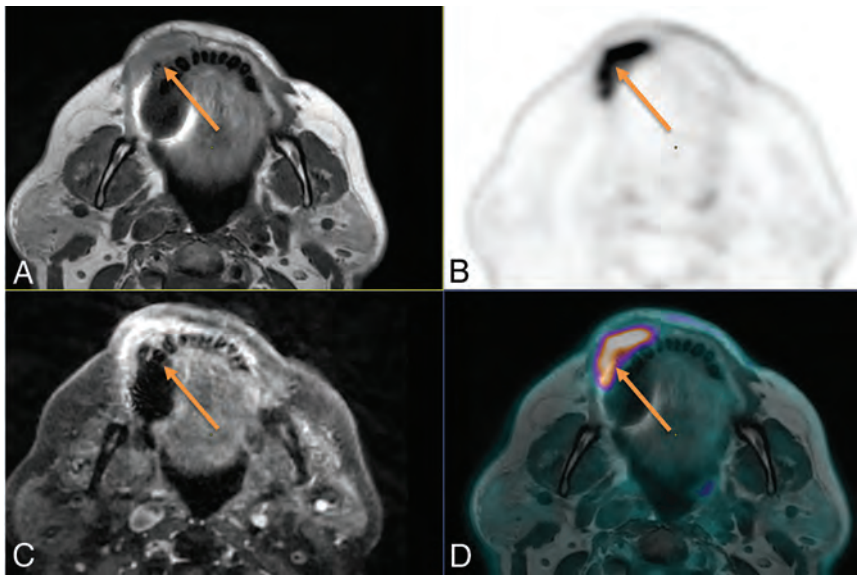

FIG 3. Local extension of a mandibular gingiva tumor in a 71-year-old woman. *A*, Axial contrast-free T1-weighted. *B*, Axial ^{18}F-FDG-PET image. *C*, 3D T1-weighted spin-echo (SE) contrast-enhanced sequence, axial plane. *D*, Fusion between axial T1-weighted and ^{18}F-FDG-PET. Both contrast-free and gadolinium-enhanced T1W MR imaging showed right vestibular invasion. Although bone invasion remained doubtful because of dental artifacts on MR alone, high FDG uptake includes a portion of the mandibular bone with margins that are clearly visible on the fusion images between PET and T1-weighted MRI, demonstrating bone involvement (*arrow*), which was pathologically confirmed.

certain patients with HNC with long follow-up times. Even though the clinical impact of these deposits remains unclear, there is a current trend of reducing the overall received dose of gadolinium, especially in patients with a good prognosis and a high life expectancy.

Although this is the first study directly investigating the value of gadolinium injection in HNC simultaneous PET/MR imaging protocols for precise assessment of tumor invasion, DWI has already been similarly examined[22,29] with the results suggesting that it has no added value in the PET/MR imaging protocol.[22,29] Indeed, significant correlation between DWI-ADC and SUV_{max} values on PET images was found.[16,21,30,31] In contrast to this, in another study, it was observed that PET/MR-DWI may help to avoid false-positive findings caused by nonspecific FDG uptake in the case of tumor recurrence.[21]

Previously, it was reported that fat-suppressed contrast-enhanced T1-weighted MR images are superior to unenhanced ones for tumor diagnosis

Table 2: Diagnostic accuracy of contrast-free and postgadolinium sessions

	First Raters Group				Second Raters Group			
	Contrast-Free Session		Postgadolinium Session		Contrast-Free Session		Postgadolinium Session	
Region extension	Se	Sp	Se	Sp	Se	Sp	Se	Sp
Median line involvement	0.67	0.96	0.67	0.95	0.83	0.95	0.83	0.95
Vascular extension	0	1	0	1	1	0.93	1	0.93
Mandibular cortical bone	0.9	0.95	0.9	0.95	0.9	0.95	0.9	0.95
Mandibular medullary bone	0.88	0.9	0.88	0.9	0.88	0.9	0.88	0.9
Intermaxillary commissure	1	0.91	1	0.86	1	0.95	1	0.89
Vestibule	0.92	1	0.92	1	0.92	1	0.92	1
Skin	0.67	1	1	1	0.67	0.92	0.67	1
Mobile tongue	0.8	1	0.8	1	0.67	1	0.67	1
Palatoglossal arch	0.67	1	0.33	1	1	0.96	0.67	1
Palatine tonsil	1	0.92	1	0.92	1	1	0.5	1
Floor of mouth	0.78	0.94	0.78	0.94	0.89	1	0.89	1
Submandibular glands	1	0.9	1	0.9	1	1	1	1
Soft palate	0.67	0.96	0.67	1	1	0.81	1	0.81
Hard palate	1	1	1	1	1	0.96	1	0.96
Maxillary bone	1	0.96	1	0.96	1	0.92	1	0.92
Maxillary sinus	1	0.96	1	0.96	1	0.96	1	0.96
Masseter muscle	1	0.96	1	0.96	1	0.96	1	1
Pterygoid muscles	1	0.89	1	0.92	1	0.88	1	0.88
Nasal fossa	1	1	1	1	0.5	0.96	1	0.96
Subarachnoid spaces	1	1	1	1	1	1	1	1
Parotid glands	0	1	1	1	1	1	0	1
Perineural extension (V)	1	1	1	1	1	0.96	1	0.96
Perineural extension (VII)	0	1	0.5	1	1	1	1	1
All locations	0.83	0.98	0.85	0.98	0.88	0.98	0.9	0.98
All locations T1-T2	0.79	0.99	0.79	0.99	0.79	0.98	0.89	0.98

Note:—Se indicates sensitivity; Sp, specificity.

in the head and neck region.[32] Contrast enhancement has shown an ability to improve lesion detection and tissue characterization and to facilitate the evaluation of tumor extension. However, some studies with advanced morphologic MR images, such as fast short inversion recovery MR imaging, have shown comparable results to postgadolinium sequences for soft tissue tumor characterization.[33]

Whereas postgadolinium contrast enhancement reflects the tumor vascularization,[34] ^{18}F-FDG reflects glucose metabolism.[35] Even if the pathophysiological mechanisms are different, our study suggests that contrast-free MR imaging morphologic sequences with simultaneous ^{18}F-FDG PET images may give the same information as that added by postgadolinium sequences. In other words, the postgadolinium sequence does not seem to improve diagnostic accuracy in patients explored by simultaneous ^{18}F-FDG-PET/MR imaging. On the basis of retrospectively fused PET/CT and MR imaging, Kuhn et al[11] previously suggested that gadolinium contrast enhancement gave added value to the evaluation of primary tumor extension compared with fused PET and T2-weighted images alone. However, in our study, using simultaneous PET/MR imaging, the diagnostic accuracy in the evaluation of precise tumor extension remains the same with or without postcontrast images, suggesting that gadolinium-enhanced MR images provide redundant information compared with simultaneously acquired nonenhanced morphologic MRI together with FDG-PET images.

Although several previous PET/MR imaging studies focused on its diagnostic performance in head and neck tumor detection,[2,18,26] the present work, to the best of our knowledge, is the first study presenting a precise mapping of the regional HNC extension areas, analyzed by means of simultaneous PET/MR imaging. Previously, it was suggested that postcontrast T1-weighted sequences allow detection of perineural spread.[11] In our study, 1 rater group correctly detected all of the 3 cases of perineural spread on both contrast-free and postgadolinium sessions, but for the second rater group, detection was facilitated by contrast enhancement in 1 case. In the present study, thorough analysis of contrast-free simultaneous PET/MR imaging alone allowed detection of perineural spread in most cases. However, studies including larger numbers of cases of perineural spread are needed to corroborate this finding. Perineural spread (PNS) is a significant element of patient prognosis and long-term survival, and noncontrast MR imaging may be limited in this regard, but PET/CT has been widely applied in patients with multiple head and neck tumors at risk of having PNS, knowing the limitation of the study. At this stage, considering that PNS can be subtle with a non-negligible risk of omission and that postgadolinium MR clearly increases the radiologist's degree of confidence, postcontrast sequences should be maintained in ^{18}F-FDG-PET/MR for salivary gland malignancy work-up (given the high propensity for nerve invasion[36]) or when PNS is clinically suspected. Still, with the exception of those particular cases, our results suggest that analyzing contrast-free MR imaging simultaneously with ^{18}F-FDG PET in the context of PET/MR provides optimal diagnostic accuracy without the need for gadolinium-enhanced sequences.

Assessment of potential tumor invasion of bony structures, such as the mandible or maxillary sinus, has been reported as challenging, and some studies have suggested, in this case, better specificity and sensitivity of CT compared with MR imaging[37] or PET/MR imaging.[11] However, other studies found good diagnostic accuracy for both CT and MR imaging.[38] Moreover, higher confidence of PET/MR imaging compared with PET/CT for bone lesion detection has been reported.[39] In our study, all cases of mandibular bone cortical and medullary invasion were correctly detected in the contrast-free session alone, with 1 exception, in which even gadolinium injection did not facilitate the detection. Therefore, PET/MR imaging diagnostic accuracy for bone lesion detection appears to be good and does not seem to be improved by contrast enhancement.

Detection of small-sized head and neck tumors can be particularly challenging.[40] In this context, one could suppose that all available MR images should be used to maximize the chances of precise lesion detection and delineation. However, in the present study, we have observed that the diagnostic accuracy was good for both reading sessions with no improvement of sensitivity or specificity when a contrast-enhanced sequence was added.

PET/MR appears to be an advantageous imaging method in HNC because it can simultaneously evaluate the locoregional tumor extension, lymph node involvement, and distant metastases by combining head and neck MR imaging and whole-body ^{18}F-FDG-PET, 2 imaging modalities recommended for HNC staging. Still, in our opinion, management of patients with HNC should also systematically include head and neck and chest CT in search of cortical bone erosion, enlargement of foramina, and lung nodules.

Our study has several limitations. First, the sample size was small in this proof-of-concept study. Still, despite this, the results appear to be significant and promising. Second, because of the clinical design of the study, there was heterogeneity concerning histopathologic tumor types, related to the local recruitment. However, the main lesions were large oral cavity squamous cell carcinoma and salivary gland adenoid cystic carcinoma, with all the detailed histologic data available. Different histologic types of tumors might be different in contrast enhancement and FDG uptake. Namely, we could expect that some adenoid cystic tumors may show important contrast enhancement with moderate hypermetabolism. Still, in our study, we have not observed added value of contrast enhancement for these tumors. In the future, it might be interesting to conduct larger scale studies focused on the adenoid cystic tumor subtype, which remains difficult because of the low prevalence of these tumors. Last, there were few cases of perineural spread, which is consistent with the rarity of adenoid cystic carcinoma and of perineural spread.

CONCLUSIONS

In our study, the diagnostic accuracy of simultaneously acquired PET/MR imaging for assessing locoregional extension in patients with HNC was comparable with or without the addition of a gadolinium-enhanced sequence. These results suggest that in the specific case of simultaneously acquired head and neck PET/MR imaging, contrast injection does not provide added value to HNC evaluation and may be avoided.

Disclosures: Nadya Pyatigorskaya—*UNRELATED: Payment for Lectures Including Service on Speakers Bureaus:* GE Healthcare. Aurelie Kas—*UNRELATED: Payment for Lectures Including Service on Speakers Bureaus:* Lecture in EANM session about clinical PET/MR imaging*; *Payment for Development of Educational Presentations:* PIRAMAL, *Comments*: Educational session for nuclear physicians about amyloid-PET imaging but without any influence on the current work.* *Money paid to institution.

REFERENCES

1. Schaarschmidt BM, Heusch P, Buchbender C, et al. **Locoregional tumour evaluation of squamous cell carcinoma in the head and neck area: a comparison between MRI, PET/CT and integrated PET/MRI.** *Eur J Nucl Med Mol Imaging* 2016;43:92–102 CrossRef Medline
2. Xiao Y, Chen Y, Shi Y, et al. **The value of fluorine-18 fluorodeoxyglucose PET/MRI in the diagnosis of head and neck carcinoma: a meta-analysis.** *Nucl Med Commun* 2015;36:312–18 CrossRef Medline
3. Gupta B, Johnson NW, Kumar N. **Global epidemiology of head and neck cancers: a continuing challenge.** *Oncology* 2016;91:13–23 CrossRef Medline
4. Widmann G, Henninger B, Kremser C, et al. **MRI sequences in head & neck radiology—state of the art.** *Rofo* 2017;189:413–22 CrossRef Medline
5. Ozturk M, Yorulmaz I, Guney E, et al. **Masses of the tongue and floor of the mouth: findings on magnetic resonance imaging.** *Eur Radiol* 2000;10:1669–74 CrossRef Medline
6. Ross MR, Schomer DF, Chappell P, et al. **MR imaging of head and neck tumors: comparison of T1-weighted contrast-enhanced fat-suppressed images with conventional T2-weighted and fast spin-echo T2-weighted images.** *Am J Roentgenol* 1994;163:173–78 CrossRef Medline
7. Weller A, Barber JL, Olsen OE. **Gadolinium and nephrogenic systemic fibrosis: an update.** *Pediatr Nephrol* 2014;29:1927–37 CrossRef Medline
8. Weinreb JC, Abu-Alfa AK. **Gadolinium-based contrast agents and nephrogenic systemic fibrosis: why did it happen and what have we learned?** *J Magn Reson Imaging* 2009;30:1236–39 CrossRef Medline
9. McDonald RJ, McDonald JS, Kallmes DF, et al. **Intracranial gadolinium deposition after contrast-enhanced MR imaging.** *Radiology* 2015;275:772–82 CrossRef Medline
10. von Schulthess GK, Veit-Haibach P. **Workflow considerations in PET/MR imaging.** *J Nucl Med* 2014;55:19S–24S CrossRef Medline
11. Kuhn FP, Hüllner M, Mader CE, et al. **Contrast-enhanced PET/MR imaging versus contrast-enhanced PET/CT in head and neck cancer: how much MR information is needed?** *J Nucl Med* 2014;55:551–58 CrossRef Medline
12. Klenk C, Gawande R, Tran VT, et al. **Progressing toward a cohesive pediatric 18F-FDG PET/MR protocol: is administration of gadolinium chelates necessary?** *J Nucl Med* 2016;57:70–77 CrossRef Medline
13. Purohit BS, Ailianou A, Dulguerov N, et al. **FDG-PET/CT pitfalls in oncological head and neck imaging.** *Insights Imaging* 2014;5:585–602 CrossRef Medline
14. Gupta T, Master Z, Kannan S, et al. **Diagnostic performance of post-treatment FDG PET or FDG PET/CT imaging in head and neck cancer: a systematic review and meta-analysis.** *Eur J Nucl Med Mol Imaging* 2011;38:2083–95 CrossRef Medline
15. Kim SY, Lee S, Nam SY, et al. **The feasibility of 18F-FDG PET scans 1 month after completing radiotherapy of squamous cell carcinoma of the head and neck.** *J Nucl Med* 2007;48:373–78 Medline
16. Varoquaux A, Rager O, Poncet A, et al. **Detection and quantification of focal uptake in head and neck tumours: (18)F-FDG PET/MR versus PET/CT.** *Eur J Nucl Med Mol Imaging* 2014;41:462–75 CrossRef Medline
17. Yamaga E, Toriihara A, Nakamura S, et al. **Clinical usefulness of 2-deoxy-2-[18F] fluoro-d-glucose-positron emission tomography/computed tomography for assessing early oral squamous cell carcinoma (cT1-2N0M0).** *Jpn J Clin Oncol* 2018;48:633–39 CrossRef Medline
18. Kubiessa K, Purz S, Gawlitza M, et al. **Initial clinical results of simultaneous 18F-FDG PET/MRI in comparison to 18F-FDG PET/CT in patients with head and neck cancer.** *Eur J Nucl Med Mol Imaging* 2014;41:639–48 CrossRef Medline
19. Queiroz MA, Hüllner M, Kuhn F, et al. **PET/MRI and PET/CT in follow-up of head and neck cancer patients.** *Eur J Nucl Med Mol Imaging* 2014;41:1066–75 CrossRef Medline
20. Schaarschmidt BM, Gomez B, Buchbender C, et al. **Is integrated 18F-FDG PET/MRI superior to 18F-FDG PET/CT in the differentiation of incidental tracer uptake in the head and neck area?** *Diagn Interv Radiol* 2017;23:127–32 CrossRef Medline
21. Becker M, Varoquaux AD, Combescure C, et al. **Local recurrence of squamous cell carcinoma of the head and neck after radio (chemo)therapy: diagnostic performance of FDG-PET/MRI with diffusion-weighted sequences.** *Eur Radiol* 2018;28:651–63 CrossRef Medline
22. Queiroz MA, Wollenweber SD, von Schulthess G, et al. **Clinical image quality perception and its relation to NECR measurements in PET.** *EJNMMI Phys* 2014;1:103 CrossRef Medline
23. Monti S, Cavaliere C, Covello M, et al. **An evaluation of the benefits of simultaneous acquisition on PET/MR coregistration in head/neck imaging.** *J Healthc Eng* 2017;2017:1–7 CrossRef Medline
24. Boss A, Stegger L, Bisdas S, et al. **Feasibility of simultaneous PET/MR imaging in the head and upper neck area.** *Eur Radiol* 2011;21:1439–46 CrossRef Medline
25. Lee SJ, Seo HJ, Cheon GJ, et al. **Usefulness of integrated PET/MRI in head and neck cancer: a preliminary study.** *Nucl Med Mol Imaging* 2014;48:98–105 CrossRef Medline
26. Platzek I, Beuthien-Baumann B, Schneider M, et al. **PET/MRI in head and neck cancer: initial experience.** *Eur J Nucl Med Mol Imaging* 2013;40:6–11 CrossRef Medline
27. Grueneisen J, Sawicki LM, Schaarschmidt BM, et al. **Evaluation of a fast protocol for staging lymphoma patients with integrated PET/MRI.** *PLoS One* 2016;11:e0157880 CrossRef Medline
28. Todd DJ, Kay J. **Gadolinium-induced fibrosis.** *Annu Rev Med* 2016;67:273–91 CrossRef Medline
29. Queiroz MA, Hüllner M, Kuhn F, et al. **Use of diffusion-weighted imaging (DWI) in PET/MRI for head and neck cancer evaluation.** *Eur J Nucl Med Mol Imaging* 2014;41:2212–21 CrossRef Medline
30. Perkins NJ, Schisterman EF. **The inconsistency of "optimal" cutpoints obtained using two criteria based on the receiver operating characteristic curve.** *Am J Epidemiol* 2006;163:670–75 CrossRef Medline
31. Fruehwald-Pallamar J, Czerny C, Mayerhoefer ME, et al. **Functional imaging in head and neck squamous cell carcinoma: correlation of PET/CT and diffusion-weighted imaging at 3 Tesla.** *Eur J Nucl Med Mol Imaging* 2011;38:1009–19 CrossRef Medline

32. Barakos JA, Dillon WP, Chew WM. **Orbit, skull base, and pharynx: contrast-enhanced fat suppression MR imaging.** *Radiology* 1991;179:191–98 CrossRef Medline
33. Tokuda O, Harada Y, Matsunaga N. **MRI of soft-tissue tumors: fast STIR sequence as substitute for T1-weighted fat-suppressed contrast-enhanced spin-echo sequence.** *Am J Roentgenol* 2009;193:1607–14 CrossRef Medline
34. Folkman J. **Clinical applications of research on angiogenesis.** *N Engl J Med* 1995;333:1757–63 CrossRef Medline
35. Mérida I, Avila-Flores A. **Tumor metabolism: new opportunities for cancer therapy.** *Clin Transl Oncol* 2006;8:711–16 CrossRef Medline
36. Amit M, Binenbaum Y, Trejo-Leider L, et al. **International collaborative validation of intraneural invasion as a prognostic marker in adenoid cystic carcinoma of the head and neck.** *Head Neck* 2015;37:1038–45 CrossRef Medline
37. Yousem DM, Gad K, Tufano RP. **Resectability issues with head and neck cancer.** *AJNR Am J Neuroradiol* 2006;27:2024–36 Medline
38. van den Brekel MW, Runne RW, Smeele LE, et al. **Assessment of tumour invasion into the mandible: the value of different imaging techniques.** *Eur Radiol* 1998;8:1552–57 CrossRef Medline
39. Samarin A, Hüllner M, Queiroz MA, et al. **18F-FDG-PET/MR increases diagnostic confidence in detection of bone metastases compared with 18F-FDG-PET/CT.** *Nucl Med Commun* 2015;36:1165–73 CrossRef Medline
40. Schroeder U, Dietlein M, Wittekindt C, et al. **Is there a need for positron emission tomography imaging to stage the N0 neck in T1-T2 squamous cell carcinoma of the oral cavity or oropharynx?** *Ann Otol Rhinol Laryngol* 2008;117:854–63 CrossRef Medline

Prediction of Human Papillomavirus Status and Overall Survival in Patients with Untreated Oropharyngeal Squamous Cell Carcinoma: Development and Validation of CT-Based Radiomics

Y. Choi, Y. Nam, J. Jang, N.-Y. Shin, K.-J. Ahn, B.-S. Kim, Y.-S. Lee, and M.-S. Kim

ABSTRACT

BACKGROUND AND PURPOSE: Human papillomavirus is a prognostic marker for oropharyngeal squamous cell carcinoma. We aimed to determine the value of CT-based radiomics for predicting the human papillomavirus status and overall survival in patients with oropharyngeal squamous cell carcinoma.

MATERIALS AND METHODS: Eighty-six patients with oropharyngeal squamous cell carcinoma were retrospectively collected and grouped into training ($n = 61$) and test ($n = 25$) sets. For human papillomavirus status and overall survival prediction, radiomics features were selected via a random forest–based algorithm and Cox regression analysis, respectively. Relevant features were used to build multivariate Cox regression models and calculate the radiomics score. Human papillomavirus status and overall survival prediction were assessed via the area under the curve and concordance index, respectively. The models were validated in the test and The Cancer Imaging Archive cohorts ($n = 78$).

RESULTS: For prediction of human papillomavirus status, radiomics features yielded areas under the curve of 0.865, 0.747, and 0.834 in the training, test, and validation sets, respectively. In the univariate Cox regression, the human papillomavirus status (positive: hazard ratio, 0.257; 95% CI, 0.09–0.7; $P = .008$), T-stage (≥III: hazard ratio, 3.66; 95% CI, 1.34–9.99; $P = .011$), and radiomics score (high-risk: hazard ratio, 3.72; 95% CI, 1.21–11.46; $P = .022$) were associated with overall survival. The addition of the radiomics score to the clinical Cox model increased the concordance index from 0.702 to 0.733 ($P = .01$). Validation yielded concordance indices of 0.866 and 0.720.

CONCLUSIONS: CT-based radiomics may be useful in predicting human papillomavirus status and overall survival in patients with oropharyngeal squamous cell carcinoma.

ABBREVIATIONS: AUC = area under the curve; HPV = human papillomavirus; OPSCC = oropharyngeal squamous cell carcinoma; OS = overall survival; rad-scores = radiomics scores; TCIA = The Cancer Imaging Archive

Oropharyngeal squamous cell carcinoma (OPSCC) is one of the most rapidly growing subtypes of head and neck cancers, primarily due to the increased incidence of human papillomavirus (HPV)-related OPSCC.[1] HPV is a well-established prognostic factor for OPSCC, with a positive HPV status carrying a better prognosis.[2-4] This distinction in HPV status has contributed to the recent change in OPSCC staging in the 8th edition of the *American Joint Committee on Cancer Staging Manual*.[5-7] Because HPV status has substantial clinical implications, tissue biopsy from a primary or neck site and a test for p16/HPV are indicated. Although biopsy is generally straightforward in the head and neck, it is conceivable that image-based differentiation of OPSCC based on HPV status could become relevant, especially if it comes with cost savings.

Imaging of head and neck cancer is often difficult due to anatomic complexity, overlapping tissue densities, and artifacts (ie, motion, dental amalgam, and so forth). Thus, describing imaging features can be challenging. Recently, the advent of radiomics in image-based research has allowed the quantification of such complex imaging features into standardized high-throughput data,

Received January 20, 2020; accepted after revision July 3.

From the Departments of Radiology (Y.C., Y.N., J.J., N.-Y.S, K.-J.A., B.-S.K.), Hospital Pathology (Y.-S.L.), and Otolaryngology-Head and Neck Surgery (M.-S.K.), Seoul St. Mary's Hospital, College of Medicine, The Catholic University of Korea, Seoul, Republic of Korea; and Division of Biomedical Engineering (Y.N.), Hankuk University of Foreign Studies, Yongin-Si, Gyeonggi-do, Republic of Korea.

Please address correspondence to Kook-Jin Ahn, MD, PhD, Department of Radiology, Seoul St. Mary's Hospital, College of Medicine, The Catholic University of Korea, 222 Banpo-daero, Seocho-gu, Seoul (06591), Korea; e-mail: ahn-kj@catholic.ac.kr

Indicates article with supplemental on-line table.

Indicates article with supplemental on-line photo.

http://dx.doi.org/10.3174/ajnr.A6756

the subsequent analysis of which could aid clinical decision-making.[8]

Before radiomics, diffusion-weighted MR imaging indicated that HPV-positive OPSCC had lower apparent diffusion coefficients than its counterpart,[9] a finding that was presumed to be due to low stromal volume[10] and abundant lymphoid cells[11] associated with HPV-positive OPSCC. Previous CT-based radiomics studies reported promise in prognostication,[12] prediction of HPV status,[9] and both prediction and prognostication in head and neck cancers.[13,14]

We hypothesized that CT-based radiomics could fulfill both purposes—HPV status and overall survival (OS) prediction. Therefore, the aim of this study was to determine whether pretreatment CT-based radiomics of primary OPSCC could predict the HPV status and OS of patients initially diagnosed with OPSCC.

MATERIALS AND METHODS

Patients

This single-center retrospective cohort study was approved by the institutional review board of Seoul St. Mary's Hospital, and the need to obtain informed consent was waived. Between January 2009 and September 2019, one hundred twenty-five patients initially diagnosed with OPSCC were retrospectively reviewed. The inclusion criteria were the following: 1) pathologically confirmed OPSCC, 2) known HPV status, and 3) available pretreatment contrast-enhanced neck CT images. Thirty-nine patients were excluded for the following reasons: 1) primary tumor not visible on CT ($n = 8$), 2) beam-hardening artifacts hampering appropriate image analysis ($n = 26$), and 3) other underlying malignancy ($n = 3$) or distant metastases ($n = 2$) at the time of OPSCC diagnosis. Finally, a total of 86 eligible patients were selected for analysis. Clinical information, including age at diagnosis, sex, smoking history, cancer staging (*American Joint Committee on Cancer Staging Manual*, 8th edition), and HPV status were retrieved via the electronic medical records of our institution. OS was defined as the interval from the date of initial diagnosis to the date of death or last documented clinical visit. The cohort was grouped into training and test cohorts (7:3 ratio) by random stratified sampling so that the survival status (dead or alive) in each group was evenly distributed. The review of patients' medical records was finalized on October 2, 2019.

Independent External Validation Dataset

An independent external cohort ($n = 137$) was retrieved from The Cancer Imaging Archive (TCIA), an open repository of various oncologic images.[15] We specifically selected the head and neck cancer dataset previously published by Aerts et al,[16] who publicly shared CT-segmented primary OPSCC for reproducibility purposes. The patients were subjected to the same selection process as described above. After screening for eligibility criteria, 59 patients were excluded for the following reasons: 1) no OPSCC ($n = 49$), 2) unknown HPV status ($n = 8$), and 3) errors in importing segmentation ($n = 2$). Finally, 78 eligible patients were included as an external validation dataset.

HPV Status Assessment

The formalin-fixed and paraffin-embedded tissues were prepared in 4-mm-thick sections, which were then mounted onto 3-aminopropylmethoxysilane-coated slides. In situ hybridization was processed on an automated BenchMark system (Ventana Medical Systems) via INFORMH HPV III Family 16 Probe (cocktail of HPV subtypes 16, 18, 31, 33, 35, 39, 45, 51, 52, 56, and 66; Ventana Medical Systems) as recommended by the manufacturer. After removal of the paraffin wax, the tissue underwent protease digestion and hybridization with a probe. The probe-target complex was detected by the action of alkaline phosphatase on the 5-bromo-4-chloro-3-indolyl phosphate, which yielded dark blue with a pink counterstain for the HPV-negative cells due to nuclear fast red. The nuclear hybridization signal was evaluated by a head and neck pathologist (Y.-S.L.).

CT Image Acquisition

CT imaging of the neck was acquired using 2 different 128-channel multidetector CT scanners (Somatom Definition AS+ and Somatom Definition; Siemens). The CT protocol included precontrast and contrast-enhanced images after intravenous injection of 100 mL of iodinated contrast agent (60-second delay) (370 mg of iodine/mL, Ultravist, iopromide; Bayer HealthCare) at 2.5 mL/s via an automatic flow power injector (MEDRAD® Stellant, Bayer, Leverkusen, Germany). The scan parameters for both scanners were the following: x-ray voltage, 120 kV(peak); automatic tube current modulation (CARE Dose, syngo CT; Siemens); rotation time, 1 second; pitch, 0.8; detector collimation, 0.6 mm; matrix size, 512×512 pixels; FOV, 25 cm; and section thickness, 3 mm. The z-axis encompassed the skull base to the aortic arch.

Image Analysis and Radiomics Feature Extraction

All image analyses were performed using syngo.via Frontier software (Siemens). Primary sites of OPSCC were semiautomatically segmented using the "lesion segmentation" function within the software,[17] which yielded a 3D ROI contour; minimal additional adjustment of the ROI was needed to avoid beam-hardening artifacts and other soft tissues surrounding the tumor. 3D ROI segmentation included both solid and necrotic portions. The semiautomatic segmentation required approximately 2 seconds of processing time per patient. A radiologist (Y.C.) with 7 years of experience in head and neck imaging segmented all ROIs; another radiologist (K.-J.A.) with 20 years of experience in head and neck imaging reviewed and confirmed the ROIs, and any discrepancy was resolved by consensus. Both radiologists were blinded to the patients' clinical information during image analysis. Representative images of ROI segmentations are provided in Fig 1.

The ROIs were initially resampled to an isometric voxel size of 1 mm. Radiomic features were extracted using PyRadiomics—a publicly maintained platform of radiomic features[18] that were embedded in syngo.via Frontier. Six different classes of features were automatically extracted, yielding a total of 854 features per patient. The detailed information regarding these features is publicly available (https://pyradiomics.readthedocs.io/en/latest/).

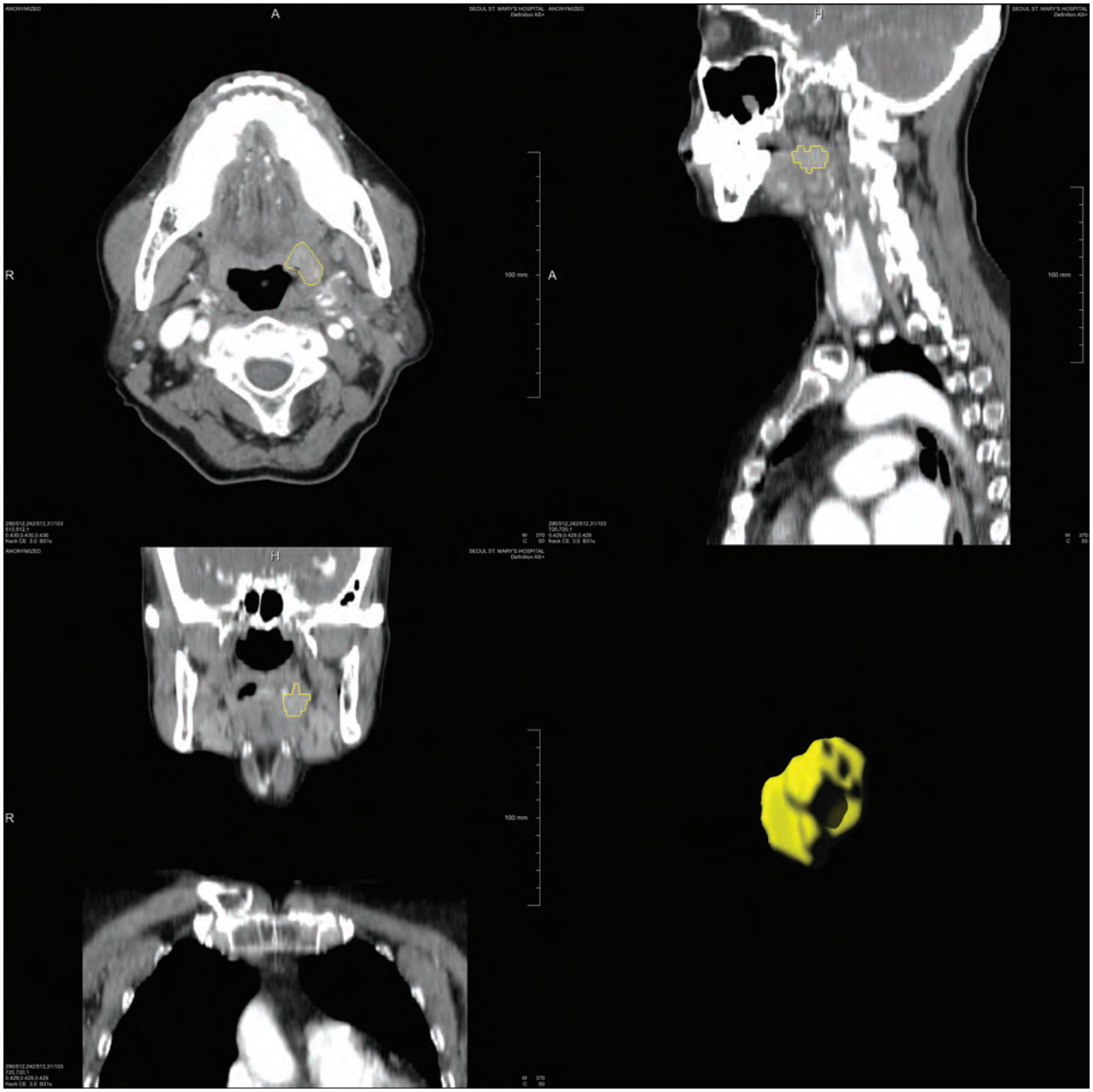

FIG 1. Representative contrast-enhanced CT images with a 3D ROI in a 73-year-old female patient. Volumetric rendering of segmentation is illustrated as a *yellow contour* (*lower right*).

Radiomics Feature Selection

For HPV-status prediction, radiomics features were selected via Boruta, which is a random forest–based wrapper algorithm for all-relevant feature selection.[19] Random forest generates an importance measure for each feature, allowing minimal parameter adjustment. In estimating feature importance, we applied the Boruta algorithm repetitively, and irrelevant features were consecutively excluded. The Boruta algorithm reached statistical significance by continuously calculating all possible feature combinations, producing an all-relevant subset of features.

Regarding OS prediction, least absolute shrinkage and selection operator–Cox regression were used for dimensionality reduction of radiomics features.[20] The selected features were weighted by their respective coefficients to calculate radiomics scores (rad-scores) for individual patients, with the median rad-score being used to dichotomize patients into high-risk and low-risk groups. All feature selections were performed in the training cohort to remove the possibility of overfitting.

Statistical Analysis

For HPV-status prediction, the Boruta-selected radiomic features from the training cohort were fitted into generalized linear models to plot receiver operating characteristic curves with calculation of the area under the curve (AUC). The same features were applied in the test and TCIA cohorts for internal and external validation, respectively, to calculate their respective AUCs. The optimal cutoff

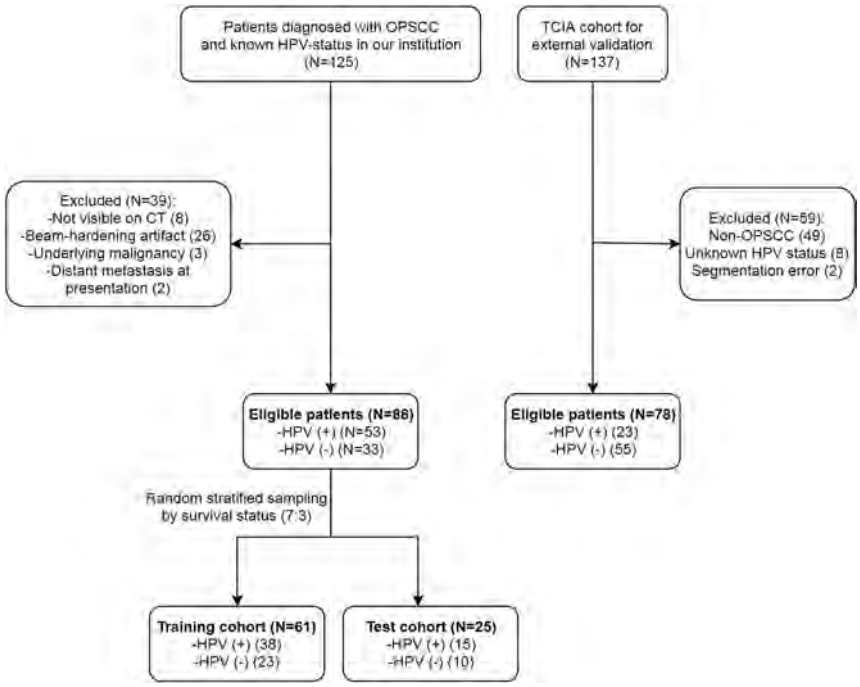

FIG 2. A flow diagram illustrating the patient-selection process.

Table 1: Clinical characteristics of the 2 study cohorts

Characteristics	Institutional Cohort ($n = 86$)	TCIA ($n = 78$)
Age (mean) (yr)	60.9 ± 8.6	60.2 ± 7.6
Sex (No.) (%)		
Male	78 (90.7)	61 (78.2)
Female	8 (9.3)	17 (21.8)
Smoking history (No.) (%)		
Smoker	50 (58.1)	NA
Nonsmoker	36 (41.9)	
HPV status (No.) (%)		
Positive	53 (61.6)	23 (29.5)
Negative	33 (38.4)	55 (70.5)
T-stage (No.) (%)		
I	19 (22.1)	13 (16.7)
II	41 (47.7)	24 (30.8)
III	20 (23.3)	10 (12.8)
IV	6 (7.0)	31 (39.7)
N-stage (No.) (%)		
0	18 (20.9)	20 (25.6)
I	32 (37.2)	11 (14.1)
II	33 (38.4)	45 (57.7)
III	3 (3.5)	2 (2.6)
Overall stage (No.) (%)		
I	25 (29.1)	5 (6.4)
II	25 (29.1)	7 (9)
III	23 (26.7)	10 (12.8)
IVA	11 (12.8)	49 (62.8)
IVB	2 (2.3)	7 (9)
No. of deaths (No.) (%)	24 (27.9)	45 (57.7)
Overall survival (mean) (day)	1290.6 ± 883.4	2243.4 ± 1370.7
Treatment (No.) (%)		
Surgery	60 (69.8)	3 (3.8)
Chemotherapy	56 (65.1)	NA
Radiation therapy	60 (69.8)	78 (100)

Note:—NA indicates not applicable.

threshold yielding the best AUC was obtained via the Youden index. Receiver operating characteristic curves with AUCs and 95% CIs were generated with 2000-times stratified bootstrapping. Comparisons among AUCs were performed using the DeLong test.

For OS prediction, a univariate Cox proportional hazard analysis was performed using variables including HPV status, smoking history, age (65 years of age or older), sex, T-stage (I/II versus III/IV), N-stage (0/I versus II/III), and rad-score (high-risk versus low-risk). Kaplan-Meier survival curves were plotted for each of these variables. Log-rank tests were used to compare the survival curves. Moreover, a nomogram for 2- and 5-year OS probabilities was constructed using the HPV status, T-stage, N-stage, and rad-score.

Multivariable Cox proportional hazards analyses were also performed to build 3 Cox regression models based on cancer stage (ie, T- and N-stage) alone (Cox model 1), cancer stage combined with the HPV status (Cox model 2), and cancer stage combined with both the HPV status and rad-score (Cox model 3). Harrell concordance indices were calculated for each model with likelihood ratio tests. Cox model 3 was both internally and externally validated in the test and TCIA cohorts to calculate the respective concordance indices. Finally, prediction error curves over survival times were plotted for the institutional and TCIA cohorts with an integrated Brier score, which ranges from 0 (perfect model) to 0.25 (meaningless model). All statistical analyses were performed using R statistical software (Version 3.5.1; http://www.r-project.org/) with "glmnet," "survival," "pROC," "pec," "caret" (for random stratified sampling), and "rms" (for nomogram) packages. The statistical significance was set at $P < .05$.

RESULTS

Patients

A flow diagram of the patient selection process is provided in Fig 2. The clinical characteristics of the study population are summarized in Table 1. Among the 86 patients in the institutional cohort (mean age, 60.9 ± 8.6 years; male, 90.7% [78/86]), 53 (61.6%) and 33 (38.4%) patients were HPV-positive and -negative, respectively. Stage II was the most prevalent for both T-stage (47.7%, 41/86) and N-stage (38.4%, 33/86). The training and test cohorts consisted of 61 and 25 patients, respectively; their clinical characteristics are provided in the On-line Table.

For the TCIA cohort (mean age, 60.2 ± 7.6 years; male, 78.2% [61/78]), 23 (29.5%) and 55 patients (70.5%) were HPV-positive and -negative, respectively. T-stage IV (39.7%, 31/78) and N-stage II (57.7%, 45/78) were the most prevalent.

Table 2: Relevant features for the prediction of human papillomavirus status and overall survival

	Mean Variable Importance	Norm Hits[a]/ Coefficients
Selected features by Boruta for prediction (Norm Hits)[a]		
original_shape_Flatness	4.753	0.812
original_shape_SphericalDisproportion	5.012	0.828
wavelet_HLH_firstorder_Mean	9.017	0.965
wavelet_HLH_firstorder_Uniformity	3.606	0.678
wavelet_HLH_glcm_ClusterShade	4.692	0.804
wavelet_LHH_glcm_Idm	3.296	0.600
wavelet_LHH_glcm_Imc1	4.201	0.753
wavelet_LHL_glszm_SmallAreaHighGrayLevelEmphasis	11.378	0.989
wavelet_LLH_glcm_Imc2	4.503	0.792
Selected features by LASSO-Cox for OS (coefficient)		
original_shape_SphericalDisproportion		3.20E-01
original_firstorder_Minimum		–2.36E-03
original_firstorder_10Percentile		–1.75E–05

Note:—LASSO indicates least absolute shrinkage and selection operator; glcm, gray-level co-occurrence matrix; glszm, gray-level size-zone matrix; idm, inverse difference moment; imc1, informational measure of correlation 1; imc2, informational measure of correlation 2.

[a] Fraction of random forest runs (Norm Hits) in which they were more important than the most important shadow value.

Relevant Radiomics Features

For each patient in the training cohort, 854 features from 6 different classes (first-order statistics, shape-based, gray-level cooccurrence matrix, gray-level run-length matrix, gray-level size-zone matrix, neighboring gray-tone difference matrix, and gray-level dependence matrix) were extracted. Among these, the Boruta algorithm selected 9 relevant features (2 shape-based, 2 first-order, 4 gray-level co-occurrence matrices, and 1 gray-level size-zone matrix) for the prediction of HPV status (Table 2).

As for OS prediction, least absolute shrinkage and selection operator–Cox regression yielded 3 radiomic features, including 1 shape-based and 2 first-order features. From these, the radscore was calculated using the follow-

Table 3: Sensitivity, specificity, and accuracy of radiomics features in predicting human papillomavirus status

Cohort	Sensitivity (95% CI)	Specificity (95% CI)	Accuracy (95% CI)	AUC (95% CI)
Training ($n = 61$)	76.3% (55.3%–100%)	91.3% (56.5%–100%)	80.3% (70.5%–90.2%)	0.865 (0.777–0.953)
Test ($n = 25$)	100% (40%–100%)	60.0% (30.0%–100%)	80.0% (60.0%–92.0%)	0.747 (0.533–0.961)
TCIA ($n = 78$)	82.6% (60.9%–100%)	80.0% (52.7%–94.6%)	80.8% (65.4%–89.7%)	0.834 (0.738–0.930)

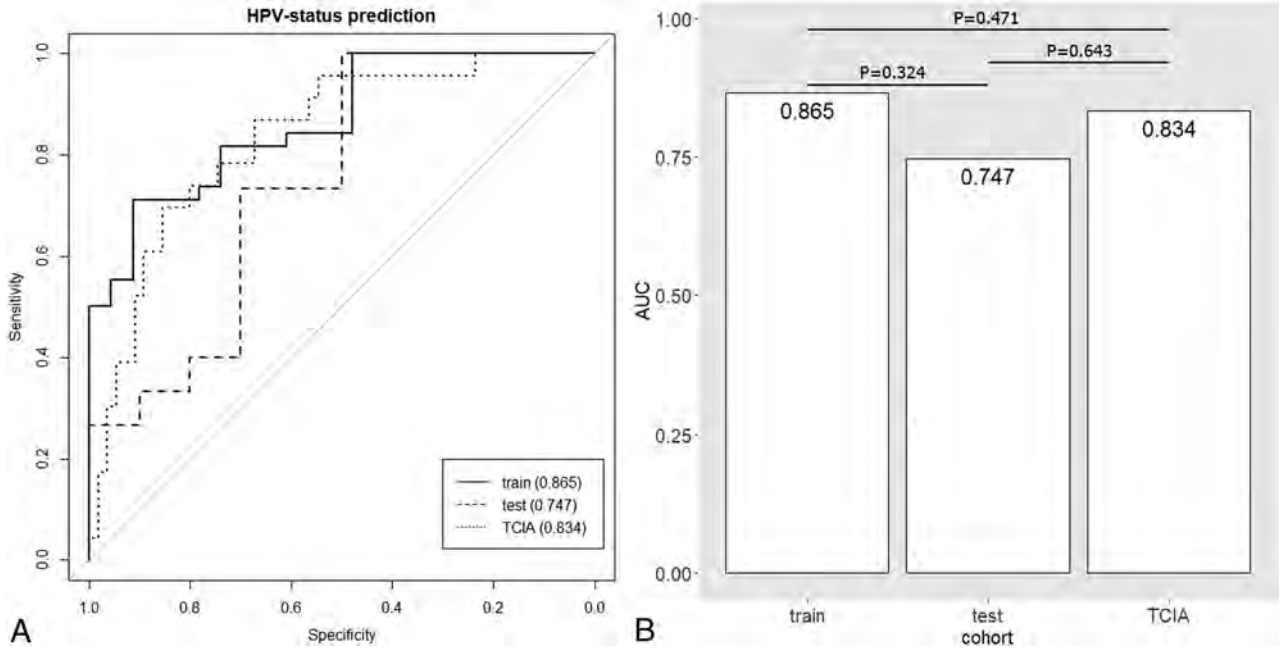

FIG 3. Receiver operating characteristic curves with AUC values for HPV-status prediction in the training, test, and TCIA cohorts (*A*). The *P* values calculated from the DeLong test between a pair of AUCs are presented above each line segment (*B*).

ing formula with Cox proportional hazard weights given to each feature as previously described:[12]

$0.32 \times$ Original_Shape_SphericalDisproportion + $(-2.363 \times 10^{-3}) \times$ Original_Firstorder_Minimum + $(-1.753 \times 10^{-5}) \times$ Original_Firstorder_10Percentile.

Performances of Radiomics Features in HPV Status Prediction

The generalized linear models fitted with 9 radiomics features in the training cohort yielded an AUC of 0.865 (95% CI, 0.777–0.953) with a sensitivity and specificity of 76.3% and 91.3%, respectively (Table 3). The internal validation, which was performed on a separate test set (30% of the initial cohort), yielded an AUC of 0.747 (95% CI, 0.533–0.961) with a sensitivity and specificity of 100% and 60%, respectively. The external validation yielded an AUC of 0.834 (95% CI, 0.738–0.930) with a sensitivity and specificity of 82.6% and 80%, respectively. Comparison of the AUCs revealed no significant differences (training versus test, $P = .324$; training versus TCIA, $P = .643$; test versus TCIA, $P = .471$) (Fig 3).

Table 4: Cox proportional hazards analyses and model validation

	HR	95%CI/C-Index	*P* Value
Clinical variable (95% CI)			
HPV status, positive	0.26	(0.09–0.7)	.008[a]
Smoking history, smoker	1.9	(0.66–5.44)	.23
Age, older than 65 years	0.97	(0.34–2.78)	.96
Sex, female	0.51	(0.07–3.83)	.51
T-stage, ≥III	3.66	(1.34–9.99)	.01[a]
N-stage, ≥II	1.62	(0.62–4.19)	.32
Overall stage, >IV	2.7	(0.95–7.68)	.06
Rad-score, high-risk	3.72	(1.21–11.46)	.02[a]
Multivariate model (C-index)			
Cancer stage (model 1)		0.621	.03
Cancer stage + HPV status (model 2)		0.702	.01
Cancer stage + HPV status + rad-score (model 3)		0.733	.01
Validation (C-index)			
Internal validation on test set		0.866	.01
External validation on TCIA set		0.72	<.001

Note:—HR indicates hazard ratio; C index, concordance index.
[a]statistically significant.

Performance of Radiomics Features in OS Prediction

In the univariate Cox analysis, the HPV status (positive: hazard ratio, 0.27; 95% CI, 0.09–0.7; $P = .008$), T-stage (≥III: hazard ratio, 3.66, 95% CI, 1.34–9.99; $P = .01$), and rad-score (high-risk: hazard ratio, 3.72; 95% CI, 1.21–11.46; $P = .02$) were found to be strongly associated with OS (Table 4). The Kaplan-Meier survival curves with log-rank tests of individual variables are provided in the On-line Figure. The nomogram for 2- and 5-year OS probabilities is illustrated in Fig 4. For the multivariate Cox analysis, Cox model 1 (T- and N-stage) had a concordance index of 0.621; the sequential addition of the HPV status and rad-score to Cox model 1 increased the concordance index to 0.702 (Cox model 2) and 0.733 (Cox model 3), respectively. The internal and external validation of Cox model 3 yielded concordance indices of 0.866 and 0.720, respectively. In addition,

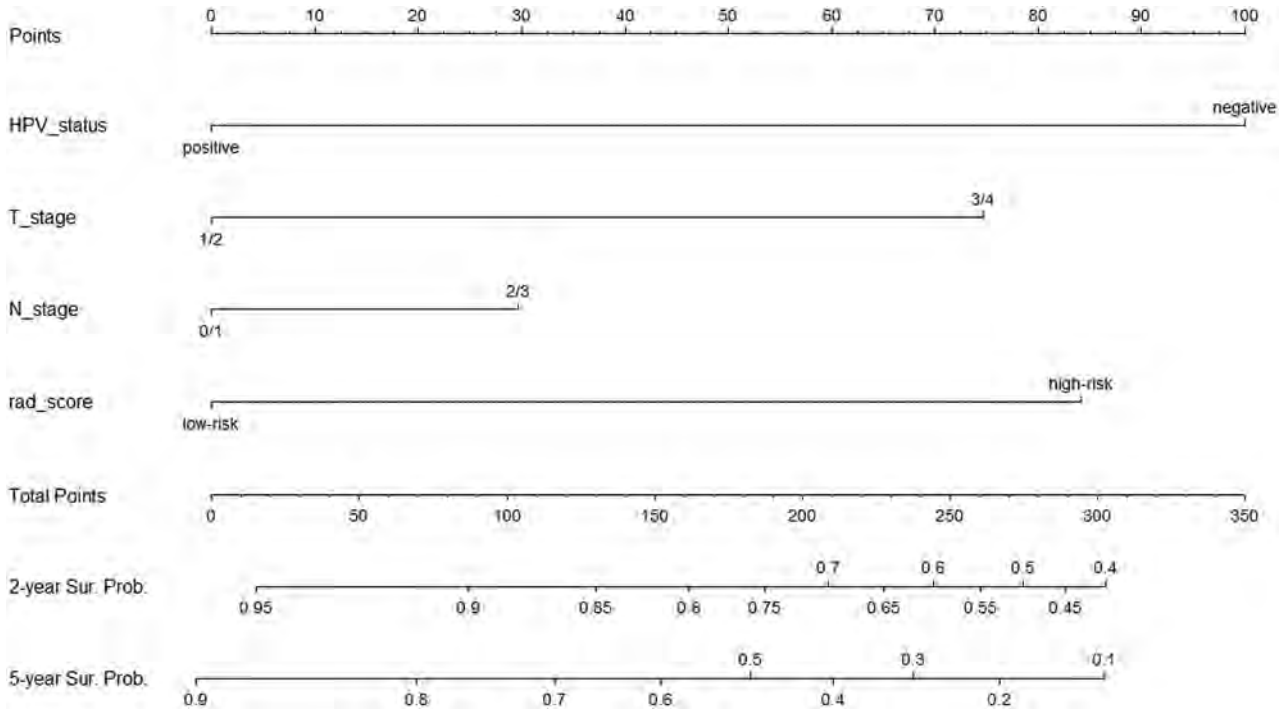

FIG 4. A nomogram of the 2- and 5-year overall survival. Sur. Prob. indicates survival probability.

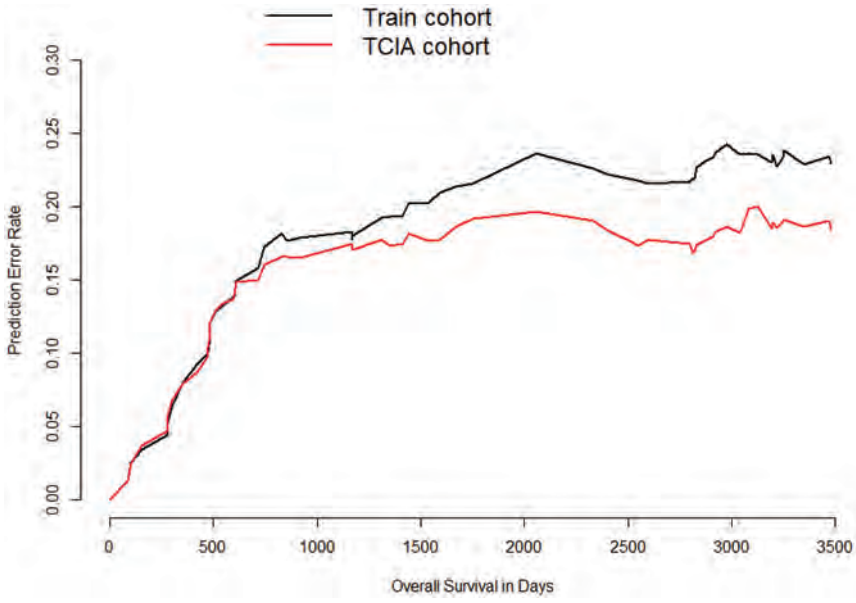

FIG 5. Prediction error curves with respect to the overall survival of the training (*black line*) and TCIA cohorts (*red line*).

Table 5: The integrated Brier scores of Cox model 3 in 2 cohorts

Survival Time (Day)	Patients at Risk	Training Cohort	TCIA
0	78	0	0
743	59	0.172	0.160
2545	40	0.217	0.173
3247	19	0.233	0.190

the external validation of Cox model 3 onto the TCIA cohort resulted in a reduction in the prediction error rates (ie, TCIA cohort curve remaining below the training cohort curve [Fig 5]). Similarly, the integrated Brier score was lower in the TCIA cohort than in the training cohort for all OS periods (Table 5).

DISCUSSION

In the current study, quantitative pretreatment CT-based radiomics features were extracted from patients with primary OPSCC, and the subsequent analysis of these features yielded robust performance in the prediction of HPV status and OS. The results were reproduced reliably in both internal and external validation sets. The findings of this study provide preliminary evidence that pretreatment CT-based radiomics could potentially aid both HPV-status prediction and prognostication for patients with OPSCC.

Several studies have considered the implications of radiomics in head and neck cancers. The present data are consistent with prior similar studies in that radiomics demonstrated additive prognostic[13,14] and predictive value for HPV status.[13,21] The studies performed by Ou et al[13] and Bogowicz et al[14] revealed that CT-based radiomics provided prognostic value in locally advanced head and neck cancers. However, the current study differs from theirs in that our target population was composed of untreated patients with OPSCC of various stages, which allowed more comprehensive risk assessment. Furthermore, our focused analysis on OPSCC minimized the potential heterogeneity that might be associated with various subtypes of head and neck cancers.

In multivariate Cox proportional hazards analysis, the addition of HPV status to the cancer stage increased the prognostic performance of the survival model. Likewise, the addition of the rad-score to the survival model fitted with HPV status and cancer stage further increased the prognostic performance. This finding suggests that rad-score—when combined with HPV status and cancer stage—may provide an incremental benefit for prognostication of patients.

An interesting additional finding in this study was the good performance observed in the external validation set, which was better than that of the internal validation set. Compared with the institutional cohort, the external validation set represented a regionally different cohort with varying clinical variables. Regardless, the CT-based radiomics models trained with the institutional cohort exhibited comparable AUCs in HPV-status prediction and better OS prediction in the external validation set. Therefore, a possible interpretation of this finding is that CT-based radiomics could be reproduced in multi-institutional cohorts.

As for the radiomics features, the most significant feature in OS prediction was the shape feature (spherical disproportion). This finding is consistent with a previous study by Leijenaar et al,[12] who also found a shape feature as the most significant prognostic marker among other features associated with survival of patients with OPSCC. Additionally, a previous study found that primary head and neck cancers displaying asphericity on pretherapeutic [^{18}F] fluorodeoxyglucose uptake appeared to be associated with a poorer prognosis.[22] Taken together, these findings suggest that the spatial heterogeneity of tumors might be associated with patients' prognosis. Future research should investigate the radiologic-pathologic correlation with regard to the spatial heterogeneity of the tumor.

The strength of the current study lies in its robust validations using internal and external datasets. While most previous radiomics studies of head and neck cancers used only internal validations[14] or lacked validations,[23,24] we used both internal and external validations to minimize the potential overfitting of radiomics models. In addition, the primary OPSCC images were segmented in 3D rather than in circular ROIs on single axial slices. These volumetric segmentations encompassed the entire oropharyngeal squamous cell carcinoma (OPSCC) and, therefore, better reflected the true intratumoral environment.

There are several limitations to this study. First, selection bias might have been present due to the retrospective nature of the study. However, we attempted to minimize the potential selection bias by strictly adhering to the predefined selection criteria.

Second, the issue of reproducibility is ongoing in most radiomics studies.[25] Thus, the open-platform PyRadiomics was adopted as our primary source of radiomics features. Furthermore, the external validation set used in this study was acquired from the TCIA, the public repository of oncologic medical images, thereby increasing the chance of reproducibility of our results. Some of the variables (ie, OS, treatment received, HPV status) differed between our cohort and the TCIA cohort; however, the differences would not have affected the outcome because the Cox models were built from the training cohort and the TCIA was used solely for external validation.

CONCLUSIONS

The current study highlighted the feasibility of CT-based radiomics in HPV status and OS prediction for patients with OPSCC. The results were good and reliably validated in both internal and external datasets. Our findings add preliminary evidence to the potential value of CT-based radiomics in risk-stratification and treatment allocation for patients with OPSCC.

ACKNOWLEDGMENT

The authors appreciate the dataset generously provided by L. Wee and A. Dekker (https://doi.org/10.7937/tcia.2019.8kap372n).

REFERENCES

1. Pytynia KB, Dahlstrom KR, Sturgis EM. **Epidemiology of HPV-associated oropharyngeal cancer.** *Oral Oncol* 2014;50:380–86 CrossRef Medline
2. Ang KK, Harris J, Wheeler R, et al. **Human papillomavirus and survival of patients with oropharyngeal cancer.** *N Engl J Med* 2010;363:24–35 CrossRef Medline
3. Chaturvedi AK, Engels EA, Pfeiffer RM, et al. **Human papillomavirus and rising oropharyngeal cancer incidence in the United States.** *JCO* 2011;29:4294–4301 CrossRef Medline
4. Ragin CC, Taioli E. **Survival of squamous cell carcinoma of the head and neck in relation to human papillomavirus infection: review and meta-analysis.** *Int J Cancer* 2007;121:1813–20 CrossRef Medline
5. O'Sullivan B, Huang SH, Siu LL, et al. **Deintensification candidate subgroups in human papillomavirus–related oropharyngeal cancer according to minimal risk of distant metastasis.** *J Clin Oncol* 2013;31:543–50 CrossRef Medline
6. Huang SH, Xu W, Waldron J, et al. **Refining American Joint Committee on Cancer/Union for International Cancer Control TNM stage and prognostic groups for human papillomavirus-related oropharyngeal carcinomas.** *J Clin Oncol* 2015;33:836–45 CrossRef Medline
7. O'Sullivan B, Huang SH, Su J, et al. **Development and validation of a staging system for HPV-related oropharyngeal cancer by the International Collaboration on Oropharyngeal Cancer Network for Staging (ICON-S): a multicentre cohort study.** *Lancet Oncol* 2016;17:440–51 CrossRef Medline
8. Gillies RJ, Kinahan PE, Hricak H. **Radiomics: images are more than pictures: they are data.** *Radiology* 2016;278:563–77 CrossRef Medline
9. Ravanelli M, Grammatica A, Tononcelli E, et al. **Correlation between human papillomavirus status and quantitative MR imaging parameters including diffusion-weighted imaging and texture features in oropharyngeal carcinoma.** *AJNR Am J Neuroradiol* 2018;39:1878–83 CrossRef Medline
10. Driessen JP, Caldas-Magalhaes J, Janssen LM, et al. **Diffusion-weighted MR imaging in laryngeal and hypopharyngeal carcinoma: association between apparent diffusion coefficient and histologic findings.** *Radiology* 2014;272:456–63 CrossRef Medline
11. Westra WH. **The morphologic profile of HPV-related head and neck squamous carcinoma: implications for diagnosis, prognosis, and clinical management.** *Head Neck Pathol* 2012;6(Supple 1):48–54 CrossRef Medline
12. Leijenaar RT, Carvalho S, Hoebers FJ, et al. **External validation of a prognostic CT-based radiomic signature in oropharyngeal squamous cell carcinoma.** *Acta Oncol* 2015;54:1423–29 CrossRef Medline
13. Ou D, Blanchard P, Rosellini S, et al. **Predictive and prognostic value of CT based radiomics signature in locally advanced head and neck cancers patients treated with concurrent chemoradiotherapy or bioradiotherapy and its added value to human papillomavirus status.** *Oral Oncol* 2017;71:150–55 CrossRef Medline
14. Bogowicz M, Riesterer O, Ikenberg K, et al. **Computed tomography radiomics predicts HPV status and local tumor control after definitive radiochemotherapy in head and neck squamous cell carcinoma.** *Int J Radiat Oncol Biol Phys* 2017;99:921–98 CrossRef Medline
15. Ren J, Tian J, Yuan Y, et al. **Magnetic resonance imaging based radiomics signature for the preoperative discrimination of stage I-II and III-IV head and neck squamous cell carcinoma.** *Eur J Radiol* 2018;106:1–6 CrossRef Medline
16. Aerts HJ, Velazquez ER, Leijenaar RT, et al. **Decoding tumour phenotype by noninvasive imaging using a quantitative radiomics approach.** *Nat Commun* 2014;5:4006 CrossRef Medline
17. Moltz JH, Bornemann L, Kuhnigk J-M, et al. **Advanced segmentation techniques for lung nodules, liver metastases, and enlarged lymph nodes in CT scans.** *IEEE J Sel Top Signal Process* 2009;3:122–34 CrossRef
18. van Griethuysen JJ, Fedorov A, Parmar C, et al. **Computational radiomics system to decode the radiographic phenotype.** *Cancer Res* 2017;77:e104–07 CrossRef Medline
19. Kursa MB, Rudnicki WR. **Feature selection with the Boruta package.** *J Stat Softw* 2010;36:1–13 CrossRef
20. Sauerbrei W, Royston P, Binder H. **Selection of important variables and determination of functional form for continuous predictors in multivariable model building.** *Statist Med* 2007;26:5512–28 CrossRef Medline
21. Huang C, Cintra M, Brennan K, et al. **Development and validation of radiomic signatures of head and neck squamous cell carcinoma molecular features and subtypes.** *EBioMedicine* 2019;45:70–80 CrossRef Medline
22. Apostolova I, Steffen IG, Wedel F, et al. **Asphericity of pretherapeutic tumour FDG uptake provides independent prognostic value in head-and-neck cancer.** *Eur Radiol* 2014;24:2077–87 CrossRef Medline
23. Buch K, Fujita A, Li B, et al. **Using texture analysis to determine human papillomavirus status of oropharyngeal squamous cell carcinomas on CT.** *AJNR Am J Neuroradiol* 2015;36:1343–48 CrossRef Medline
24. Fujita A, Buch K, Li B, et al. **Difference between HPV-positive and HPV-negative non-oropharyngeal head and neck cancer: texture analysis features on CT.** *J Compu Assist Tomogr* 2016;40:43–47 CrossRef Medline
25. Traverso A, Wee L, Dekker A, et al. **Repeatability and reproducibility of radiomic features: a systematic review.** *Int J Radiat Oncol Biol Phys* 2018;102:1143–58 CrossRef Medline

COVID-19-Associated Cytotoxic Lesions of the Corpus Callosum

P. Gaur, L. Dixon, B. Jones, H. Lyall, and W. Jan

ABSTRACT

SUMMARY: There are very limited published data on the neurologic complications associated with coronavirus disease 2019 (COVID-19) in the pediatric population. Here we present the first 2 pediatric cases of presumed COVID-19 related cytotoxic lesions of the corpus callosum. Similar to reports in adults, these cases suggest that the COVID-19 infection in children may rarely mediate a hyperinflammatory response that can cause CNS pathology. As the pandemic continues further, the presentation of cytotoxic lesions of the corpus callosum should prompt radiologists to consider COVID-19, among other known causes.

ABBREVIATIONS: CLOCC = cytotoxic lesions of the corpus callosum; COVID-19 = coronavirus disease 2019; CRP = C-reactive protein; RT-PCR = real-time reverse transcriptase polymerase chain reaction; SARS-CoV-2 = Severe Acute Respiratory Syndrome coronavirus 2

As of June 2, 2020, over 6.1 million cases of coronavirus disease 2019 (COVID-19) have been recorded and over 370,000 people have died.[1] Most confirmed cases have been in the adult population with only a small percentage (1%–2%) of reported cases being in children.[2] In the pediatric population, COVID-19 infection seems to be often asymptomatic or associated with mild respiratory symptoms.[2] As yet, there have been very limited reports of neurologic complications in children. Here we report the first series of pediatric neurologic presentations with COVID-19-associated cytotoxic lesions of the corpus callosum (CLOCC). This presentation has been related to other viral infections, but not yet demonstrated in association with COVID-19.

CASE DETAILS

A 12-year-old boy presented with a 5-day history of fever, lethargy, severe headache, vomiting, lower abdominal pain, and diarrhea. On examination, he was febrile and tender in the left iliac fossa and there was bilateral conjunctival infection, periorbital swelling, and scrotal edema. Neurologic examination was normal. Blood tests demonstrated lymphopenia and thrombocytopenia, with evidence of a systemic inflammatory response (raised D-dimer, fibrinogen, C-reactive protein [CRP], ferritin, lactate dehydrogenase, and procalcitonin). Urine and blood cultures were negative. Chest radiograph was indeterminate for COVID-19. Real-time reverse transcriptase polymerase chain reaction (RT-PCR) analysis of 2 nasopharyngeal swabs was negative. A subsequent COVID-19 serology test, an immunoassay for the in vitro detection of IgG antibody specific to Severe Acute Respiratory Syndrome coronavirus 2 (SARS-CoV-2) in human serum and plasma, was positive. No other causative agent was isolated and serologic testing showed no evidence of other infection. In the context of the serology and supportive blood test results, a diagnosis of COVID-19 was reached. MR imaging of the brain, performed early into admission, showed a small, oval-shaped, T2-weighted hyperintense lesion in the splenium of the corpus callosum that exhibited restricted diffusion (Fig 1). There was no associated intrinsic susceptibility signal drop-out; postcontrast imaging was not performed. The patient was not on any medications or therapies that could have clearly accounted for the callosal lesion at the time of imaging. Shortly after admission he became hemodynamically shocked with raised troponin levels suggesting myocardial involvement. His level of consciousness and oxygen saturation worsened, without appreciable seizure phenomenon, necessitating intubation and mechanical ventilation. Based on the evidence of both cardiac and central nervous system pathology and blood tests supporting a hyperinflammatory response, a diagnosis of COVID-19-related pediatric multisystem inflammatory syndrome was made.[3]

The patient was treated with intravenous immunoglobulin, Anakinra (Interleukin-1 antagonist), infliximab, and steroids. The patient's condition improved rapidly soon after commencing therapy and there were no neurologic symptoms at discharge.

Received June 3, 2020; accepted after revision June 11.

From the Departments of Imaging (P.G., L.D., B.J., W.J.) and Paediatric Infectious Diseases (H.L.), Imperial Healthcare NHS Trust, Charing Cross Hospital, London, United Kingdom.

Please address correspondence to Luke Dixon, Imaging Department, Charing Cross Hospital, Fulham Palace Rd, W6 8RF, London; e-mail: luke.dixon1@nhs.net

Indicates open access to non-subscribers at www.ajnr.org

http://dx.doi.org/10.3174/ajnr.A6713

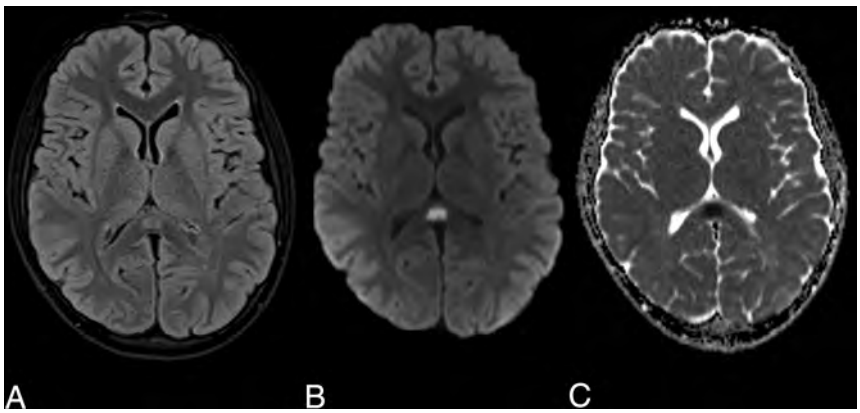

FIG 1. Axial MR images demonstrate an oval T2-weighted hyperintensity in the splenium of the corpus callosum (*A*) with associated restricted diffusion on the DWI (*B*) and ADC maps (*C*).

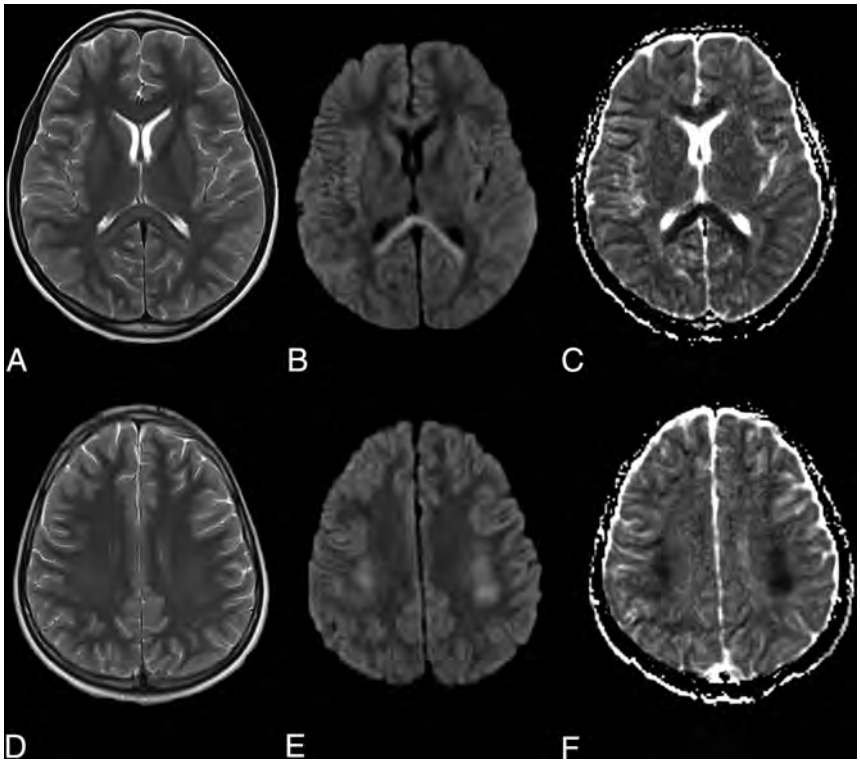

FIG 2. Axial MR images demonstrate T2-weighted hyperintensity in the splenium and genu of the corpus callosum (*A*) and symmetrically in the deep cerebral white matter (*B*) with associated restricted diffusion on the DWI (*B* and *E*) and ADC maps (*C* and *F*).

Repeat MR imaging has not yet been performed and was felt unwarranted acutely due to the clinical resolution.

A second pediatric patient, a 9-year-old boy, presented with altered mental state, fever, and lethargy. On examination he was dysarthric and ataxic. Audible lung crepitations were noted on respiratory examination. Blood tests demonstrated a lymphopenia, raised C-reactive protein and serum ferritin. Urine and blood cultures were negative, and a chest radiograph was normal. An early head MR imaging showed similar but more extensive abnormal T2-weighted hyperintense signal and restricted diffusion in the entire corpus callosum and frontoparietal cerebral white matter. This had a dorsal predilection, with greatest in-volvement of the splenium, peri-atrial white matter, and posterior frontal and parietal centrum semiovale (Fig 2). There was no intrinsic susceptibility signal drop-out. Postcontrast imaging was not performed. SARS-CoV-2 on RT-PCR testing was subsequently confirmed on broncho-alveolar lavage, despite initial negative results from nasopharyngeal swabs. No other causative agent was isolated. This second patient's symptoms improved rapidly and early follow-up MR imaging showed almost complete resolution of abnormal signal.[1]

DISCUSSION

CLOCC is a clinical-radiologic syndrome with a wide range of reported causes, including infection, trauma, drug-related, metabolic disorders, and malignancy.[4] It typically manifests in children and can present with reduced consciousness, nuchal rigidity, and seizures.[2,4]

CLOCC has been described in association with many pathogens, including influenza, malaria, Ebstein-Barr virus, adenovirus, and *E coli*.[5,6] In these cases where infection is thought to be the underlying cause, the diagnosis is also termed mild encephalitis/encephalopathy with a reversible splenial lesion. Our cases mirror clinical and radiologic features reported in a case series of 15 children with CLOCC of which 83% were presumed to be related to various different infections. Similar to our observations in presumptive COVID-19 related CLOCC, the authors of that series demonstrated evidence of systemic inflammation (raised CRP) and different degrees of nonenhancing, diffusion-restricting, white matter signal abnormality from isolated splenial lesions to more diffuse corpus callosal and extracallosal involvement.[6] To our knowledge no cases of CLOCC related to the inflammatory response to SARS-CoV-2 or other coronaviruses have been reported. CLOCC is thought to be caused by a cytokine storm that triggers T cells to breach the blood-brain barrier causing inflammation and intramyelinic edema.[5,7] This aligns with our cases of CLOCC that appeared to occur in the context of a multisystem inflammatory process with one of the cases showing more classic signs of pediatric inflammatory multisystem syndrome temporally associated with SARS-CoV-2, including myocardial and abdominal involvement.[3] These cases reflect a

new presentation of CNS inflammatory complication of SARS-CoV-2 exposure in children with pediatric inflammatory multisystem syndrome temporally associated with SARS-CoV-2. This inflammatory syndrome shares features with Kawasaki disease, toxic shock syndrome, and macrophage activation syndrome.[8-10] In our cases, the apparent rapid response to immunotherapy is encouraging and further supports the theory that this is an inflammatory and possibly cytokine-mediated process.

The diagnosis of CLOCC is based on the MR imaging demonstration of diffusion-restricting, nonenhancing lesions that usually resolve between a few days and weeks. Radiologically, as demonstrated in our cases, there is typically a lesion in the splenium of the corpus callosum with more variable involvement of the remaining corpus callosum and cerebral white matter.[5] Often clinical recovery lags behind imaging, but is usually within 3 months.[5]

This is the first reported series of presumptive COVID-19-associated CLOCC that appeared to occur in the context of pediatric inflammatory multisystem syndrome temporally associated with SARS-CoV-2. Further investigation of COVID-19-related CNS pathology in children and the potential role of immunotherapy is required. Clinicians and radiologists should be aware of this potential presentation.

REFERENCES

1. Geneva S. **World Health Organization. Coronavirus disease 2019 (COVID-19) situation report – 105.** *World Health Organization* https://www.who.int/docs/default-source/coronaviruse/situation-reports/20200504-covid-19-sitrep-105.pdf?sfvrsn=4cdda8af_2. Published 2020
2. Parri N, Lenge M, Buonsenso D. **Children with Covid-19 in pediatric emergency departments in Italy.** *N Engl J Med* 2020;383:187–90 CrossRef Medline
3. Whittaker E, Bamford A, Kenny J, et al. **Clinical characteristics of 58 children with a pediatric inflammatory multisystem syndrome temporally associated with SARS-CoV-2.** *JAMA* 2020;324:259–69 CrossRef Medline
4. Takanashi JI. **Two newly proposed infectious encephalitis/encephalopathy syndromes.** *Brain Dev* 2009;31:521–28 CrossRef Medline
5. Vanderschueren G, Schotsmans K, Maréchal E, et al. **Mild encephalitis with reversible splenial (MERS) lesion syndrome due to influenza B virus.** *Pract Neurol* 2018;18:391–92 CrossRef Medline
6. Chen WX, Liu HS, Yang SD, et al. **Reversible splenial lesion syndrome in children: Retrospective study and summary of case series.** *Brain Dev* 2016;38:915–27 CrossRef Medline
7. Starkey J, Kobayashi N, Numaguchi Y, et al. **Cytotoxic lesions of the corpus callosum that show restricted diffusion: mechanisms, causes, and manifestations.** *Radiographics* 2017;37:562–76 CrossRef Medline
8. McGonagle D, Sharif K, O'Regan A, et al. **The role of cytokines including interleukin-6 in COVID-19 induced pneumonia and macrophage activation syndrome-like disease.** *Autoimmun Rev* 2020;19:102537 CrossRef Medline
9. Inciardi RM, Lupi L, Zaccone G, et al. **Cardiac involvement in a patient with coronavirus disease 2019 (COVID-19).** *JAMA cardiology* 2020 Mar 27. [Epub ahead of Print] CrossRef Medline
10. Jones VG, Mills M, Suarez D, et al. **COVID-19 and Kawasaki disease: novel virus and novel case.** *Hosp Pediatr* 2020;10:537–40 CrossRef Medline

Maternal Anxiety and Depression during Late Pregnancy and Newborn Brain White Matter Development

R.M. Graham, L. Jiang, G. McCorkle, B.J. Bellando, S.T. Sorensen, C.M. Glasier, R.H. Ramakrishnaiah, A.C. Rowell, J.L. Coker, and X. Ou

ABSTRACT

BACKGROUND AND PURPOSE: Anxiety and depression during pregnancy have been associated with an increased risk of adverse neurodevelopmental outcomes in offspring. We aimed to study the in utero effects of maternal anxiety and depression on early brain development.

MATERIALS AND METHODS: Pregnant women were recruited at ~36 weeks of gestation for this prospective study. They were assessed for anxiety symptoms by the State-Trait Anxiety Inventory and for depression symptoms by the Beck Depression Inventory, 2nd Edition. After delivery, infant underwent an MR imaging examination of the brain without sedation, including DTI, for evaluation of white matter (WM) development. Infant fractional anisotropy values, a putative marker of WM integrity, were correlated with the mothers' State-Trait Anxiety Inventory and Beck Depression Inventory scores by using both tract-based spatial statistics and ROI methods.

RESULTS: Thirty-four infants were included in this study. Both maternal State-Anxiety and Trait-Anxiety scores negatively correlated ($P < .05$, corrected) with fractional anisotropy values in widespread brain WM regions; Beck Depression Inventory scores also negatively correlated ($P < .05$) with fractional anisotropy values in one cluster in the brain. Further ROI analyses confirmed significant negative correlations between average fractional anisotropy values in ROIs including left and right prefrontal WM, left and right middle frontal gyrus WM, and the fornix, and State-Anxiety (*R* values, –0.47 to –0.67; *P* values, .008 to <.001), Trait-Anxiety (R, –0.37 to –0.59; *P*, .04 to <.001), and Beck Depression Inventory (*R* values, –0.36 to –0.55; *P*, .05 to .002) scores.

CONCLUSIONS: Higher maternal anxiety and depression symptom scores during late pregnancy were associated with lower estimated infant brain WM development, which indicated in utero influences of maternal mental health during pregnancy on the developing brain.

ABBREVIATIONS: BDI-II = Beck Depression Inventory, 2nd ed; FA = fractional anisotropy; S-Anxiety = State-Anxiety score; SD = standard deviation; STAI = State-Trait Anxiety Inventory; T-Anxiety = Trait-Anxiety score; TBSS = tract-based spatial statistics

It is estimated that 28.8% of the US population is diagnosed with an anxiety disorder and that 20.8% will be diagnosed with a mood disorder, for example, depression, throughout life.[1] These disorders are of particular concern to women of reproductive age, which coincides with the median age of onset for these diagnoses,[1] because the physiologic and metabolic changes associated with pregnancy may play an important role in triggering these conditions. In fact, it has been estimated that ~13% of pregnant women in the United States experience an anxiety-related disorder, and 13.3% have a mood disorder, for example, depression.[2,3]

Maternal anxiety and depression during pregnancy are not only a significant health issue for the women because many of them continue to have psychiatric disorders postpartum, but also a potential health concern for their offspring. For example, offspring of women who have depression during pregnancy are almost 5 times more likely to receive a diagnosis of depression by age 16 than those who were not exposed to antenatal depression.[4] In addition, increased maternal anxiety during early pregnancy is independently associated with lower mental development scores of infants at age 1 year[5] as well as hyperactivity and inattention in boys at 4 years of age, and behavioral and emotional problems in both boys and girls.[6]

Received April 7, 2020; accepted after revision July 6.

From the Departments of Radiology (R.M.G., L.J., C.M.G., R.H.R., A.C.R., X.O.), Pediatrics (B.J.B., S.T.S., C.M.G., R.H.R., X.O.), and Psychiatry, and Obstetrics and Gynecology (J.L.C.), University of Arkansas for Medical Sciences, Little Rock, Arkansas; Arkansas Children's Nutrition Center (G.M., X.O.), Little Rock, Arkansas; and Arkansas Children's Research Institute (X.O.), Little Rock, Arkansas.

This study was supported in part by National Institutes of Health (NIH) 1P20GM121293-6283, NIH R01HD099099, and U.S. Department of Agriculture/Agricultural Research Service 6251-51000-006-00D.

Please address correspondence to Xiawei Ou, PhD, Department of Radiology, University of Arkansas for Medical Sciences, 1 Children's Way, Slot 105, Little Rock, AR 72202; e-mail: ouxiawei@uams.edu

Indicates open access to non-subscribers at www.ajnr.org

http://dx.doi.org/10.3174/ajnr.A6759

Recent advances in noninvasive neuroimaging, particularly in quantitative MR imaging methods,[7] provide an opportunity to link maternal depression and anxiety with adverse neurodevelopmental outcomes in offspring by sensitive evaluation of children's early brain development. A few new studies have revealed associations between prenatal anxiety and/or depression and infant brain structural or functional development measured by MR imaging,[8-10] which suggests the possibility of in utero influences of a mother's mental health status to fetal brain development. In addition, maternal anxiety and depression are associated with an increased risk of fetal growth restriction,[11] which has been linked to changes in later brain development.[12]

These possible in utero influences reflected by brain differences at early ages may be key to understand the relationships between prenatal maternal mental health and long-term neurodevelopment outcomes because studies have indicated the predictive value of early brain measures to later outcomes.[13,14] Moreover, studies also reported associations between maternal anxiety and/or depression during pregnancy and their offspring's brain structure and function at later ages,[15,16] although other postnatal influences may have confounded these relationships. Overall, with emerging evidence that shows the potential impact of maternal anxiety and depression on offspring neurodevelopment, more studies are needed to characterize how different brain regions may be vulnerable to this unfavorable prenatal environment and to delineate the prenatal effects with postnatal influences.

In this study, we hypothesized that both maternal anxiety and depression during pregnancy would negatively affect offspring fetal brain development, particularly for brain regions that control emotion, motivation, memory, and cognitive and/or executive functions. We aimed to determine if significant associations exist between measures of symptoms for these disorders in late pregnancy and measures of infant WM development soon after birth. To achieve that, we recruited healthy pregnant women without complications, measured their anxiety and depression symptomatology by using standardized tests, and evaluated WM microstructural development in their newborn infants during the first few weeks of life by using diffusion-tensor MR imaging.

MATERIALS AND METHODS

Subjects

All study procedures were approved by the institutional review board of the University of Arkansas for Medical Sciences, and all the participants signed informed consent to be included in this study. Healthy pregnant women without medical complications during pregnancy were recruited through the Arkansas Children's Nutrition Center for this prospective study. The inclusion criteria for the pregnant women were the following: singleton pregnancy, ~36 weeks of pregnancy, and ≥18 years of age. Exclusion criteria were the following: hypertension, diabetes, or other pre-existing medical conditions known to influence fetal growth; self-reported recreational drug, tobacco, or alcohol use while pregnant; pregnancy conception with assisted fertility treatment; and medical conditions developed during pregnancy known to influence fetal growth. Infants born preterm, with congenital defects and/or anomalies (or known chromosomal abnormalities), small for gestational age (birth weight <10th percentile), with a low Apgar score (<7) or any other medical complications at birth that suspected to affect brain WM development were also excluded. In total, 44 infants had an MR imaging examination at age 2 weeks. Among them, 34 had both valid structural and/or diffusion scans and maternal anxiety scores (2 of these did not have valid depression scores) and were included in this report. The demographics for the included subjects are presented in the Table.

Demographic information of the infants (17 male and 17 female) and their mothers' STAI, BDI-II, and IQ test scores at ~36 weeks of pregnancy

Demographic	Result	
	Mean ± SD	Range: minimum, maximum
Gestational age at birth, days	275 ± 7	259, 285
Age at MR imaging, days	18 ± 7	12, 37
Mother's IQ score	99 ± 11	74, 132
Mother's S-Anxiety score	29 ± 8	20, 52
Mother's T-Anxiety score	34 ± 10	21, 61
Mother's BDI-II score	9 ± 6	0, 29

Anxiety and Depression Assessment

Anxiety and depression symptom scores were obtained by using the State-Trait Anxiety Inventory (STAI) and the Beck Depression Inventory, 2nd ed (BDI-II),[17] respectively. Both assessments were administered by a licensed psychological examiner (GM). The STAI provides 2 results: state (S-Anxiety) and trait (T-Anxiety). The S-Anxiety score reflects the subject's current state of anxiety, that is, how the subject is feeling at the moment of filling out the evaluation. In contrast, the T-Anxiety result reflects how prone to anxiety the subject is, which can include general states of calmness and security.[18] The STAI assessment consists of 40 questions in total, with 20 dedicated to each subcategory. The result of the examination is a range of scores between 20 and 80, with a higher score indicating greater anxiety. Although the STAI manual does not indicate actual cut-points to describe clinical thresholds, results of some studies suggested a score of 39–40 to define clinically significant symptoms of S-Anxiety,[19] and results of other studies suggest a score of 45 as the cutoff for T-Anxiety.[20] For the purposes of this study, mean + 1 standard deviation (SD) (which provided a cutoff value of 38 for S-Anxiety and 45 for T-Anxiety, similar to the literature above) was used to determine whether their endorsement of anxiety symptoms was in the elevated range. The instrument manual reveals that alpha coefficients for the STAI show correlations of 0.92 to 0.94, which indicate that the STAI has very good internal consistency and is a reliable instrument for measuring anxiety. Validity evidence for the STAI also shows that this measure correlates well with other widely used measures of personality and adjustment and anxiety.[21]

The BDI-II is a 21-item questionnaire that evaluates the presence of symptoms for depression listed in the *Diagnostic and Statistical Manual of Mental Disorders,* 4th ed. The assessment includes items that measure affective, vegetative, cognitive, and somatic symptoms of depression during the past 2 weeks.[22] The Beck Depression Inventory is one of the most widely used indexes of depression due to its high validity, internal

consistency, and sensitivity to change.[23] Overall, the BDI-II has an internal consistency of 0.9 and a retest reliability range from 0.73 to 0.96. Validity research for the BDI-II when comparing it with the Beck Depression Inventory and other well-researched depression inventories shows excellent validity, which justifies its use for assessment of depression in these subjects.[24] Results are considered to indicate the presence of "minimal" depressive symptoms for scores 0–13, "mild" depressive symptoms for scores 14–19, "moderate" for scores 20–28, and "severe" for scores >29.

In addition, all pregnant women were administered the Wechsler Abbreviated Scale of Intelligence, 2nd ed,[25] which is an abbreviated scale of intellectual performance that measures verbal comprehension, perceptual reasoning, and general cognitive abilities (Full Scale IQ Index). The average reliability coefficient in adult samples when calculated with the Fisher *z* transformation is 0.97. Concurrent validity has been established with several widely used measures of intelligence.

MR Imaging Data Acquisition

At approximately age 2 weeks, the infants were brought to the radiology department of the Arkansas Children's Hospital for an MR imaging examination of the brain at natural sleep without sedation. Mini-muffs and/or headsets were placed over their ears to protect them from the noise during the scan. They were swaddled by using a MedVac infant immobilizer and warm sheets and were securely positioned. An MR imaging–compatible camera was used to monitor them. The infants were scanned by using a PRISMA scanner (Siemens Medical Solutions) and an equipped 20-channel head coil. Pulse sequences included sagittal T1 MPRAGE (TR, 1550 ms; TE, 3 ms; TI, 1100 ms; flip angle, 15°; voxel size, 1 mm × 1 mm × 1 mm) and T2 TSE (TR, 10,500 ms; TE, 168 ms; echo spacing, 15.3 ms; voxel size, 1 mm × 1 mm × 2 mm) to screen for structural abnormalities by neuroradiologists, and DWI with TR of 10,200 ms, TE of 63 ms, acquisition voxel size of 2 mm × 2 mm × 2 mm, and b-value of 1000 s/mm^2 with diffusion-weighting gradients uniformly distributed (ie, projection of diffusion directions uniformly distributed on a sphere unit) in 30 directions to evaluate brain WM development.

MR Imaging Data Analysis

Fractional anisotropy (FA) maps were calculated by using the scanner software and were exported to a workstation with FSL (version 6.0, http://www.fmrib.ox.ac.uk/fsl) installed on a VMware Linux virtual machine (VMware) for postprocessing. The postprocessing methods were similar to those in previous publications.[13,26,27] Briefly, through the use of FSL's tract-based spatial statistics (TBSS; https://fsl.fmrib.ox.ac.uk/fsl/fslwiki/TBSS) toolbox, each FA image set was eroded slightly to remove the thin and bright voxels that surround the edge of the brain, and end slices were zeroed to remove outliers, which are voxels outside the brain with noisy FA. The FA image sets were then registered to each other by using nonlinear transformation to find the most representative one, which then, consequently, served as the target images. Each FA image set was then centered and layered on top of the target images, and a mean FA map and a mean WM skeleton (with FA ≥ 0.15 as the threshold, when considering that infants have lower FA values than adults, for which 0.2 is usually the default threshold) were then generated for all the subjects and served as age-specific templates. All FA maps were then projected onto the FA skeleton to create a 4D FA maps dataset that encompassed all the subjects and, subsequently, was used for statistical analysis. Finally, voxelwise correlation analyses were used in TBSS to evaluate associations between FA values and STAI and BDI-II scores. In addition, WM ROI, showing consistent correlations between FA values and STAI and BDI-II scores in the TBSS analysis were sketched on the mean FA maps based on anatomy, and the average FA values for WM tracts in each ROI were calculated. The associations between these average FA values in these ROIs and STAI and BDI-II scores were also evaluated.

Statistical Analysis

For the voxelwise correlation analyses using TBSS, randomization with 5000 permutations was used. The threshold-free cluster enhancement option was used to identify voxels with significant correlation ($P < .05$, corrected for multiple comparisons in the voxelwise analysis) between FA values and S-Anxiety, T-Anxiety, or BDI-II scores. Potential confounders were considered, including postmenstrual age (gestational age at birth plus age at MR imaging), which has shown strong effects on infant WM development[26] as well as maternal IQ and infant sex. These parameters were included in the randomized design matrix, and their potential confounding effects were controlled by regressing out before permutation. For the ROI analysis, partial Spearmen correlation analyses were used to evaluate correlations between average FA values in each ROI and the S-Anxiety, T-Anxiety, and BDI-II scores, also with the effects of potential confounders (postmenstrual age at MR imaging, infant sex, mother's IQ) controlled. Both the correlation coefficients and the *P* values were computed and presented. $P < .05$ was regarded as significant.

RESULTS

The characteristics for the participants included in this study are listed in the Table. Most of the mothers (76%) self-reported anxiety and depressive symptoms that were within normal ranges, with overall average scores for the study group also well within established normal values. In total, 8 mothers (24%) reported elevated symptoms of depression and/or anxiety. Specifically, among 5 women (15%) with elevated depressive symptoms, 1 had severe symptoms and 4 had mild symptoms on the BDI-II. Anxiety was also considered clinically elevated in 5 women (15%) on the T-Anxiety score and 1 woman (3%) on the S-Anxiety score. There were 2 women (6%) who endorsed clinical elevations on both anxiety and depression measures. There was 1 woman who was taking sertraline (Zoloft; a selective serotonin reuptake inhibitor) 50 mg once a day and another woman who was taking Zoloft 25 mg per day during pregnancy to treat anxiety. No other women took anxiety or depression treatment medicine during pregnancy. In addition, the S-Anxiety and T-Anxiety scores showed strong correlation (correlation coefficient $R = 0.78$, $P < .001$), and both S-Anxiety ($R = 0.61$, $P < .001$) and T-Anxiety ($R = 0.65$, $P < .001$) scores showed significant correlations with Beck Depression Inventory scores.

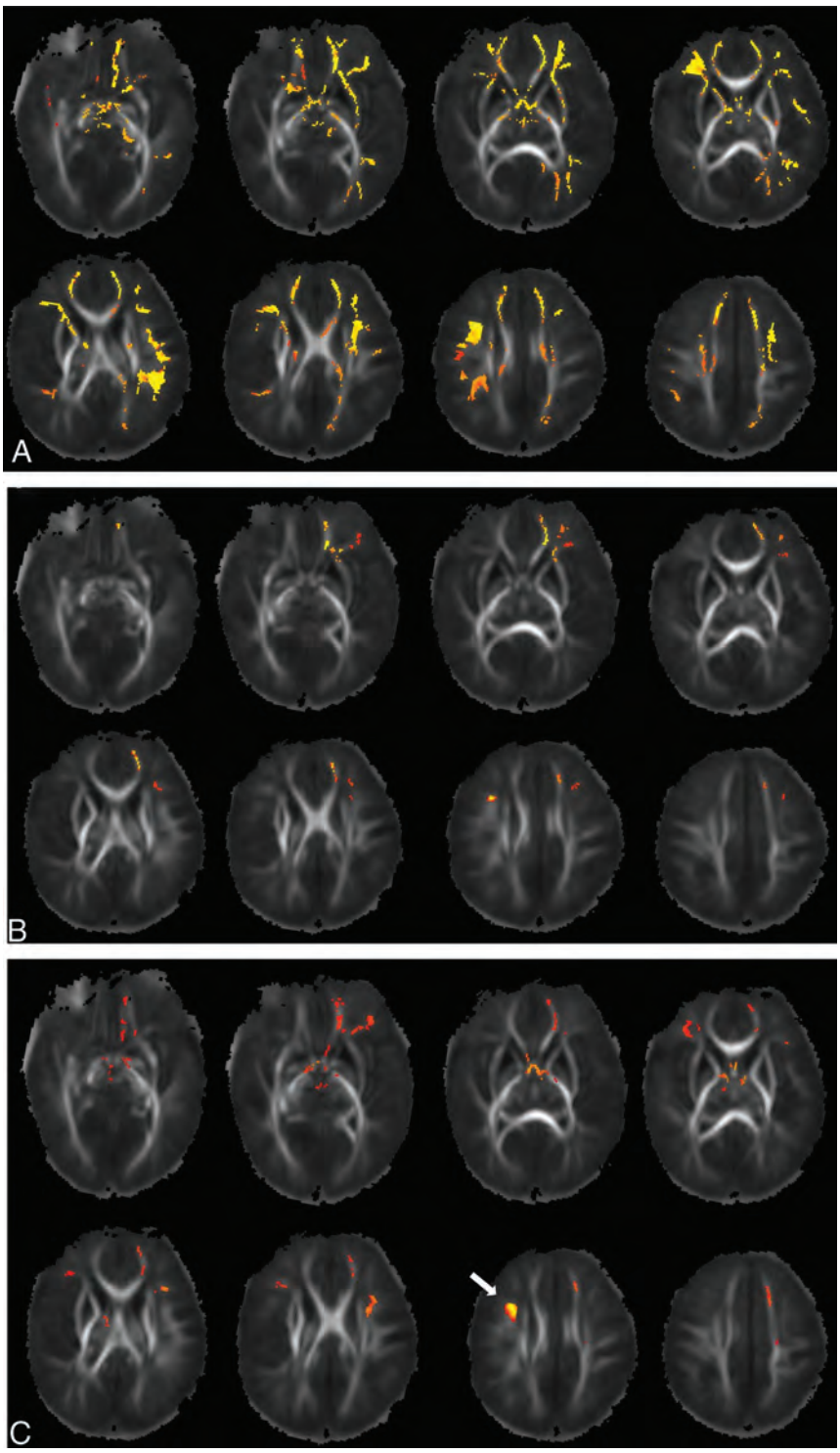

FIG 1. *A*, WM regions (*orange/red*) showing significant ($P < .05$, corrected) negative correlations between the mother's S-Anxiety score ($n = 34$) and infant FA value. B, WM regions showing significant negative correlations ($P < .05$, corrected) between the mother's T-Anxiety score ($n = 34$) and infant FA value. *C*, WM regions showing a trend ($P < .10$, corrected, except for the cluster shown by the *white arrow* in which $P < .05$) of negative correlations between mother's BDI-II score ($n = 32$) and infant FA value.

Seventeen male and 17 female infants, born at a mean ± SD gestational age of 275 ± 7 days, had successful MR imaging, with valid structural and diffusion imaging data at a mean ± SD age of 18 ± 7 days. There were no significant incidental findings that suggested WM abnormality for any of these subjects. Voxelwise TBSS analysis showed negative correlations ($P < .05$, corrected for the voxelwise multiple comparison and controlled for postmenstrual age at MR imaging, infant sex, and mother's IQ) between S-Anxiety scores in the pregnant women and FA values in the infant in widespread brain WM regions (Fig 1*A*). These regions involved frontal, parietal, and temporal WM in both brain hemispheres as well as the limbic system. In addition, the T-Anxiety score in the pregnant women also negatively and significantly ($P < .05$, corrected for multiple comparison and controlled for covariates) correlated with FA values in their infants in multiple WM regions (Fig 1*B*). These regions involved the left orbitofrontal, prefrontal, and middle frontal WM, and the right middle frontal WM. There also was a negative and significant ($P < .05$, corrected for multiple comparison and controlled for covariates) correlation between the BDI-II score in the pregnant women and FA values in their infants in 1 cluster located in the right middle frontal WM (arrow in Fig 1*C*). In addition, multiple WM regions in the left and right frontal WM as well as in the limbic system showed trends ($P < .10$, corrected for multiple comparison and controlled for covariates) of negative correlations between BDI-II scores and FA values in the TBSS analysis (Fig 1*C*). No imaging voxels or clusters in the brain showed a positive correlation ($P < .05$) between the S-Anxiety, T-Anxiety, BDI-II scores, and the FA values.[26]

Based on the TBSS results, several regions that consistently showed clusters with significant (or trend of) correlations between the S-Anxiety, T-Anxiety, BDI-II scores, and the FA values were chosen for additional ROI analysis. These ROIs were manually drawn on the mean FA maps based on anatomy and included the left-right prefrontal WM, the left-right middle frontal gyrus WM, and the fornix in the limbic system. The average FA values for the WM tracts in each of these ROIs were calculated and correlated with STAI and BDI-II scores. Specifically,

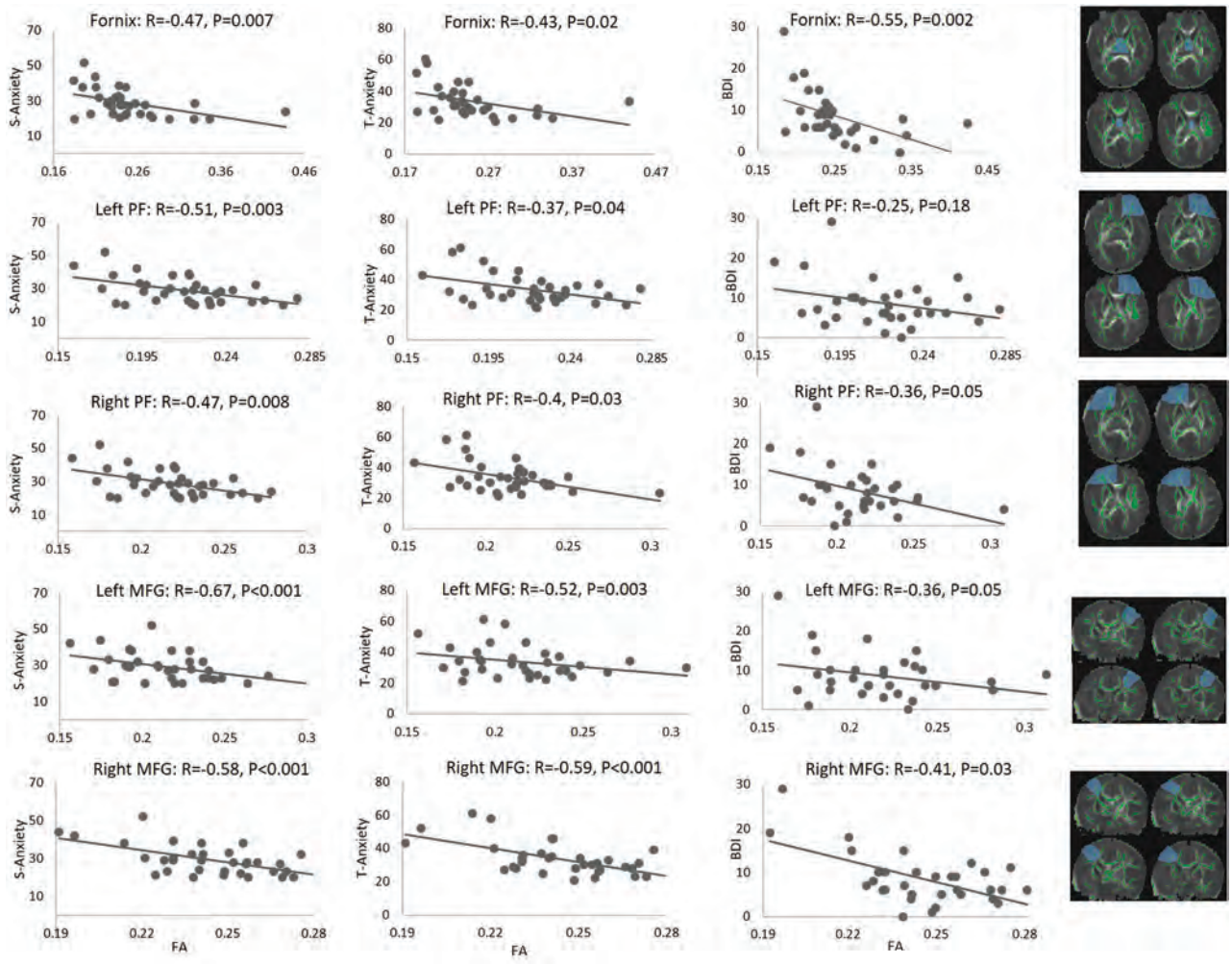

FIG 2. Correlations between infant average FA values in the selected ROIs and maternal anxiety and/or depression symptom scores (S-Anxiety, T-Anxiety, BDI-II) measured at pregnancy. The column on the right shows manually drawn regions (*shaded blue*), which, in combination with the underlying WM skeleton (*green*), defined the WM ROIs used for calculation. PF indicates prefrontal WM; MFG, middle frontal gyrus WM.

a partial correlation test (with the postmenstrual age at MR imaging, infant sex, and mother's IQ as covariates) showed negative correlations (correlation coefficient R values ranging from −0.47 to −0.67; *P* values ranging from .008 to <.001) between S-Anxiety scores in the pregnant women and the average FA values in all of the 5 ROIs (Fig 2); negative correlations (correlation coefficient R values ranging from −0.37 to −0.59; *P* values ranging from .04 to <.001) between T-Anxiety scores in the pregnant women and average FA values in all of the 5 ROIs (Fig 2); and negative correlations (correlation coefficients R values ranged from −0.36 to −0.55; *P* values ranged from .05 to .002) between BDI-II scores in the pregnant women and the average FA values in 4 of the 5 ROIs (Fig 2).

If depression scores were controlled for, then the relationships between the anxiety scores and the FA values weakened. Nevertheless, the following relationships were still significant: S-Anxiety and left prefrontal WM FA ($R = -0.40$, $P = .03$), or left ($R = -0.59$, $P < .001$) or right ($R = -0.42$, $P = .03$) middle frontal gyrus WM FA; and T-Anxiety and left ($R = -0.43$, $P = .02$) or right ($R = -0.38$, $P = .05$) middle frontal gyrus WM FA. On the other hand, if anxiety scores were controlled for, then the relationships between the depression scores and the FA values weakened as well, with only the relationship between the BDI-II score and fornix FA significant ($R = -0.40$, $P = .04$). Therefore, it seems that associations in the left prefrontal and left-right middle frontal gyrus WM may be more specific to anxiety, whereas the associations in the fornix may be more specific to depression.

DISCUSSION

Our prospective study showed that the healthy full-term infants born from uncomplicated pregnancies of mothers with symptoms for anxiety or depression (higher S-Anxiety, T-Anxiety, or BDI-II scores) had lower estimated WM development (as indicated by lower FA values) in multiple brain regions. A number of recent brain imaging studies looked into the relationships between maternal anxiety or depression during pregnancy and measurements of brain structure or function in children. For example, maternal anxiety during the second trimester of

pregnancy was associated with decreased GM volume in the prefrontal cortex and several other cerebral-cerebellar regions in 6–9-year-old children.[15] Likewise, depression symptoms at the second trimester measured by the Edinburgh Postnatal Depression Scale negatively correlated with cortical thickness in inferior frontal and middle temporal regions in 2.6–5.1-year-old children.[16] In addition, increased maternal anxiety measured at 26 weeks of pregnancy using the STAI was associated with slower growth of the hippocampus in the infant brain during the first 6 months of life.[28] Functionally, maternal depressive symptoms measured by the Edinburgh Postnatal Depression Scale at 26 weeks of gestation were also associated with lower functional connectivity between the amygdala and the corticostriatal circuitry in girls at 4 years of age.[29] Importantly, although postpartum maternal depression and a few other postnatal factors were considered in the aforementioned studies, the associations between in utero exposure to maternal depression and anxiety and brain development in childhood were inevitably confounded by many other postnatal factors, such as family environment and child nutrition. Measuring the neonatal brain soon after birth may be more indicative of the in utero effects, independent of postnatal influences. In fact, a few imaging studies with slightly different designs when compared with our study (eg, time evaluating pregnant women and infants, structural and/or microstructural parameters analyzed) looked into whether brain structures in young infants show changes associated with maternal depression or anxiety during pregnancy. For example, FA values in the amygdala in 6–14-day-old infants were lower for those born to mothers with high depression symptom scores during pregnancy versus those born to mothers with low depression symptom scores.[9] Similarly, a diffusion imaging study on 1-month-old infants showed that a higher composite symptom score of anxiety and/or depression measured at the third trimester of pregnancy in their mothers was associated with lower microstructural measures in their frontal WM.[8] Interestingly, although widespread differences in WM microstructures in 1-month-old infants were found between those born to mothers who received depression treatment with selective serotonin reuptake inhibitors during pregnancy compared with controls (mothers with no depression diagnosis or treatment during pregnancy), there were no differences in WM microstructures or GM volumes when comparing those born to mothers with a history of depression but no treatment with the same controls.[30] Analysis of these results suggests that exposure to medicine may have important confounding effects in relationships of maternal anxiety and/or depression and fetal brain development, and should not be overlooked. Analysis of these results also suggested that additional studies may be necessary to confirm the in utero effects of anxiety and depression on brain development.

Our voxel wise TBSS and subsequent ROI analysis results indicated a few brain regions that consistently showed negative correlations between higher anxiety and/or depression symptoms and lower estimated WM development. These regions mainly involved the left and right prefrontal WM, the left and right middle frontal WM, and the fornix in the limbic system. The findings in prefrontal–middle frontal WM are consistent with a few previous studies.[8,15,16] The prefrontal cortex is important for executive functioning, attention, and memory as well as speech production and language. Depression and/or anxiety has been linked with abnormalities in prefrontal WM,[31–33] and exposure to maternal depression and/or anxiety in utero has been linked to adverse development in executive functioning.[34] Likewise, WM abnormalities associated with anxiety and/or depression have been found in the middle frontal gyrus,[32] which supposedly serves as the connection between the ventral and dorsal attention network and acts as a "circuit-breaker" to transition between stimulus-driven and goal-oriented attention;[35] and, studies show that antenatal maternal depression and/or anxiety were associated with a higher risk of child attention problems.[36] The associations between maternal anxiety and/or depression during pregnancy and offspring fornix development have not been reported before, with only one study showing changes of pace in hippocampal volume growth in infants associated with maternal anxiety.[28] Development of the fornix begins at week 10 of gestation and continues rapidly throughout gestation as one of the most prominent brain fiber tracts at the fetal stage despite fornix's relatively small size in the adult brain.[37] It is understandable that the fornix is vulnerable to environmental influences during this stage of rapid development. In addition, lower fornix FA values at birth have been associated with lower cognitive scores measured at 2 years of age,[13] which indicate the functional importance of normal early development of this structure.

Although the underlying mechanism for the changes in in utero WM development associated with maternal anxiety or depression is unclear, there are a few physiologic and/or metabolic factors that may be involved. The increase of cortisol (one of the major stress and anxiety hormones) level in the maternal and fetal circulation may affect fetal neural development.[38] In addition, maternal anxiety and/or depression may lead to an increased number of inflammatory cytokines in circulation, which also could adversely affect fetal development via alteration of the in utero environment.[39] Although these potential pathways can only be speculated without appropriately designed studies, our imaging data that show infant brain differences associated with maternal anxiety and/or depression during pregnancy indicate that there are likely fetal programming effects involved. One clinical implication of our study is that focus on postpartum mental health of women at reproductive age may need to be extended to before and during pregnancy because there may be significant prenatal influences on offspring brain development.

There are a few limitations with our study. First, the sample size was small. Although significant associations between maternal anxiety and/or depression and infant WM development were revealed by using this small cohort, a larger cohort can allow consideration to more potential confounders and may potentially identify more regions with significant correlation. Second, the psychological evaluations of anxiety and depression symptoms were only measured once, at 36 weeks of pregnancy. Future studies with longitudinal observation of these symptoms throughout the pregnancy may provide a more complete characterization of fetal exposure to this unfavorable environment. Third, in our study design, we included participants on medicine for treatment of anxiety or depression ($n = 2$). Although the effects of medicine did not seem to change our results (when analyzing the data by

adding whether taking medicine as an additional covariate), the effects may need to be carefully considered with a larger cohort. Fourth, we only focused our diffusion evaluation on FA values that are commonly available on clinical scanners, while FA values are sensitive but not specific to different microstructural changes in WM. Nevertheless, our study is one of the first to reveal significant effects of both maternal anxiety and depression during pregnancy on offspring brain development, and in imaging the infant brain as early as possible to capture the in utero effects while limiting postnatal influences.

CONCLUSIONS

Higher maternal anxiety and depression symptom scores during late pregnancy were each associated with lower estimated infant brain WM development in multiple brain regions, including prefrontal and middle frontal WM and the fornix, indicating in utero influences and early brain changes, which may potentially lead to changes in long-term neurodevelopmental outcomes in offspring.

Disclosures: Ginger McCorkle—*RELATED: Grant:* NIH, *Comments:* This project is funded by NIH 1P20GM121293-6283.* Betty Jayne Bellando—*RELATED: Grant:* NIH 1P20GM121293-6283.* Charles M. Glasier—*UNRELATED: Consultancy:* Medicolegal consulting. Amy C. Rowell—*RELATED: Grant:* NIH 1P20GM121293-6283.* Jessica L. Coker—*UNRELATED: Grants/Grants pending:* Brain and Behavior Research Foundation NIH/National Institute on Drug Abuse.* Xiawei Ou—*RELATED: Grant:* NIH, Comments: 1P20GM121293-6283, 1R01HD099099.* *Money paid to the institution.

REFERENCES

1. Kessler RC, Berglund P, Demler O, et al. **Lifetime prevalence and age-of-onset distributions' of DSM-IV disorders in the national comorbidity survey replication.** *Arch Gen Psychiatry* 2005;62:593–602 CrossRef Medline
2. Vesga-López O, Blanco C, Keyes K, et al. **Psychiatric disorders in pregnant and postpartum women in the United States.** *Arch Gen Psychiatry* 2008;65:805–15 CrossRef Medline
3. American College of Obstetricians and Gynecologists Committee on Health Care for Underserved Women. **ACOG Committee Opinion No. 343: psychosocial risk factors: perinatal screening and intervention.** *Obstet Gynecol* 2006;108:469–77 CrossRef Medline
4. Pawlby S, Hay DF, Sharp D, et al. **Antenatal depression predicts depression in adolescent offspring: prospective longitudinal community-based study.** *J Affect Disord* 2009;113:236–43 CrossRef Medline
5. Davis EP, Sandman CA. **The timing of prenatal exposure to maternal cortisol and psychosocial stress is associated with human infant cognitive development.** *Child Dev* 2010;81:131–48 CrossRef Medline
6. O'Connor TG, Heron J, Golding J, et al. **Maternal antenatal anxiety and children's behavioural/emotional problems at 4 years - report from the Avon Longitudinal Study of Parents and Children.** *Br J Psychiatry* 2002;180:502–08 CrossRef Medline
7. Dubois J, Alison M, Counsell SJ, et al. **MRI of the neonatal brain: a review of methodological challenges and neuroscientific advances.** *J Magn Reson Imaging* 2020 May 18. [Epub ahead of print] CrossRef Medline
8. Dean DC III, Planalp EM, Wooten W, et al. **Association of prenatal maternal depression and anxiety symptoms with infant white matter microstructure.** *JAMA Pediatr* 2018;172:973–81CrossRef Medline
9. Rifkin-Graboi A, Bai J, Chen H, et al. **Prenatal maternal depression associates with microstructure of right amygdala in neonates at birth.** *Biol Psychiatry* 2013;74:837–44 CrossRef Medline
10. Rifkin-Graboi A, Meaney MJ, Chen H, et al. **Antenatal maternal anxiety predicts variations in neural structures implicated in anxiety disorders in newborns.** *J Am Acad Child Adolesc Psychiatry* 2015;54:313–21.e2 CrossRef Medline
11. Grote NK, Bridge JA, Gavin AR, et al. **A meta-analysis of depression during pregnancy and the risk of preterm birth, low birth weight, and intrauterine growth restriction.** *Arch Gen Psychiatry* 2010;67:1012–24 CrossRef Medline
12. Miller SL, Huppi PS, Mallard C. **The consequences of fetal growth restriction on brain structure and neurodevelopmental outcome.** *J Physiol* 2016;594:807–23 CrossRef Medline
13. Feng KY, Rowell AC, Andres A, et al. **Diffusion tensor MRI of white matter of healthy full-term newborns: relationship to neurodevelopmental outcomes.** *Radiology* 2019;292:179–87 CrossRef Medline
14. Hu HCH, McAllister AS. **The potential and promise of diffusion tensor MRI in predicting neurodevelopment in children.** *Radiology* 2019;292:188–89 CrossRef Medline
15. Buss C, Davis EP, Muftuler LT, et al. **High pregnancy anxiety during mid-gestation is associated with decreased gray matter density in 6-9-year-old children.** *Psychoneuroendocrinology* 2010;35:141–53 CrossRef Medline
16. Lebel C, Walton M, Letourneau N, et al. **Prepartum and postpartum maternal depressive symptoms are related to children's brain structure in preschool.** *Biol Psychiatry* 2016;80:859–68 CrossRef Medline
17. Beck AT, Steer RA, Brown GK. *Manual for the Beck Depression Inventory-II*. San Antonio: Psychological Corporation; 1996
18. Julian LJ. **Measures of anxiety: State-Trait Anxiety Inventory (STAI), Beck Anxiety Inventory (BAI), and Hospital Anxiety and Depression Scale - Anxiety (HADS-A).** *Arthritis Care Res* 2011;63 (suppl 11):S467–72 CrossRef Medline
19. Knight RG, Waal-Manning HJ, Spears GF. **Some norms and reliability data for the State-Trait Anxiety Inventory and the Zung Self-Rating Depression scale.** *Br J Clin Psychol* 1983;22(pt 4):245–49 CrossRef Medline
20. Bunevicius A, Staniute M, Brozaitiene J, et al. **Screening for anxiety disorders in patients with coronary artery disease.** *Health Qual Life Outcomes* 2013;11:37 CrossRef Medline
21. Guillén-Riquelme A, Buela-Casal G. **Meta-analysis of group comparison and meta-analysis of reliability generalization of the State-Trait Anxiety Inventory Questionnaire (STAI**). *Rev Esp Salud Publica* 2014;88:101–12 CrossRef Medline
22. Smarr KL, Keefer AL. **Measures of depression and depressive symptoms: Beck Depression Inventory-II (BDI-II), Center for Epidemiologic Studies Depression Scale (CES-D), Geriatric Depression Scale (GDS), Hospital Anxiety and Depression Scale (HADS), and Patient Health Questionnaire-9 (PHQ-9**.). *Arthritis Care Res (Hoboken)* 2011;63(suppl 11):S454–66 CrossRef Medline
23. Richter P, Werner J, Heerlein A, et al. **On the validity of the Beck Depression Inventory - a review.** *Psychopathology* 1998;31:160–68 CrossRef Medline
24. Wang YP, Gorenstein C. **Psychometric properties of the Beck Depression Inventory-II: a comprehensive review.** *Braz J Psychiatry* 2013;35:416–31 CrossRef Medline
25. Wechsler D. *Wechsler Abbreviated Scale of Intelligence*. 2nd ed. San Antonio: NCS Pearson; 2011
26. Ou X, Glasier CM, Ramakrishnaiah RH, et al. **Gestational age at birth and brain white matter development in term-born infants and children.** *AJNR Am J Neuroradiol* 2017;38:2373–79 CrossRef Medline
27. Ou X, Thakali KM, Shankar K, et al. **Maternal adiposity negatively influences infant brain white matter development.** *Obesity (Silver Spring)* 2015;23:1047–54 CrossRef Medline
28. Qiu A, Rifkin-Graboi A, Chen H, et al. **Maternal anxiety and infants' hippocampal development: timing matters.** *Transl Psychiatry* 2013;3:e306 CrossRef Medline

29. Soe NN, Wen DJ, Poh JS, et al. **Perinatal maternal depressive symptoms alter amygdala functional connectivity in girls.** *Hum Brain Mapp* 2018;39:680–90 CrossRef Medline
30. Jha SC, Meltzer-Brody S, Steiner RJ, et al. **Antenatal depression, treatment with selective serotonin reuptake inhibitors, and neonatal brain structure: a propensity-matched cohort study.** *Psychiatry Res Neuroimaging* 2016;253:43–53 CrossRef Medline
31. Li LJ, Ma N, Li ZX, et al. **Prefrontal white matter abnormalities in young adult with major depressive disorder: a diffusion tensor imaging study.** *Brain Res* 2007;1168:124–28 CrossRef Medline
32. Bae JN, MacFall JR, Krishnan KRR, et al. **Dorsolateral prefrontal cortex and anterior cingulate cortex white matter alterations in late-life depression.** *Biol Psychiatry* 2006;60:1356–63 CrossRef Medline
33. Kim MJ, Whalen PJ. **The structural integrity of an amygdala-prefrontal pathway predicts trait anxiety.** *J Neurosci* 2009;29:11614–18 CrossRef Medline
34. Buss C, Davis EP, Hobel CJ, et al. **Maternal pregnancy-specific anxiety is associated with child executive function at 6-9 years age.** *Stress* 2011;14:665–76 CrossRef Medline
35. Corbetta M, Shulman GL. **Control of goal-directed and stimulus-driven attention in the brain.** *Nat Rev Neurosci* 2002;3:201–15 CrossRef Medline
36. Van Batenburg-Eddes T, Brion MJ, Henrichs J, et al. **Parental depressive and anxiety symptoms during pregnancy and attention problems in children: a cross-cohort consistency study.** *J Child Psychol Psychiatry* 2013;54:591–600 CrossRef Medline
37. Huang H, Xue R, Zhang JY, et al. **Anatomical characterization of human fetal brain development with diffusion tensor magnetic resonance imaging.** *J Neurosci* 2009;29:4263–73 CrossRef Medline
38. Van den Bergh BRH, Mulder EJH, Mennes M, et al. **Antenatal maternal anxiety and stress and the neurobehavioural development of the fetus and child: links and possible mechanisms. A review.** *Neurosci Biobehav Rev* 2005;29:237–58 CrossRef Medline
39. Karlsson L, Nousiainen N, Scheinin NM, et al. **Cytokine profile and maternal depression and anxiety symptoms in mid-pregnancy-the FinnBrain Birth Cohort Study.** *Arch Womens Ment Health* 2017;20:39–48 CrossRef Medline

Intracranial Arterial Tortuosity in Marfan Syndrome and Loeys-Dietz Syndrome: Tortuosity Index Evaluation Is Useful in the Differential Diagnosis

L. Spinardi, G. Vornetti, S. De Martino, R. Golfieri, L. Faccioli, M. Pastore Trossello, C. Graziano, E. Mariucci, and A. Donti

ABSTRACT

BACKGROUND AND PURPOSE: The association of arterial tortuosity and connective tissue diseases is widely reported in the literature, but only a few studies were based on a quantitative evaluation of this arterial phenotype, and none of the latter examined the intracranial vasculature. The aim of this study was to evaluate the degree of intracranial arterial tortuosity in patients with Marfan syndrome and those with Loeys-Dietz syndrome, and to assess its usefulness in the differential diagnosis.

MATERIALS AND METHODS: We performed a retrospective analysis of 68 patients with genetically confirmed Marfan syndrome ($n = 36$) or Loeys-Dietz syndrome ($n = 32$), who underwent at least 1 MRA of the brain at our institution. Fifty-two controls were randomly selected among patients who presented with headache and without any known comorbidity. Tortuosity indexes of 4 intracranial arterial segments were measured on a 3D volume-rendered angiogram by using the following formula: $\left(\frac{\text{centerline length}}{\text{straight-line length}} - 1\right) \times 100$.

RESULTS: Both Marfan syndrome and Loeys-Dietz syndrome showed a significantly higher tortuosity index compared with controls in all examined vessels. The tortuosity index of the vertebrobasilar system showed an excellent interrater reliability (intraclass correlation coefficient, 0.99) and was the strongest independent predictor of Loeys-Dietz syndrome in patients with connective tissue disease ($P = .002$), with a 97% specificity for this pathology when its value was > 60.

CONCLUSIONS: The tortuosity index of intracranial arteries is an easily calculated and highly reproducible measure, which shows a high specificity for Marfan syndrome and Loeys-Dietz syndrome and may be useful in differentiating these 2 entities.

ABBREVIATIONS: CTD = connective tissue disease; IICA = intracranial internal carotid artery; IQR = interquartile range; LDS = Loeys-Dietz syndrome; TI = tortuosity index; VBS = vertebrobasilar system

The term arterial tortuosity defines the presence of multiple abnormal turns of one or more arteries, which likely develop as a result of aberrant vessel elongation.[1] Previous studies showed an association between arterial tortuosity and aging as well as female sex, hypertension, and other cardiovascular risk factors.[2-4] A renewed interest in this vascular biomarker emerged in recent years, especially in relation to its possible role in the diagnostic evaluation and prognostic assessment of genetic arteriopathies.[5-7]

Although arterial tortuosity has been recognized as a hallmark of Loeys-Dietz syndrome (LDS) and arterial tortuosity syndrome,[8-10] recent studies suggest that this arterial phenotype is also present in other connective tissue diseases (CTDs), such as Marfan syndrome, and familial thoracic aneurysm and aortic dissection.[5,11]

LDS is characterized by a disease course that is more severe compared with Marfan syndrome and presents with aortic dissection at a younger age and smaller aortic diameter, with vascular disease extending beyond the aortic root.[9,12] An early and accurate differential diagnosis between Marfan syndrome and LDS, therefore, is essential to ensure proper patient care. Nonetheless, a risk of misdiagnosis is present, especially in patients without specific traits of Marfan syndrome (eg, ectopia lentis) or LDS (eg, bifid uvula, cleft palate, and hypertelorism) because several other features of these syndromes demonstrate a considerable overlap.[12,13] In these scenarios, the presence of prominent intracranial arterial tortuosity may raise the suspicion of LDS and lead to early genetic testing and closer monitoring of these patients.

Several studies reported the presence of tortuous intracranial arteries in patients with LDS,[14-18] but all of them were based on subjective evaluation of tortuosity, which limits the usefulness of

Received April 5, 2020; accepted after revision June 20.

From the Neuroradiology Unit (L.S., L.F., M.P.T.), the Radiology Unit (G.V., S.D.M., R.G.), Department of Experimental, Diagnostic and Specialty Medicine, the Department of Medical Genetics (C.G.), and Pediatric Cardiology and GUCH Unit (E.M., A.D.), Sant'Orsola-Malpighi Hospital, University of Bologna, Bologna, Italy.

Please address correspondence: Gianfranco Vornetti, MD, Dipartimento di Medicina Specialistica, Diagnostica e Sperimentale, Policlinico Sant'Orsola-Malpighi, Via Giuseppe Massarenti, 9, 40138 Bologna BO, Italy;
e-mail: gianfranco.vornetti@gmail.com

http://dx.doi.org/10.3174/ajnr.A6732

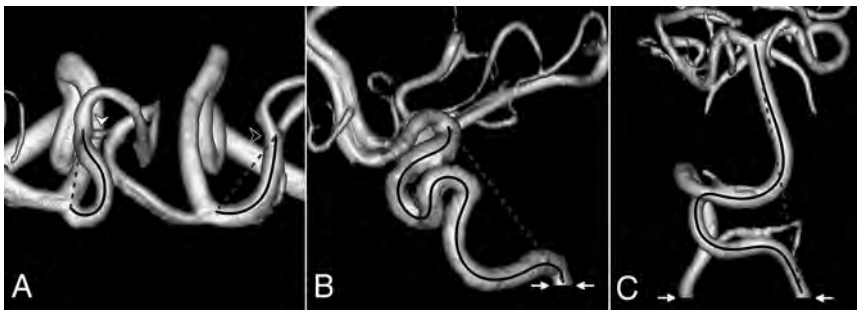

FIG 1. The TI measurement on 3D volume-rendered TOF-MRA. The *solid black line* indicates the centerline length, whereas the *dashed gray line* shows straight-line length. *A*, Superior view of A1 and M1 segments in a patient with LDS (all anterior cerebral artery segments distal to A2 have been removed; *white arrowhead*, anterior communicating artery; *black arrowhead*, right M1–M2 bifurcation). *B*, Lateral view of the right IICA in a patient with LDS (*white arrows*, level of the inferior opening of the carotid canal). *C*, Anterior view of VBS in a patient with Marfan syndrome (*white arrows*, level of the foramen magnum).

this finding due to the lack of standardization in terms of definition and measurement. Recently, more advanced quantitative methods, for example, the tortuosity index (TI), have been proposed to measure arterial tortuosity. TI is calculated as the ratio between the actual length of an arterial segment and the shortest distance measured between its end points, which has been shown to be a reproducible measure of arterial tortuosity in different vascular territories.[1,5] Recent studies used TI to measure carotid artery and vertebral artery tortuosity in the cervical region in patients with CTDs,[5,6] but no quantitative data are available with regard to the intracranial vasculature. The aim of this study was to evaluate the degree of intracranial arterial tortuosity in patients with Marfan syndrome and those with LDS, and to assess its usefulness in the differential diagnosis of these 2 pathologies.

MATERIALS AND METHODS

We retrospectively reviewed the electronic medical records and imaging studies of all patients with genetically confirmed Marfan syndrome and LDS who were referred until December 2019 to the hub center for heritable CTDs of the University of Bologna (Italy). We included in this study all patients (N= 68) who underwent at least 1 MRA of the brain at our institution.

In accordance with current guidelines,[12] at our institution, all patients diagnosed with LDS undergo full vascular imaging, including the intracranial arterial system, every 2 years to screen for the presence of aneurysms and other vascular pathology. In recent years, due to the reported association of Marfan syndrome with extra-aortic vascular pathology,[17] our patients diagnosed with Marfan syndrome undergo a screening MRA of the brain, which is not repeated if no pathologic findings are discovered. All MRAs were acquired after the diagnosis of Marfan syndrome or of LDS was already established. When more than one brain imaging study was available, only the most recent MRA was selected for analysis. All included MRAs were acquired between January 2015 and December 2019.

Fifty-two controls were randomly selected among patients who presented with headache and without any intracranial vascular pathology, and who underwent an MRA of the brain during the same period. We reviewed the electronic medical records of the controls and excluded all the patients with systemic arterial disease or cardiovascular risk factors (such as hypertension, diabetes, renal pathology, atrial fibrillation, aortic aneurysm or dissection, and fibromuscular dysplasia). In addition, patients with genetic syndromes or a history of cancer were excluded from the control group. This study was carried out in accordance with ethics standards as set out in the Declaration of Helsinki and was approved by the institutional review board as a retrospective study.

MRA Acquisition and Image Analysis

MRAs of the brain were performed with a 1.5T superconducting system (Ingenia; Philips Healthcare), with a 20-channel phased array head coil. A commercially available 3D TOF-MRA sequence was used, with the following parameters: field of view, 200 × 189 mm; matrix, 444 × 235; section thickness, 1.2 mm; number of slices, 168; echo time, 6.9 ms; repetition time, 27 ms; flip angle, 20°; and number of acquisitions, 1.

Image analysis was performed by using IntelliSpace 8.0 software (Philips Healthcare) by an examiner who was blinded to clinical data and extracranial imaging findings. A 3D volume-rendered angiogram was created from the source TOF-MRA images for each patient. The actual length of the artery was measured by using the vessel centerline, which was automatically traced by the software algorithm; manual correction was only needed in the presence of extremely tortuous vessels when the ends of a vascular loop came into contact with each other. Both centerline length and straight-line length were automatically measured by the software, whereas the end points of each vessel were manually selected. TI was calculated by using a previously described formula: $\left(\frac{\text{centerline length}}{\text{straight-line length}} - 1\right) \times 100$.[5] A second examiner (SD)calculated the TI of 20 randomly selected MRAs of the brain, and interrater reliability was assessed by using the intraclass correlation coefficient.

Arterial Segment Selection

To obtain a comprehensive estimate of intracranial arterial tortuosity, we selected vessels from both the anterior and posterior circulation, which could be defined based on easily identifiable anatomic landmarks, to maximize reproducibility and ease of segmentation (Fig 1). In the anterior circulation, the following arterial segments were analyzed: intracranial internal carotid artery (IICA) (from its entrance into the carotid canal of the temporal bone to its bifurcation into anterior and middle cerebral arteries), the A1 segment of the anterior cerebral artery (from the origin of the anterior cerebral artery to the level of the anterior communicating artery), and the M1 segment of the MCA (from the origin of the MCA to the M1–M2 bifurcation). In the posterior circulation, we segmented the vertebrobasilar system (VBS) starting

Table 1: Demographic and clinical characteristics of patients with CTD

Characteristic	CTD (*N* = 68)	Marfan Syndrome (*n* = 36)	LDS (*n* = 32)	*P*
Age at MRA, median (IQR), y	38.5 (23–48)	32.5 (25–43.5)	42 (22–50)	.21
Female, *n* (%)	33 (48.5)	15 (41.7)	18 (56.3)	.33
Aortic root dilation, *n* (%)	59 (86.8)	33 (91.7)	26 (81.3)	.29
Aortic dissection, *n* (%)	9 (13.2)	6 (16.7)	3 (9.4)	.48
Arterial dissection, *n* (%)	4 (5.9)	0 (0.0)	4 (12.5)	.04
Aortic surgery, *n* (%)	41 (60.3)	25 (69.4)	16 (50.0)	.14
Age at surgery, median (IQR), y	28 (20–37)	26 (21–35)	33 (18–44)	.47

from the level of the foramen magnum to the tip of the basilar artery. The level of the inferior opening of the carotid canal and the level of the foramen magnum were identified on MPR images. The TI of each arterial segment was calculated on both sides. For the VBS, the TI was calculated starting from both vertebral arteries. Both the average TI and maximum TI values of each segment were used for analyses. To improve clarity, we only reported data on the former because both values yielded similar results at univariate analysis, but receiver operating characteristic curve analysis showed higher sensitivity and specificity for the average TI.

Statistical Analysis

Categoric variables were compared by using the Fisher exact test, whereas the Wilcoxon rank sum test was computed for continuous variables. The Spearman rank correlation coefficient was used to evaluate the association between TI and age. Normalcy was assessed by means of the Shapiro-Wilk test. Receiver operating characteristic curve analysis was performed for each vessel TI and the binary end points of Marfan syndrome versus LDS and CTD versus control. At multivariate analysis, ORs and 95% CIs were estimated with a logistic regression model, including age, A1 TI, and VBS TI. Continuous variables were described as median and interquartile range (IQR), whereas categoric variables were summarized by absolute and relative (%) frequency. All tests were 2-sided, and $P < .05$ was considered statistically significant. Statistical analysis was performed by using R version 3.6.1 (2019; The R Foundation for Statistical Computing).

RESULTS

Subjects

Sixty-eight patients with CTD and 52 controls were included in this study. In the CTD group, 36 patients (52.9%) had Marfan syndrome and 32 (47.1%) had LDS. All the patients with Marfan syndrome had a mutation in the *FBN-1* gene, whereas, among patients with LDS, 15 (46.9%) had a mutation in *SMAD3*, 11 (34.4%) in *TGFBR2,* and 6 (18.7%) in *TGFBR1*. Univariate analysis did not show a statistically significant difference in age or sex between cases and controls. The median age at MRA was 38.5 years (IQR, 23–48 years) in patients with CTD and 35 years (IQR, 28.5–54 years) among the controls ($P = .43$); 10 patients and 5 controls were < 18 years old. There were 33 females (48.5%) in the CTD group and 28 females (53.8%) among the controls ($P = .59$). We did not find any significant difference in the examined demographic and clinical variables between the patients with Marfan syndrome and those with LDS, except for a higher prevalence of peripheral artery dissection in LDS (Table 1).

Among the patients with LDS, 7 were found to harbor a total of 8 intracranial aneurysms; in 1 patient, a dural arteriovenous fistula was reported. We did not find any intracranial vascular pathology in the patients with Marfan syndrome. The average aneurysm diameter was 3.6 mm (range, 2–5 mm), and the most frequent location was the carotid siphon (50%). No patients presented with subarachnoid hemorrhage. After evaluation by a multidisciplinary team, including neuroradiologists, neurosurgeons, and cardiologists, 2 patients underwent successful treatment of the aneurysm, 1 via endovascular coiling, the other by surgical clipping, without any complications. We did not find any significant difference in tortuosity between the patients with LDS and with and without intracranial aneurysm ($P = .71$ for A1, $P = .10$ for M1, $P = .37$ for IICA, and $P = .96$ for VBS). Among the patients with CTD, 7 (10.3%) reported a history of smoking, 8 (11.8%) presented with dyslipidemia, 1 (1.5%) had a body mass index >30 kg/m^2, and none had diabetes mellitus. No significant difference in TI was found between smokers and nonsmokers ($P = .36$ for A1, $P = .39$ for M1, $P = .24$ for IICA, and $P = .69$ for VBS) nor between patients with and patients without dyslipidemia ($P = .52$ for A1, $P = .86$ for M1, $P = .73$ for IICA, and $P = .89$ for VBS).

Interrater Reliability

The TI of the 4 examined arterial segments were measured by 2 observers in 20 randomly chosen subjects (8 patients with Marfan syndrome, 6 patients with LDS, and 6 controls) to assess for interrater reliability. Intraclass correlation coefficient for TI comparison between the 2 observers was 0.97 ($P < .001$) for A1, 0.76 ($P = .03$) for M1, 0.99 ($P < .001$) for IICA, and 0.99 ($P < .001$) for VBS.

Analysis of Intracranial Arterial Tortuosity

IICA TI and VBS TI showed a positively skewed distribution both in patients with CTD and the controls, whereas the distribution of A1 TI and M1 TI was positively skewed in LDS and normally distributed in those with Marfan syndrome and the controls. The highest TI variability was observed for M1, which may be explained by the highly variable position of the M1–M2 bifurcation relative to the origin of the MCA. The median difference between the TI of the right and left side (expressed as the percentage of the absolute value of the difference between the 2 sides compared with the less tortuous side) was 45.5% for A1 (IQR, 14.3%–64.8%), 40.7% for M1 (IQR, 21.4%–84.6%), 10.2% for IICA (IQR, 5.0%–20.1%), and 19.2% for VBS (IQR, 7.6%–33.3%). The variation in tortuosity between the 2 sides was not significantly different when comparing the patients with CTD and the controls ($P = .85$ for A1, $P = .67$ for M1, $P = .46$ for IICA, and $P = .48$ for VBS) as well as patients with Marfan syndrome and those with LDS ($P = .91$ for A1, $P = .94$ for M1, $P = .97$ for IICA, and $P = .33$ for VBS).

Table 2: The intracranial TI in patients with CTD and the controls

	Intracranial TI, median (IQR)			*P*		
	Controls ($n = 52$)	Marfan Syndrome ($n = 36$)	LDS ($n = 32$)	Marfan Syndrome vs Controls	LDS vs Controls	LDS vs Marfan Syndrome
A1	9 (6–12)	11.5 (8–16)	15.5 (11–21)	.02	<.001	.02
M1	5 (1–7)	11.5 (6–22)	12.5 (6–21)	<.001	<.001	.92
IICA	97 (80.5–110)	123.5 (105–144)	141.5 (123–160.5)	<.001	<.001	.06
VBS	12 (9–19)	28.5 (20–36)	52 (32–73.5)	<.001	<.001	<.001

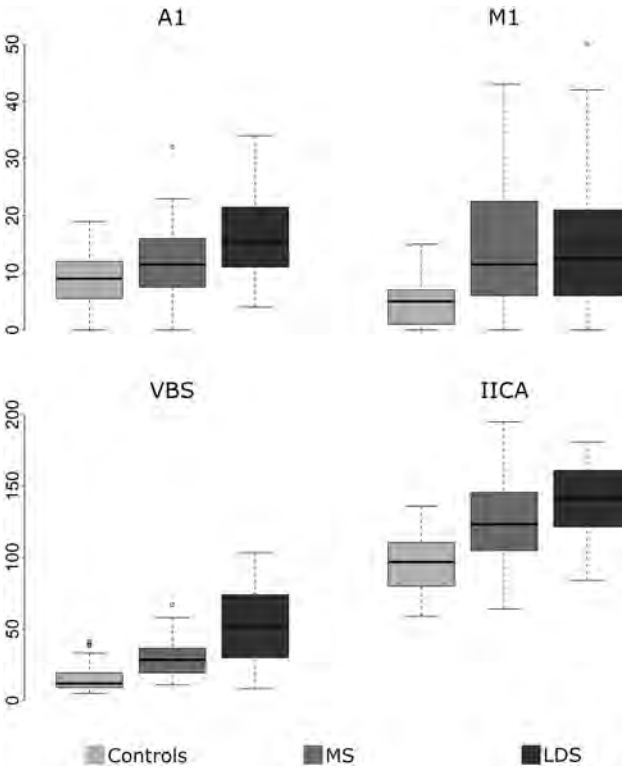

FIG 2. Boxplots of the TI of the 4 examined arterial segments for controls and patients with Marfan syndrome (MS) and LDS.

No significant differences were found between the TI of vessels from the right and left sides ($P = .90$ for M1, $P = .67$ for IICA, and $P = .37$ for VBS), except for a trend toward significance for the A1 segment ($P = .05$), which showed a higher TI on the right side (median TI, 11 [IQR, 7–17]) compared with the left side (median TI, 8 [IQR, 7–15]). No significant results were found when stratifying the patients by CTD status. The TI of the examined arterial segments did not differ significantly between males and females, even when stratifying the subjects by CTD status. The median TI in males and females was 11 (IQR, 7.5–14) and 11 (IQR, 7–18) for A1 ($P = .42$); 7 (IQR, 4–14.5) and 10 (IQR, 5–18) for M1 ($P = .50$); 117 (IQR, 93–136.5) and 117 (IQR, 97–140) for IICA ($P = .68$); and 22 (IQR, 12.5–33) and 29 (IQR, 13–49) for VBS ($P = .11$), respectively. No correlation was found between age and the TI: the correlation coefficient was −0.03 for A1 ($P = .73$), 0.05 for M1 ($P = .62$), 0.06 for IICA ($P = .50$), and 0.06 for VBS ($P = .54$). Similar results were obtained when assessing each group of patients separately.

Association between the TI and CTD

Among the patients with LDS, no significant association was found between intracranial arterial tortuosity and gene mutation; therefore, we considered these patients as a single group for further analysis. Both Marfan syndrome and LDS were characterized by a significantly higher intracranial TI compared with controls. In addition, the A1 TI and VBS TI were significantly higher in patients with LDS compared with patients with Marfan syndrome (Table 2 and Fig 2). When considering only the 59 patients with both CTD and aortic root dilation (according to Hager nomograms[19]), patients with LDS demonstrated a significantly higher TI compared with patients with Marfan syndrome for A1 (16 [IQR, 11–22] versus 11 [IQR, 8–16]; $P = .02$), IICA (145 [IQR, 125.5–164] versus 125 [IQR, 110–143]; $P = .01$), and VBS (59 [IQR, 48–80] versus 29 [IQR, 20–36]; $P < .001$). Examples of different degrees of tortuosity of the IICA and VBS are reported in Fig 3. A multivariate logistic regression model, including the TI of A1 and VBS as well as age confirmed the VBS TI to be the strongest independent predictor of LDS in patients with CTD (OR 1.68 [95% CI, 1.25–2.44]) (Table 3).

Specificity and Sensitivity Analysis

Receiver operating characteristic curve analysis of the intracranial TI for the binary outcome of LDS versus Marfan syndrome showed the VBS TI to be the best classifier, with an area under the curve of 0.84 (Fig 4). The "optimum" cutoff value of the VBS TI for maximizing sensitivity and specificity was 48, which yielded a sensitivity of 77% (95% CI, 56%–91%) and a specificity of 91% (95% CI, 76%–98%), with a positive likelihood ratio of 8.46 (95% CI, 2.82–25.40) and a negative likelihood ratio of 0.25 (95% CI, 0.12–0.52). When maximizing specificity for a value of sensitivity of at least 50%, a VBS TI > 60 returned a specificity of 97% (95% CI, 84%–100%).

To evaluate how the VBS TI performed in differentiating patients without discriminating features of either Marfan syndrome or LDS, we grouped patients with Marfan syndrome without ectopia lentis ($n = 24$ [66.6% of the patients with Marfan syndrome]) and patients with LDS without bifid uvula and/or cleft palate and hypertelorism ($n = 22$ [68.7% of the patients with LDS]). When applying the previously calculated cutoff of 48 for the VBS TI in this group of patients, it yielded a sensitivity of 82% (95% CI, 57%–96%) and a specificity of 86% (95% CI, 65%–97%) for the diagnosis of LDS. When analyzing the ability of the intracranial TI to discriminate between the patients with CTD and the controls, the IICA TI and VBS TI showed similar overall results, with an area under the curve of 0.84 and 0.87, respectively (Fig 4), but the IICA TI allowed for a higher specificity and the VBS TI allowed for a higher sensitivity. When maximizing specificity for a value of sensitivity of at least 50%, an IICA TI > 132 yielded a specificity of 98% (95% CI, 90%–100%). When maximizing sensitivity for a value of specificity of at least 50%, a VBS TI > 13 yielded a sensitivity of 96% (95% CI, 88%–99%).

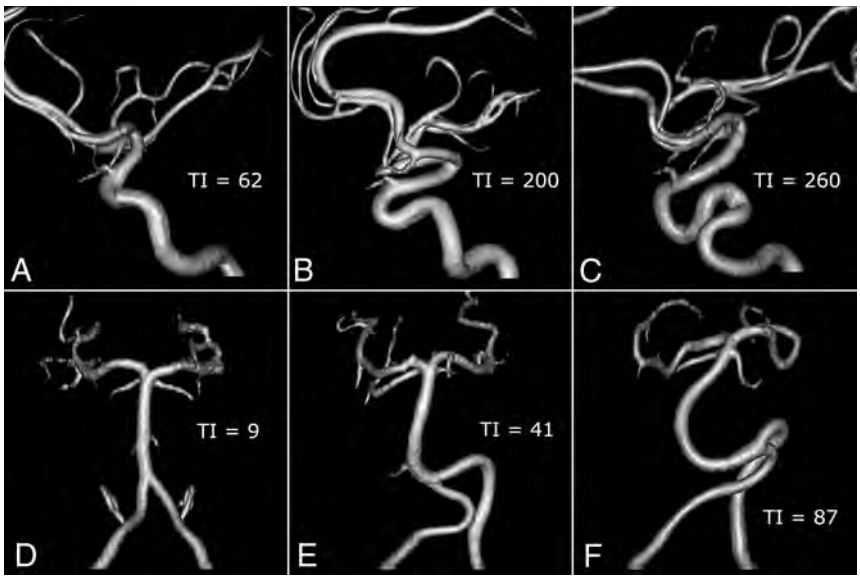

FIG 3. Examples of different degrees of tortuosity of IICA and VBS. *A–C*, Lateral view of the right IICA in a control (*A*), in a patient with Marfan syndrome (*B*), and in a patient with LDS (*C*). *D–F*, Anterior view of VBS in a control (*D*), in a patient with MS (*E*), and in a patient with LDS (*F*).

Table 3: Multivariate model for LDS versus Marfan syndrome by TI and age

	OR[a]	95% CI[a]	*P*
A1	1.61	0.73–3.93	.26
VBS	1.68	1.25–2.44	.002
Age	1.22	0.86–1.77	.28

[a] Computed for a 10-unit increase of the variable.

DISCUSSION

This study demonstrates that the TI can be reliably used in the assessment of intracranial arterial tortuosity in patients with CTDs and yields a highly reproducible quantitative measure. Importantly, our findings confirmed, on a quantitative basis, the widely reported association of LDS with intracranial arterial tortuosity but also demonstrated a significantly higher tortuosity of the intracranial vasculature in patients with Marfan syndrome compared with the controls. The TI of all examined arterial segments, except for M1, showed excellent interrater reliability, with an intraclass correlation coefficient that ranged from 0.97 to 0.99. The highly variable distance of the M1–M2 bifurcation from the origin of the MCA, as well as the presence of many different branching patterns, could explain the lower interrater reliability for the M1 segment (intraclass correlation coefficient, 0.76).

Besides the TI, other quantitative methods for measuring arterial tortuosity include the sum of angles metric, defined as the sum of the deviations from the straight line (expressed in degrees) at each point of angulation normalized by the length of the vessel, and the inflection count metric, which is calculated by multiplying the length of a vessel by the number of inflection points along its path and then dividing it by the distance between its end points.[1] Although these methods are more sensitive to local tortuosity and are effective for measuring vessels with high-frequency–low-amplitude coils, as in the coronary circulation, they require either to segment the vessel at each point of angulation or to identify inflection points, which makes their measurement more complex compared with the TI. In addition, these methods are mainly validated for 2D analysis.[1,20]

Diedrich et al[21] used tortuosity score curves to measure intracranial arterial tortuosity in a heterogeneous patient population, which also included 5 patients with LDS. Compared with the TI, this method is not dependent on the choice of 2 end points along the vessel centerline and may be used to compare images that contained different lengths of the selected artery. However, to our knowledge, no commercially available software allows for calculation of tortuosity score curves, and this method, albeit giving a more comprehensive estimate of tortuosity, might have limited applicability outside the research setting for the time being.

Although previous studies showed that older age and female sex were associated with arterial tortuosity,[2,4] the TI of the intracranial arteries did not differ significantly between males and females in our cohort, and we did not find any correlation between age and the TI (correlation coefficients ranged from −0.03 for A1 to 0.06 for the IICA). Even though we were not able to assess changes in intracranial tortuosity over time due to the small number of patients with serial MRA studies, the lack of a significant association between age and the TI is in agreement with previously reported data on the vertebral artery TI in the cervical region[5] and may support the hypothesis of a relative stability of the head and neck artery TIs over time in young patients. Although a lack of association between older age and increased arterial tortuosity is in agreement with previous studies on CTD,[5-7] this finding cannot be generalized to older patients due to the relatively young age of the subjects included in this study as well as in other studies that focused on patients with CTD. We were not able to evaluate the association of hypertension with arterial tortuosity because all of our patients were treated with antihypertensive drugs, either angiotensin II receptor blockers or β-blockers. Current guidelines recommend blood pressure control in individuals with Marfan syndrome and those with LDS to reduce hemodynamic stress and the aortic root dilation rate.[12,22]

Intracranial arterial tortuosity is a frequently reported neuroradiologic manifestation of LDS[14-18] but has never been described in Marfan syndrome. A possible explanation could be found in the lower degree of tortuosity in Marfan syndrome compared with LDS, which may not be conspicuous enough to be detected by qualitative assessment. On the contrary, quantitative analysis found a significantly higher intracranial TI in patients with Marfan syndrome compared with the controls. This finding is consistent with the increased tortuosity of the cervical vertebral arteries previously reported in patients with

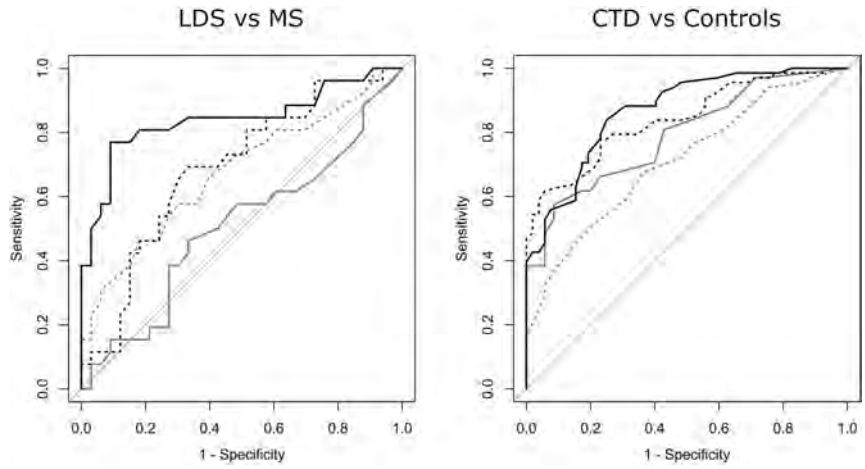

FIG 4. Receiver operating characteristic curves for the intracranial TI, with the outcome of LDS versus Marfan syndrome and CTD versus controls. *Dashed gray line* indicates the A1 TI; *solid gray line*, M1 TI; *dashed black line*, IICA TI; and *solid black line*, VBS TI.

Marfan syndrome[5] and seems to suggest the presence of a more widespread arterial tortuosity in this syndrome, which goes beyond the aorta.[7,23]

The presence of arterial tortuosity in both LDS and Marfan syndrome could be the expression of underlying vessel wall abnormality.[11,12,24] In fact, these 2 conditions share a common pathogenic mechanism because the causative mutations of both Marfan syndrome and LDS affect the transforming growth factor beta signaling pathway, which results in a disturbance in biogenesis and maintenance of elastic fiber, which, in turn, could lead to vessel wall weakening and clinical vascular manifestations.[11,24,25]

Increased arterial tortuosity has been associated with reduced perfusion pressure in different vascular territories, including the posterior circulation,[26,27] but no data are available on the association between this arterial phenotype and cerebral blood flow in patients with CTD. Although it is possible that the intracranial arterial tortuosity observed in this patient population might have an impact on cerebral perfusion, the potential clinical implications of this association have not been elucidated.

We did not find any significant difference in the examined clinical variables between patients with Marfan syndrome and patients with LDS, except for a higher prevalence of peripheral artery dissection in the latter (Table 1). This result is in contrast with early reports of LDS, which describe a more severe clinical course in this patient population compared with Marfan syndrome.[8,9] Nonetheless, our findings are congruent with more recent studies,[5] a possible explanation being the wide phenotypic variability of patients with LDS, even among individuals who belong to the same family[12,28] as well as the tendency of early reports to characterize the most severe cases.

Although previous studies showed higher arterial tortuosity of head and neck arteries in patients with intracranial aneurysm,[20,29,30] we did not find any significant difference in tortuosity between the patients with LDS and with or without intracranial aneurysm. This finding may suggest a difference in some of the underlying mechanisms of aneurysm formation in patients with CTD compared with the general population, but further studies, including greater numbers of patients with CTD and intracranial aneurysm, are needed to further elucidate these results. Our results show that the intracranial TI could be helpful in the differential diagnosis between Marfan syndrome and LDS. The VBS TI is the strongest independent predictor of LDS (Table 3) and yields the best results in classifying these 2 entities compared with other arterial segments (Fig 2), which demonstrates a 97% specificity for LDS when its value is > 60.

No formal diagnostic criteria have been established for the diagnosis of LDS, which is currently based on the presence of a mutation in one of the known LDS genes in a patient with aortic aneurysms or dissection.[13] Nevertheless, some of these patients may not undergo genetic testing due to a misdiagnosis of Marfan syndrome. According to the Revised Ghent Nosology,[31] Marfan syndrome can be diagnosed without genetic testing in the presence of aortic root dilation ($Z > 2$) and either ectopia lentis or a systemic score of >7 if no discriminating feature of LDS or other CTDs are present. Although ectopia lentis is not reported in LDS, many of the features included in the systemic score can also be found among these patients, including scoliosis, pes planus, anterior chest deformity, spontaneous pneumothorax, joint hyperextension, mitral valve prolapse, and dural ectasia.[12,13] In addition, craniofacial anomalies that are absent in Marfan syndrome, such as bifid uvula, cleft palate, and hypertelorism, are not always found in patients with LDS.[9]

In our cohort, 24 patients with Marfan syndrome (66.6%) did not show ectopia lentis and 22 patients with LDS (68.7%) had neither bifid uvula and/or cleft palate nor hypertelorism. The VBS TI also demonstrated high sensitivity and specificity in this group of patients. In the absence of ectopia lentis, an increased VBS TI, therefore, should prompt genetic testing, even if characteristic craniofacial features are lacking, to avoid misdiagnosis of patients with LDS. All the examined arterial segments show a significantly higher tortuosity in both Marfan syndrome and LDS compared with the controls. An increased intracranial TI, therefore, may raise the suspicion for CTD in the appropriate clinical setting. IICA and the VBS TI demonstrated similar overall results in classifying patients and controls, but the IICA TI showed a higher specificity for CTD, which reached 98% for values > 132.

Limitations

The present study has some limitations, including its retrospective nature and the small number of enrolled patients. In addition, the study design did not allow estimating CTD prevalence, which thus precluded computation of positive and negative predictive values. Because our control group had similar demographic characteristics to the CTD group and included only healthy subjects, without cardiovascular risk factors, our data on

intracranial tortuosity cannot be generalized to older individuals or those with comorbidities, for example, hypertension, because these factors are known to be associated with increased vascular tortuosity. Our sample is limited to Marfan syndrome and LDS, therefore, our results need to be validated in larger prospective studies, enrolling a larger number of subjects and also including patients with other CTDs.

CONCLUSIONS

Our results confirmed a significantly increased tortuosity of the intracranial vasculature in LDS compared with Marfan syndrome and controls but also demonstrated that patients with Marfan syndrome have significantly more tortuous intracranial arteries compared with healthy subjects, which has not been previously reported. The TI of the intracranial arteries is an easily calculated and highly reproducible measure, which shows a high specificity for CTD and may raise the suspicion for the diagnosis of Marfan syndrome or LDS in the appropriate clinical setting as well as helping in differentiating between these 2 entities.

REFERENCES

1. Ciurică S, Lopez-Sublet M, Loeys BL, et al. **Arterial tortuosity**. *Hypertension* 2019;73:951–60 CrossRef Medline
2. Del Corso L, Moruzzo D, Conte B, et al. **Tortuosity, kinking, and coiling of the carotid artery: expression of atherosclerosis or aging?** *Angiology* 1998;49:361–71 CrossRef Medline
3. Pancera P, Ribul M, Presciuttini B, et al. **Prevalence of carotid artery kinking in 590 consecutive subjects evaluated by echocolordoppler. Is there a correlation with arterial hypertension?** *J Intern Med* 2000; 248:7–12 CrossRef
4. Cha KS, Kim MH, Kim HJ. **Prevalence and clinical predictors of severe tortuosity of right subclavian artery in patients undergoing transradial coronary angiography.** *Am J Cardiol* 2003;92:1220–22 CrossRef Medline
5. Morris SA, Orbach DB, Geva T, et al. **Increased vertebral artery tortuosity index is associated with adverse outcomes in children and young adults with connective tissue disorders.** *Circulation* 2011; 124:388–96 CrossRef Medline
6. Chu LC, Haroun RR, Beaulieu RJ, et al. **Carotid artery tortuosity index is associated with the need for early aortic root replacement in patients with Loeys-Dietz syndrome.** *J Comput Assist Tomogr* 2018;42:747–53 CrossRef Medline
7. Welby JP, Kim ST, Carr CM, et al. **Carotid artery tortuosity is associated with connective tissue diseases.** *AJNR Am J Neuroradiol* 2019;40:1738–43 CrossRef Medline
8. Loeys BL, Chen J, Neptune ER, et al. **A syndrome of altered cardiovascular, craniofacial, neurocognitive and skeletal development caused by mutations in TGFBR1 or TGFBR2.** *Nat Genet* 2005;37: 275–81 CrossRef Medline
9. Loeys BL, Schwarze U, Holm T, et al. **Aneurysm syndromes caused by mutations in the TGF-beta receptor.** *N Engl J Med* 2006;355: 788–98 CrossRef Medline
10. Beyens A, Albuisson J, Boel A, et al. **Arterial tortuosity syndrome: 40 new families and literature review.** *Genet Med* 2018;20:1236–45 CrossRef Medline
11. Morris SA. **Arterial tortuosity in genetic arteriopathies.** *Curr Opin Cardiol* 2015;30:587–93 CrossRef Medline
12. MacCarrick G, Black JH III, Bowdin S, et al. **Loeys-Dietz syndrome: a primer for diagnosis and management.** *Genet Med* 2014;16:576–87 CrossRef Medline
13. Meester JAN, Verstraeten A, Schepers D, et al. **Differences in manifestations of Marfan syndrome, Ehlers-Danlos syndrome, and Loeys-Dietz syndrome.** *Ann Cardiothorac Surg* 2017;6:582–94 CrossRef Medline
14. Johnson PT, Chen JK, Loeys BL, et al. **Loeys-Dietz syndrome: MDCT angiography findings.** *AJR Am J Roentgenol* 2007;189: W29–35 CrossRef Medline
15. Rodrigues VJ, Elsayed S, Loeys BL, et al. **Neuroradiologic manifestations of Loeys-Dietz syndrome type 1.** *AJNR Am J Neuroradiol* 2009;30:1614–19 CrossRef Medline
16. Van Laer L, Dietz H, Loeys B. Loeys-Dietz syndrome. In: Halper J, eds. *Progress in Heritable Soft Connective Tissue Diseases*. Dordrecht: Springer-Verlag; 2014:95–105
17. Kim ST, Brinjikji W, Lanzino G, et al. **Neurovascular manifestations of connective-tissue diseases: a review.** *Interv Neuroradiol* 2016;22: 624–37 CrossRef Medline
18. Spinardi L, Mariucci E, Vornetti G, et al. **High prevalence of arterial dissection in patients with Loeys–Dietz syndrome and cerebral aneurysm**. *Vasc Med* 2020;25:218–20 CrossRef Medline
19. Hager A, Kaemmerer H, Rapp-Bernhardt U, et al. **Diameters of the thoracic aorta throughout life as measured with helical computed tomography.** *J Thorac Cardiovasc Surg* 2002;123:1060–66 CrossRef Medline
20. Kliś KM, Krzyżewski RM, Kwinta BM, et al. **Computer-aided analysis of middle cerebral artery tortuosity: association with aneurysm development**. *J Neurosurg* 2019;130:1478–84 CrossRef Medline
21. Diedrich KT, Roberts JA, Schmidt RH, et al. **Medical record and imaging evaluation to identify arterial tortuosity phenotype in populations at risk for intracranial aneurysms.** *AMIA Annu Symp Proc* 2011;2011:295–304 Medline
22. Brooke BS, Habashi JP, Judge DP, et al. **Angiotensin II blockade and aortic-root dilation in Marfan's syndrome**. *N Engl J Med* 2008; 358:2787–95 CrossRef Medline
23. Kono AK, Higashi M, Morisaki H, et al. **High prevalence of vertebral artery tortuosity of Loeys-Dietz syndrome in comparison with Marfan syndrome.** *Jpn J Radiol* 2010;28:273–77 CrossRef Medline
24. Pepe G, Giusti B, Sticchi E, et al. **Marfan syndrome: current perspectives.** *Appl Clin Genet* 2016;9:55–65 CrossRef Medline
25. Franken R, El Morabit A, de Waard V, et al. **Increased aortic tortuosity indicates a more severe aortic phenotype in adults with Marfan syndrome.** *Int J Cardiol* 2015;194:7–12 CrossRef Medline
26. Vorobtsova N, Chiastra C, Stremler MA, et al. **Effects of vessel tortuosity on coronary hemodynamics: an idealized and patient-specific computational study.** *Ann Biomed Eng* 2016;44:2228–39 CrossRef Medline
27. Peng YF, Zhang HL, Zhang DP, et al. **Perfusion by delayed time to peak in vertebrobasilar dolichoectasia patients with vertigo.** *Ann Clin Transl Neurol* 2018;5:1562–73 CrossRef Medline
28. Jondeau G, Ropers J, Regalado E, et al. **International Registry of Patients Carrying TGFBR1 or TGFBR2 Mutations: results of the MAC (Montalcino Aortic Consortium).** *Circ Cardiovasc Genet* 2016;9:548–58 CrossRef Medline
29. Labeyrie P-E, Braud F, Gakuba C, et al. **Cervical artery tortuosity is associated with intracranial aneurysm.** *Int J Stroke* 2017;12:549–52 CrossRef Medline
30. Kim BJ, Lee SH, Kwun BD, et al. **Intracranial aneurysm is associated with high intracranial artery tortuosity.** *World Neurosurg* 2018;112: e876–80 CrossRef Medline
31. Loeys BL, Dietz HC, Braverman AC, et al. **The revised Ghent nosology for the Marfan syndrome.** *J Med Genet* 2010;47:476–85 CrossRef Medline

Fetal Intraventricular Hemorrhage in Open Neural Tube Defects: Prenatal Imaging Evaluation and Perinatal Outcomes

R.A. Didier, J.S. Martin-Saavedra, E.R. Oliver, S.E. DeBari, L.T. Bilaniuk, L.J. Howell, J.S. Moldenhauer, N.S. Adzick, G.G. Heuer, and B.G. Coleman

ABSTRACT

BACKGROUND AND PURPOSE: Fetal imaging is crucial in the evaluation of open neural tube defects. The identification of intraventricular hemorrhage prenatally has unclear clinical implications. We aimed to explore fetal imaging findings in open neural tube defects and evaluate associations between intraventricular hemorrhage with prenatal and postnatal hindbrain herniation, postnatal intraventricular hemorrhage, and ventricular shunt placement.

MATERIALS AND METHODS: After institutional review board approval, open neural tube defect cases evaluated by prenatal sonography between January 1, 2013 and April 24, 2018 were enrolled ($n = 504$). The presence of intraventricular hemorrhage and gray matter heterotopia by both prenatal sonography and MR imaging studies was used for classification. Cases of intraventricular hemorrhage had intraventricular hemorrhage without gray matter heterotopia ($n = 33$) and controls had neither intraventricular hemorrhage nor gray matter heterotopia ($n = 229$). A total of 135 subjects with findings of gray matter heterotopia were excluded. Outcomes were compared with regression analyses.

RESULTS: Prenatal and postnatal hindbrain herniation and postnatal intraventricular hemorrhage were more frequent in cases of prenatal intraventricular hemorrhage compared with controls (97% versus 79%, 50% versus 25%, and 63% versus 12%, respectively). Increased third ventricular diameter, specifically >1 mm, predicted hindbrain herniation (OR = 3.7 [95% CI, 1.5–11]) independent of lateral ventricular size and prenatal intraventricular hemorrhage. Fetal closure ($n = 86$) was independently protective against postnatal hindbrain herniation (OR = 0.04 [95% CI, 0.01–0.15]) and postnatal intraventricular hemorrhage (OR = 0.2 [95% CI, 0.02–0.98]). Prenatal intraventricular hemorrhage was not associated with ventricular shunt placement.

CONCLUSIONS: Intraventricular hemorrhage is relatively common in the prenatal evaluation of open neural tube defects. Hindbrain herniation is more common in cases of intraventricular hemorrhage, but in association with increased third ventricular size. Fetal closure reverses hindbrain herniation and decreases the rate of intraventricular hemorrhage postnatally, regardless of the presence of prenatal intraventricular hemorrhage.

ABBREVIATIONS: NTD = neural tube defects; BPD = biparietal diameter; GA = gestational age by sonography; IVH = intraventricular hemorrhage; HC = head circumference; HH = hindbrain herniation; GMH = gray matter heterotopia; ONTD = open neural tube defects; MMC = myelomeningocele; MS = myeloschisis; MOMS = Management of Myelomeningocele Study; HC/AC = head circircumferenceto abdominal circumference ratio

Neural tube defects (NTD) can be classified as open (eg, myelomeningocele [MMC] and myeloschisis [MS]) or closed, and detailed radiologic evaluation is key to their differentiation.[1] Fetal sonography is effective in the assessment and characterization of NTD, with important implications for patient counseling and management.[2-5] Fetal MR imaging provides supplementary or additional diagnostic information in these disorders.[6] Both imaging modalities have similar performance in the evaluation of NTD prenatally[5] and when compared with postnatal imaging.[7]

The association between open neural tube defects (ONTD) and hindbrain herniation (HH) has long been described.[8] In animal studies, surgically created MMC produced HH that could be reversed with prenatal repair.[9,10] The Management of Myelomeningocele Study (MOMS) trial demonstrated clinical

Received March 4, 2020; accepted after revision June 16.

From the Departments of Radiology (R.A.D., J.S.M-S., E.R.O., S.E.D., L.T.B., B.G.C.), Center for Fetal Diagnosis and Treatment (R.A.D., E.R.O., S.E.D., L.T.B., L.J.H., J.S.M., N.S.A., G.G.H., B.G.C.), and Surgery (L.J.H., J.S.M., N.S.A., G.G.H.), The Children's Hospital of Philadelphia, Philadelphia, Pennsylvania; and Perelman School of Medicine (R.A.D., E.R.O., L.T.B., J.S.M., N.S.A., G.G.H., B.G.C.), University of Pennsylvania, Philadelphia, Pennsylvania.

Preliminary results previously presented at: Annual Meeting of the Society of Pediatric Radiology, May 3, 2019; San Francisco, California.

Please address correspondence to Ryne A. Didier, MD, Children's Hospital of Philadelphia, 3401 Civic Center Blvd, Philadelphia, PA 19104; e-mail: didierr@email.chop.edu

Indicates article with supplemental on-line table.

http://dx.doi.org/10.3174/ajnr.A6745

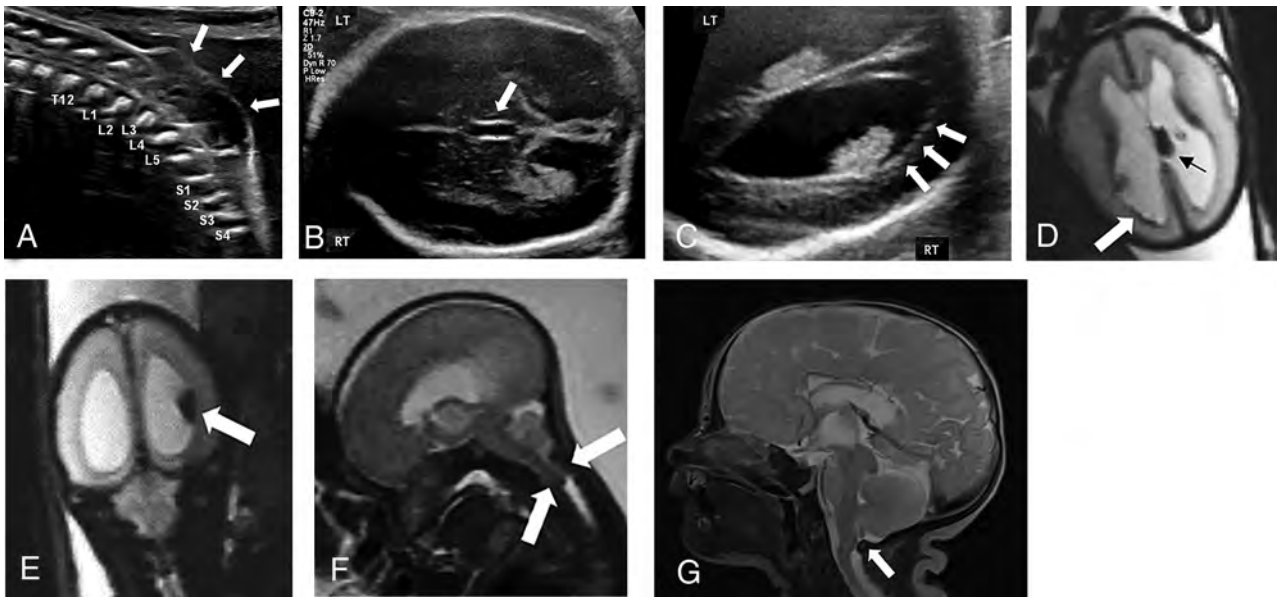

FIG 1. Prenatal intraventricular hemorrhage in open neural tube defect of a fetus (24 weeks and 2 days gestational age) with myelomeningocele and intraventricular hemorrhage with resolution of hindbrain herniation and intracranial blood products postnatally following in utero surgical closure. *A,* Sagittal grayscale sonography image of the fetal spine demonstrating the lumbosacral myelomeningocele (*white arrows*). Transverse gray-scale sonography images through the fetal skull demonstrate *(B)* dilation of the third ventricle measuring 2.8 mm in transverse dimension and *(C)* ependymal nodularity of the right lateral ventricle concerning for intraventricular hemorrhage. Corresponding fetal MR imaging demonstrates multiple foci of susceptibility artifact *(D)* within the left choroid plexus (*black arrow*) and along the right ventricular wall *(white arrow)* and *(E)* layering within the right lateral ventricle on axial and coronal EPI through the fetal brain, respectively, consistent with germinal matrix and intraventricular hemorrhage. *F,* Sagittal T2WI through the fetal brain demonstrates hindbrain herniation. Following in utero surgical closure at 25 weeks and 6 days gestational age, postnatal MR imaging performed at 3 days of age demonstrates *(G)* resolution of hindbrain herniation on sagittal T2WI through the neonatal brain and there was no evidence of intraventricular hemorrhage on any sequence. RT, right; LT, left.

effectiveness[11] and further studies have supported these initial results.[11-16] In the MOMS trial, the safety and efficacy of fetal closure was proved with slight outcome discrepancies in subsequent studies.[17-20] Prenatal identification of HH is crucial for patient counseling and management and serves as an important outcome variable in conjunction with ventricular shunt placement. However, none of the reported studies have evaluated the significance of prenatal intraventricular hemorrhage (IVH) on these important outcomes.[21,22]

The incidence of IVH in ONTD has not been reported. This may be partially explained by the challenge in identification by both sonography and MR imaging. For example, sonography is less sensitive in detecting blood products and MR imaging may confuse normal germinal matrix vessels as hemorrhage, particularly on EPI sequences. Furthermore, imaging findings of IVH, including ependymal nodularity, overlap with those of gray matter heterotopia (GMH), a common finding in NTD. The aim of this study is to investigate fetal sonography and MR imaging findings of patients with ONTD with attention to prenatal IVH to determine the incidence and its associations with prenatal and postnatal HH, postnatal IVH, and ventricular shunt placement to better inform patient management and family counseling.

MATERIALS AND METHODS

Setting

As a large referral center for ONTD diagnosis and management, including fetal surgery, our institution evaluates approximately 100 new patients per year with this diagnosis. A single-institution retrospective case-control study was conducted after approval from our institutional review board. All patients who underwent evaluation for suspected NTD with fetal sonography at our institution between January 1, 2013 and April 24, 2018 were screened. Patients with a confirmed diagnosis of MMC or MS were included.

Study Population and Case Selection

Patients with discrepant diagnoses of the type of NTD (MMC or MS) between imaging modalities, those without fetal MR imaging, inconclusive HH, or multiple congenital anomalies or chromosomal abnormalities were excluded. The presence or absence of IVH and GMH by both prenatal sonography and MR imaging studies was used for classification. Cases of IVH were determined by the presence of IVH and the absence of GMH by both modalities (Figs 1 and 2). Controls were defined as fetuses with neither IVH nor GMH ($n = 229$). Studies were excluded from final analyses if there was disagreement between imaging modalities of the presence or absence of IVH or the presence of GMH to maximize the true-positive rate of IVH. Ultimately, a total of 135 subjects with findings of GMH were excluded from the final analyses.

Data Sources

Data were extracted from electronic medical records. If imaging reports were incomplete, variables were unavailable, or if an inconsistency in the report was discovered (ie, dictation error), images were evaluated by a pediatric radiologist for resolution and to verify data accuracy. Report data were intentionally

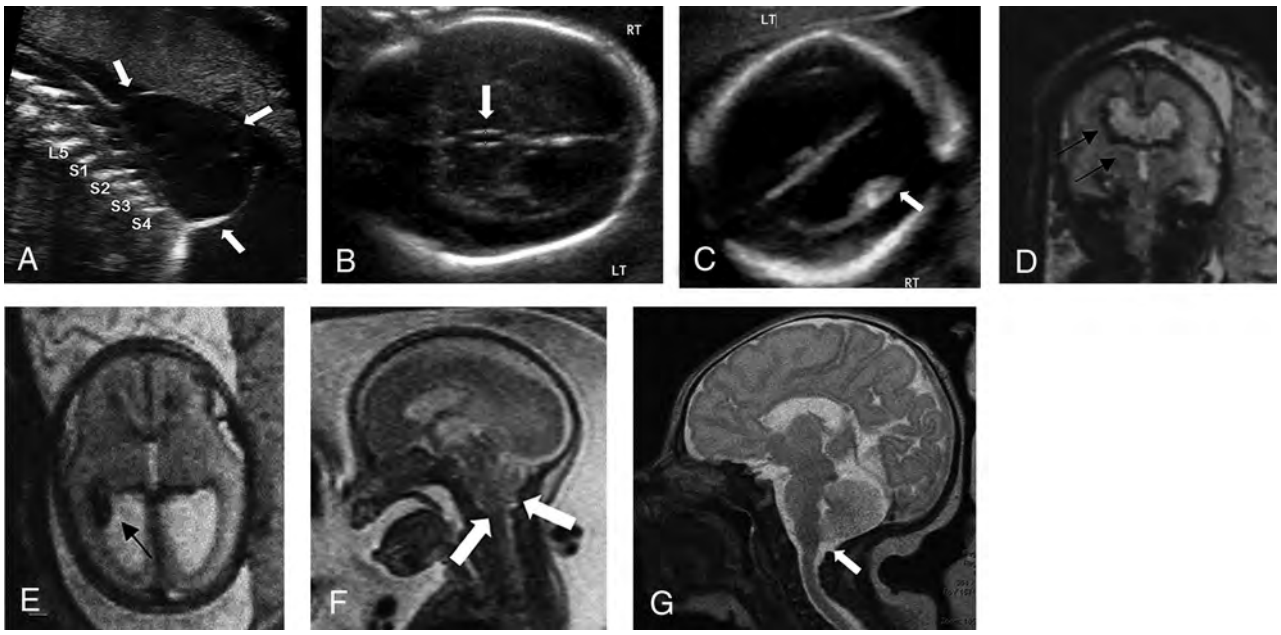

FIG 2. Prenatal intraventricular hemorrhage in open neural tube defect of a fetus (22 weeks and 3 days gestational age) with myelomeningocele and intraventricular hemorrhage with resolution of hindbrain herniation and intracranial blood products postnatally following in utero surgical closure. *A,* Sagittal gray-scale sonography image through the fetal lumbosacral spine demonstrates a myelomeningocele with a large, thin-walled sac. Transverse gray-scale sonography images through the fetal skull demonstrate *(B)* dilation of the third ventricle measuring 2 mm in transverse dimension and *(C)* layering echogenic material within the right lateral ventricle concerning for intraventricular hemorrhage. Corresponding fetal MR imaging demonstrates multiple foci of susceptibility artifact within the right lateral ventricle on *(D)* transverse and *(E)* coronal EPI through the fetal brain consistent with intraventricular hemorrhage. *F,* Sagittal T2WI through the fetal brain demonstrates hindbrain herniation. Following in utero surgical closure at 24 weeks and 5 days gestational age, postnatal MR imaging performed at 7 days of age demonstrates *(G)* resolution of hindbrain herniation on sagittal T2WI through the neonatal brain and there was no evidence of intraventricular hemorrhage on any sequence. RT, right; LT, left.

included in this retrospective study as it is the actionable information used to make critical treatment and management decisions during prenatal evaluation and consultation.

Imaging Protocols

Sonography and MR imaging examinations were performed per clinical protocols and before any surgical intervention. Detailed fetal sonography evaluation included transabdominal gray-scale and Doppler evaluation to assess the ventricular size, presence of ependymal nodularity, intraventricular debris/blood products, and the NTD. Transvaginal sonography was performed in all patients considering in utero fetal closure or for further anatomic evaluation of the brain and/or spine if transabdominal images were suboptimal. MR imaging examinations were performed on a 1.5T or 3T magnet using an 18-channel body coil in line with a spine coil with the following sequences: T2-weighted HASTE and steady-state free precession, and EPI performed in orthogonal planes through the fetal brain and spine. Postnatal MR imaging was performed with sequences including T2-weighted FSE, FLAIR, and CISS, T1-weighted FLASH or MPRAGE, gradient-echo, spin-labeled perfusion imaging, and DWI.

Variables and Study Outcomes

Clinical data included: fetal sex, gestational age, ventricular shunt placement within 12 months of birth, type of pregnancy (singleton or multiple), presence of an additional anomaly, and age at the time of imaging studies and surgical interventions. Eligibility for in utero closure was determined by institutional protocol and in accordance with the MOMS trial criteria, and all were performed as an open procedure.[11] Prenatal sonography data included: gestational age (GA) by sonography, biparietal diameter (BPD), head circumference (HC), head circumference to abdominal circumference ratio (HC/AC), cerebellar diameter, transverse third ventricular size, level of the osseous defect (T12 or higher, L1–L3, or L4 or lower), transverse lateral cerebral ventricles measurement at the level of the glomus of the choroid plexus, and absolute difference in lateral ventricular size (left versus right). Prenatal MR imaging data included: transverse measurement of the lateral ventricles at the level of the atria and absolute difference in lateral ventricular size. HH was defined as cerebellar tonsillar tissue below the foramen magnum on prenatal or postnatal MR imaging. Secondary outcomes were IVH by postnatal MR imaging (if performed $<$30 days of age and before surgical intervention) and requirement of ventricular shunt placement within 12 months of birth.

Bias Assessment

Patients were selected consecutively. All data were extracted by experienced research personnel using the Research Electronic Data Capture (REDCap) platform. Data were reviewed and validated by a board-certified radiologist with 3 or 8 years of experience. Concordance between prenatal imaging modalities identifying IVH was evaluated. Study personnel were blinded to postnatal findings of IVH at the time of data extraction and image review.

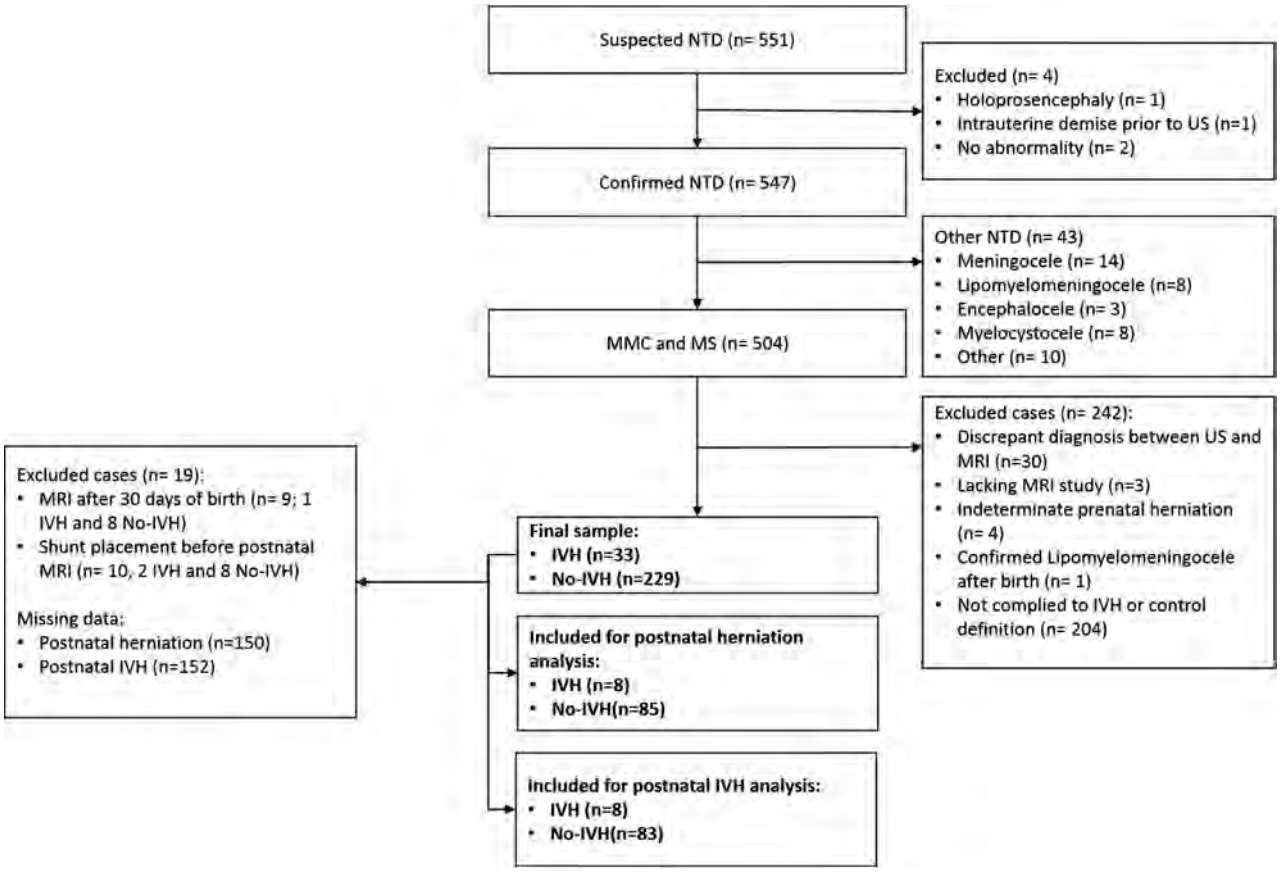

FIG 3. Population flow chart. US indicates sonography.

Statistical Analysis

R statistical software (version 3.5.1 for Windows, R Core Team) and packages 'vcd', 'aod', 'pscl', and 'ggplot2' were used. Cases and controls were compared using χ^2 or Fisher exact test and independent t Student or Wilcoxon rank sum, as appropriate. Concordance was evaluated with Cohen κ.[23] Primary outcomes were evaluated using multivariate logistic regression models. Variables were included if univariate regression was significant (Wald test, $P < .05$), and McFadden pseudoR^2 was used to determine effect size. Cut-points for significant continuous predictors were established using predicted probabilities and were included in an additional model as binary predictors. Analyses were considered significant at $P < .05$.

RESULTS

Five hundred four cases with confirmed MMC ($n = 369$, 73.2%) or MS ($n = 135$, 26.8%) by prenatal sonography were included (Fig 3). Four hundred eighty-seven of 504 (96.6%) also underwent fetal MR imaging. Overall, mean gestational age at prenatal sonography and MR imaging was 22 weeks and 4 days (±17 days), and mean maternal age was 29.75 (±5.37) years. IVH was reported prenatally in 83 of 504 (16.5%) sonography and 108 of 487 (22.2%) MR imaging examinations. Agreement between imaging modalities was observed in 404 of 487 cases (83%). Of these, IVH was reported in 52 of 404 (13%) ($\kappa = 0.454$, $P < .001$). On postnatal MR imaging, IVH was reported in 38 of 223 (17.0%) neonates. Compared with postnatal MR imaging, concordance with prenatal imaging modalities was lower but remained significant ($\kappa = 0.131$, $P = .049$ and $\kappa = 0.223$, $P = .001$ for fetal sonography and MR imaging, respectively).

The On-line Table compares the findings between IVH and controls. In cases of IVH, there was a higher prevalence of HH, on both prenatal and postnatal imaging studies, though this only reached statistical significance prenatally ($P < .05$). In cases of IVH, we found significantly increased bilateral lateral ventricular size ($P < .001$), increased head biometric measurements ($P < .001$), and third ventricle diameter ($P < .001$).

A multivariate model evaluating the association between prenatal IVH and HH was performed and included the presence of IVH, largest lateral ventricle by sonography, BPD, HC, GA, level of osseous defect, and transverse third ventricular diameter by sonography (Wald test, $\chi^2 = 31.8$, $P < .001$, pseudo$R^2 = 0.27$). IVH was more common in prenatal HH but not independently predictive (OR = 3.1 [95% CI, 0.5–60]). Decreased BPD (OR = 0.02 [95% CI, 0.001–0.37]), decreased HC (OR = 0.38 [95% CI, 0.16–0.89]), increased GA (OR = 5.89 [95% CI, 2–19]), and increased third ventricular size (OR = 8.4 [95% CI, 2.2–37]) were predictive of prenatal HH (Table 1 and Fig 4). The level of the osseous defect was not shown to be predictive of HH in our cohort. After calculating cut-points, an additional multivariate logistic regression model showed good fit ($\chi^2 = 46.4$, $P < .001$,

Table 1: Coefficient results of multivariate logistic regression models for prenatal HH including continuous variable and categorical variables with cut-points

Predicted Outcome	Predictor	β	SE	P
Prenatal HH (continuous variables)	IVH presence	1.6	1.1	1.6
	Right ventricular size by US (mm)	0.1	0.1	.08
	BPD (cm)	−3.6	1.5	.02[a]
	Head circumference (cm)	−1.1	0.4	.01[a]
	AUA	1.7	0.6	.003[a]
	Third ventricular diameter (mm)	2.5	0.7	<.001[a]
Prenatal HH (categoric variables with cut-points)	BPD (>4.5 cm)	−0.7	0.7	.34
	HC (>18 cm)	−1.2	0.7	.1
	AUA (>21 weeks)	0.6	0.7	.44
	Third ventricle diameter (>1 mm)	1.2	0.4	.001[a]

Note:—HH indicates hindbrain herniation; IVH, intraventricular hemorrhage; mm, millimeters; cm, centimeters; US, ultrasound; AUA, average ultrasound age; β, regression coefficient; SE, standard error.
[a] Significant difference $P < .05$.

pseudoR^2 = 0.07) (Table 1). From this second model, only a third ventricular diameter >1 mm (OR = 3.4 [95% CI, 1.7–7.5]) was independently predictive of prenatal HH. Mean third ventricular size was higher in the setting of HH (1.15 ± 0.74 mm versus 0.83 ± 0.35 mm; $P < .001$). A multivariate model evaluating variables associated with postnatal HH was performed and included: IVH, largest ventricular size by MR imaging, GA at birth, prenatal HH, and history of in utero surgical closure (Wald test, $\chi^2 = 13.3$, $P = .02$, pseudoR^2 = 0.31). Prenatal IVH was not predictive of postnatal HH (OR = 2.8 [95% CI, 0.5–16]) (Table 2). Not surprisingly, prenatal HH predicted postnatal HH (OR 11.4 [95% CI, 2.4–75]), but a history of in utero surgical closure was negatively predictive (OR = 0.04 [95% CI, 0.01–0.16]).

A final multivariate regression model showed that prenatal IVH was predictive (OR = 15.7 [95% CI, 2.8–80]) of postnatal IVH, while a history of in utero surgical closure (OR = 0.08 [95% CI, 0.01–0.39]) was negatively predictive (Wald test, $\chi^2 = 25.4$, $P < .001$, pseudo$R^2 = 0.24$), suggesting that fetal closure is protective against persistent IVH. No association between prenatal IVH and postnatal ventricular shunt placement was observed (On-line Table).

DISCUSSION

IVH is commonly detected by sonography and MR imaging in prenatal evaluation of ONTD and frequently described on postnatal MR imaging. Prenatal IVH is associated with, but not independently predictive of, prenatal and postnatal HH likely related to its close association with increased ventriculomegaly. Third ventricular size was strongly associated and a 1 mm cut-point predicted prenatal HH. Postnatal HH was associated with prenatal HH and history of fetal closure was negatively predictive. These findings confirm that in utero surgical closure reverses HH, and we found that this outcome is independent of the presence of prenatal IVH. Last, prenatal IVH was not associated with a requirement for postnatal ventricular shunt placement.

Ventriculomegaly is a common finding in MMC and is thought to be secondary to obstruction of CSF by HH.[24-26] In cases of open NTD, associated HH is an important factor in determining eligibility for prenatal surgical intervention and contributes to predictions of patient outcomes.[11,12,21,22] We found an expected association between HH and decreased head biometric measurements as the HH limits normal calvarial expansion, which may serve as an additional clue to the presence of HH. We also found an association between HH and increased GA, suggesting that the progression of HH is possible later in gestation. Therefore, patients initially excluded from fetal surgery due to absent HH may benefit from follow-up evaluation for subsequent HH development.

In delineating the influence of prenatal IVH in our cohort, we found that ventricular size and head biometric parameters were significantly larger in cases of IVH, suggesting that hemorrhage may contribute to ventriculomegaly. Despite this association, we found that neither IVH nor increased lateral ventricular size was independently predictive of HH, suggesting that ventriculomegaly is a consequence of HH rather than causative. Interestingly, third ventricular enlargement was strongly predictive and size ≥1 mm may be a more specific sign for HH. While this measurement falls within the reported normal range for midgestation fetuses,[27] these values are established from healthy fetuses without congenital anomalies and our data suggest that these normograms may not be applicable to our patient population and this is supported by our results demonstrating a smaller mean third ventricular diameter in cases without HH. Therefore, sonography assessment of the third ventricle may aid in influencing the suspicion for HH and be of particular benefit when MR imaging is inconclusive or not readily available.

Importantly, our results demonstrate that prenatal IVH does not affect the efficacy of fetal closure in reversing HH. While concordance for IVH detection was moderate prenatally and reduced postnatally, overall concordance remained statistically significant. These findings may be explained by the self-limited nature of IVH, time-associated factors, the potential for interval hemorrhage, and unavoidable differences in the timing of imaging. Our results are similar to those reported comparing prenatal and postnatal imaging studies for GMH.[28] In addition, our multivariate model shows that fetal closure may even promote IVH resolution; we suspect by reversal of HH and improvement in CSF flow dynamics thus allowing clearance of blood products. This is concordant

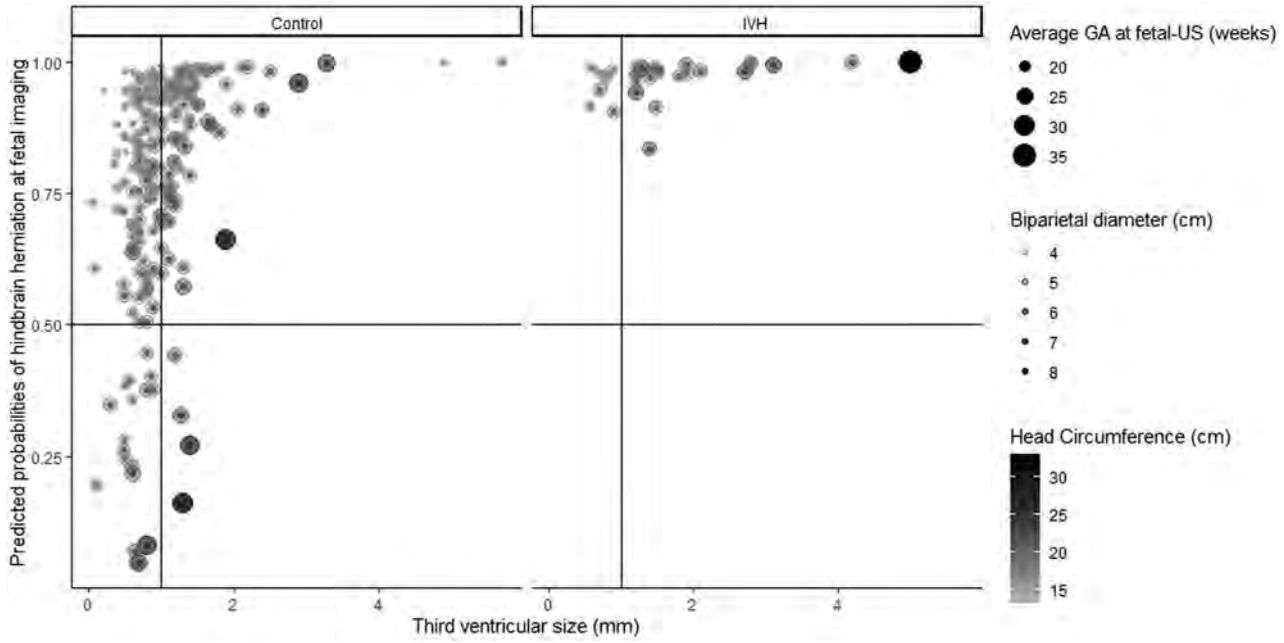

FIG 4. Effect of third ventricular diameter, biparietal diameter, and head circumference per study group according to logistic regression results. Scatterplots depicting the effect of the model described in Table 1 for controls (*left*) and cases of intraventricular hemorrhage (*right*). Y-axis shows the predicted probability for finding prenatal hindbrain herniation (horizontal line indicates the probability of 50%). The x-axis shows the third ventricle diameter (mm). The size of the geometric point corresponds to gestational age, color intensity illustrates head circumference, and transparency shows biparietal diameter for each subject. Most subjects with intraventricular hemorrhage had a third ventricle at or above 1 mm (*vertical line*), hence its strong predictive effect (Table 1).

Table 2: Coefficient results of multivariate logistic regression model for postnatal hindbrain herniation

Predicted Outcome	Predictor	β	SE	*P*
Postnatal HH	IVH presence	1.0	0.9	.23
	Largest ventricular size by MR (mm)	0.11	0.1	.38
	GA at birth	−0.01	0.2	.86
	Prenatal HH	1.8	0.7	.007[a]
	Fetal closure	−3.2	0.7	<.001[a]

Note:—β indicates regression coefficient; SE, standard error.
[a] Significant difference $P < .05$.

with results reporting a higher prevalence of IVH in infants who did not undergo in utero surgery.[21] Ultimately previously considered possible exclusion criteria, prenatal IVH should not preclude eligibility for in utero closure, and families should be counseled and treated accordingly.

The limitations of this study are the retrospective nature and decision to use imaging report data, though this accounts for variability in clinical practice. We ran concordance analyses among imaging studies before case classification and defined IVH based on findings by both sonography and MR imaging to account for this bias and increase data reliability. Previous studies have implemented a grading system in the severity of HH, which would be of benefit for more detailed characterization, but the severity has not been shown to significantly change without fetal closure, does not influence patient counseling or management at our institution, and would be challenging to implement given the variability in the timing of postnatal MR imaging in our cohort; but could be a source of further study. Lastly, subtle changes in sonography and MR image acquisition over the study period may affect the study results, though performing statistical analyses as case-control series may decrease any potential influence on outcomes.

CONCLUSIONS

IVH is prevalent in the prenatal evaluation of fetuses with ONTD. While IVH is associated with prenatal HH, this is not independent and seen in conjunction with increased ventricular size. The transverse third ventricular diameter appears to be a good radiologic marker of prenatal HH and, if larger than 1 mm, it is strongly predictive. The presence of prenatal IVH does not prevent resolution of HH following fetal surgical closure and does not increase the need for postnatal shunt placement. Overall, our results support that prenatal IVH in ONTD is self-limited, particularly in those with fetal closure that is protective against postnatal IVH, likely secondary to the restoration of CSF flow dynamics and clearance of blood products.

REFERENCES

1. Coleman BG, Langer JE, Horii SC. **The diagnostic features of spina bifida: the role of ultrasound.** *Fetal Diagn Ther* 2015;37:179–96 CrossRef Medline
2. Goldstein RB, Podrasky AE, Filly RA, et al. **Effacement of the fetal cisterna magna in association with myelomeningocele.** *Radiology* 1989;172:409–13 CrossRef Medline

3. D'Addario V, Rossi AC, Pinto V, et al. **Comparison of six sonographic signs in the prenatal diagnosis of spina bifida.** *J Perinat Med* 2008;36:330–34 CrossRef Medline
4. Pretorius DH, Russ PD, Rumack CM, et al. **Diagnosis of brain neuropathology in utero.** *Neuroradiology* 1986;28:386–97 CrossRef Medline
5. Araujo Júnior E, Nakano ML, Nardozza LMM, et al. **Comparison between 2D ultrasonography and magnetic resonance imaging for assessing brain and spine parameters in fetuses with spina bifida.** *Arch Gynecol Obstet* 2013;287:845–49 CrossRef Medline
6. Aertsen M, Verduyckt J, De Keyzer F, et al. **Reliability of MR imaging-based posterior fossa and brain stem measurements in open spinal dysraphism in the era of fetal surgery.** *AJNR Am J Neuroradiol* 2019;40:191–98 CrossRef Medline
7. Aaronson OS, Hernanz-Schulman M, Bruner JP, et al. **Myelomeningocele: prenatal evaluation–comparison between transabdominal US and MR imaging.** *Radiology* 2003;227:839–43 CrossRef Medline
8. Variend S, Emery JL. **Cervical dislocation of the cerebellum in children with meningomyelocele.** *Teratology* 1976;13:281–89 CrossRef
9. Bouchard S, Davey MG, Rintoul NE, et al. **Correction of hindbrain herniation and anatomy of the vermis after in utero repair of myelomeningocele in sheep.** *J Pediatr Surg* 2003;38:451–58 CrossRef Medline
10. Paek BW, Farmer DL, Wilkinson CC, et al. **Hindbrain herniation develops in surgically created myelomeningocele but is absent after repair in fetal lambs.** *Am J Obstet Gynecol* 2000;183:1119–23 CrossRef Medline
11. Adzick NS, Thom EA, Spong CY, et al. **A randomized trial of prenatal versus postnatal repair of myelomeningocele.** *N Engl J Med* 2011;364:993-1004 CrossRef Medline
12. Moldenhauer JS, Soni S, Rintoul NE, et al. **Fetal myelomeningocele repair: the post-MOMS experience at the Children's Hospital of Philadelphia.** *Fetal Diagn Ther* 2015;37:235–40 CrossRef Medline
13. Moldenhauer JS, Adzick NS. **Fetal surgery for myelomeningocele: after the Management of Myelomeningocele Study (MOMS).** *Semin Fetal Neonatal Med* 2017;22:360–66 CrossRef Medline
14. Heuer GG, Moldenhauer JS, Adzick NS. **Prenatal surgery for myelomeningocele: review of the literature and future directions.** *Childs Nerv Syst* 2017;33:1149–55 CrossRef Medline
15. Kabagambe SK, Jensen GW, Chen YJ, et al. **Fetal surgery for myelomeningocele: a systematic review and meta-analysis of outcomes in fetoscopic versus open repair.** *Fetal Diagn Ther* 2018;43:161–74 CrossRef Medline
16. Nagaraj UD, Bierbrauer KS, Zhang B, et al. **Hindbrain herniation in Chiari II malformation on fetal and postnatal MRI.** *AJNR Am J Neuroradiol* 2017;38:1031–36 CrossRef Medline
17. Bennett KA, Carroll MA, Shannon CN, et al. **Reducing perinatal complications and preterm delivery for patients undergoing in utero closure of fetal myelomeningocele: further modifications to the multidisciplinary surgical technique.** *PED* 2014;14:108–14 CrossRef Medline
18. Moron AF, Athanasiou A, Barbosa M, et al. **Amniotic fluid lactic acid and matrix metalloproteinase-8 levels at the time of fetal surgery for a spine defect: association with subsequent preterm prelabour rupture of membranes.** *BJOG* 2018;125:1288–92 CrossRef Medline
19. Zaretsky MV, Liechty KW, Galan HL, et al. **Modified hysterotomy closure technique for open fetal surgery.** *Fetal Diagn Ther* 2018;44:105–11 CrossRef Medline
20. Elbabaa SK, Gildehaus AM, Pierson MJ, et al. **First 60 fetal in-utero myelomeningocele repairs at Saint Louis Fetal Care Institute in the post-MOMS trial era: hydrocephalus treatment outcomes (endoscopic third ventriculostomy versus ventriculo-peritoneal shunt).** *Childs Nerv Syst* 2017;33:1157–68 CrossRef Medline
21. Zamłyński J, Olejek A, Koszutski T, et al. **Comparison of prenatal and postnatal treatments of spina bifida in Poland–a non-randomized, single-center study.** *J Matern Neonatal Med* 2014;27:1409–17 CrossRef Medline
22. Pedreira DAL, Zanon N, Nishikuni K, et al. **Endoscopic surgery for the antenatal treatment of myelomeningocele: the CECAM trial.** *Am J Obstet Gynecol* 2016;214:111.E1–111.E11 CrossRef Medline
23. Cohen J. **A coefficient of agreement for nominal scales.** *Educ Psychol Meas* 1960;20:37–46 CrossRef
24. Adzick NS. **Fetal myelomeningocele: natural history, pathophysiology, and in-utero intervention.** *Semin Fetal Neonatal Med* 2010;15:9–14 CrossRef Medline
25. Danzer E, Johnson MP, Adzick NS. **Fetal surgery for myelomeningocele: progress and perspectives.** *Dev Med Child Neurol* 2012;54:8–14 CrossRef Medline
26. Partridge EA, Flake AW. **Maternal-fetal surgery for structural malformations.** *Best Pract Res Clin Obstet Gynaecol* 2012;26:669–82 CrossRef Medline
27. Sari A, Ahmetoglu A, Dinc H, et al. **Fetal biometry: size and configuration of the third ventricle.** *Acta Radiol* 2005;46:631–35 CrossRef Medline
28. Nagaraj UD, Peiro JL, Bierbrauer KS, et al. **Evaluation of subependymal gray matter heterotopias on fetal MRI.** *AJNR Am J Neuroradiol* 2016;37:720–25 CrossRef Medline

Expanding the Neuroimaging Phenotype of Neuronal Ceroid Lipofuscinoses

A. Biswas, P. Krishnan, A. Amirabadi, S. Blaser, S. Mercimek-Andrews, and M. Shroff

ABSTRACT

BACKGROUND AND PURPOSE: Neuronal ceroid lipofuscinoses are a group of neurodegenerative disorders characterized by the accumulation of autofluorescent lipopigments in neuronal cells. As a result of storage material in the brain and retina, clinical manifestations include speech delay, cognitive dysfunction, motor regression, epilepsy, vision loss, and early death. At present, 14 different ceroid lipofuscinosis (CLN) genes are known. Recently, the FDA approved the use of recombinant human proenzyme of tripeptidyl-peptidase 1 for CLN2 disease, while phase I/IIa clinical trials for gene therapy in CLN3 and CLN6 are ongoing. Early diagnosis is, therefore, key to initiating treatment and arresting disease progression. Neuroimaging features of CLN1, CLN2, CLN3, and CLN5 diseases are well-described, with sparse literature on other subtypes. We aimed to investigate and expand the MR imaging features of genetically proved neuronal ceroid lipofuscinoses subtypes at our institution and also to report the time interval between the age of disease onset and the diagnosis of neuronal ceroid lipofuscinoses.

MATERIALS AND METHODS: We investigated and analyzed the age of disease onset and neuroimaging findings (signal intensity in periventricular, deep, and subcortical white matter, thalami, basal ganglia, posterior limb of the internal capsule, insular/subinsular regions, and ventral pons; and the presence or absence of supratentorial and/or infratentorial atrophy) of patients with genetically proved neuronal ceroid lipofuscinoses at our institution. This group consisted of 24 patients who underwent 40 brain MR imaging investigations between 1993 and 2019, with a male preponderance (male/female ratio = 15:9).

RESULTS: The mean ages of disease onset, first brain MR imaging, and diagnosis of neuronal ceroid lipofuscinoses were 4.70 ± 3.48 years, 6.76 ± 4.49 years, and 7.27 ± 4.78 years, respectively. Findings on initial brain MR imaging included T2/FLAIR hypointensity in the thalami ($n = 22$); T2/FLAIR hyperintensity in the periventricular and deep white matter ($n = 22$), posterior limb of the internal capsule ($n = 22$), ventral pons ($n = 19$), and insular/subinsular region ($n = 18$); supratentorial ($n = 21$) and infratentorial atrophy ($n = 20$). Eight of 9 patients who had follow-up neuroimaging showed progressive changes.

CONCLUSIONS: We identified reported classic neuroimaging features in all except 1 patient with neuronal ceroid lipofuscinoses in our study. CLN2, CLN5, and CLN7 diseases showed predominant cerebellar-over-cerebral atrophy. We demonstrate that abnormal signal intensity in the deep white matter, posterior limb of the internal capsule, and ventral pons is more common than previously reported in the literature. We report abnormal signal intensity in the insular/subinsular region for the first time. The difference in the median time from disease onset and diagnosis was 1.5 years.

ABBREVIATIONS: CLN = ceroid lipofuscinosis; DWM = deep white matter; IQR = interquartile range; I-SI = insular/subinsular region; NCL = neuronal ceroid lipofuscinoses; PLIC = posterior limb of the internal capsule; PVWM = periventricular white matter; SCWM = subcortical white matter

Neuronal ceroid lipofuscinoses (NCL) are a group of clinically and genetically heterogeneous lysosomal storage disorders characterized by the accumulation of autofluorescent lipopigments in neuronal cells of the brain and retina.[1] They constitute the most common neurodegenerative disorders of childhood, with an estimated incidence of 1.6–2.4/100,000 in the United States, 2.2/100,000 in Sweden, 2–2.5/100,000 in Denmark, 3.9/100,000 in Norway, 4.8/100,000 in Finland, and 7/100,000 in Iceland.[1,2] Clinical manifestations include speech delay, cognitive

Received May 2, 2020; accepted after revision June 16.

From the Department of Diagnostic Imaging (A.B., P.K., A.A., S.B., M.S.), The Hospital for Sick Children, Toronto, Canada; Division of Clinical and Metabolic Genetics (S.M.-A.), Department of Pediatrics, University of Toronto, The Hospital for Sick Children, Toronto, Canada.

Previously presented in poster format at: Annual Meeting of the American Society of Pediatric Neuroradiology, January 10–12, 2020; Miami Beach, Florida.

Please address correspondence to Asthik Biswas, MD, MBBS, Department of Diagnostic Imaging, The Hospital for Sick Children, 555 University Ave, Toronto, ON, M5G 1X8, Canada; e-mail: asthik.biswas@sickkids; caasthikbiswas@gmail.com; @stikkman11

http://dx.doi.org/10.3174/ajnr.A6726

Table 1: Subgroups of NCL, their genes, protein names, and MIM numbers

Locus Name	Gene Symbol	Protein Name	MIM Number
CLN1	PPT1	Palmitoyl protein thioesterase 1	600722
CLN2	*TPP1*	Tripeptidyl peptidase 1	607998
CLN3	*CLN3*	CLN3	607042
CLN4	*DNAJC5*	DnaJ homolog	611203
CLN5	*CLN5*	CLN5	608102
CLN6	*CLN6*	CLN6	601780
CLN7	*MFSD8*	Major facilitator superfamily	611124
CLN8	*CLN8*	CLN8	607837
CLN9	N/A	Unknown	609055
CLN10	*CTSD*	Cathepsin D	116840
CLN11	*GRN*	Granulins	138945
CLN12	*ATP13A2*	Probable cation transporting	610513
CLN13	*CTSF*	Cathepsin F	603539
CLN14	*KCTD7*	BTB/POZ domain-containing	611725

Note:—MIM indicates Mendelian Inheritance in Man; N/A, not applicable.

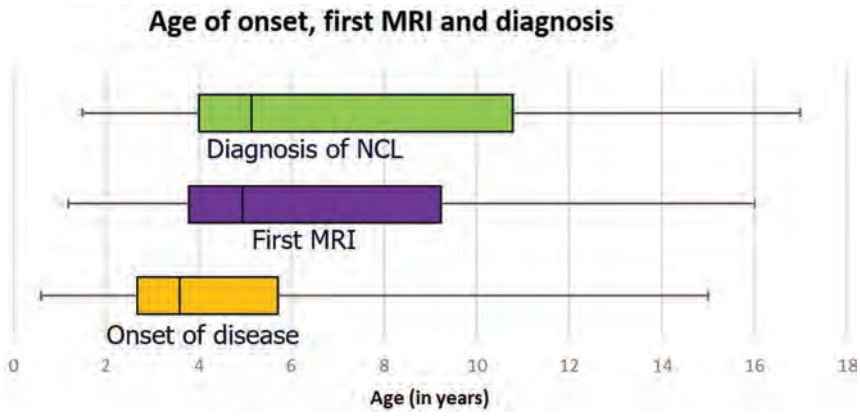

FIG 1. Time delay between disease onset (median, 3.6 years; IQR, 3 years) and clinical, radiologic, and histopathologic diagnoses (median, 5.1 years; IQR, 6.7 years) of NCL is depicted.

dysfunction, developmental regression, epilepsy, vision loss, and early death.[3] Although traditionally classified on the basis of the age of onset (infantile, late-infantile, juvenile, and adult), classification is now based on genetic etiology, with 14 different ceroid lipofuscinosis (CLN) genes known at present (Table 1).[4] Several new insights into the cell biology of NCL have emerged,[5-7] with ongoing translational research likely to have therapeutic implications.[8] Furthermore, it has been proposed that the different subtypes of NCL are actually distinct disorders, each with a unique underlying molecular pathomechanism sharing a common end point in the form of neuronal loss and autofluorescent storage material.[8] Recently, the FDA approved the use of cerliponase alfa (Brineura), a recombinant human proenzyme of tripeptidyl-peptidase 1, for CLN2 disease.[9] The treatment arrests disease progression; therefore, early diagnosis is essential for optimal treatment outcomes. In addition, phase I/IIa clinical trials with gene therapy are currently in progress for CLN3[10] and CLN6 diseases.[11]

The classic neuroimaging features in brain MR imaging of NCL reported in the literature include T2-hypointense thalami, T2-hyperintense periventricular white matter, and progressive cerebral and cerebellar volume loss.[12-19] Subtype-specific imaging findings are well-described in CLN1, CLN2, CLN3, and CLN5 diseases,[20-25] with scarce literature on other subtypes.[26-31] Given the rapidly changing landscape in cell biology and translation in NCL and the need for early diagnosis facilitating early treatment, we performed a retrospective review study to investigate and expand the MR imaging features of the disease in patients with genetically confirmed NCL diagnosed at our institution. We also report the time interval between the age of disease onset, first brain MR imaging, and diagnosis in this study.

MATERIALS AND METHODS

The institutional Research Ethics Board approved the study (REB 1000065260). Patients were identified from a previous study data base.[32] Patient demographics and clinical features were obtained through electronic chart review. Brain MR imaging examinations were reviewed for quality and co-read by 2 of the authors (A.B. and P.K.) with consensus review. Specifically, the nature of T2 signal intensity in the thalami, periventricular white matter (PVWM), deep white matter (DWM), subcortical white matter (SCWM), basal ganglia, posterior limb of the internal capsule (PLIC), insular/subinsular region (I-SI), and ventral pons, along with the presence or absence of supratentorial and infratentorial atrophy, was documented. Atrophy was graded subjectively as mild, moderate, and severe. Note was made of the degree of cerebral atrophy relative to cerebellar atrophy. Volumetric analysis was not performed due to insufficient numbers of cases with volume data. The age of disease onset was determined by documented history in the hospital records system (Chartmaxx; https://chartmaxx.software.informer.com/). A working diagnosis of NCL was defined either by a histopathologic basis with positive conjunctival or skin biopsy demonstrating curvilinear profiles, fingerprint profiles, or granular osmiophilic profiles; or by a clinicoradiologic basis when clinical presentation or family history, or both in conjunction with MR imaging findings were highly suggestive of the diagnosis. All patients in the cohort eventually had confirmed genetic diagnoses via direct Sanger testing, the details of which have been published previously.[32] Data were entered into Excel (Microsoft). Data were analyzed with descriptive statistics (median and interquartile range [IQR] for age calculated in Excel).

RESULTS

Thirty-four patients with genetically confirmed neuronal ceroid lipofuscinosis were identified between 1993 and 2019. Most of these patients and their molecular genetic investigations have

Table 2: Clinical features of patients with NCL[a]

NCL Subtypes	Sex	Speech Delay *n* (%)	Visual Impairment *n* (%)	Seizures *n* (%)	Behavioral Abnormalities *n* (%)	Cognitive Decline *n* (%)	Developmental Regression *n* (%)
CLN1 disease ($n = 6$)	M ($n = 4$), F ($n = 2$)	5 (83)	5 (83)	4 (67)	3 (50)	5 (83)	5 (83)
CLN2 disease ($n = 5$)	M ($n = 5$)	4 (80)	3 (60)	4 (80)	2 (40)	4 (80)	4 (80)
CLN3 disease ($n = 2$)	M ($n = 2$)	2 (100)	2 (100)	1 (50)	2 (100)	2 (100)	2 (100)
CLN5 disease ($n = 1$)	F ($n = 1$)	1 (100)	1 (100)	1 (100)	1 (100)	1 (100)	1 (100)
CLN6 disease ($n = 2$)	M ($n = 1$), F ($n = 1$)	1 (50)	1 (50)	1 (50)	1 (50)	2 (100)	2 (100)
CLN7 disease ($n = 6$)	M ($n = 4$), F ($n = 2$)	6 (100)	2 (33)	6 (100)	2 (33)	6 (100)	6 (100)
CLN8 disease ($n = 2$)	M (n = 1), F ($n = 1$)	2 (100)	0 (0)	2 (100)	0 (0)	2 (100)	2 (100)

[a] Data are number of patients (percentage in parenthesis).

Table 3: Brain MR imaging features of patients with NCL

		T2 Hyperintensity n (%)				Volume Loss n (%)	
NCL Subtypes	T2 hypointense thalami n (%)	Corpus Striatum	STWM (PVWM and/or DWM and/or SCWM and/or PLIC)	Insular/Sub-Insular	Pons	Supratentorial	Cerebellar
CLN1 disease ($n = 6$)	6 (100)	6 (100)	6 (100)	4 (67)	6 (100)	6 (100)	6 (100)
CLN2 disease ($n = 5$)	5 (100)	3 (60)	5 (100)	4 (80)	3 (60)	4 (80)	4 (80)
CLN3 disease ($n = 2$)	0 (0)	0 (0)	1 (50)	1 (50)	0 (0)	2 (100)	0 (0)
CLN5 disease ($n = 1$)	1 (100)	1 (100)	1 (100)	1 (100)	1 (100)	1 (100)	1 (100)
CLN6 disease ($n = 2$)	2 (100)	1 (50)	2 (100)	1 (50)	2 (100)	1 (50)	1 (50)
CLN7 disease ($n = 6$)	6 (100)	2 (33)	6 (100)	5 (83)	5 (83)	5 (83)	6 (100)
CLN8 disease ($n = 2$)	2 (100)	2 (100)	2 (100)	2 (100)	2 (100)	2 (100)	2 (100)

Note:—STWM indicates supratentorial white matter.

been reported.[32] Of these, 24 patients (male/female ratio = 15:9) had 40 MR imaging examinations and were therefore included in the study. The time delay between disease onset and diagnoses is depicted in Fig 1. The median (IQR) age of disease onset, first brain MR imaging, and age of genetic diagnoses were 3.6 (3.0), 4.9 (5.4), and 5.1 (6.7) years, respectively (Fig 1). The NCL subtypes were CLN1 ($n = 6$), CLN2 ($n = 5$), CLN3 ($n = 2$), CLN5 ($n = 1$), CLN6 ($n = 2$), CLN7 ($n = 6$), and CLN8 ($n = 2$) diseases. The most common symptom was developmental and cognitive regression ($n = 22$). Other presenting symptoms included speech delay ($n = 21$), seizures ($n = 19$), impaired vision ($n = 14$), and behavioral abnormalities ($n = 11$). Clinical features and their distribution to each subgroup of NCL are listed in Table 2.

Brain MR imaging features are summarized in Table 3. Findings on initial brain MR imaging included the following: 1) T2/FLAIR hypointensity in the thalami ($n = 22$); 2) T2/FLAIR hyperintensity in the PVWM and DWM ($n = 22$); 3) T2/FLAIR hyperintensity in the PLIC ($n = 22$); 4) T2/FLAIR hyperintensity in the ventral pons ($n = 19$); 5) T2/FLAIR hyperintensity in the I-SI region ($n = 18$); 6) supratentorial atrophy ($n = 21$; mild, [$n = 10$]; moderate-severe, [$n = 11$]; and 7) cerebellar atrophy [$n = 20$]). Eight of 9 patients who had follow-up neuroimaging showed progressive changes. Imaging findings in each subtype are summarized below.

CLN1 Disease

In CLN1 disease ($n = 6$), the median (IQR) age of onset was 3 (8.5) years, while the median (IQR) age at first MR imaging was 3.5 (11.5) years. On the initial MR imaging, all patients ($n = 6$) showed T2/FLAIR hypointensity in the thalami and T2 hyperintensity in the basal ganglia. All patients had T2/FLAIR hyperintensity in the PVWM, DWM, PLIC, and pons, while only 1 patient showed abnormality in the SCWM. Four patients demonstrated T2/FLAIR hyperintensity in the I-SI region. All patients showed supratentorial atrophy (mild = 2; moderate = 2; severe = 2) and cerebellar atrophy (mild = 4; moderate = 2), with 5 patients showing brain stem atrophy. In all 6 patients, the degree of cerebral atrophy was greater than that of cerebellar atrophy.

Three of 6 patients had follow-up imaging. All 3 patients demonstrated progressive supratentorial and cerebellar volume loss, and 2 patients showed progressive white matter T2/FLAIR hyperintensity now extending to involve the SCWM.

CLN2 Disease

In CLN2 disease ($n = 5$), the median (IQR) age of onset was 3.5 (5.3) years. The median (IQR) age the first MR imaging was 8.7 (8.4) years. All patients ($n = 5$) showed T2/FLAIR hypointensity in the thalami, whereas 3 patients showed T2 hyperintensity in basal ganglia. All patients showed T2/FLAIR hyperintensity in the PLIC, PVWM, and DWM, with 1 patient demonstrating abnormality involving the SCWM. Four patients showed T2/FLAIR hyperintensity in the I-SI region, and 3 showed signal abnormality in the pons.

Four patients showed supratentorial atrophy (mild = 1; moderate = 1; severe = 2) and cerebellar atrophy (mild = 2; severe = 2), with 4 patients showing brain stem atrophy. In 3 of 5 patients, cerebellar atrophy was greater than cerebral atrophy.

Three patients had follow-up imaging. All 3 showed progressive supratentorial atrophy, and 2 showed progression in cerebellar atrophy. One patient who had normal signal in the I-SI region and pons on the initial MR imaging showed signal abnormality in both regions on follow-up MR imaging.

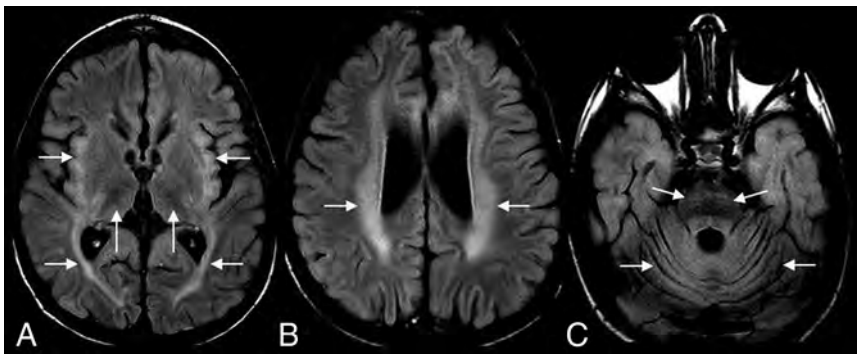

FIG 2. A 4-year-old boy with CLN2 disease. Axial FLAIR MR imaging shows hypointense thalami and hyperintense insular/subinsular region and posterior limb of the internal capsule (*A*); hyperintense periventricular and deep white matter (*B*), and hyperintense ventral pons (*C*). Note diffuse cerebral and cerebellar volume loss (*A–C*).

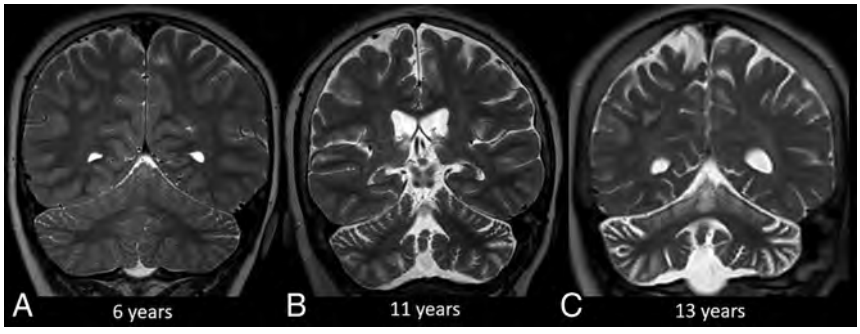

FIG 3. Progression of CLN2 disease. Coronal T2-weighted MR imaging at 6 years of age (*A*) shows no discernible volume loss. Follow-up MR imaging at 11 and 13 years of age (*B* and *C*) shows progressive cerebral and cerebellar volume loss. Note the greater degree of cerebellar volume loss relative to the cerebrum.

Sample cases of CLN2 disease are shown in Figs 2 and 3.

CLN3 Disease

In CLN3 disease ($n = 2$), the age of onset was 10 years in patient 3A and was unknown in patient 3B. MR imaging of patient 3A performed at 6 years of age showed no signal abnormality or volume loss on the initial MR imaging. Follow-up MR imaging at 10 years of age showed supratentorial volume loss with PVWM and DWM signal abnormality. MR imaging of patient 3B performed at 1.2 years of age showed only mild supratentorial atrophy without signal change and no obvious progression on follow-up imaging after 6 years (the first MR imaging for patient 3B was actually performed for follow-up of intraventricular hemorrhage; therefore, the atrophy was possibly not related to NCL). Neither patient had cerebellar atrophy.

CLN5 Disease

In CLN5 disease ($n = 1$), the disease onset was at 3.5 years of age. MR imaging at 6.5 years of age showed T2/FLAIR hypointense thalami; and T2/FLAIR hyperintensity in basal ganglia, PVWM, DWM, PLIC, I-SI region, and pons, along with mild supratentorial and severe cerebellar atrophy. There was no follow-up MR imaging.

CLN6 Disease

In CLN6 disease ($n = 2$), the age at disease onset was 4 years in a female and 9 years in a male patient. MR imaging of both patients (6A and 6B, at 8.6 years and 10.8 years of age) showed T2/FLAIR hypointense thalami, and both showed T2/FLAIR hyperintense signal in the PLIC, PVWM, DWM, and pons (none in the SCWM). One (patient 6A) had T2/FLAIR hyperintensity in the basal ganglia. Patient 6A showed severe supratentorial and cerebellar atrophy and brain stem atrophy. Patient 6B did not have atrophy on the initial MR imaging but showed mild supratentorial atrophy on follow-up imaging after 4.5 years. Both patients showed a greater degree of cerebral atrophy compared with cerebellar atrophy.

CLN7 Disease

In CLN7 disease ($n = 6$), the median age of onset of disease was 3.75 years (IQR, 3.1 years), while the median age at first MR imaging was 4.5 years (IQR, 4 years). All patients showed T2/FLAIR hypointense thalami; 2 showed a T2/FLAIR hyperintense basal ganglia; all showed T2/FLAIR hyperintense PLIC, PVWM, and DWM (none in the SCWM) and 5 showed abnormal signal in the I-SI region and pons. Five patients showed supratentorial atrophy (mild = 3; moderate = 2), while all 6 patients showed cerebellar atrophy (mild = 1; moderate = 4; severe = 1). Four patients had brain stem atrophy. In 5 of 6 patients, the degree of cerebellar atrophy was greater than cerebral atrophy (Fig 4), with equal atrophy in 1 patient. None of the patients had follow-up MR imaging.

CLN8 Disease

In CLN8 disease ($n = 2$), the age of disease onset was 3.7 years in a male (8A) and 3.3 years in a female (8B) patient. MR imaging of both patients (at 4.5 and 3.3 years, respectively) showed T2/FLAIR hypointense thalami and T2/FLAIR hyperintense basal ganglia, PVWM, DWM, PLIC, I-SI region, and pons. None had SCWM signal abnormality. Both showed supratentorial (mild = 1; moderate = 1) and cerebellar (mild = 1, moderate = 1) atrophy. Patient 8A had greater cerebellar atrophy compared with cerebral atrophy while patient 8B had an equal degree of atrophy. Neither of the patients had follow-up MR imaging.

DISCUSSION

We report 24 patients with genetically confirmed NCL and their brain MR imaging features, which is one of the largest patient

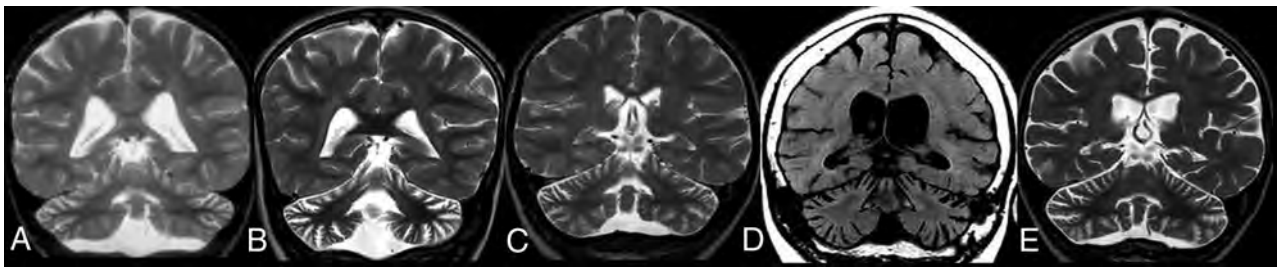

FIG 4. CLN7 disease. Coronal T2-weighted MR imaging of 4 different patients (*A*, *B*, *C*, and *E*) and coronal reformatted CT of 1 patient (*D*). Note cerebellar more than cerebral volume loss in all patients.

cohorts, to the best of our knowledge. Brain MR imaging findings of atrophy and white matter signal changes in NCL were first reported by Machen et al,[33] expanding the findings on previously reported brain MR imaging features of NCL on CT.[34] To the best of our knowledge, thalamic T2 hypointensity and periventricular T2 hyperintense rims in infantile-onset NCL were reported by Vanhanen et al[35] for the first time in 1994. The white matter signal change was hypothesized to represent loss of myelin due to Wallerian degeneration based on histopathologic and microscopic studies.[7,36-38] The thalamic T2 darkening was speculated to represent accumulation of iron, though this was debated.[38] Vanhanen et al[14] studied postmortem MR imaging with histopathologic correlation in 8 patients with infantile NCL in 1995 and demonstrated almost complete loss of cortical neurons, axons, and myelin sheaths in all patients, along with astrocytic proliferation containing periodic-acid-Schiff-positive storage material. They also demonstrated loss of thalamic neurons and loss of granular and Purkinje cells in the cerebellar cortex. They speculated that the thalamic T2 hypointense signal was due to accumulation of saposin (similar to GM2 gangliosides) and also by hypertrophic astrocytes containing storage protein and glial fibrillary acid protein.

In addition to their previous reports, Vanhanen et al,[18] in 1995, reported progressive cerebral atrophy in infantile-onset NCL starting from 13 months of age and peaking at 4 years of age, redemonstrated by the same group in 2004 in patients with proved CLN1,[20] with cerebellar atrophy lagging behind cerebral atrophy. All 6 of our patients with CLN1 disease (infantile onset) showed this pattern of initial early-onset cerebral atrophy followed by later-onset cerebellar atrophy.

Patients with late infantile-onset NCL have been reported to show early-onset cerebellar atrophy.[23,39,40] We also identified similar findings in our late-infantile-onset CLN2, CLN5, and CLN7 diseases, wherein most patients showed earlier onset and, in most, a greater degree of cerebellar atrophy compared with cerebral atrophy. Interestingly, this was most remarkable in our CLN7 disease cohort wherein 5 of 6 patients showed this finding. On the other hand, both patients with CLN6 disease (early-juvenile and late-infantile NCL) had a greater degree of cerebral atrophy compared with cerebellar atrophy.

Juvenile NCL generally demonstrates cerebral and cerebellar atrophy, usually after the ages of 9 and 13 years respectively,[19] though quantitative white matter signal intensities may be abnormal at a younger age.[19] Studies have also demonstrated progressive hippocampal atrophy,[25] altered white matter microstructure,[22] and decreased volume of the dorsomedial thalami and corona radiata in CLN3 disease.[24] One of our patients (3A) with CLN3 disease had mild PVWM and DWM signal abnormality and mild supratentorial volume loss at 14 years of age, while the other patient (3B) was only imaged up to 7 years of age and had no discernible signal abnormality. Unfortunately, we do not have morphometric data on these images.

White matter signal abnormalities, starting from the periventricular white matter with progression to deep and subcortical white matter in NCL, have been reported and have been attributed to white matter degeneration or abnormal myelin.[18,19] We noted a distinctive abnormality in our cohort with involvement of the insular/subinsular region seen in 75% of our patients. To the best of our knowledge, this brain MR imaging feature has not been reported previously. Additionally, we identified T2/FLAIR hyperintensity of the PLIC and ventral pons in 91% and 79%, respectively, in our study cohort, which has been rarely reported in the literature.[17,18] Jadav et al[17] reported PLIC hyperintensity as an uncommon-but-characteristic brain MR imaging feature of CLN3 disease, though Holmberg et al[23] also had previously reported this finding in a CLN5 disease cohort. In our study, this was seen not only in juvenile-onset but also in infantile and late-infantile onset NCL.

The differences in imaging phenotypes (eg, predominant cerebral over cerebellar atrophy and vice versa) is intriguing. As alluded to earlier, different subtypes of NCL may represent distinct disorders, each with its own molecular pathway converging to a common end point (including storage of autofluorescent material and neuronal death). The NCL genes encode several types of gene products that include lysosomal enzymes, soluble lysosomal proteins, transmembrane domain–containing proteins, and other proteins with different subcellular localizations.[1,41] The precise localization and function of many of these proteins remain elusive. However, several roles of these proteins have now been elucidated, including apoptosis and autophagy, endocytosis, vesicular trafficking, cell proliferation, pH homeostasis, synaptic functioning, and protein secretion.[1,41] Furthermore, researchers[42] have demonstrated interaction among NCL proteins, with the CLN5 protein interacting with CLN2 and CLN3 polypeptides, suggesting the possibility of common pathways among these subtypes. In a recent study, CLN1, CLN3, CLN6, and CLN8 diseases have been linked to endoplasmic reticulum stress resulting in apoptosis.[43] Whether the cerebral cortex is particularly susceptible to endoplasmic reticulum stress–related apoptosis accounting for

predominant cerebral atrophy in these subtypes is unclear but appears plausible. The pathogenesis of NCL is therefore multifactorial and occurs not only due to the accumulation of lipopigments but also due to mitochondrial dysfunction, endoplasmic reticulum stress, and alterations in cellular pH, which lead to excessive production of mitochondrial reactive oxygen species and disturbed calcium homeostasis, resulting in apoptosis and neuronal loss. Each of the NCL proteins has varying effects on these cellular functions, resulting in slight differences in phenotypes and neuroimaging features.

This study has several limitations. First, because it was a retrospective study, MR imaging performed in different machines and protocols was analyzed, with nonuniform imaging parameters. Second, because images were analyzed during a 30-year period, there was an insufficient number of cases with the data required to perform meaningful quantitative analyses. We, therefore, restricted the study to qualitative analysis of signal intensity and volume loss. Third, only 9 patients had follow-up imaging, making it difficult to assess progression of disease. Last, there was under-representation of certain subtypes (eg, CLN3 disease) in this study cohort.

CONCLUSIONS

CLN1 and CLN7 diseases were the most common subgroups in our study cohort. The difference in the median time from disease onset and diagnosis was 1.5 years. Given recent FDA approval of the use of cerliponase alfa for treatment of CLN2 disease and ongoing phase I/IIa clinical trials with gene therapy for CLN3 and CLN6 diseases, it is imperative to reduce this time gap to arrest disease progression. In patients with a history of developmental regression, brain MR imaging and referral to a neurologist and geneticist are crucial to diagnose patients at the disease onset.

We identified reported classic neuroimaging features in all except 1 patient with NCL in our study, including predominant cerebellar-over-cerebral atrophy in CLN2, CLN5, and CLN7 diseases and minimal abnormality up to early adolescence in CLN3 disease. We confirmed less frequently reported findings of abnormal signal intensity in the deep white matter, posterior limb of the internal capsule, and ventral pons and demonstrated that these findings are more common than previously reported in the literature. We report abnormal signal intensity in the insular/subinsular region for the first time.

ACKNOWLEDGMENTS

A.B. is partially funded by Ontasian Imaging Laboratory (OIL), Toronto.

Disclosures: Saadet Mercimek-Andrews—*UNRELATED*: *Board Membership*: Recordati, BioMarin advisor; *Consultancy*: Canadian Medical Protective Association expert reviewer, Borden Ladner Gervais expert reviewer; *Grants/Grants Pending*: Physician Services Incorporation grant*; *Payment for Lectures Including Service on Speakers Bureaus*: BioMarin, Recordati. Manohar Shroff—*RELATED*: *Other*: BioMarin, *Comments*: I received a one-time honorarium (November 2019) for participating in an afternoon discussion on CLN2 hosted by BioMarin, which manufactures an enzyme-replacement treatment for CLN2. This was 2 months before we started this project. *Money paid to the institution.

REFERENCES

1. Nita DA, Mole SE, Minassian BA. **Neuronal ceroid lipofuscinoses.** *Epileptic Disord* 2016;18:73–88 CrossRef Medline
2. Uvebrant P, Hagberg B. **Neuronal ceroid lipofuscinoses in Scandinavia: epidemiology and clinical pictures.** *Neuropediatrics* 1997;28:6–8 CrossRef Medline
3. Mole SE, Williams RE, et al. Neuronal ceroid-lipofuscinoses. In: Adam MP, Ardinger HH, Pagon RA, eds. *GeneReviews*. University of Washington, Seattle; 1993
4. Geraets RD, Koh Sy, Hastings ML, et al. **Moving towards effective therapeutic strategies for neuronal ceroid lipofuscinosis.** *Orphanet J Rare Dis* 2016;11:40 CrossRef Medline
5. Mukherjee AB, Appu AP, Sadhukhan T, et al. **Emerging new roles of the lysosome and neuronal ceroid lipofuscinoses.** *Mol Neurodegener* 2019;14:4 CrossRef Medline
6. Kline RA, Wishart TM, Mills K, et al. **Applying modern Omic technologies to the neuronal ceroid lipofuscinoses.** *Biochim Biophys Acta Mol Basis Dis* 2020;1866:165498 CrossRef Medline
7. di Ronza A, Bajaj L, Sharma J, et al. **CLN8 is an endoplasmic reticulum cargo receptor that regulates lysosome biogenesis.** *Nat Cell Biol* 2018;20:1370–77 CrossRef Medline
8. Cooper JD, Mole SE. **Future perspectives: what lies ahead for neuronal ceroid lipofuscinosis research?** *Biochim Biophys Acta Mol Basis Dis* 2020;866:165681 CrossRef Medline
9. Kohlschütter A, Schulz A, Bartsch U, et al. **Current and emerging treatment strategies for neuronal ceroid lipofuscinoses.** *CNS Drugs* 2019;33:315–25 CrossRef Medline
10. **Gene Therapy for Children with CLN3 Batten Disease.** ClinicalTrials.gov. Accessed May 7, 2020
11. **Gene Therapy for Children with Variant Late Infantile Neuronal Ceroid Lipofuscinosis 6 (vLINCL6).** ClinicalTrials.gov. Accessed May 7, 2020
12. D'Incerti L. **MRI in neuronal ceroid lipofuscinosis.** *Neurol Sci* 2000;21:S71–73 CrossRef Medline
13. Baker EH, Levin SW, Zhang Z, et al. **MRI brain volume measurements in infantile neuronal ceroid lipofuscinosis.** *AJNR Am J Neuroradiol* 2017;38:376–82 CrossRef Medline
14. Vanhanen SL, Raininko R, Santavuor P, et al. **MRI evaluation of the brain in infantile neuronal ceroid-lipofuscinosis, Part 1: postmortem MRI with histopathologic correlation.** *J Child Neurol* 1995;10:438–43 CrossRef Medline
15. Jiangxi X, Li G, Yuanchun Z, et al. **MRI findings in childhood with neuronal ceroid lipofuscinosis.** *Chinese Journal of Radiology* 2003;37:802–04
16. Peña JA, Cruz EM, Leendertz R, et al. **MRI and proton spectroscopy in children with late infantile neuronal ceroid lipofuscinosis: preliminary results.** *J Pediatr Neurol* 2015;05:215–20 CrossRef
17. Jadav RH, Sinha S, Yasha TC, et al. **Magnetic resonance imaging in neuronal ceroid lipofuscinosis and its subtypes.** *Neuroradiol J* 2012;25:755–61 CrossRef Medline
18. Vanhanen SL, Raininko R, Autti T, et al. **MRI evaluation of the brain in infantile neuronal ceroid-lipofuscinosis, Part 2: MRI findings in 21 patients.** *J Child Neurol* 1995;10:444–50 CrossRef Medline
19. Autti T, Raininko R, Vanhanen SL, et al. **MRI of neuronal ceroid lipofuscinosis. I: cranial MRI of 30 patients with juvenile neuronal ceroid lipofuscinosis.** *Neuroradiology* 1996;38:476–82 CrossRef
20. Vanhanen SL, Puranen J, Autti T, et al. **Neuroradiological findings (MRS, MRI, SPECT) in infantile neuronal ceroid-lipofuscinosis (infantile CLN1) at different stages of the disease.** *Neuropediatrics* 2004;35:27–35 CrossRef Medline
21. Dyke J, Sondhi D, Voss H, et al. **Brain region specific degeneration with disease progression in late infantile neuronal ceroid lipofuscinosis (CLN2 disease).** *AJNR Am J Neuroradiol* 2016;37:1160–69 CrossRef Medline
22. Roine U, Roine TJ, Hakkarainen A, et al. **Global and widespread local white matter abnormalities in juvenile neuronal ceroid lipofuscinosis.** *AJNR Am J Neuroradiol* 2018;39:1349–54 CrossRef Medline
23. Holmberg V, Lauronen L, Autti T, et al. **Phenotype-genotype correlation in eight patients with Finnish variant late infantile NCL (CLN5).** *Neurology* 2000;55:579–81 CrossRef Medline

24. Autti T, Hämäläinen J, Aberg L, et al. **Thalami and corona radiata in juvenile NCL (CLN3): a voxel-based morphometric study.** *Eur J Neurol* 2007;14:447–50 CrossRef Medline
25. Tokola AM, Salli EK, Åberg LE, et al. **Hippocampal volumes in juvenile neuronal ceroid lipofuscinosis: a longitudinal magnetic resonance imaging study.** *Pediatr Neurol* 2014;50:158–63 CrossRef Medline
26. Lauronen L, Santavuori P, Hirvasniemi A, et al. **Northern epilepsy syndrome (NES, CLN8): MRI and electrophysiological studies.** *Eur J Paediatr Neurol* 2001;5(Suppl A):167–73 CrossRef Medline
27. Alkhars FZ, Bo Ali AY, Almohanna MA, et al. **Neuronal ceroid lipofuscinoses type 8: expanding genotype/phenotype diversity-first report from Saudi Arabia.** *Neurosciences (Riyadh)* 2020;25:65–69 CrossRef Medline
28. Doccini S, Sartori S, Maeser S, et al. **Early infantile neuronal ceroid lipofuscinosis (CLN10 disease) associated with a novel mutation in CTSD.** *J Neurol* 2016;263:1029–32 CrossRef Medline
29. Varvagiannis K, Hanquinet S, Billieux MH, et al. **Congenital neuronal ceroid lipofuscinosis with a novel CTSD gene mutation: a rare cause of neonatal-onset neurodegenerative disorder.** *Neuropediatrics* 2018;49:150–53 CrossRef Medline
30. Kamate M, Detroja M, Hattiholi V. **Neuronal ceroid lipofuscinosis type-11 in an adolescent.** *Brain Dev* 2019;41:542–45 CrossRef Medline
31. Di Fabio R, Colonnese C, Santorelli FM, et al. **Brain imaging in Kufs disease type B: case reports.** *BMC Neurol* 2015;15:102 CrossRef Medline
32. Jilani A, Matviychuk D, Blaser S, et al. **High diagnostic yield of direct Sanger sequencing in the diagnosis of neuronal ceroid lipofuscinoses.** *JIMD Rep* 2019;50:20–30 CrossRef Medline
33. Machen BC, Williams JP, Lum GB, et al. **Magnetic resonance imaging in neuronal ceroid lipofuscinosis.** *J Comput Tomogr* 1987;11:160–66 CrossRef Medline
34. Valavanis A, Friede RL, Schubiger O, et al. **Computed tomography in neuronal ceroid lipofuscinosis.** *Neuroradiology* 1980;19:35–38 CrossRef Medline
35. Vanhanen SL, Raininko R, Santavuori P. **Early differential diagnosis of infantile neuronal ceroid lipofuscinosis, Rett syndrome, and Krabbe disease by CT and MR.** *AJNR Am J Neuroradiol* 1994;15:1443–53 Medline
36. Haltia M, Rapola J, Santavuori P. **Infantile type of so-called neuronal ceroid-lipofuscinosis. histological and electron microscopic studies.** *Acta Neuropathol* 1973;26:157–70 CrossRef Medline
37. Haltia M, Rapola J, Santavuori P, et al. **Infantile type of so-called neuronal ceroid-lipofuscinosis, Part 2: morphological and biochemical studies.** *J Neurol Sci* 1973;18:269–85 CrossRef
38. Heiskala H, Gutteridge JM, Westermarck T, et al. **Bleomycin-detectable iron and phenanthroline-detectable copper in the cerebrospinal fluid of patients with neuronal ceroid-lipofuscinoses.** *Am J Med Genet Suppl* 1988;5:193–202 CrossRef Medline
39. Wisniewski KE, Kida E, Connell F, et al. **New subform of the late infantile form of neuronal ceroid lipofuscinosis.** *Neuropediatrics* 1993;24:155–63 CrossRef Medline
40. Autti T, Raininko R, Launes J, et al. **Jansky-Bielschowsky variant disease: CT, MRI, and SPECT findings.** *Pediatr Neurol* 1992;8:121–26 CrossRef Medline
41. McLaren MD, Mathavarajah S, Huber RJ. **Recent insights into NCL protein function using the model organism *Dictyostelium discoideum*.** *Cells* 2019;8:115 CrossRef Medline
42. Vesa J, Chin MH, Oelgeschläger K, et al. **Neuronal ceroid lipofuscinoses are connected at molecular level: interaction of CLN5 protein with CLN2 and CLN3.** *Mol Biol Cell* 2002;13:2410–20 CrossRef Medline
43. Marotta D, Tinelli E, Mole SE. **NCLs and ER: a stressful relationship.** *Biochim Biophys Acta Mol Basis Dis* 2017;1863:1273–81 CrossRef Medline

CT-Based Measurements of Facial Parameters of Healthy Children and Adolescents in Thailand

N. Jullabussapa, K. Khwanngern, C. Pateekhum, C. Angkurawaranon, and S. Angkurawaranon

ABSTRACT

BACKGROUND AND PURPOSE: Facial parameters are used for evaluating normal growth patterns, diagnosing patients with craniofacial abnormalities, and planning surgical procedures. However, these parameters vary by ethnicity and race. This study aims to describe soft-tissue and bony facial parameters based on CT of healthy pediatric and adolescent patients in Thailand.

MATERIALS AND METHODS: CT imaging of the brain, orbit, facial bones, and neck was performed at Maharaj Nakorn Chiangmai Hospital, in patients from birth to 19 years old. Patients with known syndromic disease, craniofacial syndrome, facial trauma and/or infection, and previous surgery that deformed the study area were excluded. The key points of measurement were soft-tissue intercanthal, bony interorbital, and bony lateral orbital distances.

RESULTS: There were 932 patients: 554 males (59.4%) and 378 females (40.6%). Facial parameters rapidly increased in the first 2 years of life. Significant differences in these parameters between the males and females were found at the age of ≥15 years. However, ratios of the interorbital to the lateral orbital distance were generally consistent among age groups in both sexes, at 0.25.

CONCLUSIONS: This study, in Thailand, provides detailed age- and sex-specific normative data of the craniofacial measurements in children and adolescences based on CT imaging. These data can be used for evaluating individual patients with craniofacial abnormalities as well as determining the treatment in Thai and Asian populations, in whom craniofacial abnormalities, for example, frontoethmoidal encephalomeningocele, are common.

ABBREVIATIONS: IC = intercanthal; IO = interorbital; LO = lateral orbital; SD = standard deviation

Facial parameters and proportions play important roles in medicine because they are used for evaluating normal growth patterns, diagnosing patients with craniofacial abnormalities, and planning surgical procedures.[1,2] One of the most common craniofacial abnormalities in southeast Asia is frontoethmoidal encephalomeningocele,[3] a congenital pediatric disorder characterized by herniation of the brain and the meninges through an anterior skull defect that usually involves the orbits.[3-5] Although rare in Europe and the United States, it has been described in several pediatric groups of different races in southeast Asia, including Thais, Malaysians, and Burmese.[3] The incidence of frontoethmoidal encephalomeningocele in Thailand and Burma is 1:5000 to 1:6000 live births.[6] Treatment for frontoethmoidal encephalomeningocele includes surgery, which requires normal facial parameters for orbital reconstruction.

Existing data of the facial parameters have been collected by using one or more of these methods: direct measurement (anthropometric), radiographic measurement (cephalometric), and sonography measurement of the fetus in utero.[7] Each method has its own limitations in accurately measuring normative standards for craniofacial measurements. Most of the data were collected and applied to adult populations.[1,2,8-11] Available data for the pediatric population is reported to a much lesser extent.[11-13] CT is now considered as the main technique for diagnosis, follow-up, and surgical planning for reconstructive surgery. There is literature that indicates that CT is more accurate and reliable than other cephalometric measures.[14] Furthermore, CT measurements are reliable and reproducible; results of studies have suggested that the accuracy, interobserver error, and intraobserver error are often within an acceptable range (within 1 mm) for craniofacial measurements.[15,16]

Facial characteristics vary across multiple ethnicities.[1,2,8,17,18] There are limited normative craniofacial parameters based on CT

Received March 17, 2020; accepted after revision June 23.

From the Department of Radiology (N.J., S.A.); Division of Plastic Surgery (K.K.), Department of Surgery; Department of Family Medicine (C.P., C.A.), Faculty of Medicine, Chiang Mai University, Sriphum, Muang, Chiang Mai, Thailand.

Please address correspondence to Salita Angkurawaranon, MD, Department of Radiology, Faculty of Medicine, Chiang Mai University, 110 Intawaroros Rd, Sriphum, Muang, Chiang Mai, Thailand 50200; e-mail: salita.ang@cmu.ac.th

Indicates open access to non-subscribers at www.ajnr.org

Indicates article with supplemental on-line photos.

http://dx.doi.org/10.3174/ajnr.A6731

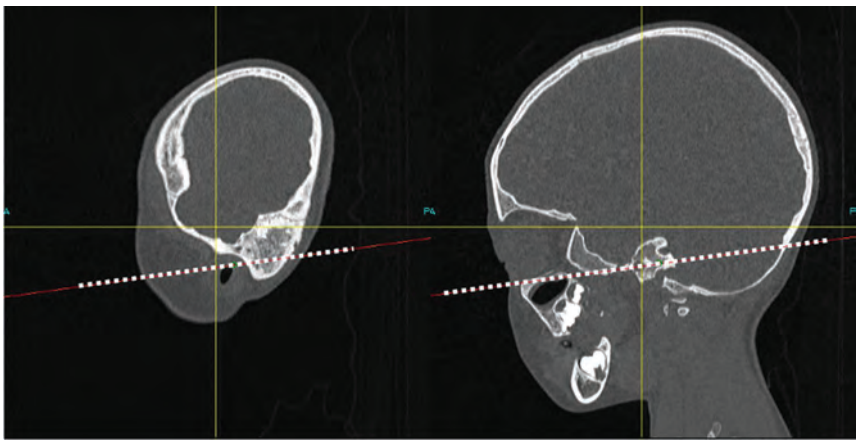

FIG 1. Multiplanar reconstruction CT of the facial bone in the sagittal view. The *dotted line* represents the Frankfort horizontal plane.

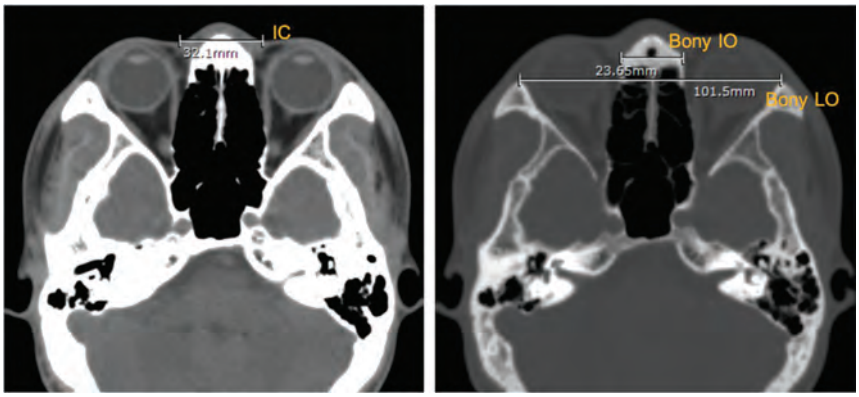

FIG 2. An axial CT of the brain. Left, soft-tissue intercanthal (IC); right, bony interorbital (IO) and bony lateral orbital (LO) distances, which measure 32.10, 23.65, and 101.50 mm, respectively.

among populations in Asian countries, for example, Thailand. One study was conducted in India and used CT from 100 adults,[19] and one study was from Thailand and used CT from 349 patients (ages, 0-21 years), with a broad categorization of age groups into 2- to 3-year age bands with both sexes grouped together.[20] These limited data with relatively small sample sizes make the establishment of normative data difficult because the facial parameters may change rapidly in early life due to cranial growth. The cranium triples in size during the first year of life, is 75% complete at age 2 years, and is 95% complete by age 10 years. Some biologic variation between the sexes also exists because additional growth thereafter is usually complete by ages 16–18 years in girls and 18–20 years in boys. Thus, more-detailed normative data are needed to document normal growth patterns. This will be useful for monitoring and diagnosing those suspected with craniofacial anomalies, such as telecanthus, pseudohypertelorism, or ocular hypertelorism as well as for pediatric patients with frontoethmoidal encephalomeningocele who require surgical reconstruction.

MATERIALS AND METHODS

All CT imaging of the brain, orbit, facial bone, and neck performed at Maharaj Nakorn Chiang Mai Hospital between 2013 and 2016, in patients from birth to 19 years old was retrospectively reviewed. Maharaj Nakorn Chiang Mai Hospital is a tertiary university hospital that acts as a referral center for northern Thailand. Based on the patient's history review and evaluation of imaging, we excluded any patient with a known syndromic disease, craniofacial syndrome, facial trauma and/or infection, and previous surgery that deformed the study area.

All the scans were produced by using 2 multidetector CT machines: 1) Dual sources Somatom Force (Siemens), and 2) Dual sources Somatom Definition, (Siemens). The CT images were reviewed in soft-tissue and bone windows. The 4 key points measured were intercanthal (IC), bony interorbital (IO), bony lateral orbital (LO) distances, and the IO:LO ratio. These points of measurement, determined by the craniofacial surgeon (K.K.) and the radiologists (N.J., S.A.), were considered to be useful for clinical purposes and reproducibility. These points of measure were also those suggested by a previous study from Thailand.[20] All measurements were performed by research assistants who were trained by a board-certificated diagnostic neuroradiologist (S.A.) by using the PACS.

Orientation was in the Frankfort horizontal plane, defined as the highest point on the upper margin of the opening of the external auditory canal and the lowest point on the lower margin of the orbit (Fig 1). After the Frankfort horizontal plane was identified, the measurements of the soft-tissue IC, bony IO, and bony LO distances in millimeters (Fig 2) were performed. The IC distance was defined as the distance between medial canthi. IO and LO distances were defined as the distance between the medial wall of orbits and the distance between the lateral wall of orbits, respectively. Key points of measurement were summarized by using descriptive statistics with the calculation of means and standard deviations (SDs). Data were divided by different age groups. Due to the rapid growth of the skull and face during early life, age groups were categorized by every 3 months until 2 years of age, then every year until age 19 years. Male and female patients were analyzed separately, and comparisons between the sexes within each age group were conducted by using *t*-tests.

RESULTS

A total of 983 scans from 932 individuals were reviewed, of whom 554 were males (59.4%) and 378 were females (40.6%). The mean ± SD age for males was 9.0 ± 6.5 years and for females

Table 1: Values for soft-tissue intercanthal distances by age group and sex

Age Group	IC Distance, Mean ± Standard Deviation, mm			
	All	Males	Females	*P*
0–3 months ($n = 76$)	22.1 ± 2.8	22.6 ± 2.7	21.3 ± 2.7	.05
>3–6 months ($n = 41$)	23.9 ± 2.7	24.5 ± 2.9	23.3 ± 2.4	.15
>6–9 months ($n = 40$)	24.1 ± 2.5	24.8 ± 2.2	23.7 ± 2.7	.17
>9–12 months ($n = 30$)	24.3 ± 2.1	24.0 ± 2.1	24.8 ± 2.1	.34
>12–15 months ($n = 25$)	26.1 ± 3.3	26.3 ± 3.9	25.9 ± 2.3	.75
>15–18 months ($n = 14$)	25.6 ± 3.3	24.8 ± 2.1	26.3 ± 4.0	.42
>18–21 months ($n = 21$)	26.4 ± 3.4	26.5 ± 3.6	26.4 ± 3.3	.95
>21–24 months ($n = 12$)	27.3 ± 3.8	26.2 ± 3.8	28.7 ± 3.8	.29
>2–3 years ($n = 49$)	27.1 ± 3.3	27.8 ± 3.1	26.1 ± 3.2	.08
>3–4 years ($n = 36$)	27.8 ± 3.3	28.3 ± 2.5	27.1 ± 3.0	.26
>4–5 years ($n = 42$)	28.0 ± 2.8	27.4 ± 3.0	28.9 ± 2.3	.08
>5–6 years ($n = 41$)	27.7 ± 2.9	28.2 ± 3.0	27.0 ± 2.7	.21
>6–7 years ($n = 36$)	29.3 ± 3.4	30.1 ± 3.9	28.7 ± 2.8	.20
>7–8 years ($n = 29$)	29.2 ± 3.8	28.7 ± 3.4	30.1 ± 4.5	.37
>8–9 years ($n = 26$)	29.3 ± 2.6	29.4 ± 2.7	29.1 ± 2.6	.71
>9–10 years ($n = 30$)	30.7 ± 3.3	31.4 ± 3.8	30.0 ± 2.3	.19
>10–11 years ($n = 31$)	29.5 ± 3.6	29.0 ± 2.7	30.3 ± 4.5	.31
>11–12 years ($n = 33$)	30.2 ± 3.9	30.3 ± 4.6	30.0 ± 2.0	.80
>12–13 years ($n = 32$)	31.1 ± 3.2	31.8 ± 3.1	29.2 ± 2.7	.03
>13–14 years ($n = 42$)	31.4 ± 4.4	30.9 ± 3.7	31.9 ± 5.2	.50
>14–15 years ($n = 43$)	31.5 ± 3.9	31.6 ± 3.4	31.1 ± 5.0	.68
>15–16 years ($n = 69$)	32.9 ± 4.6	33.9 ± 4.6	31.8 ± 4.3	.05
>16–17 years ($n = 71$)	32.8 ± 3.9	32.9 ± 4.0	32.8 ± 3.5	.91
>17–18 years ($n = 57$)	32.7 ± 3.9	33.6 ± 3.8	30.4 ± 3.2	<.01
>18–19 years ($n = 57$)	32.7 ± 4.2	34.2 ± 4.1	30.2 ± 2.7	<.01

Table 2: Values for bony interorbital distances by age group and sex

Age Group (No. Scans Per Group)	IO Distance, Mean ± Standard Deviation, mm			
	All	Males	Females	*P*
0–3 months (76)	16.4 ± 1.9	16.5 ± 2.1	16.1 ± 1.8	.39
>3–6 months (41)	18.2 ± 2.0	18.4 ± 2.6	18.0 ± 1.3	.57
>6–9 months (40)	17.7 ± 2.1	19.5 ± 2.4	17.2 ± 1.8	.07
>9–12 months (30)	18.1 ± 2.0	18.1 ± 1.6	17.9 ± 2.6	.79
>12–15 months (25)	18.8 ± 2.2	18.9 ± 2.0	18.5 ± 2.5	.66
>15–18 months (14)	18.5 ± 2.3	18.2 ± 1.6	18.7 ± 2.7	.67
>18–21 months (21)	19.1 ± 2.8	19.2 ± 2.0	19.0 ± 3.7	.90
>21–24 months (12)	18.6 ± 1.4	19.1 ± 1.6	18.1 ± 1.7	.22
>2–3 years (49)	19.3 ± 2.1	20.0 ± 2.0	18.3 ± 1.8	<.01
>3–4 years (36)	19.8 ± 2.3	19.8 ± 2.4	19.8 ± 2.3	.94
>4–5 years (42)	20.4 ± 2.6	20.1 ± 2.0	20.8 ± 3.3	.37
>5–6 years (41)	20.5 ± 2.4	20.7 ± 2.3	20.3 ± 2.7	.69
>6–7 years (36)	22.3 ± 2.4	22.9 ± 2.8	21.9 ± 2.0	.25
>7–8 years (29)	22.5 ± 3.0	22.2 ± 2.8	21.1 ± 3.3	.43
>8–9 years (26)	22.2 ± 2.1	22.8 ± 2.1	21.1 ± 1.7	.04
>9–10 years (30)	23.1 ± 2.5	24.1 ± 2.1	21.7 ± 2.3	<.01
>10–11 years (31)	23.1 ± 2.0	22.9 ± 2.4	23.3 ± 1.2	.66
>11–12 years (33)	22.8 ± 2.3	23.0 ± 2.7	22.4 ± 1.6	.48
>12–13 years (32)	24.3 ± 3.5	24.6 ± 3.6	23.6 ± 3.7	.49
>13–14 years (42)	24.2 ± 3.3	23.9 ± 3.1	24.4 ± 3.5	.64
>14–15 years (43)	24.6 ± 3.1	24.8 ± 3.2	24.1 ± 2.8	.48
>15–16 years (69)	24.6 ± 3.0	25.4 ± 3.3	23.7 ± 2.5	.02
>16–17 years (71)	25.3 ± 3.1	25.6 ± 3.0	24.4 ± 3.3	.13
>17–18 years (57)	24.7 ± 2.9	25.3 ± 2.6	23.2 ± 3.2	.01
>18–19 years (57)	24.8 ± 2.6	25.7 ± 2.2	23.4 ± 2.7	<.01

was 7.8 ± 6.4 years. The mean measurements of soft tissue IC, bony IO, and bony LO distances for both sexes, categorized by age group, are shown in Tables 1–3. As expected, there was a rapid increase in the IC distance in the first 2 years of life. The average ± SD IC distance was 22.1 ± 2.8 mm among neonates (0–3 months). At 22–24 months, the average ± SD IC distance was 27.3 ± 3.8 mm or approximately 80% of the mean IC distances among adults ages > 18 years (Table 1 and On-line Fig 1). The average IC distances increased with age. By the age of 8 years, the mean IC distance was 29.2 mm or approximately 90% of the mean IC distance among adults aged > 18 years. Small differences between the sexes, between 1 and 2 mm, were also detected among those >15 years of age. On average, after the age of 15 years, males tended to have larger IC distances than did the females. By age 15 years, among the males, the average IC distance was approximately 90% of the mean IC distances among adult men at >18 years. For females, by age 15 years, the average IC distance was already similar to the mean IC distances among adult women at age >18 years (Table 1).

This pattern of rapid growth in early life and difference between males and females aged >15 years was also observed from IO distances and LO distances. Among neonates (ages, 0–3 months), the average IO distance was 16.4 mm and was 18.6 mm by age 2 years. By the age of 8 years, the average IO distance as 22.5 mm or 90% of the mean IO distance in adulthood. Among those >15 years of age, the mean IO distance was 1–2 mm longer for men compared with women (Table 2 and On-line Fig 2). As demonstrated in Table 3, by 2 years of age, the average LO distance (77.3 mm) was also nearly 80% of the average LO distances among adults >18 years (90.0 mm). By the age of 8 years, the average LO distance (88.1 mm) was also almost 90% of the average adult LO distance at the age of 18 years. Similar to IC and IO distances, after the age of 15 years, the average LO size was 3–5 mm longer among men compared with women (On-line Fig 3). Although there is evidence for rapid growth and small differences between the sexes in IO and LO distances after the age of 15 years, the mean ratios between IO/LO were relatively stable, at 0.25, across age groups and between the sexes (Table 4). Ninety percent of all the scans had an IO:LO ratio between 0.22 and 0.28 (Fig 3).

DISCUSSION

This study aimed to document normative facial parameters among children, adolescents, and young adults in Thailand by using CT. Consistent patterns emerged that facial parameters were approximately 80% developed within the first 2 years of life and 90% developed by the age of 8 years. However, small differences between the sexes in distances after the age of 15 years also existed. Despite different growth rates across different ages and sexes, the ratios between IO:LO were relatively constant.

Table 3: Values for bony lateral orbital (LO) distances by age group and sex

Age Group (No. Scans Per Group)	LO Distance, Mean ± Standard Deviation, mm			
	All	Males	Females	*P*
0–3 months (76)	63.3 ± 4.4	63.7 ± 4.5	62.5 ± 4.2	.23
>3–6 months (41)	69.3 ± 4.4	69.6 ± 4.8	69.0 ± 4.1	.67
>6–9 months (40)	72.6 ± 3.5	64.7 ± 3.0	71.2 ± 3.1	<.01
>9–12 months (30)	73.1 ± 3.4	73.9 ± 3.3	71.9 ± 3.2	.12
>12–15 months (25)	75.5 ± 3.4	76.1 ± 3.3	74.6 ± 3.4	.30
>15–18 months (14)	76.1 ± 3.9	76.7 ± 3.8	75.6 ± 4.2	.63
>18–21 months (21)	77.3 ± 3.2	78.0 ± 3.1	76.3 ± 3.1	.22
>21–24 months (12)	77.3 ± 2.8	78.3 ± 2.9	75.7 ± 2.1	.12
>2–3 years (49)	80.1 ± 3.6	81.8 ± 3.0	77.8 ± 3.1	<.01
>3–4 years (36)	80.6 ± 4.6	81.5 ± 4.8	79.5 ± 4.2	.20
>4–5 years (42)	82.5 ± 3.7	82.2 ± 4.0	83.0 ± 3.4	.45
>5–6 years (41)	83.4 ± 3.5	83.9 ± 4.0	82.7 ± 2.6	.31
>6–7 years (36)	86.5 ± 3.7	87.5 ± 3.6	85.7 ± 3.6	.13
>7–8 years (29)	88.1 ± 3.7	88.8 ± 3.4	87.0 ± 4.0	.23
>8–9 years (26)	88.4 ± 3.7	89.2 ± 3.4	87.1 ± 3.9	.16
>9–10 years (30)	90.7 ± 3.9	91.7 ± 3.3	89.4 ± 4.3	.11
>10–11 years (31)	90.4 ± 3.6	90.7 ± 4.3	90.1 ± 2.6	.66
>11–12 years (33)	91.0 ± 4.3	91.1 ± 4.7	90.7 ± 3.5	.77
>12–13 years (32)	83.9 ± 5.4	94.6 ± 5.6	92.3 ± 4.7	.28
>13–14 years (42)	93.9 ± 4.7	94.0 ± 4.4	93.9 ± 5.1	.97
>14–15 years (43)	96.3 ± 5.0	97.2 ± 4.9	94.3 ± 4.7	.08
>15–16 years (69)	97.1 ± 4.6	99.0 ± 4.3	95.0 ± 4.0	<.01
>16–17 years (71)	98.6 ± 4.5	99.5 ± 4.7	96.2 ± 3.2	<.01
>17–18 years (57)	98.9 ± 5.0	100.6 ± 3.7	94.2 ± 5.1	<.01
>18–19 years (57)	99.0 ± 5.3	100.8 ± 4.9	96.0 ± 4.6	<.01

Table 4: Values for bony interorbital (IO) to lateral orbital (LO) distances by age group and sex

Age Group (No. Scans Per Group)	IO to LO Distance, Mean ± Standard Deviation, mm			
	All	Males	Females	*P*
0–3 months (76)	0.26 ± 0.02	0.26 ± 0.02	0.26 ± 0.02	.85
>3–6 months (41)	0.26 ± 0.02	0.26 ± 0.02	0.26 ± 0.02	.79
>6–9 months (40)	0.24 ± 0.03	0.25 ± 0.03	0.24 ± 0.02	.50
>9–12 months (30)	0.25 ± 0.02	0.25 ± 0.02	0.25 ± 0.03	.76
>12–15 months (25)	0.25 ± 0.02	0.25 ± 0.02	0.25 ± 0.03	.95
>15–18 months (14)	0.24 ± 0.02	0.24 ± 0.02	0.25 ± 0.02	.45
>18–21 months (21)	0.25 ± 0.03	0.24 ± 0.02	0.25 ± 0.04	.82
>21–24 months (12)	0.24 ± 0.01	0.24 ± 0.01	0.24 ± 0.01	.53
>2–3 years (49)	0.24 ± 0.02	0.24 ± 0.02	0.24 ± 0.02	.10
>3–4 years (36)	0.25 ± 0.02	0.24 ± 0.02	0.25 ± 0.03	.46
>4–5 years (42)	0.25 ± 0.03	0.24 ± 0.02	0.25 ± 0.03	.45
>5–6 years (41)	0.25 ± 0.02	0.25 ± 0.02	0.25 ± 0.03	.96
>6–7 years (36)	0.26 ± 0.02	0.26 ± 0.03	0.26 ± 0.02	.48
>7–8 years (29)	0.26 ± 0.03	0.25 ± 0.03	0.26 ± 0.03	.20
>8–9 years (26)	0.25 ± 0.02	0.26 ± 0.02	0.24 ± 0.02	.10
>9–10 years (30)	0.25 ± 0.02	0.26 ± 0.02	0.24 ± 0.02	.02
>10–11 years (31)	0.25 ± 0.02	0.25 ± 0.02	0.26 ± 0.01	.36
>11–12 years (33)	0.25 ± 0.02	0.25 ± 0.02	0.25 ± 0.01	.49
>12–13 years (32)	0.26 ± 0.03	0.26 ± 0.03	0.25 ± 0.03	.72
>13–14 years (42)	0.26 ± 0.03	0.25 ± 0.03	0.26 ± 0.03	.55
>14–15 years (43)	0.25 ± 0.03	0.26 ± 0.03	0.25 ± 0.02	.99
>15–16 years (69)	0.25 ± 0.02	0.26 ± 0.03	0.25 ± 0.02	.29
>16–17 years (71)	0.26 ± 0.02	0.26 ± 0.02	0.25 ± 0.03	.58
>17–18 years (57)	0.25 ± 0.02	0.25 ± 0.02	0.25 ± 0.03	.43
>18–19 years (46)	0.25 ± 0.02	0.26 ± 0.02	0.24 ± 0.02	.07

Compared with a study conducted in the United States that examined orbital measurements of healthy infants and children,[12] our average soft-tissue IC distances were slightly lower, whereas, the average bony LO distances were of similar values and our bony IO average distance was longer. The findings were not surprising because facial parameters differ among difference ethnicities.[1,21,22] Our facial parameters were in the line with a recent report from Thailand.[20]

Similar to previous literature, there were no significant differences in our measured parameters between males and females from birth until the early teenage years.[23,24] However, we noticed differences in our measured parameters between the sexes at ages ≥15 years. A previous study conducted in Thailand by using direct anthropometric measurements also found significant differences between the sexes in their binocular width, which was concordant with our bony LO distance in the adolescent age group.[22] Another study, from Malaysia, that used 3D facial imaging and anthropometric techniques also found some differences in LO and IC distances between the sexes in late adolescence.[25] This is not surprising because studies documented that, unlike males, facial growth is usually completed by the age of 14–15 years among females.[26,27]

Our study has some limitations with regard to using samples from a single referral center in northern Thailand and of using a hospital-based sample. However, our results were in line with the recent study conducted in Bangkok, which indicated that their sample was representative of the normal Thai population.[20] There were limited longitudinal data because most of the scans used were of unique individuals rather than repeated follow-up. There is literature that indicates that the cross-sectional design is likely to underestimate growth rates but is useful for determining cutoff normative values because they are more likely to be representative of the healthy population.[20,28] The strength of our study is the large number of scans, which allowed more-detailed age- and sex-specific normative values not previously published in an Asian population.

Based on the strengths of our study, our findings have several clinical implications. Establishing normative values is important

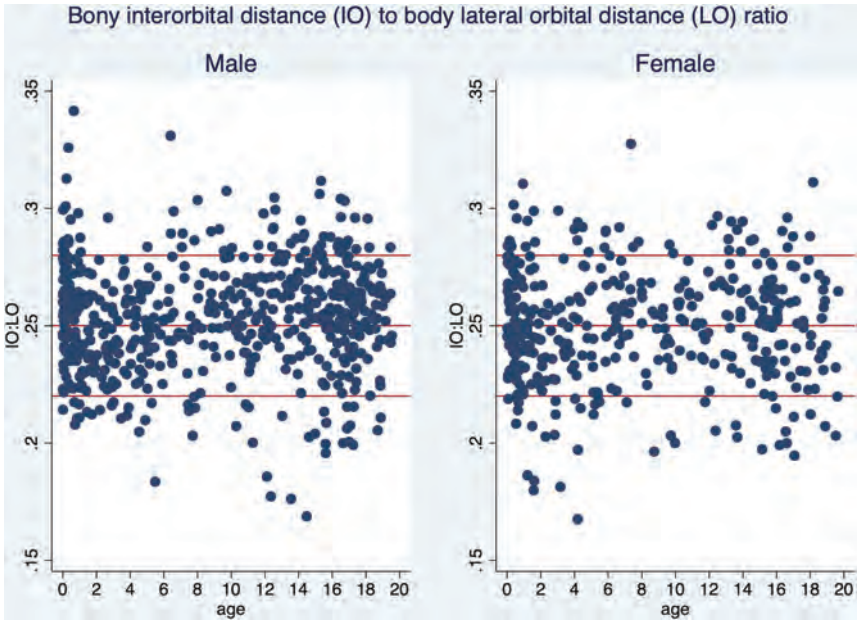

FIG 3. The ratio of the interorbital (IO) to bony lateral orbital (LO) distances by age and sex.

because a diagnosis of craniofacial abnormality, for example, telecanthus, relies on age- and sex-specific means and SDs. To avoid or reduce the number of unnecessary postoperative CTs, the values of soft-tissue IC can be used for follow-up of patients after craniofacial surgery, such as frontoethmoidal encephalomeningocele correction, craniofacial cleft correction, orbital translocation, and facial bipartition. The understanding of normal growth development also helps identify the timing of surgery of craniofacial anomalies, such as frontonasal dysplasia, hypertelorism, and craniofacial cleft because correction of the orbital complex or glabella region should be performed when the bones are nearly fully grown. Results of our study suggest that the facial parameters are almost fully developed around the age of 8 years in this population. The finding that the IO:LO ratio is relatively constant, at 0.25, across ages and sexes helps inform surgeons on the aesthetic or cosmetic facial ratio for pre-, intra-, and postoperative evaluations.

CONCLUSIONS

This study provides detailed age-and sex-specific normative data of the craniofacial measurement in children and adolescents in Thailand based on CT imaging. These data can be used for evaluating individual patients with craniofacial abnormalities as well as determining the treatment in Thai and Asian populations where craniofacial abnormalities, for example, frontoethmoidal encephalomeningocele, are common.

REFERENCES

1. Farkas LG, Katic MJ, Forrest CR. **Comparison of craniofacial measurements of young adult African-American and North American white males and females.** *Ann Plast Surg* 2007;59:692–98 CrossRef Medline
2. Patil SB, Kale SM, Math M, et al. **Anthropometry of the eyelid and palpebral fissure in an Indian population.** *Aesthet Surg J* 2011;31:290–94 CrossRef Medline
3. Richards CG. **Frontoethmoidal meningoencephalocele: a common and severe congenital abnormality in South East Asia.** *Arch Dis Child* 1992;67:717–19 CrossRef Medline
4. Dumrongpisutikul N, Triampo A, Janthanimi P, et al. **Incidence of associated brain and ophthalmic anomalies in frontoethmoidal encephalomeningocele evaluated by multidetector computed tomography facial bone imaging.** *J Craniofac Surg* 2017;28:454–58 CrossRef Medline
5. Meling TR, Due-Tønnessen BJ, Helseth E, et al. **Frontoethmoidal meningoencephaloceles.** *Tidsskr Nor Laegeforen* 2000;120:2250–52 Medline
6. Chowchuen B, Thanapaisal C, Chowchuen P, et al. **Frontoethmoidal meningoencephalocele: challenges and the Tawanchai center's long-term integrated management.** *J Med Assoc Thai* 2011;94(Suppl):S129–40 Medline
7. Harris R, Nagarkar P, Amirlak B. **Varied definitions of nasolabial angle: searching for consensus among rhinoplasty surgeons and an algorithm for selecting the ideal method.** *Plast Reconstr Surg Glob Open* 2016;4:e752 CrossRef Medline
8. Le TT, Farkas LG, Ngim RCK, et al. **Proportionality in Asian and North American Caucasian faces using neoclassical facial canons as criteria.** *Aesthetic Plast Surg* 2002;26:64–69 CrossRef Medline
9. Farkas LG, Tompson BD, Katic MJ, et al. **Differences between direct (anthropometric) and indirect (cephalometric) measurements of the skull.** *J Craniofac Surg* 2002;13:105–10; discussion 109–10 CrossRef Medline
10. Park DH, Choi WS, Yoon SH, et al. **Anthropometry of Asian eyelids by age.** *Plast Reconstr Surg* 2008;121:1405–13 CrossRef Medline
11. Laestadius ND, Aase JM, Smith DW. **Normal inner canthal and outer orbital dimensions.** *J Pediatr* 1969;74:465–68 CrossRef Medline
12. Pool GM, Didier RA, Bardo D, et al. **Computed tomography-generated anthropometric measurements of orbital relationships in normal infants and children.** *J Neurosurg Pediatr* 2016;18:201–06 CrossRef Medline
13. Farkas LG, Hreczko TM, Katic MJ, et al. **Proportion indices in the craniofacial regions of 284 healthy North American white children between 1 and 5 years of age.** *J Craniofac Surg* 2003;14:13–28 CrossRef Medline
14. Matteson SR, Bechtold W, Phillips C, et al. **A method for three-dimensional image reformation for quantitative cephalometric analysis.** *J Oral Maxillofac Surg* 1989;47:1053–61 CrossRef Medline
15. Christiansen EL, Thompson JR, Kopp S. **Intra- and inter-observer variability and accuracy in the determination of linear and angular measurements in computed tomography: an in vitro and in situ study of human mandibles.** *Acta Odontol Scand* 1986;44:221–29 CrossRef Medline
16. Waitzman AA, Posnick JC, Armstrong DC, et al. **Craniofacial skeletal measurements based on computed tomography: part I. Accuracy and reproducibility.** *Cleft Palate Craniofac J* 1992;29:112–17 CrossRef Medline
17. Farkas LG. **Accuracy of anthropometric measurements: past, present, and future.** *Cleft Palate Craniofac J* 1996;33:10–18; discussion 19–22 CrossRef Medline
18. Richtsmeier JT, Paik CH, Elfert PC, et al. **Precision, repeatability, and validation of the localization of cranial landmarks using**

computed tomography scans. *Cleft Palate Craniofac J* 1995;32:217–27 CrossRef Medline
19. Gupta V, Prabhakar A, Yadav M, et al. **Computed tomography imaging-based normative orbital measurement in Indian population.** *Indian J Ophthalmol* 2019;67:659–63 CrossRef Medline
20. Chatdokmaiprai C, Kiranantawat K, Lertsithichai P, et al. **Normative data of the interorbital distance in Thai population.** *J Craniofac Surg* 2018;29:1939–44 CrossRef Medline
21. Prendergast PM. Facial proportions. In: Erian A, Shiffman MA, eds. *Advanced Surgical Facial Rejuvenation*. New York: Springer-Verlag Berlin Heidelberg; 2012:15–22
22. Farkas LG, Katic MJ, Forrest CR, et al. **International anthropometric study of facial morphology in various ethnic groups/races.** *J Craniofac Surg* 2005;16:615–46 CrossRef Medline
23. Freihofer HP. **Inner intercanthal and interorbital distances.** *J Maxillofac Surg* 1980;8:324–26 CrossRef Medline
24. Méhes K, Kitzvéger E. **Inner canthal and intermamillary indices in the newborn infant.** *J Pediatr* 1974;85:90–92 CrossRef Medline
25. Othman SA, Majawit LP, Wan Hassan WN, et al. **Anthropometric study of three-dimensional facial morphology in Malay adults.** *PLoS One* 2016;11:e0164180 CrossRef Medline
26. Palmert MR, Dunkel L. **Clinical practice. Delayed puberty.** *N Engl J Med* 2012;366:443–53 CrossRef Medline
27. Ferrario VF, Sforza C, Poggio CE, et al. **Craniofacial growth: a three-dimensional soft-tissue study from 6 years to adulthood.** *J Craniofac Genet Dev Biol* 1998;18:138–49 Medline
28. Preece MA. **Standardization of growth.** *Acta Paediatr Scand Suppl* 1989;78:57–64; discussion 81–83 CrossRef Medline

MRI Spectrum of Brain Involvement in Sphingosine-1-Phosphate Lyase Insufficiency Syndrome

K.W. Martin, N. Weaver, K. Alhasan, E. Gumus, B.R. Sullivan, M. Zenker, F. Hildebrandt, and J.D. Saba

ABSTRACT

SUMMARY: *SGPL1* encodes sphingosine-1-phosphate lyase, the final enzyme of sphingolipid metabolism. In 2017, a condition featuring steroid-resistant nephrotic syndrome and/or adrenal insufficiency associated with pathogenic *SGPL1* variants was reported. In addition to the main features of the disease, patients often exhibit a range of neurologic deficits. In a handful of cases, brain imaging results were described. However, high-quality imaging results and a systematic analysis of brain MR imaging findings associated with the condition are lacking. In this study, MR images from 4 new patients and additional published case reports were reviewed by a pediatric neuroradiologist. Analysis reveals recurring patterns of features in affected patients, including isolated callosal dysgenesis and prominent involvement of the globus pallidus, thalamus, and dentate nucleus, with progressive atrophy and worsening of brain lesions. MR imaging findings of abnormal deep gray nuclei, microcephaly, or callosal dysgenesis in an infant or young child exhibiting other typical clinical features of sphingosine-1-phosphate lyase insufficiency syndrome should trigger prompt genetic testing for *SGPL1* mutations.

ABBREVIATIONS: PKAN = pantothenate kinase-associated neurodegeneration; S1P = sphingosine-1-phosphate; SPLIS = sphingosine-1-phosphate lyase insufficiency syndrome

Sphingosine-1-phosphate lyase insufficiency syndrome (SPLIS), also referred to as nephrotic syndrome type 14, is a recently discovered severe inborn error of metabolism caused by biallelic pathogenic variants of *SGPL1*, the gene encoding sphingosine-1-phosphate lyase.[1] Sphingosine-1-phosphate lyase is an intracellular enzyme responsible for catalyzing the final step in sphingolipid degradation, in which the universal sphingolipid breakdown product sphingosine-1-phosphate (S1P) is irreversibly degraded (Fig 1).[2] S1P is a bioactive lipid that mediates signals through a family of G protein-coupled receptors that regulate lymphocyte trafficking, vascular integrity, and other physiologic and developmental processes.[3,4]

The first descriptions of a human syndrome of sphingosine-1-phosphate lyase insufficiency associated with inactivating mutations in *SGPL1* and sphingolipid accumulation were reported in 2017, and during the subsequent 2 years, approximately 45 patients have been identified in total worldwide (including our unpublished cohort of 7 new patients).[5-11] A wide spectrum of severity has been observed, ranging from nonimmune hydrops fetalis to survival into at least the third decade. However, most patients with SPLIS exhibit severe manifestations of ≥1 of the main clinical features including steroid-resistant nephrotic syndrome, primary adrenal insufficiency, lymphopenia, ichthyosis, hypothyroidism, micropenis, and neurologic defects.

Neurologic abnormalities were reported in >50% of the cases. The incidence of neurologic complications may be higher than reported because neurologic status could not be determined in cases resulting in fetal loss or in patients requiring basic life support. Neurologic manifestations may include macrocephaly, microcephaly, hypotonia, cranial nerve palsies, sensorineural hearing loss, seizures, Charcot-Marie-Tooth-type peripheral neuropathy, ataxia, developmental delay and/or regression, developmental brain anomalies, and severe neurologic deterioration resulting in death.

Brain imaging results have been reported for some patients with SPLIS (On-line Table). Lesions including cortical atrophy; contrast enhancement of the midbrain, pons, and/or cerebellum;

Received March 4, 2020; accepted after revision June 1.

From the Department of Radiology (K.W.M.), UCSF Benioff Children's Hospital Oakland, Oakland, California; Division of Human Genetics (N.W.), Cincinnati Children's Hospital Medical Center, Cincinnati, Ohio; Department of Pediatrics (K.A.), College of Medicine, King Saud University, Riyadh, Saudi Arabia; Department of Medicine (E.G.), Harran University, Sanliurfa, Turkey; Division of Clinical Genetics (B.R.S.), Children's Mercy, Kansas City, Missouri; Department of Pediatrics (B.R.S.), University of Missouri, Kansas City, Missouri; Institute of Genetics (M.Z.), Otto von Guericke Universitat, Magdeburg, Germany; Department of Pediatrics (F.H.), Boston Children's Hospital, Harvard Medical School, Boston, Massachusetts; and UCSF Department of Pediatrics (J.D.S.), University of California, San Francisco, San Francisco, California.

This work was supported by Public Health Service grant R01DK115669 (J.D.S.), a grant from the Swim Across America Foundation (J.D.S.), and the National Institutes of Health grant R01 NIH-DK076683 (F.H.).

Please address correspondence to Julie D. Saba, MD, PhD Children's Hospital, Oakland Research Institute, 5700 Martin Luther King Jr. Way, Oakland, CA 94609; e-mail: Julie.Saba@ucsf.edu

Indicates open access to non-subscribers at www.ajnr.org
Indicates article with supplemental on-line table.

http://dx.doi.org/10.3174/ajnr.A6746

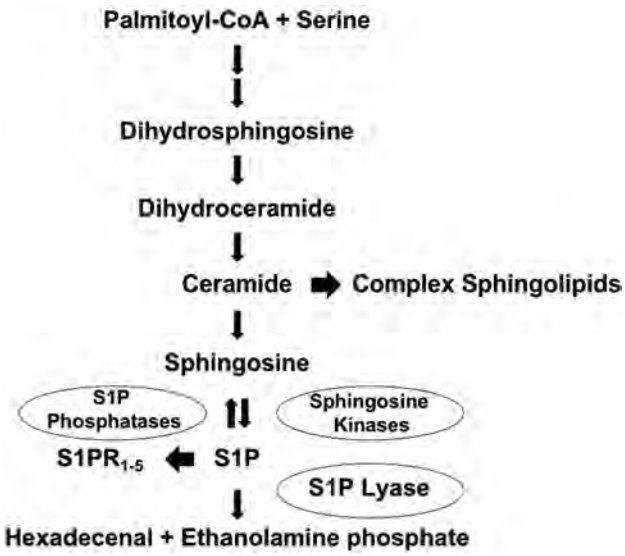

FIG 1. Sphingolipid metabolic pathway. Sphingolipid biosynthesis leads to the formation of ceramide, the main building block of complex sphingolipids. Ceramide is degraded to sphingosine. Sphingosine is phosphorylated by sphingosine kinases, leading to formation of S1P, which has intracellular activities and also serves as a ligand for S1P receptors ($S1PR_{1–5}$). S1P can be dephosphorylated by specific and nonspecific lipid phosphatases, regenerating sphingosine. Alternatively, S1P can be irreversibly degraded by sphingosine-1-phosphate lyase (S1P lyase), which controls the sole exit point of sphingolipid metabolism. S1P catabolism by sphingosine-1-phosphate lyase results in formation of hexadecenal and ethanolamine phosphate. CoA indicates coenzyme A.

and developmental anomalies were described. We have performed a detailed study of 4 new patients with genetically confirmed SPLIS including 1 infant in whom the progressive nature of the disease was evident on serial MR imaging. Interpreted in the context of other reported cases of SPLIS, our findings reveal several patterns of MR imaging changes that may aid in the recognition of this novel and atypical (nonlysosomal) sphingolipidosis.

MATERIALS AND METHODS

The main focus of this study is the MR images of the brain from 4 new unrelated patients with biallelic *SGPL1* pathogenic variants identified by whole-exome sequencing and referred to us from the King Saud University College of Medicine in Saudi Arabia, the Cincinnati Children's Hospital Medical Center in the United States, and the Harran University Department of Medicine in Turkey. Individuals had testing that was interpreted by a College of American Pathologists/Clinical Laboratory Improvement Amendments–certified molecular testing lab. Pathogenicity calling followed the American College of Medical Genetics guidelines. MR imaging studies were systematically reviewed by a qualified pediatric neuroradiologist. Images from a fifth patient who had been previously reported were obtained for review.[5] CT imaging, when available, did not reveal abnormalities even when MR imaging findings for the same patient at the same time point were abnormal. We have not included these negative CT results in our report. We retrospectively reviewed MR images from published case reports by Lovric et al,[5] Prasad et al,[6] Bamborschke et al,[10] and Settas et al.[11] The study was conducted in accordance with human subject protocols and consent forms that were reviewed and approved by the institutional review boards of UCSF Benioff Children's Hospital Oakland, Cincinnati Children's Hospital Medical Center, King Saud University College of Medicine, and the Harran University Department of Medicine.

Patients

The first patient, from Saudi Arabia, was homozygous for c.1079G>T; p. Gly360Val *SGPL1* pathogenic variant as determined by whole-exome sequence analysis at 3 years of age. She developed a squint at 1 year of age requiring surgical correction, steroid-resistant nephrotic syndrome at 3 years of age, and left-radial neuritis several months later. At 4 years of age, she lost the ability to walk or sit with support. Despite treatment for presumed autoimmune encephalitis with intravenous immunoglobulin, high-dose prednisolone, baclofen, biotin, trihexphenydyl, clonazepam, and, later, pyridoxine, she continued to deteriorate from chronic progressive encephalopathy. Her course was further complicated by suppression of the thyroid gland due to biotin, which resolved without medication. She also exhibited lymphopenia and was being investigated for adrenal insufficiency. However, testing for the latter could not be completed because she was on high corticosteroid doses. She died of presumed sepsis at 4.5 years of age. MR imaging was performed at 4 years of age.

The second patient, from Saudi Arabia, was homozygous for c.665G>A; p.Arg222Gln *SGPL1* pathogenic variant as determined by whole-exome sequence analysis at 9 years of age. The patient presented at 6 years of age with convulsions, electrolyte disturbance, and hyperpigmentation and was diagnosed with ichthyosis and adrenal insufficiency, which was treated with fludrocortisone and hydrocortisone. The patient exhibited proteinuria at first presentation, followed by fluctuating renal dysfunction during the next 3 years. Renal biopsy at 9 years of age revealed focal segmental glomerulosclerosis. Dialysis was instituted due to chronic renal failure at that time. He also exhibited lymphopenia. Other than seizures at presentation, the patient had no neurologic problems until he was diagnosed with severe left carpal tunnel syndrome at 6 years of age with persistent severe weakness in the left arm. The patient remains alive and is scheduled for kidney transplantation at the time of this report. MR imaging was performed at 6 years of age.

The third patient, from the United States, was compound heterozygous for c.868-T > C; p.Phe290Leu; c.993C>G; p.Tyr331* *SGPL1* pathogenic variants as determined by whole-exome sequence analysis at 13 months of age. This patient had adrenal calcifications and polyhydramnios on fetal sonography imaging. Prenatal MR imaging findings of the brain were normal. His perinatal course was complicated by apnea, bilateral hearing loss, immunodeficiency including lymphopenia, and nephrotic syndrome accompanied by massive kidney enlargement. The latter required bilateral nephrectomy and peritoneal dialysis at 3 months of age. At 1 year of age, he was diagnosed with adrenal insufficiency and esotropia. At 13 months, the patient began exhibiting developmental regression. His neurologic status

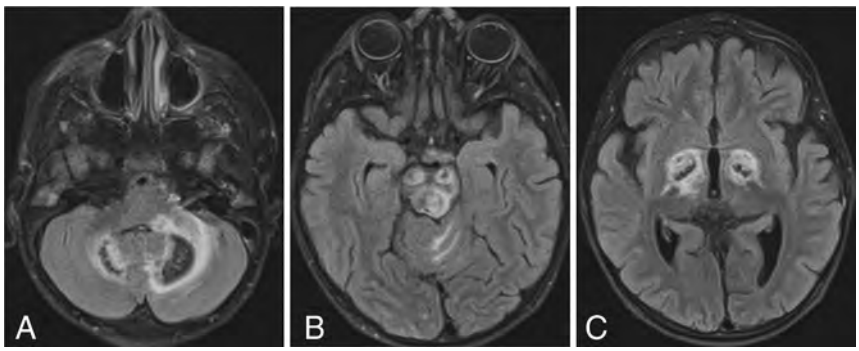

FIG 2. SPLIS with mineral deposition and edema. T2-FLAIR axial MR images of a 4-year-old child with SPLIS show involvement of the dentate nuclei (*A*), cerebral peduncles and tectum (*B*), and globi pallidi (*C*). There is surrounding edema. Loss of central signal is attributed to calcium on the basis of the analysis of susceptibility-weighted images in another patient. The findings predominantly involve dopaminergic neurons.

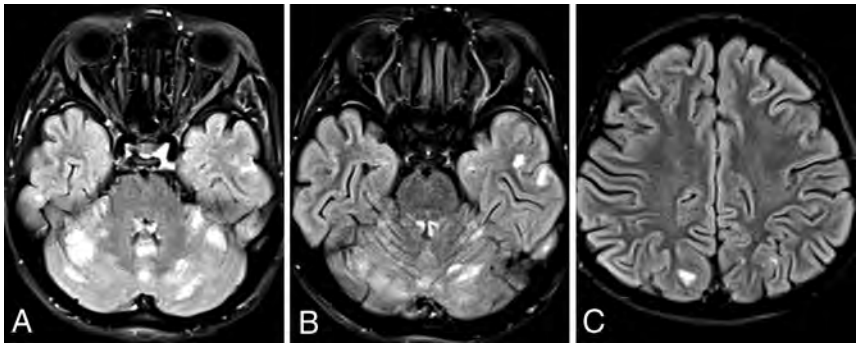

FIG 3. SPLIS with cerebral and cerebellar cortical lesions. T2-FLAIR axial images of an 8-year-old child with SPLIS show multiple focal hyperintense lesions involving cerebellar and cortical gray matter with some lesions extending into the subcortical white matter (*B* and *C*).

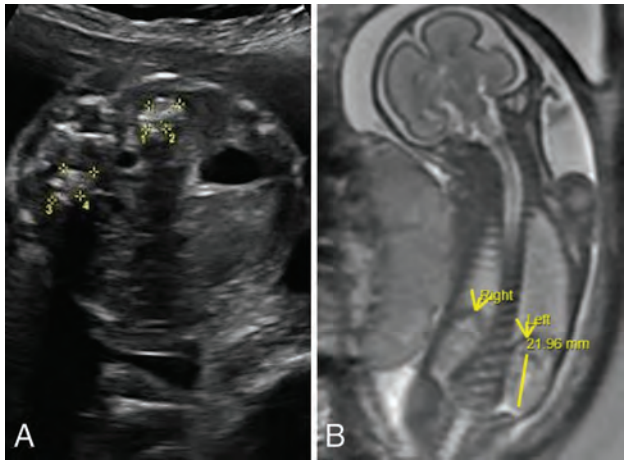

FIG 4. SPLIS at 25 weeks' gestation. Fetal sonography shows a transverse image of the abdomen (*A*) with echogenic enlarged adrenal glands with posterior shadowing presumably due to calcification. Fetal whole-body MR imaging (*B*) shows normal-appearing kidneys and adrenal glands. Mineralization of the adrenal glands is not apparent on this T2-weighted sequence.

deteriorated steadily with intermittent seizures until his death at 17 months of age. MR imaging of the brain was performed at 25 weeks' gestation, and postnatally at 6 weeks, 13 months, and 15 months of age.

The fourth patient, from Turkey, was homozygous for c.44A>G; p.Tyr15Cys *SGPL1* pathogenic variant as determined by whole-exome sequence analysis at 2 years of age. The parents were consanguineous, and the presence of the pathogenic variant in each parent was confirmed by Sanger sequencing. The patient had a healthy infancy, but experienced a fall from the bed at 1 year of age, resulting in a hospital emergency department visit, with no traumatic injuries found. At 2 years of age, she was noted to have macrocephaly, ptosis, loss of developmental milestones, hypotonia, and incontinence. Dysmorphic features and abnormal dentition, including structural and numeric dental problems and a dentinogenesis imperfecta-like appearance, were noted. The patient remains alive at the time of this report. MR imaging of the brain was performed at 1 and 2 years of age.

Additional clinical information related to these cases is being provided separately in a therapy-related report.[12]

MR Imaging

MR imaging was performed on a variety of scanners using T1- and T2-weighted sequences, FLAIR, and occasionally more sophisticated methods, including diffusion-weighting, susceptibility-weighting, and postcontrast imaging. Complete studies were not available for our review. Imaging studies consisted mostly of selected key images that had been submitted with other medical data for clinical consultation. Available images from each patient were reviewed and compared.

RESULTS

Our 4 new patients were combined with 11 patients from prior publications that included patients with SPLIS who had imaging of the brain. The clinical and imaging features are summarized in the On-line Table. Five of these 15 patients had cortical atrophy or clinical findings of microcephaly. Five had edema, calcification, necrosis, or atrophy of the globus pallidus, caudate, putamen, or thalamus. Seven patients exhibited involvement of the pons or cerebellum. Gadolinium contrast, when administered, typically caused enhancement of the affected deep gray nuclei or central structures in the midbrain, medulla, and cerebellum, including the olivocerebellar circuits. The 3 patients who underwent CT scanning all reportedly had normal findings, suggesting

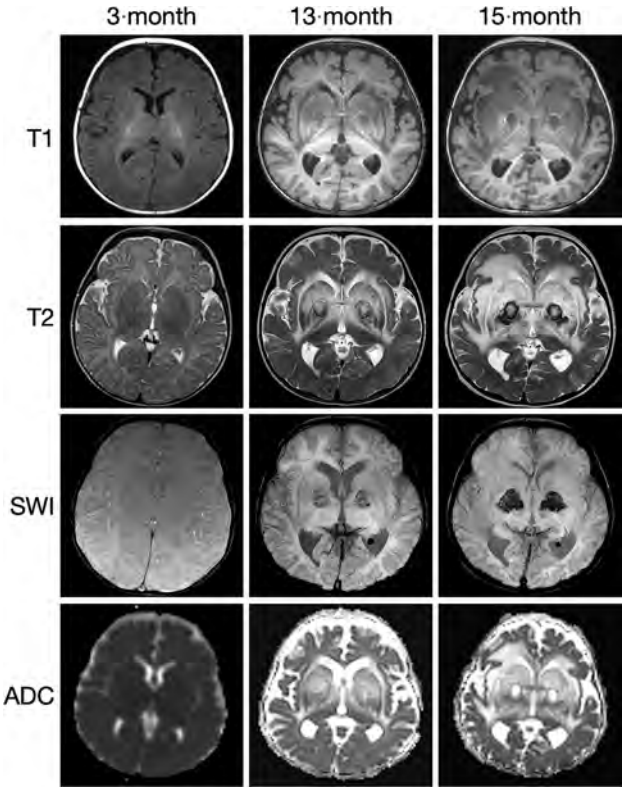

FIG 5. SPLIS appearance and progression of MR imaging findings with age. Sequential MR imaging performed in this infant with SPLIS between 6 weeks and 15 months of age has initially normal findings. At 13 and 15 months of age, there is progressive involvement of the globus pallidus with extensive edema of the caudate, putamen, and thalamus. Diffusivity is increased, and there is a susceptibility effect with a ring of T1- and T2- shortening. The susceptibility-phase images indicate the presence of calcium.

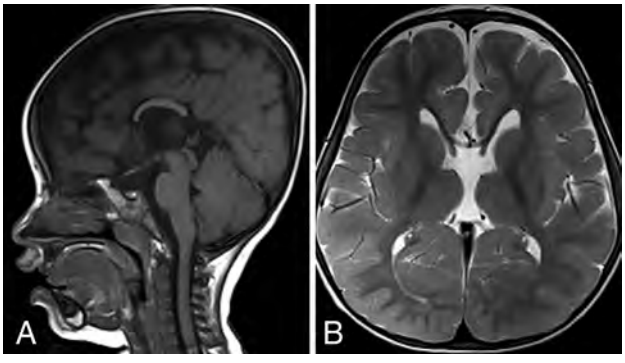

FIG 6. SPLIS with dysgenesis of the corpus callosum and hypoplasia with an absent rostrum, genu, and splenium. This 2-year-old patient with SPLIS has dysgenesis of the corpus callosum. The sagittal T1- and axial T2-weighted MR images show absence of the rostrum, genu, and splenium (*A*). The body of the corpus callosum is hypoplastic. Brain volume, gyral complexity, and myelin maturation are grossly normal (*B*).

the insensitivity of this method to detect the earliest brain abnormalities observed in patients with SPLIS.

New patient 1 had 3 scans showing similar-but-progressive findings. Deep gray nuclear involvement was present, including the globus pallidus, thalamus, substantia nigra, and dentate nuclei of the cerebellum, all of which were associated with extensive surrounding FLAIR hyperintensity, presumably representing edema (Fig 2). Across time, the lesions appeared to consolidate and edema diminished, and there was a loss of central or peripheral T2 signal. Brain stem involvement was present, which could not be separated into primarily gray or white matter disease.

New patient 2 had a single scan at 6 years of age showing multiple small areas of cerebral and cerebellar cortical T2-FLAIR hyperintensity, some of which extended into the adjacent subcortical white matter (Fig 3). The deep gray nuclei and deep white matter structures appeared completely spared.

New patient 3 had fetal imaging at 25 weeks' gestation. Sonography demonstrated enlarged echogenic adrenal glands with posterior shadowing. The concurrent fetal MR images showed prominent adrenal glands with a normal signal character suggesting calcification rather than hemorrhage (Fig 4). Postnatal MR imaging was performed at 6 weeks, 13 months, and 15 months of age (Fig 5). Initial brain imaging findings at 6 weeks were normal. At 13 and 15 months, there was extensive and progressive bilateral caudate, putaminal, and thalamic involvement, which appears to be centered on the globus pallidus. A rim of T1- and T2-shortening developed about the en-larged globi pallidi associated with the susceptibility effect and increased diffusivity. Analysis of phase images suggests the presence of calcium rather than iron.

New patient 4 underwent MR imaging of the brain at 1 and 2 years of age. There was callosal dysgenesis with absence of the rostrum, genu, and splenium. Otherwise, the T2-weighted images of the brain and progression of myelin maturation appeared normal at 1 and 2 years of age (Fig 6).

DISCUSSION

SPLIS is a newly recognized nonlysosomal sphingolipidosis caused by recessive mutations in the gene encoding S1P lyase, an intrinsic protein of the endoplasmic reticulum outer membrane. Analysis of these patients demonstrates the variety of neuroimaging findings in SPLIS. Appearances included callosal agenesis, dysgenesis, or hypoplasia or a rapidly progressive neurodegenerative disease in other patients. The developmental malformation could range from the callosal dysgenesis alone to generalized microcephaly, or it could result in widespread gyral simplification and hypoplasia of the frontal and temporal lobes, as described by Bamborschke et al.[10] Patient 4 does not exhibit typical features of SPLIS, and sphingolipid accumulation was not observed in the patient's plasma (our unpublished findings). Thus, the clinical and imaging findings observed in this case could potentially have another etiology. Considering that another reported patient with SPLIS with biochemically confirmed pathogenic biallelic *SGPL1* variants also exhibited callosal dysgenesis,[5] we included this patient in our analysis. Both patients with callosal dysgenesis were Turkish, but they do not share *SGPL1* pathogenic variants. This feature raises the possibility of a separate genetic defect as the cause of the developmental malformation.

Two of our patients and a total of 5 of the 15 patients reviewed in this report had progressive damage to the deep gray nuclei, including the thalamus, globus pallidus, caudate, putamen, brain

stem, and cerebellum. One older patient progressed to develop multiple focal lesions in the cerebral and cerebellar cortex and subcortical white matter. The cause of deep and cortical gray matter injury in patients with SPLIS is not known with certainty. The appearance is not specific and resembles other toxic, metabolic, mitochondrial, infectious, and postinfectious disorders. The simultaneous presence of nephrotic syndrome with renal dysfunction, adrenal insufficiency, immunodeficiency, and sphingolipid deposition disease creates a complicated mix of possible pathophysiologic mechanisms of brain injury.

One pattern of injury affects the dopaminergic pathways, particularly the globus pallidus and dentate nucleus, but also the red nucleus and substantia nigra. These dopaminergic neural pathways are characterized by high rates of metabolism and mineral transport. Thus, they may be especially sensitive to changes in energy production, myelin composition, vascular supply, or the abnormal accumulation of cellular sphingolipids, which influences mitochondrial function and cell fate decisions in response to stress.[13] The progressive nature of these changes has been shown on serial imaging. Routine and susceptibility-weighted imaging sequences have shown mineral deposition within or at the margin of lesions affecting the globus pallidus, thalamus, and dentate nucleus. Microhemorrhage and necrosis were suspected. However, analysis of phase images in 1 patient suggested the presence of calcium rather than iron or manganese. Disorders of calcium phosphate metabolism are known to lead to mineral deposition in the basal ganglia, particularly the globus pallidus; however, the deposition appears passive and less destructive than that observed in patients with SPLIS. Neurodegeneration with brain iron accumulation, including pantothenate kinase-associated neurodegeneration (PKAN), leads to iron deposition in the dopaminergic pathways. The appearance resembles that of some of our patients, but the presence of iron has not been proved in patients with genetically proved SPLIS. We recently had the opportunity to image and review many patients with PKAN as part of a novel drug-treatment trial.[14] Other variants of neurodegeneration with brain iron accumulation were excluded. All patients had symmetric SWI signal changes in the globus pallidus, substantia nigra, red nucleus, and dentate nucleus. Some patients with SPLIS have involvement of these structures, which progresses to a much more robust disease than typical of PKAN. The presence of cortical and cerebellar gray and white matter involvement seems to distinguish SPLIS from PKAN in this regard.

The 1 patient whose fetal images we reviewed demonstrated adrenal enlargement and calcification. Among the known causes of adrenal calcification are Wolman disease and Niemann-Pick disease, both of which, like SPLIS, are disorders of lipid metabolism.

The molecular pathogenesis of SPLIS neuropathy is unknown. Mice constitutively lacking *SGPL1* in brain neurons exhibit cognitive and motor deficits.[15] *SGPL1* disruption blocks autophagic flux and induces accumulation of aggregation-prone proteins in hippocampal neurons and brain tissue.[15,16] S1P can act as a neurotoxin by inducing inappropriate elevations in cellular calcium, activating the unfolded protein response.[17,18] In addition, sphingolipids such as S1P and ceramide exert effects on apoptosis, autophagy, exosome release, neuroinflammation, mitochondrial function, and the vasculature.[19] Knockout mice lacking the ability to produce S1P or signal through S1P receptor 1 have interrupted angiogenesis and neurogenesis, are embryonic lethal, and exhibit neural tube closure defects and increased neuronal apoptosis.[20]

Due to the novelty of SPLIS and its diverse clinical presentations, patients with SPLIS may be challenging to recognize. Most are identified by next-generation sequencing studies of patients presenting with congenital or infantile nephrotic syndrome or nephrotic syndrome associated with other congenital anomalies. Some commercially available diagnostic panels for genetic testing of patients with these conditions include *SGPL1*, but this is not universal. Furthermore, gene panels focused on other disease characteristics have not yet incorporated *SGPL1*. Therefore, clinicians in all areas of pediatrics including radiologists who may encounter the MR imaging patterns described in this report should have a high index of clinical suspicion. Delay in diagnosis may lead to complications due to unrecognized conditions such as primary adrenal insufficiency or immunodeficiency. Early diagnosis would provide a window of opportunity for intervention before progression of clinical sequelae. Current treatments for SPLIS are largely supportive. However, targeted therapeutic strategies are in development and could potentially be leveraged to avert the devastating neurodegenerative component of the syndrome.[12]

Disclosures: Nicole Weaver—*UNRELATED*: *Grants/Grants Pending*: National Institutes of Health, *Comments*: K08 award through the National Heart, Lung, and Blood Institute; *Travel/Accommodations/Meeting Expenses Unrelated to Activities Listed*: hotel accommodations for 2 nights at Costello Syndrome Family Network meeting in July 2019. Evren Gumus—*UNRELATED*: *Employment*: Mu la Sıtkı Koçman University. Friedhelm Hildebrandt—*UNRELATED*: *Board Membership*: Goldfinch Bio, *Comments*: cofounder and scientific advisory board member. Julie D. Saba—*RELATED*: *Grant*: National Institutes of Health and Swim Across America Foundation, *Comments*: This work was supported by a grant from the National Institutes of Health DK115669 to myself, and funds for research from the Swim Across America Foundation.* *Money paid to the institution.

REFERENCES

1. Choi YJ, Saba JD. **Sphingosine phosphate lyase insufficiency syndrome (SPLIS): a novel inborn error of sphingolipid metabolism.** *Adv Biol Regul* 2019;71:128–40 CrossRef Medline
2. Saba JD. **Fifty years of lyase and a moment of truth: sphingosine phosphate lyase from discovery to disease.** *J Lipid Res* 2019;60:456–63 CrossRef Medline
3. Dixit D, Okuniewska M, Schwab SR. **Secrets and lyase: control of sphingosine 1-phosphate distribution.** *Immunol Rev* 2019;289:173–85 CrossRef Medline
4. Kumar A, Saba JD. **Lyase to live by: sphingosine phosphate lyase as a therapeutic target.** *Expert Opin Ther Targets* 2009;13:1013–25 CrossRef Medline
5. Lovric S, Goncalves S, Gee HY, et al. **Mutations in sphingosine-1-phosphate lyase cause nephrosis with ichthyosis and adrenal insufficiency.** *J Clin Invest* 2017;127:912–28 CrossRef Medline
6. Prasad R, Hadjidemetriou I, Maharaj A, et al. **Sphingosine-1-phosphate lyase mutations cause primary adrenal insufficiency and steroid-resistant nephrotic syndrome.** *J Clin Invest* 2017;127:942–53 CrossRef Medline
7. Atkinson D, Nikodinovic Glumac J, Asselbergh B, et al. **Sphingosine 1-phosphate lyase deficiency causes Charcot-Marie-Tooth neuropathy.** *Neurology* 2017;88:533–42 CrossRef Medline
8. Janecke AR, Xu R, Steichen-Gersdorf E, et al. **Deficiency of the sphingosine-1-phosphate lyase SGPL1 is associated with congenital nephrotic syndrome and congenital adrenal calcifications.** *Hum Mutat* 2017;38:365–72 CrossRef Medline

9. Linhares N, Arantes R, Araujo S, et al. **Nephrotic syndrome and adrenal insufficiency caused by a variant in SGPL1.** *Clin Kidney J* 2018;11:462–66 CrossRef Medline
10. Bamborschke D, Pergande M, Becker K, et al. **A novel mutation in sphingosine-1-phosphate lyase causing congenital brain malformation.** *Brain Dev* 2018;40:480–83 CrossRef Medline
11. Settas N, Persky R, Faucz FR, et al. **SGPL1 deficiency: a rare cause of primary adrenal insufficiency.** *J Clin Endocrinol Metab* 2018;104:1484–90 CrossRef Medline
12. Zhao P, Liu ID, Hodgin JB, et al. **Responsiveness of sphingosine phosphate lyase insufficiency syndrome to vitamin B6 cofactor supplementation.** *J Inherit Metab Dis* 2020 Mar 31. [Epub ahead of print] CrossRef Medline
13. Milstien S, Gude D, Spiegel S. **Sphingosine 1-phosphate in neural signalling and function.** *Acta Paediatr* 2007;96:40–43 CrossRef Medline
14. Klopstock T, Tricta F, Neumayr L, et al. **Safety and efficacy of deferiprone for pantothenate kinase-associated neurodegeneration: a randomised, double-blind, controlled trial and an open-label extension study.** *Lancet Neurol* 2019;18:631–42 CrossRef Medline
15. Mitroi DN, Deutschmann AU, Raucamp M, et al. **Sphingosine 1-phosphate lyase ablation disrupts presynaptic architecture and function via an ubiquitin-proteasome mediated mechanism.** *Sci Rep* 2016;6:37064 CrossRef Medline
16. Mitroi DN, Karunakaran I, Graler M, et al. **SGPL1 (sphingosine phosphate lyase 1) modulates neuronal autophagy via phosphatidylethanolamine production.** *Autophagy* 2017;13:885–99 CrossRef Medline
17. Hagen N, Hans M, Hartmann D, et al. **Sphingosine-1-phosphate links glycosphingolipid metabolism to neurodegeneration via a calpain-mediated mechanism.** *Cell Death Differ* 2011;18:1356–65 CrossRef Medline
18. Hagen N, Van Veldhoven PP, Proia RL, et al. **Subcellular origin of sphingosine-1-phosphate is essential for its toxic effect in lyase deficient neurons.** *J Biol Chem* 2009;284:11346–53 CrossRef Medline
19. Wang G, Bieberich E. **Sphingolipids in neurodegeneration (with focus on ceramide and S1P).** *Adv Biol Regul* 2018;70:51–64 CrossRef Medline
20. Mizugishi K, Yamashita T, Olivera A, et al. **Essential role for sphingosine kinases in neural and vascular development.** *Mol Cell Biol* 2005;25:11113–21 CrossRef Medline

Paraspinal Myositis in Patients with COVID-19 Infection

W.A. Mehan, B.C. Yoon, M. Lang, M.D. Li, S. Rincon, and K. Buch

ABSTRACT

SUMMARY: Myalgia is a previously reported symptom in patients with COVID-19 infection; however, the presence of paraspinal myositis has not been previously reported. We report MR imaging findings of the spine obtained in a cohort of 9 patients with COVID-19 infection who presented to our hospital between March 3, 2020 and May 6, 2020. We found that 7 of 9 COVID-19 patients (78%) who underwent MR imaging of the spine had MR imaging evidence of paraspinal myositis, characterized by intramuscular edema and/or enhancement. Five of these 7 patients had a prolonged hospital course (greater than 25 days). Our knowledge of the imaging manifestations of COVID-19 infection is expanding. It is important for clinicians>a to be aware of the relatively high frequency of paraspinal myositis in this small cohort of patients with COVID-19 infection.

ABBREVIATIONS: COVID-19 = coronavirus disease 2019; SARS-CoV-2 = Severe Acute Respiratory Syndrome coronavirus 2

Information regarding the imaging manifestations in patients infected with Severe Acute Respiratory Syndrome coronavirus 2 (SARS-CoV-2) has been rapidly evolving; however, most of the imaging studies have primarily focused on the pulmonary, gastrointestinal, and cardiac manifestations of coronavirus disease 2019 (COVID-19).[1-15] Emerging case reports have described neuroimaging manifestations seen in patients with COVID-19 infection, including acute intracranial hemorrhage, demyelinating lesions, and encephalitis.[16]

The presence of paraspinal muscular pathology in the setting of COVID-19 infection has not been previously reported. Although the most common symptoms of COVID-19 infection include cough, shortness of breath, and fever, myalgia has been reported in up to 50% of patients with the infection.[17-18] The purpose of this study was to describe the imaging findings of suspected myositis in a small cohort of patients with COVID-19 infection undergoing MR imaging of the spine.

Received May 26, 2020; accepted after revision June 12.

From the Department of Radiology, Massachusetts General Hospital, Boston, Massachusetts.

Please address correspondence to Karen Buch, MD, Department of Radiology, Massachusetts General Hospital, 55 Fruit St, Boston, MA 02118, United States; e-mail: kbuch@partners.org; @MGHNeuroRad; @KBuchRad

Indicates open access to non-subscribers at www.ajnr.org

Indicates article with supplemental on-line table.

http://dx.doi.org/10.3174/ajnr.A6711

CASE SERIES

This study was an institutional review board–approved, retrospective study performed at a single large academic institution. Between March 3, 2020 and May 6, 2020, 641 patients presented to our institution for medical care and tested positive for COVID-19 by reverse transcriptase polymerase chain reaction. A total of 9 patients with COVID-19 infection at our institution underwent MR imaging of the spine for evaluation of spinal pathology with indications including back pain, lower extremity weakness, and lower extremity paresthesia.

All imaging was performed on either a 1.5T (Signa HX and Signa Excite HDx, GE Healthcare; Avanto, Siemens) or 3T scanner (Discovery MR750, GE Healthcare; Tim Trio and Skyra, Siemens). All MR imaging examinations of the spine included sagittal T1-weighted imaging, sagittal non-fat-saturated T2-weighted imaging, sagittal fat-saturated T2-weighted imaging, and axial T2-weighted imaging. Postcontrast sequences were performed in a subset of this cohort.

Evaluation of the MR imaging included an assessment for spinal cord signal abnormality and clumping or thickening of the cauda equina nerve roots, bone marrow edema suggestive of an acute process, edema and/or enhancement within the intervertebral disks, and edema and/or enhancement within the paraspinal musculature. Myositis was defined as intramuscular edema manifested by T2 hyperintensity and/or enhancement within the paraspinal muscles which was present in the absence of, or disproportionate to the presence of minimal edema in the posterior subcutaneous soft tissues. The locations of these findings were

FIG 1. A 56-year-old man with COVID-19. *A*, sagittal fat-saturated T2-weighted image of the lumbar spine demonstrating increased T2 signal intensity within the posterior paraspinal muscles. *B*, post-contrast fat-saturated T1-weighted image of the lumbar spine demonstrating diffuse enhancement within the posterior paraspinal muscles.

recorded in reference to the vertebral body level for each patient. Indications for spine MR imaging included a report of back pain in 5 patients, bilateral leg pain in 2 patients, imbalance in 1 patient, and 1 patient who was found unconscious after a suicide attempt.

A complete cervical, thoracic, and lumbar spine MR imaging was performed in 3 patients, an isolated cervical spine MR imaging was performed in 1 patient, thoracolumbar MR imaging was performed in 3 patients, and isolated lumbar spine MR imaging was performed in 2 patients (On-line Table). Four of the 9 MR imaging examinations were performed with contrast and the remaining 5 MRIs were performed without contrast.

Prior MR imaging of the spine was available for 3 patients in this cohort confirming that no findings of myositis were seen on prior spine MR imaging. Additionally, the electronic medical records were searched for each patient and confirmed that none of these patients had been previously treated for myositis. One patient in this cohort had a single-level laminectomy in the thoracic spine for treatment of an epidural abscess 5 years earlier. No history of prior spine surgery was present in the remaining 8 patients.

Imaging findings were correlated with clinical parameters. Patient age, sex, length of hospital stay, respiratory failure requiring intubation, presence of a superimposed bacterial infection, and serum inflammatory markers were recorded for each patient. The recorded serum inflammatory

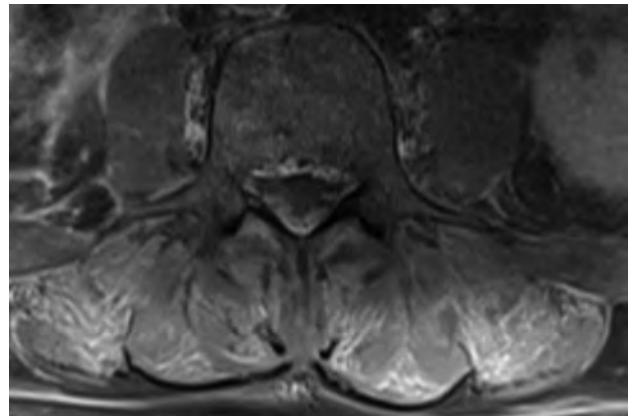

FIG 2. Same 56-year-old man with COVID-19 seen in Fig 1. Axial post-contrast, fat-saturated T1-weighted image of the lumbar spine demonstrates symmetric areas of intramuscular enhancement involving the erector spinae and multifidus muscles bilaterally.

markers included creatine kinase levels (normal range 60–400 U/L), erythrocyte sedimentation rate (normal range 0–20 mm/h), C-reactive protein (normal range $<$8.0 mg/L), creatinine level (normal range 0.6–1.5 mg/dL), and D-dimer (normal range $<$500 mg/mL). All serum inflammatory markers recorded were performed within 12 hours of the MR imaging examination.

Of the 9 patients included in this cohort, the mean age was 55 years (standard deviation 17 years, range: 30–87). Six of the 9 patients required admission to the hospital for treatment of COVID-19 infection, and 4 of these patients were intubated. The mean time between hospital admission and/or symptom onset and acquisition of the MR imaging scan was 17 days (range 1–35 days following admission). None of the patients in this cohort were diagnosed with having a superimposed bacterial infection over the duration of their hospital courses.

Seven of 9 (78%) patients who underwent spine MR imaging demonstrated evidence of myositis on MR imaging with involvement of the erector spinae muscles and multifidus muscles (Figs 1–3). In all 7 patients with MR imaging findings of myositis, it occurred exclusively in the lumbar spine and involved multiple vertebral body levels (On-line Table). In all cases, the myositis was bilateral.

All patients with lumbar spine imaging (8 total) had trace to mild edema within the superficial subcutaneous soft tissues. In the 7 patients with lumbar spine MR imaging who had imaging findings suggestive of myositis, the edema in the paraspinal musculature was out of proportion to the degree of superficial subcutaneous edema.

None of the patients in this cohort demonstrated signal abnormality or enhancement within the visualized portion of the spinal cord or clumping or thickening of the cauda equina nerve roots. Abnormal edema and/or enhancement within the intervertebral disks was not seen in any patient in this cohort. Two of the 9 patients in this cohort had degenerative changes related to moderate facet hypertrophy confined to 2 levels within the lumbar spine. There was no evidence of reactive marrow edema in these patients related to degenerative disease.

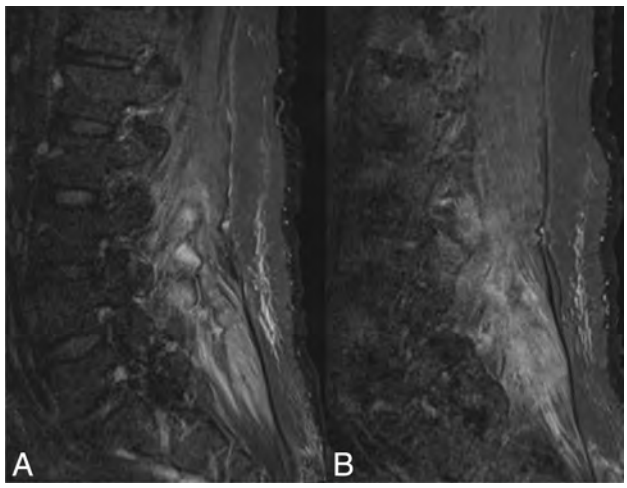

FIG 3. A 54-year-old woman with COVID-19. Sagittal fat-saturated T2-weighted imaging of the lumbar spine demonstrates nearly symmetric areas of increased T2 signal intensity within the posterior paraspinal muscles bilaterally. *A*, right parasagittal view of the T2 signal hyperintensity in the right paraspinal musculature. *B*, left parasagittal view of the T2 signal hyperintensity in the left paraspinal musculature.

One patient included in this cohort had a history of adrenal carcinoma with a known metastatic lesion at the L5 level, which was unchanged in appearance from multiple prior MR imaging examinations, and was not associated with new marrow edema or extension of disease.

Of the 7 patients with MR evidence of myositis, 5 were admitted to the hospital with a length of stay greater than 25 days, and 4 of these 5 patients were intubated over the course of their hospital admission. Three of the 7 patients with myositis demonstrated elevated serum inflammatory markers (as shown in the On-line Table). MR findings suggestive of myositis were seen in 2 patients who did not require hospital admission, did not have symptoms of respiratory failure, and did not have serum inflammatory markers collected.

None of the patients in this cohort received hydroxychloroquine or remdesivir for treatment of COVID-19 infection.

DISCUSSION

Of the small cohort of patients with COVID-19 infection who underwent MR imaging at our institution for evaluation of the spine, 78% (7 of 9) of patients had intramuscular edema and imaging findings suggestive of myositis, and all cases of myositis were found in the lumbar spine. These findings occurred in the absence of spine trauma. Three of the 7 patients in this cohort with MR imaging findings suggestive of myositis had elevated inflammatory markers. Two patients in our cohort did not demonstrate imaging manifestations of lumbar myositis; 1 had a relatively short hospital admission of 10 days, and the other patient was asymptomatic and did not require hospital admission. The patients in this cohort who had imaging of the cervical and thoracic spine demonstrated no MR imaging findings to suggest myositis in these segments of the spine.

Possible etiologies of the observed paraspinal myositis include direct muscular viral infection with SARS-CoV-2, an immune-mediated, parainfectious inflammatory response given the elevated serum inflammatory markers in several patients, or drug-mediated effects. An additional consideration for these findings includes sequelae of a critical illness myopathy that has been previously described in up to 62% of intensive care unit patients who failed to be wean from the ventilator.[19-20] While it is possible that these findings could be compounded by third spacing with gravitationally dependent edema, this is felt to be less likely as edema and/or paraspinal muscular enhancement was found to be out of proportion to the degree of overlying superficial subcutaneous edema, which was found to be trace to mild in all patients. Of the 7 patients with MR imaging findings of myositis, 3 patients were never intubated, and 4 patients had MR imaging findings suggestive of myositis with MR imaging performed within 10 days of admission. These findings suggest that patients may have been relatively early in their COVID-19 infection course and these findings may be unrelated to a critical illness myopathy. Viral myositis is a known entity reportedly caused by several other viruses including influenza, HIV, hepatitis C, and Middle East Respiratory Syndrome Coronavirus.[21-25] The results of this study are consistent with Beydon et al[19] who demonstrated MR features of myositis involving the pelvis and thighs in a patient with COVID-19 infection.

This is a small series of patients, in part related to the low frequency of back pain complaints in patients with COVID-19 infection. Furthermore, severe manifestations of COVID-19 may render patients too unstable or unable to undergo MR imaging of the spine. There are numerous confounders in these patients including heterogeneous sampling of serum inflammatory markers, lack of clear information regarding how long patients had the infection before experiencing symptoms of back pain and weakness, and heterogeneous treatment algorithms. These variations in practice patterns, documentation, and recorded histories make it difficult to determine dominant etiologies contributing to these imaging manifestations.

In conclusion, the findings of this study demonstrate a high frequency of myositis in patients with COVID-19 infection reporting myalgia in a small series. It is important for health care providers and radiologists to be aware of these clinical features and imaging findings.

Disclosures: William A. Mehan—*UNRELATED: Consultancy:* Kura Oncology, *Comments:* Independent reviewer of head and neck imaging studies for a clinical trial; *Expert testimony:* CRICO and other health insurance companies, *Comments:* Expert opinion for medicolegal cases involving neuroimaging.

REFERENCES

1. Zeng Z, Xu L, Xie XY, et al. **Pulmonary pathology of early phase COVID-19 pneumonia in a patient with a benign lung lesion.** *Histopathology* 2020 May 6. [Epub ahead of print] CrossRef Medline
2. Jafari R, Cegolon L, Jafari A, et al. **Large saddle pulmonary embolism in a woman infected by COVID-19 pneumonia.** *Eur Heart J* 2020;41:2133 CrossRef Medline
3. Ji M, Yuan L, Shen W, et al. **Characteristics of disease progress in patients with coronavirus disease 2019 in Wuhan, China.** *Epidemiol Infect* 2020;148:e94 CrossRef Medline

4. Yu Q, Wang Y, Huang S, et al. **Multicenter cohort study demonstrates more consolidation in upper lungs on initial CT increases the risk of adverse clinical outcome in COVID-19 patients.** *Theranostics* 2020;10:5641–48 CrossRef
5. Wu J, Pan J, Teng D, et al. **Interpretation of CT signs of 2019 novel coronavirus (COVID-19) pneumonia.** *Eur Radiology* 2020 May 4. [Epub ahead of print] CrossRef Medline
6. Pozzessere C, Rotzinger DC, Ghaye B, et al. **Incidentally discovered COVID-19 pneumonia: the role of diagnostic imaging.** *Eur Radiology* 2020 May 4. [Epub ahead of print] CrossRef Medline
7. Liya G, Yuguang W, Jian L, et al. **Studies on viral pneumonia related to novel coronavirus SARS-CoV-2, SARS-CoV, and MERS-CoV: a literature review.** *APMIS* 2020 May 4. [Epub ahead of print] CrossRef Medline
8. Guneyli S, Atceken Z, Dogan H, et al. **Radiological approach to COVID-19 pneumonia with an emphasis on chest CT.** *Diagn Interv Radiology* 2020;26:323–32 CrossRef
9. Ding X, Xu J, Zhou J, et al. **Chest CT findings of COVID-19 pneumonia by duration of symptoms.** *Eur J Radiology* 2020;127:109009 CrossRef
10. Middeldorp S, Coppens M, van Haaps TF, et al. **Incidence of venous thromboembolism in hospitalized patients with COVID-19.** *J Thromb Haemost* 2020 May 5. [Epub ahead of print] CrossRef Medline
11. Scialpi M, Scialp S, Piscioli I, et al. **Pulmonary thromboembolism in critically ill COVID-19 patients.** *Int J Infect Dis* 2020;95:361–62 CrossRef Medline
12. Leonard-Lorant I, Delabranche X, Severac F, et al. **Acute pulmonary embolism in COVID-19 patients on CT angiography and relationship to D-dimer levels.** *Radiology* 2020 Apr 23. [Epub ahead of print] CrossRef Medline
13. Grillet F, Behr J, Calame P, et al. **Acute pulmonary embolism associated with COVID-19 pneumonia detected by pulmonary CT angiography.** *Radiology* 2020 Apr 23. [Epub ahead of print] CrossRef Medline
14. Babapoor-Farrokhran S, Gill D, Walker J, et al. **Myocardial injury and COVID-19: possible mechanisms.** *Life Sci* 2020;253:117723 CrossRef Medline
15. Liu K, Pan M, Xiao Z, et al. **Neurological manifestations of the coronavirus (SARS-CoV-2) pandemic 2019-2020.** *J Neurol Neurosurg Psychiatry* 2020;91:669–70 CrossRef Medline
16. Zanin L, Saraceno G, Panciani PP, et al. **SARS-CoV-2 can induce brain and spine demyelinating lesions.** *Acta Neurochir (Wien)* 2020;162:1491–94 CrossRef Medline
17. Chen Y, Zhao M, Wu Y, et al. **Epidemiological analysis of the early 38 fatalities in Hubei, China, of the coronavirus disease 2019.** *J Glob Health* 2020;10:011004 CrossRef Medline
18. Beydon M, Chevalier K, Al Tabaa O, et al. **Myositis as a manifestation of SARS-CoV-2.** *Ann Rheum Dis* 2020 CrossRef
19. Latronico N, Bolton CF. **Critical illness polyneuropathy and myopathy: a major cause of muscle weakness and paralysis.** *Lancet Neurol* 2011;10:931–41 CrossRef
20. Shepherd S, Batra A, Lerner DP. **Review of critical illness myopathy and neuropathy.** *Neurohospitalist* 2017;7:41-48 CrossRef Medline
21. Gibson SB, Majersik JJ, Smith AG, et al. **Three cases of acute myositis in adults following influenza-like illness during the H1N1 pandemic.** *J Neurosci Rural Pract* 2013;4:51–54 CrossRef Medline
22. Dalakas MC, Pezeshkpour GH, Gravell M, et al. **Poly-myositis associated with AIDS retrovirus.** *JAMA* 1986;256:2381–83 CrossRef
23. Dalakas MC, Pezeshkpour GH. **Neuromuscular diseases associated with human immunodeficiency virus infection.** *Ann Neurol* 1988; 23:S38–S48 CrossRef
24. Villanova M, Caudai C, Sabatelli P, et al. **Hepatitis C virus infection and myositis: a polymerase chain reaction study.** *Acta Neuropathol* 2000;99:271–76 CrossRef Medline
25. Alsaad KO, Hajeer AH, Al Balwi M, et al. **Histopathology of Middle East respiratory syndrome coronovirus (MERS-CoV) infection—clinicopathological and ultrastructural study.** *Histopathology* 2018; 72:516–24 CrossRef Medline

Safety of Consecutive Bilateral Decubitus Digital Subtraction Myelography in Patients with Spontaneous Intracranial Hypotension and Occult CSF Leak

M.C. Pope, C.M. Carr, W. Brinjikji, and D.K. Kim

ABSTRACT

BACKGROUND AND PURPOSE: Digital subtraction myelography performed with the patient in the lateral decubitus position has the potential for increased sensitivity over prone-position myelography in the detection of spinal CSF-venous fistulas, a well-established cause of spontaneous intracranial hypotension. We report on the safety of performing routine, consecutive-day right and left lateral decubitus digital subtraction myelography in these patients.

MATERIALS AND METHODS: In this retrospective case series, all patients undergoing consecutive-day lateral decubitus digital subtraction myelography for suspected spinal CSF leak between September 2018 and September 2019 were identified. Chart review was performed to identify any immediate or delayed adverse effects associated with the procedures. Procedural parameters were also analyzed due to inherent variations associated with the positive-pressure myelography technique that was used.

RESULTS: A total of 60 patients underwent 68 pairs of consecutive-day lateral decubitus digital subtraction myelographic examinations during the study period. No major adverse effects were recorded. Various minor adverse effects were observed, including pain requiring analgesics (27.2%), nausea/vomiting requiring antiemetics (8.1%), and transient neurologic effects such as syncope, vertigo, altered mental status, and autonomic dysfunction (5.1%). Minor transient neurologic effects were correlated with increasing volumes of intrathecal saline injectate used for thecal sac prepressurization.

CONCLUSIONS: In patients with spontaneous intracranial hypotension and suspected spontaneous spinal CSF leak, consecutive-day lateral decubitus digital subtraction myelography demonstrates an acceptable risk profile without evidence of neurotoxic effects from cumulative intrathecal contrast doses. Higher intrathecal saline injectate volumes may correlate with an increased incidence of minor transient periprocedural neurologic effects.

ABBREVIATIONS: DSM = digital subtraction myelography; SIH = spontaneous intracranial hypotension

Spontaneous intracranial hypotension (SIH) is a syndrome of orthostatic headaches and other potentially debilitating neurologic symptoms attributable to spontaneous spinal CSF leaks.[1,2] Distinct subtypes of spinal CSF leaks have been described, including dural tears and CSF-venous fistulas along the nerve root sleeves. Ventral dural tears are often associated with epidural fluid collections, which can be longitudinally extensive along the spinal axis.[3,4] These leaks usually are well-characterized by conventional spinal MR imaging and CT or MR myelography. Conversely, CSF-venous fistulas and some nerve root sleeve dural tears may present without identifiable extradural fluid collections.[5-7] Adjunctive techniques such as dynamic CT myelography and digital subtraction myelography (DSM) can be used to increase the sensitivity for these occult leaks and provide precise localization for subsequent surgical repair or blood patching.[8-11]

In particular, digital subtraction myelography has proved effective for detecting occult CSF leaks due to its superior spatial and temporal resolution.[9,12] Various procedural variations have recently been described in the literature, most notably the performance of DSM imaging with the patient in the lateral decubitus position. Schievink et al[13] demonstrated a 5-fold increase in the detection rate of previously occult CSF-venous fistulas by performing DSM with patients in the lateral decubitus position instead of conventional prone positioning. Farb et al[5] also reported success with the lateral decubitus DSM technique in detecting spinal CSF-venous fistulas as well as a case of nerve root sleeve dural tear.

At our institution, right and left lateral decubitus DSM was typically performed on consecutive days for patients being evaluated for SIH without an identifiable CSF leak on prior MR

Received March 23, 2020; accepted after revision July 1.

From the Department of Radiology, Mayo Clinic, Rochester, Minnesota.

Please address correspondence to Matthew C. Pope, Mayo Clinic, 200 First St SW, Rochester, MN 55905; e-mail: Pope.matthew@mayo.edu

http://dx.doi.org/10.3174/ajnr.A6765

imaging and/or conventional CT myelography. This approach provided several advantages over targeted or unilateral DSM. For example, performing a comprehensive bilateral decubitus DSM examination with accompanying decubitus CT myelography within a 24-hour window was less burdensome for our patients, simplifying scheduling and potentially reducing travel expense. This also ensured that no multifocal bilateral leaks were overlooked.

While the relative safety of intrathecal iodinated contrast and various lumbar puncture techniques for myelography has been well-documented,[14-19] the risk profile of performing consecutive myelographic procedures as discussed above has not been previously described. Specifically, there are currently no data on the potential for increased adverse effects related to a cumulative intrathecal iodinated contrast load within such a short timeframe. Additional considerations include increased patient exposure to radiation, sedation, and general procedural risk. We report on our experience with this unique practice during a 13-month period.

MATERIALS AND METHODS

Study Cohort

In this single-institution retrospective case series, we identified all patients with SIH undergoing lateral decubitus DSM to evaluate occult CSF leaks between September 2018 and September 2019. Inclusion criteria were the following: 1) clinical suspicion of SIH based on evaluation by neurologists with subspecialty experience in CSF dynamics disorders; 2) prior brain and spinal MR imaging deemed inconclusive for definitive spinal CSF leak; and 3) the availability of intraprocedural and postprocedural care documentation in the electronic medical record. Given our primary concern with cumulative effects of consecutive-day procedures, any lateral decubitus DSM procedures performed on 1 side only or bilaterally on nonconsecutive days were excluded. These were generally in the case of patient scheduling exceptions or repeat examinations due to extradural injections on the initial procedure.

Procedural Technique

Lateral decubitus DSM procedures were conducted per our recently described technique.[20] All examinations were performed by a core group of 10 subspecialty neuroradiologists who received training from a single individual. Because this was a new procedure for our institution, some changes to the protocol were made early in the study period. For example, Omnipaque 240 (iohexol; GE Healthcare) was the intrathecal contrast agent used initially, but Omnipaque 300 was subsequently found to produce higher quality images due to higher concentration and became the agent of choice for most cases in the study group. Additionally, varying amounts of sterile preservative-free normal saline (Baxter) were injected before main contrast runs in an attempt to create positive intrathecal pressure and facilitate a CSF leak, which can be intermittent, thereby improving detection of the leak.[21,22] The volume of saline injected was variable and ultimately based on operator preference. Both 20- and 22-ga Quincke spinal needles (Becton Dickinson) were used, and this was also based on operator preference and consideration of factors such as patient body habitus. Imaging was performed with Allura Xper FD 20/20 (Philips Healthcare) or Axion Artis dTA ceiling-mounted (Siemens) systems. Procedures were intended to be performed 24 hours apart, though in practice, the time interval in a small number of cases was as short as 19 hours or as long as 28 hours.

Data Collection

Retrospective chart review of procedure reports, clinical notes, medication administration logs, and radiation logs within the institutional electronic medical record was performed to identify relevant periprocedural data. In addition to demographic data, the following variables were recorded for each DSM procedure: spinal level accessed (L1–L5), needle gauge (20- versus 22-ga), volume of intrathecal contrast injectate (milliliters), volume of intrathecal saline injectate (milliliters), type of intrathecal contrast material (Omnipaque 240 or Omnipaque 300), total fluoroscopy time (seconds), and total radiation skin dose (milligray). Radiation dose parameters were obtained from the automated software recording on the angiographic equipment. The type of anesthesia (local, moderate, or general) was also recorded, given the potential for confounding of documented adverse effects. All postprocedural clinical encounters were reviewed for documentation of delayed adverse effects, extending to 3 months after the conclusion of the study period. If a leak was identified and subsequent definitive treatment with spinal surgery or intrathecal blood patching was performed, these steps were considered an end point due to potential confounding as to the source of the adverse effect.

Adverse Effects

Adverse effects were classified as major or minor. Major adverse effects included procedure-site infections, procedure-site bleeding requiring intervention, acute radiation injury, or a variety of major, rare neurotoxic effects classically associated with intrathecal iodinated contrast such as seizures, arachnoiditis, and long-term mental status changes.[23] Minor adverse effects included intraprocedural and immediate postprocedural complications such as pain (for example, headache, backache, or leg pain) or nausea/vomiting. Specifically, pain and nausea/vomiting were recorded if analgesic or antiemetic medication was administered and symptoms resolved within 24 hours. Any other transient neurologic symptoms such as vertigo were also categorized as minor, in keeping with the spectrum of effects seen in prior studies of iodinated contrast myelography.[14-19] Adverse effects were documented either in the procedure report or periprocedural nursing logs including standardized institutional pain and Richmond Agitation Sedation Scale neurologic scores. Final categorization as a minor effect was contingent on complete spontaneous resolution of the effect within 24 hours. Any reported inadvertent extradural injections were also recorded.

Statistics

Descriptive statistics were performed to summarize patient demographics and general procedural factors. Mixed binomial logistic regression modeling and χ^2 analysis were performed to evaluate any association between procedural factors and the probability of adverse effects. Any missing data points were excluded from comparative analyses. JMP, Version 14.1, (SAS Institute; 1989–2019) and SPSS, Version 25.0 (IBM; released 2017) were used for all statistical calculations. A P value $< .05$ was considered statistically significant.

Table 1: Number of procedures with adverse effects recorded

Type	No. of Procedures (% of Total)			P Value
	Day 1 (n = 68)	Day 2 (n = 68)	Day 3 (n = 136)	
Major adverse effect	0 (0)	0 (0)	0 (0)	
Local bleeding	0 (0)	0 (0)	0 (0)	
Local infection	0 (0)	0 (0)	0 (0)	
Seizures	0 (0)	0 (0)	0 (0)	
Acute radiation injury	0 (0)	0 (0)	0 (0)	
Minor adverse effect	28 (41.2)	26 (38.2)	54 (39.7)	$P = .730$
Subdural injection	5 (7.4)	4 (5.9)	9 (6.6)	$P = .753$
Pain	21 (30.9)	16 (23.5)	37 (27.2)	$P = .335$
Nausea	5 (7.4)	6 (8.8)	11 (8.1)	$P = .753$
Transient neurologic effect	3 (4.4)	4 (5.9)	7 (5.1)	$P = .698$

Table 2: Volume of injectate in patients experiencing transient neurologic adverse effects

Patient	Day 1 Volume (mL)	Day 2 Volume (mL)	Symptom/Sign
A	20	31[a]	Syncope
B	33	41[a]	Autonomic disturbance
C	26	41[a]	Altered mental status
D	21	41[a]	Autonomic disturbance
E	27[a]	52	Syncope
F	61[a]	31	Vertigo
G	43[a]	33	Altered mental status

[a] Occurrence of transient neurologic adverse effects.

Institutional review board approval with waived consent was granted for this Health Insurance Portability and Accountability Act–compliant retrospective research study.

RESULTS

Study Cohort

Of 151 lateral decubitus DSM procedures identified in the study period, 15 were not performed as consecutive pairs. These cases were excluded, and a total of 60 unique patients undergoing 68 pairs of consecutive lateral decubitus DSMs were evaluated. The excess procedural pairs were accounted for by 2 patients who underwent 3 separate procedural pairs each and 4 patients who underwent 2 separate procedural pairs each. These patients undergoing multiple procedural pairs generally had definitive treatment for CSF leaks after the initial study and subsequently developed recurrent symptoms meeting the inclusion criteria at least 1 month after the most recent dural puncture. The study population included 37/60 women (62%) and 23/60 men (38%) with a mean age of 54.6 ± 11.9 years. Chart review follow-up for a minimum of 3 months was performed in all cases, with the exception of patients undergoing targeted spinal therapy before the 3-month period ended.

Procedural Parameters

Mean contrast injectate per single procedure was 11.5 mL, and mean saline injectate per procedure was 20.7 mL. The mean fluoroscopy time per procedure was 8.0 minutes (median, 7.9 minutes). The average cumulative radiation exposure for each procedural pair was 666 mGy (median, 349 mGy), not including subsequent CT scans, though this varied widely on the basis of patient body habitus (range, 45–2678 mGy). Lumbar punctures were performed at L3–L4 most commonly (70/136, 51.5%) followed by L2–L3 (57/136, 41.9%), L4–L5 (7/136, 5.1%), and L1–L2 (2/136, 1.5%). Twenty-two-gauge Quincke spinal needles were used in 73/136 cases (53.7%), and 20-ga, in 63/136 cases (46.3%). General anesthesia was used in 71/136 cases (52.2%); moderate sedation, in 44/136 cases (32.3%); and local anesthesia alone, in 21/136 cases (15.5%). Omnipaque 240 was used in 18/136 cases (13.2%), and Omnipaque 300, in 118 cases (86.8%). There were several missing data points, including saline injectate volume (n = 13), fluoroscopy time (n = 1), and total radiation dose (n = 1), with the associated cases being excluded from comparative analyses.

Adverse Effects

No major adverse effects were recorded for any of the 68 procedural pairs (Table 1). A single patient with severe postprocedural vertigo, nausea, and vomiting was admitted for observation but recovered overnight and was discharged home after undergoing the second part of the procedure the following morning. An additional patient elected for overnight admission between procedures for baseline pain control. Otherwise, all procedures were performed in an outpatient setting with no major or minor adverse effects requiring admission.

Minor adverse effects were recorded in 54 of 136 total procedures (39.7%), all of which resolved in the intraprocedural or immediate postprocedural period except as previously described (Table 1). Documented cases of pain included headache (23/136, 17.0%), backache (2/136, 1.5%), and leg pain (1/136, 0.7%). The remaining cases of pain (11/136, 8.1%) received a numeric score and analgesic treatment, but the location was not specified in the nursing log. The category of transient neurologic effect included cases of syncope, vertigo, altered mental status, and autonomic dysfunction (Table 2). Altered mental status included patients who briefly entered a trancelike state after intrathecal prepressurization and did not respond to verbal prompts from the proceduralist. Autonomic disturbance was used as a descriptor for 2 patients who, during general anesthesia, demonstrated transient hypertension/tachycardia and bigeminal pulse, respectively. Overall, there was no significant difference in the distribution of minor adverse effects between first- and second-day procedures.

An increased total injectate volume was noted in the patients experiencing minor transient neurologic effects. The mean injectate volume (contrast + saline) in the neurologic-effect group was 40.7 ± 10.8 mL, while the mean injectate volume in the remaining patients was 31.7 ± 8.6 mL. The mean injectate-volume variance was almost entirely accounted for by differences in saline volume used for thecal sac prepressurization because the contrast volume was constant. There was a statistically significant

association between total injectate volume and the probability of transient neurologic effects ($P = .017$), with no significant contributory effects from the procedure day ($P = .46$). Injectate volume demonstrated no significant association with the probability of pain ($P = .25$), nausea ($P = .29$), or pooled minor adverse effects ($P = .97$). Minor transient neurologic effects were also associated with the use of a 20-ga spinal needle ($P = .004$). The type of anesthesia performed was not correlated with minor neurologic effects ($P = .33$), pain ($P = .64$), or nausea/vomiting ($P = .21$).

DISCUSSION

No major adverse effects were demonstrated during the 13-month study period in any of the DSM procedural pairs. The rates of minor adverse effects such as pain (27.2%), nausea (8.1%), and other minor transient neurologic effects (5.1%) were comparable with complication rates in many of the original studies on lumbar myelography using iohexol.[16–19,24,25] For example, Kieffer et al[18] reported symptoms of headache (21%), nausea (10%), dizziness (3%), and "other" symptoms (7%), which included hypotension, paresthesia, photophobia, syncope, and somnolence. Manufacturer's studies for intrathecal Omnipaque describe adverse effects such as headache/pain (26%), nausea/vomiting (9%), dizziness (2%), and other reactions (<0.1%).[26] Other more recent studies of myelography with iodinated contrast have demonstrated lower rates of adverse effects, ranging from 7.4% to 14%.[14,15] This discrepancy can probably be at least partially accounted for by differences in patient populations, with other studies focusing on myelography for lumbar spinal stenosis and disc herniation, while our patient population included patients with SIH who demonstrated similar symptoms at baseline with known derangement of CSF volumes.

Most important for our study, despite injecting at least the maximum daily recommended intrathecal dose of Omnipaque 300 or 240 twice within a 24-hour interval, no significant differences were noted in the rate of minor adverse effects between day 1 and day 2 of the procedural pairs. This suggests that there is no accumulative toxicity from subsequent-day intrathecal contrast injections. Because of the low overall systemic dose of iodinated contrast and the relative health of this patient cohort, pre- and postprocedural renal function was not recorded. In patients with renal impairment or renal failure, it may be advisable to adjust contrast dosing or forgo the procedure altogether. However, we suspect that equilibration of the relatively small volume of water-soluble contrast from the CSF to the systemic circulation would presumably limit any increase in CNS toxicity related to delayed renal excretion.[23] Also, we did not routinely screen for seizure-threshold-lowering medications before performing the procedures, a practice that may further reduce the risk of seizures.[27]

Most interesting, a statistically significant correlation was noted between the volume of intrathecal injectate and transient minor neurologic effects such as vertigo, syncope, altered mental status, and autonomic dysfunction. Specifically, variable amounts of saline injectate were sometimes used to prepressurize the thecal sac in these patients with chronically low CSF volume, which may have resulted in vasovagal reactions or mechanical effects on pain-sensitive nerves and vessels related to CSF pressurization. This effect did not appear to result in any lasting neurologic sequelae. Contrast volumes were relatively constant but were included in the mean injectate calculations because they did constitute a large component of the total injectate volume. Griauzde et al[22] also reported transient neurologic symptoms in their experience with intrathecal preservative-free normal saline challenge in patients with SIH. However, their injection rate was reported at 1 mL/min in contrast to our fast injection rate of 1 mL/s, and even higher average volumes of saline were injected in their study (75.8 mL). Although the sample size of our study is too small to fully characterize the relationship between injectate rate/volume and neurologic symptoms and no true control group was present, our results suggest that standardizing and reducing the volume of intrathecal injectate might be considered to help reduce patient discomfort.

No acute radiation injury occurred, and the average cumulative fluoroscopic skin dose from each procedural pair was comparable with doses seen with common diagnostic visceral and cerebral angiographic procedures.[28] Medical radiation exposure should always be minimized when possible, and these examinations would certainly not be considered the first-line examination for localization of spinal CSF leaks, given a cumulative dose of 2 DSMs and 2 entire spine CT examinations. However, in the case of patients with SIH with debilitating symptoms and multiple prior nondiagnostic radiographic examinations, a thorough bilateral decubitus DSM examination could be considered.

There are several limitations of this study, most notably its retrospective nature. The sample size is too small to adequately assess certain rare serious adverse effects related to parenteral iodinated contrast exposure such as seizure, coma, or death, which have an expected incidence of <0.01%.[26] Additionally, the postprocedural effects of moderate and general anesthesia could account for some of the patients' recorded symptoms as well as mask other symptoms. Other factors potentially contributing to adverse effects could include the needle gauge, orientation of needle bevel during insertion, and stylet use.[29-31] All 7 patients categorized as having minor neurologic transient effects underwent lumbar puncture with 20-ga rather than 22-ga needles, and it is unclear whether this association is clinically significant, given the lack of similar correlation for pain or nausea. The difference in the injection flow rate is one possibility, but the flow rate differences due to needle gauge would be small. Although preservative-free normal saline has been safely used intrathecally, its hypertonicity relative to the CSF could play a role in adverse symptoms, and further studies comparing the use of artificial CSF (Elliotts B solution; Baxter Laboratories) with saline would be helpful. Finally, opening CSF pressures were not recorded before saline or contrast injection, and variations in the baseline CSF pressure could serve as a confounding factor in the development of minor adverse effects.

Our results are pertinent to a unique group of patients with SIH and may be of limited generalizability for other types of myelography. A core group of 10 fellowship-trained neuroradiologists who specialize in spine intervention performed the lateral decubitus DSM procedures, and all received training from a single individual. The specialty training of these interventionalists may result in lower adverse effect rates, reducing generalizability of our results.

CONCLUSIONS

In patients with SIH without evidence of spinal CSF leak on conventional imaging, consecutive-day lateral decubitus DSM procedures have demonstrated an acceptable risk profile in our 13-month experience, and there is no evidence of an increased neurotoxic effect from the cumulative intrathecal contrast dose. Adverse effect rates are comparable with those previously reported for general myelography studies. Increasing volumes of total intrathecal injectate, mostly attributable to prepressurization with saline, may have a correlation with the incidence of transient minor neurologic effects such as syncope, vertigo, autonomic dysfunction, and altered mental status. In patients who are undergoing this procedure with moderate sedation or local anesthesia only, decreasing the volume of injectate could help in reducing patient discomfort. Careful patient selection is warranted, given the cumulative radiation exposure associated with this technique.

REFERENCES

1. Davidson B, Nassiri F, Mansouri A, et al. **Spontaneous intracranial hypotension: a review and introduction of an algorithm for management.** *World Neurosurg* 2017;101:343–49 CrossRef Medline
2. Mokri B. **Spontaneous low pressure, low CSF volume headaches: spontaneous CSF leaks.** *Headache* 2013;53:1034–53 CrossRef Medline
3. Akbar JJ, Luetmer PH, Schwartz KM, et al. **The role of MR myelography with intrathecal gadolinium in localization of spinal CSF leaks in patients with spontaneous intracranial hypotension.** *AJNR Am J Neuroradiol* 2012;33:535–40 CrossRef Medline
4. Wang YF, Lirng JF, Fuh JL, et al. **Heavily T2-weighted MR myelography vs CT myelography in spontaneous intracranial hypotension.** *Neurology* 2009;73:1892–98 CrossRef Medline
5. Farb RI, Nicholson PJ, Peng PW, et al. **Spontaneous intracranial hypotension: a systematic imaging approach for CSF leak localization and management based on MRI and digital subtraction myelography.** *AJNR Am J Neuroradiol* 2019;40:745–53 CrossRef Medline
6. Clark MS, Diehn FE, Verdoorn JT, et al. **Prevalence of hyperdense paraspinal vein sign in patients with spontaneous intracranial hypotension without dural CSF leak on standard CT myelography.** *Diagn Interv Radiol* 2018;24:54–59 CrossRef Medline
7. Schievink WI, Maya MM, Jean-Pierre S, et al. **A classification system of spontaneous spinal CSF leaks.** *Neurology* 2016;87:673–79 CrossRef Medline
8. Schievink WI. **Novel neuroimaging modalities in the evaluation of spontaneous cerebrospinal fluid leaks.** *Curr Neurol Neurosci Rep* 2013;13:358 CrossRef Medline
9. Hoxworth JM, Trentman TL, Kotsenas AL, et al. **The role of digital subtraction myelography in the diagnosis and localization of spontaneous spinal CSF leaks.** *AJR Am J Roentgenol* 2012;199:649–53 CrossRef Medline
10. Hoxworth JM, Patel AC, Bosch EP, et al. **Localization of a rapid CSF leak with digital subtraction myelography.** *AJNR Am J Neuroradiol* 2009;30:516–19 CrossRef Medline
11. Luetmer PH, Mokri B. **Dynamic CT myelography: a technique for localizing high-flow spinal cerebrospinal fluid leaks.** *AJNR Am J Neuroradiol* 2003;24:1711–14 Medline
12. Schievink WI, Moser FG, Maya MM, et al. **Digital subtraction myelography for the identification of spontaneous spinal CSF-venous fistulas.** *J Neurosurg Spine* 2016;24:960–64 CrossRef Medline
13. Schievink WI, Maya MM, Moser FG, et al. **Lateral decubitus digital subtraction myelography to identify spinal CSF-venous fistulas in spontaneous intracranial hypotension.** *J Neurosurg Spine* 2019 Sept 13. [Epub ahead of print] CrossRef Medline
14. Matsumoto T, Imagama S, Inoue H, et al. **Outpatient myelography: a prospective trial comparing complications after myelography between outpatients and inpatients in Japan.** *Asian Spine J* 2015;9:928–34 CrossRef Medline
15. Albrecht A, Golebiowski M, Kornienko VN, et al. **A double-blind, prospective, randomized, multicenter group comparison study of iopromide 240 vs iohexol 240 in myelography.** *Eur Radiol* 1999;9:1901–08 CrossRef Medline
16. Wang H, Binet EF, Gabrielsen TO, et al. **Lumbar myelography with iohexol in outpatients: prospective multicenter evaluation of safety.** *Radiology* 1989;173:239–42 CrossRef Medline
17. Sand T, Myhr G, Stovner LJ, et al. **Side effects after ambulatory lumbar iohexol myelography.** *Neuroradiology* 1989;31:49–54 CrossRef Medline
18. Kieffer SA, Binet EF, Davis DO, et al. **Lumbar myelography with iohexol and metrizamide: a comparative multicenter prospective study.** *Radiology* 1984;151:665–70 CrossRef Medline
19. Eldevik OP, Nakstad P, Kendall BE, et al. **Iohexol in lumbar myelography: preliminary results from an open, noncomparative multicenter clinical study.** *AJNR Am J Neuroradiol* 1983;4:299–301 Medline
20. Kim DK, Brinjikji W, Morris PP, et al. **Lateral decubitus digital subtraction myelography: tips, tricks, and pitfalls.** *AJNR Am J Neuroradiol* 2020;41:21–28 CrossRef Medline
21. Gatica-Moris SR, Welch TL, Abcejo AS, et al. **Anesthesia during positive-pressure myelogram: a new role for cerebral oximetry.** *J Neurosurg Anesthesiol* 2019 Oct 23. [Epub ahead of print] CrossRef Medline
22. Griauzde J, Gemmete JJ, Pandey AS, et al. **Intrathecal preservative-free normal saline challenge magnetic resonance myelography for the identification of cerebrospinal fluid leaks in spontaneous intracranial hypotension.** *J Neurosurg* 2015;123:732–36 CrossRef Medline
23. Junck L, Marshall WH. **Neurotoxicity of radiological contrast agents.** *Ann Neurol* 1983;13:469–84 CrossRef Medline
24. Skalpe IO, Nakstad P. **Myelography with iohexol (Omnipaque); a clinical report with special reference to the adverse effects.** *Neuroradiology* 1988;30:169–74 CrossRef Medline
25. Laasonen EM. **Iohexol and metrizamide in lumbar myelography: comparison of side effects.** *Acta Radiol Diagn (Stockh)* 1985;26:761–65 CrossRef Medline
26. Omnipaque [package insert]. GE Healthcare, Marlborough, MA; 2018
27. Shah LM, Kranz PG, Anzai Y, et al. **Critical assessment of myelography practices: a call for rational guideline revision.** *AJNR Am J Neuroradiol* 2018;39:2378–84 CrossRef Medline
28. Mahesh M. **Fluoroscopy: patient radiation exposure issues.** *Radiographics* 2001;21:1033–45 CrossRef Medline
29. Strupp M, Brandt T, Müller A. **Incidence of post-lumbar puncture syndrome reduced by reinserting the stylet: a randomized prospective study of 600 patients.** *J Neurol* 1998;245:589–92 CrossRef Medline
30. Halpern S, Preston R. **Postdural puncture headache and spinal needle design: meta-analyses.** *Anesthesiology* 1994;81:1376–83 CrossRef Medline
31. Norris MC, Leighton BL, DeSimone CA. **Needle bevel direction and headache after inadvertent dural puncture.** *Anesthesiology* 1989;70:729–31 CrossRef Medline

Time to Resolution of Inadvertent Subdural Contrast Injection during a Myelogram: When Can the Study Be Reattempted?

D.P. Shlapak, D.K. Kim, F.E. Diehn, J.C Benson, V.T. Lehman, G.B. Liebo, J.M. Morris, P.P. Morris, J.T. Verdoorn, and C.M. Carr

ABSTRACT

BACKGROUND AND PURPOSE: Inadvertent subdural contrast injections can occur during any myelogram. Currently, there are no guidelines defining when residual subdural iodinated contrast will be cleared and no longer interfere with subsequent procedure and imaging. We investigated the time to resolution of subdural contrast using a 2-day lateral decubitus digital subtraction myelogram and associated CT myelogram data in patients undergoing evaluation for spontaneous intracranial hypotension.

MATERIALS AND METHODS: Retrospective review of 63 patients with lateral decubitus digital subtraction myelograms from September 4, 2018, to October 1, 2019, was performed. Patients with 2-day lateral decubitus digital subtraction myelograms on 2 consecutive days, with or without a same-day CT myelogram on day 1 and with a same-day CT myelogram on day 2, were included. Patients with next-day CT covering at least the abdomen and pelvis after either-day injection were also included. In cases of subdural injection, next-day CT scans were evaluated for residual subdural contrast.

RESULTS: Of 49 included patients, 5 had subdural injection on day 1, with the second-day CT myelogram available for review. One of these 5 patients had subdural injections on 2 different days and subsequently had chest/abdomen/pelvis CTA a day after the second subdural injection. In all 6 cases of subdural injections, there was complete resolution of subdural contrast on the next-day CT, with the shortest time to resolution of approximately 20.5 hours (range, 20.5–28.5 hours).

CONCLUSIONS: Our study suggests that resolution of inadvertently injected subdural contrast occurs within 1 day, and the myelogram can be reattempted as early as the next day.

ABBREVIATIONS: CTM = CT myelogram; eGFR = estimated glomerular filtration rate; LDDSM = lateral decubitus digital subtraction myelogram

Since the introduction of myelography in the mid-1900s, inadvertent subdural contrast injections during myelographic procedures have been called "the anathema to the myelographer" because they can make interpretation of the findings more difficult and potentially inaccurate.[1,2] Moreover, when a procedure is reattempted, residual subdural contrast could confound the interpretation of the repeat examination. This issue has led some practices to routinely wait several days or even a week before reattempting myelography, which can potentially cause delay in diagnosis and management.

Given the intricacy of the anatomy of the spinal meningeal spaces, by "subdural," we are referring to a cellular interface between a laminar arachnoid and the inner surface of the dura—a so-called "dura-arachnoid interface" or "subdural compartment," composed of neurothelial cells with an amorphous substance.[3,4] This interface has also been previously described as the medial border of the spinal dura mater,[5] dural border cell layer,[6] and subdural mesothelium.[7]

Suboptimal contrast injections are usually mixed, intrathecal, and subdural, with a variable degree of subdural contrast amount. The timeline to resolution of inadvertent subdural injections has not been evaluated, and currently, there are no guidelines on when a myelogram should or can be reattempted. At our institution, we have been regularly performing lateral decubitus digital subtraction myelograms (LDDSMs) to evaluate CSF leaks since 2018, with alternating sides down on 2 consecutive days, usually immediately followed by a lateral decubitus CT myelogram (CTM). These types of myelograms have a higher rate of subdural injections compared with conventional myelography due to multiple factors, including low CSF pressure, patient positioning, tenting of the dura, and the rate of injection.[8] Given its consecutive-day nature, this new aspect

Received April 10, 2020; accepted after revision June 15.

From the Department of Radiology, Mayo Clinic, Rochester, Minnesota.

Please address correspondence to Darya Shlapak, MD, MBA, Department of Radiology, Mayo Clinic, 200 1st St SW, Rochester, MN 55905; e-mail: shlapak.darya@mayo.edu

Indicates article with supplemental on-line table.

http://dx.doi.org/10.3174/ajnr.A6725

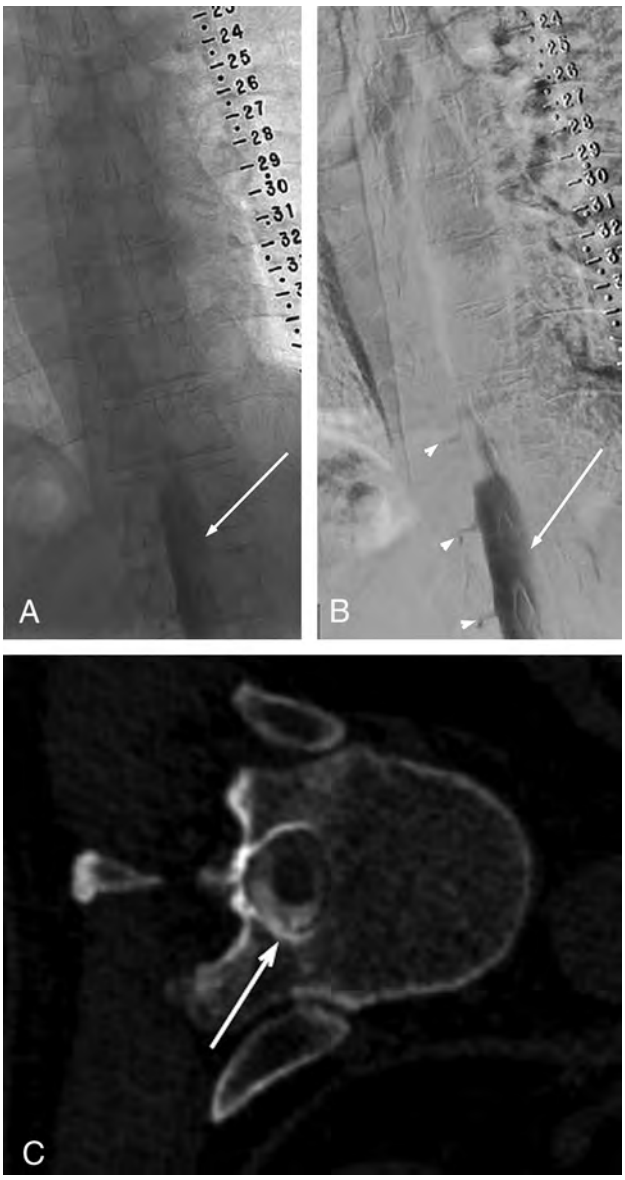

FIG 1. Unsubtracted (*A*) and subtracted (*B*) left-side-down LDDSM images on day 1 demonstrate subdural contrast injection at the lower thoracic/upper lumbar levels. Notice nondependent masslike subdural contrast overlying the middle of the osseous spinal canal (*solid arrows* in *A* and *B*). Given the predominantly subdural injection, only minimal intrathecal contrast is seen filling nerve root sheaths (*arrowheads* in *B*). The study was terminated without obtaining a CTM. The next-day CTM following the repeat left LDDSM injection shows no residual subdural contrast at the level of T11 and a homogeneous appearance of the intrathecal contrast clearly outlining a nerve root traversing the intrathecal space (*arrow* in *C*). The time interval between images *A*/*B* and *C* is approximately 20.5 hours.

of modern myelography provides a unique opportunity to evaluate CTM images for resolution of inadvertently injected subdural contrast.

MATERIALS AND METHODS

This retrospective Health Insurance Portability and Accountability Act–compliant study involving human participants was performed

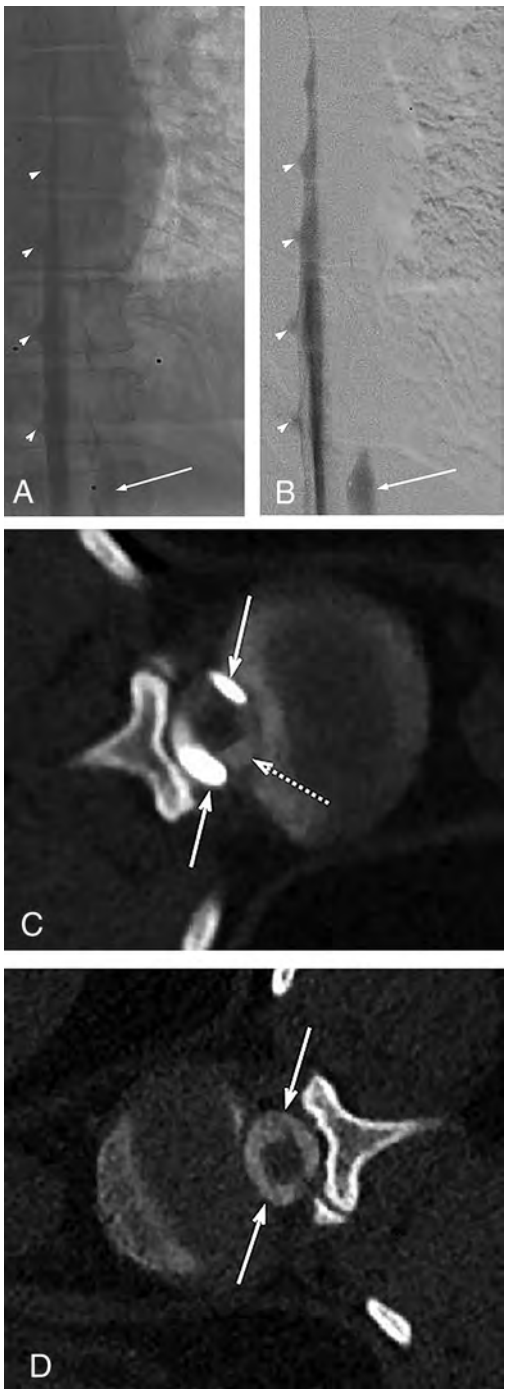

FIG 2. Unsubtracted (*A*) and subtracted (*B*) left LDDSM images on day 1 demonstrate subdural contrast injection at the thoracolumbar junction that appears as a nondependent thick contrast column overlying the middle of the osseous spinal canal (*solid arrows* in *A* and *B*). Given the predominantly intrathecal injection, compare the subdural contrast appearance with the dependently layering menisci of intrathecal contrast filling the nerve root sheaths (*arrowheads* in *A* and *B*). On the same-day left lateral decubitus CTM (*C*), subdural contrast appears as nondependent collections (*solid arrows* in *C*), more hyperattenuating than the intrathecal contrast (*dashed arrow* in *C*). The next-day CTM (immediately following the contralateral right LDDSM) shows no residual subdural contrast at the T12/L1 level (*solid arrows* in *D*). The time interval between images *A*/*B*/*C* and image *D* is approximately 22.5 hours.

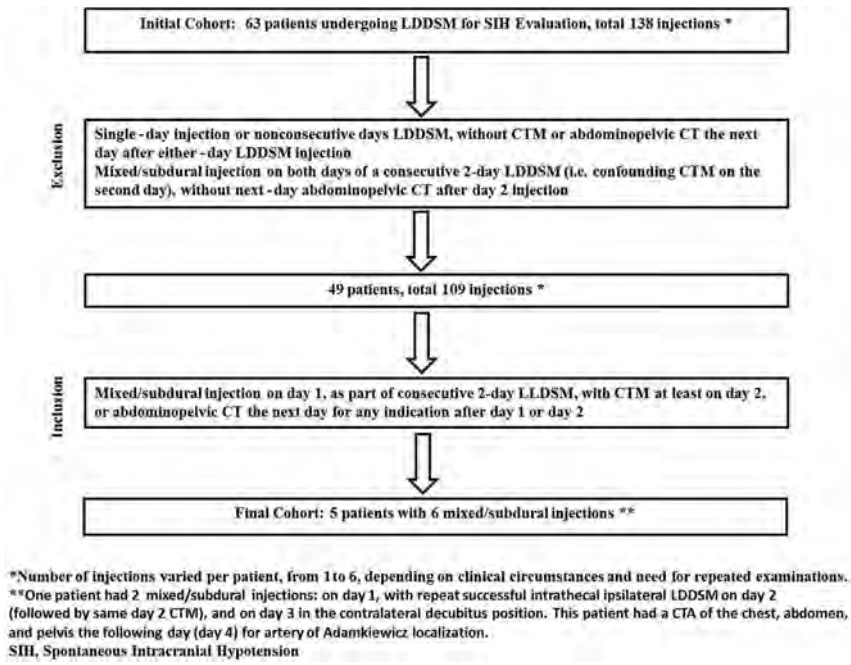

FIG 3. Patient selection flow chart.

in accordance with the ethical standards of the Institutional and National Research Committee and with the 1964 Declaration of Helsinki and its later amendments or comparable ethical standards. The institutional review board reviewed and approved this study (No. 19-002405). Informed consent was waived.

Patients with symptoms of postural headaches and suspected spontaneous intracranial hypotension were first evaluated for a potential CSF leak by subspecialty neurologists and referred to our service for an LDDSM. The LDDSM technique including patient positioning and needle placement has been recently described.[8]

Subsequent CTMs were performed with the patient in the same lateral decubitus position as the LDDSM covering the skull base to the sacrum. Typically, CTM images were obtained in a single pass with a dual-energy setting (100 kV and 140 kV) and 50-keV monoenergetic reconstructions to increase the sensitivity for subtle contrast leakage.[9,10] We reconstructed 0.75- and 3-mm slices from 0.6-mm slices. Next-day CTA of the chest, abdomen, and pelvis in one of the further described subdural contrast injection cases was performed according to routine CTA protocol in arterial and delayed phases from the lung apices to the ischial tuberosities with 1- and 2-mm slices reconstructed from 0.6-mm slices.

We reviewed imaging studies and reports of 63 patients who underwent LDDSMs at our institution as part of an evaluation for spontaneous intracranial hypotension, without or with same-day concurrent CTM from September 4, 2018, to October 1, 2019, for 138 separate contrast injections. Demographic data including patient sex and age at the time of LDDSM were recorded. Additionally, the estimated glomerular filtration rate (eGFR) in patients with mixed, subdural, and intrathecal contrast injections around the time of LDDSM if available was also recorded.

To be included in the final study group, patients had to complete both days of the LDDSM (left and right side down) performed on 2 consecutive days, with a CTM immediately following the LDDSM at least on the second day of the 2-day study. Additionally, patients who had the next-day CT covering at least the abdomen and pelvis after either-day injection or after a single-day study were also included.

Unsubtracted and subtracted LDDSM and CTM images were reviewed for the presence of subdural contrast. The relative degree of intrathecal-versus-subdural contrast was subjectively estimated on the basis of visual inspection of the images and graded as entirely intrathecal, predominantly subdural, or predominantly intrathecal, with "predominantly" qualitatively referring to >50% of the total volume of injected contrast. Subdural contrast was usually evident on unsubtracted and subtracted LDDSM images as a nondependent masslike thick column of contrast overlying the middle of the osseous spinal canal, rather than dependently layering menisci of intrathecal contrast filling the nerve root sheaths (Figs 1 and 2*A* and -*B*). On subsequent lateral decubitus CT myelograms, subdural contrast appeared as a nondependent collection or a more globular-like area of contrast, more hyperattenuating and confined than contrast seen intrathecally (Fig 2*C*).

RESULTS

Of 63 patients with 138 injections, 49 patients with 109 injections met the inclusion criteria and composed the final study group: 31 women and 18 men, with an average age of 56 years (range, 28–78 years). A flow chart demonstrating the selection of the final patient study cohort is presented in Fig 3. Of these 49 patients, 5 had a mixed (subdural and intrathecal) injection on the first day of the study: 3 women and 2 men, with the average age of 59 years (range, 36–78 years). One of these 5 patients with subdural injection on the first day (injection 2 in the On-line Table) had a repeat successful intrathecal ipsilateral LDDSM on the second day but then again had a mixed injection on the third day in the contralateral decubitus position (injection 3 in the On-line Table). This patient had a CTA of the chest, abdomen, and pelvis on the following day (fourth day) for artery of Adamkiewicz localization. Therefore, in total, there were 5 patients with 6 mixed injections who had next-day CT images available for evaluation. Of the 5 patients with subdural injections, 3 had an eGFR of >60 (injections 1–4 in the On-line Table), 1 patient had an eGFR of 51 (injection 5), and 1 had no renal function panel available around the time of the LDDSM (injection 6).

All 5 second-day CTMs and a next-day CTA in injection 3 demonstrated complete resolution of subdural contrast injected on the previous day (Figs 1 and 2). The shortest time between

the LDDSM subdural injection and the next-day CT was approximately 20.5 hours. Resolution of the other 5 subdural injections was confirmed on the next-day CT images after approximately 22.5, 24, 26, 26, and 28.5 hours after the previous-day LDDSM injection, respectively, with a mean time interval of 24.6 hours.

Patient position, total contrast amount/type, relative degree of subdural contrast, needle gauge, postinjection imaging, outcomes, and time to subdural contrast resolution per next day CT are summarized in the On-line Table.

Patients with mixed injections 1, 5, and 6 in the On-line Table did not have a spinal CSF leak on either day of the study on LDDSM or CTM images. Patient 2 (injection 2 in the On-line Table) did not have a left CSF leak on the first day of mixed injection or next-day repeat left LDDSM or CTM images but had an identifiable right T6/T7 CSF-venous fistula on the right LDDSM despite another mixed injection (injection 3 in the On-line Table). Subdural contrast in injection 3 extended from the lowest visualized level on the LDDSM of L1 to the T7 inferior endplate level and from the S1 to T7 superior endplate on the same-day right-side-down CTM images.

Finally, the patient with a mixed injection 4 in the On-line Table did not have a left spinal CSF leak on the first-day left LDDSM or same-day CTM images at the time of the mixed injection. However, on the next-day right LDDSM and the same-day right-side-down CTM, there was an identifiable right CSF leak presumably due to a dural tear at L2/L3. Subdural contrast from the mixed injection on day 1 on the left LDDSM extended from the lowest visualized level of L2 to T7 and on the same-day left-side-down CTM from L3 to T4.

DISCUSSION

Our study suggests that subdural contrast resolves within approximately 24 hours. While mixed intrathecal and subdural injections can still be diagnostic, in nondiagnostic cases due to predominantly subdural injection, our findings suggest that the examination can be repeated as early as the next day. Because there are currently limited data and lack of consensus as to when a myelogram can be reattempted after subdural injection, leading to many practices waiting days to weeks before repeat examination, our study results can facilitate an earlier reattempt at performing the myelogram and avoiding further delay in diagnosis.

Although these findings are applicable to any type of myelography using iodinated contrast, they are particularly helpful for proceduralists performing LDDSMs. As noted by Kim et al,[8] subdural injections are more common during these examinations due to multiple factors, including low CSF pressure, patient positioning, tenting of the dura, and the rate of injection.

The mechanism of clearance of subdural contrast remains unclear and is not addressed by the present study. A case report by Yi et al[11] described spontaneous resolution of an idiopathic lumbar subdural hygroma after approximately 2 weeks, documented by a CT myelogram and lumbar spine MR imaging. On the basis of 65 radiographic studies in the mid-1900s of iophendylate distribution being injected in the subdural space, Hugh,[12] in 2010, suggested that contrast could be rapidly reabsorbed by a rich lymphatics network.

Of 5 patients with subdural injections in our study, 3 had an eGFR of >60, one had an eGFR of 51, and 1 had no renal function panel available around the time of the LDDSM. Although we suspect that renal function is unrelated to subdural contrast clearance, more research with larger study groups and more variable renal function is needed.

Additionally, given resolution of subdural contrast in all 6 cases of mixed injections on the next-day CT images with or without a CSF leak, it seems unlikely that close approximation of the CSF leak site to subdural contrast would impact its time to resolution.

Our study has several additional limitations, including its small number of patients with mixed contrast injections who had next-day CT images available for review. Additionally, the results of a mixed injection, even predominately subdural, might not apply to a full subdural injection.

Finally, all patients in our study group had a presumptive diagnosis of spontaneous intracranial hypotension, and the results may not be generalizable to other patient populations. For example, patients with severe spinal canal stenosis or prior spine surgery may have alteration of subdural contrast clearance.

Future work could include larger retrospective studies by centers performing a high volume of 2-day LDDSMs with concurrent CTMs confirming next-day resolution of subdural contrast as well as evaluating the diagnostic yield of mixed injections. Prospective studies could include obtaining a limited CT within 24 hours in cases of mixed injection for various indications and different types of myelograms.

CONCLUSIONS

Our study suggests that subdural contrast inadvertently injected during a myelographic procedure resolves after approximately 24 hours and as early as after 20.5 hours. A myelogram could be reattempted as early as the next day, without concerns that residual subdural contrast could interfere with diagnostic quality of the repeat examination.

REFERENCES

1. Camp JD. **Contrast myelography past and present.** *Radiology* 1950;54:477–506 CrossRef
2. Schultz EH Jr, Brogdon BG. **The problem of subdural placement in myelography.** *Radiology* 1962;79:91–96 CrossRef Medline
3. Collier CB. **The intradural space: the fourth place to go astray during epidural block.** *Int J Obstet Anesth* 2010;19:133–41 CrossRef Medline
4. Reina MA, Collier CB, Prats-Galino A, et al. **Unintentional subdural placement of epidural catheters during attempted epidural anesthesia: an anatomic study of spinal subdural compartment.** *Reg Anesth Pain Med* 2011;36:537–41 CrossRef Medline
5. Waggener JD, Beggs J. **The membranous coverings of neural tissues: an electron microscopy study.** *J Neuropathol Exp Neurol* 1967;26:412–26 CrossRef Medline

6. Alcolado R, Weller RO, Parrish EP, et al. **The cranial arachnoid and pia mater in man: anatomical and ultrastructural observations.** *Neuropathol Appl Neurobiol* 1988;14:1–17 CrossRef Medline
7. Orlin JR, Osen KK, Hovig T. **Subdural compartment in pig: a morphologic study with blood and horseradish peroxidase infused subdurally.** *Anat Rec* 1991;230:22–37 CrossRef Medline
8. Kim DK, Brinjikji W, Morris PP, et al. **Lateral decubitus digital subtraction myelography: tips, tricks, and pitfalls.** *AJNR Am J Neuroradiol* 2020;41:21–28 CrossRef Medline
9. Postma AA, Das M, Stadler AA, et al. **Dual-energy CT: what the neuroradiologist should know.** *Curr Radiology Rep* 2015;3:16 CrossRef Medline
10. Shuman WP, Chan KT, Busey JM, et al. **Dual-energy CT a ortography with 50% reduced iodine dose versus single-energy CT aortography with standard iodine dose.** *Acad Radiol* 2016;23:611–18 CrossRef Medline
11. Yi CK, Biega TJ, Burgos RM. **Spontaneous resolution of idiopathic lumbar subdural hygroma on CT myelography and lumbar spine MRI.** *BMJ Case Rep* 2014;2014:bcr2014206223 CrossRef Medline
12. Hugh AE. **The subdural space of the spine: a lymphatic sink? Myodil's last message.** *Clin Anat* 2010;23:829–39 CrossRef Medline

Recanalized Aneurysms: Is Rupture Further Preventable?

I read with great interest the article by Funakoshi et al,[1] "Predictors of Cerebral Aneurysm Rupture after Coil Embolization: Single-Center Experience with Recanalized Aneurysms." They reviewed their results of coil embolization of unruptured and ruptured saccular cerebral aneurysms retrospectively and analyzed the rate of recanalization and bleeding from treated aneurysms.

It is noteworthy that 44.1% of treated unruptured aneurysms are paraclinoid aneurysms, which usually account for less than 1% of SAH in Japan.[2] Presumably, their institution has a lot of referrals for difficult paraclinoid cases, but considering the real-world frequency of the origin of SAH cases, the risk of bleeding from paraclinoid aneurysms should be small. Hence, while I reserve a small leap in argument, it makes sense to assume that filling this low-risk aneurysm with coils will not result in enlargement or bleeding, though some paraclinoid aneurysms recanalized in their Results section.

The authors calculated the rupture risk after coil embolization to be 0.20%/year by a person-year method. If the number of low-risk aneurysms, ie, paraclinoid aneurysms, increases in the cohort, the observation period without recanalization or rupture becomes large and results in smaller apparent bleeding and recanalization rates. Therefore, aneurysms that cause SAH in actual clinical practice and these low-risk aneurysms, like paraclinoid aneurysms, should be better analyzed separately, though they are usually discussed in a mixed bag.

The authors claim that coiled aneurysms with class IIIb recanalization should have an early retreatment from analysis of rupture after coil embolization, which would be reasonable. As is mentioned in the Discussion section, those aneurysms that showed new blebs were treated, and more than 40% of all recanalized aneurysms were retreated. The ruptures occurred in the remaining patients. Five of 8 ruptures after coil embolization seem to have occurred in patients with mRS $>$ 3 (Table 2), which might have affected the indication of retreatment, and the rupture may be a simple result of "natural history" of observation of recanalized aneurysms.

As they mentioned in the Limitations section, cases of the ruptured group with severe neurologic deficit were not followed up, and the information is limited, which is not to be blamed. However, they should have referred to the grade of SAH and provided the survival curve with the number at risk because the mean follow-up duration of the ruptured group is much shorter than that of the unruptured group, which may be the result of the percentage of patients with poor grades. If the number of patients followed up differs substantially, the interpretation of the results needs to be kept in mind. In addition, the maximum duration of recanalized aneurysms is longer than that of all aneurysms in Table 1. I wonder if this was interquartile range or range.

Last, I appreciate the authors for frankly presenting their clinical results. It will contribute to the discussion about treatment decisions for cerebral aneurysms.

REFERENCES

1. Funakoshi Y, Imamura H, Tani S, et al. **Predictors of cerebral aneurysm rupture after coil embolization: single-center experience with recanalized aneurysms.** *AJNR Am J Neuroradiol* 2020;41:828–35 CrossRef Medline
2. Yoshiteru Tada SN. **Classification of subarachnoid hemorrhage severity and frequency by aneurysm location and CT findings..** In: Kobayashi S, ed. *Japanese Stroke Data Bank 2015*. Nakayama Shoten Co, Ltd; 2015:152–53

T. Kimura
Department of Neurosurgery
Japanese Red Cross Medical Center
Tokyo, Japan

http://dx.doi.org/10.3174/ajnr.A6734